

# Designing Multifunctionality and Confined Environments in Porphyrin-based Metal-Organic Frameworks

Karina Hemmer

Vollständiger Abdruck der von der TUM School of Natural Sciences der Technischen  
Universität München zur Erlangung einer  
Doktorin der Naturwissenschaften (Dr. rer.nat.)  
genehmigten Dissertation.

Vorsitz: Prof. Dr. Klaus Köhler

Prüfer\*innen der Dissertation:

1. Prof. Dr. Dr. h.c. Roland A. Fischer
2. Prof. Dr. Torben Gädt
3. Prof. Dr. Mathias O. Senge

Die Dissertation wurde am 12.07.2023 bei der Technischen Universität München eingereicht  
und durch die TUM School of Natural Sciences am 31.07.2023 angenommen.

Die vorliegende Arbeit wurde im Zeitraum von Dezember 2019 bis Juli 2023 im Fachgebiet Anorganische und Metallorganische Chemie der Technischen Universität München angefertigt.

## Danksagung

Zuerst möchte ich mich bei Ihnen, **Prof. Dr. Dr. h.c. Roland A. Fischer**, bedanken. Ihre stetige Unterstützung, seien es Forschungsprojekte, Konferenzbesuche oder Stipendien, weiß ich sehr zu schätzen. Sie brennen für die Wissenschaft, was man stetig in wissenschaftlichen Diskussionen und Ihrem Ideenreichtum spürt. Ihre Motivation, etwas zu verändern oder neue Ansätze zu liefern, die die Forschung und Lehre auf die nächste Stufe heben, haben mich sehr inspiriert. Gerade Ihr Interesse an interdisziplinärem Zusammenarbeiten und gegenseitigem Austausch ist für mich äußerst vorbildlich. Danke, dass Sie uns zeigen, wie wichtig der Blick über den Tellerrand hinaus ist. Auch, dass Sie immer versuchen „the beauty of science“ an neue Generationen weiterzugeben, beeindruckt mich sehr. Generell kann ich Ihnen nur danken, dass Sie an Ihrem Lehrstuhl so ein tolles Umfeld geschaffen haben, in dem man sich aufgehoben fühlt und gegenseitige Unterstützung und Motivation Standard sind. Mit vielen Freiheiten haben Sie mich über die letzten Jahre gefördert und gleichzeitig gefordert, woran ich auch über die Wissenschaft hinaus wachsen konnte. Danke für alles!

Ein besonderer Dank geht auch an Dich, **Dr. Mirza Cokoja**. Während meiner Promotion stand Deine Tür jederzeit für mich offen. Für Dein Vertrauen, Deine Unterstützung und Deinen Rat möchte ich Dir herzlichst danken. Neben den wissenschaftlichen Aspekten möchte ich vor allem Dein Mentoring hervorheben. Du hast es geschafft, dass ich mich persönlich weiterentwickeln konnte, und Deine Ratschläge werde ich sicherlich in meinem Leben weiter mitnehmen. Deine ständige Erreichbarkeit und Dein Zuspruch sind nicht selbstverständlich, das weiß ich sehr zu schätzen.

Zudem möchte ich mich bei **Dr. Christian Gemel, Dr. Alexander Pöthig, Dr. Dominik Halter, Dr. Markus Drees** und **Dr. Gabriele Raudaschl-Sieber** für Ihre Hilfe, Unterstützung und Ihren besonderen Beitrag zur Lehrstuhlfamilie in den letzten Jahren bedanken. A special thanks to **Dr. Julien Warnan** for the fantastic cooperation and your support, I really enjoyed the excursion into the world of photons and excitons. Des Weiteren möchte ich mich herzlich bei Dir, **Dr. Gregor Kieslich** bedanken. Dein Vertrauen, mich direkt am Anfang mit auf Strahlzeit zu nehmen, beeindruckt mich immer noch – genauso wie Deine Unterstützung, sei es im gemeinsamen Projekt oder darüber hinaus. Dankeschön auch an **Dr. Dana Weiß** und **Martin Schellerer** für Eure stetige organisatorische Unterstützung.

Thank you to my external cooperation partners **Prof. Mathias Senge, Dr. Nitika Grover, Prof. Bettina Lotsch, Dr. Simon Krause, Dr. Hanna Boström, Prof. Martin Elsner, Prof. Didier Bourissou** and **Dr. Julien Monot**. I really enjoyed the projects and the different perspectives you brought to my topic and science in general. Thanks for your trust in the last years.

Außerdem möchte ich mich für das Mentoring bei **Dr. Ulrich Müller** und **Dr. Stefan Marx** herzlichst bedanken – seien es Einblicke in die Industrie, Stipendien oder Ratschläge für die weitere Zukunft. Ich freue mich sehr und bin sehr dankbar, diese Unterstützung zu haben.

Ein weiterer Dank gebührt **Prof. Richard W. Fischer**. Bereits im Masterstudium haben Sie mich für die industrielle Katalyse inspiriert und mit Ihrem Wissen beeindruckt. Die gemeinsamen Kolloquien habe ich immer sehr genossen. Sie haben es geschafft, mir einen Überblick über dieses faszinierende Feld zu geben und mein Interesse daran sehr verstärkt.

Zusätzlich möchte ich mich beim **Fonds der chemischen Industrie (FCI)** für das Kekulé-Stipendium und die Möglichkeit zur Teilnahme am Lindauer Nobelpreisträgertreffen bedanken. Des Weiteren danke ich der **DECHEMA** und der **Gesellschaft Deutscher Chemiker (GDCh)** für die Unterstützung für Konferenzbesuche.

Zudem bedanke ich mich bei **Christine Benning**, **Ulrike Ammari** und **Bircan Dilki** für ihre Bereitschaft und analytische Messungen. **Jürgen Kudermann** danke ich für die Unterstützung und zahlreichen Einblicke in verschiedene analytische Methoden. Ein besonderer Dank auch an Dich, **Dr. Eliza Gemel**. Neben deinen Aufgaben im CRC versuchst du immer, für uns Doktoranden geeignete Lösungen zu finden und bist für uns da, wofür ich dir sehr danken möchte.

Ganz herzlich möchte ich mich bei meinen Studenten **Mihyun Park**, **Annika Schulz**, **Constantin Hagemann**, **Markus Hegelmann** und **Anna Tratter** für Ihr Engagement und ihr Vertrauen bedanken. Ich habe sehr gerne mit Euch zusammengearbeitet und schätze Eure Beiträge sehr! Besonders dankbar bin ich dafür, dass Du, **Markus Hegelmann**, nach Deinem Praktikum dich entschlossen hast, Deine Masterarbeit auch unter meiner Betreuung zu machen. Dein Engagement und Dein Fleiß beeindruckten mich immer wieder. Ich habe die gemeinsamen Diskussionen und allgemein die Zeit sehr genossen und freue mich unendlich, dass Du dem Lehrstuhl erhalten bleibst.

Des Weiteren möchte ich mich bei der gesamten **AMC-Crew** (alt und neu) für die schöne Zeit und die tolle Atmosphäre bedanken. Insbesondere danke ich **Lisa Semrau**, **David Mayer**, **Kathrin Weger**, **Sarah Dummert**, **Raphael Bühler**, **Maxi Muhr**, **Johannes Stephan**, **Laura Kronthaler**, **Thomas Pickl** und **Simon Deger**. Vor allem meine Laborboxkollegen **Jan Berger**, **Pia Vervoorts** und **Johanna Haimerl** möchte ich hervorheben. Ihr habt signifikant zum Spaß an der Laborarbeit beigetragen. Besonderer Dank auch an die ACS-Gruppe **Maxi Muhr**, **Johanna Haimerl**, **Kathrin Kollmannsberger**, **Silva Kronawitter** und **Philip Stanley** für die schöne Zeit in Amerika!

Mein herzlichster Dank geht an Dich, **Lena Staiger**, für Deine Unterstützung und Dein Mentoring während der Masterarbeit (und darüber hinaus) – vor allem aber für die Freundschaft, die sich daraus entwickelt hat und die schönen gemeinsamen Erinnerungen! Vor allem an unseren gemeinsamen Urlaub und die Summer School in Slowenien mit **Fabian Schmidt** denke ich sehr gerne zurück. Danke an Euch beide für die schöne Zeit in der Catalysis Subgroup und dass ihr mich so gut aufgenommen habt.

Besonderer Dank auch an die „Neufahrn-Crew“ **Fabian Schmidt, Melanie Schmid, Patricia Weishäupl, Sebastian Weishäupl, Margit Aust, Lukas Niederegger, Alexandra Heidecker, Philip Keil, Lena Staiger, Simon Deger** und **Stefan Burger**. Die gemeinsame Zeit auch außerhalb der Uni hat mir sehr viel Spaß gemacht.

Darüber hinaus möchte ich mich bei meinen Studiumsfreunden **Kerstin Halama, Lilla Koser, Kathrin Kollmannsberger, Florian Tschernuth, Amelie Mühlbach** und **Johanna Löhr** bedanken für die unvergessliche Zeit während des Studiums und die Freundschaft darüber hinaus. Ihr habt meinen Uni-Alltag sehr bereichert. Zudem danke ich meinen Bamberger Freunden **Anna-Lena, Franziska, Vincent** und **Alexandra**, die mich teilweise seit dem Kindergarten über viele Jahre hinweg begleiten. Danke, dass wir auch trotz teilweise größerer Distanzen weiterhin so gut befreundet sind.

Vielen herzlichen Dank auch an Dich, **Silva**. Auf dich kann man sich immer verlassen und die gemeinsame Zeit am Lehrstuhl hat mir sehr viel Spaß gemacht. Vor allem aber möchte ich unseren gemeinsamen Amerika-Urlaub mit **Torben** und **Philip** hervorheben, der für mich unvergessen bleibt, sowie die Zeit im Schollbach. Ich danke dir so sehr, für deine Freundschaft und alles, was wir zusammen erleben.

Besonders möchte ich mich bei dir, **Sonja**, bedanken für dein allzeit offenes Ohr, die unzähligen gemeinsamen Erlebnisse und dass du immer für mich da bist. Seit unserem gemeinsamen Protokollschreiben und der Zeit in Garching bist du mir richtig ans Herz gewachsen und gehörst schon mit zur Familie.

Unendlicher Dank gebührt meiner Familie, **Mama, Papa** und **Melissa**, für Ihre bedingungslose Unterstützung mein ganzes Leben lang. Danke, dass ihr immer stolz auf mich seid, mir blind vertraut und zur Seite steht. Ohne euch wäre das alles hier nicht möglich gewesen. Egal wo ich bin, Ihr seid immer mein Zuhause und ich bin so gerne bei euch.

Insbesondere möchte ich mich bei dir, **Philip**, von Herzen bedanken. Du bist mein Ruhepol, hast immer Verständnis für mich und bist immer für mich da. Ich danke dir für deinen unfassbaren Rückhalt und dass du mehr an mich glaubst, als ich selbst tue. Ich bin sehr froh, dass uns das AC-Praktikum damals zusammengebracht hat und daraus etwas so Bedeutendes entstanden ist. Ich freue mich unfassbar, mein Leben mit dir zu verbringen.

*"Life is like a box of chocolates. You never know what you're gonna get."*

Forrest Gump

# Table of Content

Kurzzusammenfassung .....	IX
Abstract .....	10
List of Abbreviations .....	11
1. Introduction.....	1
1.1. Enzymes – From Nature to Artificial Systems.....	1
1.2. Metal-Organic Frameworks .....	3
1.3. MOFs in Catalysis .....	4
1.3.1. Catalyst Integration.....	6
1.3.1.1. Node Manipulation.....	9
1.3.1.2. Node Anchoring.....	10
1.3.1.3. Linker Functionalization and Anchoring .....	12
1.3.1.4. Catalyst Encapsulation in Pores .....	15
1.3.2. Confinement Effects in MOF Catalysis.....	16
1.3.3. Multifunctionality in MOF Catalysis .....	22
1.4. Porphyrin-based Zr-MOFs – From Opportunities to Challenges and vice versa .....	25
1.4.1. Synthetic Challenges .....	26
1.4.2. Catalytic Applications – the Porphyrin Motif .....	29
1.5. Principles of Catalysis .....	31
2. Motivation and Research Questions .....	33
3. Results and Discussion .....	36
3.1. Synthetic Procedure Investigations .....	36
3.1.1. Porphyrin Linker .....	36
3.1.2. MOFs .....	37
3.1.2.1. MOF Synthesis Investigations .....	37
3.1.2.2. MOF Characterization.....	40
3.1.2.3. Metalated Porphyrin MOFs.....	42
3.2. Design of Catalyst – MOF Hybrids and their Applications.....	67

3.2.1. Framework-integrated Catalysts .....	67
3.2.1.1. Rh-porphyrin MOFs for Confinement Effect Studies .....	68
3.2.1.2. Metalloporphyrin MOFs as Epoxidation Catalysts .....	79
3.2.1.3. Metalloporphyrin MOFs in CO <sub>2</sub> Cycloaddition Catalysis .....	83
3.2.1.4. Multifunctionality Design for Sequential Catalysis .....	85
3.2.1.5. Non-planar Porphyrin Integration .....	91
3.2.2. Pore-anchored Catalysts .....	99
3.2.2.1. A Node-anchored Non-planar Porphyrin .....	99
3.2.2.2. Anchoring Studies for Pd Pincer Complex Incorporation .....	102
3.2.2.3. Re-Photocatalyst Anchoring in Pores via Coordinative Bonds .....	106
3.3. Resumé Confinement Effects and Multifunctionality .....	114
4. Conclusion .....	117
5. Experimental .....	120
5.1. Materials .....	120
5.2. Analytical Methods and Characterization Techniques .....	120
5.3. Synthetic Procedures .....	125
5.3.1. (Metallo-)Porphyrin Syntheses .....	125
5.3.2. MOF Syntheses .....	134
5.3.3. Porphyrin MOF Metalation .....	136
5.3.4. SED and Photocatalyst Synthesis .....	146
5.3.5. Functional Linker and Catalyst (analogue) Integration .....	147
5.4. Catalysis .....	149
5.4.1 Cyclopropanation Catalysis .....	149
5.4.2. Epoxidation Catalysis .....	151
5.4.3. CO <sub>2</sub> Cycloaddition .....	152
5.4.4. Sequential Conversion of Epoxides to Cyclic Carbonates .....	153
5.4.5. Thia-Michael Addition .....	154
5.4.6. Henry Reaction .....	154
5.4.7. Photocatalytic CO <sub>2</sub> Reduction .....	155
5.4.8. Cycloisomerization of 5-Hexynoic acid .....	155



6. References .....	156
7. Appendix .....	169
7.1. Material Characterization .....	169
7.2. Metalation Strategies .....	178
7.3. Cyclopropanation Catalysis.....	213
7.4. Epoxidation Catalysis.....	231
7.5. CO <sub>2</sub> Cycloaddition Catalysis .....	240
7.6. Sequential Olefin to Cyclic Carbonate Catalysis.....	240
7.7. Non-planar Porphyrin Framework Integration.....	243
7.8. Node-anchored Non-planar Porphyrin.....	259
7.9. Anchoring of Pd Pincer Complexes – Pre-study.....	262
7.10. Re-photocatalyst Anchoring in MOF Pores .....	270
7.11. Author Contributions .....	278
7.12. List of Publications .....	279

## Kurzzusammenfassung

Die Natur bietet faszinierende, ausgereifte Strategien in der Katalyse, mit Enzymen als typisches Beispiel dafür, Reaktionen mit ausgezeichneter Aktivität und hervorragender Selektivität katalysieren können, was bisher in synthetischen Systemen nicht erreicht werden kann. Daher ist die Nachahmung von Konzepten der Natur in künstlichen Systemen eine vielversprechende Strategie in der Materialforschung. Insbesondere in der biomimetischen Katalyse stellen die Prinzipien des enzymatischen Taschendesigns, insbesondere die präzise Umgebung des aktiven Zentrums, vielversprechende Werkzeuge für synthetische Materialien dar. Ein großer Nachteil natürlicher Systeme ist jedoch die begrenzte Stabilität, wobei kommen synthetische Systeme ins Spiel kommen. Eine Materialklasse, die in dieser Hinsicht vielversprechende Möglichkeiten bietet, sind metallorganische Gerüste (MOFs). Diese aus organischen Linkern und anorganischen Metallknoten aufgebauten Materialien bieten poröse Reaktionsumgebungen und eine hohe Variabilität, was den Einbau von Multifunktionalität und begrenzten Umgebungen ermöglicht – also Schlüsselprinzipien der Enzymkatalyse.

Daher konzentriert sich diese Arbeit auf den Einbau verschiedener katalytisch aktiver Spezies in MOFs, insbesondere in (porphyrinbasierte) Zr-MOFs, und deren Platzierung in einer definierten, porösen Reaktionsumgebung. Zu diesem Zweck werden verschiedene Strategien wie die Linkerfunktionalisierung oder Knotenverankerung angewandt - mit einem Schwerpunkt auf dem Einbau von Metallen in Porphyrinmoleküle, die als MOF-Linker fungieren. Hier werden synthetische Leitlinien in Abhängigkeit vom gewünschten Metall (im Porphyrinkern) vorgestellt, mit Fallstudien für Rh, Ru, Mn, Co, Zn, Ni, Cu, Mg und Fe. Die vorgestellten Strategien erlauben eine freie Wahl des Metalls, der Metallkombination und eine flexible Variation des Verhältnisses, was eine enorme Designflexibilität für verschiedene Anwendungen ermöglicht.

Mit diesen synthetischen Werkzeugen ist die Untersuchung anspruchsvoller katalytischer Ansätze in Proof-of-Concept-Reaktionen möglich. Ein faszinierendes Merkmal dieser porphyrinbasierten Zr-MOFs ist die Synthese verschiedener Topologien aus denselben Bausteinen, wodurch die Untersuchung der Auswirkungen von Topologie auf die katalytischen Eigenschaften möglich ist. Detaillierte Untersuchungen liefern somit Einblicke in die Ursachen für eine Selektivitätskontrolle – in Thermo- und Photokatalyse. Darüber hinaus ist durch die Integration von Multifunktionalität, d.h. zwei verschiedener aktiver Zentren, die Katalyse gekoppelter Reaktionen in einem Material möglich. Die katalytischen Eigenschaften können hier durch die synthetische Flexibilität angepasst werden. Ein Beispiel bietet die sequentielle Umwandlung von Olefinen zu cyclischen Carbonaten über das Epoxid. Diese beiden Arten der katalytischen Anwendung unterstreichen das Potenzial von MOFs als Plattform für den Einbau von Multifunktionalität, die das Design spezifischer (katalytischer) Eigenschaften nach Bedarf und damit die Kontrolle der katalytischen Leistung ermöglicht.

## Abstract

Nature provides fascinating mature strategies for catalysis, with enzymes as a typical example which are able to catalyze reactions with excellent activities and outstanding selectivities – unrivaled by synthetic systems. Thus, imitating concepts provided by nature in artificial systems is a promising strategy in materials research and has gained tremendous attention in the last years. In particular in biomimetic catalysis, the principles of enzymatic pocket design, especially the close environment around the active site, present promising tools for the implementation in synthetic materials. However, a major drawback of natural systems is their limited stability – which is where artificial/synthetic systems come into play. A class of materials with promising opportunities in this regard are metal-organic frameworks (MOFs). Constructed from organic linkers and inorganic metal nodes these materials offer porous reaction environments and high tunability, allowing for the integration of enzymatic pocket principles with multifunctionality and confined environments as key concepts.

Therefore, this Thesis focuses on the integration of different catalytically active species into MOFs, in precise (porphyrin-based) Zr-MOFs, and placing them in a defined porous reaction environment. Various strategies are applied for this purpose such as linker functionalization or node anchoring – with a focus on metal incorporation into porphyrin molecules acting as MOF linkers. Here, synthetic guidelines are provided depending on the desired metal (in the porphyrin core), with case studies for Rh, Ru, Mn, Co, Zn, Ni, Cu, Mg and Fe. The presented strategies allow for a free choice of metal, metal combination and flexible ratio variation which enables high design flexibility for several applications – beyond the ones described in this Thesis.

With these synthetic tools in hand, the study of demanding catalytic approaches in proof-of-concept reactions is possible. An intriguing feature of those porphyrin-based Zr-MOFs is the synthesis of different topologies from the same building blocks which permits the study of topology and reaction environment effects on catalytic properties. Detailed investigations thus provide further insights into origins causing a selectivity control which is studied both for thermal- and photocatalysis. Model reactions for this purpose are the thermal cyclopropanation and the photocatalytic CO<sub>2</sub> reduction. Moreover, by integration of multifunctionality, i.e., two different active sites, catalysis of coupled reactions within one material is possible with catalytic property tuning feasible by the synthetic flexibility. This is exemplarily shown for the sequential conversion of olefins to cyclic carbonates via the epoxide. These two types of catalytic applications emphasize the potential of using MOFs as a platform for multifunctionality integration allowing for the design of specific (catalytic) properties on demand and thereby the control of catalytic performances.

## List of Abbreviations

<b>ALD</b>	Atomic layer deposition
<b>AS</b>	Aminostyrene
<b>BA</b>	Benzoic acid
<b>BET</b>	Brunauer-Emmett-Teller
<b>BIH</b>	1,3-dimethyl-2-phenyl-2,3-dihydro-1 <i>H</i> -benzo[ <i>d</i> ]imidazole
<b>C</b>	Conversion
<b>CDCl<sub>3</sub></b>	Deuterated chloroform
<b>DCM</b>	Dichloromethane
<b>DED</b>	Difference envelope density
<b>DEF</b>	<i>N,N</i> -Diethylformamide
<b>DFT</b>	Density functional theory
<b>DMF</b>	<i>N,N</i> -Dimethylformamide
<b>DMSO</b>	Dimethylsulfoxide
<b>DUT</b>	Dresden University of Technology
<b>EDA</b>	Ethyl diazoacetate
<b>EtP</b>	2,3,7,8,12,13,17,18-octaethyl-5,10,15,20-tetrakis(4-carboxyphenyl)-porphyrin
<b>Et-TCPPH<sub>2</sub></b>	2,3,7,8,12,13,17,18-octaethyl-5,10,15,20-tetrakis(4-carboxyphenyl)-porphyrin
<b>HCOO<sup>-</sup></b>	Formate
<b>HKUST</b>	Hong Kong University of Science and Technology
<b>ICP-MS</b>	Inductively coupled plasma – mass spectrometry
<b>IR</b>	Infrared
<b>IRMOF</b>	Isorecticular MOF (= MOF-5)
<b>LED</b>	Light emitting diode
<b>M</b>	Metal
<b>MeCN</b>	Acetonitrile
<b>MeOH</b>	Methanol
<b>MIL</b>	Materials Institute Lavoisier
<b>MOF</b>	Metal-Organic framework
<b>MUF</b>	Massey University Framework
<b>MW</b>	Microwave
<b>n</b>	Amount of substance
<b>NMR</b>	Nuclear magnetic resonance
<b>Cl<sub>2</sub>pyNO</b>	2,6-Dichloropyridine N-oxide
<b>NP</b>	Nanoparticle
<b>NU</b>	Northwestern University
<b>Oac</b>	Acetate
<b>OMS</b>	Open metal site
<b>ORR</b>	Oxygen reduction reaction
<b>PCN</b>	Porous coordination network

---

<b>PMOF</b>	Porphyrin MOF
<b>PPA</b>	Phenylphosphonic acid
<b>PS</b>	Photosensitizer
<b>PXRD</b>	Powder X-ray diffraction
<b>S</b>	Selectivity
<b>SALE</b>	Solvent assisted linker exchange
<b>SALI</b>	Solvent assisted ligand incorporation
<b>SEM</b>	Scanning electron microscopy
<b>STY</b>	Space-time-yield
<b>t</b>	Time
<b>T</b>	Temperature
<b>TBAB</b>	Tetrabutylammonium bromide
<b>TBAPy</b>	1,3,6,8-Tetrakis( <i>p</i> -benzoic-acid)pyrene
<b>TBHP</b>	<i>tert</i> -Butyl hydroperoxide
<b>TCPPH<sub>2</sub></b>	5,10,15,20-Tetrakis(4-carboxyphenyl)-porphyrin
<b>TEM</b>	Transmission electron microscopy
<b>TEMPO</b>	2,2,6,6-Tetramethylpiperidinyloxy
<b>TGA</b>	Thermogravimetric analysis
<b>TOF</b>	Turnover frequency
<b>TON</b>	Turnover number
<b>UiO</b>	Universitetet i Oslo
<b>UV</b>	Ultraviolet
<b>VT</b>	Variable temperature
<b>Y</b>	Yield
<b>ZIF</b>	Zeolitic imidazolate framework
<b>ΔG</b>	Gibbs free energy

# 1. Introduction

## 1.1. Enzymes – From Nature to Artificial Systems

Nature provides fascinating concepts and structures for organic transformations – such as enzymes. The latter are able to catalyze challenging reactions with excellent activities and selectivities and high substrate affinity under mild conditions. Next to a tremendous number of biological processes, enzymes are applied in industrial processes, e.g., for pharmaceutical synthesis. However, their broad applications are still hindered due to their limited thermal and chemical stability and high costs.<sup>[1–3]</sup>

The unique properties arise from the presence of several functionalities – active sites, coordination functionalities, cofactors etc. – working in synergy and their defined and close arrangement in enzymatic pockets. Functionalities in the microenvironment of enzymes, like amino acids, allow for the precise orientation alignment of substrates by secondary interactions enabling excellent performances (Figure 1).<sup>[4–7]</sup> While at first glance, this is extremely beneficial and sophisticated the elucidation of underlying enzymatic mechanisms is a major challenge since several functionalities need to be considered. Therefore, combination of elaborate experimental efforts and theoretical modelling is particularly important.<sup>[4,5]</sup>

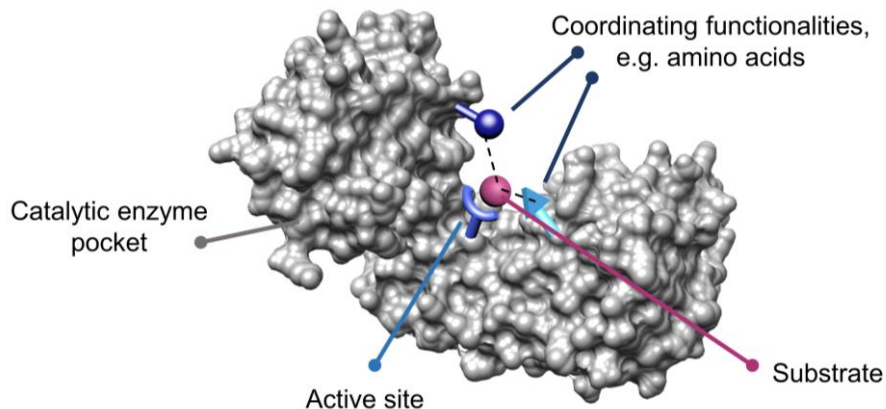


Figure 1: Schematic representation of a catalytic enzyme pocket containing the active site, the substrate and coordinating functionalities, e.g., amino acids, responsible for substrate alignment.

Due to their above-described outstanding properties and to overcome the disadvantages, enzyme mimicking and designing artificial enzymes gained significant interest in research – simulating their concepts in catalysis, like specific, multifunctional reaction environments or enzyme – substrate interactions.<sup>[7,8]</sup> Beside enzyme immobilization for stability enhancement, new, biomimetic systems are reported resembling principles of enzymes.<sup>[1,9,10]</sup> Here, tools in chemical synthesis – in particular in supramolecular chemistry – can be applied for this purpose resulting in a high number of reported artificial enzyme systems.

Thus, the design of confined cavities comparable to enzymatic pockets is possible in supramolecular systems.<sup>[1,9,11]</sup> However, the stability, catalytic efficiencies and selectivity control in biomimetic systems is still a challenge.<sup>[2]</sup> Therefore, further studies and new materials are necessary to gain further insights and provide approaches to come closer to enzymatic performances.

A material class which has attracted high interest in biomimetics, is metal-organic frameworks (MOFs) which will be described in the following. In addition to their intrinsic large design flexibility and multifunctionality, biomimetic motifs can be incorporated, such as porphyrins, offering great potential towards artificial enzyme systems.<sup>[1,3,12,13,14]</sup>

## 1.2. Metal-Organic Frameworks

A material class meeting the requirements for the design of artificial enzymes are metal-organic frameworks (MOFs). According to the definition of the International Union of Pure and Applied Chemistry (IUPAC) a MOF is a “coordination network with organic ligands containing potential voids” while a coordination network is defined as “a coordination compound extending, through repeating coordination entities, in 1 dimension, but with cross-links [...], or a coordination compound extending through repeating coordination entities in 2 or 3 dimensions.”<sup>[15]</sup> In MOFs organic polytopic ligands (= linkers; usually carboxylates or imidazoles) and inorganic metal clusters or ions (= node) are assembled forming a porous, at least 2D, crystalline network, see Figure 2.<sup>[16]</sup>

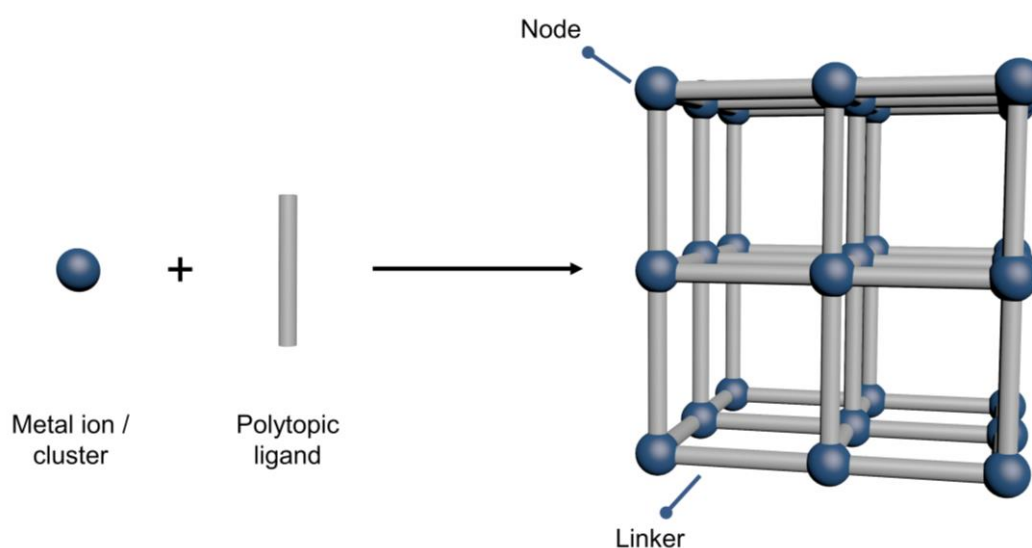


Figure 2: Conceptual representation of the MOF building principle. Reaction of a metal ion or cluster with a polytopic ligand results in the formation of a crystalline, porous framework. The metal ions/clusters form the MOF nodes while the ligands act as so-called linkers.

An intriguing feature is the high porosity of MOFs since more than 50% of the MOF crystal volume are porous – resulting in high surface areas from 1000 to 10 000 m<sup>2</sup>/g and thus significantly extend zeolites or activated carbon surface area wise.<sup>[17]</sup> Most fascinating, an almost unlimited number of MOF systems is imaginable by the concept of reticular synthesis since several organic and inorganic compounds could be combined for MOF design. Thus, until now more than 100 000 MOFs have been reported.<sup>[18,19]</sup> Simultaneously, the void space of MOFs enables the incorporation and heterogenization of guest species (complexes, enzymes, nanoparticles etc.).<sup>[1,20–22]</sup> Therefore, it is not unexpected that MOFs reveal interesting properties for a large variety of applications, such as adsorption, sensing, gas separation, drug delivery or catalysis.<sup>[19,23]</sup> In particular the high tunability of MOFs is an appealing feature allowing for the tailoring of MOF properties for desired applications – either *in-situ* or by post-synthetic approaches – which will be discussed in the following.<sup>[24,25]</sup>



### 1.3. MOFs in Catalysis

According to a *Web of Science* search, more than 3 900 publications on “MOF catalysis” have been published since 2004.<sup>[26]</sup> The large surface areas, defined pore spaces, the tremendous tunability possibilities and high density of active sites render MOFs as excellent candidates for applications in thermal, electro- or photocatalysis. The catalytic activity can either result from the MOF building blocks themselves and is thus intrinsically given or by integration of active species (Figure 3). In particular metal nodes as MOF components were intensively studied in catalysis. Coordinatively unsaturated (=open metal) sites (OMS) at the nodes show Lewis acidic properties able to catalyze different reactions, such as the cyanosilylation, CO<sub>2</sub> cycloaddition, oxidation or hydrogenation reactions.<sup>[27–31]</sup>

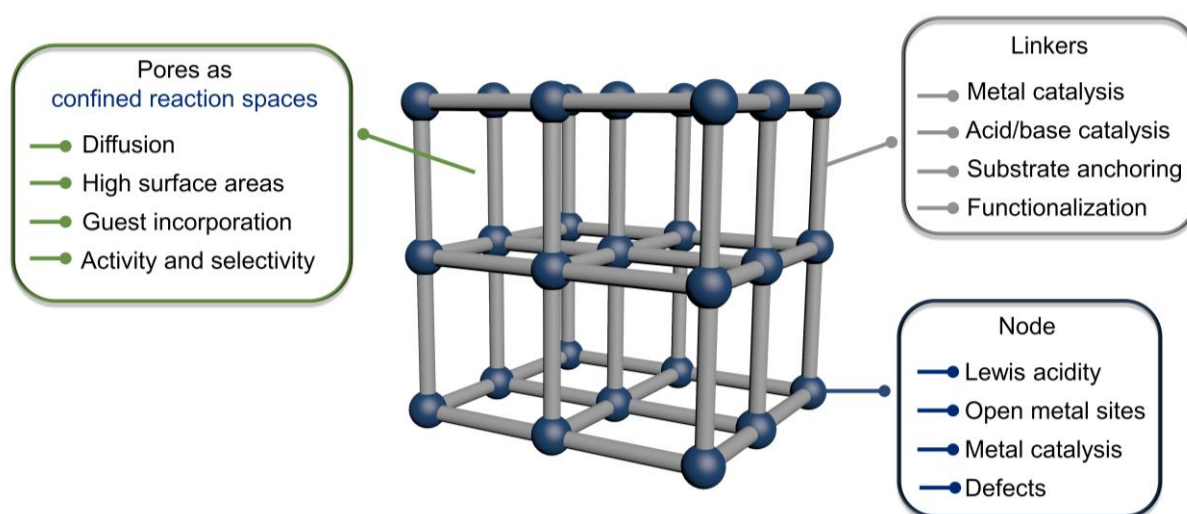


Figure 3: Summary of MOF properties in catalysis. The porous space restricts a defined reaction space and allows for diffusion, high surface areas, guest incorporation and activity and selectivity control. Linkers can be applied in MOF catalysis containing catalytically active metals as catalysts in acid/base reactions, and as a platform for substrate anchoring or functionalization affecting catalytic properties. Lewis acidic properties and the presence of open metal sites at the metal node allow for catalytic applications. Additionally, metal catalysis and defect engineering are possible.

Open metal sites can arise from intrinsic node undercoordination (e.g. for 6-fold coordinated MOF nodes which could coordinate 12 carboxylates) or the presence of defects in the crystal lattice.<sup>[27,28,32]</sup> The latter result from missing nodes or linkers or the absence of a coordinating solvent at the node.<sup>[33]</sup> Consequently, the presence or introduction of defects can enhance the catalytic activity of a MOF, with UiO-66 materials as common examples.<sup>[34,35]</sup> Thus, defect engineering in MOFs is an appealing strategy for tuning catalytic performances.<sup>[33]</sup> Similar to MOF nodes as active sites, the organic linkers can be applied in catalysis – in particular by functionalities at the linker active in acid, base or organocatalysis.<sup>[28,30,36]</sup> A typical example is the linker functionalization with an amino group acting as the basic site and active for example in the Knoevenagel condensation reaction.<sup>[30]</sup> Moreover, linker metalation introduces catalytically active sites which is a prominent example in porphyrin-based systems.<sup>[36,37]</sup>

In addition to intrinsic active sites, a prominent approach is using MOF scaffolds as hosts for several catalysts like metal nanoparticles, enzymes or molecular catalysts – enabled by the porous MOF nature.<sup>[1,20,21]</sup> Beside the classic heterogenization effect, the restricted pore environment allows for the control of selectivities which is a phenomenon typically known from zeolite catalysis.<sup>[38,39]</sup> Although the latter outperform MOFs stability wise – which hinders the broad application of MOFs in catalysis – the design flexibility of MOFs is an immense advantage compared to zeolites.<sup>[28,30,40]</sup> While zeolite formation is constrained to certain building units, the tunability of MOFs allows for numerous catalyst integration strategies.<sup>[28]</sup> Thus, the latter will be presented in more detail in the following chapter which serve as core synthesis strategies for the MOF catalyst design studied in this Thesis.

Another approach of MOFs in catalysis emerging during the last years is the usage of MOFs as precursors for single-site catalysis – which is extensively studied for electrocatalysis.<sup>[27]</sup> Here, MOFs with precise catalytically active sites are synthesized and afterwards decomposed, e.g. by pyrolysis, to achieve MOF derivative materials while maintaining the single-site nature of the active sites. This has been shown to enhance catalytic performances and presents a further dimension of using MOFs for catalytic applications – i.e. serving as precursors for catalytic materials.<sup>[41]</sup> This concept is exemplarily shown for a MOF with metalated linkers in Figure 4.

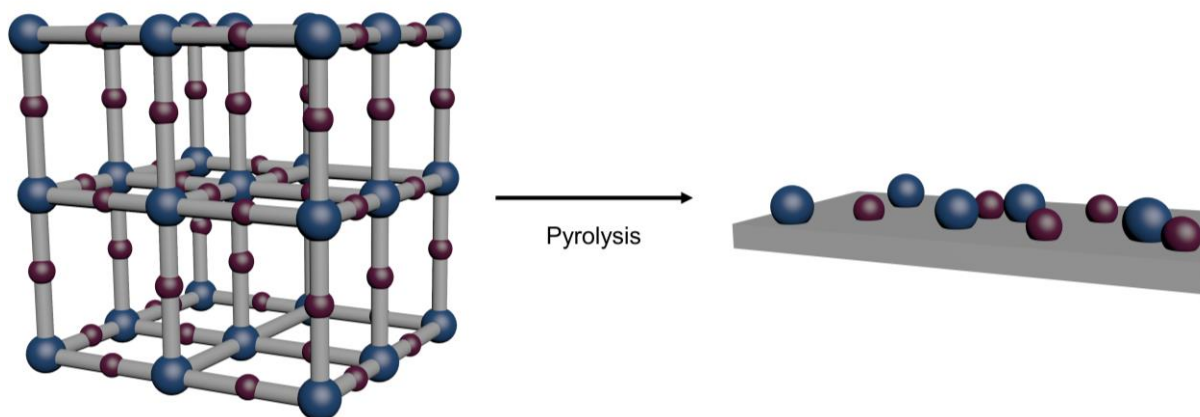


Figure 4: Illustration of a metalated MOF used as precursor for a MOF derived material. Decomposition results from pyrolysis resulting in single-metal sites deposited on a carbon matrix.

In general, several limitations have to be considered when using MOFs in catalysis. Especially the thermal and chemical stability of MOFs is limited due to the presence of organic species – as mentioned above – resulting in potential framework collapse or catalyst leaching during catalysis.<sup>[42,43]</sup> Thus, stability studies before catalytic applications are essential – in addition to long-term stability investigations important for catalyst recycling. Moreover, sufficient pore space for reactants, intermediates and products has to be available to ensure reaction inside the pores instead of at the outer surface.<sup>[43]</sup>

The impact of the external surface in catalysis can be studied by MOF particle size reduction which should increase the activity when the catalysis proceeds at the outer surface exclusively. The downsizing effect of particle size on the catalytic performance, i.e. increasing the activity, has been reported previously and presents an appealing strategy for rate enhancement in catalysis.<sup>[44–46]</sup>

### 1.3.1. Catalyst Integration

As discussed in the previous chapter, different catalytically active components can be integrated into MOFs. This catalyst integration can be achieved by different strategies, either in direct MOF synthesis or by post-synthetic modification which is extremely beneficial since the incorporation strategy can be selected depending on the desired property.<sup>[27]</sup> While catalyst embedment into MOF pores possibly results in diffusion limitations, linker functionalization can serve as alternative without significant pore space alteration. Simultaneously, the distance between active sites is adjustable by the choice of integration strategy: in contrast to linker functionalization with a fixed location predetermined by the MOF topology, catalyst anchoring into the pores can decrease the distance to further functionalities. The latter has been reported as an important feature for a molecular Co catalyst incorporated in NU-1000 which is used in the photocatalytic hydrogen evolution favoring electron transfer and affecting the catalytic activity.<sup>[47]</sup> Different catalyst integration strategies are presented in Figure 5 and will be discussed in the following chapters.

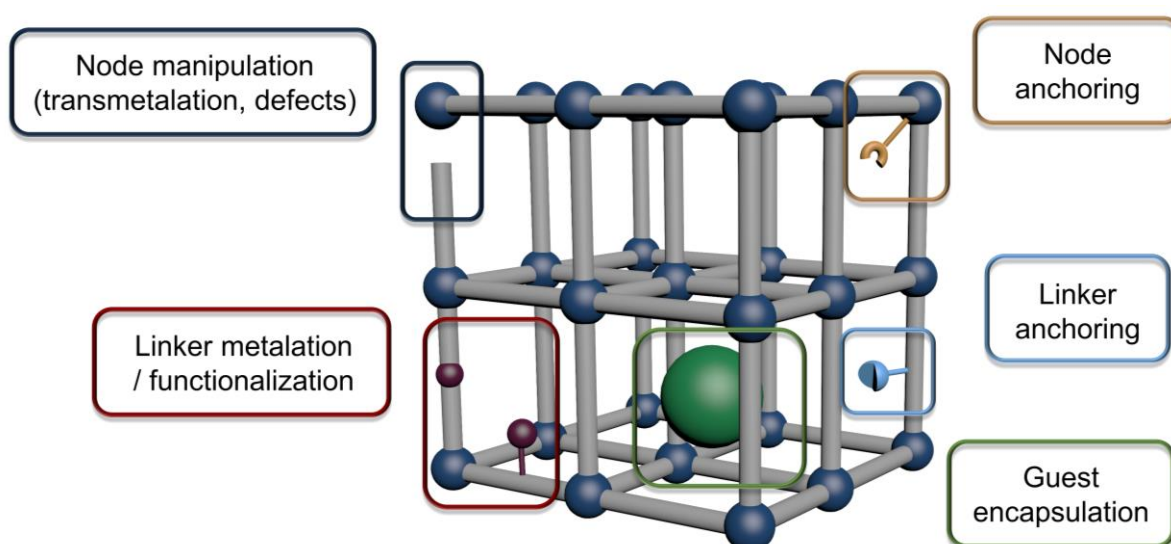


Figure 5: Conceptual visualization of different catalyst integration strategies for MOFs. Node manipulation can be achieved by transmetalation or defect engineering. Additionally, linker metalation or functionalization is possible. Anchoring of catalytically active species is accomplished by tethering these catalysts to the node or linker. Moreover, guest encapsulation in the MOF pores is a common strategy.

In general, several *in-situ* or post-synthetic strategies were reported for catalyst integration in MOFs.<sup>[25,48,49]</sup> Beside the above-mentioned tuning of intrinsic node or linker properties, catalyst anchoring to the MOF node or linker is possible. Moreover, a common strategy for nanoparticles or enzymes is the immobilization into MOF pores without precise coordination/anchoring of the catalyst to the MOF.<sup>[1,20,21]</sup> In the following, those strategies will be presented in further detail.

However, before discussing each approach individually, typical strategies in MOF synthesis (*de novo* and post-synthetic), which are recurrent in the following, will be defined. In *de novo* synthesis, MOF manipulation via a modulation approach or a mixed-linker strategy is possible.<sup>[27,30,33]</sup> In the **modulation approach** monocarboxylic acids (“modulators”) are added during MOF synthesis which reduces crystallization kinetics by influencing the equilibrium (Figure 6). However, increasing the modulator amount prevents the exchange of some modulator with linker molecules, thus, creating a defect in the framework.<sup>[33]</sup>

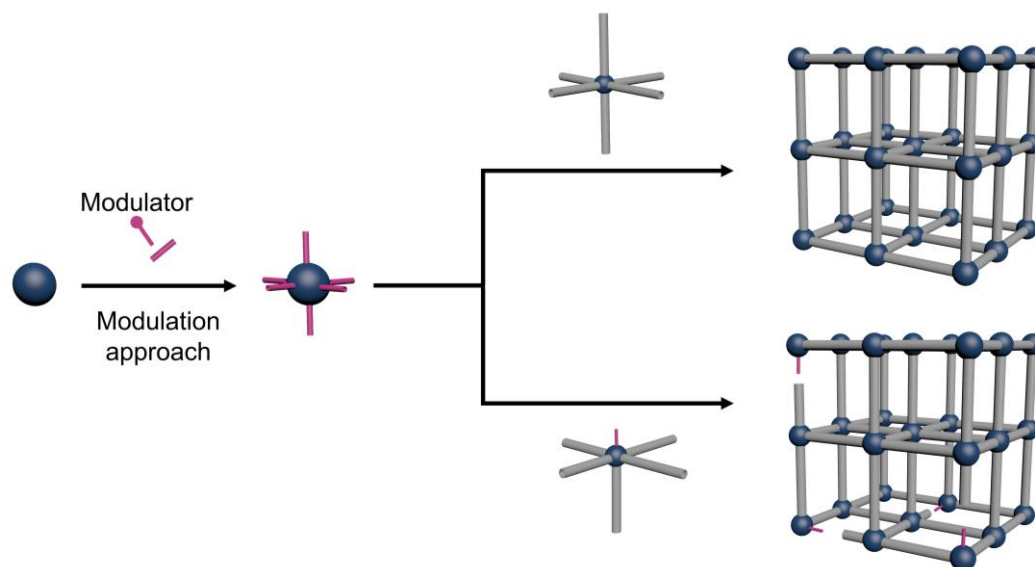


Figure 6: Schematic representation of the modulation approach: A modulator is applied in MOF synthesis to affect crystallization kinetics. Simultaneously, the application of modulators allows for the creation of defects.

For the **mixed-linker strategy**, a different linker is incorporated by partial substitution of the original linker during MOF synthesis introducing multifunctionality (Figure 7).<sup>[27,30,50]</sup> Usually, both linkers are similar in terms of length or structure while the newly incorporated linker contains a further functionality. Example combinations are  $\text{NH}_2\text{-H}_2\text{bdc}/\text{H}_2\text{bdc}$  (bdc = benzene-1,4-dicarboxylate) or metalloporphyrin/free-base porphyrin systems.<sup>[28,50,51]</sup> Although the linkers are in general very comparable, differences in MOF synthesis might occur which can influence MOF crystallization and thus the success of the synthesis.

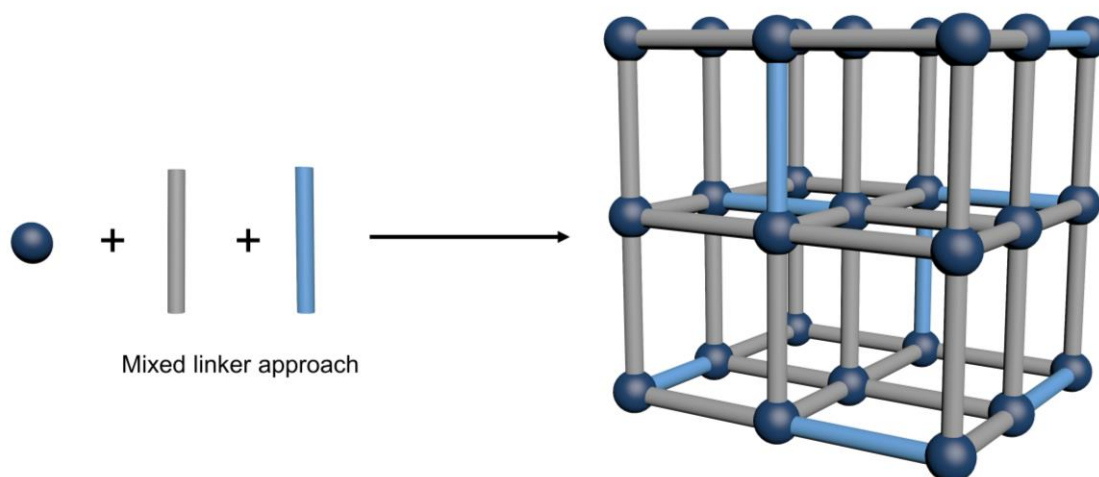


Figure 7: Visualization of the mixed linker approach in MOF in *de novo* MOF synthesis. In addition to the original linker, a second (functionalized) linker is applied resulting in a framework where both linkers are integrated.

Classic strategies in post-synthetic modifications are the so-called **SALE** (solvent-assisted linker exchange) and **SALI** (solvent-assisted ligand incorporation) approaches.<sup>[48]</sup> Both methods start with the pristine MOF obtained by its typical synthesis. During SALE, the MOF is soaked in a solution of the second linker at elevated temperatures – replacing some of the initial MOF linker (Figure 8). Simultaneously, this strategy allows for the engineering of the pore space which can be increased by exchanging the previous linker with longer linkers.<sup>[48,52]</sup>

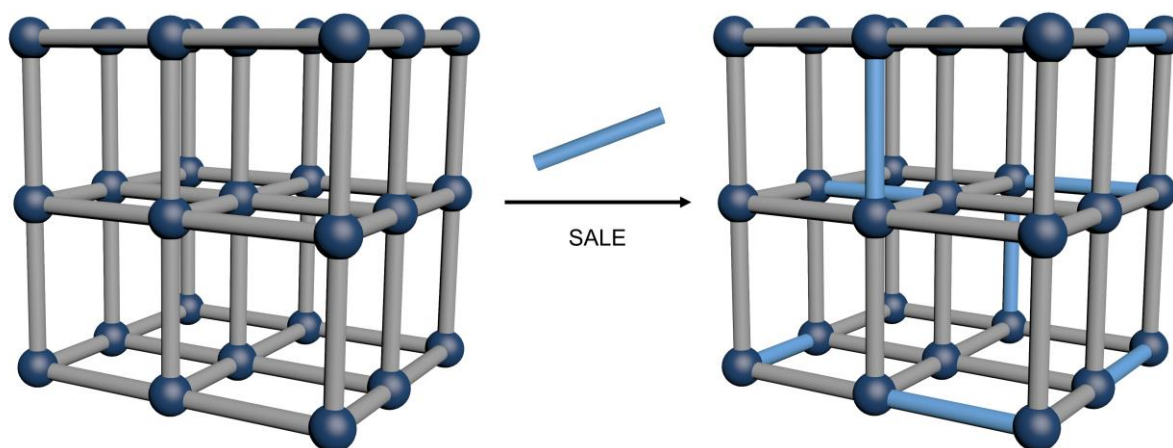


Figure 8: Conceptual representation of the post-synthetic MOF modification using the SALE method. Here an original linker is post-synthetically substituted with a new (functionalized) one.

In the SALI approach, a non-bridging ligand (usually containing a carboxylate function) is attached to the node based on acid-base chemistry or ligand exchange (Figure 9).<sup>[48]</sup> This method is frequently applied in the Zr-based MOF NU-1000 where different molecules have been successfully anchored to the node via an acid-base equilibrium between the hydroxyl ligands at the node and the carboxylate functionality of the new ligand.<sup>[48,53]</sup>

These post-synthetic methods are advantageous since the synthesis of the pristine MOF is not affected – preventing the challenges occurring upon addition of further molecules/functionalities in *de novo* synthesis since the MOF is already formed. Moreover, the MOF structure is usually unaffected by this method when its general stability under the applied modification conditions is ensured. A further benefit of SALI/SALE is the control of the functionalization degree provided by both strategies.<sup>[48,49,54]</sup>

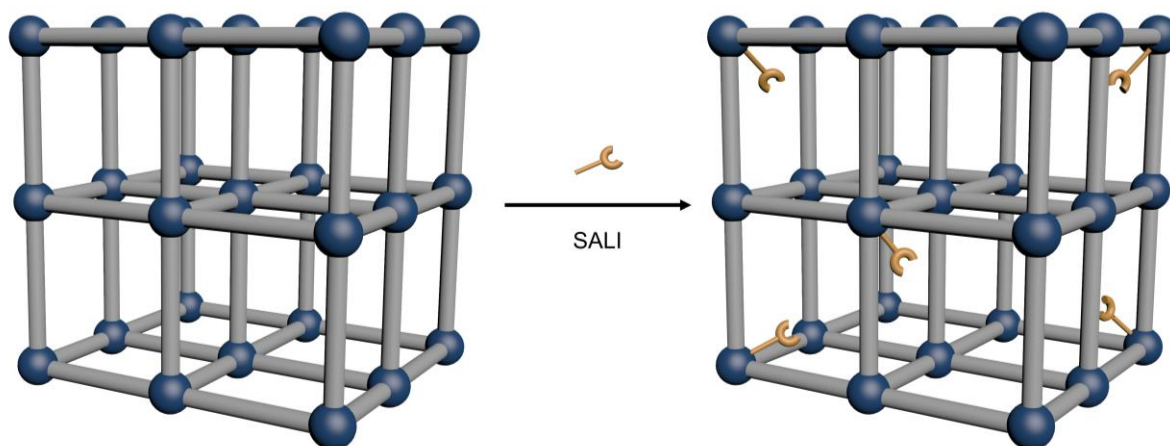


Figure 9: Conceptual representation of the post-synthetic MOF modification using the SALI method. Here a non-bridging ligand is post-synthetically anchored to the node.

### 1.3.1.1. Node Manipulation

The catalytic activity of the node is tunable in several ways. As indicated above, defect engineering is a fascinating approach and shows significant impact on the catalytic properties of the material.<sup>[30,33,37]</sup> The introduction of defects is achievable by *de novo* synthesis (modulation or mixed-linker approach) or by post-synthetic methods such as SALE/SALI, chemical or mechanical treatment, or recently presented thermal defect engineering, i.e. the controlled thermal removal of coordinating functionalities (modulator or linker), see Figure 10.<sup>[33,55]</sup> Several reports show a correlation between the defect concentration and catalytic activity. As an example, a higher activity of different Zr/Hf-based MOFs in the epoxide ring opening of styrene oxide – catalyzed by Lewis acidic sites – was obtained upon increasing defect amounts resulting in more coordinatively unsaturated sites.<sup>[35]</sup> The phenomenon of activity enhancement upon defect incorporation was also shown in the MOF catalyzed Pall-Knorr reaction, ethylene dimerization or cyanosilylation.<sup>[33]</sup>

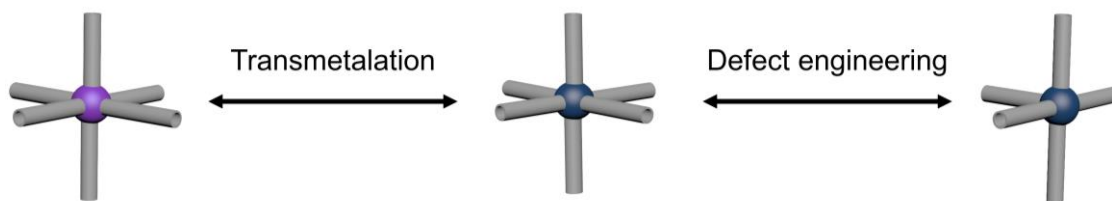


Figure 10: Schematic representation of different node manipulation approaches, via transmetalation or defect engineering. Both are possible in *de novo* synthesis or post-synthetically.

In addition to defect engineering at the metal node, transmetalation of metal nodes can introduce catalytic properties in MOFs (Figure 10).<sup>[37,48]</sup> During *de novo* synthesis, a mixture of metal node precursors can be applied for the synthesis of mixed-metal nodes. This has exemplarily been shown for Cu-doped ZIF-67 ( $\rightarrow$  Co/Cu) or Fe/Ni-MIL-53 forming a solid solution.<sup>[37]</sup> Post-synthetically, transmetalation is achieved by ion metathesis where the metal ion is exchanged in a solution of the synthesized MOF with the new metal precursor – allowing for concentration control while maintaining the framework. This was demonstrated for several Zn-MOFs (partially) exchanging Zn with Cu, Co or Ni to introduce catalytically active sites for coupling reactions, CO oxidation or ethylene oligomerization.<sup>[48]</sup>

Combined, these strategies allow for the general introduction of catalytic activity or the increase of the latter by precise design of active sites at MOF nodes with a plethora of synthetic methods available in MOF synthesis and modification. Simultaneously, the catalytically active sites can be categorized as framework compounds without affecting molecular diffusion inside the pores and have a defined location.

### 1.3.1.2. Node Anchoring

Beside the modification of intrinsic MOF node properties, anchoring of catalytically active molecules or atoms to the node is possible – post-synthetically.<sup>[25,37,49,56]</sup> Cluster metalation occurs by the integration of an atom interacting with hydroxy functionalities at the node. Synthetically, the anchoring of a metal at the node can be achieved by solvothermal deposition or atomic layer deposition (ALD), see Figure 11.<sup>[25,49]</sup> A prominent example for this approach is the node functionalization of NU-1000 studied by *Hupp* and co-workers where metals like Cu, Al, V or Ni were anchored to the node acting as single-site catalysts at the node.<sup>[57,58]</sup>

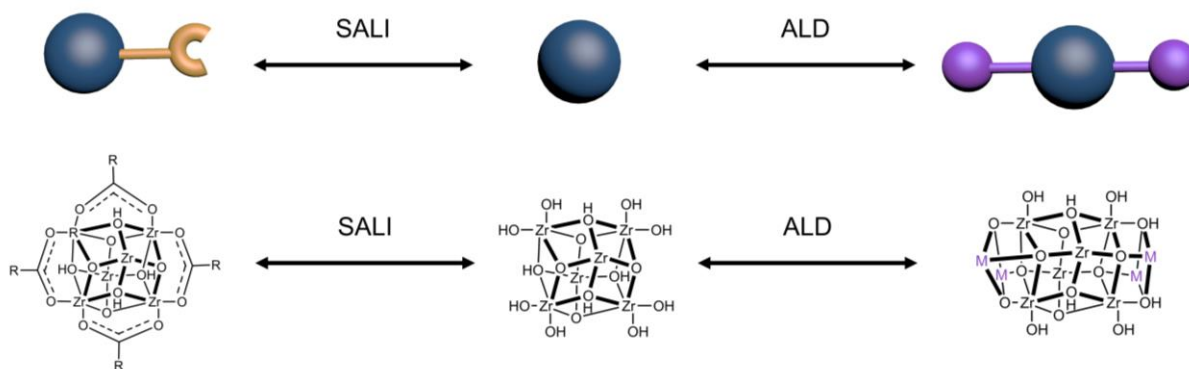


Figure 11: Schematic representation of different node anchoring strategies. Metal anchoring can be achieved via atomic layer deposition (ALD) while several ligands can be anchored to the node via the SALI (solvent assisted ligand incorporation) method. The figure is designed according to Ref [25].

Ligand attachment to the node is possible by coordination of functional groups at the ligand to coordinatively unsaturated sites at the node (e.g. hydroxy groups), similar to metal anchoring (Figure 11).<sup>[25,48,49]</sup> This strategy is extremely appealing since several species, such as organic molecules, metal complexes or inorganic acids, can be grafted onto the node – offering a plethora of functionalization and catalyst integration opportunities.<sup>[21,25,37,53,59,60]</sup> Typical platforms for the node anchoring are Zr-based MOFs, e.g. the UiO series (-66, -67, -68) or NU-1000, where organic molecules or metal complexes are commonly introduced via the SALI method.<sup>[21,53,59]</sup> Most fascinating and beyond the possibility of concentration control, the immobilization of two different molecular catalysts (a Re- and Co catalyst) was shown via this method in NU-1000 offering a highly appealing strategy for the design of multifunctional catalysts.<sup>[47]</sup>

A great advantage offered by the post-synthetic node anchoring is the site isolation of anchored species which can decrease their intermolecular deactivation due to the local separation of nodes by the MOF linkers. Simultaneously, the tailorability of MOFs enables precise tuning of steric or electronic properties close to the integrated species – which in turn can affect the catalytic properties of the material.<sup>[25]</sup>



### 1.3.1.3. Linker Functionalization and Anchoring

Catalyst integration or catalytic property tuning at the linker is achievable by different techniques. Linker functionalization was indicated above and is among the most studied approaches for tailoring catalytic MOF properties – introducing metal sites, organometallic complexes, Brønsted acid sites or basic functions (Figure 12). The scope of linker functionalization reaches from rather simple linker substitution with functional groups to tethering of catalysts to the linker via coordinative or chemical bonds. Functionalization at the linker and integration into a MOF scaffold can be achieved *in-situ* and/or post-synthetically.<sup>[37,48]</sup> Therefore, the following chapter is structured according to the different functionalization approaches with indications on the incorporation techniques (pre- versus post-synthetic).

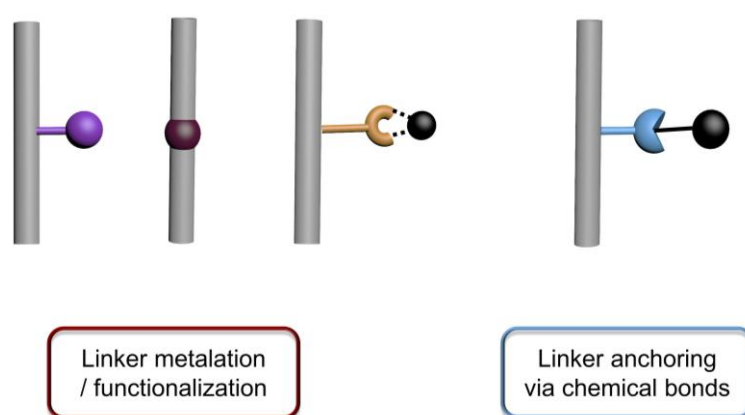


Figure 12: Schematic representation of different linker functionalization or anchoring strategies. From left to right: Linker substitution, direct linker metalation, linker functionalization followed by metalation and anchoring of organocatalysts to the linker via chemical bonds.

Integrating functional groups at the linker – by linker substitution – can significantly impact the catalytic properties of active sites in close proximity.<sup>[30,37,61]</sup> This has been shown for  $\text{-NH}_2$  functionalized linkers or substituted metalloporphyrins.<sup>[28,36]</sup> Beside influencing the catalytic properties itself, amino functionalities showed great potential in enhancing the  $\text{CO}_2$  adsorption capacity of the material which in turn affects the performance of the catalyst in reactions involving  $\text{CO}_2$ .<sup>[61,62]</sup> Linker substitution is usually performed pre-synthetically while the functionalized linker can be incorporated into the MOF structure as exclusive linker or by a mixed-linker approach allowing for the control of linker ratios.<sup>[28,37]</sup>

Beside linker substitution, metalation of linkers is an important approach for catalyst integration. Here, it can be distinguished between two types: i) metal complexation by chelating groups intrinsically present at the linker and ii) linker functionalization with chelating groups as prerequisite for subsequent metalation (Figure 13). Classic examples for i) are salen-, bipyridine or porphyrin-based systems.

While metalation of the chelating ligand can be performed before MOF synthesis, followed by a mixed-linker approach, or post-synthetically for salen or porphyrin-based systems, bipyridyl metalation is usually achieved post-synthetically.<sup>[31,36,37,49]</sup> This design principle is in general extremely beneficial since several catalytically active (transition) metals can be introduced. For the porphyrin core in MOFs, Fe, Pd, Zn, Mn, Co, Ru, and Cu – amongst others – were reported, able to catalyze tremendous amounts of reactions like oxidations, CO<sub>2</sub> cycloadditions, Heck reaction, epoxidations, CO<sub>2</sub> reduction or hydrogen evolution. Simultaneously, different porphyrin-based MOF structures such as PCN-222, PCN-224, MOF-525, PCN-602, Ir-PMOF-1 are accessible allowing for the variation of framework topology.<sup>[36]</sup> Regarding ii), an example for this strategy is the design of a Pd(II) Schiff-base complex in IRMOF-3 by post-synthetic PdCl<sub>2</sub> addition able to catalyze a C-C coupling reaction.<sup>[30]</sup>

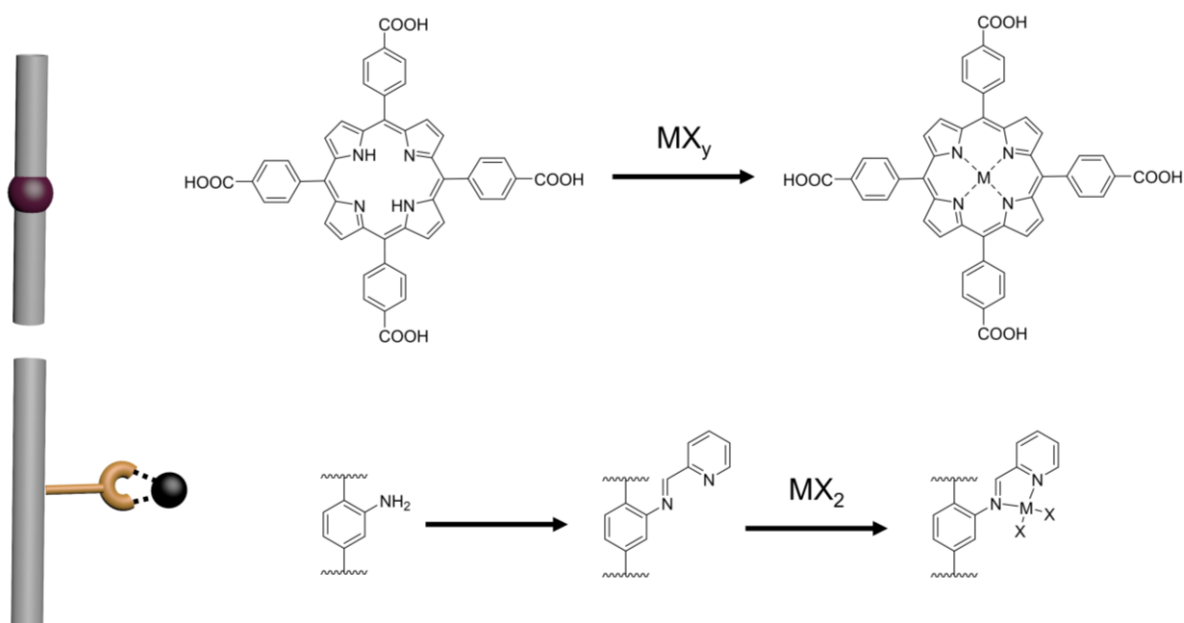


Figure 13: Representation of different linker metalation strategies. Top: direct linker metalation, bottom: linker functionalization and subsequent metalation.

In general, the approach of *in-situ* linker metalation and subsequent MOF integration could also be categorized as heterogenization of a molecular complex within a framework structure – however, will be addressed in the chapters on linker functionalization in accordance to several literature reports.

An interesting alternative to post-synthetic metal coordination is the functionalization of ligands in metal complexes with coordinating groups (e.g. carboxylic acids, pyridines) to be able to act as linkers in MOF synthesis (Figure 14).<sup>[36]</sup> In addition to the already described porphyrin systems, this approach was presented for Re, Ir or Ru complexes bearing a dicarboxylic acid functionalized ligand (e.g. 2,2'-bipyridine-5,5'-dicarboxylic acid) which was applied as linker in UiO-66.<sup>[21,63]</sup>

Moreover, functionalization of the salen ligand motif enabled their incorporation into MOF structures. Simultaneously, metal-salen complexes allow for enantioselective catalysis due to the chiral character of the salen ligand.<sup>[64]</sup>

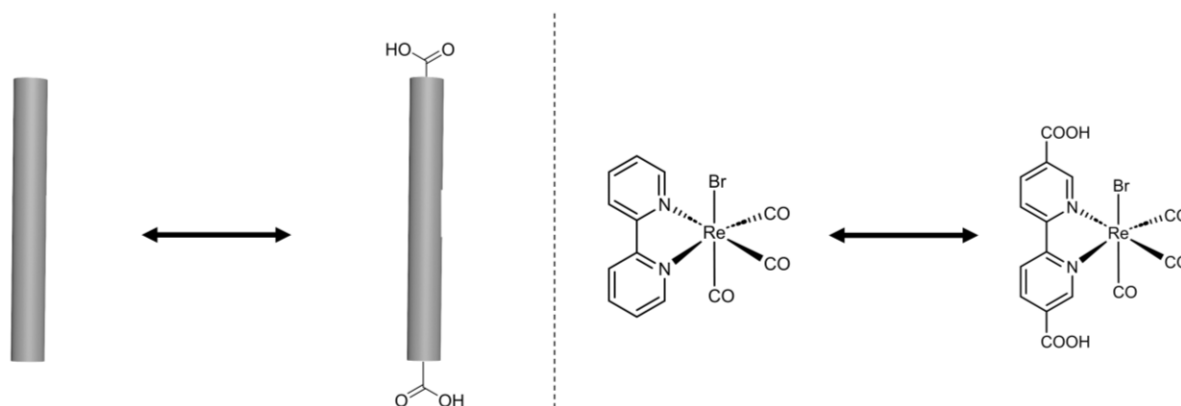


Figure 14: Schematic representation of functionalizing a ligand of an organometallic complex to allow for MOF integration as linker.

Additionally, metal- or organocatalysts can be anchored to linkers by chemical bonds. This was exemplarily shown for proline functionalized UiO-67 and UiO-68 where the organocatalytic proline is anchored to the MOF linker via an amide motif and subsequently applied in MOF synthesis. Moreover, linker functionalization with a urea moiety was presented in UiO-67 catalyzing the Friedel-Crafts reaction or Henry reaction. For this type of linker functionalization both direct MOF synthesis and post-synthetic modification are possible – which has been shown for the urea case by reaction of isocyanates with amino functionalities at the linker.<sup>[36]</sup>

Note that the here described methods present a selection of modification approaches, since large numbers of techniques have been presented in literature. For more specific approaches the reader is referred to respective reviews. Simultaneously, for the categorization of techniques several reviews were compared extracting common categories which – however – can vary in the plethora of published review articles on MOF catalysis.

### 1.3.1.4. Catalyst Encapsulation in Pores

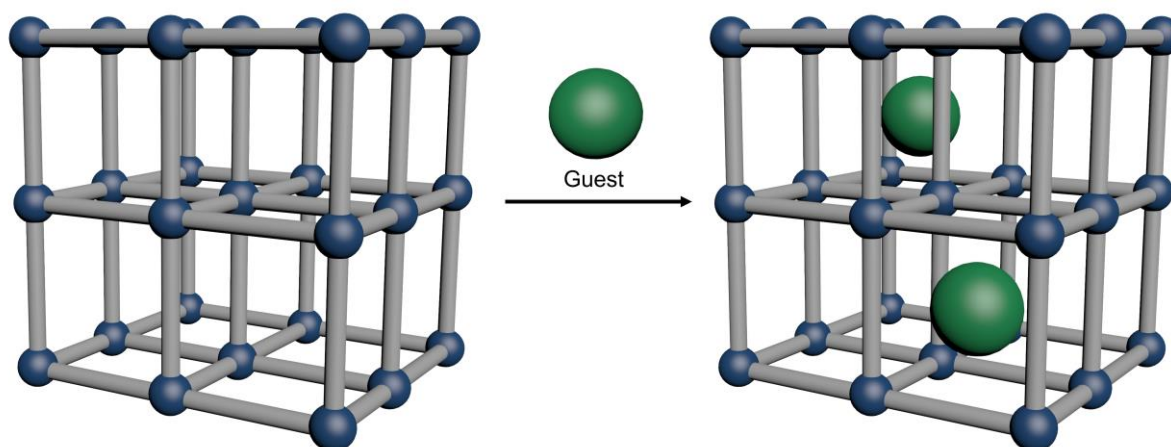


Figure 15: Illustration of guest encapsulation in MOF pores.

Applying MOFs as host for guest species like nanoparticles, polyoxometalates or enzymes is an approach frequently studied in MOF catalyzed reactions – starting in early MOF catalysis research (Figure 15). The MOF scaffold enables activity and stability enhancement of guest species and prevents aggregation and leaching of guests (by pore space restriction).<sup>[1,20,21,65]</sup> However, sufficient pore space needs to be provided for guest species to ensure their encapsulation within the pores instead of the outer surface.<sup>[21]</sup> Several techniques are reported for guest encapsulation, e.g. ship-in-bottle, *in-situ* encapsulation, impregnation, chemical vapor deposition.<sup>[20]</sup> Functionalities at the node or linker in guest@MOF systems allows for synergistic effects, changes in electronic properties or chemical environments.<sup>[25,27,61]</sup> In particular nanoparticle@MOF systems show large potential in catalysis since several NP@MOF systems are reported catalyzing CO<sub>2</sub> utilization reactions, hydrogenation and dehydrogenation or C-C coupling reactions, among others.<sup>[20]</sup>

Beside the general catalytic application arising from the introduction of guest species in MOFs, guest encapsulation results in the design of multifunctionality in MOFs allowing for synergistic effects or the application in multi-step reactions which will be covered in chapter 1.3.3.

### 1.3.2. Confinement Effects in MOF Catalysis

The intrinsic properties of MOFs and the controlled reactive site incorporation in precise environments of pores allows for the potential exploitation of confined reaction space effects on catalysis – inspired by principles of enzyme catalysis. Beyond using MOFs for heterogenization of catalytically active species (e.g. molecular catalysts, nanoparticles), the design of multifunctionality possible in MOFs and their intrinsic properties enable the construction of tailor-made reaction environments with specific substrate – catalyst interactions.<sup>[61]</sup> Strategies to integrate multifunctionality within MOFs are described in chapter 1.3.1. In combination with intrinsic MOF properties – such as the pore walls restricting the reaction space of specific size and shape and predetermined distances between building blocks – cooperative effects and performance control in catalysis is possible.<sup>[25,61]</sup> While neighboring groups can result in precise alignment of substrates close to active sites, deactivation of the latter is prevented by the defined positioning within the MOF.<sup>[61,66,67]</sup> Conceptually, this resembles principles in enzymatic catalysis (enzyme pockets) with amino acid residues placing substrates in ideal distance and conformation to the active site (Figure 16).

Recently, the author published a concept paper focussing on this topic in the journal *ChemCatChem*.<sup>[68]</sup>

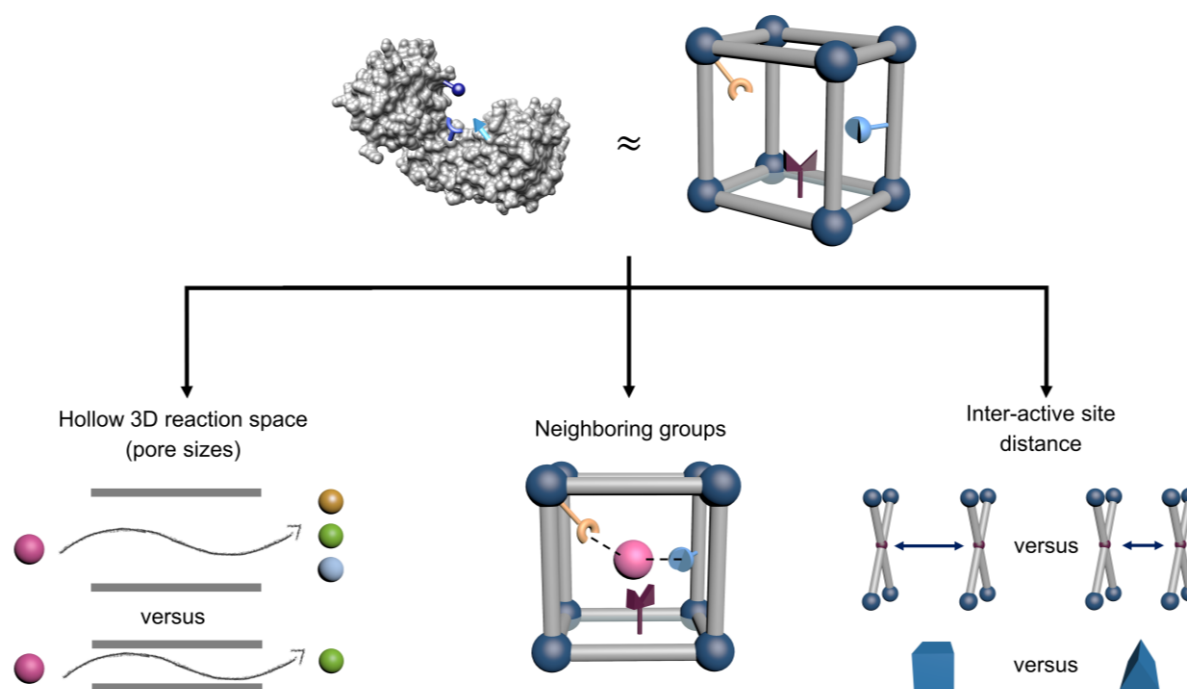


Figure 16: Schematic representation of confinement effects in MOFs – resembling enzymatic pockets. Confinement effects include a hollow 3D reaction space (pore size effects), the influence of neighboring groups and the impact of inter-active site distances (and topology).

Therefore, in the following section such “confinement effects” in MOFs are summarized which allow for the control of activity and selectivity in catalysis. In contrast to the frequently applied term of confinement for heterogenization, this Thesis defines confinement as a property of the MOF cavity – i.e. structural properties and functionalities.<sup>[61]</sup> These properties determine distances and accessibility of catalysts and are tunable by specific (synthetic) modifications. Thus, three categories are identified in the term of confinement effects allowing for the control of performances in MOF catalysis: 1) pore size effects, 2) neighboring groups and 3) topology effects and active site alignment (Figure 16), which will be summarized in the following. Noteworthy, categorizing the present publications, where performance improvements upon MOF integration are given, is challenging since reasons for observed properties are often not fully understood. This arises from the challenging characterizations of interactions in MOFs and the combination of different factors which might be responsible for the respective performances. Therefore, categorization is achieved according to the feature which is most likely to cause the observed catalytic behaviors. Examples are described in more detail since the exploitation of confinement effects is key for the presented Thesis and an understanding of their underlying principles is essential to allow for the design of sophisticated catalysts with specific secondary interactions.

### **Pore size effects**

The pore size effects (1) present the most tangible category of confinement effects, since this concept is widely used in catalysis by porous materials, especially for zeolites. Here, the selectivity is enhanced by pore size adjustment excluding specific reactants, transition states or products.<sup>[30,38]</sup> Thus it is not unexpected, that these effects were among the first confinement effects reported in MOF catalysis – in particular for polymerization catalysis. By pore space restriction, the control of cross linking or tacticity was shown. An example presents the porous coordination polymer  $[\text{Cu}_2(\text{pzdc})_2(\text{L})]_n$  (pzdc = pyrazine-2,3-dicarboxylate, L = pillar ligands) active in monosubstituted acetylene polymerization.<sup>[69]</sup> The reduced channel size results in an enhanced *trans*-product formation since the reaction to the *cis*-product is prevented by the limited available space. This concept of selectivity control by limited pore size is also shown in divinylbenzene polymerization with  $[\text{M}_2(1,4\text{-bdc})_2(\text{ted})]_n$  (bdc = benzenedicarboxylate; ted = triethylenediamine; M = Zn(II) or Cu(II)).<sup>[70]</sup> In contrast to larger channels allowing for the cross-linking of polymers, isotactic linear polymers are obtained in the smaller channels – highlighting the potential of reaction space limitation to steer the selectivity.

Moreover, Cr-MIL-100/-101 with various activator ligands was described as isoprene polymerization catalyst.<sup>[71]</sup> Here, the activator ( $\text{Ph}_3\text{C}$  versus  $\text{PhNMe}_2$ ) plays a crucial role influencing the channel dimensions and thus controlling the reaction. While  $\text{Ph}_3\text{C}$  as non-coordinating activator results in large pores facilitating the  $\beta$ -H elimination side reaction,  $\text{PhNMe}_2$  with coordinating ability enables a more restricted reaction space forming the desired linear polyisoprene.

Additionally, confinement effects can arise from the MOF linker itself, i.e. by its substitution, which was presented for a Cu MOF with BINOL (BINOL = 1,1'-bis-2-naphthol) phosphoric acid linkers.<sup>[72]</sup> Substitution of the linker results in altered steric properties and carboxylate location, accomplished with the construction of varied MOF topologies with different pore voids. In enantioselective Friedel-Crafts catalysis the enantioselectivity is lowered in the MOF with 4,4'-substituted BINOL linker due to the larger pore space. Beside enhancing the enantioselectivity for the 3,3'-substituted BINOL analogue – and in contrast to the 4,4'-substitution – a reverse of enantioselectivity was observed resulting in the (*R*)-enantiomer compared to the (*S*)-enantiomer achieved in the homogeneous system. This is assumed to arise from substrate – pore wall interactions. Such a enantioselectivity reversal was also discernible in aldol reaction using a L-proline functionalized MIL-101(Al) catalyst with large channel size compared to smaller channel MOFs DUT-5 and MIL-53 and the homogeneous analogue.<sup>[73]</sup> These studies suggest the importance of providing sufficient space for substrate alignment and the potential of controlling the selectivity by reaction space restriction.

### Neighboring group effects

Another example of stereoselectivity reversal was shown in aldol addition catalysis upon the incorporation of L-proline in UiO-67 and UiO-68.<sup>[74]</sup> For both MOFs the *syn*-product was formed compared to the *anti*-product obtained in the homogeneous case – ascribed to the restricted reaction space in the MOFs. In another example of L-proline functionalized DUT-67 selectivity enhancement in the same reaction resulting in the *syn*-product is ascribed to the presence of missing linker defects of the Zr-node.<sup>[75]</sup> The importance of metal nodes was affirmed in L-proline-MIL-101(Al) – however, the substrate is assumed to coordinate to a more distant node instead of the one next to the catalyst.<sup>[76]</sup> Further alteration of the reaction environment around L-proline was performed in MUF-77 with three different linkers (either containing L-proline or modulators) to design secondary interactions with neighboring groups. Combining experiment and theory revealed the importance of the local pore environment on the catalytic properties increasing the enantioselectivity in asymmetric aldol catalysis. Simultaneously, the designed environment can be exploited to reverse the enantioselectivity – depending on MOF modification.<sup>[77]</sup>

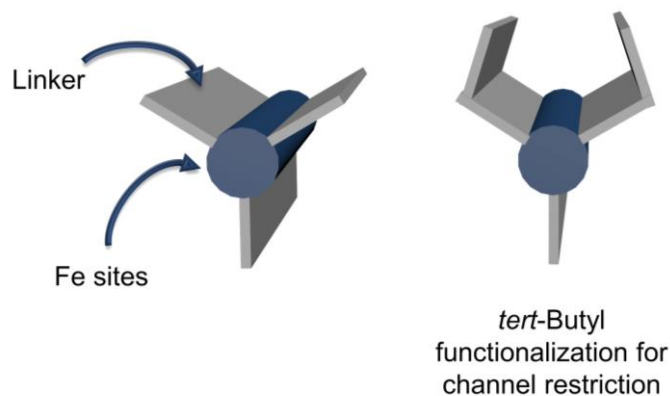


Figure 17: Schematic representation of the active Fe sites in  $\text{Fe}_2(\text{dotpdc})$  MOFs – non-functionalized (left) and functionalized with *tert*-butyl (right). The latter results in a more restricted channel.<sup>[78]</sup>

The potential of neighboring groups affecting the selectivity was highlighted in the different Fe containing frameworks  $\text{Fe}_2(\text{dobdc})$  ( $\text{dobdc} = 2,5\text{-dioxido-1,4-benzenedicarboxylate}$ ),  $\text{Fe}_2(\text{dobpdc})$  ( $\text{dobpdc} = 4,4'\text{-dihydroxy-[1,1'-biphenyl]-3,3'-dicarboxylic acid}$ ), and  $\text{Fe}_2(\text{dotpdc})$  ( $\text{dotpdc} = 4,4''\text{-dihydroxy-[1,1':4',1''-terphenyl]-3,3''-dicarboxylic acid}$ ). These can be distinguished by different pore sizes affecting diffusion and catalyst stability in the cyclohexane oxidation.<sup>[78]</sup> However, significant importance of neighboring groups on the catalytic performance was revealed by integrating -H, -F, - $\text{CH}_3$  and - $^t\text{Bu}$  (*tert*-butyl) functionalities to  $\text{Fe}_2(\text{dotpdc})$ . With non-polar functionalities (e.g. - $^t\text{Bu}$ ) the conversion and alcohol selectivity were significantly enhanced caused by more pronounced channel restriction towards the catalytically active Fe sites (Figure 17). Simultaneously, van der Waals interactions between - $^t\text{Bu}$  and the substrate likely support the direction of the substrate to Fe increasing the local cyclohexane concentration at the active sites. In addition to the positive impacts on conversion and selectivity upon - $^t\text{Bu}$  functionalization, the latter increase the Fe site stability – underlining the advantages of neighboring groups close to active sites provided by the high tailorability of MOFs.

### Influence of topology and alignment of active sites

The topology is an intrinsic property of MOFs determined by its structure upon building block combination. Thus, different topologies result in varied pore shapes and sizes, e.g., triangular versus cubic pores. This allows for the study of confinement effects since by topology active sites are located in a specific environment with a predetermined distance towards each other. In contrast to previous sections with only one catalytically active site in the pore, the topology effects on catalysis imply the importance of inter-active site distances and their alignment.



A Co(salen) MOF is presented as an example where the proximity of the Co sites allows for cooperative interactions between the Co centers and thus both substrates are activated simultaneously.<sup>[79]</sup> This enhances the activity and enantioselectivity in the hydrolytic kinetic resolution in the MOF catalyzed reaction compared to the homogeneous counterpart.

Similarly, a close contact between the Zn-nodes and the catalytic site of the linker in a Zn-BCTA-MOF (BCTA = bis[4-(5-carboxy-2-thienyl)-phenyl](4-carboxyphenyl)amine) is assumed to increase the efficiency in the photocatalytic alkene sulfonylation and cyclization by simultaneous substrate fixation and its activation. The latter is possibly due to the two-fold interpenetration of the framework decreasing the inter-active site distance. Moreover, the diastereoselectivity was enhanced compared to the homogeneous system – highlighting the possibility of selectivity control by the confined environment in MOFs.<sup>[80]</sup>

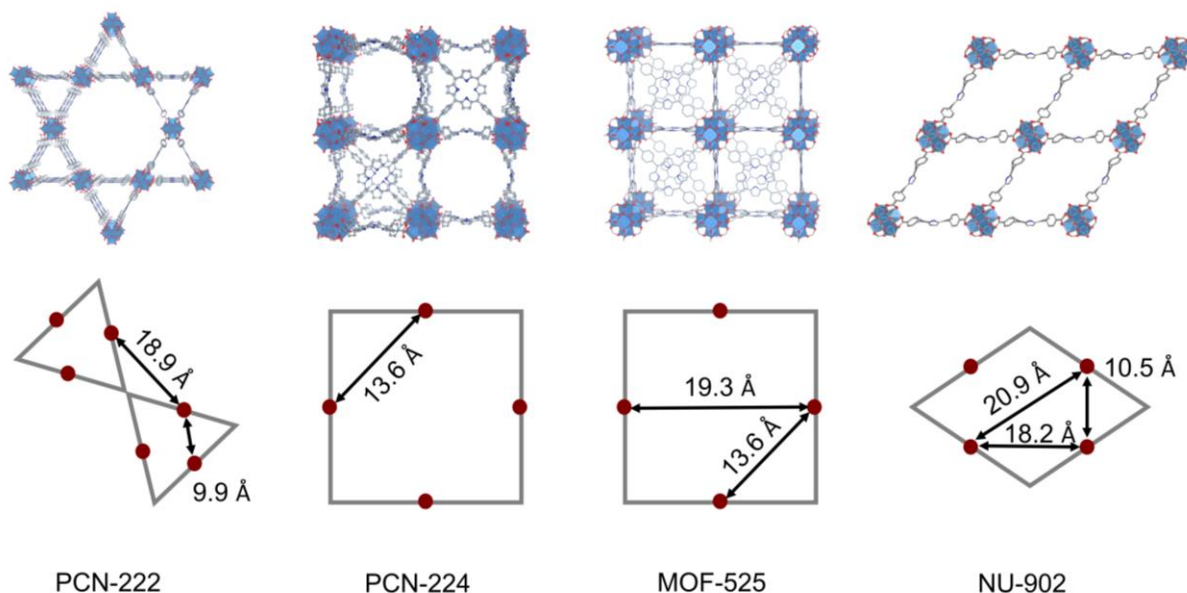


Figure 18: Representation of the different crystal structures of PCN-222, PCN-224, MOF-525 and NU-902 (top). The bottom shows the respective pore structures. The red dots represent the porphyrin core (which could be a metal). Additionally, the interactive site distances, i.e. distances between the porphyrin cores, are depicted which were taken from Ref <sup>[81]</sup> and <sup>[82]</sup>.

A predestined subclass of MOFs for performance control by confinement effects are porphyrin-based MOFs. By using the same building units (Zr-oxo metal nodes and porphyrin linkers) but altering their connection and structural alignment different topologies are accessible (Figure 18).<sup>[82]</sup> Synthetically, this is accomplished by changing the reaction conditions which will be described in more detail in chapter 1.4.1. The influence of active site distances was studied by Deng *et al.* applying such topologically different frameworks (PCN-221, PCN-222, PCN-223, PCN-224, MOF-525 and Al-PMOF, all constructed from the same building units) in the photocatalytic dehydrogenation of tetrahydroquinoline.<sup>[82]</sup> Here, a linear dependency of the catalytic activity on the active site distance was elucidated since a closer contact of active porphyrins resulted in an enhanced activity.

The importance of close active site contacts for activity augmentation was confirmed in an In-TBP MOF (TBP = tetrakis(4-benzoic acid)porphyrinato). Here, twofold interpenetration of the framework resulted in a shorter distance between the parallel aligned active Co sites (located in the porphyrin core) which allows for cooperative substrate activation and thus an increased activity. Moreover, the restricted space between two Co sites excludes the conversion of some substrates, namely meta-substituted aromatic alkynes due to the different steric demand.<sup>[67]</sup>

Similarly, reaction environment restriction for selectivity control was applied in an Ir-metalated porphyrin MOF where the catalytically active Ir-porphyrin ligands define a molecular nanoreactor. Reactant diffusion was facilitated by larger pores next to the nanoreactor. This design strategy allowed for chemoselectivity control in the carbenoid insertion into Si-H bonds – favoring primary silanes. Contrary, in the homogeneous analogue the highest reactivity was observed for tertiary silanes.<sup>[83]</sup>

A fascinating result of confinement effects is the potential of inducing stereoselectivity by the MOF without any intrinsic stereoinformation present (e.g. chiral auxiliaries/ligands).<sup>[84–88]</sup> This stereoselectivity is assumed to arise from specific substrate alignment close to the active center – resembling enzymatic pockets. In MIL-101(Cr) Pd nanoparticles were encapsulated acting as multi-step catalyst with Cr(III) catalyzing citronellal cyclization and Pd responsible for the hydrogenation step. Here, a diastereoselectivity of 81% towards (–)-menthol was observed.<sup>[84]</sup> An increased diastereoselectivity was also apparent in styrene cyclopropanation with HKUST-1 as catalyst resulting in 71% *trans* isomer.<sup>[85]</sup> MOF-808 applied in estradiol synthesis achieved a 40:60 (*alpha:beta*) diastereoselectivity which is ascribed to the confined porous environment.<sup>[86]</sup> Diastereoselectivity control by pore confinement was also addressed in the styrene cyclopropanation comparing different Rh-porphyrin-based Zr-MOFs (PCN-222(Rh) and PCN-224(Rh)). Importantly, specific styrene functionalization drastically enhanced the *trans*-selectivity. This is assumed to arise from coordination of these functional (amino- and hydroxy) groups to neighboring Rh sites (in the same pore) resulting in a specific alignment of the substrate close the catalytically active site favoring the transition state towards the *trans*-product. Further diastereoselectivity enhancement was observed upon decreasing the Rh-Rh distance by changing the MOF topology – from PCN-224 to PCN-222. The Kagomé topology of the latter shows short Rh distances of ~10 Å in the triangular pores which is in accordance to the length of a Rh-carbene and amino-functionalized styrene substrate coordinated to a neighboring Rh site.<sup>[87]</sup>

In another series of topologically different porphyrin-based MOFs (PCN-222, NU-902 and MOF-525), Zn was incorporated into the porphyrin core and subsequently applied in the acyl transfer catalysis with pyridylcarbinols (PC).<sup>[81]</sup> Here, an impact of orientation in the MOFs on the preconcentration (affected by the single porphyrin site number per volume) and substrate alignment (influenced by porphyrin pair number per MOF volume) and therefore the activity was discernible. DFT calculation confirmed the importance of substrate orientation which is affected by the different topologies and thus Zn-porphyrin alignments favoring transition state formation. This study emphasizes the effect of active site density and location to enhance catalytic activities by precise substrate coordination and is a key example where the significance of neighboring groups for substrate alignment and network topology are combined.

Concluding, this chapter on confinement effects accentuates the potential of exploiting such effects in MOFs to control catalytic performances but simultaneously underlines the importance of understanding underlying reasons for observed behaviors. The latter will allow for the custom design of reaction spaces in porous catalysts with specific substrate – catalyst interactions for the control of desired properties.

### 1.3.3. Multifunctionality in MOF Catalysis

The large design space provided by MOFs is extremely appealing in terms of introducing multifunctionality in MOFs – accomplished amongst others with the above-described techniques. Several combinations of multifunctionality are imaginable, e.g., OMS and linker functionalities, OMS and metal catalysts, two molecular catalysts, NP with node, linker or molecular catalyst. In theory, the type of possible combinations is unlimited – however, restricted by the synthetic feasibility. For catalysis, multifunctionality allows for two key applications: 1) exploiting multifunctionality for synergistic effects in catalysis and 2) the catalysis of coupled catalytic transformations, e.g., tandem or cascade reactions (Figure 19). Both approaches will be discussed in the following with selected examples from the high number of publications on both applications.

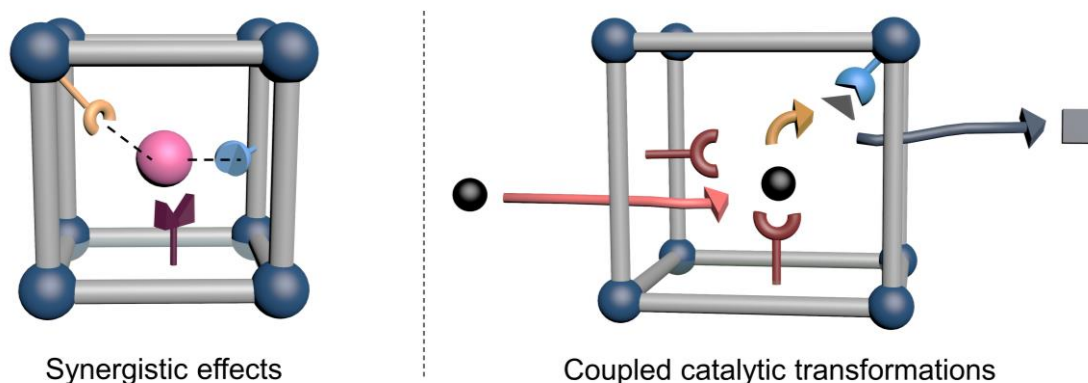


Figure 19: Conceptual illustration of synergistic effects and the catalysis of coupled transformations within one multifunctional MOF material. Left: the substrate (pink) is converted by one center (red) in synergy with further functionalities. Right: The substrate (black) is converted by the first active center (red) and subsequently by a second active site (blue) to result in the final product.

### Synergistic effects

Synergistic effects in multifunctional MOFs have been demonstrated in numerous literature reports.<sup>[28,61]</sup> A typical and probably the most prominent example is the combination of acid and base functionalities, e.g. Lewis acidic MOF nodes and amino groups at the linker. UiO-66-NH<sub>2</sub> with Lewis acidic Zr<sup>4+</sup> and basic amino groups was studied in this regard – where the proximity of both sites resulted in increased kinetics and higher selectivities of a cross-aldol condensation.<sup>[89]</sup> Moreover, ZIF-8, containing Lewis acidic Zn<sup>2+</sup> and basic imidazole groups, showed high activity in the transesterification of triglycerides and CO<sub>2</sub> cycloaddition of styrene.<sup>[90]</sup> For the latter reaction, the presence of both Lewis acidic and basic sites is beneficial since usually a Lewis-basic co-catalyst is added which could be prevented by its direct integration into the MOF matrix. This was exemplarily reported for imidazolium based ionic liquids incorporated into UiO-66 or PCN-222(Mn).<sup>[91,92]</sup> Furthermore, defect engineering can promote synergistic effects in catalysis which was shown for HKUST-1 enhancing the activity in the click reaction of azide-alkyne cycloaddition.<sup>[93]</sup> Other reaction examples of synergistic effects in MOFs are the cyanosilylation, Suzuki-Miyaura or Sonogashira coupling or Knoevenagel condensation resulting from synergy between acid/base, two metals or metal catalysts with intrinsic MOF building units.<sup>[28,61,94]</sup>

## Multifunctionality for coupled catalytic transformations

Before focussing on example reactions in multifunctional MOFs different terms for coupled catalytic transformations catalysis are defined in the following. In “tandem catalysis” all catalysts (or their precursors) are present from the beginning. Another prerequisite is the existence of at least two different catalytic mechanisms. Further differentiation of tandem catalysis into orthogonal catalysis, auto-tandem or assisted-tandem catalysis is possible depending on the amount of catalysts and if a trigger is necessary to start the reaction.<sup>[95]</sup>

Further types of multifunctional (one-pot) catalytic reactions such as “cooperative”, “relay” or “sequential” catalysis are classified in literature. In cooperative catalysis interactions between two catalytic cycles are necessary. While in relay catalysis both catalysts are present from the onset, delayed addition of the second catalyst is required in sequential catalysis.<sup>[96]</sup> Note that the term “cascade” catalysis is often equal to “tandem” catalysis.

In general, several reaction combinations were successfully applied with multifunctional MOFs as catalysts e.g., oxidation/hydrogenation, oxidation/esterification, epoxidation/rearrangement, deacetalization/Knoevenagel condensation, isomerization/hydrogenation. Multifunctionality for those reactions is accomplished by combination of acidic and basic sites, acid or base with metal NPs or base and metal complexes.<sup>[97]</sup> Noteworthy, and crucial for this Thesis, the incorporation of two molecular catalysts and their concentration and ratio control is still limited in literature. Literature reports include the incorporation of a Au – and a Pd complex in UiO-67 for alkyne hydration/Suzuki coupling or integration of two different metalloporphyrins or metallosalen catalysts, respectively, in a MOF for epoxidation/CO<sub>2</sub> cycloaddition.<sup>[98,99]</sup> Very recently, the incorporation of both a molecular Co- and a Re-catalyst was presented in NU-1000 for photocatalytic CO<sub>2</sub> reduction/hydrogen evolution.<sup>[47]</sup>

For future multifunctional catalyst design for coupled reactions, detailed studies are necessary to investigate compatibilities, and present strategies for straightforward catalyst integration – which seems to be restricted for the combination of molecular catalysts. In an ideal case, such synthesis strategies are adjustable “on-demand” and transferrable to a large variety of molecular catalysts enabling the catalysis of several tandems or cascades – which is still in its infancy in literature.

## 1.4. Porphyrin-based Zr-MOFs – From Opportunities to Challenges and vice versa

The great advantages of porphyrin-based Zr-MOF systems were accentuated in previous chapters. Combining the possibility of integrating various metals into the porphyrin core, the high chemical and thermal stability of Zr-MOFs and the numerous modification opportunities of both building units allow for great flexibility in multifunctional catalyst design.<sup>[100–102]</sup> Intriguingly, the accessibility of different topologies from the same building units described above is extremely beneficial for confinement effect studies, in particular since all three confinement categories can be met in those MOFs (see chapter 1.3.2.). Combination of  $Zr_6$ -oxo nodes and the tetratopic porphyrin linker TCPPH<sub>2</sub> (5,10,15,20-tetrakis(4-carboxyphenyl)porphyrin) results in at least six topologically different MOFs: MOF-525, PCN-222, PCN-223, PCN-224, PCN-225 and NU-902 (Figure 20). The different topologies arise from deviations in linker conformation and node connectivity. The highest connectivity of the Zr node with a value of 12 is present in MOF-525 (**ftw** topology) and PCN-223 (**shp** topology). In PCN-222 (often called MOF-545, **csq** topology), PCN-225 (**sqc**) and NU-902 (**scu**) the node is 8-connected. The lowest connectivity is observed for PCN-224 (**she**) where only 6 linkers are coordinated to the node – leaving six coordinatively unsaturated sites.<sup>[103]</sup>

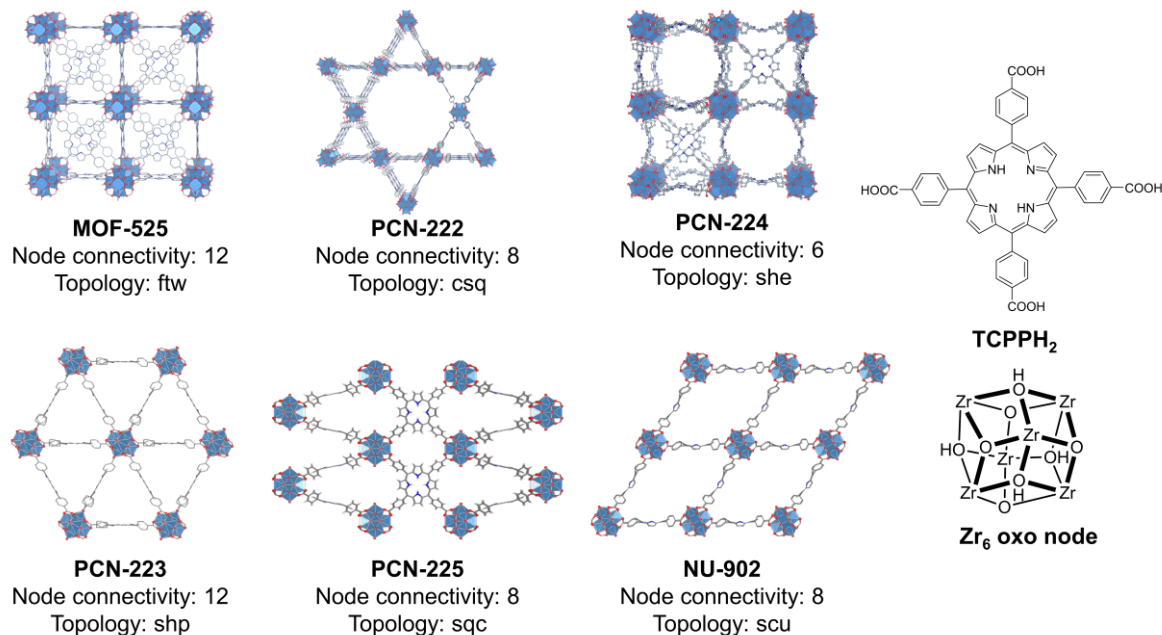


Figure 20: Overview of different structures of porphyrin-based Zr-MOFs (MOF-525, PCN-222, PCN-224, PCN-223, PCN-225 and NU-902) built from the same porphyrin linker (TCPPH<sub>2</sub>) and a  $Zr_6$  oxo node. Additionally, node connectivity and topologies are represented. The Figure was adapted from Ref <sup>[103]</sup>.

### 1.4.1. Synthetic Challenges

However, this appealing feature of accessing several topologies from the same building blocks results in a major drawback and challenge: the synthesis of phase-pure, crystalline compounds. This problem is widely spread among researchers working with those porphyrin-based systems. In general, all six MOFs are synthesized under solvothermal conditions – however with subtle differences in reaction conditions or procedures. In general, stoichiometry, Zr source, acidic modulator, temperature, solvent and reaction time are variables altered in different synthesis approaches. Usually,  $\text{ZrCl}_4$  or  $\text{ZrOCl}_2 \cdot 8\text{H}_2\text{O}$  are used as Zr source. Importantly, modulators (monocarboxylic acids) seem to be crucial for successful synthesis. Although this synthesis problem is known, only a few papers focus on detailed synthesis investigations to elucidate parameters affecting the phase-purity of the solvothermal synthesis, discussed in the following.

#### Temperature effect

Farha *et al.* studied the effect of temperature variation on the resulting polymorph formation with the result that MOF-525 and PCN-224 are kinetic products while PCN-222 is thermodynamically favored. Thus, by precise temperature adjustment, polymorph control was possible.<sup>[103]</sup> The hypothesis of MOF-525 as the kinetically favored product is in accordance with a high-throughput synthesis study presented by Harris *et al.* and findings of Deng *et al.*<sup>[82,104]</sup>

#### Modulator effect

Simultaneously, the hypothesis of a crucial role of the modulator emerged. In a comprehensive study, Morris *et al.* varied the acidity and concentration of the modulator for the synthesis – studying impacts on crystallinity and selectivity.<sup>[105]</sup> Regarding crystallinity, for low modulator concentrations ([Mod/Linker] low) the crystallinity is significantly decreased leading to amorphous products – emphasizing the importance of the modulation approach described in chapter 1.3.1. Too high modulator concentrations, however, prevented MOF formation, thus, leaving a finite range of suitable modulator concentrations ([Mod/Linker]; 1000 – 3000 equiv. for weakly acidic modulators, 500 – 1000 equiv. for strong acids). Addressing the modulator effect on polymorph selectivity, strongly acidic modulators result in very high [Mod/Linker<sup>4-</sup>] enhancing the deprotonated species concentration. At the same time, the acid-base equilibrium is shifted – leading to an enhanced concentration of protonated ligand and thus lowering [Linker<sup>4-</sup>]. Thus, the modulator is preferentially incorporated which in turn results in the growth of the most stable clusters (since labile ones dissolve preventing cluster growth) and therefore the most stable/thermodynamically favored polymorph, which is PCN-222.

Note that since only completely deprotonated modulator and ligand species are responsible for MOF formation, in the following the ratio of deprotonated species will be used for description. For intermediately strong acids PCN-223 was obtained as the major product. Since for lower  $[\text{Mod}^{\ominus}/\text{Linker}^{4\ominus}]$  crystal growth is expected to proceed faster, kinetically favored products are synthesized (i.e., PCN-223). Low  $[\text{Mod}^{\ominus}/\text{Linker}^{4\ominus}]$  concentrations resulting from weakly acidic modulators lead to the formation of MOF-525 – assumed as the least stable polymorph and thus favored by kinetics. The observations on thermodynamic versus kinetic products (PCN-222 vs. MOF-525) are in line with hypotheses from temperature variation studies above. Similar results were found in a comparative study presented by Deng *et al.*: with a general low acidity, PCN-221 and PCN-223 (both 12-connected, energetically demanding) were formed while PCN-222 was obtained upon increasing acid concentrations.<sup>[82]</sup>

### **Possible reasons for phase-mixtures and synthesis challenges**

In particular the synthesis of MOF-525 as the kinetically favored product has emerged as a major challenge. From a structural perspective, in the 12 connected topology of MOF-525 the carboxylate groups of the TCPPh<sub>2</sub> linkers need to adopt a coplanar arrangement with the porphyrin macrocycle. This results in a highly symmetric but extremely energetically demanding conformation.<sup>[106]</sup>

Additionally, Zr-based MOFs were reported as very tolerant towards defects.<sup>[33,82,105,107,108]</sup> This is of particular importance for MOF-525. While hypotheses on phase formation are mainly conform in literature, discrepancies regarding defect formation are given. While almost no defects were present in MOF-525 synthesized in the approach presented by Harris *et al.*,<sup>[104]</sup> both Deng *et al.* and Morris *et al.* agree on an extremely high defect tolerance with linker deficiencies up to 50%.<sup>[82,105]</sup> High defect concentrations were also elucidated for PCN-222 (~25% of missing linkers per cluster, 2 out of 8). In contrast, PCN-223 was less defective with only ~10% of missing linkers (1 out of 12).<sup>[105]</sup> In general, modulators, specifically their acidity and concentration, were shown to have a crucial effect on the defect presence.<sup>[82,105]</sup> Exemplarily, high concentrations of strongly acidic modulators result in high defect incorporations due to the favored coordination to the node compared to the linker.<sup>[105]</sup> Here it is important to note that the characterization of defects and in particular their identification (e.g. missing node or missing linker defects) remains challenging.<sup>[33]</sup>

Another important aspect for the MOF formation, often neglected however, is the water content in the synthesis. It is assumed that the association/dissociation equilibrium during nucleation is – in addition to the modulator – also affected by water. Noteworthy, the modulator acidity is solvent dependent and thus varied upon water addition.<sup>[109]</sup> Water is either intrinsically provided by the Zr source ( $\text{ZrOCl}_2 \cdot 8\text{H}_2\text{O}$ ) or present in the solvent. Thus, the choice of a suitable Zr precursor is key.



This was intensively studied by Lotsch *et al.* for the formation of disordered PCN-224 (dPCN-224) elucidating different stages during the MOF formation (organic product → metal-organic intermediate → metal-organic intermediate microrods → nucleation → growth → single crystal).<sup>[110]</sup> The results indicate that water is essential for the  $Zr_6O_4(OH)_4$  cluster formation since for a reaction with neat  $ZrCl_4$  no dPCN-224 was received. Simultaneously, an effect of water on the reaction kinetics was revealed showing faster dPCN-224 formation with more water. Moreover, PCN-222 occurred as side product. Thus, since water is in general required for the Zr-MOF formation but subtle deviations in water content could result in the formation of an undesired polymorph, precise adjustment of water contents is essential. From a more critical point of view, determining the water content and including the respective values in the synthesis protocol might allow for an increased reproducibility which is currently rarely practiced in literature.

For an increase in reproducibility and to enhance the success rate of phase-pure MOF synthesis, the addition of nucleation seeds has emerged as a helpful tool. This was shown for PCN-222, PCN-224(Ni) and PCN-225 and is a rather straightforward approach – however with the prerequisite of having phase-pure seeds at hand.<sup>[111]</sup>

In MOF catalysis, crystal sizes can impact the catalytic performance.<sup>[44]</sup> Since the crystal sizes of porphyrin-based systems obtained by the classical synthesis approaches are usually on a macroscale decreasing the size to the nanoscale was investigated by high-throughput experiments. These revealed significant deviations of synthetic protocols from the “classical” ones and the importance of acidic concentrations.<sup>[104]</sup>

Due to their inherent properties described above, applying porphyrin-based Zr-MOFs in catalysis is highly attractive – in particular the integration of multifunctionality or directing substrate – catalyst interactions. However, for the elucidation of such interactions and their precise tuning a detailed knowledge on the MOF structure is key. Therefore, in-depth characterization is necessary to access linker conformations or node composition. The latter was recently revisited for PCN-221, which was originally reported to consist of  $Zr_8O_6$  clusters. Contrary, precise, sophisticated characterization revealed the presence of four disordered  $Zr_6O_4(OH)_4$  clusters in the PCN-221 structure. Due to the structural similarities and high linker deficiencies of about 50% compared to PCN-224, PCN-221 is described as disordered PCN-224(dPCN-224).<sup>[107]</sup> Concluding, such studies are of extreme importance and will pave the way for designing specific structure – property relations.

The different factors summarized above emphasize the challenges faced in porphyrin-based Zr-MOF synthesis and show that detailed synthesis procedures and characterizations are essential for this MOF subclass. In future research, this could increase reliability and reproducibility of the different MOFs in high purity and crystallinity and thus allow for further applications of these materials – also beyond catalysis.

### 1.4.2. Catalytic Applications – the Porphyrin Motif

In recent chapters, various applications and properties of porphyrins were mentioned. In addition to the high stability and node tunability of Zr-MOFs, here, the advantages of using porphyrin linkers in MOF design are highlighted, which will be important for the following Thesis.

Beside the intrinsic catalytic activity of the Zr node or the role of the MOF as the host for catalyst immobilization, the catalytically most fascinating active center is the metal in the porphyrin core. As described above – several metals can be integrated possessing catalytic activity. Exemplarily, Mn, Ru or Fe are able to catalyze oxidation reactions, Zn or Co are known for CO<sub>2</sub> cycloadditions, Co or Ni for CO<sub>2</sub> reduction or Cu for esterifications (Figure 21).<sup>[112,113,114]</sup> Since the porphyrin motif is present in different natural systems such as chlorophyll or heme (in cytochrome P450), the design of biomimetic materials with porphyrins is feasible.<sup>[115]</sup>

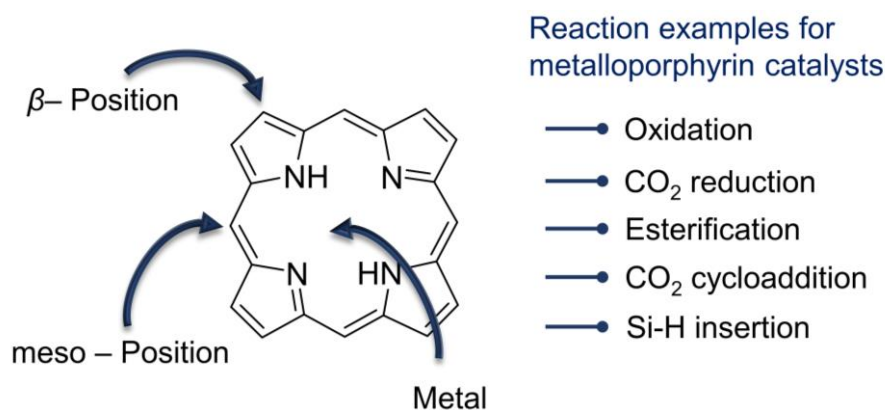


Figure 21: Functionalization positions of the porphyrin macrocycle and examples of catalytic applications of metalloporphyrins.

Moreover, the porphyrin macrocycle allows for several functionalizations at the core and periphery and thus, large design flexibility. Substitution is either possible at the  $\beta$ - or meso-position (Figure 21).<sup>[115]</sup> The latter is functionalized with carboxyphenyl moieties in the porphyrin MOF examples described in this chapter, enabling the coordination of the carboxylate groups to the Zr node.

This porphyrin functionalization results in more structural diversity on one side but also affects the catalytic properties of the metal in the porphyrin core which was shown for MOF integrated Fe-porphyrin systems functionalized with halides or an alkyl group at the  $\beta$ -position.<sup>[116,117]</sup>

Summarized, the intrinsic beneficial properties of porphyrins combined with the large design flexibility is extremely appealing for the fabrication of multifunctional, enzyme inspired MOF catalysts. Moreover, the accessibility of different topologies from the same building units allows for the study of confinement effects in MOF catalysis since the catalytically active metalloporphyrins have a defined location in the structure.

## 1.5. Principles of Catalysis

During the last decades catalysis emerged as one of the most important “tools” for reaction improvement. Inspired by the natural catalysis in enzymes, several synthetic catalysts were reported for a large number of applications. Catalysts are defined as substances accelerating a reaction, i.e., increasing the rate of reaching an equilibrium – in theory without being consumed. In practice, catalyst poisoning or catalyst decomposition can indeed result in catalyst “consumption”. Importantly, thermodynamics remain unaffected by the catalyst. Catalysis is extremely advantageous from an economic point of view, saving energy and resources.<sup>[118–120]</sup>

In general, two major types of catalysis can be classified, namely homogeneous and heterogeneous catalysis. In homogeneous catalysis the catalyst structure and mechanism are usually known achieving high selectivities under mild conditions where diffusion limitations are typically absent. In contrast, in heterogeneous catalysis the active site structure is often unknown and mechanism determination more challenging. Usually, harsh reaction conditions are applied. Catalyst deactivation by poisoning or diffusion limitations are factors which need to be considered in heterogeneous systems. Although the large number of drawbacks of the latter compared to homogeneous systems, the potential of catalyst separation and recycling is extremely beneficial for heterogeneous catalysts.<sup>[118,120]</sup>

In the following, standard concepts and characteristic parameters in catalysis are defined to provide a general understanding necessary for the evaluation of the presented values and results. For catalytic performance investigations, the activity, selectivity and stability of the catalyst are investigated. The activity describes the rate of the reaction with the typical values: conversion, space-time-yield (STY), turnover number (TON), turnover frequency (TOF). The conversion (C or X) refers to one reactant (usually the limiting component) and defines the ratio of reactants converted ( $n_{i0} - n_i$ ) versus the starting amount of reactant ( $n_{i0}$ ; both in mol).

$$C_i = \frac{n_{i0} - n_i}{n_{i0}} = \frac{\text{amount of substance converted}}{\text{initial amount of substance}}$$

The STY is a typical value in heterogeneous catalysis in reactors and describes the amount of product formed ( $m_{product}$ ) per time ( $t$ ) and volumetric unit in the reactor ( $V_R$ ).

$$STY = \frac{m_{product}}{V_R \cdot t}$$

The ratio of converted reactant ( $n_{\text{substrate converted}}$ ) and amount of catalyst ( $n_{\text{catalyst}}$ , i.e. active sites, both in mol) represents the TON while the TON per time unit ( $t$ , usually seconds) is determined as TOF ([1/s]). Note that for catalytic processes a TON > 1 is required. While in homogeneous and enzymatic catalysis the number of active sites equals the molar amount of catalyst, the determination of active sites is required in heterogeneous catalysis accomplished by the dispersion.<sup>[118,120]</sup>

$$TON = \frac{n_{\text{substrate converted}}}{n_{\text{catalyst}}}$$

$$TOF = \frac{TON}{t}$$

The yield (Y) describes the ratio of formed amount of a product ( $n_{\text{product, formed}}$ ) and the maximum amount of product possible ( $n_{\text{product max.}}$ ). For the selectivity (S), the ratio of formed product and converted reactant (both in mol) is calculated. Following relation between conversion, yield and selectivity can be deduced: The selectivity is the quotient of yield and conversion (yield/conversion). In general, different types of selectivities are described for catalytic reactions, e.g., chemo-, regio-, diastereo- and enantioselectivity. Since of particular importance for this Thesis, the diastereoselectivity is important for reactions where two diastereomers are formed and describes which diastereomer is the favored product.<sup>[120]</sup>

$$Y = \frac{n_{\text{product, formed}} *}{n_{\text{product max.}}}$$

$$S = \frac{n_{\text{product, formed}} *}{n_{\text{reactant, converted}}}$$

$$S = \frac{Y}{C}$$

\*Note that stoichiometric coefficients need to be considered.

A crucial consideration in catalysis is the catalyst stability, since usually the catalytic performance is decreased with enhanced reaction time – requiring catalyst replacement at some point. Additionally, several factors can decrease the catalyst lifetime/stability, e.g., high temperatures, catalyst poisoning, leaching or aggregation. Thus, stability tests under reaction conditions are essential to evaluate the compatibility of the catalyst and the process conditions.<sup>[121]</sup>

## 2. Motivation and Research Questions

Multifunctionality in porous material catalysis emerged as an important feature for the design of biomimetic systems. Resembling catalytic pockets in enzymes, the precise tuning of reaction environments is highly desirable to allow for high efficiencies and excellent selectivities – close to enzymes. Therefore, a material platform is necessary, which meets the requirements for such studies. As described in detail in chapter 1, all these properties are combined in MOFs which possess a tremendous design flexibility allowing for the precise tuning of (intrinsic) catalytic properties and the integration of several catalytic species in a confined space. Due to the immense advantages of systems containing porphyrins – a motif known from nature – that were discussed above (chapter 1.4.2.), this subclass of MOFs with the focus on metalloporphyrins is targeted in this Thesis for the design of multifunctional catalysts with the potential of performance control. The latter was recently shown for porphyrin MOFs with different topologies where the latter is assumed to affect the activity and selectivity in catalysis. While this presents the conceptual appeal of these systems, from a synthetic point of view challenges in the porphyrin MOF synthesis are anticipated according to previous literature (chapter 1.4.1.). Thus, key research questions arise from a synthetic perspective towards the design of metalloporphyrin-based MOF catalysts:

*“Is the synthesis of topologically different (metallo-) porphyrin-based Zr-MOFs possible in high phase-purity and crystallinity – allowing for topology effect studies? Can we present a strategy for the integration of different catalytically active metals into the porphyrin core and their integration into a MOF?”*

Successful integration of metalloporphyrins in different MOF structures would present a “bifunctional” system considering the metalloporphyrin and the Zr node. However, this could serve as an ideal platform to expand this concept of multifunctionality integration possible by the tailorability of MOFs and the large quantity of further MOF functionalization and catalyst incorporation presented in chapter 1.3.1. Thus, the incorporation of two different metalloporphyrins, linker functionalization and catalyst anchoring are imaginable, augmenting the scope of such multifunctional materials in catalysis – leading to the following question:

*“Can we expand the metalloporphyrin integration and incorporate two different metalloporphyrins in one framework – with free choice of metal combination and ratio? Is it possible to use different design strategies to embed various types of catalysts (e.g., by node or linker anchoring; as a framework building block or directed into the pores)?”*

With such multifunctional systems at hand studies towards confinement effects reminiscent of enzyme systems are possible. As described in chapter 1.3.2, different types of confinement are possible, i.e., pore size and neighboring group effects or the alignment of active sites (which can result from different topologies). Since topologically different porphyrin-based systems with integrated catalytic functions could possess all three types of confinement, detailed studies are necessary to i) find potential effects of the confined reaction environment on the catalytic performance and ii) elucidate underlying principles and the origin of the potentially improved performance in the confined MOF space. Insights in previous studies indicated the importance of such confined spaces in two porphyrin MOFs with different inter-active site distances significantly improving the selectivity, however, require further understanding. Thus, following questions arise:

*Can we build on the previously described selectivity enhancement by confinement effects and identify the origin of the observed behavior? Is it possible to transfer this concept of confinement effects and the impact of topology to different MOF catalyst systems – e.g., with catalytic functionalities directing into the MOF pore?*

Gaining insights on the origin of performance variations and underlying principles in confined spaces is crucial to transfer these concepts to other materials. This will allow for the precise design of confined reaction environments or secondary interactions, which enable the control of performances. This is of particular importance for applications desiring a specific stereoselectivity which is usually accompanied with demanding synthetic or purification strategies.

Beside the study of confinement effects for catalytic performance control, the designed multifunctionality would allow for the investigation of coupled reactions performed within one catalyst. From a conceptual perspective, this is an attractive approach – preventing work-up between the reactions but more importantly exploiting the tailorability offered by MOFs to integrate specific functionalities for desired, sophisticated purposes. Although some multifunctional MOFs for such combined reaction sequences were reported, in particular the integration of two molecular catalysts is still in an early stage – indicating synthetic challenges. This gives rise to following questions:

*Can we use the designed multifunctional MOF catalysts in combined reaction sequences – studied by a proof-of-concept reaction? Can the performance be tuned by changes in material synthesis, e.g., catalyst combination or ratios?*

These combined reaction catalysis studies as proof-of-concepts with the tailor-made multifunctional catalysts – and in particular the variation of catalyst combination and ratio – would allow for the evaluation, if the presented design strategies are suitable for such purposes. This could enable the transfer of this concept to several reaction combinations. Therefore, this Thesis shall present key advances in multifunctionality and confined environment design in metal-organic framework catalysts for sophisticated applications.

In Figure 22, the workflow and complexity of the different studies presented in this Thesis is depicted. A crucial point is the feedback loop which enables the implementation of the learnings from the different projects by using this knowledge e.g., for variations in material synthesis which in turn can affect the catalytic performance.

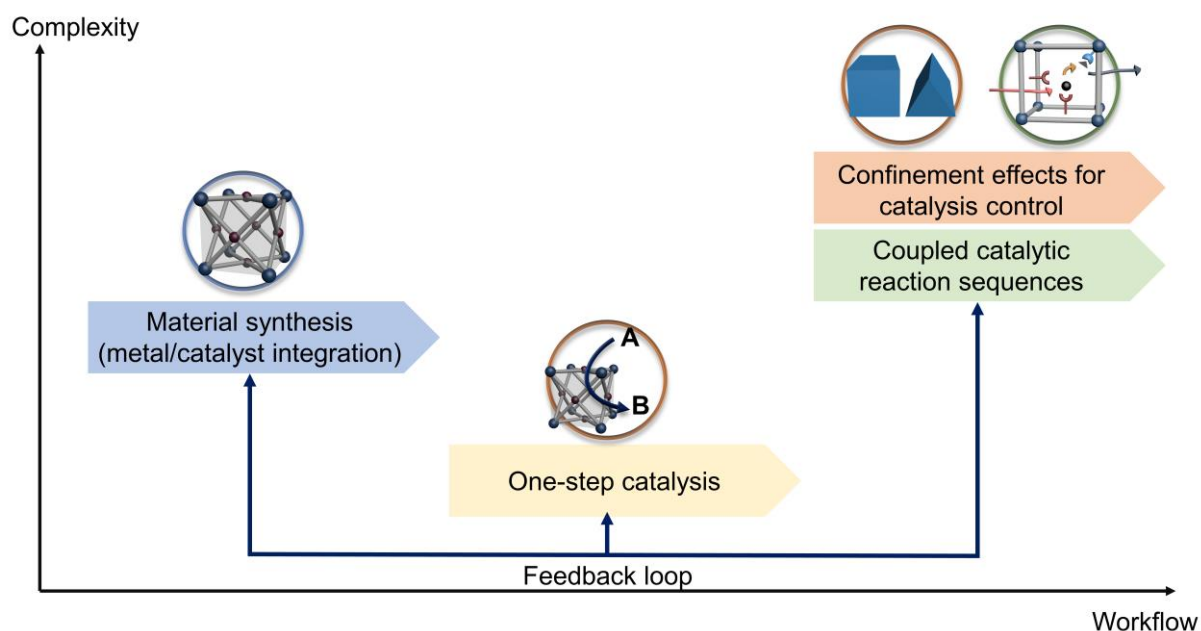


Figure 22: Workflow and complexity of the different projects covered in this Thesis which include the material synthesis (incl. metalation and catalyst integration), one-step catalysis, confinement effect studies and the performance of coupled catalytic reaction sequences. A feedback loop between all these projects is necessary to allow for the implementation of the different learnings.



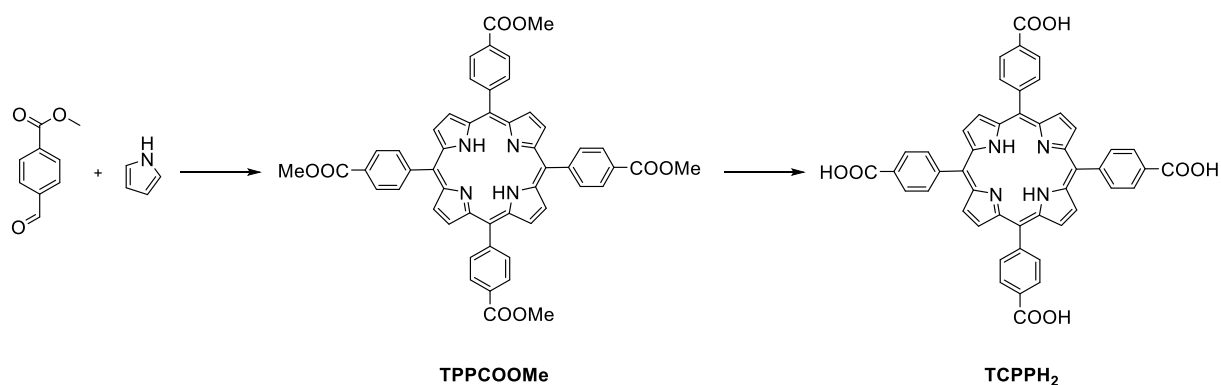
## 3. Results and Discussion

### 3.1. Synthetic Procedure Investigations

The following subchapters will describe synthetic procedures and investigations on influencing parameters for linker and MOF synthesis. For the latter, particular focus is placed on reaction conditions affecting phase-purity and high crystallinity of the material – essential for different applications. Additionally, the porphyrin metalation with a large variety of different metals will be discussed since several catalytic applications with the respective metals as active sites are targeted (see chapters 3.2.1.1 – 3.2.1.5).

#### 3.1.1. Porphyrin Linker

In general, all MOFs used in this Thesis were synthesized from the same linker: 5,10,15,20-tetrakis(4-carboxyphenyl)porphyrin (TCPPH<sub>2</sub>, see Scheme 1). This linking molecule was prepared by a literature known two-step synthesis refluxing pyrrole and methyl 4-formylbenzoate in propionic acid (Scheme 1, details see chapter 5.3.1.).<sup>[14]</sup> The resulting ester 5,10,15,20-tetrakis(4-methoxycarbonylphenyl)-porphyrin (TPPCOOMe) of purple color was converted to TCPPH<sub>2</sub> with blue color via a saponification procedure (details see chapter 5.3.1.).<sup>[14]</sup> The successful synthesis of both molecules was confirmed by <sup>1</sup>H NMR and UV-vis spectroscopy and elemental analysis where the analytic results match literature reports.<sup>[14,122]</sup> The resulting TCPPH<sub>2</sub> linker was applied for all following synthesis of porphyrin-based Zr-MOFs (PCN-222, PCN-224 and MOF-525). Note that the content of crystallized water was determined by elemental analysis (calculated with the program *Jasper* v1.0 (JavaScript Percentage Elemental Calculator)) and thus the amount of linker used as weigh-in for MOF synthesis adjusted accordingly.



Scheme 1: Synthesis of TCPPH<sub>2</sub> from methyl 4-formylbenzoate and pyrrole in propionic acid via TPPCOOMe.

### 3.1.2. MOFs

Over the course of this Thesis, the focus was placed on three porphyrin-based Zr-MOFs, namely PCN-222, PCN-224 and MOF-525. The three MOFs are built from the same building units where TCP<sub>2</sub> acts as linker and the node consists of a Zr<sub>6</sub> cluster with different connectivity (6 for PCN-224, 8 for PCN-222 and 12 for MOF-525, see Figure 20).<sup>[14,100,123]</sup> PCN-222 crystallizes in the space group *P6/mmm* with **csq** topology while PCN-224 has the space group *Im $\bar{3}m$*  and **she** topology.<sup>[14,100,123]</sup> The space group of MOF-525 is *Pm $\bar{3}m$*  with a **ftw** topology.<sup>[123]</sup> These three MOFs were selected according to their varied node connectivity and different pore shapes and sizes. While PCN-222 consists of trigonal and hexagonal pores (and pores between Zr nodes), the pores of PCN-224 and MOF-525 are cubic.<sup>[14,100,123]</sup>

#### 3.1.2.1. MOF Synthesis Investigations

For the synthesis of these porphyrin-based MOFs, different procedures have been published. However, several attempts following literature known procedures were unsuccessful either leading to no product precipitation or the formation of product mixtures which could not be purified afterwards (for PCN-222: <sup>[14]</sup>, <sup>[124]</sup>, <sup>[123]</sup>, <sup>[125]</sup>, <sup>[126]</sup>, <sup>[127]</sup>, <sup>[128]</sup>, <sup>[103]</sup>; PCN-224: <sup>[100]</sup>, <sup>[103]</sup>; MOF-525: <sup>[123]</sup>, <sup>[82]</sup>). The exact reason for the failure of the applied reported synthetic procedures could not be clarified over the course of laboratory work for this Thesis. Explanations for the lack in phase-purity presented in literature are described in chapter 1.4.1., which mainly results from the presence of identical building blocks and comparable synthetic protocols for different phases.<sup>[103,105]</sup> Due to these (and the above-described) challenges of phase-pure Zr-porphyrin MOF synthesis, the following syntheses will be described in more detail. In general, all three MOF structures were obtained under solvothermal conditions with the TCP<sub>2</sub> linker, a Zr source and a modulator, see Figure 23.

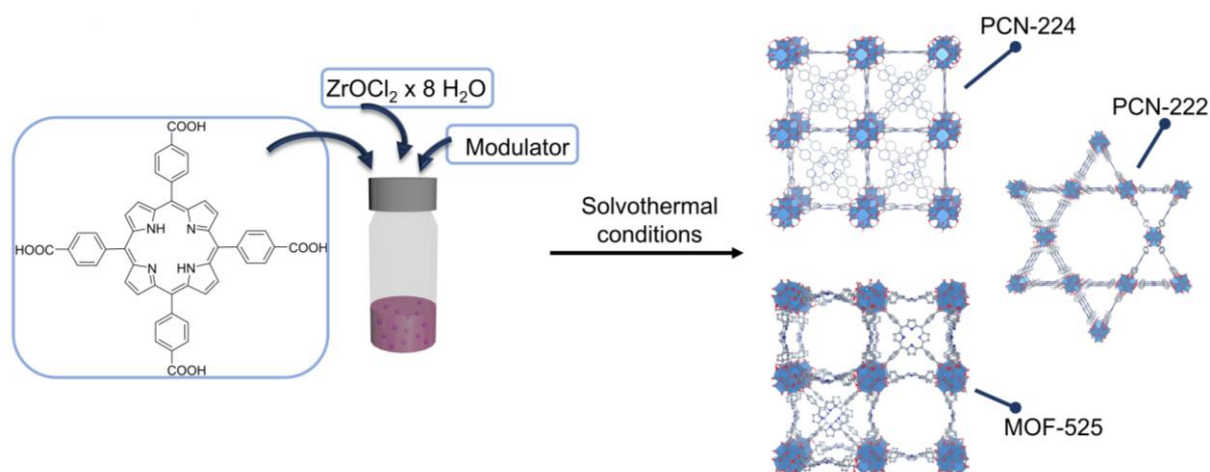


Figure 23: Schematic illustration of the general solvothermal synthesis procedure of the different porphyrin-based MOFs PCN-222, PCN-224 and MOF-525 from TCPPH<sub>2</sub>, ZrOCl<sub>2</sub> · 8H<sub>2</sub>O and a modulator.

Phase-pure products of PCN-222 and PCN-224 were obtained following a procedure from Deng *et al.* where the choice of modulator seems to have a significant impact on the phase-purity.<sup>[82]</sup> Here, for PCN-222 4-*tert*-butylbenzoic acid was applied in excess while for PCN-224 both 3,3-dimethylbutanoic acid and formic acid acted as modulators. In both cases, the Zr source was ZrOCl<sub>2</sub> · 8H<sub>2</sub>O. The solvothermal synthesis of both MOFs was performed similarly except for the amount of reactants and differences in solvent (*N,N*-diethyl formamide (DEF) for PCN-222 and *N,N*-dimethyl formamide (DMF) for PCN-224) and modulator. For both synthesis, 20 mL screw cap vials were used as reaction vessels. After addition of all reactants the suspension was ultrasonicated – however, without complete dissolution of all starting materials – and heated in an oven under identical conditions (temperature and time, without stirring). Further details on the synthesis are given in chapter 5.3.2. Interestingly, the different texture of the two MOFs was directly observable by eye after solvothermal synthesis. Here, for PCN-222 a very fine, purple precipitate was obtained (sticking to the walls of the reaction vessel) whereas the product of the PCN-224 synthesis was more large-grained (purple-brownish color) and could be easily removed from the reaction vial. Both MOF syntheses resulted in similar yields which are in general very low (approx. 20%). This probably results from the competing coordination between modulator and linker to the Zr node and competing formation of different phases. Since for the applications desired in this work purity is essential a low yield is accepted. The powder texture of both MOFs was unaltered after work-up (washing, solvent exchange, drying and activation – details see chapter 5.3.2). Interestingly, a tenfold scale-up of the syntheses was possible (changing the volume of the reaction vessel accordingly) yielding 80 – 100 mg instead of 8 – 10 mg per synthesis batch (Figure A 3).

Noteworthy, the positive impact of seed crystals on the phase-pure MOF synthesis has been described in literature which was also applied here in the synthesis of PCN-222 and PCN-224.<sup>[111]</sup> The seeds for both MOFs were obtained by previous syntheses and added after ultrasonication (before heating the MOF precursor solution in an oven). Seed addition resulted in an enhancement of the number of successful synthesis batches: without seed addition approximately 7 out of 10 batches resulted in the desired material whereas with seeds the number was increased to 10 out of 10 batches – however, with the prerequisite of obtaining phase-pure MOF seeds.

Additionally, the influence of water on the MOF synthesis was studied. The potential of water to significantly impact the MOF synthesis has been described recently.<sup>[110]</sup> In the study presented in this work, dried solvents were applied in the synthesis of PCN-222 and PCN-224 and specific volumes of water were added (the total liquid volume did not change). DMF was purchased in anhydrous form from *Sigma Aldrich* while DEF (*TCI*) was dried over molecular sieve for seven days. The MOFs were characterized by PXRD after synthesis to evaluate the impact of water on the crystallinity and phase-purity. For PCN-222 a solid material of high crystallinity and phase-purity was obtained when up to 1 vol% of water was added (Figure A 1). From 3 – 7 vol% the crystallinity of the product slightly decreased – however still achieving good results and pure PCN-222. Using 10 and 15 vol%, respectively, resulted in a material of insufficient crystallinity. The synthesis of PCN-224 was not affected by additional water of 0.1 – 3 vol% whereas higher water contents resulted in an amorphous product (Figure A 2). Thus, a small water content did not significantly influence the outcome of the applied synthetic method. Furthermore, the success of the synthesis was independent from the time the solvent bottle was opened, i.e. synthesis with solvent from a freshly opened bottle resulted in the same MOF compared to solvent from a bottle which was already opened for more than four weeks (this counts for both DMF and DEF). Again, while such details may appear benign, it's important to highlight for the reader that slight differences/inaccuracies in reporting protocols can significantly detrimentally impact MOF crystallinity and yields – as discussed in detail in chapter 1.4.1.

After MOF synthesis, PCN-222 and PCN-224 can be treated with HCl in DMF to remove the modulator from the node.<sup>[14,32]</sup> This step is not necessarily required since the modulator could also be exchanged by the addition of coordinating molecules to the synthesized MOFs and depends on the desired application. Note that it will be described in the respective chapter whether the MOF was treated with acid for modulator removal.

For MOF-525 a different MOF synthesis strategy was followed since other procedures (also the one described by Deng *et al.*) were not successful.<sup>[82,122]</sup> First, the Zr precursor ( $\text{ZrOCl}_2 \cdot 8\text{H}_2\text{O}$ ) was diluted in DMF while ultrasonicated for 30 min. As a reaction vessel, a Schott<sup>®</sup> bottle (100 mL) was used. Afterwards, the linker TCPPH<sub>2</sub> was added to the node solution and after further sonification also the modulator acetic acid. The solvothermal synthesis was performed in an oven yielding a purple, grained product (optically comparable to PCN-224).<sup>[129]</sup> Interestingly, over the course of this Thesis, obtaining MOF-525 with high crystallinity remained challenging which is shown in the PXRD pattern and N<sub>2</sub> sorption measurements indicating amorphous contributions (see chapter 3.1.2.2.). This again highlights the challenges faced in literature which is in the case of MOF-525 likely reinforced by the energetically demanding linker conformation of TCPPH<sub>2</sub> in MOF-525.<sup>[105]</sup>

In general, for each project (including metalation) different batches of each MOF were combined to increase comparability, reproducibility, and accuracy by avoiding influences of different defect and metalation contents on the desired property (e.g., catalytic activity and selectivity).

### 3.1.2.2. MOF Characterization

As indicated above, all solid MOF materials were characterized by PXRD to confirm phase-purity and crystallinity. The PXRD pattern of PCN-222 and PCN-224 synthesized according to the above-described procedure matched the positions of *Bragg* reflections and showed high crystallinity and purity (compared to the pattern simulated from their single crystal structures CCDC:893545 (PCN-222), 1001133 (PCN-224)), see Figure A 4, Figure A 5. For PCN-224, the superstructure reflections were observable at  $2\theta = 3.2^\circ$  and  $5.5^\circ$ .<sup>[107]</sup> The structure also remained intact upon acid treatment since no change in PXRD pattern was detected. In contrast, the PXRD pattern of MOF-525 recorded after synthesis revealed a generally lower crystallinity and amorphous background (Figure A 6, pattern for comparison from <sup>[123]</sup>).

Moreover, the surface area and pore volume of the MOFs was evaluated by N<sub>2</sub> sorption measurements and the Brunauer-Emmett-Teller (BET) method (Figure A 7 – Figure A 9). Here, high specific surface areas for PCN-222 ( $1989 \pm 7.7 \text{ m}^2\cdot\text{g}^{-1}$ ) and PCN-224 ( $1978 \pm 26 \text{ m}^2\cdot\text{g}^{-1}$ ) were obtained which are comparable to values reported in literature.<sup>[32,81]</sup> Upon modulator removal, the surface areas for PCN-222 and PCN-224 changed:  $2154 \pm 5.7 \text{ m}^2\cdot\text{g}^{-1}$  and  $1572 \pm 26 \text{ m}^2\cdot\text{g}^{-1}$ , respectively. In general, an increase in surface area was expected upon modulator removal.<sup>[14]</sup> However, during HCl treatment the MOF was partially decomposed and reconstructed – observable by the dissolution of solid material upon HCl addition which could result in a varied surface area (and defect content, see below).

For MOF-525, however, the surface area was lower as expected ( $1014 \pm 9.5 \text{ m}^2\cdot\text{g}^{-1}$ ; Lit.<sup>[129]</sup>:  $2128 \text{ m}^2\cdot\text{g}^{-1}$ ), supporting the presence of amorphous phases.

The thermal stability of the MOFs was investigated via thermogravimetric analysis (TGA), see Figure A 10 – Figure A 14. Simultaneously, the method allows for the determination of defects since porphyrin-based Zr-MOFs are very prone to defect formation. The measured TGA curves revealed a comparably high thermal stability of all synthesized MOFs (decomposition in the range of 370-415 °C) in accordance to published temperatures.<sup>[14,87]</sup> The defect content, i.e. the linker deficiency which can be used to evaluate the overall deficiency of the MOF structure, was calculated according to a procedure presented by Lillerud *et al.* where the amount of linker molecules present in the MOF is accessible resulting in an altered sum formula and Zr:linker content.<sup>[105,108,130]</sup> However, for precise determination further characterization, e.g. of the Zr content via ICP-MS, is necessary to conclude on the type of defects (i.e. missing node or missing linker defects) Therefore, within this Thesis, defects are referred to as the amount of linkers deviating from the ideal amount (accessible from the sum formula). For PCN-222 the amount of linkers from the sum formula per  $\text{Zr}_6$  node was 2 ( $\text{Zr}_6(\text{OH})_{16}(\text{TCPP-H}_2)_2$ ), 1.5 for PCN-224 ( $\text{Zr}_6\text{O}_4(\text{OH})_{10}(\text{H}_2\text{O})_6(\text{TCPP-H}_2)_{1.5}$ ) and 3 for MOF-525 ( $\text{Zr}_6\text{O}_4(\text{OH})_4(\text{TCPP-H}_2)_3$ ) resulting in Zr:linker ratios of  $6:2 = 3$  for PCN-222,<sup>[14,102]</sup>  $6:1.5 = 4$  for PCN-224<sup>[100,102]</sup> and  $6:3 = 2$  for MOF-525.<sup>[123]</sup> Especially MOF-525 has been shown to be very tolerant towards defect formation where up to 50 % of defects (missing linkers) are possible which might also affect the synthesis toward a crystalline, phase-pure product.<sup>[82]</sup> The TGA of the here synthesized MOFs revealed a large defect range for PCN-222 (1.77 - 2.67) depending on the synthesis batch whereas the range was more narrow in the case of PCN-224 (1.44 - 1.67) and closer to the theoretical value of linker molecules. For MOF-525 a linker value of 2.13 instead of 3 was extracted from the TGA curve highlighting the high defect tolerance of this framework. The linker defects changed upon HCl treatment. During this process, part of the solid material was dissolved again and recrystallized afterwards. Thus, a change in defect concentration is not surprising. After HCl treatment, the number of  $\text{TCPPH}_2$  linkers decreased in both cases and resulted in smaller values compared to the theoretical numbers (e.g., 1.77 for PCN-222 and 1.44 for PCN-224) indicating the removal of linkers which are not sufficiently incorporated into the framework. This characterization again highlights the challenges faced by researchers working with porphyrin-based MOFs and that the defects have to be taken into account especially when comparing properties of different materials.

Since the porphyrin linker is a dye with specific absorption bands, solid-state UV-vis spectroscopy allows for the characterization of its absorption bands upon MOF incorporation (Figure A 15). The different solid-state UV-vis spectra of PCN-222, PCN-224 (both not treated with HCl) and MOF-525 showed the typical TCPPH<sub>2</sub> absorption bands in the range of 420 – 469 nm. A sharp Soret band was detected for PCN-222 at 429 nm while for PCN-224 and MOF-525 broader peaks in the region of 420 – 446 nm were observable. The Q bands arised at 510, 544, 592 and 649 nm for PCN-222 at 513 – 533, 559, 591, 648 nm and at 504, 533, 588 and 645 nm for MOF-525. Differences in absorption peak shifts and also peak broadening can arise from the different symmetry of the porphyrin linker which is altered depending on the framework it is integrated in.<sup>[103,105]</sup> The solid-state UV-vis method is especially beneficial when comparing metalated with non-metalated porphyrins incorporated in the respective MOFs which will be described in chapter 3.1.2.3.

Further spectroscopic analysis via infrared (IR) spectroscopy allowed for conclusions on different vibrational peaks and in particular supports the evaluation of porphyrin metalation discussed below (chapter 3.1.2.3). The spectra of non-metalated PCN-222, PCN-224 and MOF-525 (Figure A 16) generally showed peaks at comparable positions – however, with varied intensity relations.

The particle morphology of the different MOFs was characterized with scanning electron microscopy (SEM, Figure A 17, Figure A 18). While for PCN-222 rod-shaped crystals of 10 – 20 µm length and a diameter of 0.5 – 2 µm were observable matching literature reports,<sup>[82,125]</sup> for PCN-224 cubic crystals were expected while rather irregular spherical particles were observed in SEM measurements – which was also the case for MOF-525.<sup>[82]</sup>

### 3.1.2.3. Metalated Porphyrin MOFs

The potential of porphyrin metalation with a large variety of different metals is extremely beneficial since several applications of the resulting materials are conceivable and have been reported, e.g., from sensing to catalysis. Over the course of this Thesis, different transition metals were introduced into the porphyrin core allowing for the catalysis of various reaction types and evaluation of material properties and performances depending on the incorporated metal. In general, metalated porphyrin-MOFs are frequently presented in literature – however, the methods of metalation are often very similar: usually, porphyrin metalation is performed before the solvothermal synthesis of the MOFs with the respective metal chlorides as precursors. An alternative procedure is the post-synthetic metalation of the porphyrins already integrated into the framework.

Both methods intrinsically feature different advantages and disadvantages: the pre-metalation of the porphyrins can be easily followed and quantified by  $^1\text{H}$  NMR and UV-vis spectroscopy – which remains challenging for the post-synthetic method since these characterization techniques are more complicated in the solid-state and thus, the metal content is typically followed by methods like elemental analysis or ICP-MS. Here it has to be noted that a combination of the presented techniques (paired with  $\text{N}_2$  sorption or transmission electron microscopy (TEM)) is necessary to determine the location of the metal and if it is indeed incorporated into the porphyrin core instead of coordinating to the node or agglomerating inside the pores. At the same time, applying a pre-synthetic metalation can result in metal loss during solvothermal synthesis which can also be evaluated by ICP-MS and results in challenges determining the precise metal location.

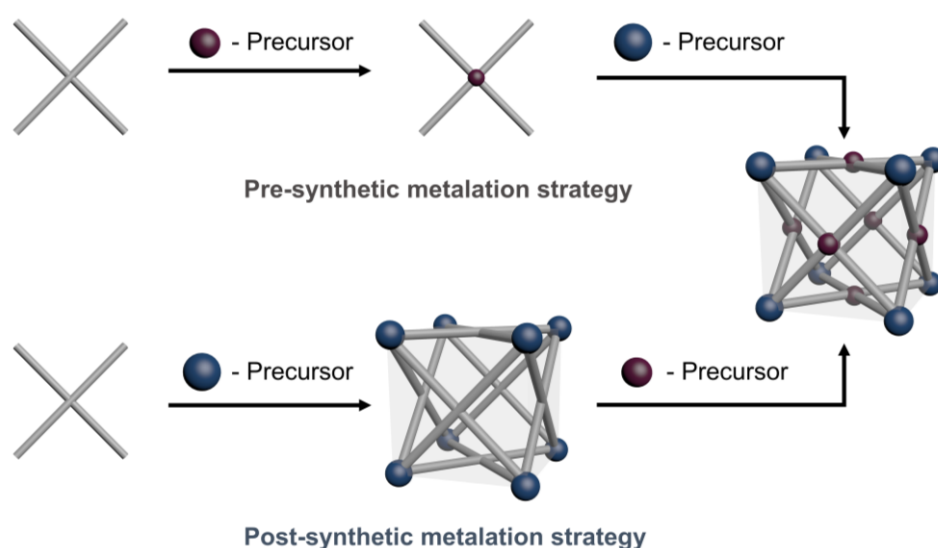


Figure 24: Schematic representation of the pre- and post-synthetic metalation approach for porphyrin-based Zr-MOFs. The pre-metalation procedure includes the metalation of the linker (here in grey, TCPFH2) with a metal (red) and subsequent MOF formation (top). For the post-synthetic approach, the MOF is first formed by reaction of the linker (grey) with a Zr-precursor (blue) and afterwards metalated upon addition of a precursor of the metal which shall be integrated into the porphyrin core.

In this Thesis, both approaches – the pre- and post-synthetic porphyrin metalation – were studied revealing preferred procedures for different metals used (Figure 24). The procedures were performed with the respective precursors for Rh, Ru, Mn, Co, Zn, Cu, Ni, Fe and Mg (Figure 25). In the course of this work, the different metals were selected according to their properties desired for the targeted applications (described in the respective chapters below). Thus, this Thesis provides synthetic guidelines for metalated porphyrin MOFs for up to nine different metals by several strategies by comparing different approaches – currently unpublished on this magnitude and adding value to existing literature. Beside the metal chloride precursors typically applied for metalated porphyrin MOFs in literature, further precursors like  $\text{Ru}_3(\text{CO})_{12}$  are used according to procedures published for homogeneous porphyrin systems.<sup>[131,132]</sup>



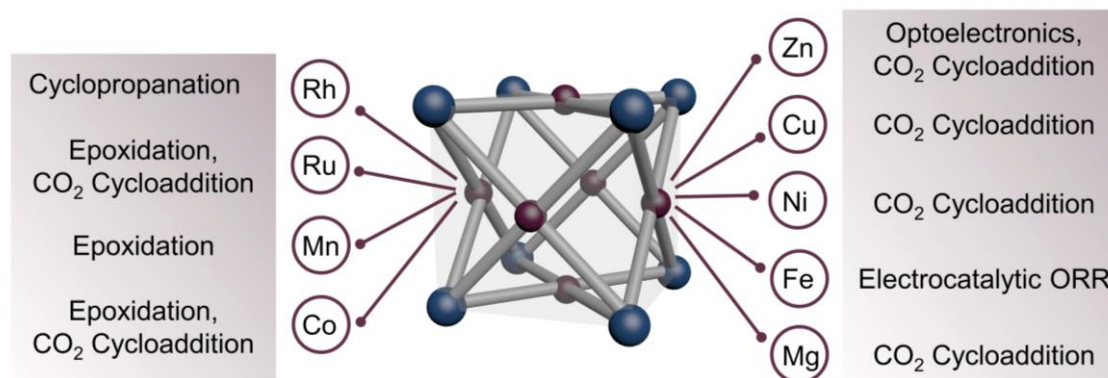
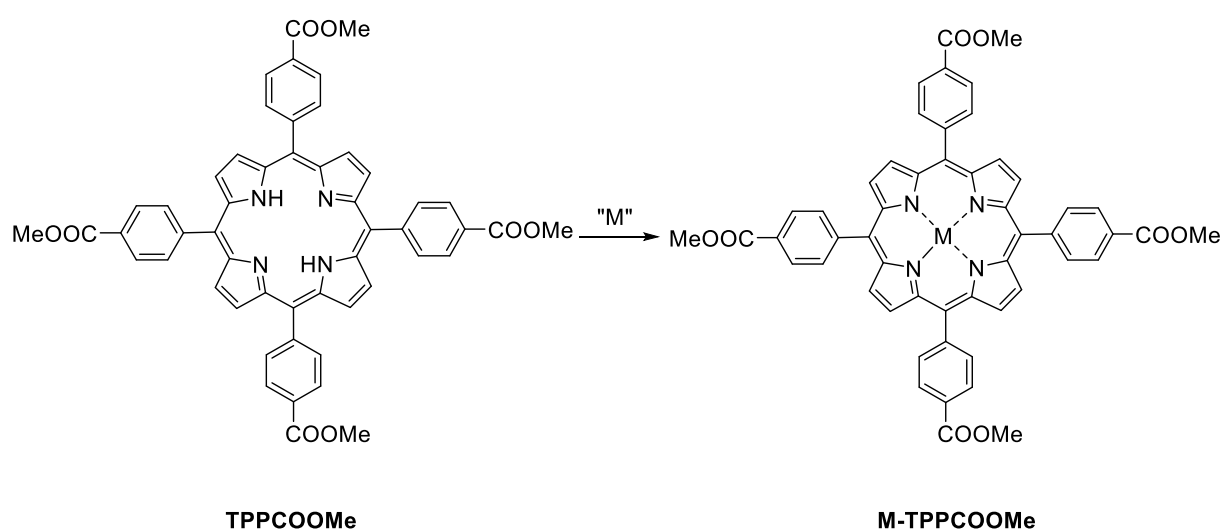


Figure 25: Metals incorporated into the porphyrin core of the different MOF frameworks of this Thesis. Additionally, the respective in this work targeted applications of the metalated MOFs for are depicted.

In the following the general procedure of the pre- and post-synthetic metalation will be described before discussing each metal individually and evaluating the degree of metal incorporation in the final metalated MOF. In the course of this Thesis, a more detailed description and analysis of the metalation procedure and the resulting MOFs is presented since the synthesis and reproducibility of phase-pure metalated porphyrin MOFs remains challenging – requiring precise information on the reaction conditions.

### Pre-metalation



Scheme 2: Metalation of TPPCOOMe with a suitable metal precursor "M" to incorporate M into the porphyrin core.

The pre-synthetic procedure typically involves the metalation of TPPCOOMe with a metal precursor under reflux conditions and the respective purification, e.g., column chromatography or recrystallization – depending on the metal (Scheme 2, for details see 5.3.1), followed by the saponification of the ester group resulting in M-TCPP.

After drying, the M-TCPPP molecule was characterized by  $^1\text{H}$  NMR spectroscopy. Here, the metalation was followed by the change of the porphyrin -NH signals at -2.93 ppm in the  $^1\text{H}$  NMR. Upon complete metalation this signal disappears and is therefore a key hallmark characterization tool. Simultaneously, metalation results in a change of the Q bands of the UV-vis spectrum of the dissolved M-TCPPP: the number of Q bands decreases from 4 to 2 due to a change in symmetry.<sup>[133]</sup> The metalated linkers were then applied in the respective MOF synthesis. Here, depending on the desired metal loading, either M-TCPPP can be solely applied or in different quantities with another linker, e.g., non-metalated TCPPH<sub>2</sub>. The resulting MOFs were analyzed with PXRD, IR and solid-state UV-vis spectroscopy. However, the metalation could not be followed by solid-state  $^1\text{H}$  NMR due to peak overlapping. At the same time, dissolving the metalated MOF in DCl/DMSO-d<sub>6</sub> for solution-based  $^1\text{H}$  NMR could release metal previously incorporated into the porphyrin core and would result in errors in metal content determination and was thus not applied in this work. Therefore, the metal content was evaluated with ICP-MS, in particular by comparing the measured Zr:M ratio with the theoretical one:  $\text{Zr:M}_{\text{theo, PCN-222}} = 3$ ;  $\text{Zr:M}_{\text{theo, PCN-224}} = 4$ ;  $\text{Zr:M}_{\text{theo, MOF-525}} = 2$ . Note that these ratios were calculated from the ideal sum formula and did not take defects into account, thus they only serve as an estimation. Additionally, a rough estimation on the percentage of porphyrins metalated in the MOF can be given, which is also calculated from the ideal sum formula.

### Post-metalation

For the post-synthetic metalation, the MOFs are synthesized using TCPPH<sub>2</sub> as the linker molecule. Following this, the solid MOF was suspended in a solution of the metal precursor and heated at elevated temperatures. Here, different setups were tested (Figure 26): a) applying reflux conditions while stirring, b) a microwave reactor with stirring, c) an oven comparable to the MOF synthesis itself and d) using an aluminum heating block, also while stirring. After the reaction the MOF was washed, followed by solvent exchange, and drying. The characterization of the MOFs after post-synthetic treatment for evaluating if the metalation was successful was also performed by PXRD, IR and UV-vis spectroscopy and ICP-MS.

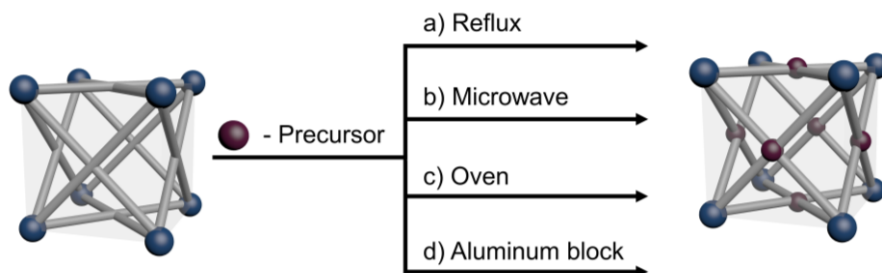


Figure 26: Post-synthetic MOF metalation strategy with different approaches: a) reflux conditions, b) using a microwave setup, c) heating in an oven comparable to the solvothermal MOF synthesis and d) heating of the MOF/metal precursor suspension in an aluminum block.

## Rhodium

Rhodium metalated MOFs are applied in the study of confinement effects in the cyclopropanation catalysis of styrene and styrene derivatives.<sup>[87]</sup> In the course of elucidating potential topology effects, the three topologically different porphyrin-based Zr-MOFs PCN-222, PCN-224 and MOF-525 were synthesized which were metalated with Rh acting as the active site in the cyclopropanation catalysis. Since cooperative effects between neighboring Rh centers are assumed from previous studies, a high degree of porphyrin metalation is essential ensuring potential proximity of Rh sites which requires an appropriate metalation procedure.<sup>[87]</sup> Here, both methods – the pre- and post-synthetic MOF metalation were studied and described in the following.

### Rhodium – pre-metalation

Rhodium-metalated TCPP (Rh-TCPP) was synthesized by refluxing TPPCOOMe with  $\text{RhCl}_3 \cdot x\text{H}_2\text{O}$  in benzonitrile for 2 h and subsequent purification by column chromatography according to a literature known procedure. Saponification of metalated TPPCOOMe (Rh-TPPCOOMe) yielded Rh-TCPP (for details see 5.3.1).<sup>[87,134]</sup> The purity of all (metalated) porphyrin molecules was confirmed by  $^1\text{H}$  NMR and UV-vis spectroscopy (Figure A 19). The percentage of Rh-metalation was calculated via  $^1\text{H}$  NMR spectroscopy by comparison of the integrals of the -NH groups at  $\delta = -2.93$  ppm with the aromatic signals at  $\delta = 8.38 - 8.95$  ppm resulting in 84% of porphyrin molecules with Rh incorporated. The Rh-porphyrin was applied in the synthesis of the different MOFs by substituting TCPPH<sub>2</sub> with Rh-TCPP. For PCN-222(Rh) and MOF-525(Rh) the procedures described above were followed – i.e. identical to pristine MOF syntheses.<sup>[82,129]</sup> Synthesis attempts for PCN-224(Rh) were performed following additional published procedures.<sup>[82,87,134]</sup> For PCN-222(Rh) a crystalline product is obtained in good purity (additional Bragg reflection at  $2\theta = 8.8^\circ$ , Figure A 20) with Rh-TCPP (4.5 wt% Rh in PCN-222, Zr:Rh = 3.6; Zr:Rh<sub>theo</sub> = 3) while for PCN-224(Rh) and MOF-525(Rh) either no product precipitation or the formation of product mixtures are received.

### Rhodium – post-metalation

Since only the synthesis of PCN-222(Rh) from Rh-TCPP resulted in a phase-pure product a post-synthetic metalation approach was studied using the different procedures described above (a – d in Figure 26). The success of the metalation was firstly evaluated by analyzing the phase-purity and crystallinity of the metalloporphyrin MOF with PXRD and metal quantification via ICP-MS.

Under refluxing conditions (Figure 26, path a), i.e. heating a suspension of as-synthesized MOF (in this case PCN-222) with  $\text{RhCl}_3 \cdot x\text{H}_2\text{O}$  in DMF and acetone respectively (details 5.3.3.), a Rh content of 1.8 wt% and a Zr:Rh ratio of 7.5 (theo: 2) was obtained by refluxing in DMF while the phase-purity and crystallinity was unaffected during this process (Table A 1, Figure A 21). In acetone, the metal content deviated more from the theoretical value (9.6 wt% Rh, Zr:Rh = 1.3, theoretically more than 100% metalated, Table A 1). Here an effect of decreased metal equivalents (1.2 vs 2.5 for acetone and DMF, respectively) has to be considered for the comparison. Thus, a more precise adjustment of metal equivalents is required – potentially leading to quantitative metalation of PCN-222 with Rh by refluxing the precursors in acetone.

In a standard post-synthetic metalation procedure using a microwave reactor (Figure 26, path b), PCN-222(Rh), PCN-224(Rh) and MOF-525(Rh) were prepared by reacting the as-synthesized MOF with  $\text{RhCl}_3 \cdot x\text{H}_2\text{O}$  (5 equivalents regarding the porphyrins in the respective MOFs) in DMF in a microwave vessel for 10 min (85 W, 130 °C, high stirring, details see 5.3.3.). Porphyrin metalation using a microwave reactor was reported as successful in literature, however, for the porphyrin molecule itself which was afterwards applied in MOF synthesis (pre-metalation approach).<sup>[113]</sup> After synthesis, all MOFs remained phase-pure with high crystallinity (Figure A 22 – Figure A 24, Figure A 25, Figure A 26). The Rh contents determined by ICP-MS were 1.7 wt% for PCN-222(Rh), 3.2 wt% for PCN-224(Rh) and 1.8 wt% for MOF-525(Rh). The Zr:Rh ratios indicated insufficient metalation using this procedure since as a maximum only ~45% of porphyrins in PCN-224(Rh) were metalated with only ~20% for PCN-222(Rh) and MOF-525(Rh). Thus, the Rh precursor, metal equivalents and reaction time were varied, exemplarily for PCN-222(Rh) (Table A 2).  $\text{Rh}_2(\text{OAc})_4$  as a precursor resulted in comparable metal contents and Zr:Rh ratios as for  $\text{RhCl}_3 \cdot x\text{H}_2\text{O}$  and was thus not further applied. The metal loading could be slightly enhanced by decreasing metal equivalents (2 vs 5): 2.1 wt% Rh and Zr:Rh = 8.8. Increasing the reaction time (10 to 20 min) was not beneficial since counterintuitively higher reaction times resulted in decreased metal contents (1.7 wt% vs 1.2 wt%), supported by the metal contents achieved after 5 min of reaction determined as 2.2 wt%). An increased metal content of 4.1 wt% Rh (Zr:Rh = 4.9) could be realized by enhancing both the reaction time (to 60 min) and the Rh equivalents (9 equivalents). The Zr:Rh ratios are schematically illustrated in Figure 27 (and compared to the other techniques described below). The microwave metalation presents a promising method maintaining phase-purity and crystallinity of the MOF, however achieving rather low metal contents for Rh – which can be disadvantageous depending on the desired application.

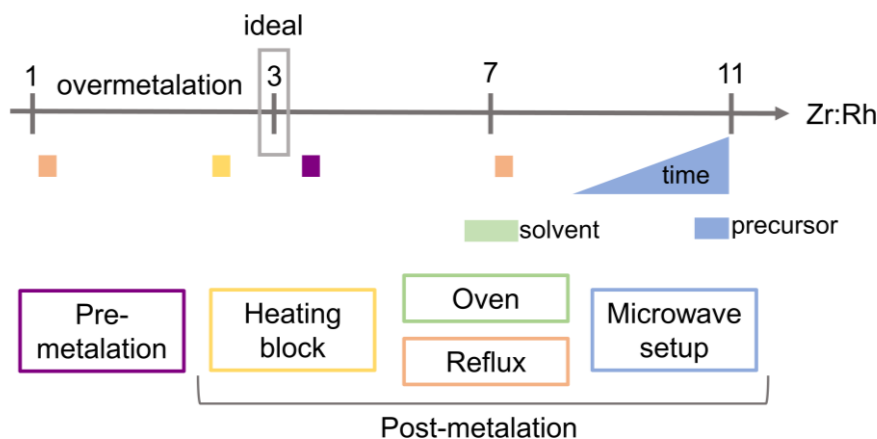


Figure 27: Semi-quantitative representation of the Zr:Rh ratios of PCN-222(Rh) synthesized via different approaches (pre-metalation in purple, reflux conditions in orange, microwave setup in blue, oven, heating block in yellow). For the microwave setup a dependency of the Zr:Rh ratio on the reaction time and a solvent dependency for the oven setup, respectively, are apparent while the metal precursor does not affect the Zr:Rh ratio significantly. Additionally, the ideal Zr:Rh ratio of 3 accessible from the sum formula of PCN-222 is shown.

An alternative route is presented by post-synthetic metalation of the as-synthesized MOFs with  $\text{RhCl}_3 \cdot x\text{H}_2\text{O}$  in an oven (Figure 26, path c) which is the same as used for the MOF synthesis itself, i.e., without stirring (details see 5.3.3). The setup was tested for PCN-222(Rh), varying the solvent (DMF vs DEF) with 9 equivalents of Rh precursor. For both attempts Rh contents of 2.4-2.8 wt% were detected with Zr:Rh ratios of 8.2 (DMF) and 6.8 (DEF) (see Figure 27), which were comparably high considering the theoretical value of 2 (~30% of porphyrins metalated). The phase-purity and crystallinity of PCN-222 could be maintained during this process (Figure A 27Figure A 27).

For method d) (Figure 26) suspensions of as-synthesized MOFs with  $\text{RhCl}_3 \cdot x\text{H}_2\text{O}$  in DMF were heated in an aluminum block while stirring (details see 5.3.3.). The syntheses were performed with 9 equivalents Rh for PCN-222(Rh) and 8 equivalents for PCN-224(Rh) and MOF-525(Rh). In general, this method resulted in higher metal contents compared to the previously described post-synthetic procedures: For PCN-222(Rh) 8.3 wt% Rh (Zr:Rh = 2.5;  $\text{Zr:Rh}_{\text{theo}} = 3$ ), for PCN-224(Rh) 6.5 wt% (Zr:Rh = 3.4;  $\text{Zr:Rh}_{\text{theo}} = 4$ ) and for MOF-525(Rh) 9.4 wt% (Zr:Rh = 2.8;  $\text{Zr:Rh}_{\text{theo}} = 2$ ), see Figure 27. Considering the ideal sum formula, the measured Zr:Rh values were in good agreement for all Rh-MOFs (90-100% of porphyrins metalated). Noteworthy, a value above 100% can be caused by physisorbed metal species in the MOF pores which are, however, challenging to distinguish. Additionally, especially PCN-222 and MOF-525 are very defect-rich (see TGA results and literature)<sup>[82,105]</sup> which needs to be taken into account for these calculations.

Interestingly, a lower success rate of this method has to be considered since in only about 50 % of the synthesis batches the MOF remained crystalline while the other half became amorphous during this process. This presumably arises from the high amounts of HCl formed during the reaction. However, since the highest metal loadings were achieved using this method, the products were synthesized in various batches, combined and analyzed in more detail in the following.

The PXRD pattern recorded after metalation revealed no changes for PCN-222(Rh) and MOF-525(Rh) compared to their non-metalated analogs (Figure A 28, Figure A 30). Additionally, the *Bragg* reflections in PCN-222(Rh) were slightly shifted. In contrast to PCN-222 and MOF-525, the crystallinity of PCN-224 decreased slightly during the metalation process (Figure A 29). The crystallinity was estimated by comparing the signal-to-noise ratios and peak intensities of the different MOFs. Performing N<sub>2</sub> sorption measurements of the metalloporphyrin MOFs revealed changing adsorption capacity between the non-metalated and metalated MOFs where in every case a decline in BET surface areas was measurable: for PCN-222 from 2154 m<sup>2</sup>/g to 1692 m<sup>2</sup>/g, for PCN-224 from 1572 m<sup>2</sup>/g to 1314 m<sup>2</sup>/g and for MOF-525 from 1014 m<sup>2</sup>/g to 743 m<sup>2</sup>/g (Figure A 31 – Figure A 33). The decrease in BET surface area upon MOF metalation was in accordance to a previously published study.<sup>[129]</sup> In particular the BET surface area of MOF-525 and MOF-525(Rh) has been described before and possibly – in the case presented in this Thesis – resulted from amorphous contributions and the decreased crystallinity described above.

Moreover, spectroscopic analysis substantiated the presence of Rh-porphyrins. In particular, altered vibrational modes in the IR spectra at ~990 cm<sup>-1</sup> and ~1600 cm<sup>-1</sup> were observable arising from the pyrroles' N-H plane modes which decreased upon metalation. Additionally, peak changes in the region of 650 cm<sup>-1</sup> – 970 cm<sup>-1</sup> were detected which is the typical range for the porphyrins' in- and out-of-plane vibrational modes. Upon Rh-metalation differences could be found from ~750 cm<sup>-1</sup> – 800 cm<sup>-1</sup> and ~660 cm<sup>-1</sup> – 690 cm<sup>-1</sup> – suggesting the presence of Rh-N bonds (Figure A 34 – Figure A 39).<sup>[135]</sup>

The solid-state UV-vis spectra of the Rh-metalated MOFs revealed a broadening and shift of signals at 510 nm to 655 nm assigned to the Q bands of the framework porphyrins (Figure A 40 – Figure A 42). This phenomenon has been previously described in literature – comparing TCPPH<sub>2</sub> with dissolved PCN-222(Zn).<sup>[81]</sup>

## Ruthenium

In the course of this Thesis, ruthenium metalated porphyrin-based MOFs were studied for the potential application in the epoxidation of olefins with the capability of establishing multifunctional systems for sequential catalysis. For this project PCN-222(Ru) was selected as model catalyst since PCN-222 synthesis was suggested to be more reliable than e.g., the synthesis of MOF-525. The ability of molecular Ru-porphyrins catalyzing epoxidation reactions has been demonstrated previously.<sup>[114,136]</sup> For Ru-metalation of PCN-222 also the two approaches (pre- and post-synthetic) were investigated.

### Ruthenium – pre-metalation

For Ru metalation of TCPPH<sub>2</sub> in a first step the ester TPPCOOMe was refluxed for 72 h in propionic acid with the metal precursor Ru<sub>3</sub>(CO)<sub>12</sub> under an inert atmosphere (ensuring higher metal loadings) following a literature known procedure (for details see 5.3.1.).<sup>[137]</sup> The solid product was purified by column chromatography (note that the use of HPLC grade chloroform is empirically crucial). The Ru incorporation could be followed by UV-vis spectroscopy, reducing the number of Q bands upon Ru metalation which were shown at 529 nm and 563 nm due to symmetry changes.<sup>[133]</sup> Additionally, the Soret band was shifted from 418 to 411 nm compared to the non-metalated porphyrin. Saponification of Ru-TPPCOOMe(CO) resulted in Ru-TCPP(CO) where the same observations in band changes in the UV-vis spectra compared to the porphyrin ester could be made. Note, that in the case of Ru a CO ligand is coordinated to the Ru located in the porphyrin center. This Ru carbonyl species is beneficial for characterization since different CO species can be clearly distinguished by the CO vibrations in the IR spectra (Figure A 43). Ru-TCPP(CO) showed Ru-CO vibrations in the range of 1934 cm<sup>-1</sup> to 1938 cm<sup>-1</sup> which is in the characteristic range for ruthenium carbonyl vibrations.<sup>[132]</sup> <sup>1</sup>H NMR spectroscopy allowed for the evaluation of purity and the degree of metalation which was determined by comparing the intensity of the -NH signals of the porphyrin core. Although a high purity of the compound could be reinforced a quantification of the metalation degree could not be achieved due to a broadening of the -NH signal. Thus, for metal quantification ICP-MS was used resulting in 12 wt% Ru (complete porphyrin metalation).

The MOF metalation with Ru was only performed for PCN-222. Thus, Ru-metalation of PCN-224 and MOF-525 will be neither described in the pre-metalation nor post-metalation chapters. PCN-222(Ru) was synthesized by substituting TCPPH<sub>2</sub> with Ru-TCPP(CO) which yielded a red solid. PXRD confirmed high crystallinity and phase-purity of the product since the *Bragg* reflections matched the simulated pattern of PCN-222 (Figure A 44). PCN-222(Ru) showed a characteristic CO vibration at 1941 cm<sup>-1</sup> in the IR spectrum (Figure A 43). Comparison to the bands of Ru-TCPP(CO) (at 1936 cm<sup>-1</sup>) and the spectrum of the precursor Ru<sub>3</sub>(CO)<sub>12</sub> substantiated that Ru remains incorporated into the porphyrin core during MOF synthesis.

The solid-state UV-vis spectra (Figure A 45) revealed a decrease in the number of Q bands in PCN-222(Ru) compared to PCN-222 which is in accordance to previously described observations for molecular Ru-TCPP(CO). A high N<sub>2</sub> adsorption capacity and BET surface area of  $1368 \pm 25 \text{ m}^2/\text{g}$  for PCN-222(Ru) was reinforced by N<sub>2</sub> sorption measurements (Figure A 46). A decrease in BET surface area upon metalation (PCN-222:  $\sim 2000 \text{ m}^2/\text{g}$ ) has been previously described.<sup>[87,129]</sup> A Ru content of 6.6 wt% and a Zr:Ru ratio of 2.68 (Figure 28,  $\text{Zr:Ru}_{\text{theo}} = 3$ ) were determined by ICP-MS suggesting slight overmetalation of PCN-222, however, not considering MOF defects. In general, the synthesis of PCN-222(Ru) with pre-metalated Ru-TCPP(CO) resulted in a phase-pure product with an excellent degree of metalation.

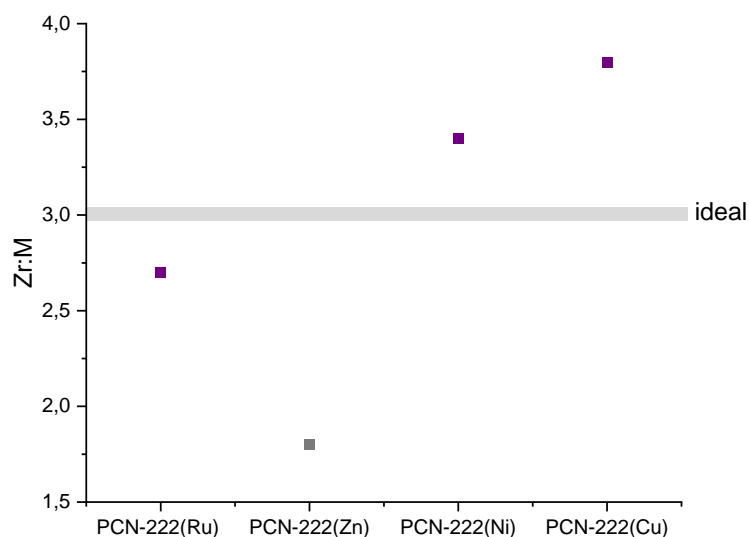


Figure 28: Zr:M ratios determined by ICP-MS for the different PCN-222(M) MOFs. PCN-222(Ru), PCN-222(Ni) and PCN-222(Cu) were synthesized with the pre-metalation approach while for PCN-222(Zn) a post-synthetic strategy was followed. The ideal Zr:M ratio of 3 for PCN-222 is additionally highlighted.

### Ruthenium – post-metalation

In a post-synthetic metalation approach, refluxing conditions (a) were applied. Here, PCN-222 was suspended with Ru<sub>3</sub>(CO)<sub>12</sub> in DMF and heated under an Ar atmosphere (comparable to the metalation of the molecular porphyrin). The brown product was characterized by PXRD where no deviations from the pattern of PCN-222 were discernible (Figure A 44). In contrast to PCN-222(Ru) obtained with the pre-metalation method, the IR spectrum of PCN-222(Ru) accessible via the post-synthetic approach showed two bands at 1942 and 2031 cm<sup>-1</sup> (Figure A 43) indicating the presence of an additional CO species within the framework with an altered Ru-CO environment compared to porphyrinic Ru-CO.<sup>[132]</sup>



Interestingly, the N<sub>2</sub> sorption measurements (Figure A 46) revealed a drastic drop in N<sub>2</sub> uptake and BET surface area (from ~2000m<sup>2</sup>/g for PCN-222 to 611 m<sup>2</sup>/g for PCN-222(Ru) obtained via post-synthetic metalation). Combined with the results from IR spectroscopic measurements this affirms the physisorption of Ru species (e.g. the Ru precursor) in the MOF pore where only a slight amount of Ru might be incorporated into the porphyrin core. ICP-MS analysis for PCN-222(Ru) synthesized with different equivalents of Ru<sub>3</sub>(CO)<sub>12</sub> (3, 6 and 9, respectively) resulted in Ru contents of 4.8 to 16.9 wt% with Zr:Ru ratios ranging from 3.7 to 0.3 (Table A 5). The latter significantly underlines the presence of physisorbed Ru in the MOF. Thus, precise synthesis of PCN-222(Ru) was not possible with this post-synthetic metalation approach – strongly limiting its applicability in precision studies such as those targeted in this Thesis which involve catalytic mechanisms and confinement effects.

## Manganese

The metalation of the framework porphyrins with manganese was studied due to the reported catalytic activity of Mn in epoxidation reactions – also after incorporation into MOFs.<sup>[138,139]</sup> Thus, as this Thesis also aimed to the design a porphyrin MOF-based epoxidation catalyst, the incorporation of this metal was studied via different approaches which will be presented in the following. Here, Mn-metalation was examined for PCN-222, PCN-224 and MOF-525 with the aim of studying potential confinement effects in epoxidation catalysis.

### Manganese – pre-metalation

Metalation of TCPPH<sub>2</sub> with Mn was achieved via Mn-TPPCOOMe by refluxing TPPCOOMe with the Mn precursor (MnCl<sub>2</sub> · 4H<sub>2</sub>O) in DMF and subsequent saponification yielding a dark green solid (details see 5.3.1.). The metalation was characterized by UV-vis and <sup>1</sup>H NMR spectroscopy confirming successful metal incorporation (Figure A 47, Figure A 48). Afterwards, the Mn-TCPP linker was reacted with the Zr precursor and modulator in DEF or DMF for the synthesis of PCN-222(Mn) and PCN-224(Mn), respectively, according to the procedure for PCN-222 and PCN-224 syntheses described above. PXRD measurements reinforced the phase-purity and crystallinity of the products (Figure A 49, Figure A 50). Here, for PCN-224(Mn) the crystallinity was lower compared to the non-metalated analog. ICP-MS analysis revealed a Mn content of 0.7 wt% and a Zr:Mn ratio of 8.9 for PCN-222(Mn), where a value of 3 was expected for complete metalation, and 0.7 wt% Mn and a Zr:Mn ratio of 15.8 (expected: 4) for PCN-224(Mn) suggesting a generally low degree of metalation (Table A 6, Table A 7).

The solid-state UV-vis spectrum of PCN-222(Mn) showed changes in the region of 450 nm to 700 nm compared to PCN-222 (Figure A 51). For PCN-224(Mn) a UV-vis absorption spectrum was not detectable. Note, that the pre-synthetic approach for MOF-525(Mn) was not studied within this Thesis.

### **Manganese – post-metalation**

For post-synthetic Mn metalation of PCN-222, PCN-224 and MOF-525 the synthesis was performed in a microwave reactor (Figure 26, path b) or using an aluminum heating block (Figure 26, path d). The as-synthesized MOFs were suspended in DMF with  $\text{MnCl}_2 \cdot 4\text{H}_2\text{O}$  as a Mn source and heated in the different setups. For PCN-222 and PCN-224 also the metalation of HCl treated samples were studied to conclude on possible influences if modulator molecules are attached to the node. The PXRD pattern of all PCN-222(Mn) samples achieved via the different routes showed high crystallinity and phase-purity while the crystallinity was decreased for PCN-222(Mn) treated with HCl prior to metalation without affecting the purity (Figure A 49). While the MOF structure during the metalation of MOF-525 and PCN-224 with Mn using a microwave setup remained intact, amorphization occurred during reaction in a heating block (Figure A 50, Figure A 55). Metal contents (summarized in Table A 6 – Table A 8 and Figure 29) revealed an increased metal content for PCN-222 (1.8 wt% vs 3.1 wt%) and PCN-224 (1.1 wt% vs 3.5 wt%) previously treated with HCl compared to as-synthesized MOFs when using the microwave setup. In general, for the microwave reaction the Zr:Mn ratios were in the range of 3.1 – 4.5 for PCN-222(Mn), 3.8 – 7.1 for PCN-224(Mn) and 7.7 for MOF-525(Mn). Using a heating block resulted in drastically increased metal contents (9.1 wt% for PCN-222(Mn), 6.3 wt% for PCN-224(Mn) and 8.7 wt% for MOF-525(Mn)) with Zr:Mn ratios of 0.9 – 1.0 which highlight large amounts of excessive metal in the pores. Exemplarily, solid-state UV-vis spectra of PCN-222(Mn) were analyzed where all materials showed changes (shift and peak broadening) in the region of 450 nm to 700 nm – the degree of change depended on the metalation procedure applied and a correlation between observed changes and metal content could be deduced (Figure A 51 – Figure A 56). Additionally, IR spectra of all Mn metalated MOFs were recorded (Figure A 53 – Figure A 57). In general, sufficient Mn metalation with the post-synthetic method remains challenging if complete metalation is desired – while smaller amounts of Mn can be readily incorporated using the microwave setup.

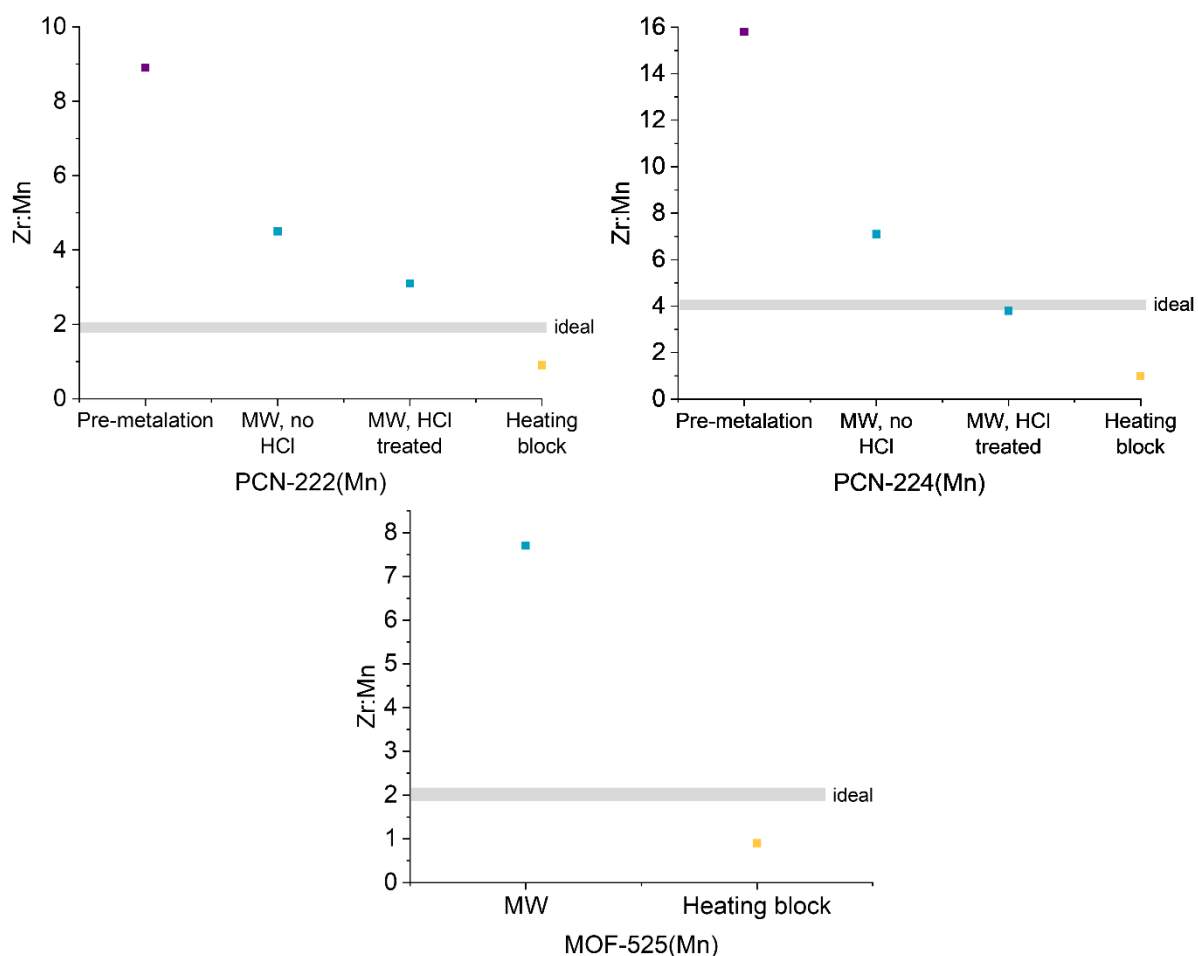


Figure 29: Zr:Mn ratios for PCN-222(Mn), PCN-224(Mn) and MOF-525(Mn) synthesized via different methods: pre-metalation, microwave setup (MW), heating in an aluminum block (heating block). Additionally, for PCN-222(Mn) und PCN-224(Mn) the modulator of the as-synthesized MOFs (no HCl) was removed by an HCl treatment prior to MOF metalation.

## Cobalt

Cobalt-porphyrins have been presented as catalysts in both epoxidation and CO<sub>2</sub> cycloaddition.<sup>[113,140,141]</sup> For the accomplishment of a multifunctional catalyst system able to perform sequential reactions these both reactions – and in particular their combination – was studied which will be presented in chapter 3.2.1.4. Thus, Co incorporation into porphyrin-MOFs (here PCN-222, PCN-224 and MOF-525) was investigated using several methods described below.

### Cobalt – pre-metalation

Metalation of TPPCOOMe with Co was performed by refluxing the porphyrin molecule with  $\text{CoCl}_2 \cdot 6\text{H}_2\text{O}$  in DMF according to literature.<sup>[14]</sup> Successive purification and saponification resulted in Co-TCPP (details see 5.3.1.). Co metalation was confirmed by UV-vis spectra of Co-TCPP and TCPPH<sub>2</sub> where metalation resulted in an expected decrease in the number of Q bands (occurring at 544 nm and 589 nm) and a shift of the Soret band (to 425 nm) as described previously (Figure A 47). The high Co content of 7.7 wt% determined by ICP-MS suggested quantitative porphyrin metalation. Detailed molecule characterization via <sup>1</sup>H NMR spectroscopy was not possible due to the paramagnetic nature of the product. Solvothermal MOF synthesis with Co-TCPP as linker resulted in phase-pure and crystalline PCN-222(Co) and PCN-224(Co) confirmed by PXRD (Figure A 58, Figure A 59). Note that the synthesis of MOF-525(Co) starting with Co-TCPP was not studied over the course of this Thesis. Solid-state UV-vis spectroscopy showed a change of absorption bands in the range of 500 – 700 nm in line with successful metalation (Figure A 64 – Figure A 66). The latter was further reinforced by ICP-MS measurements yielding 2.3 wt% Co and a Zr:Co ratio of 3.0 for PCN-222(Co), indicating complete metalation, and 2.6 wt% Co and a Zr:Co ratio of 5.2 for PCN-224(Co).

### Cobalt – post-metalation

For post-synthetic MOF metalation with Co three approaches were followed: a microwave setup (Figure 26, path b, for PCN-222, PCN-224 and MOF-525), metalation in an oven (Figure 26, path c, for PCN-222 only) and heating the reaction suspensions in an aluminum block (Figure 26, path d, for PCN-222, PCN-224 and MOF-525), details see 5.3.3. In every case, MOF and metal precursor ( $\text{CoCl}_2 \cdot 6 \text{H}_2\text{O}$ ) were suspended in DMF and heated in the respective setup. With all setups the crystallinity and structure of the as-synthesized MOFs PCN-222 and PCN-224 were maintained upon Co metalation while the crystallinity decreased for MOF-525(Co) (Figure A 64 – Figure A 66) metalated in a heating block or microwave setup. Metalation in an oven was not performed for MOF-525(Co).

ICP-MS analysis showed generally high values of metal loadings, especially using an aluminum block for heating (Table A 9 – Table A 11, Figure 30). Here a Co content of 10.8 – 12.9 wt% was obtained for the three different MOFs with Zr:Co ratios of 0.6 – 0.8 highlighting a large excess of Co present and potentially physisorbed in the MOF pores. The metal content was decreased (but still high) using a microwave technique. Here, Co contents of 4.5 wt% (Zr:Co = 2.0) for PCN-222(Co), 4.0 wt% (Zr:Co = 2.5) for PCN-224(Co) and 4.0 wt% (Zr:Co = 2.6) for MOF-525(Co) were calculated. Also, with this approach overmetalation of PCN-222 and PCN-224 with Co was indicated.

Post-synthetic metalation of PCN-222 with Co in an oven resulted in a Co content of 5.4 wt% and a Zr:Co molar ratio of 1.2. Thus, in all post-metalation procedures overmetalation is observed. The successful porphyrin metalation with Co was further supported by IR spectroscopy of PCN-222(Co) where the band at  $2969\text{ cm}^{-1}$  disappeared and changes in the region of  $650 - 800\text{ cm}^{-1}$  were discernible (Figure A 61 – Figure A 63) and solid-state UV-vis spectroscopy revealed changes in the range of the porphyrin's Q bands (Figure A 64 – Figure A 66).

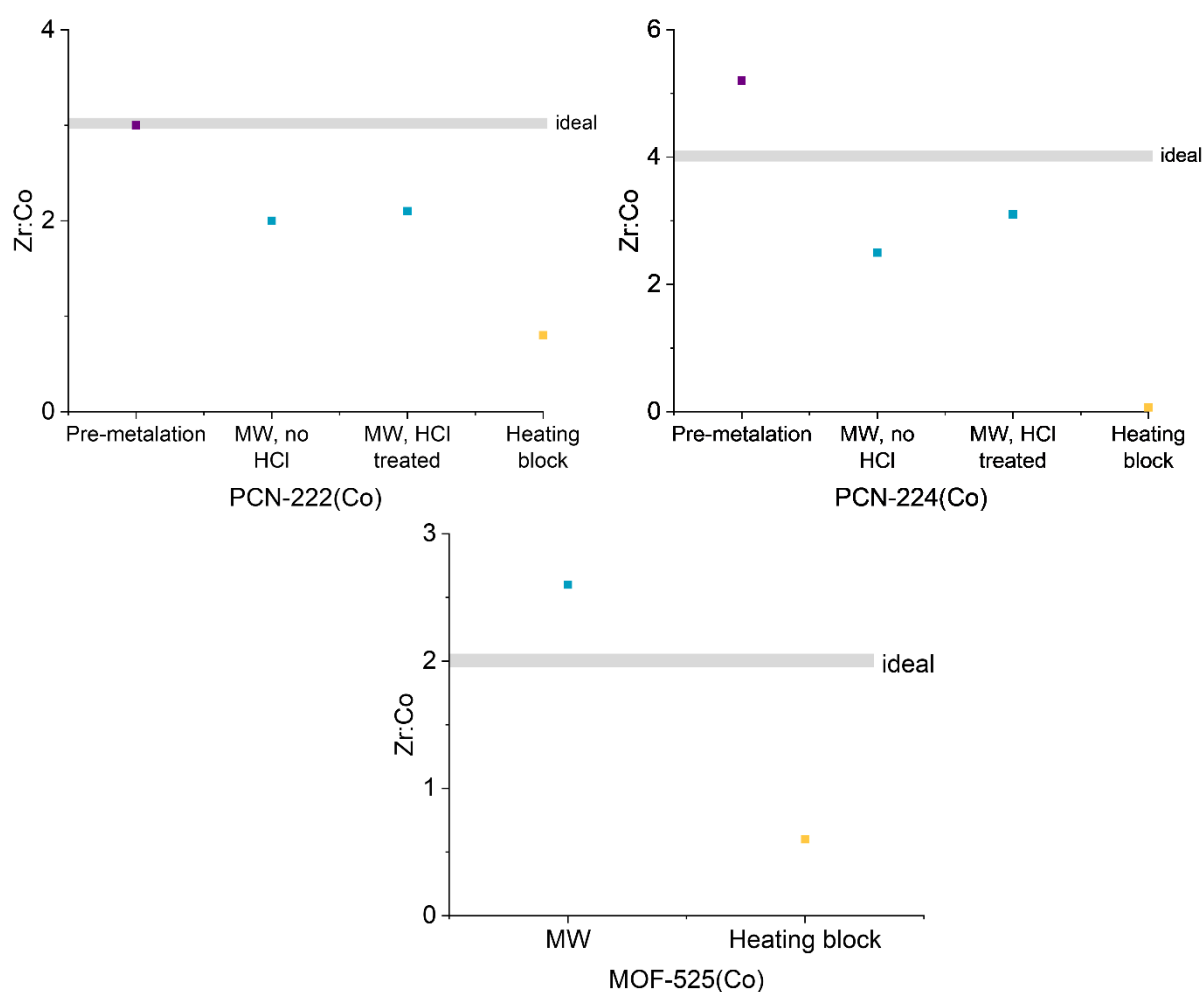


Figure 30: Zr:Co ratios for PCN-222(Co), PCN-224(Co) and MOF-525(Co) synthesized via different methods: pre-metalation, microwave setup (MW), heating in an aluminum block (heating block). Additionally, for PCN-222(Co) und PCN-224(Co) the modulator of the as-synthesized MOFs (no HCl) was removed by an HCl treatment prior to MOF metalation.

## Zinc

The incorporation of Zn was studied in more detail due to its previously evidenced cycloaddition activity,<sup>[92,113,140]</sup> and the possibility of serving as anchoring point for N-containing molecular species shown in literature.<sup>[142]</sup> The latter is important for the study of photocatalyst – MOF assemblies presented in chapter 3.2.2.3.

### Zinc – pre-metalation

While in literature  $\text{ZnCl}_2$  is often reported as Zn source, the pre-synthetic porphyrin metalation in this Thesis was performed with Zinc(II) acetate ( $\text{Zn(OAc)}_2$ ) to prevent the presence of  $\text{Cl}^-$  anions.<sup>[14,143]</sup> Metalation under refluxing conditions and following saponification resulted in Zn-TCPP. Noteworthy, significant amounts of Zn were released during the saponification process, reinforced by ICP-MS where the Zn content decreased from 7.2 wt% for Zn-TPPCOOMe to 1.0 wt% for Zn-TCPP. The low metal content was supported by only minor changes in the UV-vis spectra, i.e., a weak bathochromic shift of the Soret band and the presence of four Q bands in both Zn-TCPP and TCPPH<sub>2</sub> (Figure A 67). The low metal content of Zn-TCPP and the high metal loss during reaction at increased temperature renders this an unappealing strategy for the synthesis of PCN-222(Zn) since during this process further Zn might be released.

### Zinc – post-metalation

PCN-222(Zn) and PCN-224(Zn) were obtained via a post-synthetic approach where a suspension of the as-synthesized MOF and  $\text{ZnCl}_2$  in DMF was heated in an oven (pathway c for metalation, Figure 26) for 24 h at 100 °C (details see 5.3.3).<sup>[92,143]</sup> MOF-525(Zn) was not synthesized during this Thesis. A post-synthetic approach was followed according to the above-described Zn loss observed during linker saponification. The phase-purity and crystallinity of both MOFs was confirmed by PXRD after Zn metalation where the pattern match the simulated ones (Figure A 68, Figure A 69). Symmetry changes of the porphyrin upon Zn metalation were detected by UV-vis spectroscopy as shown by an altered Q band structure (Figure A 70, Figure A 71). The degree of Zn incorporation measured by ICP-MS after MOF digestion indicated quantitative porphyrin metalation since Zr:Zn ratios of 1.8 and 1.9 were obtained for PCN-222(Zn) (Figure 28) and PCN-224(Zn), respectively. At the same time, these low values suggested overmetalation and thus physisorbed Zn species in the MOF pores. The high porosity of both MOFs was preserved during the metalation procedure which was characterized by  $\text{N}_2$  sorption measurements (Figure A 72) allowing for the extraction of BET surface areas of  $\sim 1550 \text{ m}^2\cdot\text{g}^{-1}$  for PCN-222(Zn) and  $\sim 1750 \text{ m}^2\cdot\text{g}^{-1}$  for PCN-224(Zn), respectively, compared to  $\sim 2000 \text{ m}^2\cdot\text{g}^{-1}$  for the pristine MOFs. The decrease in BET surface upon metalation was described prior and will be additionally caused by the presence of Zn in the MOF pores.<sup>[129]</sup>

In general, this post-synthetic approach presents a promising technique for MOF metalation with Zn. However, since kinetics of Zn incorporation into the porphyrin core are rather fast (compared to other metals like Co, Rh etc.) precise adjustment of the metal equivalents is required preventing undesired overmetalation.

## Nickel

Due to the previously reported activity of Ni as an active site in the catalytic CO<sub>2</sub> cycloaddition into epoxides,<sup>[62,113]</sup> PCN-222(Ni) was synthesized towards a multifunctional catalyst of the sequential olefin to cyclic carbonate reaction where Ni is designed to act as the active catalyst for the second reaction step – the CO<sub>2</sub> cycloaddition. For this project only the metalation of PCN-222 was studied.

### Nickel – pre-metalation

The synthesis of Ni-TCPP was performed by adapting a published procedure. Here, TPPCOOMe was refluxed with Ni(II) acetyl acetonate in toluene and saponificated to achieve Ni-TCPP as solid of dark purple color. Successful synthesis was confirmed by <sup>1</sup>H NMR (indicating 100% metalation) and UV-vis spectroscopy where an expected change in the Q bands and a shift in the Soret band compared to TCPPh<sub>2</sub> was apparent (Figure A 73, Figure A 67). Subsequent synthesis of PCN-222(Ni) from Ni-TCPP resulted in a phase-pure product with high crystallinity (Figure A 74). The Ni content was calculated from ICP-MS data as 3.2 wt% with a Zr:Ni ratio of 3.4 (indicating approximately 70% of linkers metalated, Figure 28). The Ni incorporation into PCN-222 was also discernible from the solid-state UV-vis spectrum where changes in the range of 500 nm to 680 nm were apparent compared to non-metalated PCN-222 (Figure A 75). Since this approach successfully resulted in PCN-222(Ni) with a high Ni content, a post-synthetic metalation procedure was not studied.

## Copper

In line with the purpose of Ni incorporation, Cu metalation of PCN-222 was performed due to the ability of copper to catalyze the cycloaddition of epoxides and CO<sub>2</sub>.<sup>[62,113,144]</sup> Similarly, only the framework incorporation of previously metalated Cu-TCPP via solvothermal synthesis was analyzed.

### Copper – pre-metalation

For Cu-TCPP, TPPCOOMe and copper (II) acetate hydrate were refluxed in chloroform yielding Cu-TPPCOOMe which was saponified to result in purple Cu-TCPP where analytics confirmed the successful synthesis (see  $^1\text{H}$  NMR and UV-vis spectroscopy data, Figure A 73, Figure A 67). Synthesis of PCN-222(Cu) was performed using Cu-TCPP as the linker according to the procedure described above. Phase-purity and high crystallinity of the product were reinforced by PXRD analysis (Figure A 74). ICP-MS measurements revealed a Cu content of 3.1 wt% with a Zr:Cu ratio of 3.8 (which refers to a porphyrin metalation of approximately 62%, Figure 28). Within the scope of this Thesis, post-synthetic MOF metalation was not further investigated since the pre-synthetic approach results in an adequate metalation.

### Magnesium

Previously, the catalytic activity of Mg-porphyrins in the synthesis of cyclic carbonates has been demonstrated.<sup>[140,145]</sup> Thus, toward the aim of designing a catalyst for sequential epoxidation/cycloaddition and elucidating potential effects of different metal combinations, PCN-222(Mg) was targeted.

### Magnesium – pre-metalation

Mg-TCPP was obtained from TPPCOOMe and  $\text{MgBr}_2$  which was reacted at room temperature with triethyl amine ( $\text{Net}_3$ ) resulting in Mg-TPPCOOMe and subsequent saponification. Only minor changes in  $^1\text{H}$  NMR and UV-vis spectroscopy (Figure A 73, Figure A 67) indicated insufficient Mg metalation. Thus, metalation of PCN-222 with Mg using Mg-TCPP was not further investigated. However, for further studies and the synthesis of PCN-222(Mg) a post-synthetic metalation procedure – comparable to one for PCN-222(Zn) – is suggested which is however not part of this Thesis. Noteworthy, also in the case of Mg the importance of metal equivalent adjustment preventing overmetalation might be essential.

### Iron

Porphyrin metalation with iron and its incorporation into a MOF framework has been studied due to the activity of Fe in the electrocatalytic oxygen reduction reaction (ORR).<sup>[146]</sup> Here, single-site catalysts showed high activity which can be obtained from pyrolysis of MOFs. Thus, PCN-222(Fe) was synthesized which subsequently acted as precursor for a MOF-derived catalyst material investigated for ORR (not described in this work).



### Iron – pre-metalation

TPPCOOMe was refluxed with  $\text{FeCl}_2 \cdot 4 \text{H}_2\text{O}$  in DMF yielding Fe(III)-TPPCOOMe which was converted to Fe-TCPP by saponification. Quantification of the Fe metalation with  $^1\text{H}$  NMR spectroscopy was not possible due to the paramagnetic nature of the molecule. The successful metalation was confirmed by UV-vis spectroscopy where the Soret band at 415 nm and two Q bands at 575 nm and 625 nm were apparent (Figure A 76).<sup>[122]</sup> The change upon Fe metalation was also observable by IR spectroscopy (Figure A 77). Here, changes in the region at  $\sim 1000 \text{ cm}^{-1}$  presumably arised from the formed Fe-N bond.<sup>[147]</sup> Fe-TCPP was applied in the solvothermal synthesis of PCN-222 following the previously described procedure. The measured PXRD pattern of the product matched the calculated one of PCN-222 and showed high crystallinity and phase-purity (Figure A 78). ICP-MS measurements substantiated the successful synthesis of PCN-222(Fe) with a high degree of Fe metalation due to an Fe content of 1.9 wt% and a Zr:Fe ratio of 2.6 close to the theoretical value (note that in the case of PCN-222 defects need to be taken into account).

### Iron – post-metalation

For iron metalation, a post-synthetic approach using a microwave setup (Figure 26, path b) or an aluminum heating block (Figure 26, path d), respectively, was investigated ((see 5.3.3. for details).  $\text{FeCl}_2 \cdot 4 \text{H}_2\text{O}$  acted as an iron source and was in both cases suspended with the as-synthesized PCN-222 in DMF. For the microwave reaction, the reaction time was varied from 30 min to 60 min. After synthesis, the PXRD pattern recorded for both products revealed that the structure and phase-purity of PCN-222 was preserved (Figure A 78). Additionally, the metal incorporation was followed by ICP-MS measurements where a Fe content of 2.5 wt% after 30 min corresponding to a Zr:Fe ratio of 4.3 and a content of 5.3 wt% and a Zr:Fe ratio of 2.1 after 60 min (Figure 31) were calculated. The latter indicated a slight overmetalation of PCN-222 with Fe (however, also not considering linker defects in PCN-222). After Fe metalation using an aluminum block where the reaction vials were heated in, the MOF was completely decomposed as evidenced by PXRD (Figure A 78). Thus, this approach was not further studied while the microwave setup is indeed suitable for Fe metalation. Here it has to be noted that a more detailed characterization with a larger quantity of PCN-222(Fe) would be necessary.

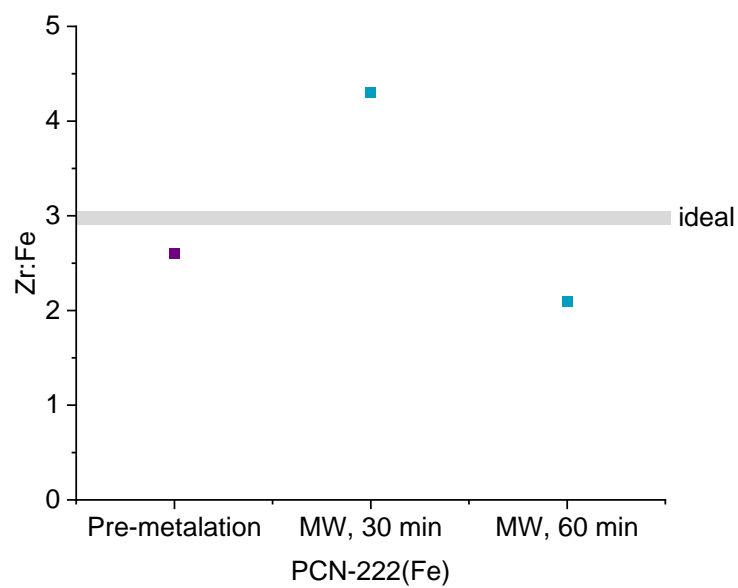


Figure 31: Zr:Fe ratios determined by ICP-MS for PCN-222(Fe) prepared via different strategies: pre-metalation (purple), with a microwave set-up (MW, blue). For the microwave setup reaction times were varied (30 vs 60 min). Additionally, the ideal Zr:Fe ratio of 3 calculated from the sum formula of PCN-222 is shown.

### Comparison of metalation strategies

The detailed studies of different metalation procedures for the various metals (Rh, Ru, Mn, Co, Zn, Ni, Cu, Fe, Mg, see Figure 25) allows to conclude on most promising techniques for each specific metal to be integrated in a porphyrin-based MOF framework. This is a key advance and an important insight provided by this Thesis, as such a detailed overview across nine metals, up to five synthesis strategies, and up to three topologies is unprecedented in literature and is designed to guide researchers in material development. Table 1 provides an overview on suitable metalation strategies. Note that the table gives an estimation if the technique is in general possible and does not include details on metal loadings and post-synthetic strategies. The latter will be described below.

Table 1: Comparison of suitable metalation strategies for different metals. If the synthesis was successful with the respective technique, this is marked with a green check mark, if not, a red cross is used. If the method was not tested, the approach is marked with -. Note that for the metalation with Cu, Ni and Fe only PCN-222 was tested.

Metal	Pre-metalation	Post-metalation
Rh	✓*	✓
Ru	✓	✗
Cu	✓	-
Ni	✓	-
Fe	✓	✓
Co	✓	✓
Mn	✓	✓
Zn	✗	✓
Mg	✗	-

\*only for PCN-222

A pre-metalation approach, i.e., substituting TCPPH<sub>2</sub> with M-TCPP in the solvothermal MOF synthesis, is suggested for Ru, Cu, Ni, Fe, Co and to some extent Rh. The latter was only successful for PCN-222(Rh) while PCN-224(Rh) and MOF-525(Rh) could not be formed with this method. In literature, this pre-metalation is mainly approached when metalated porphyrin-MOFs are targeted.<sup>[12,14,100,113,134,148]</sup> Moreover, the study indicates that PCN-222 is more tolerant towards porphyrin substitution than PCN-224 and MOF-525 using the pre-metalation approach demonstrated in the case of Rh. For the Rh case, heating of the metal precursor and as-synthesized MOFs in a post-synthetic approach is more promising, in particular with the intent of comparing different MOF topologies ensuring that performance differences might not arise from different preparation procedures.

While under refluxing conditions or heating in an aluminum block high metal loadings could be obtained, the latter resulted in MOF decomposition in several cases which needs to be considered. Here, the microwave technique is a suitable alternative if non-quantitative porphyrin metalation is desired.

For Manganese, high metal loadings were not possible with the pre-metalation technique. Therefore, if higher metal contents are desired a post-synthetic metalation using a microwave setup with precise metal equivalent adjustment is suggested. This microwave technique also showed promising results for the synthesis of PCN-222(Fe).

Especially for Zn and likely Mg post-synthetic MOF metalation seems to be crucial since a significant loss of metal occurs during heating processes. This was observed during saponification and will most probably also be the case during solvothermal synthesis. Therefore, exact adjustment of metal equivalents during post-synthetic metalation is crucial to prevent overmetalation by physisorption of metal in the MOF pores.

Noteworthy, an impact of metal precursor for porphyrin metalation – particularly important for the pre-metalation strategy – on the material properties cannot be excluded (and might affect the solvothermal MOF synthesis). However, more detailed studies are necessary for precise conclusions on the counterion effects.

In literature, both strategies – the pre- and post-synthetic metalation – have been demonstrated. Exemplarily, metalation of MOF-525 with Cu or Fe was achieved via a post-synthetic approach since pre-metalation of the porphyrin and subsequent MOF synthesis was not successful.<sup>[123]</sup> Metalation of TCPPH<sub>2</sub> with Fe, Ni, Co, Cu, Mn and Zn and its application in the solvothermal synthesis of PCN-222 is also published in literature<sup>[14,100]</sup> – however could not be reproduced for this Thesis. Therefore, more detailed descriptions in literature as discussed for the synthesis of the MOFs itself (see chapter 1.4.1) would be necessary and important to ensure synthesis reproducibility among different laboratories. Additionally, the focus in most of the published work is not on the metalation procedure itself but on the desired application. Thus, a more comprehensive material characterization should be presented in literature which is in particular important for localizing the incorporated metal, i.e. if it is indeed incorporated into the porphyrin core. This can potentially be achieved by spectroscopic methods. Especially for syntheses under higher temperatures and upon indications in N<sub>2</sub> sorption measurements (significant decrease in BET surface area after metalation) material characterization using transmission electron microscopy (TEM) can exclude the formation of metal nanoparticles.

### Metalation strategy for mixed-metal MOFs

For the design of a multifunctional MOF system able to catalyze sequential reactions the incorporation of two different metals – where each one is active in one catalysis step – is targeted. Due to the high conceptual and synthetic challenge of such a project, as a proof-of-concept reaction the sequential catalysis consisting of an epoxidation and a CO<sub>2</sub> cycloaddition step is selected – which is described in chapter 3.2.1.4. in more detail. For this purpose of a mixed-metal MOF, two strategies were pursued (Figure 32): the pre-metalation of TCPPH<sub>2</sub> with the respective metals and subsequent MOF synthesis with a mixed-linker approach (i) and the synthesis of the MOF where the first metal is incorporated during the solvothermal synthesis and the second metal integration is achieved via post-synthetic metalation of the synthesized metalated MOF with an appropriate precursor (ii). For this project PCN-222 was chosen as framework. As the epoxidation site metal Ru is selected while for the CO<sub>2</sub> cycloaddition Co, Ni, Cu and Zn are considered.

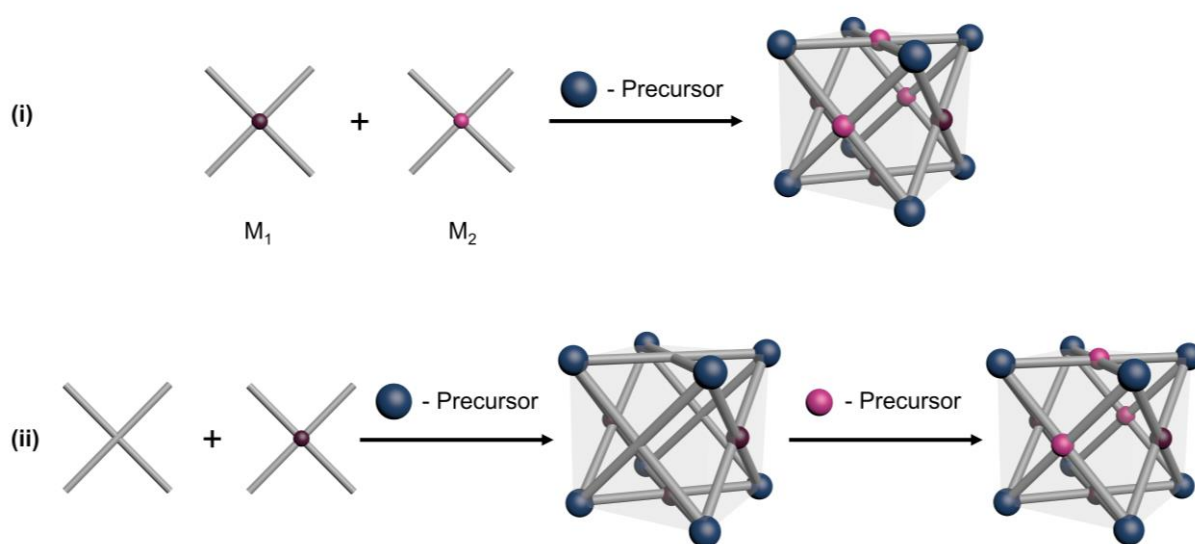


Figure 32: Schematic representation for the synthesis of mixed-metal porphyrin-MOFs via different strategies: A mixed-linker approach from two different metalloporphyrins in combination with a metal node precursor (blue, i) and the synthesis of the porphyrin-MOF containing one metal by solvothermal synthesis (mixed metal between non-metalated porphyrin and metalloporphyrin) and subsequent metalation with a second metal precursor (pink) forming the mixed-metal porphyrin-MOF (ii).

In both cases, the incorporation of Ru was achieved via the pre-metalation approach (see synthesis investigations for single-metalated PCN-222(Ru) above). For the synthesis of PCN-222(Ru,Cu) and PCN-222(Ru,Ni) the mixed-linker approach resulted in the desired material while for PCN-222(Ru,Zn) and PCN-222(Ru,Co) the post-synthetic metalation of PCN-222(Ru) proved to be more fruitful (details see 5.3.3.). Successful synthesis was confirmed by PXRD (Figure A 79) and solid-state UV-vis spectroscopy revealed the expected changes in the region of the porphyrin's Q bands upon metalation (Figure A 80). The metal contents determined by ICP-MS are summarized in Table A 12.

### Different concentrations of metals

Additionally, the here investigated metalation strategies allow for the adjustment of metal concentration and metal ratios in the resulting metalloporphyrin-MOFs. Concentration variations were achieved via a mixed-linker strategy exemplarily for Ru-TCPP(CO) and TCPPH<sub>2</sub> in the solvothermal synthesis of PCN-222 (Figure 33). As described, this allows for the integration of a second metal into the core of TCPPH<sub>2</sub> via a post-synthetic approach – where Zn was chosen (Figure 34). The results for both approaches are presented in the following.

### Ru variation in PCN-222(Ru) via mixed-linker approach

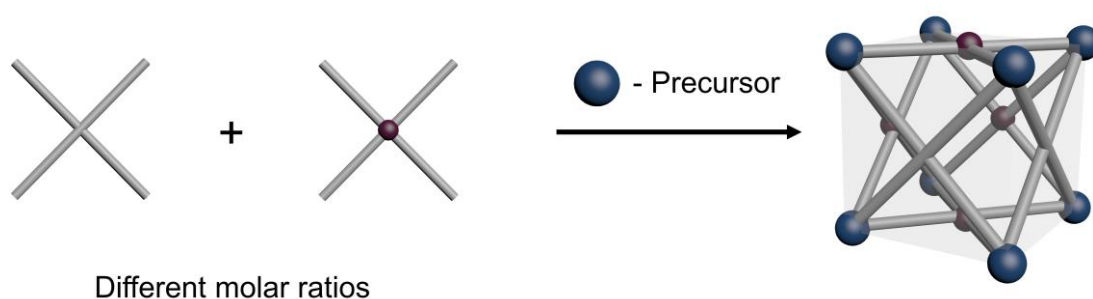


Figure 33: Schematic representation for the Ru (red) variation in metalloporphyrin-MOFs by a mixed linker approach, varying the molar ratios of non-metalated porphyrin and metalloporphyrin in solvothermal synthesis with a metal node precursor (blue).

For the synthesis of different PCN-222(Ru) materials with varied Ru content (and dispersion), the ratios of Ru-TCPP(CO) and TCPPH<sub>2</sub> were adjusted in the synthesis with following Ru-TCPP(CO):TCPPH<sub>2</sub> ratios: 100:0; 50:50; 15:85. The other parameters of the synthesis (e.g., modulator concentration, temperature, reaction time) were kept constant. Thus, three different PCN-222(Ru) materials with varied Ru loadings of 6.6 wt%, 3.2 wt% and 1.2 wt% (calculated by ICP-MS) were accessible, i.e., resulting in different metal dispersions in metalated MOFs, while the MOF structure was preserved (Figure A 81). This enables the study of dispersion effects in catalysis and presents a further strategy of catalyst loading variation (which will be discussed in chapter 3.2.1.2.). The successful incorporation of different metal amounts underlines the general applicability of the mixed-linker approach and is of particular importance for porphyrin metalation with two different metals since free TCPPH<sub>2</sub> in mixed linker PCN-222(Ru) are available for further metal incorporation.

### PCN-222(Ru,Zn) with different Zn concentrations via post-synthetic metalation

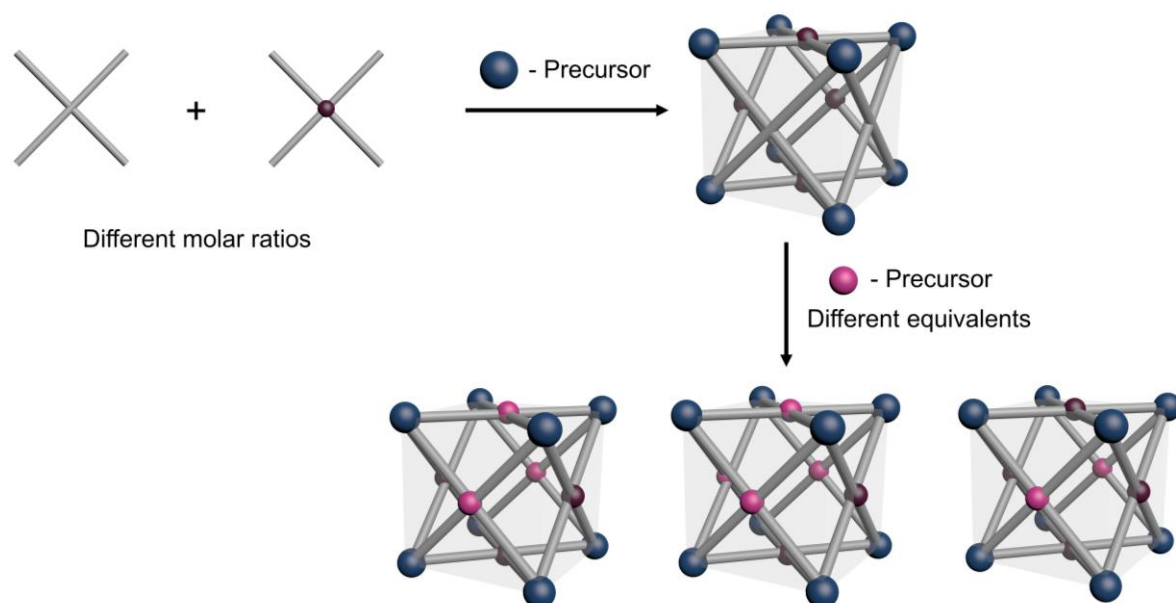


Figure 34: Schematic representation for the metal ratio variation in a mixed-metal porphyrin-MOF. First, the porphyrin-MOF containing one metal is synthesized via solvothermal synthesis from a metal node precursor (blue) and a combination of non-metalated porphyrin and metalloporphyrin (metal = red) as linkers. Here, the molar ratios between both linkers can be varied to obtain different dispersions of the first metal in the porphyrin (top). Subsequently, the resulting metalloporphyrin-MOF can be post-synthetically metalated with a second metal precursor (pink) to obtain the mixed-metal porphyrin-MOF. In the second step, the ratio of metal one (red) and metal two (pink) can be adjusted by using different equivalents of the precursor for metal two (pink).

Due to the above-described challenges of Zn-TCPP incorporation into PCN-222 during solvothermal synthesis, Zn metalation in PCN-222(Ru,Zn) was achieved by a mixed-linker approach (Ru-TCPP(CO) and TCPPH<sub>2</sub>) and subsequent post-synthetic metalation with Zn (see above). Here, different equivalents of ZnCl<sub>2</sub> were applied (1; 2 and 5 equiv.) resulting in Ru contents of 2.3 – 2.4 wt% and Zn loadings of 0.7 wt%, 1.7 wt% and 2.1 wt%, respectively. The Zr: M (M = Ru + Zn) ratios calculated from ICP-MS data ranged from 3.2 (5 equiv. ZnCl<sub>2</sub>) to 5.3 (1 equiv. ZnCl<sub>2</sub>) – where a theoretical value of 3 was expected according to the sum formula of PCN-222. Thus, while in the Zr:M = 5.3 case free porphyrin was present, almost complete porphyrin metalation was assumed for Zr:M = 3.2. Thus, in addition to the mixed-linker strategy, the post-synthetic metalation of a pre-metalated porphyrin MOF presented in this Thesis is an appealing strategy for the synthesis of mixed metal MOFs allowing for the free variation of metal ratios which is rather unexplored in literature.

## 3.2. Design of Catalyst – MOF Hybrids and their Applications

### 3.2.1. Framework-integrated Catalysts

In chapter 1.3.1. different strategies for catalyst integration into MOFs are described. One possibility is incorporating the catalytically active site as part of the framework itself, exemplarily by coordinatively unsaturated sites at the node able to perform catalytic transformations or linker functionalization. In this Thesis, the latter approach is followed by incorporation of a catalytically active metal into the porphyrin linkers of porphyrin-based Zr-MOFs presented in chapter 3.1.2.3. As indicated here, the usage of such MOF systems is appealing since they can be metalated with a large variety of different metals and yield topological diversity despite identical building units. Especially the latter allows for the sophisticated study of confinement effects in MOF catalyzed reactions, i.e. whether the topology of the MOF affects the catalytic performance. Additionally, the possibilities of combining differently metalated porphyrins into one framework are theoretically almost unlimited allowing for the design of multifunctional systems for several reaction types. Despite this high conceptual appeal, research efforts are still in their infancy. The benefits of exploiting confinement effects for steering catalytic reactions or the design of sophisticated, multifunctional systems is of particular interest over the course of this Thesis and are the reason why these porphyrin-based MOFs were selected.

Moreover, the integration of metalated porphyrins as linkers in the framework does not affect the porosity – allowing unhindered diffusion of molecules – compared to the approach of integrating catalytically active molecules in the MOF pores, e.g., by attaching them to the node. Thus, the high porosity is maintained while simultaneously accessibility of the active sites for substrates is enabled. Thus, the subsequent chapters 3.2.1.1 – 3.2.1.4. present applications in catalysis where the strategy of metalated porphyrins as MOF linkers is followed.



### 3.2.1.1. Rh-porphyrin MOFs for Confinement Effect Studies

This chapter is based on the publication: Karina Hemmer, Raphael Bühler, Martin Elsner, Mirza Cokoja, Roland A. Fischer, *Catal. Sci. Technol.* **2023**, *13*, 3304-3312.

Experiments were conducted by K. Hemmer including design and optimization. DFT calculations were performed by R. Bühler. ICP-MS measurements were conducted at the chair of M. Elsner. M. Cokoja and R. Fischer also designed the project and gave overarching academic guidance. The manuscript was written by K. Hemmer and edited by all co-authors.

While the potential of exploiting confinement effects for reactions catalyzed by MOFs and thus controlling activities or selectivities is high, only a few studies to date have contributed to understanding the effect of MOF confinement.<sup>[67,78,81–83,87]</sup> Such fundamental investigations are important, as the gained conceptual insights are key in advanced catalyst design. Previous work of Fischer *et al.* indicated the importance of topological differences for the diastereoselectivity enhancement in the cyclopropanation of styrene and its derivatives.<sup>[87]</sup> The cyclopropanation activity of Rh has been demonstrated in literature for homogeneous and heterogeneous Rh (porphyrin) systems.<sup>[87,149,150]</sup>

Thus, Rh was incorporated into the porphyrin core of the framework creating single catalytic sites and embedded in a MOF framework (namely PCN-222 and PCN-224, as linking molecule between the nodes). The in this Thesis performed study builds upon the previous publication of Fischer *et al.* and aims to gain deeper insights and a fundamental understanding of their findings.<sup>[87]</sup> Precisely, an increase in diastereoselectivity toward the *trans* cyclopropanation product was observed for styrene derivatives with -NH or -OH functionalization. The diastereomeric ratio (toward *trans*) could be further enhanced by changing the MOF topology – from PCN-224(Rh) to PCN-222(Rh). The results indicated that both a coordinating functionality and a close contact of active sites are crucial since coordination of the styrene derivative to a neighboring Rh center is anticipated – controlling the selectivity by a pre-alignment of the substrate. Nevertheless, further studies are necessary to confirm this hypothesis. This is the starting point for the investigations presented herein. First, reaction conditions were screened and optimized prior to mechanistic studies. For mechanism elucidation, a third MOF – MOF-525(Rh) – is included which has also cubic pores (like PCN-224) but an increased connectivity (12 vs 6 for PCN-224) resulting in a higher linker density in the material (Figure 35). Since potential Rh – Rh contacts seem to be important, this might affect the selectivity.

Moreover, an additive approach is followed where molecules with a coordinating function like pyridine, aniline, phenol, or ethylene diamine were added to the catalytic reaction (Figure 35). The aim here is to investigate potential interference with the substrates by coordination of the additive to a neighboring Rh center, thus, decreasing the diastereoselectivity by preventing substrate pre-alignment.

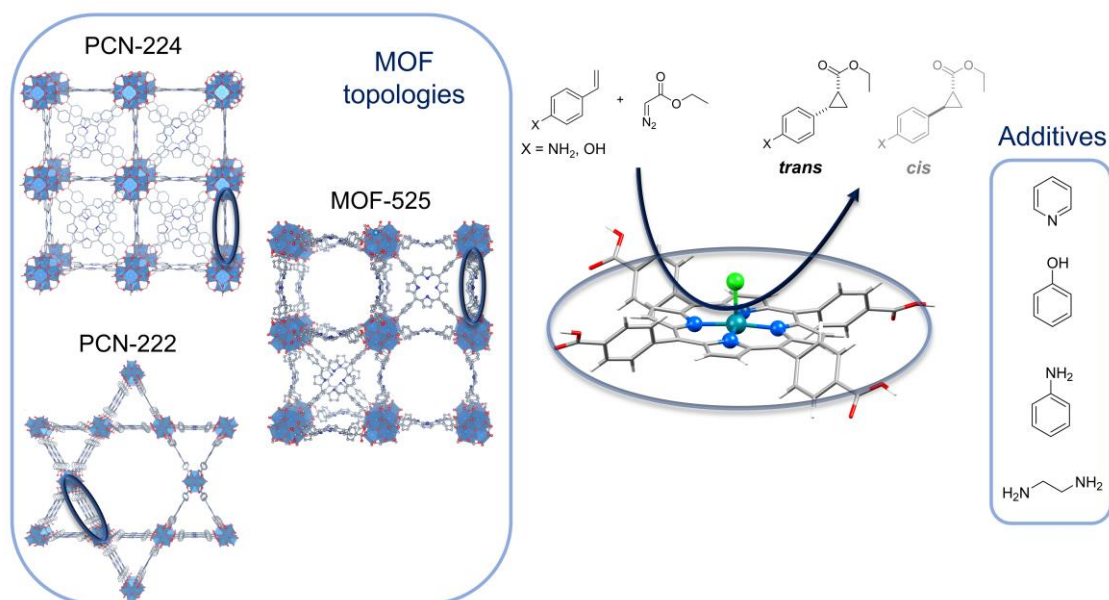


Figure 35: Schematic representation of the cyclopropanation of styrene (-derivatives) with EDA as carbene source using Rh-TCPP as catalyst (blue: Nitrogen, turquoise: Rhodium, green: Chlorine, grey: Carbon, red: Oxygen, white: Hydrogen). The Rh-porphyrin is incorporated as linker in the different topologies of PCN-224, PCN-222 and MOF-525 allowing for the study of topology differences. While for styrene as substrate the ratio of *trans* and *cis* product is 1:1, an increased diastereoselectivity towards the *trans* product for -NH<sub>2</sub> or -OH functionalized styrene was described previously.<sup>[87]</sup> Moreover, coordinating molecules (pyridine, aniline, phenol, ethylenediamine) are added to investigate their impact on the catalytic performance.

Importantly, the reaction was selected as a proof-of-concept reaction for the study of potential confinement/topology effects. Thus, optimizing the performance to outperform reported cyclopropanation catalysts is not aspired to.

Material synthesis of PCN-222(Rh), PCN-224(Rh) and MOF-525(Rh) was described in chapter 3.1.2.3. Since only PCN-222(Rh) was accessible via the pre-metalation approach all three MOFs were synthesized first and metalated post-synthetically in an aluminum block setup. Here, a suspension of the respective MOF and RhCl<sub>3</sub>·xH<sub>2</sub>O in DMF were heated (120 °C) in a closed vessel. A uniform procedure for all MOFs was applied to exclude that catalytic performance differences arise from varied synthesis strategies. Detailed descriptions of the procedure and material characterization can be found in chapter 5.3.3. Noteworthy, the synthesis was repeated for several times and the batches were combined to obtain a sufficient amount of (metalated) MOF material for all experiments while simultaneously precluding the potential impact of material property differences (between the varied batches) – such as the defect concentration or metal content.

In the following, the results on the optimization of reaction conditions and the mechanistic studies (i.e., with the additive approach) will be presented and discussed.

### Reaction condition optimization

The reaction setup previously published serves as the starting point for parameter optimization.<sup>[87]</sup> Here, cyclopropanation catalysis was performed at room temperature in a heterogeneous system where the MOF was suspended in the substrate styrene (thus, the substrate was used in excess) while a solution of ethyl diazoacetate (EDA) in dichloromethane (DCM) was added dropwise. In this Thesis, reaction temperature, solvent (important for solid styrene derivatives or decreased substrate amounts) and the stoichiometry of the reactants were altered. Analysis of the reaction solution should reveal potential impacts on the catalytic performance (activity and selectivity) while the main focus is placed on the diastereoselectivity of the reaction which is described by the *cis/trans* product ratio. In this work, the reaction setup described above and in literature was used where the styrene derivatives were dissolved in DCM.<sup>[87]</sup> After the addition of EDA via a motorized syringe pump an aliquot was taken from the reaction mixture, the catalyst removed by filtration and analyzed via gas chromatography. The latter allows for the determination of the catalytic activity and (diastereo-)selectivity (for details see 5.4.1.). For the calculation of the reaction selectivities the sum of *cis* and *trans* cyclopropanation products and side products – including coupling products of EDA, linear allyl species etc. – were considered.

For the reaction setup it is important to note that the calculation of reaction rates was not possible since samples could not be taken during EDA addition to prevent changes in reactant stoichiometry.

As mentioned above, in the context of the confinement effect studies, MOF-525(Rh) was included as catalyst for styrene(-derivative) cyclopropanation. The catalytic activity decreases in the following order: PCN-222(Rh) > PCN-224(Rh) > MOF-525(Rh) (Figure 36, Figure A 82). Note that minor amorphous contents in MOF-525(Rh) may contribute to a lower activity. Importantly, in accordance to previous findings, MOF variation revealed that the *cis/trans* selectivity was not affected by altered topologies in the case of styrene. The calculated *cis:trans* ratio was 1:1 for all three Rh-MOFs (Figure 36). The catalytic performance indeed arised by the Rh-porphyrin incorporated into the framework since control experiments without adding one of the three MOFs and with their non-metalated analogues, respectively, did not give any conversion (Figure A 83, Figure A 84, Figure A 85). PXRD characterization after cyclopropanation catalysis showed that all three MOFs are stable under the applied conditions (Figure A 99, Figure A 100, Figure A 101).

Moreover, catalyst recycling was possible as exemplarily shown for PCN-222(Rh) where an activity loss after each cycle needs to be taken into account (Figure A 92). Especially the catalytic setup itself, i.e., centrifugation and washing of the MOF between the different cycles and the generally small amounts of MOFs used in the experiments, were problematic regarding the recycling.

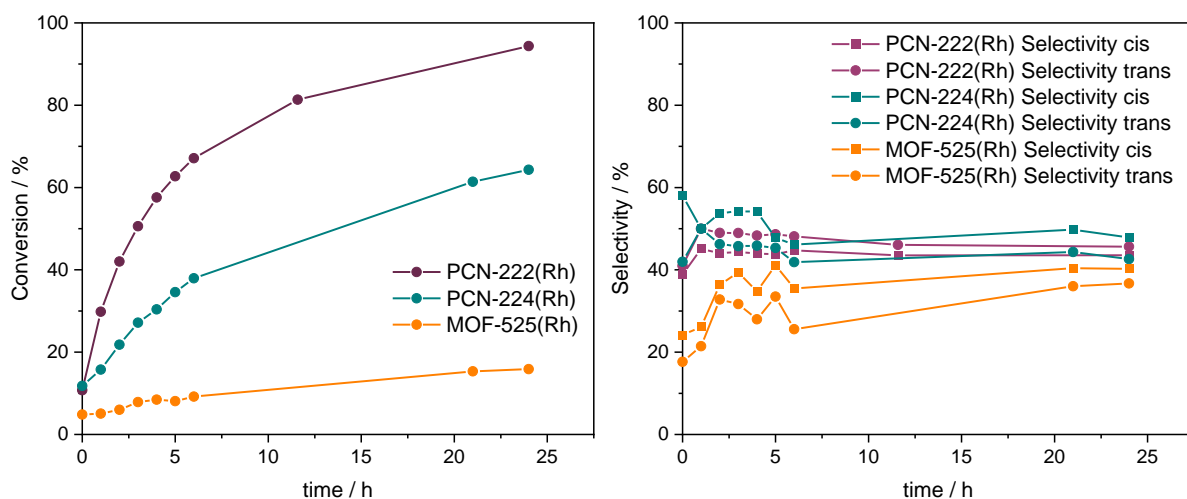


Figure 36: Conversion and selectivity of the styrene cyclopropanation with EDA as carbene source under standard reaction conditions. PCN-222(Rh) (violet), PCN-224(Rh) (turquoise) and MOF-525(Rh) (orange), respectively, were used as catalysts.

Further parameter optimization was conducted with PCN-222(Rh) as a model catalyst due to its increased activity compared to PCN-224(Rh) and MOF-525(Rh). The *cis:trans* selectivity was also not affected by solvent variation (acetonitrile (MeCN) vs DCM)) remaining at 1:1. However, the activity was decreased which was probably caused by MeCN coordination to the Rh centers (Figure A 86) resulting in a decreased accessibility of the Rh sites by the substrate. Temperature enhancement (r.t. vs 50 °C, MeCN as solvent) led to a higher conversion while the formation of the *trans* isomer was slightly favored (Figure A 87). However, for further investigations DCM was used as solvent due to the higher activity of the latter at room temperature compared to MeCN.

### Mechanistic Studies

In a previous study, an alteration of substrates, i.e. using styrene derivatives with an amino- or hydroxy functionality, resulted in a drastic increase in the diastereomeric ratio, preferentially forming the *trans* diastereomer which could additionally be affected by changing the MOF topology.<sup>[87]</sup> Here, a correlation between interactive site distance (arising from the different MOF topologies) and the diastereoselectivity was anticipated – as stated above.

For more detailed insights and to elucidate potential causes of the diastereoselectivity enhancement, in this Thesis, kinetic measurements were performed where the activity and in particular the *cis:trans* selectivity of the styrene derivative cyclopropanation were followed. Analysis during catalysis reveals an exclusive *trans* isomer formation of 4-aminostyrene (4-AS) as substrate (Figure 37 and Figure 38). Cyclopropanation of 4-hydroxystyrene resulted in a very limited activity (~17% after 24 h) and a significant presence of side products which might also arise from the stabilizers of the substrate. Since no unambiguous conclusions can be drawn from this experiment, this substrate was not further studied. In contrast to 4-AS, the cyclopropanation of 4-chlorostyrene yielded both the *cis* and *trans* isomers with a molar ratio of 1:1 – comparable to unfunctionalized styrene – which is in line with previous observations (Figure 37, Figure A 88).<sup>[87]</sup>

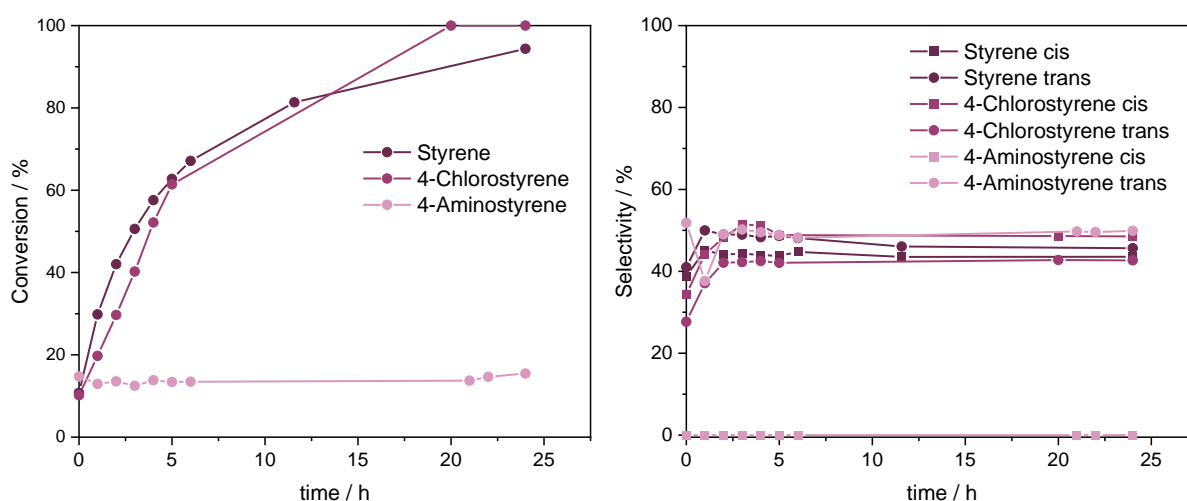


Figure 37: Conversion and Selectivity during the reaction progress of the cyclopropanation with EDA using PCN-222(Rh) as catalyst under standard reaction conditions with substrate variation: styrene versus 4-chlorostyrene versus 4-aminostyrene.

Simultaneously, these results strengthen the hypothesis that the amino- and hydroxy group (from previous studies) have a common feature which allows for the increase of the diastereoselectivity which is not present in the case of chloro- or non-functionalized styrene. Both first mentioned functional groups have a coordinating ability on the one hand and the potential of hydrogen bonding on the other hand which are both absent for chlorostyrene and styrene.

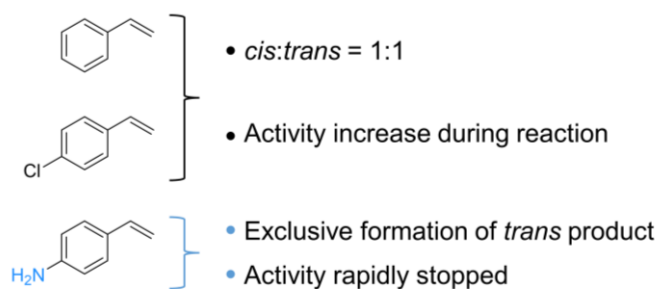


Figure 38: Summary of the main findings of substrate variation in the cyclopropanation.

Most intriguingly, topology variation did not cause a change in *cis:trans* selectivity. All tested topologies, namely PCN-222(Rh), PCN-224(Rh) and MOF-525(Rh) resulted in the *trans* diastereomer exclusively (Figure 39, Figure A 89). These results suggest that the increase in the diastereoselectivity does not arise from topology effects as indicated previously. In the previous study diastereomeric ratios of 42:1 (*trans:cis*) for PCN-222(Rh) and 23:1 (*trans:cis*) for PCN-224(Rh) were obtained where the difference between both values is in general rather small.<sup>[87]</sup>

Particularly in the case of the here applied porphyrin-based MOF catalysts the synthetic challenges need to be considered which might have caused these observed differences in the diastereoselectivity of 4-AS cyclopropanation. However, studying the homogeneous porphyrin system Rh-TPPCOOMe revealed a *trans:cis* ratio of 4.9:1 for the substrate 4-AS (C(36 h) = 52%) which was significantly lower than with all compared MOF catalyst systems. This indicates that the incorporation of the Rh-porphyrin into a MOF scaffold is essential in favoring the *trans* cyclopropanation product.

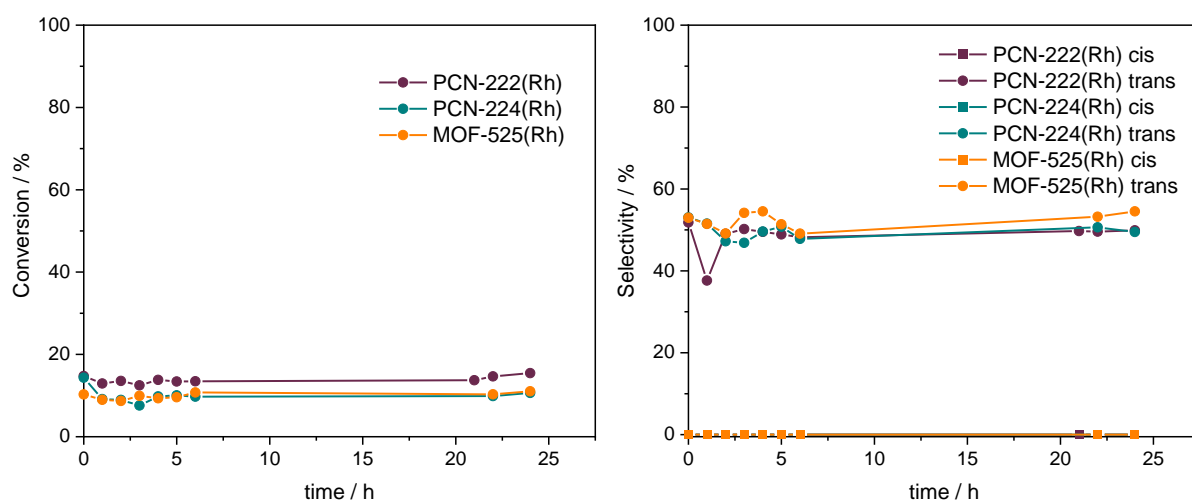


Figure 39: Conversion and Selectivity during the reaction progress of the 4-aminostyrene cyclopropanation with EDA under standard reaction conditions varying the catalyst: PCN-222(Rh) versus PCN-224(Rh) versus MOF-525(Rh).

In addition to effects on the selectivity, the kinetic measurements revealed a second interesting feature. In contrast to styrene and chlorostyrene, where the conversion showed a rather “classical” progress during catalysis, the activity in the case of 4-AS did not increase during the reaction and remained unchanged for the complete catalysis at ~13% (Figure 39). This suggests that the coordinating ability of the amino group (stated above – in contrast to the chloro functionality) prevents further catalysis at the Rh center for carbene intermediate formation by blocking this site via coordination of the amino group to Rh. Previously, the importance of the olefin nature and concentration has been investigated where the Rh-carbene formation can be either negatively influenced by competition between the olefin and the carbene source for the vacant coordination sites or accelerated.<sup>[151]</sup> Supported by prior studies,<sup>[152,153]</sup> the first case is assumed in the cyclopropanation investigations performed in this Thesis decreasing the substrate conversion, which is in particular observable in the kinetic profile. Thus, lowering the concentration of 4-AS (i.e. the ratio of 4-AS:EDA) resulted in an increased conversion (Figure A 90) – in line with the reaction rate dependence on the olefin concentration described in literature.<sup>[151]</sup> Noteworthy, 4-AS concentration variations did not change the *cis:trans* ratio and the kinetic profile. Upscaling of the reaction setup (by factor 2) did not affect the activity and selectivity of the cyclopropanation catalysis (Figure A 91).

Therefore, two aspects need to be clarified for a more detailed understanding of the cyclopropanation with the here studied MOF catalysts: the kinetic behavior observed for 4-AS differing to styrene and chlorostyrene and the selectivity enhancement for 4-AS compared to styrene upon porphyrin incorporation into a confined MOF scaffold. Here it is important to highlight again the independence of diastereoselectivity on the MOF topology.

For further insights, molecules with a coordinating ability such as pyridine, aniline, ethylene diamine and phenol were added respectively in the cyclopropanation of 4-AS to study their potential influence on the performance (Figure 40). Due to the small size of the additives, pore blocking and thus limiting substrate diffusion are excluded. For the experiments two cases are imaginable: 1) the additive acts as placeholder for EDA, preventing the blocking of active sites by the olefin and 2) a diastereoselectivity decrease is observable assuming that the presence of neighboring Rh sites for substrate pre-alignment is important as suggested previously.<sup>[87]</sup> The results highlight that the diastereoselectivity is in general not affected independent of the molecule added and its concentration – only obtaining the *trans* product (Figure 40, Figure A 93 – Figure A 97). Although the selectivity was not influenced by the additive, a significant effect of the additive concentration on the catalyst activity was apparent. High concentrations (50 mol% additive regarding Rh) resulted in a decreased conversion (less than 10%, Figure A 98) suggesting that larger amounts of additive resulted in active center blocking.

Interestingly, small amounts of additives (0.05 mol%) positively impacted the activity – observable for all different molecules added. This effect was more pronounced in the case of pyridine and aniline where the conversion could be increased by almost 100% (with pyridine, C = 22% instead of C = 13% after 24 h, Figure 40, Figure A 93), suggesting the importance of relative binding strength of both the substrate and the additive for the conversion.

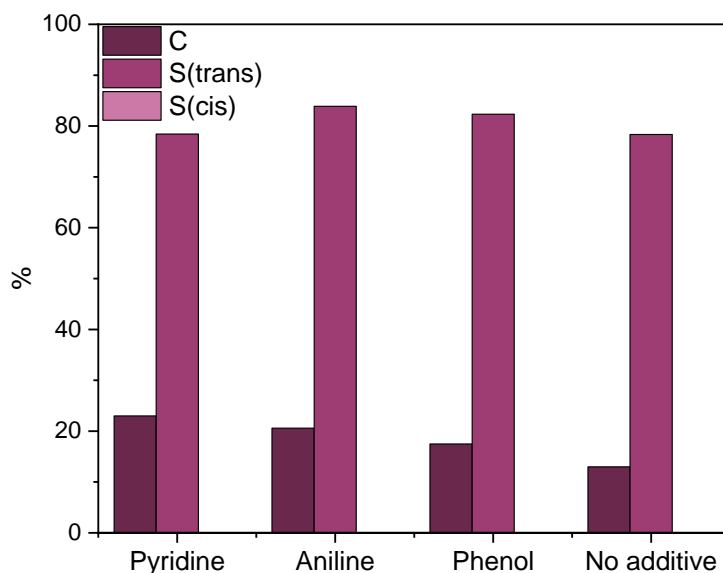


Figure 40: Conversion and Selectivity for the *cis* and *trans* cyclopropanation product of 4-AS with EDA under standard reaction conditions using PCN-222(Rh) as catalyst and 0.05 mol% additive (regarding mol Rh) after 6 h of reaction time.

The effect of donor molecule addition on the cyclopropanation activity was studied by DFT calculations – exemplarily performed for the additive pyridine. Since the carbene intermediate formation upon  $N_2$  release is reported as the rate-determining step,<sup>[151]</sup> transition states of model complexes, where 4-AS or pyridine act as spectator ligands, were calculated and validated by analytical frequency calculations with a single negative frequency (corresponding to the C-N vibration). The energy difference between the calculated transition state of the 4-AS containing carbene ( $\Delta G = 17.5$  kcal/mol) and the pyridine coordinated complex ( $\Delta G = 7.4$  kcal/mol) was calculated as 10.1 kcal/mol (Figure 41). This shows that the energetic barrier for the olefin coordinated Rh-carbene is almost twice as high compared to the pyridine analogue, supporting the empirical observations. Here it is important to note that the mechanistic studies in literature were performed for Rh complexes bearing iodide as the ligand instead of chloride. Thus, the different binding strength of the Rh-I and Rh-Cl bonds need to be taken into account for the mechanistic considerations in this study. Since the Rh-Cl bond is in general stronger than the Rh-I bond, release of  $Cl^-$  is rather unlikely and the mechanism for Cl-bearing Rh porphyrin complexes might deviate from the iodide case.<sup>[154]</sup>



Therefore, more detailed investigations on the mechanism with the Cl<sup>-</sup> bearing Rh complex are necessary in future study and the here presented results aim to give a rough estimation on the influence of the additive.

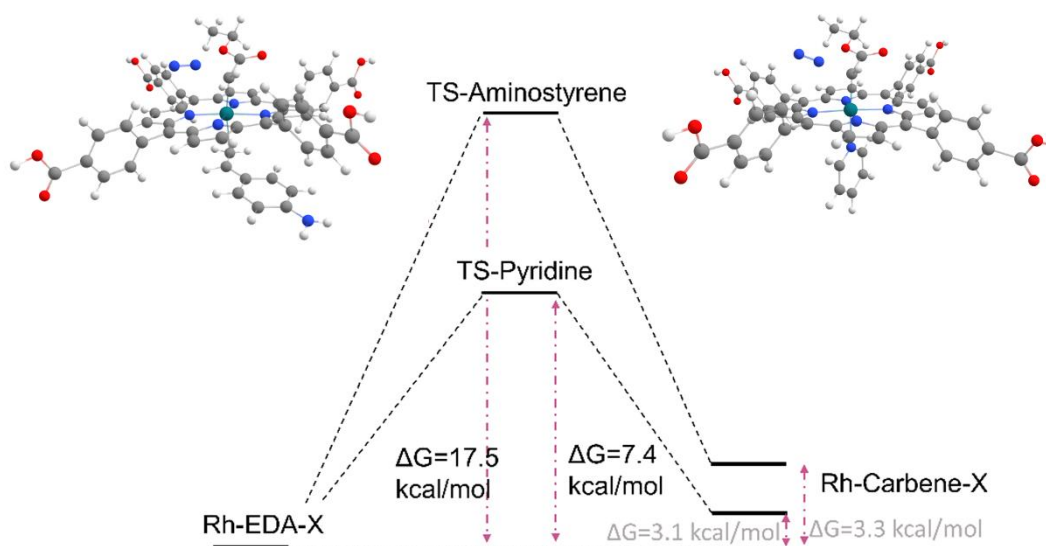


Figure 41: Energy diagram for the carbene formation transition states calculated for model complexes with 4-AS and pyridine as spectator ligand (B3LYP/def2-svp). Atom colors: orange = Rhodium, pink = Nitrogen, grey = Carbon, white = Hydrogen.

As described above, most importantly, the *cis:trans* selectivity of the cyclopropanation of 4-AS was not affected by an additive. Thus, coordination of the substrate to a neighboring Rh center resulting in substrate pre-alignment is assumed to be not essential. Therefore, the increased diastereoselectivity has to arise from another feature. In literature, several Rh-porphyrin complexes have been reported to catalyze the cyclopropanation of styrene in homogeneous phase. In general, it is assumed that the porphyrin skeleton and the macrocycle substitution significantly impact the diastereoselectivity of the reaction.<sup>[150,155]</sup> Although no general trend is apparent, both the porphyrin – by its steric demand and electronic hinderance – and the substrate itself (e.g. by  $\pi$ - $\pi$ -interactions for styrene substrates) can steer the diastereoselectivity.<sup>[150,156]</sup> As an example, the formation of the *trans* diastereomer is favored for terminal olefins by a parallel alignment of the olefin to the Rh-carbene.<sup>[150,152]</sup> This is in agreement with the *cis:trans* selectivity detected in the experiments of this Thesis. However, the *trans* selectivity was increased to an extremely high extent – compared to literature and the here studied homogeneous counterpart – since the formation of the *cis* product was completely excluded with 4-AS as the substrate. Since this effect was less pronounced in homogeneous phase and absent for styrene as the substrate, an interaction between the amino group of 4-AS and a feature emerging upon porphyrin integration into the MOF scaffold seems to be the key for the diastereoselectivity enhancement.

Additionally, the hypothesis of a topology influence and the importance of neighboring Rh sites could not be confirmed in this Thesis (also see the additive approach), consequently a feature present in the MOFs independent on the topology is assumed to interact with the amino group (see Table 2). Here, an interaction with the Zr-oxo node seems to be a promising option. Thus, IR measurements were performed to gain information on possible interactions. After soaking PCN-222(Rh) for example in a solution of 4-AS and DCM for two hours, the solvent was evaporated for the measurement. The spectrum was compared to the ones of PCN-222(Rh) and 4-AS (Figure 42) where small deviations were apparent in the NH<sub>2</sub> stretching vibration regions.<sup>[157]</sup> Here, peak broadening at 3439 cm<sup>-1</sup> and a peak shift from 3356 cm<sup>-1</sup> to 3341 cm<sup>-1</sup> of the 4-AS peaks were apparent upon MOF addition indicating the presence of hydrogen bonding of the substrate to the MOF.<sup>[157,158]</sup> This is supported by the diastereoselectivity increase for 4-hydroxystyrene as substrate presented in literature, which is also able to form hydrogen bonds, and the absence of diastereomer favoritism for chloro- and dimethylaminostyrene where hydrogen bonding is not possible.<sup>[87]</sup> It is important to note that for this hypothesis of hydrogen bonding interactions to the Zr-node indicated here, further studies are essential, e.g. DFT calculations or DRIFTS (Diffuse reflectance infrared Fourier transform spectroscopy) analysis with the opportunity of revealing interactions at the Zr node.<sup>[47]</sup>

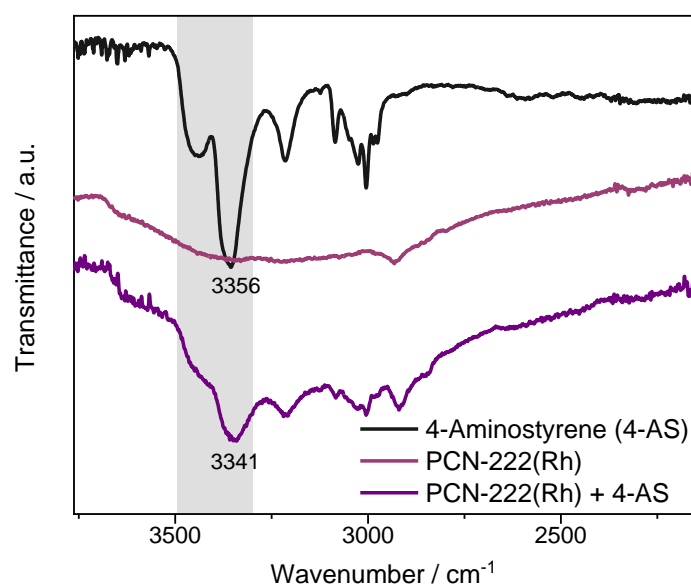




Figure 42: Comparison of IR spectra of 4-AS, PCN-222(Rh) and PCN-222(Rh) soaked for 2 h in a 4-AS/DCM solution. The area of changes is marked in grey.

As a resumé, hypotheses for the diastereoselectivity increase of this work and described previously are summarized in Table 2.<sup>[87]</sup> Additionally, observations and corresponding experiments are described which enable the evaluation of the different hypotheses – including an assessment of the hypothesis status.

Table 2: Summary of hypotheses for the diastereoselectivity increase in the cyclopropanation of specific styrene derivatives (in particular for 4-AS), observations made in this Thesis and the corresponding experiment. Additionally, the status of hypothesis investigation is evaluated.

Hypotheses for selectivity increase	Observations (this Thesis)	Experiment	Status
Topology difference (Rh-Rh distance) <sup>[87]</sup>	<ul style="list-style-type: none"> <li>• Diastereoselectivity independent on MOF topology</li> </ul>	MOF variation	Negated
	<ul style="list-style-type: none"> <li>• Diastereoselectivity unaffected by Lewis basic additives</li> </ul>	Additive approach	
MOF incorporation (Interaction with Zr nodes)	<ul style="list-style-type: none"> <li>• Absence of diastereoselectivity enhancement in homogeneous phase for 4-AS</li> </ul>	Cyclopropanation of 4-AS with Rh-TCPP	Further investigation
	<ul style="list-style-type: none"> <li>• Common feature in all MOF topologies (Zr nodes)</li> </ul>	Topology variation	
	<ul style="list-style-type: none"> <li>• H-bond interactions of NH<sub>2</sub> group</li> </ul>	IR spectroscopy	

In conclusion, this chapter highlights the potential of exploiting the confinement of a homogeneous catalyst, e.g. a metalloporphyrin, to steer the selectivity of a reaction which has been exemplarily shown for the cyclopropanation of styrene(-derivatives) with Rh-porphyrins in the framework of PCN-222, PCN-224 and MOF-525. Although in this case no topology impact could be confirmed, the potential of these materials to influence catalytic reactions by their different topology and interactive site distance has been demonstrated previously<sup>[81,82]</sup> and presents an appealing strategy for future catalyst design for targeted applications, in particular with the aim of resembling principles in enzymatic systems. Simultaneously, the detailed characterization and elucidation of underlying principles and interactions of e.g. selectivity enhancements, have been shown to be challenging, however, key for further design strategies and require extensive (multidisciplinary) investigation, in particular by combining experiment and theory.

### 3.2.1.2. Metalloporphyrin MOFs as Epoxidation Catalysts

Comparable to the cyclopropanation of styrene, the epoxidation of olefins is a second proof-of-concept reaction studied in this Thesis. Recently, several metal-organic framework catalysts have been reported to successfully perform this type of reaction.<sup>[62]</sup> Importantly, as stated, the reaction serves as a model test to design catalysts with specific properties: 1) for the exploitation of potential confinement effects – reminiscent of the cyclopropanation studies and 2) for the engineering of multifunctional catalysts for sequential reactions where the epoxidation catalysis could be the first reaction step. Therefore, differently metalated porphyrins were incorporated into MOF networks – again PCN-222, PCN-224 and MOF-525 – to allow for their performance study in the epoxidation catalysis. In literature, manganese, iron, cobalt or ruthenium porphyrins are prominent catalysts for this type of reaction.<sup>[159]</sup> In general, an oxidizing agent is required in combination with the metal catalysts. Here, various combinations have been reported which have proven successful, e.g. Mn with TBHP (*tert*-butyl hydroperoxide) or O<sub>2</sub>, Fe with molecular hydrogen peroxide, Co with TBHP, or Ru with N-oxides (e.g. 2,6-dichloropyridine N-oxide (Cl<sub>2</sub>pyNO)).<sup>[29,114,139,160]</sup> Since previous studies revealed a limited activity (5% after 17 h) of Fe-porphyrins incorporated into a MOF framework (PCN-222(Fe)) for the epoxidation activity, this metal was excluded in this Thesis.<sup>[122]</sup> Instead, Mn and Co were incorporated into the porphyrin core of the different Zr-porphyrin MOFs (see chapter 3.1.2.3.). For metalated PCN-222 systems, namely PCN-222(Mn), epoxidation with O<sub>2</sub> as oxidizing agent (with an aldehyde as co-reductant) and TBHP were described in literature.<sup>[91,122,139]</sup>

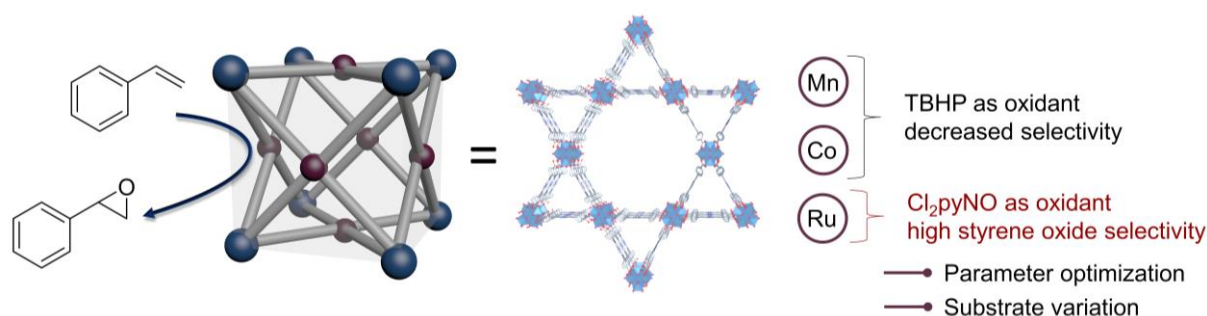


Figure 43: Conceptual representation of the styrene epoxidation catalysis with different PCN-222(M) (M = Mn, Co, Ru) catalysts. In addition to oxidant variation, parameter optimization and substrate variation were performed.

The following investigations were exemplarily performed for PCN-222(M), since its synthesis – also with different metals in the porphyrin core – has been shown in this Thesis as most reliable (Figure 43). Details on the catalysis procedures and the characterizations for the different PCN-222(M) catalysts can be found in chapter 5.4.2. In a first step, their stability towards different oxidizing agents was tested. For PCN-222(Mn) and PCN-222(Co) TBHP (70% in water) was selected as oxidizing agent while for PCN-222(Ru) Cl<sub>2</sub>pyNO was used.

The stability of each compound under the applied conditions (with oxidizing agent present) was confirmed via PXRD after 24 h of soaking (Figure A 102, Figure A 103). Although the stability of PCN-222(Ru) was maintained with TEMPO present, no conversion of styrene with TEMPO as an oxidant and PCN-222(Ru) as the catalyst was detected.

Epoxidation of styrene with PCN-222(Mn) and PCN-222(Co), respectively, resulted in minor conversion (19% and 15%, respectively) after 24 h at room temperature analyzed by  $^1\text{H}$  NMR spectroscopy (Figure A 104). The conversion could be enhanced by a temperature increase to  $50^\circ\text{C}$  yielding 62% for PCN-222(Mn) and 52% for PCN-222(Co). While reactions without TBHP did not result in any conversion, attempts without MOF catalyst yielded 1-phenylethane-1,2-diol but no styrene oxide. Kinetic measurements (after each hour for the first 7 h and after 24 h) showed a constant increase in conversion, however, the highest selectivity towards styrene oxide after 7 h (e.g., below 40% for PCN-222(Co)). In general, significant amounts of by-products like 1-phenylethane-1,2-diol, benzaldehyde, 2-phenylacetaldehyde and acetophenone (Figure A 105) were formed – strongly suggesting the presence of radical mechanisms as supported by literature.<sup>[161]</sup> In the course of this Thesis, and in particular for the control of reaction sequences and the study of potential confinement effects, radical reaction paths are undesired and therefore the epoxidation of styrene with PCN-222(Mn) and PCN-222(Co) was not further investigated.

Accordingly, further studies on the epoxidation of styrene focus on PCN-222(Ru) as catalyst. Since epoxidation with  $\text{Cl}_2\text{pyNO}$  showed promising results,<sup>[114]</sup> this oxidizing agent was applied in all following studies. Noteworthy, a pre-catalytic formation of the active Ru(IV) species, e.g. by reaction with metachloroperbenzoic acid (MCPBA) reported in literature,<sup>[136]</sup> was not necessary since the active species was generated *in-situ*. Analysis of the conversion as a function of reaction time in this Theses indicated an induction period within the first hour of epoxidation catalysis supporting the proposed oxygen transfer from  $\text{Cl}_2\text{pyNO}$  to Ru(II) resulting in the active Ru(IV)-oxo-species (Figure A 106).

In the following, parameter variation such as solvent, reaction temperature, concentrations or catalyst loading are described. Benzene, DCM and deuterated chloroform ( $\text{CDCl}_3$ ) yielded the desired product styrene epoxide with 32, 100 and 100 % conversion after 24 h at  $40^\circ\text{C}$ , respectively, while in acetonitrile styrene was not converted probably by coordination to Ru (Figure A 107, Figure A 108). Temperature increase (from room temperature to  $40^\circ\text{C}$ ) with DCM or  $\text{CDCl}_3$  as solvent resulted in higher conversions for both cases (Figure A 107, Figure A 108). Since the selectivity is slightly lower for  $\text{CDCl}_3$  (83% vs 92% for DCM after 8 h) further catalyses were performed at  $40^\circ\text{C}$  with DCM as solvent.

The enhancement of oxidant equivalents from 1.1 equiv. to 2.2 equivalents  $\text{Cl}_2\text{pyNO}$  (regarding the substrate) did not result in an improvement of the performance – instead, decreasing the conversion – which might indicate that both the oxidant and the substrate compete for Ru coordination (Figure A 109, Figure A 110).<sup>[162]</sup> In general, the catalyst loading (Ru) can be influenced in different ways, i.e. by the different metalation strategies described above (see 3.1.2.3.) and thus different metal contents within PCN-222 or by using the same PCN-222(Ru) material, however, with varied quantities of the material. For the latter case, i.e. adjusting the catalyst loading via different amounts of PCN-222(Ru), an improvement of reaction rates was achieved by increased catalyst loadings (0.05 mol% vs 0.10 mol% vs 0.25 mol% Ru regarding the substrate, Figure A 109) in combination with selectivities of 100%, 96% and 91% (Figure A 110), respectively. Adjusting the catalyst loading via the different metalation strategies, e.g., by post-synthetic metalation with different amounts of  $\text{Ru}_3(\text{CO})_{12}$  or a mixed linker approach with varied ratios of TCPPh<sub>2</sub> and Ru-TCPPhCO, allows for the study of different metal dispersion (different amounts of Ru) within PCN-222. Since the post-synthetic metalation of PCN-222 with  $\text{Ru}_3(\text{CO})_{12}$  was not successful (see 3.1.2.3.), the mixed-linker approach was followed for dispersion regulation. This approach resulted in the three Ru loadings: 1.17 wt%, 3.22 wt% and 6.56 wt%. Catalytic tests showed that the dispersion of Ru did not alter the catalytic performance significantly (Figure A 111, note that for the high conversion of 3.22 wt% Ru the small experimental scale might play an important role).

Upon parameter variation optimized conditions could be deduced which were applied in all further studies resulting in 100% conversion and a styrene oxide selectivity of 91% after 5 h: a catalyst loading of 0.25 mol% (Ru), 1.1 equiv. of oxidant ( $\text{Cl}_2\text{pyNO}$ ) with the solvent DCM at 40 °C.

In control experiments performed without  $\text{Cl}_2\text{pyNO}$  or PCN-222(Ru) no conversion of styrene could be detected confirming the importance of both compounds (Figure A 112). Hot filtration of the catalyst after 2 h prevented further conversion precluding Ru leaching (Figure A 113). Noteworthy, catalysis with PCN-222(Ru) where the modulator of MOF synthesis was removed from the Zr-oxo nodes (procedure described above) lead to the formation of the by-product 1-phenylethane-1,2-diol, thus, decreasing the overall styrene oxide selectivity (Figure A 114, Figure A 115). This is assumed to arise from the contribution of Lewis acidic Zr sites inducing epoxide opening.<sup>[163]</sup> Additionally, recycling experiments showed that PCN-222(Ru) could be reused for four times maintaining its high activity and selectivity (Figure A 116). Comparing the styrene epoxidation with PCN-222(Ru) of this work with RuTMP(O<sub>2</sub>), a Ru-porphyrin epoxidation catalyst in homogeneous phase, a higher reaction rate and slightly enhanced selectivity is obtained with the homogeneous system (100% vs 92% for RuTMP(O<sub>2</sub>) and PCN-222(Ru), respectively).<sup>[114]</sup>

The in this work performed epoxidation with Ru-TCPP(CO) in homogeneous phase showed a similar catalytic performance compared to PCN-222(Ru) (Figure A 117, Figure A 118). However, the benefits of heterogenization of the metalloporphyrin – such as recyclability and the potential of incorporating further functionalities into the MOF scaffold rather easily – legitimate the application of PCN-222(Ru) for the epoxidation of styrene.

In addition to parameter optimization, the general applicability of the PCN-222(Ru) catalyst for the epoxidation was studied by expanding the substrate scope. Following styrene derivatives were tested as substrates: 4-methyl-, 4-chlorostyrene and  $\beta$ -methylstyrene, *cis*- and *trans*-stilbene (Figure 44, Figure A 119). High activities and selectivities (up to 99%) were achieved for aromatic olefins (except 4-methylstyrene, Figure 44). The latter might arise from auxiliary interaction between the aromatic substrates and the porphyrin macrocycle via  $\pi$ - $\pi$ -interactions.<sup>[164]</sup> The stereoselectivity remained unchanged upon epoxidation with PCN-222(Ru), since *cis*-stilbene oxide was formed from *cis*-stilbene and the *trans* oxide from the *trans*-substrate while in literature the conversion of *cis*-olefins to *trans*-epoxides has also been reported.<sup>[165]</sup> Since inductive and mesomeric effects are reported to influence the performance of metalloporphyrins,<sup>[166]</sup> 4-chlorostyrene (-I effect) and 4-methylstyrene (+I effect) were tested where both cases resulted in slower reaction rates – to a greater extent for 4-methylstyrene with a decreased selectivity of 78%. Concluding, substrate variation underlines the general applicability of the synthesized catalyst system for a broad range of styrene derivatives.

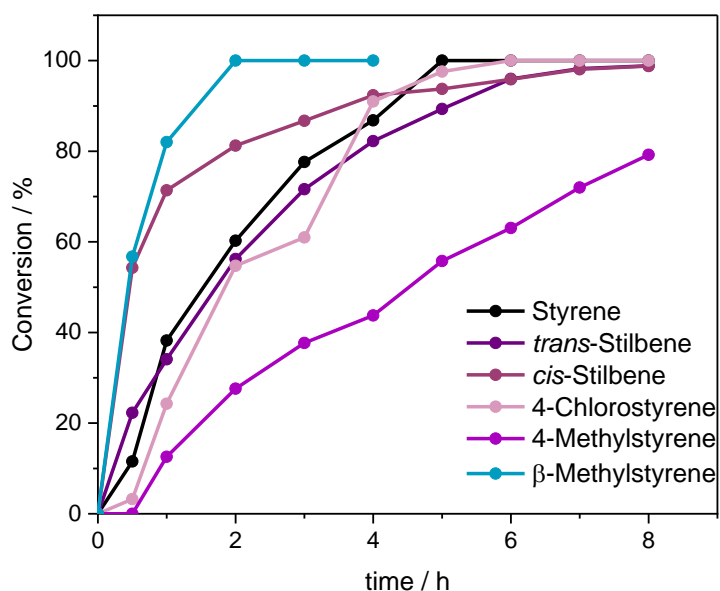


Figure 44: Conversions of different substrates (styrene, *trans*- and *cis*-stilbene, 4-chlorostyrene, 4-methylstyrene,  $\beta$ -methylstyrene) in the epoxidation catalysis using PCN-222(Ru) as catalyst. Reaction conditions: 40 °C, DCM, 1.0 equiv. of olefin, 1.1 equiv. of Cl<sub>2</sub>pyNO, 0.25 mol% catalyst loading.

Concluding, this chapter summarizes the study of different metals incorporated into the porphyrin core as catalysts in epoxidation catalysis. Upon parameter optimization, the best performing reaction parameters could be deduced. Here, a high conversion and selectivity of the epoxidation is important for the realization of a reaction sequence where the epoxidation product acts as intermediate which is further converted in a second reaction step. While the epoxidation with PCN-222(Mn) and PCN-222(Co) did not result in sufficient performances, PCN-222(Ru) showed an excellent performance for styrene(-derivative) epoxidation and is therefore applied in the studies for the design of a sequential catalyst (see chapter 3.2.1.4).

### 3.2.1.3. Metalloporphyrin MOFs in CO<sub>2</sub> Cycloaddition Catalysis

The reaction sequence combining the epoxidation of an olefin and the CO<sub>2</sub> cycloaddition to the epoxide resulting in a cyclic carbonate has been demonstrated previously and presents an attractive proof-of-concept sequence.<sup>[91,99,167]</sup> While the first step – the epoxidation – was studied and discussed in chapter 3.2.1.2, this chapter will cover the CO<sub>2</sub> cycloaddition as the second reaction step of the sequential catalysis (Figure 45). The reaction most commonly requires a Lewis acidic site for epoxide coordination and a nucleophilic co-catalyst (Lewis base) – mainly tetraalkylammonium halides – for epoxide ring opening.<sup>[62,168]</sup> In general, several transition metals like Co, Zn, Ni and Cu are reported to be active in the CO<sub>2</sub> cycloaddition reaction.<sup>[113,169]</sup> A great benefit of the porphyrin-based MOFs described in this Thesis is their ability to incorporate an large variety of metals – also the ones reported as catalysts for the CO<sub>2</sub> cycloaddition – and the possibility of metal content adjustment. The synthesis of different PCN-222(M) (M = Zn, Co, Cu, Ni, Ru) was presented in chapter 3.1.2.3: While PCN-222(Co), PCN-222(Cu), PCN-222(Ni) and PCN-222(Ru) were accessible via pre-synthetic porphyrin metalation, metalation with Zn was performed post-synthetically due to significant Zn leaching upon porphyrin saponification. The successful synthesis was confirmed by PXRD, ICP-MS and solid-state UV-vis spectroscopy (see chapter 3.1.2.3).



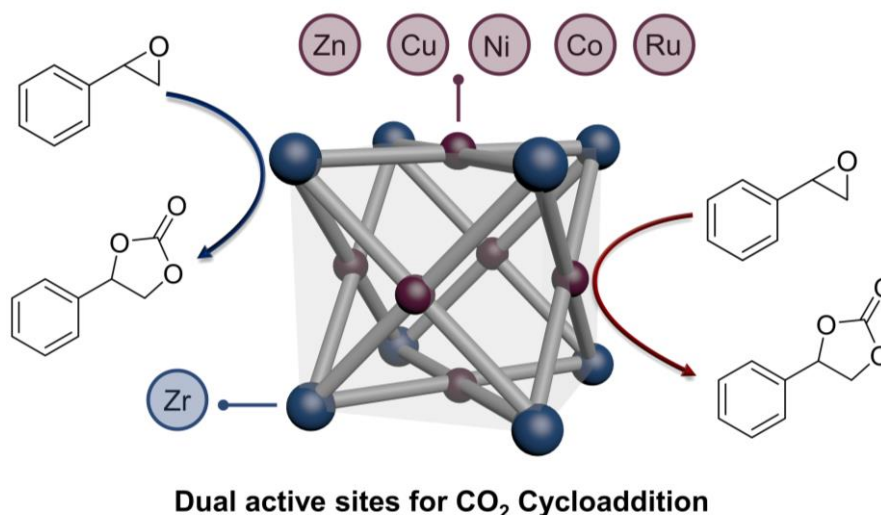


Figure 45: Conceptual representation of the cycloaddition of CO<sub>2</sub> and styrene with a metalloporphyrin-based Zr-MOF. Both the Zr node and the metal incorporated into the porphyrin core (Zn, Cu, Ni, Co, Ru) can act as catalytically active sites.

The CO<sub>2</sub> cycloaddition catalysis was performed with styrene oxide as a substrate (which will be produced in the reaction sequence by the epoxidation catalysis of styrene), 4 bar CO<sub>2</sub> and tetrabutylammonium bromide (TBAB) as nucleophilic co-catalyst while the different PCN-222(M) materials were applied as catalysts (Table 3, Figure A 120). The highest conversion (~90% after 24 h) was detected for PCN-222(Ru) and PCN-222(Cu) – with Cu possessing an excellent selectivity of 98%. In contrast, a decreased activity was measured for PCN-222(Ni) resulting in 18% conversion of styrene oxide after 24 h with a styrene carbonate selectivity of only 45%. Since the Zr-node of PCN-222 itself is Lewis acidic due to its undercoordinated nature,<sup>[32]</sup> non-metalated PCN-222 was applied as CO<sub>2</sub> cycloaddition catalyst yielding 13% conversion with 85% styrene carbonate selectivity after 24 h. The superior activity of porphyrins containing Lewis acidic metalloporphyrins compared to the activity of the Zr node has been highlighted previously and again underlines the outstanding advantages of porphyrin-based MOFs in catalysis.<sup>[32]</sup> Since catalytic attempts of the CO<sub>2</sub> cycloaddition with different PCN-222(M) catalysts have proven successful, in the following both reactions (epoxidation and CO<sub>2</sub> cycloaddition) will be combined within one material achieving a reaction sequence.

Table 3: Styrene oxide conversions and selectivities of the cyclic carbonate in the CO<sub>2</sub> cycloaddition of styrene with PCN-222(M) (M = Ru, Zn, Co, Cu, Ni) as catalyst after 24 h. Reaction conditions: 40 °C, DCM, 4 bar CO<sub>2</sub>, 5 mol% TBAB (regarding olefin), 0.25 mol% M loading.

Catalyst	Conversion / %	Selectivity / %
PCN-222	13	85
PCN-222(Ru)	91	96
PCN-222(Zn)	70	76
PCN-222(Co)	75	76
PCN-222(Cu)	91	98
PCN-222(Ni)	18	46

### 3.2.1.4. Multifunctionality Design for Sequential Catalysis

After both reaction steps – the epoxidation of styrene and CO<sub>2</sub> cycloaddition – were studied in detail separately, the reaction sequence by combination of the two reactions will be discussed in the following (Figure 46). The sequence of epoxidation and CO<sub>2</sub> cycloaddition was selected since both individual reactions have been intensively studied in literature and also their combination has been reported successfully – although only in rare examples.<sup>[62,91,99,167,170]</sup> Especially the compatibility of both reaction conditions is a critical issue for this reaction e.g. since bromide ions (applied as co-catalysts in the CO<sub>2</sub> cycloaddition) can open the epoxide and thus result in decreased selectivity.<sup>[91]</sup> Therefore, the sequence serves as a proof-of-concept supporting the catalyst integration strategies to design a multifunctional catalyst.

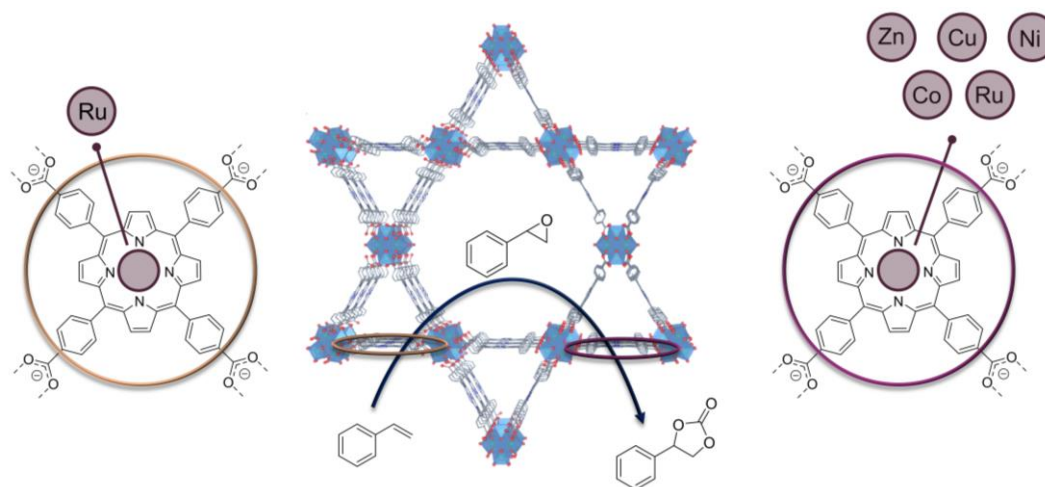


Figure 46: Schematic representation of the sequential styrene epoxidation/CO<sub>2</sub> cycloaddition using PCN-222 as catalyst containing different metalated porphyrin cores acting as active sites for the epoxidation (Ru) and CO<sub>2</sub> cycloaddition (Ru, Co, Cu, Ni, Zn), respectively.

As described in chapter 1.3.3, the implementation of different homogeneous catalysts within one material is synthetically challenging and still in an early stage. With the metalation strategies studied in this Thesis a synthetically rather straightforward approach is presented which allows for the integration of two molecular catalysts within one MOF, where both the active metal itself (i.e., the metal in the porphyrin core) can be freely chosen and the ratio of e.g. two active sites can be adjusted depending on the desired purpose. In MOF catalysis research, this intensive study is very rare and almost unique – however – it is of significant importance for the design of sophisticated catalyst materials. For the following studies Ru was implemented into PCN-222 via the pre-metalation approach where the Ru concentration was adjustable by the mixed-linker strategy (see chapter 3.1.2.3.). For CO<sub>2</sub> cycloaddition, Co, Cu, Ni, Ru and Zn, respectively, were applied as active sites. Thus, PCN-222(Ru,M) (M = Ru, Co, Cu, Ni, Zn) was synthesized either via the mixed-linker approach (Ru, Co, Cu, Ni) or by post-synthetic metalation of PCN-222(Ru) for M = Zn (see chapter 3.1.2.3.). The characterization of all materials is described in section 3.1.2.3. Additionally, details on the catalytic procedures and performance calculations are described in chapter 5.4.4.

### Reaction setup

In general, a one-pot, two-step reaction can be performed with different setups, e.g., adding all reactants and catalysts at the beginning (“tandem catalysis”), or sequentially where the reactants for the first reaction and the catalysts of both reactions are present from the beginning but with a delayed addition of reactants for the second reaction step. In literature, the two-step epoxidation/CO<sub>2</sub> cycloaddition catalysis is often performed in a one-pot setup where all reactants and catalysts are present at the beginning. However, for this Thesis, both setups were tested – with PCN-222(Ru) as an ideal catalyst candidate as it showed high activity for both reactions (see chapters 3.2.1.2. and 3.2.2.3.). The following two catalysis setups were evaluated: 1) the addition of all starting materials (styrene, oxidant, catalyst – PCN-222(Ru) – and co-catalyst (TBAB)) from the beginning and CO<sub>2</sub> addition after 4 h of reaction, and 2) a setup where the reactants for epoxidation (styrene and oxidant) and the catalyst are present at the beginning and the reactants necessary for the CO<sub>2</sub> cycloaddition (TBAB and CO<sub>2</sub>) are added after 4 h of epoxidation. The concentration of the co-catalyst TBAB was 5 mol% regarding the olefin – independent of the reaction setup. A drastically lowered conversion of styrene and styrene carbonate selectivity was apparent from kinetic measurements during catalysis for the addition of the co-catalyst directly at the beginning (C = 47% vs C = 100% after 24 h; S(Styrene carbonate) = 58% vs S = 84%, Figure A 121). It is assumed that coordination of the co-catalyst to the Ru center prevents sufficient epoxidation.

In contrast, the delayed addition of the co-catalyst resulted in complete conversion of styrene after 24 h (S(styrene carbonate) = 84%). Thus, in all further experiments, TBAB and CO<sub>2</sub> were both added after 4 h of epoxidation reaction.

### **Influence of second metal on catalytic performance**

The metalation approaches for a large variety of different metals and the possibility to adjust the ratio between different incorporated metals presented in this work allows for the design of several, multifunctional materials and thus the study of metal combination effects – in this case on the different reaction steps of the sequential catalysis. The different catalytic performances of single-metal PCN-222(M) (M = Ru, Co, Cu, Ni, Zn) has already been described in chapter 3.2.1.3. Thus, with the provided opportunity of synthesizing multifunctional PCN-222 analogues, mixed-metal PCN-222 materials and potential cooperative effects of different metal combinations in the sequential epoxidation/CO<sub>2</sub> cycloaddition catalysis can be studied. While the catalytic metal for the epoxidation is Ru for all materials, the second metal – for the CO<sub>2</sub> cycloaddition – was varied since a drastic difference between the different metals has been deduced. Therefore, different PCN-222(Ru,M) (M = Ru, Co, Cu, Ni, Zn) have been synthesized (details on synthesis and characterization are described in chapter 5.3.1. and 6.2.).

In a first step, the PCN-222(Ru, M) (M = Ru, Co, Cu, Ni, Zn) was applied in the epoxidation catalysis separately, to conclude on possible effects of metal combination affecting the epoxidation performance. Although all PCN-222(M) (M = Co, Cu, Ni, Zn) did not show any conversion in styrene epoxidation, except for PCN-222(Ru), a positive influence of Ni and Cu could be determined using PCN-222(Ru,Ni) and PCN-222(Ru,Cu) as catalysts in the epoxidation. While for PCN-222(Ru,Ru) 86% of styrene was converted, the activity was increased to 92% and 100% conversion after 4 h for PCN-222(Ru,Cu) and PCN-222(Ru,Ni), respectively (Table 4). In contrast, Zn and Co negatively impacted the epoxidation activity resulting in 66% conversion (4 h) for PCN-222(Ru,Zn) and only 14% conversion (4 h) for PCN-222(Ru,Co). The latter is assumed to arise from the high oxophilicity and thus a transfer of oxygen from the oxidizing agent to non-active metal centers reducing the amount of active Ru-oxo species. Noteworthy, an impact of metal variation on the epoxide selectivity was not apparent (Table 4).

Table 4: Styrene conversion and epoxide selectivity for styrene epoxidation with PCN-222(Ru,M) (M = Ru, Co, Ni, Cu, Zn) catalysts. Reaction conditions: 4 h, 40 °C, DCM 1.0 equiv. styrene, 1.1 equiv. Cl<sub>2</sub>pyNO, 0.25 mol% Ru.

Catalyst	C(Styrene) / %	S(Epoxyde) / %
PCN-222(Ru,Ru)	86	93
PCN-222(Ru,Co)	14	90
PCN-222(Ru,Cu)	92	93
PCN-222(Ru,Ni)	100	91
PCN-222(Ru,Zn)	66	87

The two-step sequential catalysis of olefin → epoxide → carbonate was conducted with the different PCN-222(Ru,M) (M = Ru, Zn, Co, Cu, Ni) MOFs, styrene as substrate, Cl<sub>2</sub>pyNO as oxidant, TBAB as co-catalyst and 4 bar of CO<sub>2</sub> (both added after 4 h of epoxidation) in DCM. The catalyst loading was constant with 0.25 mol% Ru and the amount of MOF adjusted accordingly. For kinetic measurements, samples were taken after 4 h of epoxidation, after 4 h of CO<sub>2</sub> addition (in total 8 h of reaction) and after 24 h (20 h after CO<sub>2</sub> addition). Reactant, intermediate and product yields during catalysis are exemplarily depicted in Figure 47 for PCN-222(Ru,Zn).

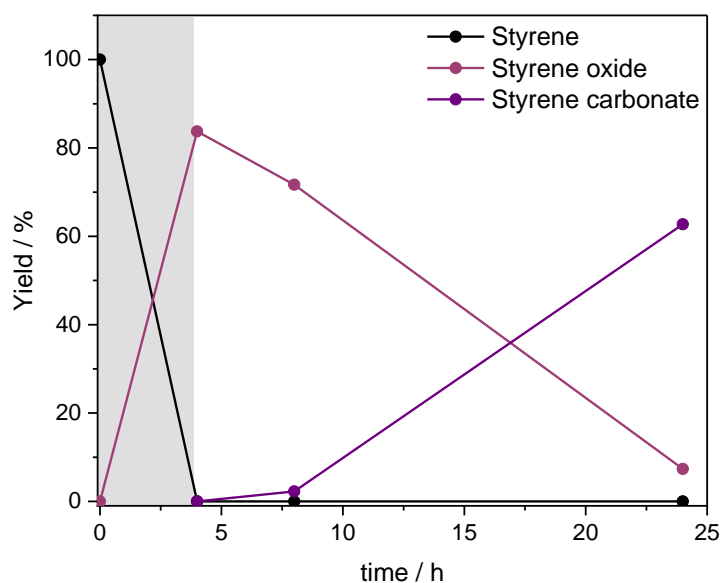


Figure 47: Yields of styrene (reactant), styrene oxide (intermediate) and styrene carbonate (product) in the sequential epoxidation/CO<sub>2</sub> cycloaddition of styrene using PCN-222(Ru,Zn) (Ru/Zn = 0.72) as catalyst.

In the sequential catalysis with different PCN-222(Ru,M) PCN-222(Ru,Cu) and PCN-222(Ru,Ru) showed 100% conversion after 8 h total reaction time (4 h after CO<sub>2</sub> addition, Figure A 122) while more than 80 % conversion of styrene was reached after 24 h with PCN-222(Ru,Zn) and PCN-222(Ru,Co) (Table 5, Figure A 122, Figure A 123).

The three catalysts PCN-222(Ru,Cu), PCN-222(Ru,Zn) and PCN-222(Ru,Co) outperformed the other catalyst materials – in particular PCN-222(Ru,Ni) – with high conversions and sufficient carbonate selectivities (60 – 80%, Table 5). This is in line with the above-described activity of Cu and Co for the cycloaddition of CO<sub>2</sub> – suggesting the independence of both reaction steps. Thus, while combining Ru and Ni negatively influenced the catalytic performance, Ru/Cu and Ru/Zn combinations were advantageous for the reaction sequence. Note that differences in catalyst loading between the catalysts need to be taken into account (for metal amounts see Table A 12) as physical amounts of MOFs were calculated according to the Ru content which is kept constant for all different catalyst materials. In particular for the second reaction step, ratios of substrate (epoxide) and catalyst vary for the different metal combinations due to their effect on the epoxidation activity.

Table 5: Styrene and epoxide conversions and carbonate selectivity for the sequential conversion of styrene to the cyclic carbonate with PCN-222(Ru,M) (M = Ru, Co, Cu, Ni, Zn) catalysts. Reaction conditions: 24 h, 40 °C, DCM 1.0 equiv. styrene, 1.1 equiv. Cl<sub>2</sub>pyNO, 4 bar CO<sub>2</sub> (added after 4 h reaction time), 5 mol% TBAB (regarding styrene), 0.25 mol% Ru.

Catalyst	Styrene Conversion / %	Epoxide Conversion / %	Carbonate Selectivity / %
PCN-222(Ru, Ru)	100	60	84
PCN-222(Ru,Co)	84	88	60
PCN-222(Ru,Cu)	100	100	70
PCN-222(Ru,Ni)	100	38	76
PCN-222(Ru,Zn)	92	75	81

Since the presented synthesis strategy allows for the adjustment of metal concentrations and thus, metal ratios which might affect the catalytic performance, different PCN-222(Ru,Zn) catalysts with varied Ru/Zn ratios were synthesized (Ru/Zn = 2.08, 0.93, 0.72). Zn was chosen as example due to the possibility of a straightforward adjustment of the metal ratio during the post-synthetic metalation by variation of the Zn precursor equivalents. While for higher Ru/Zn ratios a decrease in styrene conversion was observable (33% and 66% after 4 h for 2.08 and 0.93, respectively) – without influencing the selectivity (Figure A 124) – high Zn amounts (0.72) resulted in a boost of styrene conversion (100% after 4 h), see Figure 48. In the latter case, the CO<sub>2</sub> cycloaddition activity was also enhanced which is assumed to arise from the increased amount of active Zn sites. Thus, highlighting the crucial effect of metal ratio on the catalytic performance which is of importance when optimizing reaction conditions.

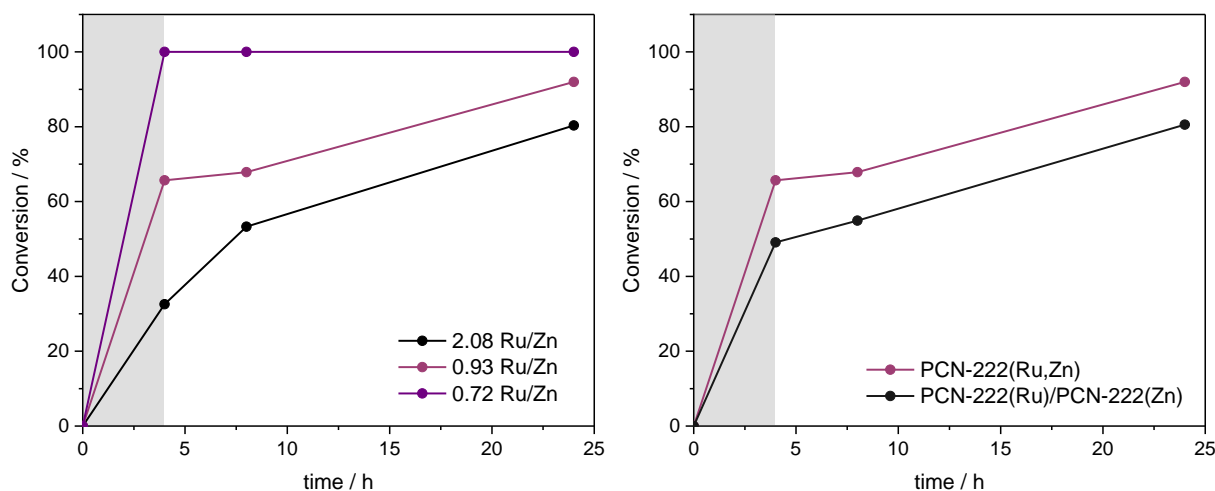


Figure 48: Styrene conversions in the sequential epoxidation/ $\text{CO}_2$  cycloaddition. Left: Ru/Zn ratio variation (2.08 versus 0.93 versus 0.72). Right: Variation of catalyst system (multifunctional PCN-222(Ru,Zn) versus physical mixture of PCN-222(Ru)/PCN-222(Zn)).

Although from a conceptual point of view very appealing, the design of multifunctional systems, i.e., with two catalysts incorporated in one material is synthetically challenging. Thus, advantages of those systems or superior properties compared to physical mixtures of two catalysts need to exist to legitimate efforts in synthesis and characterization of multifunctional systems. Therefore, the sequential catalysis was performed with the synthesized PCN-222(Ru,Zn) material – with both catalysts incorporated in one structure – and with a physical mixture of PCN-222(Ru) and PCN-222(Zn). The experiments revealed an increased conversion in the multifunctional PCN-222(Ru,Zn) compared to PCN-222(Ru)/PCN-222(Zn) (Figure 48) – underlining the potential multifunctional catalysts offer by placing different active sites in close proximity.<sup>[92,171]</sup> Note that the carbonate selectivities are comparable for both systems (~81%).

Additionally, the results were compared to previously published PCN-222(Mn) system applied in the one-pot olefin  $\rightarrow$  epoxide  $\rightarrow$  carbonate catalysis (5 bar  $\text{CO}_2$ , 50 – 70 °C,  $\text{O}_2$  as oxidant). For the PCN-222(Mn) case conversions of 45 – 100 % after 8 h (depending on the reaction temperature) and styrene carbonate selectivities of 83 – 96% were obtained.<sup>[91]</sup> Although the in this Thesis presented PCN-222(Ru,M) catalysts show decreased activities compared to the PCN-222(Mn) system, varied reaction conditions and the incorporation of the co-catalyst (ImBr = 1-methyl-3-(2-carboxyethyl)imidazolium bromide) into PCN-222(Mn) enhancing the performance need to be considered. Especially the co-catalyst integration offers an interesting strategy to further increase the system's multifunctionality.

As a resumé, the presented strategy which incorporated two different catalytically active metals with varied metal ratios successfully allows for the performance of the sequential epoxidation/CO<sub>2</sub> cycloaddition catalysis. Parameter optimization and metal variation revealed important influences on the performance. However, and most importantly, this concept is transferrable to several multifunctional reactions since the synthesis method of the bimetalated porphyrin MOFs allows for the free variation of metals and thus the broad application of this concept for other catalysis combinations which have been presented previously.<sup>[43,96]</sup>

### 3.2.1.5. Non-planar Porphyrin Integration

A great advantage of porphyrin motifs is their high substitution potential – introducing further functionalities or altering the electronic or structural properties of the porphyrin. In addition to functionalization at the phenyl groups, porphyrin substitution at the pyrrole moieties (*beta*-position) is a common approach. This has been extensively studied by the group of *Mathias Senge* (Trinity College Dublin), resulting in a cooperation project presented in this chapter. Upon porphyrin functionalization with ethyl groups in  $\beta$  position, a non-planar arrangement of the porphyrin core arises (in contrast to planar TCPPH<sub>2</sub>) introducing increased basicity of the nitrogen groups and allowing for its application in metal-free base catalysis.<sup>[172,173]</sup> The altered arrangement and acid/base properties of the porphyrin are assumed to result in beneficial kinetics for metal incorporation.<sup>[172]</sup> Since the integration of some metals (e.g. Rh) has proven challenging, this might pave the way for a more straightforward metal integration which is essential for the design of metalated porphyrin MOF catalysts. Therefore, this project aimed to incorporate the non-planar porphyrin 2,3,7,8,12,13,17,18-octaethyl-5,10,15,20-tetrakis(4-carboxyphenyl)-porphyrin (here referred to as Et-TCPPH<sub>2</sub>) into the structure of PCN-222 (note that Et-TCPPH<sub>2</sub> was provided by Senge *et al.* – Trinity College Dublin) and the study of resulting material properties, e.g. metalation capability or catalytic properties of metal free, non-planar porphyrin after MOF incorporation (Figure 49).



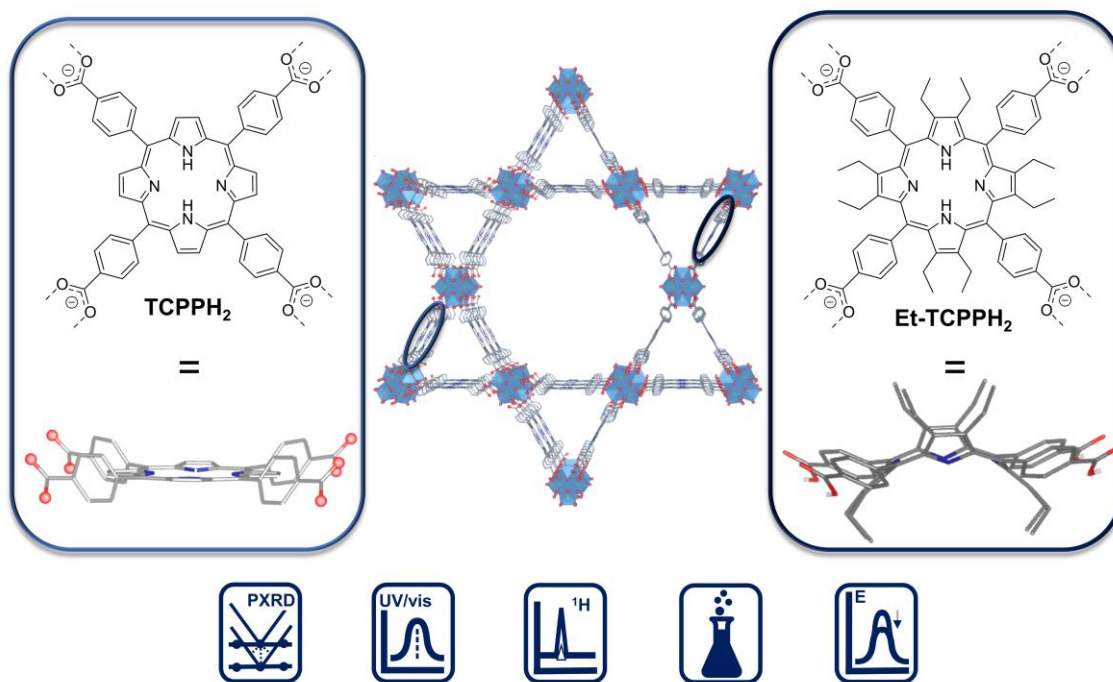


Figure 49: Schematic representation of the incorporation of Et-TCPPh<sub>2</sub> in PCN-222 via a mixed-linker approach of TCPPh<sub>2</sub> and Et-TCPPh<sub>2</sub>. Additionally, structures of TCPPh<sub>2</sub> and Et-TCPPh<sub>2</sub> are depicted. For structural elucidation a combination of PXRD, UV-vis and <sup>1</sup>H NMR is necessary while chemical and catalytical properties of the resulting materials were studied.

Et-TCPPh<sub>2</sub> was integrated into the MOF framework via a mixed-linker approach with TCPPh<sub>2</sub>, varying the molar ratios of Et-TCPPh<sub>2</sub> and TCPPh<sub>2</sub> in the solvothermal synthesis (details see 5.3.5.). Determination of the molar ratios of TCPPh<sub>2</sub> and Et-TCPPh<sub>2</sub> was possible by <sup>1</sup>H NMR spectroscopy (Figure 50, Figure A 125, Figure A 126) by digesting the solid MOFs in a DCI/DMSO-d<sub>6</sub> solution (0.1 mL/0.3 mL). Comparison of the integrals of the phenyl signals of TCPPh<sub>2</sub> (8.55 ppm, 8.62 ppm, 8.75 ppm) and Et-TCPPh<sub>2</sub> (8.38 ppm, 8.64 ppm), respectively, allowed for the quantification of the molar ratio of both linkers (Table A 13, for details see Figure A 126). A slight peak shift of both linkers in the digested MOF spectrum (8.49, 8.55 and 8.69 ppm for TCPPh<sub>2</sub> and 8.35 and 8.61 ppm for Et-TCPPh<sub>2</sub>) arised from slightly varied acid concentration in the samples. The linkers' molar ratios were calculated as averaged values from three NMR measurements of the same MOFs.

To enable the study of properties of functionalized PCN-222 depending on the Et-TCPPh<sub>2</sub> content, a series of functionalized PCN-222 analogues was synthesized with following Et-TCPPh<sub>2</sub> contents – determined by <sup>1</sup>H NMR spectroscopy: 20EtP-PCN-222 (20 mol% Et-TCPPh<sub>2</sub>, 80 mol% TCPPh<sub>2</sub> in PCN-222), 59EtP-PCN-222 (59 mol% Et-TCPPh<sub>2</sub>, 41 mol% TCPPh<sub>2</sub> in PCN-222) and 72EtP-PCN-222 (72 mol% Et-TCPPh<sub>2</sub>, 28 mol% TCPPh<sub>2</sub> in PCN-222). Intriguingly, both 20EtP-PCN-222 and 72EtP-PCN-222 were synthesized with a weigh-in of 20 mol% Et-TCPPh<sub>2</sub> (80 mol% TCPPh<sub>2</sub>) – however – with different batches of Et-TCPPh<sub>2</sub> of different crystallinity.

This indicates that the latter significantly influences the amount of Et-TCPPh<sub>2</sub> incorporation since with the more crystalline Et-TCPPh<sub>2</sub> batch 20EtP-PCN-222 was synthesized with 20 mol% Et-TCPPh<sub>2</sub> weigh-in while with the powdered Et-TCPPh<sub>2</sub> batch the content was drastically enhanced resulting in 72EtP-PCN-222. The increased Et-TCPPh<sub>2</sub> integration might result from the higher solubility of the powdered sample – in line with the weigh-in of 10 mol% Et-TCPPh<sub>2</sub> for 59EtP-PCN-222. This is an important fact and needs to be considered for the integration of guest molecules into MOFs by solvothermal synthesis and their content adjustment – in particular when some reactants are not completely dissolved prior to starting the synthesis.

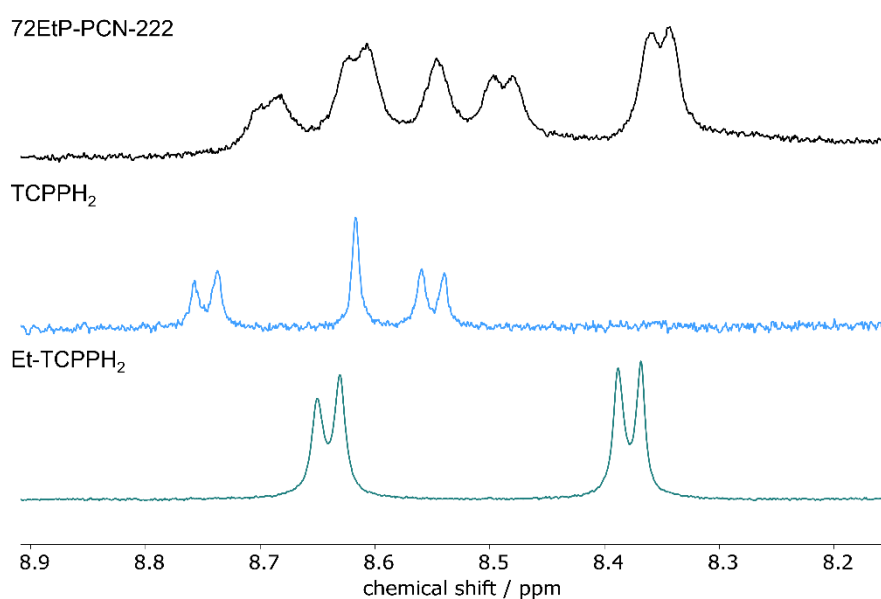


Figure 50: <sup>1</sup>H NMR spectra of Et-TCPPh<sub>2</sub>, TCPPh<sub>2</sub> and digested 72EtP-PCN-222 (all samples were measured in DCI/DMSO-d<sub>6</sub>). The depicted range was applied for the quantification of the respective (functionalized) porphyrin contents (Et-TCPPh<sub>2</sub> and TCPPh<sub>2</sub>).

The crystallinity and phase-purity of PCN-222 upon Et-TCPPh<sub>2</sub> incorporation was preserved until approximately 80 mol% of Et-TCPPh<sub>2</sub> (Figure 51, Figure A 127) underlining the tolerance of the MOF towards linker functionalization. Synthesizing functionalized PCN-222 exclusively from Et-TCPPh<sub>2</sub> (100 mol%) resulted in a significant decrease in crystallinity apparent from PXRD data – however still obtaining the main PCN-222 *Bragg* reflections (Figure 51, Figure A 127). Therefore, the 100EtP-PCN-222 was excluded from the subsequent material properties study.

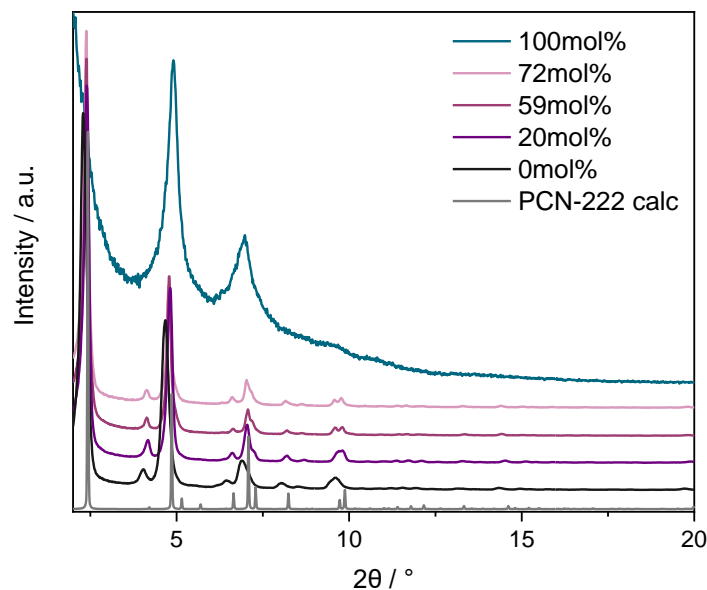


Figure 51: PXRD pattern of PCN-222 analogues with different amounts of Et-TCPPh<sub>2</sub> (0 mol% - 100 mol%) incorporated via a mixed-linker approach.

An imaginable approach for enhancing the Et-TCPPh<sub>2</sub> content above 80 mol% – while preserving the crystallinity – is the solvent-assisted linker exchange which is often applied for (linker) molecule incorporation (SALE, see chapter 1.3.1.) – performed for 72EtP-PCN-222 already containing 72 mol% of Et-TCPPh<sub>2</sub>. However, due to the similarities in reaction conditions for SALE and the solvent-assisted linker incorporation SALI (see chapter 1.3.1), i.e. heating a suspension of linker and MOF in an appropriate solvent, control of linker coordination and its characterization is challenging.<sup>[49,53,174]</sup> As the coordination of the newly introduced Et-TCPPh<sub>2</sub> linker to the node cannot be excluded this approach was not performed.

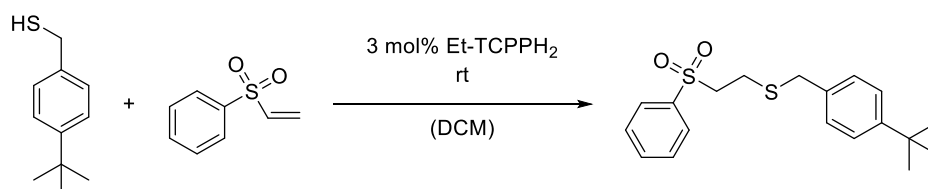
Further material characterization with N<sub>2</sub> sorption measurements of the EtP-PCN-222 series revealed a type IV isotherm – indicating the presence of micro- and mesopores.<sup>[14]</sup> The adsorbed N<sub>2</sub> quantity (Figure A 128 – Figure A 130) and BET surface area decreased upon enhancing the Et-TCPPh<sub>2</sub> content resulting in following BET surface areas: 2079 ± 6.9 m<sup>2</sup>·g<sup>-1</sup> for PCN-222, 1744 ± 15 m<sup>2</sup>·g<sup>-1</sup> for 20EtP-PCN-222, 1594 ± 12 m<sup>2</sup>·g<sup>-1</sup> for 59EtP-PCN-222 and 1512 ± 10 m<sup>2</sup>·g<sup>-1</sup> for 72EtP-PCN-222. This might result from to contribution of ethyl groups at the porphyrin linker while its contribution increases with increasing Et-TCPPh<sub>2</sub> amounts in the MOF. Such a decrease in surface area is in line with declines observed for porphyrin metalation.<sup>[14,87,129]</sup> In literature, the synthesis of Et-TCPPh<sub>2</sub> functionalized PCN-224 was reported. Here a smaller decrease of BET surface area upon porphyrin functionalization with ethyl groups was apparent.<sup>[116]</sup> However, general differences in BET surface area analysis and the importance of defects affecting the surface area need to be considered.

Additionally, IR spectra of the functionalized EtP-PCN-222 series were recorded (Figure A 131) – without apparent significant differences between the individual materials. Successful Et-TCPPh<sub>2</sub> integration could be followed by solid-state UV-vis spectroscopy showing differences in the Soret and Q bands of the porphyrin upon ethyl functionalization in the ranges of 450-530 nm and 680-720 nm (Figure A 132, Figure A 133). The thermal stability of the different PCN-222 analogues – accessible by TGA – confirmed comparable stabilities for each material (405-415 °C) in good agreement to reported values for PCN-222 (Figure A 134, Figure A 137).<sup>[14,32]</sup> Note that a trend in thermal stability and also defect concentration (Table A 14) upon increased Et-TCPPh<sub>2</sub> amounts was absent. Moreover, the morphology of PCN-222 was preserved with Et-TCPPh<sub>2</sub> incorporated which was apparent by scanning electron microscopy (SEM) of the powdered MOFs (Figure A 138 – Figure A 141). Crystal sizes were in the same order of magnitude, thus, precluding a dependency of crystal size on the Et-TCPPh<sub>2</sub> content. Qualitative analysis of confocal microscopy images revealed a decrease in fluorescence upon Et-TCPPh<sub>2</sub> integration (Figure A 142) – in line with the low fluorescence intensity of non-planar porphyrins compared to planar ones.<sup>[117]</sup> However, no trend depending on the Et-TCPPh<sub>2</sub> amount could be extracted.

In general, the presented study highlights the importance of characterization technique combination to draw conclusions on functionalized linker integration. By combining findings from structural information on phase purity (PXRD) with methods quantifying molecular contents (like NMR spectroscopy) – supported by classical MOF characterizations like N<sub>2</sub> sorption or TGA – the evaluation of MOF functionalization is allowed.

### Material Properties

Towards potential applications, further material properties of the EtP-PCN-222 series were studied. The pH stability of PCN-222 was previously validated in the range of pH = 0-11.<sup>[100]</sup> Thus, the pH stability was investigated – for PCN-222 and 59EtP-PCN-222 as examples – to conclude on potential stability differences. Adjusting different pH values (8.0, 8.5, 10.3, 11.0, 12.3) in NaOH/H<sub>2</sub>O and soaking of the MOFs in the respective solutions revealed a stability until pH = 11.0 while in a pH = 12.3 solution both MOFs were decomposed. The stability was verified by PXRD measurements and comparison with the calculated pattern of PCN-222 (Figure A 143, Figure A 144). Note that the background for 59EtP-PCN-222 in pH = 11 solution arises from sample preparation for the measurement.



Scheme 3: Reaction scheme of the thia-Michael addition of phenyl vinyl sulfone and *tert*-butylbenzyl mercaptan with Et-TCPPh<sub>2</sub> as catalyst at rt in DCM.

Since the functionalized PCN-222 analogs are stable in basic solutions (to a certain extent) the basic treated EtP-PCN-222 was applied in the thia-Michael addition of phenyl vinyl sulfone and *tert*-butylbenzyl mercaptan at room temperature in DCM (Scheme 3). This reaction was chosen based on the activity of Et-TCPPh<sub>2</sub> in a homogeneous catalyst system reported prior.<sup>[173]</sup> The experiment was designed to evaluate the general performance of Et-TCPPh<sub>2</sub> upon MOF integration, i.e. if the activity is preserved – and potential heterogenization impacts. However, Et-TCPPh<sub>2</sub> functionalized PCN-222 did not show any conversion of the substrate analyzed by <sup>1</sup>H NMR analysis (see 5.4.5.). Additionally, the Henry reaction of benzaldehyde and nitromethane was tested (MeOH, 55 °C) with EtP-PCN-222 as catalyst – however also showing no activity.

In addition to the metal-free catalysis metalloporphyrins show promising catalytic activities. Therefore, EtP-PCN-222 was metalated with Rh to evaluate the metalation potential upon Et-TCPPh<sub>2</sub> incorporation. Due to the conformational changes of the porphyrin upon ethyl functionalization and the resulting out of plane location of the porphyrin N atoms, metalation of Et-TCPPh<sub>2</sub> compared to TCPPh<sub>2</sub> is assumed to be faster (Figure 49).<sup>[172]</sup> Therefore, Rh was chosen for metalation since its post-synthetic incorporation was shown to be more challenging (chapter 3.1.2.3.). For post-synthetic MOF metalation, a suspension of MOF and metal precursor (RhCl<sub>3</sub> · xH<sub>2</sub>O) in DMF was heated using different setups (reflux vs oven). Structural analysis by PXRD after synthesis did not show changes in phase-purity and crystallinity upon Rh metalation in EtP-PCN-222 – independent on the heating setup (Figure A 145, Figure A 146). In comparison, for unfunctionalized PCN-222(Ru) a crystallinity decrease was apparent under reflux conditions (*Bragg* reflection broadening and lower signal-to-noise ratio). The Rh contents after metalation were calculated from ICP-MS measurements. A porphyrin metalation less than 30% was calculated for both EtP-PCN-222(Rh) and PCN-222(Rh). In general, lower Rh contents were achieved for the oven setup compared to refluxing conditions (Table A 15). The metalation experiments confirm that Et-TCPPh<sub>2</sub> metalation after MOF incorporation is still possible – however not beneficial compared to unfunctionalized TCPPh<sub>2</sub> – and enables the synthesis of metalated EtP-PCN-222 for catalytic applications.

Concluding, this chapter highlights the large design flexibility provided by the porphyrin motif and the potential of incorporating functionalized porphyrins (introducing altered properties, e.g. structural conformations of the macrocycle) within known porphyrin-based MOF structures. This allows to manipulate the material's catalytic performances and study substitution effects on catalysis.<sup>[116]</sup> Although no superior properties were obtained upon Et-TCPPH<sub>2</sub> integration within PCN-222, the presented mixed-linker approach and combination of different characterization techniques allows for the straightforward embedment of functionalities in existing MOF structures which can be exploited for the design of specific (catalytic) material properties.

### **Excursion – Structural investigation by variable temperature PXRD (VT PXRD)**

Due to the conformational differences between TCPPH<sub>2</sub> and Et-TCPPH<sub>2</sub> variations in framework flexibility are assumed – studied by PXRD evaluating the material's response to temperature variations. Such effects have already been investigated in literature, e.g. evaluating the thermal expansion of frameworks upon temperature changes.<sup>[175]</sup> The behavior of PCN-222 under variable temperature (i.e. the thermal expansion) was recently studied depending on the pore contents (e.g. solvent, water) in the MOF. Although not directly comparable to the here synthesized PCN-222 – due to the modulator present in PCN-222 synthesized for this study in this Thesis which was absent in the literature study – the high complexity of the PCN-222 material was apparent.<sup>[176]</sup>

This study was conducted in cooperation with the group of *Gregor Kieslich*. VT PXRD measurements and data evaluation was performed by *Silva Kronawitter* and will thus be described in summary way in the following.

For the EtP-PCN-222 series described above PXRD measurements were recorded in a temperature range of 150 – 400 K allowing for the comparison of the lattice parameters and cell volume of the PCN-222 structure – accessible by Pawley profile fitting – depending on the Et-TCPPH<sub>2</sub> content. Pawley refinements of all synthesized (functionalized) PCN-222 materials at 310 K are depicted in Figure A 147 - Figure A 150.

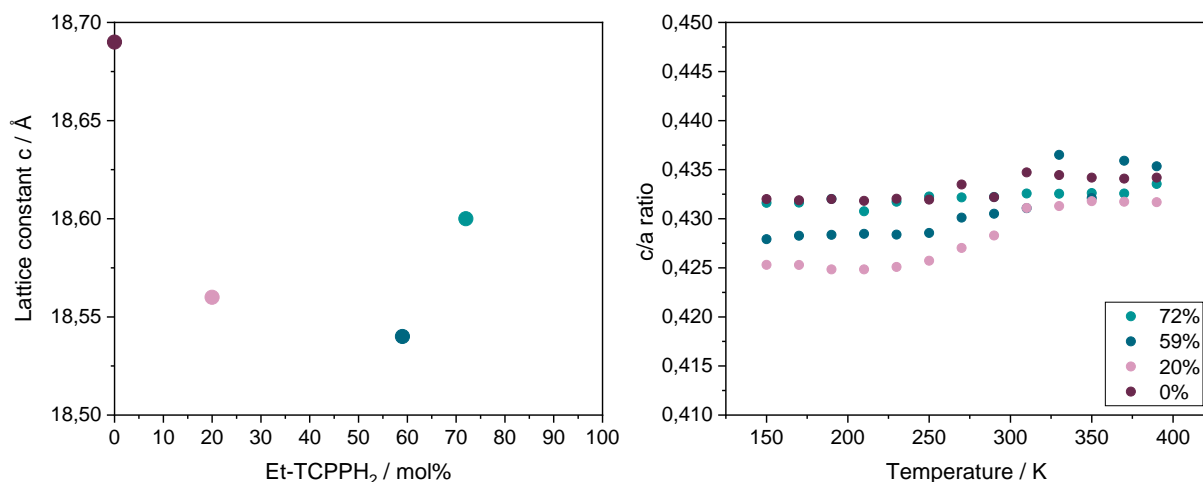


Figure 52: Structural parameters in the EtP-PCN-222 series (PCN-222, 20EtP-PCN-222, 59EtP-PCN-222 and 72EtP-PCN-222). Left: Lattice parameter  $c$  as a function of Et-TCPPh<sub>2</sub> content. Right:  $c/a$  ratio as function of temperature.

Depending on the Et-TCPPh<sub>2</sub> content differences in lattice parameters  $a$ ,  $c$  and  $c/a$  (which are considered for a hexagonal structure as in PCN-222) were apparent from refinement results at 310 K which was most obvious for  $c$  changing  $\sim 0.1$  Å Et-TCPPh<sub>2</sub> integration (Figure 52, Figure A 151). Upon heating, the lattice volume of PCN-222 remained almost unchanged (Figure A 153) – in contrast to previous studies of (dehydrated) PCN-222 – suggesting the importance of modulator on the thermal response by limiting the framework flexibility.<sup>[176]</sup> Although the functionalized PCN-222 series revealed temperature dependent changes in unit cell parameters ((Figure 52, Figure A 152), the possibility of thermal expansion coefficient calculation was prevented by the lack of a linear trend of the data as a function of temperature, thus, only allowing for qualitative conclusions. Compared to PCN-222 and 72EtP-PCN-222 (showing similar behavior), the unit cell volume and  $c/a$  ratio for 20EtP-PCN-222 and 59EtP-PCN-222 changed to a greater extent with varying temperature (Figure 52, Figure A 153). A possible explanation for the observed temperature dependent behavior is the defectiveness of the material (Table A 14) since PCN-222 and 72EtP-PCN-222 were more defective compared to 20EtP-PCN-222 and 59EtP-PCN-222 – probably allowing for more flexibility of the framework for the latter two. Note that a higher defectiveness implicates an increased amount of porphyrin linker compared to the theoretical value, e.g., 2.5 for PCN-222 and 2.1 for 20EtP-PCN-222 compared to the theoretical value of 2 (Table A 14). Such a defect dependent behavior is in line with literature reports (studied for UiO-66(Hf)).<sup>[177]</sup> Summarized the VT PXRD study allows for the investigation of temperature dependent structural properties upon linker functionalization, i.e. Et-TCPPh<sub>2</sub> incorporation. However, the results underline the challenge in the characterization of those materials and the importance of considering several aspects, e.g., guest molecules, for conclusions on structural/material properties.

### 3.2.2. Pore-anchored Catalysts

In addition to catalyst incorporation as a linker described above, heterogenization of molecular catalyst by node anchoring into MOFs is a common approach studied in literature.<sup>[27,31,37]</sup> The SALI method (see chapter 1.3.1.) presents an appealing strategy since it is a synthetically straightforward technique which can be easily followed by standard characterization techniques (e.g. UV-vis spectroscopy) and is compatible with a variety of molecular catalysts. Simultaneously, this strategy enables the integration of a catalyst into a precise reaction environment – defined by the MOF pores – and allows for the study of potential confinement effects and catalytic performance control.<sup>[48,49]</sup>

For this purpose, an anchoring functionality at the catalyst (e.g. at the ligand) able to coordinate to the MOF node is required – usually a (carboxylic or phosphonic) acid group.<sup>[48,53,178]</sup> However, for this strategy – and in particular the anchoring via carboxylic acids – stability tests are essential to conclude on potential catalyst leaching and thus the absence of potential incorporation/confinement effects. Additionally, and in contrast to the catalyst embedment as framework linker – tethering of the catalyst at the node and thus directing into the pores might result in pore blocking and thus diffusion limitations. Therefore, sufficient pore space has to be ensured to prevent such phenomena which would likely decrease the catalytic activity.

In the following, this SALI approach for catalyst anchoring will be described for two different molecular catalyst – MOF combinations: a) a non-planar porphyrin coordinated to the node of PCN-222 and b) a Pd<sub>2</sub>S<sub>2</sub> pincer catalyst in NU-1000. The performed studies will allow for the evaluation of the general applicability of this approach for the two different systems and – as an outlook – the investigation on potential confinement effects, e.g., *endo/exo* selectivity preferences upon catalyst into MOF integration.

#### 3.2.2.1. A Node-anchored Non-planar Porphyrin

The catalytic activity of the non-planar porphyrin Et-TCPPh<sub>2</sub> in basic catalysis (described above) and the improved metalation kinetics render this molecule as interesting candidate to be incorporated in a framework and subsequently study heterogenization effects (in particular of MOF pores) on catalysis.<sup>[173]</sup> In contrast to the Et-TCPPh<sub>2</sub> anchoring presented in chapter 3.2.1.5, in this chapter the anchoring of this molecule to the MOF node via the SALI approach is described and aims to elucidate if anchoring via this method is in general possible for this catalyst and potentially beneficial compared to the mixed-linker strategy. Thus, PCN-222 was selected as model host to allow for comparison of both integration strategies.



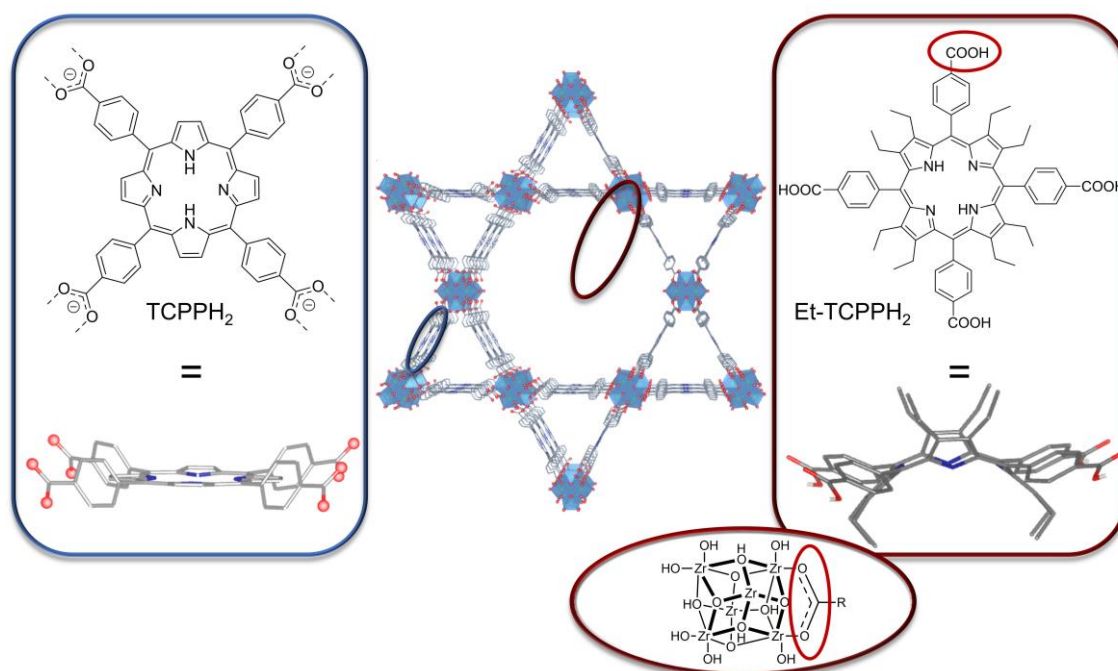


Figure 53: Illustrative representation of Et-TCPPh<sub>2</sub> incorporated via SALI into the framework of PCN-222. The anchoring motif is highlighted in a red circle and shows that the coordination of the porphyrin to the node occurs via the carboxylic acid groups. Additionally, the (chemical) structure of TCPPh<sub>2</sub> is depicted.

Experimentally, PCN-222 was soaked in a solution of Et-TCPPh<sub>2</sub> in DMF (1 equiv. per node) at 80 °C for 24 h with occasional swirling. The successful incorporation of Et-TCPPh<sub>2</sub> was visually apparent by the color of the supernatant after the SALI process which changed its color from green to colorless. Upon washing, no Et-TCPPh<sub>2</sub> release was apparent from the color of the washing solution (remains colorless). For a quantitative evaluation of the porphyrin embedment, UV-vis measurements of the supernatant were performed showing the absence of the porphyrin absorption bands after SALI (Figure 54 left) and thus indicating complete porphyrin integration.

The crystallinity and phase purity of PCN-222 was preserved during the process (Figure A 154). Solid-state UV-vis spectra of the resulting Et-TCPPh<sub>2</sub>@PCN-222 material substantiated the presence of Et-TCPPh<sub>2</sub> in PCN-222 by comparison of absorption bands in the region of 450 – 490 nm and 670 – 730 nm (Figure A 155).

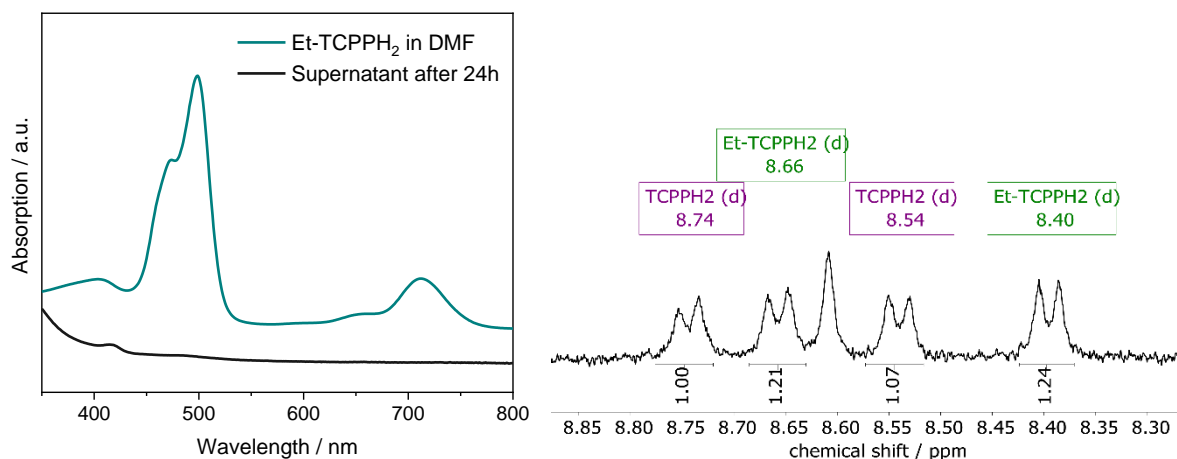


Figure 54: Left: UV-vis spectra of Et-TCPPh<sub>2</sub> in DMF and supernatant after soaking PCN-222 in the Et-TCPPh<sub>2</sub>/DMF solution for 24 h at 80 °C. Right: <sup>1</sup>H NMR spectrum of Et-TCPPh<sub>2</sub>@PCN-222 digested in DCI/DMSO-d<sub>6</sub>. Peaks corresponding to TCPPh<sub>2</sub> shown in purple, peaks for Et-TCPPh<sub>2</sub> in green.

Quantification of Et-TCPPh<sub>2</sub> in Et-TCPPh<sub>2</sub>@PCN-222 was achieved by <sup>1</sup>H NMR spectroscopy of the digested MOF hybrid and comparison of the integrals of Et-TCPPh<sub>2</sub> and TCPPh<sub>2</sub> (see chapter 3.2.1.5, Figure 54 right). Here, a ratio of ~1:1 Et-TCPPh<sub>2</sub>:TCPPh<sub>2</sub> was calculated which deviates from the synthetically adjusted 1:1 ratio of Zr<sub>6</sub>: Et-TCPPh<sub>2</sub> which would result in a Et-TCPPh<sub>2</sub>:TCPPh<sub>2</sub> ratio of 1:2. The increased amount of Et-TCPPh<sub>2</sub> might arise from errors in porphyrin weigh-in (~3 mg) and the high defect tolerance of Zr nodes reported in literature.<sup>[107,108,179]</sup> Nevertheless, the presented analytical techniques confirm the successful anchoring of Et-TCPPh<sub>2</sub> into PCN-222 via the SALI approach. Note that N<sub>2</sub> sorption measurements of PCN-222 and Et-TCPPh<sub>2</sub>@PCN-222 resulted in comparable BET surface areas (1977 ± 2 m<sup>2</sup>/g and 2089 ± 4 m<sup>2</sup>/g, respectively, Figure A 156) while decreased incremental pore volumes of the hexagonal channels in Et-TCPPh<sub>2</sub>@PCN-222 compared to PCN-222 were calculated (Figure A 157) supporting the presence of Et-TCPPh<sub>2</sub> in the MOF pores.

Although the incorporation of Et-TCPPh<sub>2</sub> into PCN-222 was in general possible, evidenced by the results above, the integration strategy was not further followed since i) the mixed-linker strategy was also successful – however preventing pore blocking and diffusion limitations which might be present with the SALI approach and ii) the absence of catalytic properties and metalation advantages of Et-TCPPh<sub>2</sub> (compared to TCPPh<sub>2</sub>) presented in chapter 3.2.1.5.

### 3.2.2.2. Anchoring Studies for Pd Pincer Complex Incorporation

This project was performed in cooperation with the group of *Didier Bourissou* and *Julien Monot* (Université Paul Sabatier Toulouse) responsible for catalyst preparation and potential catalyst functionalizations which are thus not described in this Thesis. Indenediide-based Pd pincer catalysts can be applied in a large variety of organic transformations with different types of selectivities – e.g., *endo/exo* selectivity – which could be affected upon MOF incorporation.<sup>[180]</sup> Note that for the studies performed in this Thesis the Pd pincer complex Pd<sub>2</sub>S<sub>2</sub> catalyst (Figure 55) was applied.

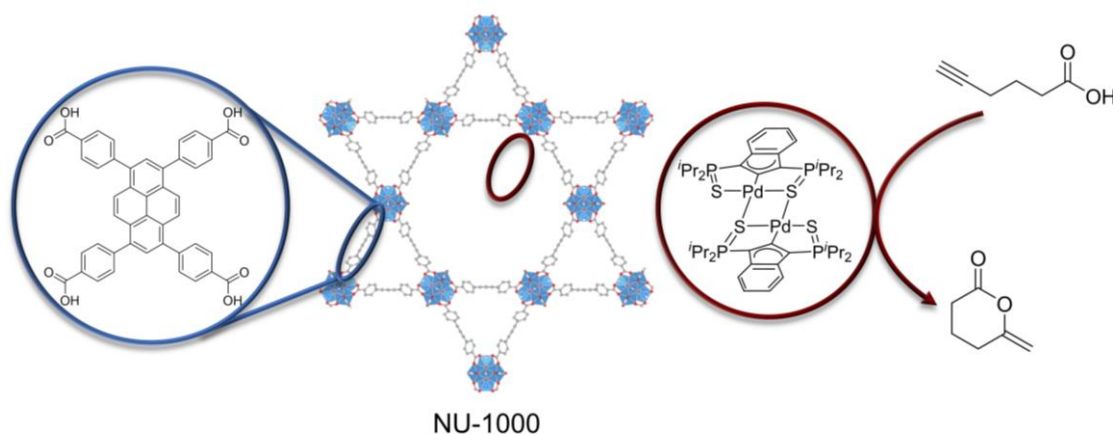


Figure 55: Schematic illustration of NU-1000 including its linker (TBAPy) and the Pd<sub>2</sub>S<sub>2</sub> pincer complex which shall be anchored to the node of NU-1000 via a SALI approach. The Pd complex shall be applied in the cyclization catalysis of 5-hexynoic acid.

For this Thesis, the cyclization of 5-hexynoic acid was selected for a proof-of-concept reaction while NU-1000 was chosen as framework for catalyst incorporation – which is intensively studied in literature for the SALI approach (Figure 55, details on NU-1000 synthesis see 5.3.2.).<sup>[47,53,59]</sup> NU-1000 consists of Zr<sub>6</sub> nodes and a pyrene linker 1,3,6,8-tetrakis(*p*-benzoic-acid)pyrene) (TBAPy) forming a Kagomé like topology (**csq**, comparable to PCN-222) with pore sizes of 13 and ~30 Å.<sup>[58,181]</sup> As for the porphyrin-based MOF systems discussed above, the synthesis of different topologies from the same building units is possible (NU-1000 and NU-901), allowing for the investigation of topology effects on catalysis.<sup>[182]</sup> In contrast to PCN-222, NU-1000 has a light yellow color (PCN-222: (dark) violet) and thus different light absorbing properties which facilitates the characterization by spectroscopic techniques, in particular when following catalyst integration and is thus beneficial in the course of this project.

For the design of a hybrid Pd<sub>2</sub>S<sub>2</sub>@NU-1000 catalyst system, different pre-experiments are essential. In a first step, solid NU-1000 was added to a standard catalysis experiment of Pd<sub>2</sub>S<sub>2</sub> as catalyst for the 5-hexynoic acid cyclization in homogeneous phase (details see chapter 5.3.5). This experiment was aimed to give insights into i) the stability of NU-1000 under catalysis conditions and ii) possible effects of MOF presence on the catalysis. <sup>1</sup>H NMR measurements after 6 h revealed 100% conversion of the substrate (Figure A 159) – in accordance to (unpublished) results from the *Bourissou* group – verifying that the performance is not affected upon MOF addition. MOF stability was confirmed by PXRD measurements after catalysis by comparison to the pattern of as-synthesized NU-1000 and the calculated pattern from structural data (CCDC: 1825881, Figure A 160).

### **Anchoring of model acids in NU-1000**

Since the chosen catalytic reaction involves a substrate containing a carboxylic acid group, the substrate could anchor to the Lewis acidic Zr node and also substitute a catalyst molecule when anchored to the node via a carboxylic acid. The increased coordination strength of phosphonates to Zr compared to carbonates was presented in literature.<sup>[178]</sup> Thus, both carboxylic acid and phosphonic acid groups were tested as functionalities for Zr-node coordination. For first attempts, benzoic acid (BA) and phenylphosphonic acid (PPA) were applied as model acids due to the elaborate synthesis of functionalized catalyst (Figure 56). NU-1000 was soaked in a solution of the respective acid in DMF (1 equiv. per node, details see 5.3.), resulting in NU-1000-BA and NU-1000-PPA, respectively. After 22 h at 60 °C the MOF was separated by centrifugation, washed and dried and digested in DCI/DMSO-d<sub>6</sub> for <sup>1</sup>H (and <sup>31</sup>P) NMR measurements. Comparison of the <sup>1</sup>H NMR spectra of BA, TBAPy and NU-1000-BA revealed the successful incorporation of BA into NU-1000 (Figure A 162). Similarly, <sup>1</sup>H NMR signals of PPA were apparent in the spectrum of NU-1000-PPA (Figure A 163) – supported by the presence of PPA peaks in the <sup>31</sup>P NMR spectrum (Figure A 164). The structure and phase purity of NU-1000 was preserved for both acids, confirmed by PRXD analysis (Figure A 161), which validates the use of Zr-MOFs for such purposes tolerating the presence of acids without decomposing.

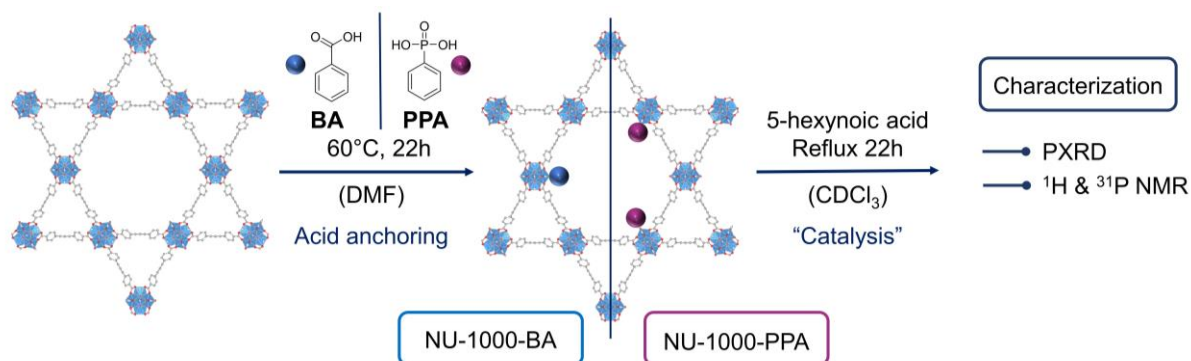


Figure 56: Schematic representation of the synthesis approach for NU-1000-acid materials. Benzoic acid (BA) and phenylphosphonic acid (PPA) were used as acids. The resulting NU-1000-acid MOFs were tested under “catalytic” conditions and characterized afterwards to evaluate their stability.

### Stability of acid anchoring under catalysis conditions

NU-1000-BA and NU-1000-PPA were introduced into a solution of 5-hexynoic acid (substrate for catalysis) in  $\text{CDCl}_3$  (for BA) and  $\text{DMSO-d}_6$  (for PPA due to the limited solubility of PPA in  $\text{CDCl}_3$ ) and heated under reflux conditions for 22 h – resembling catalytic conditions.  $^1\text{H}$  (and  $^{31}\text{P}$ ) NMR measurements were performed of the mother liquor and of the digested MOF to evaluate the stability of BA and PPA anchoring under catalytic conditions (Figure 56). Note that the interpretation of NMR spectra of digested MOFs remains challenging due to the minor amounts of acids (maximum of 1 equiv. per node) compared to the signals of e.g. the linker. Thus, no conclusion on the amount of acid in the MOF could be drawn from the  $^1\text{H}$  NMR spectra of digested NU-1000-BA and NU-1000-PPA after catalysis. However, in both spectra (of NU-1000-BA and NU-1000-PPA) signals assigned to 5-hexynoic acid were significantly apparent (Figure A 166, Figure A 167, Figure A 170, Figure A 172). Since both solid MOFs were washed after catalysis, the presence of 5-hexynoic acid signals in the digested MOF spectra might result from a rather strong binding of this substrate to the MOF. While peaks of BA were apparent in the spectrum of the mother liquor after catalysis, no signals of PPA were observable in the  $^1\text{H}$  NMR and  $^{31}\text{P}$  spectra for the mother liquor with NU-1000-PPA (Figure A 168, Figure A 173, Figure A 174) indicating a stronger bonding of PPA compared to BA – in line with previous results.<sup>[178]</sup> Noteworthy, no signal of PPA was detected in the  $^{31}\text{P}$  NMR of NU-1000-PPA after catalysis (compared to NU-1000-PPA, Figure A 171) which might result from the general challenges of MOF digestion for NMR. Thus, NMR spectra of the mother liquor appeared more reliable and were used for conclusions. Moreover,  $^1\text{H}$  NMR spectra recorded in  $\text{DMSO-d}_6$  after catalysis (NU-1000-PPA case) reveal significant amounts of TBAPy linker in the reaction solution suggesting MOF decomposition (Figure A 169).

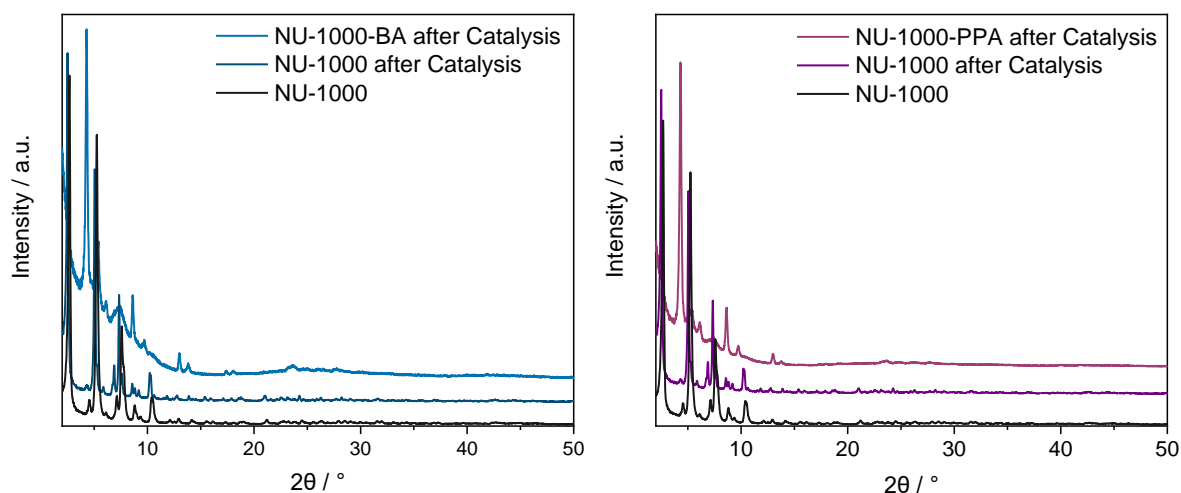


Figure 57: PXR D pattern of benzoic acid (BA, left) and phenylphosphonic acid (PPA, right) anchoring in NU-1000. For comparison, diffraction pattern of NU-1000, NU-1000 after cycloisomerization catalysis and NU-1000-acid after catalysis are depicted.

The instability of the acid incorporated MOFs after catalysis was supported by PXR D pattern after catalysis (Figure 57). Here, in both cases additional peaks were observable which could not be assigned to NU-1000. Additionally, the crystallinity decreased significantly (shown by the reduced signal-to-noise ratio), and amorphous substances might be present (see background at  $2\theta = 20 - 30^\circ$  for NU-1000-BA after Catalysis). Thus, this approach of catalyst anchoring via carboxylic or phosphonic acid groups to the nodes of NU-1000 via SALI is not suitable for the desired catalytic application and is thus not further followed in this Thesis. For the approach of catalyst anchoring to the node as design principle, a different reaction should be chosen excluding the involvement of acidic substrates able to substitute catalyst tethered to the node. If, however, such acidic substrates are required for a specific purpose, highly stable catalyst anchoring to the MOF, e.g., by covalent bonding to the linker, is crucial. Both aspects need to be addressed in further studies – beyond this Thesis – for the implementation of a hybrid  $\text{Pd}_2\text{S}_2@$ MOF catalyst able to induce potential confinement effects in catalysis.

Thus, the above-described study allows for the presentation of following key findings: 1) the selection of an appropriate catalytic reaction, MOF and anchoring motif prior to synthetic approaches are key for the design of a hybrid catalytic system, 2) pre-experiments are essential to evaluate on the stability of the material – during catalyst incorporation and under catalytic conditions and 3) the stability of the MOF material might change upon catalyst integration.

### 3.2.2.3. Re-Photocatalyst Anchoring in Pores via Coordinative Bonds

This chapter is based on the publication: Philip M. Stanley,<sup>‡</sup> Karina Hemmer,<sup>‡</sup> Markus Hegelmann, Annika Schulz, Mihyun Park, Martin Elsner, Mirza Cokoja, Julien Warnan, *Chem. Sci.* **2022**, *13*, 12164-12174.

Experiments were conducted by P. Stanley and K. Hemmer including design and optimization, with contributions from M. Hegelmann, A. Schulz and M. Park. ICP-MS measurements were conducted at the chair of M. Elsner. M. Cokoja and J. Warnan also designed the project and gave overarching academic guidance.

Another appealing strategy of catalyst incorporation provided by the high design flexibility of MOFs is the anchoring of a molecular catalyst via coordinative bonds to a linker molecule. In this Thesis, this approach was studied for the two porphyrin-based MOFs PCN-222 and PCN-224 where the porphyrin linkers – which show photosensitizing properties<sup>[126,128,183,184]</sup> – were metalated with Zn which serves as anchoring point for a molecular Re-based CO<sub>2</sub>-to-CO photocatalyst (Figure 58). Here, the coordination occurs between the Zn in the porphyrin core with a nitrogen group of a pyridine analogue applied as ligand for the Re complex (Figure 58). For the preparation of the Zn-metalated porphyrin (Zn-TCPP), the metalated porphyrin MOFs PCN-222(Zn) and PCN-224(Zn) and the catalyst *fac*-ReBr(CO)<sub>3</sub>(qtpy) (qtpy = 4,4':2',2'':4'',4'''-quarterpyridine) and their respective characterization the reader is referred to chapters 3.1.2.3 and 5.3.3. Note that the focus of this Thesis is set on the synthesis and characterization of the dyadic catalyst-host systems. The photocatalytic experiments were performed in cooperation with *Philip Stanley* and will be shortly summarized in this work.

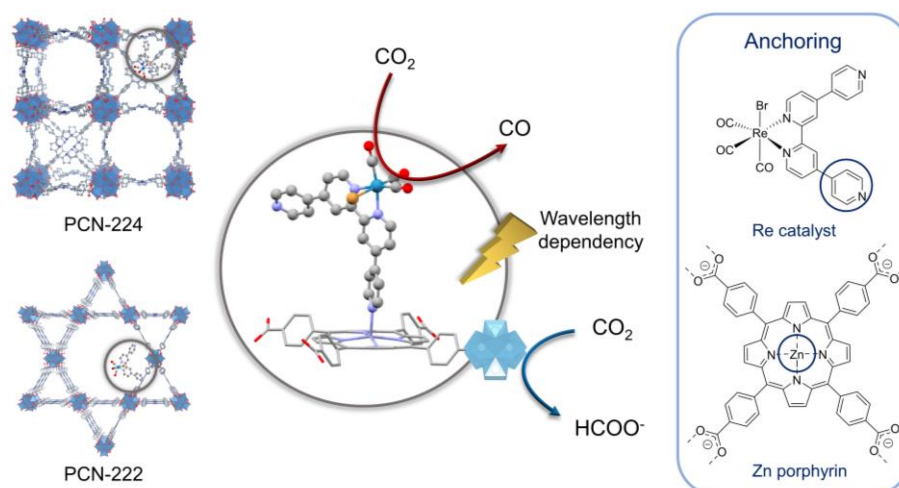


Figure 58: Schematic representation of the photocatalytic CO<sub>2</sub> reduction at a Re catalyst (*fac*-ReBr(CO)<sub>3</sub>(qtpy)) anchored to a MOF incorporated Zn-porphyrin and at the MOF node. In addition to different MOF structures, the irradiation wavelength was varied. The dyadic Re catalyst – porphyrin assemblies are shown in grey circles while blue circles highlight the anchoring motif. Chemical structures of Re catalyst and Zn-porphyrin are depicted. Colors in DFT optimized structure of assembly: Red: Oxygen, Grey: Carbon, Purple: N, Gold: Br, Cyan: Re. MOF structures were rendered from crystal structure data (CCDC: 893545 and 1001133).

## Material Preparation and Properties

For the incorporation of the Re complex into PCN-222(Zn) and PCN-224(Zn) the MOFs were soaked in a stock solution (0.1 mM) of the catalyst in MeCN yielding powdered  $\text{ReBr}(\text{CO})_3(\text{qtpy})@\text{PCN-222}(\text{Zn})$  (Re-PCN-222(Zn)) and  $\text{ReBr}(\text{CO})_3(\text{qtpy})@\text{PCN-224}(\text{Zn})$  (Re-PCN-224(Zn)). The catalyst integration was followed by UV-vis spectroscopy of the supernatant, revealing an intensity decrease of the  $\text{ReBr}(\text{CO})_3(\text{qtpy})$  absorption bands after 24 h of soaking (Figure A 175). Catalyst leaching upon MOF washing was excluded by UV-vis measurements where the catalyst absorption bands were absent in the washing solutions (Figure A 176 – confirming the presence of strong Zn-N bonds. The importance of Zn for catalyst anchoring was supported by soaking PCN-222 and PCN-224, respectively, (both without Zn) in a catalyst solution where no decrease in catalyst absorption bands was apparent (Figure A 177).

PXRD measurements confirmed the stability of both MOFs upon Zn and catalyst integration (Figure A 178) since the phase-purity and crystallinity remained unchanged. The successful incorporation of the  $\text{ReBr}(\text{CO})_3(\text{qtpy})$  catalyst was followed by IR spectroscopy showing peaks at 1926 and 2025  $\text{cm}^{-1}$  and 1927 and 2024  $\text{cm}^{-1}$ , respectively, corresponding to the Re catalyst's characteristic symmetric and asymmetric CO vibrations (Figure A 179).<sup>[185]</sup> At the same time these peaks prove that the molecular structure of  $\text{ReBr}(\text{CO})_3(\text{qtpy})$  was preserved upon MOF incorporation. Moreover, IR spectra indicated Zn-N coordination by a peak shift at  $\sim 398 \text{ cm}^{-1}$  after catalyst embedment (Figure A 179).<sup>[186]</sup>

In a proof-of-concept experiment in solution (without MOF catalyst), UV-vis spectra verified the formation of a dyad between Zn-TCPP and  $\text{ReBr}(\text{CO})_3(\text{qtpy})$  in MeCN showing a bathochromic shift of 5 nm of Zn-TCPP's Soret band (414 to 419 nm) supporting the self-assembly of both molecular species (Figure A 180).<sup>[187]</sup>

For the catalyst – MOF hybrid, the absorption bands of both MOFs (apparent from solid-state UV-vis measurements) were preserved upon Re-catalyst integration (Figure A 181, Figure A 182). Since the catalyst did not affect the absorption bands it is assumed that mainly the MOF matrix – not the catalyst – is excited by visible light, which is key and desired for photocatalytic applications as such Re-based molecular catalysts often perform extremely modestly without a photosensitizer.<sup>[188,189]</sup> The amount of Re in the molecular catalyst – MOF hybrids was obtained with ICP-MS measurements. Here, similar Re contents of  $\sim 82$  and  $\sim 75 \text{ nmol}_{\text{Re}}\text{-mg}_{\text{MOF}}^{-1}$  for Re-PCN-222(Zn) and Re-PCN-224(Zn), respectively, were calculated corresponding to approximately 0.1 Re catalyst per linker in accordance to metal loadings reported for molecule anchoring via nodes or linkers in MOFs (e.g. by carboxylic or phosphonic acids).<sup>[128,190,191]</sup>



Thus, the here described synthesis strategy presents an appealing, straightforward way of catalyst integration within a MOF matrix – provided by the high design flexibility of MOF materials – achieving comparable loadings to previously studied catalyst anchoring via acid groups. Note that the anchoring of the catalyst to physisorbed Zn cannot be ruled out completely with the here presented techniques. N<sub>2</sub> sorption measurements of Re-PCN-222(Zn) and Re-PCN-224(Zn) exhibit a drastic decline of adsorbed N<sub>2</sub> quantity upon Re-catalyst integration (Figure A 183, Figure A 184). Supported by the decreased BET surface areas of ~1219 m<sup>2</sup>·g<sup>-1</sup> for Re-PCN-222(Zn) and ~618 m<sup>2</sup>·g<sup>-1</sup> for Re-PCN-224(Zn) compared to ~1550 m<sup>2</sup>·g<sup>-1</sup> for PCN-222(Zn) and ~1750 m<sup>2</sup>·g<sup>-1</sup> for PCN-224(Zn), pore blocking is implied upon catalyst integration – significantly present in the case of Re-PCN-224(Zn).

### Photocatalysis

For photocatalytic experiments, the catalyst – MOF hybrid was suspended in an MeCN/H<sub>2</sub>O solution with 1,3-dimethyl-2-phenyl-2,3-dihydro-1H-benzo[d]imidazole (BIH) as a single electron donor (SED). After saturation of the suspension with CO<sub>2</sub> the setup was irradiated with a Xenon Light Source (300 W, λ = 430-740 nm, ~10 mW·cm<sup>-2</sup>). Analysis of the reaction headspace, i.e., quantities of CO and H<sub>2</sub>, was performed by gas chromatography. In contrast, for the evaluation of formate formation <sup>1</sup>H NMR spectroscopy of the solution was applied.

As a reference, the ReBr(CO)<sub>3</sub>(qtpy) catalyst was studied in homogeneous phase under identical conditions (compared to the described heterogeneous conditions above) selectively forming CO with a TON<sub>CO</sub> of ~5 after 2 h which could be increased to a TON<sub>CO</sub> ~10 when Zn-TCPP as photosensitizer was added in equimolar amounts (Table A 16).

Although, the low stability of Re catalysts during photocatalysis is reported in literature, the activity observed in this work is significantly lower than in prior reports of Re(CO)<sub>3</sub>X(bpy)-based (bpy = 4,4'-dicarboxy-2,2'-bipyridine) catalyst and porphyrin-Rhenium-catalyst dyads where TONs above 100 are achieved.<sup>[188,192,193]</sup> This observation indicates the importance of the linking unit within the molecular complex, e.g. qtpy versus bpy, on the photocatalytic performance.

Under heterogeneous conditions, Re-PCN-222(Zn) mainly produced formate (~27 μmol<sub>HCOO</sub><sup>-</sup>·g<sup>-1</sup>·h<sup>-1</sup>, TON<sub>HCOO</sub><sup>-</sup> per node ~5) after 80 h and only marginal amounts of CO (~4 μmol<sub>CO</sub>·g<sup>-1</sup>·h<sup>-1</sup>; TON<sub>CO</sub> per Re < 1), see Figure 59, Figure 60 and Table A 17. A high formate selectivity was also apparent for PCN-222(Zn) (without Re catalyst) resulting in a comparable rate of formate production but no CO formation (Figure 59, Figure 60, Table A 17). In control experiments without light or BIH no products (CO, H<sub>2</sub>, formate) could be detected (Table A 16).

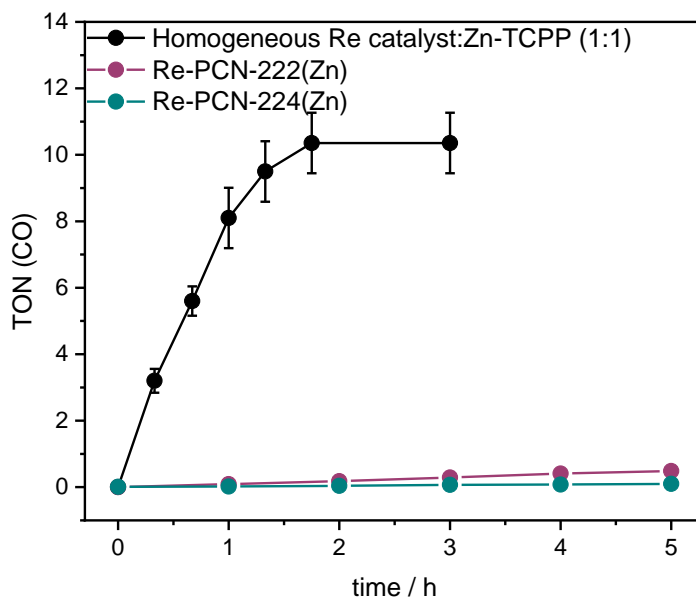


Figure 59: TONs(CO) as a function of reaction time for Re-PCN-222(Zn), Re-PCN-224(Zn) and a homogeneous reference system of *fac*-ReBr(CO)<sub>3</sub>(qtpy)/Zn-TCPP. Reaction conditions: 1.5 mg MOF, MeCN/H<sub>2</sub>O (4 mL/0.12 mL), 225 mg BIH, rt, irradiation >430 nm.

During photocatalysis, the light is absorbed by Zn-TCPP. Subsequently, electrons can be transferred to the Re catalyst or the Zr-oxo node of the MOF. While the Re catalyst selectively forms CO, formate is produced at the MOF node, thus, two competing mechanisms are present in the catalyst – MOF hybrid for the photocatalytic CO<sub>2</sub> reduction, as reported prior.<sup>[126,183,194,195]</sup> For Re-PCN-224(Zn), significantly decreased activities compared to Re-PCN-222(Zn) were measured, however, also forming formate preferentially ( $\sim 2 \mu\text{mol}_{\text{CO}} \cdot \text{g}^{-1} \cdot \text{h}^{-1}$  and  $\sim 9 \mu\text{mol}_{\text{HCOO}^-} \cdot \text{g}^{-1} \cdot \text{h}^{-1}$ , Figure 60, Table A 17).

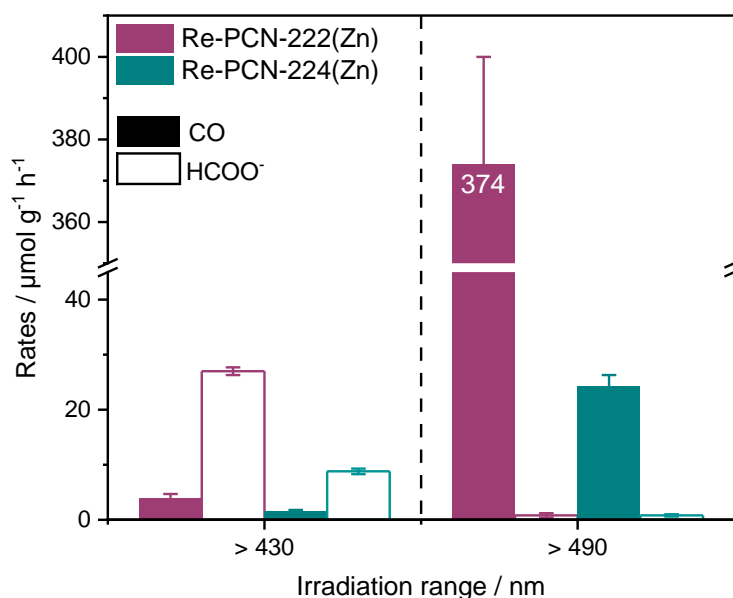


Figure 60: Product evolution rates of CO and HCOO<sup>-</sup> for the first two hours of irradiation. Rates for different wavelengths of irradiation (>430 nm and >490 nm) are compared for Re-PCN-222(Zn) and Re-PCN-224(Zn).

Characterization after photocatalysis confirmed the stability of both MOFs by PXRD measurements (Figure A 178). In contrast, the Re catalyst decomposed during photocatalysis indicated by the disappearance of its CO bands in the IR spectrum (Figure A 185) – which is in accordance to the limited stability observed under homogeneous conditions and in literature.<sup>[190,193,196]</sup>

These experiments showed three main findings: 1) the lifetime of the Re catalyst could be significantly enhanced by integration into the MOF matrix, 2) a selectivity switch between CO formation and formate production is apparent: while under homogeneous conditions  $\text{ReBr}(\text{CO})_3(\text{qtpy})$  selectively yields CO, upon MOF incorporation and under heterogeneous conditions, formate is the major product in the  $\text{CO}_2$  photoreduction catalysis, and 3) an influence of the MOF host on the photocatalytic activity has been shown, since the activity was decreased in the PCN-224 case compared to the PCN-222 MOF. In particular 2) and 3) are intriguing – especially as this Thesis studies effects of MOF confinement – and thus required further investigations of the underlying mechanism which will be presented in an abridged version in the following. A more detailed description can be found in the publication<sup>[197]</sup>.

To elucidate the potential impact of MOF structure on the photocatalytic performance, both topologies need to be compared. Summarized briefly here, beside the different sizes of pore channels ( $\sim 35 \text{ \AA}$  and  $\sim 10 \text{ \AA}$  for PCN-222 and  $\sim 20 \text{ \AA}$  for PCN-224), the pore shapes are significantly different: the topology of PCN-222 shows hexagonal and trigonal channels while PCN-224 consists of cubic pores (Figure 18).<sup>[81,87]</sup>

Due to the size of the Re catalyst ( $\sim 13.5 \text{ \AA}$  van der Waals sphere diameter deduced from DFT calculations) and the apparent decrease in  $\text{N}_2$  uptake pore blocking is suggested which is more distinct in the PCN-224 case. Additionally, DED (difference envelope density) analysis was performed visualizing the electron density of the Re catalyst inside the MOF pores – in brief by comparison of PXRD patterns of pristine and catalyst incorporated MOFs (details can be found in the respective publication<sup>[197]</sup>).<sup>[198]</sup> While in the case of Re-PCN-222(Zn) sufficient space is left in the hexagonal pores after catalyst incorporation, the pores of Re-PCN-224(Zn) are almost completely occupied. Additional DFT calculations confirmed the DED analysis results and the drastic pore blocking for Re-PCN-224(Zn) (details see<sup>[197]</sup>). Interestingly, exclusively for the latter, DFT calculations showed that coordination of the catalyst to two neighboring Zn-porphyrins is possible – supporting the hypothesis of significant pore blocking. Summarized, the presented techniques underline a more restricted environment for Re-PCN-224(Zn) compared to the PCN-222 analogue which might affect substrate diffusion (e.g., BIH max. diameter =  $10.6 \text{ \AA}$ ),<sup>[199]</sup> and thus result in a decreased photocatalytic activity. It is important to note that the crystal size of both MOFs is not considered – however is known to affect catalytic performances.<sup>[44,45]</sup>

In addition to the mass transport considerations and dissimilarities between both MOFs, differences in exciton migration and thus charge separation have been reported in literature depending on the MOF topology, suggesting increased exciton hopping rates and a lower Förster radius  $R$  between the chromophores (Förster resonance energy transfer scaling with  $R^{-6}$ ) for Re-PCN-222(Zn).<sup>[184,200]</sup> Here, the translational hopping distance of the exciton along the  $c$ -axis (which is almost the half for PCN-222 compared to PCN-224) and the triangular pore shape are beneficial in PCN-222.<sup>[201,202]</sup>

For a further understanding the luminescence of Zn-TCPP (emission bands at  $\lambda = 649$  and 714 nm) in the presence of the Re catalyst and a discrete Zr<sub>6</sub>-oxo node (synthesized with methacrylate ligands capping the cluster avoiding aggregation)<sup>[203]</sup> was studied simulating the conditions given in the MOF environment. The measurements revealed significantly altered properties of the porphyrin when the other two components were added – dependent on the excitation wavelength (415 nm and 515 nm corresponding to the Soret and Q band, respectively). For both irradiation wavelengths the emission is comparably reduced upon addition of the Re catalyst to Zn-TCPP, attributed to an electron transfer (i.e. luminescence quenching) of Zn-TCPP to the catalyst. Importantly, a drastic wavelength dependency of the emission upon Zr-node addition was apparent: while the emission was almost unaffected by the Zr node for 515 nm irradiation, with a wavelength of 415 nm and the addition of the Zr node the emission of the porphyrin is quenched almost completely (Figure A 186, Figure A 187).

The observations of the luminescence studies indicate different energy relaxation pathways (Figure 61) where Soret band excitation ( $S_0 \rightarrow S_2$ ) probably results in a fast transfer of electrons from the  $S_2$  state ( $E_{00} \approx 2.9$  eV) to the Zr node.<sup>[183]</sup> In contrast, supported by the absence of fluorescence quenching for Q band irradiation ( $S_0 \rightarrow S_1$ ), electron transfer from  $S_1$  ( $E_{00} \approx 2.0$  eV) to the energy level of the Zr node is not possible since the energy level of the Zr node is assumed to be located between the  $S_2$  and  $S_1$  state. At the same time the observations indicate that the electron transfer of  $S_2$  to the Zr-oxo-node energy level is faster than the internal conversion ( $S_2 \rightarrow S_1$ ) which is in accordance to the relaxation mechanisms and electron transfers in molecular dyadic and heterogeneous systems reported in literature.<sup>[204]</sup> The reduction of the Re catalyst is assumed to result from electron transfer of the  $S_1$  excited state since the fluorescence quenching described above is wavelength independent.

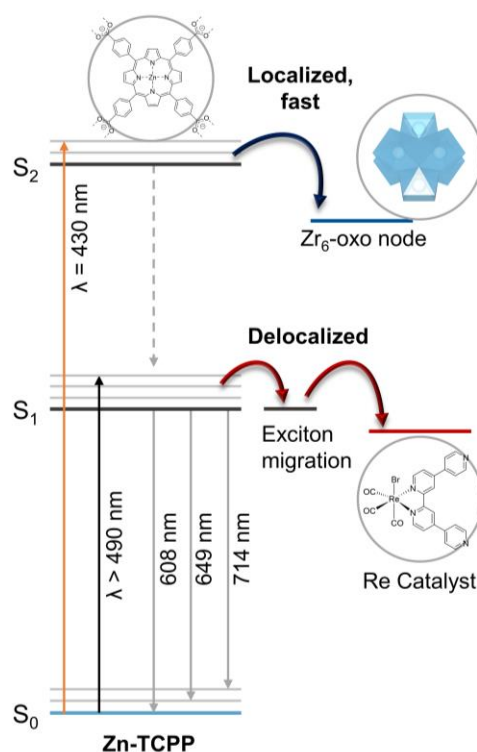


Figure 61: Schematic representation of the energy levels describing different paths upon irradiation with different wavelength. While electrons from the S<sub>2</sub> level of the Zn-porphyrin are transferred to the Zr<sub>6</sub>-oxo node, electrons from the S<sub>1</sub> state are directed to the Re catalyst via exciton migration.

The identified wavelength dependency on the photocatalytic performance was tested for both Re-PCN-222(Zn) and Re-PCN-224(Zn). For excitation a wavelength of  $\lambda = 490\text{-}740\text{ nm}$  ( $\sim 8\text{ mW}\cdot\text{cm}^{-2}$ ) was applied, excluding the excitation of the Soret band and thus occupation of the S<sub>2</sub> energy level, which showed a drastically enhanced activity for Re-PCN-222(Zn) ( $\text{TON}_{\text{CO}} \sim 100$  after 80 h) compared to irradiation with  $\lambda > 430\text{ nm}$  ( $\text{TON}_{\text{CO}} < 1$ , Figure 60). Most interestingly, the selectivity of the CO<sub>2</sub> reduction was reversed forming CO as the main product and only minor amounts of formate ( $\sim 370\text{ }\mu\text{mol}_{\text{CO}}\cdot\text{g}^{-1}\cdot\text{h}^{-1}$  and  $< 1\text{ }\mu\text{mol}_{\text{HCOO}^-}\cdot\text{g}^{-1}\cdot\text{h}^{-1}$ , Figure 60). The photocatalytic performance of Re-PCN-224(Zn) followed the same trend ( $\sim 24\text{ }\mu\text{mol}_{\text{CO}}\cdot\text{g}^{-1}\cdot\text{h}^{-1}$  ( $\text{TON}_{\text{CO}} \sim 12$ ) and  $< 1\text{ }\mu\text{mol}_{\text{HCOO}^-}\cdot\text{g}^{-1}\cdot\text{h}^{-1}$  after  $\sim 60\text{ h}$ ) but with an in general lower activity compared to Re-PCN-222(Zn) which is ascribed to the topology effects discussed above (Figure 60). Irradiation for 80 h with  $> 490\text{ nm}$  did not affect the phase-purity and crystallinity of both MOF – molecular catalyst assemblies confirmed by PXRD measurements (Figure A 178). However, also for this wavelength the catalyst was not stable under reaction conditions apparent from IR spectroscopy (Figure A 185). ICP-MS analysis after catalysis revealed a Re leaching of 27% and 17% for Re-PCN-222(Zn) and Re-PCN-224(Zn), respectively, which is in accordance to previously reported catalyst decomposition.<sup>[190,193,196,205]</sup>

Accordingly, the wavelength dependency allows for a switch in product selectivities of the molecular catalyst – MOF assembly by simply adjusting the irradiation wavelength. Since this presents a very appealing strategy it needs to be clarified if this concept is also transferrable to another Re-catalyst – MOF hybrid. Thus, control experiments with *fac*-ReBr(CO)<sub>3</sub>(4,4'-dicarboxy-2,2'-bipyridine) which was anchored to the node of PCN-222 and PCN-224, respectively (details on the synthesis see 5.3.4.), were performed confirming the described wavelength dependency using identical conditions (Table A 17). This highlights the importance of irradiation wavelength on the selectivity independent on the anchoring motif. The observation is also in agreement with a ReCl(CO)<sub>3</sub>(4,4'-dicarboxy-2,2'-bipyridine)/PCN-222 hybrid acting as CO<sub>2</sub>-to-CO reduction catalyst reported in literature with an irradiation > 500 nm.<sup>[206]</sup>

From a mechanistic point of view – combining the results from luminescence measurements and catalysis, electrons are either selectively transferred from the S<sub>2</sub> state (Soret band excitation) to the Zr-node forming formate or from the S<sub>1</sub> level (Q band excitation) to the CO<sub>2</sub> reduction catalyst yielding CO depending on the excitation energy.<sup>[126,183,194]</sup> The ground state is assumed to be regenerated by bimolecular reaction with BIH.<sup>[206]</sup> CO<sub>2</sub> reduction to formate at the node occurs at Zr(III) sites as a one-electron process and due to the presence of four nodes for each linker, localized electron channeling is assumed.<sup>[126,195]</sup> In contrast, CO<sub>2</sub> to CO reduction at the catalyst is considered as a two-electron process.<sup>[190,206]</sup> Since only at approximately every tenth linker a photocatalyst is anchored, excitons can migrate within the MOF structure providing a delocalized electron channel.<sup>[202,206]</sup>

Concluding, the here presented study demonstrates a straightforward catalyst anchoring strategy in porphyrinic MOFs with the possibility of tailoring the photocatalytic performance of a molecular catalyst – MOF assembly either by topology or wavelength alteration. While the confinement of the catalyst within different topologies was shown to affect the activity of the reaction, selectivity control was achievable by variation of irradiation wavelength.

### 3.3. Resumé Confinement Effects and Multifunctionality

The presented studies in this Thesis allow to evaluate the two strategies for 1) exploiting confinement effects in MOF catalysis to control the catalytic performance and 2) the design of multifunctionality within one MOF via different approaches, e.g. mixed-linker or SALI techniques. The different strategies and goals of this Thesis are summarized in Figure 62.

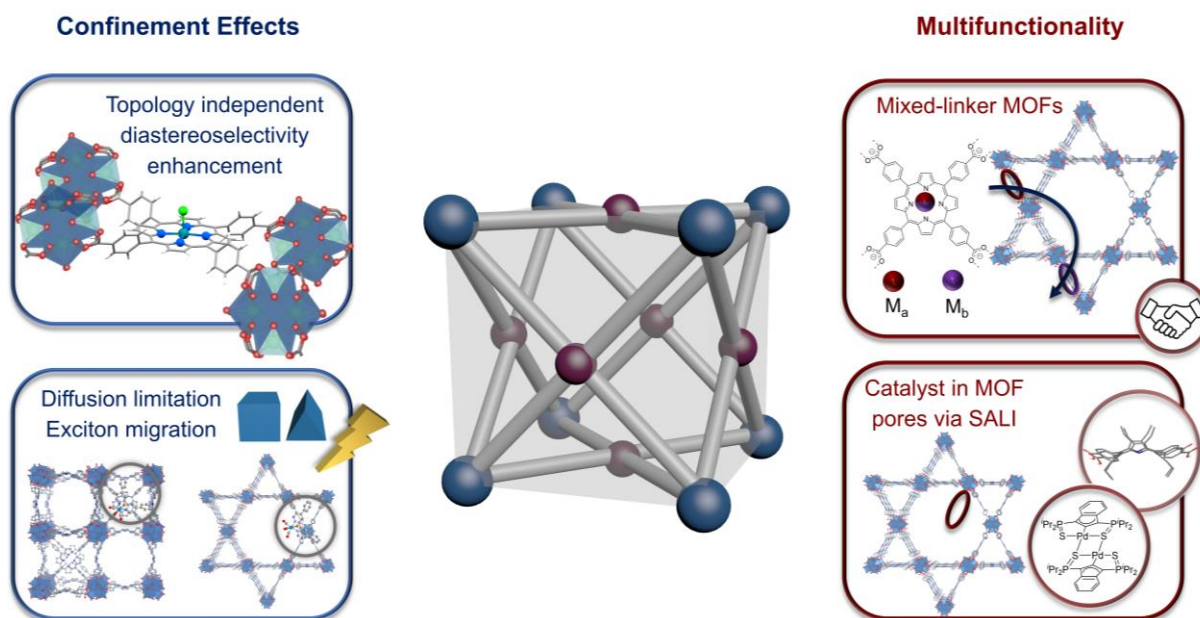


Figure 62: Schematic visualization of the confinement effect studies and multifunctional material designs performed in this Thesis. The illustration highlights the topology independent diastereoselectivity enhancement in the catalytic cyclopropanation with Rh-porphyrin MOFs, the photocatalytic CO<sub>2</sub> reduction of a Re-catalyst in PCN-222 and PCN-224 revealing topological differences. For designing multifunctionality, a mixed-linker strategy and catalyst incorporation via SALI has been presented. The mixed-linker approach designing multimetal PCN-222 MOFs allows for the successful application in sequential catalysis.

Addressing 1) the presented investigations highlighted the importance of framework effects upon molecular catalyst incorporation. Although the previous hypothesis of topology dependent diastereoselectivity enhancement could not be confirmed for cyclopropanation catalysis, embedding the Rh-porphyrin in the MOF and possible interaction with Zr nodes seem to be crucial for the observed selectivities. Here, comparisons of topologically different MOFs (formed from the same building units) and to analogous homogeneous systems was essential. The importance of substrate interactions with Zr nodes in catalysis has been assumed in literature resulting in altered selectivities and requires more detailed investigations for the cyclopropanation catalysis.<sup>[207]</sup>

Remarkably, a topology impact could be identified in the application of two topological different porphyrin-based MOFs (PCN-222 and PCN-224): Due to increased diffusion limitations and pore blocking upon molecular catalyst integration a decrease in photocatalytic CO<sub>2</sub> reduction activity was apparent for PCN-224.

Additionally, the exciton migration is most likely affected by the pore shape where the triangular motif in PCN-222 is beneficial – supported by several reports in literature. Combined this results in drastically increased CO<sub>2</sub> reduction activities of the Re catalyst tethered in the latter framework. More crucially, this study manifests the importance of host selection. Thus, the choice of using a porphyrin-based framework where the porphyrin acts as photosensitizer allowed for product selectivity (CO<sub>2</sub> versus formate) control – so far unreported in literature. Note that morphology and particle size effects were not investigated in this Thesis which – however – have been shown to impact the catalytic performances.<sup>[44,45]</sup>

Regarding 2), in particular the mixed-linker strategy is appealing for the design of multifunctional systems where the porphyrin-based MOFs (in this case PCN-222) seems to be an ideal platform allowing several degrees of functionalization (different metals, functionalized porphyrins). Especially the presented possibility of free metal combination choice and metal/metal ratio adjustment is unmatched in previous literature studies. However, this is an extremely attractive method to incorporate two catalytically active sites – fixed in a framework – within one MOF allowing for several reaction combinations enabling one-pot tandem or sequential catalysis. Simultaneously, diffusion limitations are almost absent due to the lack of molecular catalysts directing into the MOF pores which was shown for the Re-photocatalyst in PCN-224. Beyond the general possibility of integrating two different molecular catalysts within one framework the study of confinement effects in these multifunctional systems is interesting since the importance of interactive site distance for catalytic performance control has been presented which could be exploited in specific catalytic reactions.<sup>[67,82]</sup>

On top of the potential of achieving multifunctionality by incorporating molecular systems into MOF pores by SALI techniques (shown for a non-planar porphyrin and the pre-experiments of Pd catalyst anchoring) the catalytic application of these hybrid materials and confinement effects studies are appealing. The framework effects of the MOF host on the performance of incorporated catalysts has been presented in rare example and has a huge potential for further research.<sup>[77,207]</sup>

A critical point – however – especially for the confinement effect study, is the understanding of respective MOF structures (e.g., linker arrangement, topology, defectiveness), catalyst locations and intriguingly present interactions which might cause catalytic property control. In the case of porphyrin-based MOF systems this is of particular importance since the structures are still not completely understood. The high defect tolerance of those materials is also an issue which needs to be considered. Thus, sophisticated characterization is essential to conclude on structure – property relations which enable the future design of specific interactions in those materials, e.g., exploiting the confinement provided in MOFs.



Simultaneously, this Thesis underlines the difficulty of systematic studies regarding confinement effects. On the one hand, a suitable material class is required offering the general possibility for such studies (e.g., the porphyrin-MOF systems) and on the other hand reliable synthesis of the MOF – catalyst hybrid needs to be ensured (which is a problem for the PCN systems). Although large MOF pores are attractive to preserve sufficient diffusion after catalyst incorporation into MOF pores, confinement effects might be more pronounced in more restricted pores allowing for interactions with neighboring pore walls.<sup>[82]</sup> After identifying a suitable material platform as host and a suitable catalyst, the selection of the catalyst integration strategy is important since distances between functionalities are tunable depending on the catalyst anchoring methodology. Beyond material synthesis, the choice of (proof-of-concept) catalytic reaction is crucial since a general potential of steering e.g., selectivities needs to be provided (like *cis/trans* or *exo/endo* selectivities).

## 4. Conclusion

The studies presented in this Thesis focus on the design and catalytic applications of multifunctional (porphyrin-based) Zr-MOFs – allowing for the transfer of concepts in enzymatic catalysis to synthetic MOF materials. Although these materials offer several advantages, synthetic challenges need to be faced when working with these MOFs. Therefore, studies on the phase-pure synthesis of the materials and parameter influences were discussed (chapters 1.4.1. and 3.1.2.).

The first major part presents design strategies to integrate catalytically active species into the MOF by different approaches. Here, the most significant achievement is the comprehensive study of different (transition) metals (Rh, Ru, Mn, Co, Zn, Ni, Cu, Fe, Mg) included into the porphyrin core of topologically different MOFs (Figure 63). While for most of the metals the synthesis of metalloporphyrins and subsequent MOF formation from these ligands is possible, in particular for Zn and Mg post-synthetic metalation is recommended (see chapter 3.1.2.3.). Thus, this Thesis provides guidelines which allow for the free choice of metals, the combination of different ones and their ratio adjustment. This is extremely beneficial for the materials' applications, e.g., in catalysis, since the properties resulting from metal incorporation can be precisely tuned. Details on the synthetic techniques for specific metals are summarized in chapter 3.1.2.3. Regarding all those strategies, studies on the compatibility of reaction conditions and the MOF stability and detailed characterization were essential. Although several metalation protocols were reported in literature, their reproducibility was limited. Together with the challenges of non-metalated porphyrin-MOF synthesis, this emphasizes the importance of detailed protocols in literature.

In addition to the catalyst incorporation as a building block in the MOF which was intensively shown for (metallo-)porphyrins, the anchoring of further catalytic species into the pores was achieved. Here, different strategies were followed, e.g., SALI or coordination of a catalyst ligand to a metalloporphyrin. Therefore, several techniques for catalyst integration provided in this Thesis enable a high design flexibility and allow for various applications – depending on the desired purpose.

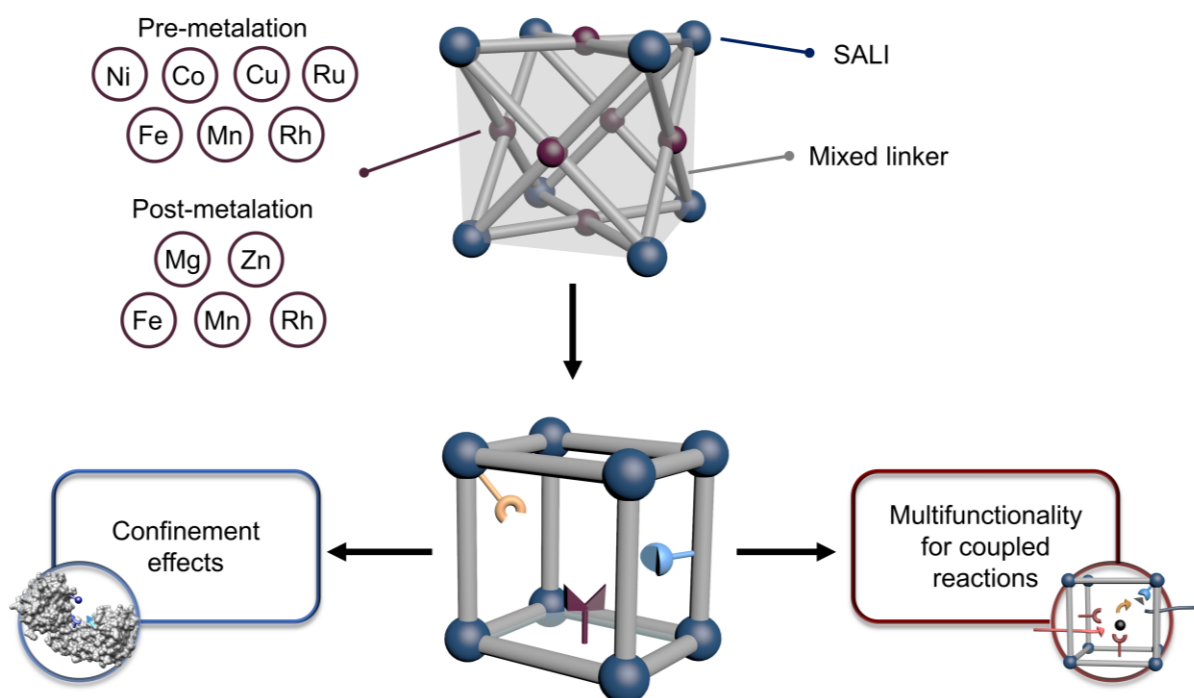


Figure 63: Summary of different catalyst integration strategies: porphyrin metalation (pre- and post-synthetic), SALI and mixed-linker strategy (top). The catalyst integration and design of multifunctionality allows for the study of confinement effects – resembling enzymatic pockets – and coupled catalytic reactions.

In the second part of this Thesis, the materials bearing catalysts incorporated by different strategies were applied in catalysis using proof-of-concept reactions. This allows to study a) confinement effects affecting the catalytic performance and b) multifunctional catalysts for coupled reaction sequences (Figure 63).

Indeed, confinement effects resulting in performance variations either between the heterogeneous and homogeneous systems (chapter 3.2.1.1.) or between different topologies (chapter 3.2.2.3.) could be elucidated. While for the first case the presence of Zr nodes seems crucial to increase the selectivity, the activity of two different MOFs is significantly influenced by the pore space and shape. This highlights the potential of such effects to be exploited for the specific control of catalytic reactions.

Addressing b), the multifunctional porphyrin-based MOFs (PCN-222 analogues) were successfully applied as catalyst materials coupling two reactions in a sequence and achieving promising activities and selectivities. Here, the variation of metal combination and their ratios revealed significant impacts on the performance. Thus, the design strategy allowed for the precise tuning of catalytic properties.

In general, this Thesis emphasizes the suitability of porphyrin-based MOFs for the integration of multifunctionality and different catalysts within one structure – presented in chapter 3.2. Simultaneously, the accessibility of different topologies from the same building blocks renders these MOFs as an ideal platform for the investigation of confined reaction environments which can allow for performance control. This provides further understanding and allows for the future precise design of active site surroundings and interactions – resembling enzymatic systems. However, the presented studies also show the key role of choosing a suitable MOF host, catalyst, its anchoring into the MOF and a proof-of-concept reaction. Although this seems straightforward, the results indicated significant challenges, if one of these aspects is inappropriate (in particular in chapter 3.2.2.2.). Suitable MOF host systems should show high chemical and thermal stability to allow for different modification approaches to incorporate functionalities, which is for example met in Zr-based MOFs. Especially regarding tandem or sequential catalysis, time and cost intensive multi-step material preparation in combination with the limited stability of MOF systems represents a drawback hindering the broad application of such materials in catalysis and requires significant further studies.

Summarized, the different studies highlight the beauty of MOF materials – in particular their tailorability – which allows for their property adjustment “on-demand” for a broad scope of applications. In particular in material design for catalysis, their potential is currently not fully exhausted. Thus, fundamental studies are crucial to present design strategies and gain understandings of principles and interactions to transfer this to new sophisticated catalytic materials. Additionally, the emerging field of machine learning and artificial intelligence might provide helpful tools for the specific design of material properties.

## 5. Experimental

### 5.1. Materials

Acetonitrile (MeCN, HPLC grade), methanol (HPLC grade), chloroform (HPLC grade), absolute ethanol, *n*-propanol (HPLC grade), ethyl acetate (HPLC grade), ethylene glycol dimethyl ether, hexane (HPLC grade), tetrahydrofuran (THF, HPLC grade), *N,N*-dimethylformamide (DMF, HPLC grade), dichloromethane (DCM, HPLC grade),  $\text{ReBr}(\text{CO})_5$ , polyphosphoric acid, *o*-phenylenediamine, benzoic acid, methyl iodide, sodium borohydride, anhydrous sodium sulfate, potassium oxalate, Celite® S,  $\text{ZrOCl}_2 \cdot 8 \text{H}_2\text{O}$ , pyrrole, propionic acid, 4-*tert*-butylbenzoic acid, 3,3-dimethylbutanoic acid, formic acid, ethyl diazo acetate (10wt% in DCM), mesitylene, Pd/C (10 wt. %), triruthenium dodecacarbonyl ( $\text{Ru}_3(\text{CO})_{12}$ ), cobalt(II) chloride octahydrate ( $\text{CoCl}_2 \cdot 8 \text{H}_2\text{O}$ ), sodium hydroxide and potassium hydroxide were purchased from *Sigma Aldrich*. Copper acetate ( $\text{Cu}(\text{OAc})_2$ ) and zinc chloride ( $\text{ZnCl}_2$ ) were purchased from *Alfa Aesar*. Nickel acetylacetonate ( $\text{Ni}(\text{acac})_2$ ) and manganese(II) chloride tetrahydrate ( $\text{MnCl}_2 \cdot 4 \text{H}_2\text{O}$ ) were purchased from *abcr*. Methyl-*p*-formylbenzoate was purchased from *ChemPUR*. 2,2'-Bipyridine, 4,4'-bipyridine, 4,4'-dicarboxyl-2,2'-bipyridine and *N,N*-Diethylformamide (DEF) was purchased from *TCI Chemicals*. Methacrylic acid was purchased from *ACROS Organics*.  $\text{RhCl}_3 \cdot x\text{H}_2\text{O}$  was purchased from *Carbolution*.  $\text{FeCl}_3$  and 8-dram vials for MOF synthesis (TraceClean®) were purchased from *VWR*. The required argon 4.6 and the  $\text{CO}_2$  4.5 for catalytic reactions were purchased from the company *Westfalen*. All purchased chemicals were used without further purification. All synthesis and catalysis runs were carried out under air, if not stated other. Where specified, inert gas conditions entail standard *Schlenk* techniques under an argon atmosphere.

### 5.2. Analytical Methods and Characterization Techniques

#### Adsorption measurements

Adsorption measurements with  $\text{N}_2$  (99.999 vol%) at 77 K were carried out on a 3Flex Physisorption from *Micromeritics Instrument Corp.*, which uses a volumetric method to determine the amount adsorbed under an equilibrated gas pressure. Adsorption data were processed using the 3Flex Software Version 5.01 by *Micromeritics Instrument Corp.* and plotted in OriginPro 2019b by *OriginLab Corp.* Samples were transferred into pre-weighed sample tubes and capped with *Micromeritics* CheckSeals. Samples were subsequently activated at 393 K for 12 hours under a dynamic vacuum of approx.  $10^{-3}$  mbar using a SmartVac Prep by *Micromeritics Instrument Corp.* to ensure absence of unwanted adsorbates and identical pre-measurement states of all samples.

In particular, this unusually low activation temperature and time was chosen for all samples to ensure structural integrity of the immobilized molecular complexes which are known to sublime and decompose comparatively readily. The mass of the adsorbents was then recorded, generally in the range of 25 – 40 mg. The free space of the sample tube was determined prior to measuring each adsorption isotherm using Helium (99.999 vol%). A liquid nitrogen bath was used for measurements at 77 K.

The apparent surface area was derived using the Brunauer-Emmett-Teller (BET) model, is hence given as the 'BET area' and based on N<sub>2</sub> isotherms measured at 77 K. To determine this value for microporous materials, care was taken to adhere to the Rouquerol criteria.<sup>[208]</sup>

The pore size distribution (PSD) was derived by fitting N<sub>2</sub> isotherms measured at 77 K with sets of theoretical isotherms (kernel) derived from two-dimensional non-local-density functional theory (2D-NLDFT) based methods for specific pore sizes and geometry. As an approximation, cylindrical pores on an oxide surface were assumed for all materials to allow comparability within this series. Fitting was done using the respective kernel available via the 3Flex Software Version 5.01 by *Micromeritics Instrument Corp.*

### **Attenuated total reflectance infrared spectroscopy (ATR-IR)**

ATR-IR measurements were carried out on a *PerkinElmer* Frontier FT-IR spectrometer featuring an ATR plate with a diamond crystal with a 2 cm<sup>-1</sup> resolution and 16 accumulated scans.

### **Confocal microscopy**

Fluorescence images were recorded with a STELLARIS 8 FALCON (*Leica Microsystems*, Germany) equipped with the HC PL APO CS2 63x/1.10 OIL objective (*Leica*). Solid samples were directly used without further preparation and placed in chambered coverslip wells. Excitation was performed at 405 nm (Diode 405 laser). Images were obtained in the emission range of 700 – 760 nm. Merging of channels and localization of their fluorescence intensity was performed with the software *ImageJ*.

### **Density functional theory (DFT) calculations – Cyclopropanation project**

Geometries of the model complexes were performed using the ORCA5.0<sup>[209]</sup> software package with the 3-parameter hybrid functional B3LYP<sup>[210]</sup>. Grimme's Dispersion correction including Becke-Johnson damping (D3BJ)<sup>[211]</sup> was used. The structure optimization and analytical calculations of the Hessian were performed using Ahlrich's def2-SVP basis set.<sup>[212]</sup>

### Gas chromatography (GC)

GC is performed with an *Agilent Technologies* 7890B GC with a flame ionization detector (FID). The substance separation occurs via a capillary column HP-5 (length 30 m, inside diameter 0.32 mm, film 0.25  $\mu\text{m}$ , stationary phase (5%-phenyl)-methylpolysiloxane)). Sample preparation is performed by retrieving 50  $\mu\text{L}$  aliquot from the reaction suspension, adding 1.5 mL of the respective solvent and removing the MOF by a syringe filter (13 mm PTFE membrane with 0.2  $\mu\text{m}$  pore size).

### Inductively coupled plasma mass spectrometry (ICP-MS)

To obtain an accurate quantification of the Zr, Rh, Zn, Co, Cu, Ni, Ru, Fe, Mn, and Re amount immobilized in MOF samples, ICP-MS was conducted on a *Perkin Elmer* Nexlon 350D ICP-MS instrument. The respective samples were immersed in concentrated 7.5 mL nitric acid and 2.5 mL  $\text{H}_2\text{O}_2$  30 % (v/v) and treated in the microwave at 150  $^\circ\text{C}$  for 10 min. Subsequently, the microwave-digested samples were diluted 1/100 with Millipore Milli-Q® water. Each solvent was extra pure and checked for possible analyte contaminations before measurement.  $^{103}\text{Rh}$ ,  $^{66}\text{Zn}$ ,  $^{187}\text{Re}$ ,  $^{102}\text{Ru}$ ,  $^{59}\text{Co}$ ,  $^{63}\text{Cu}$ ,  $^{60}\text{Ni}$  and  $^{94}\text{Zr}$  were used as target masses for the analytes and  $^{103}\text{Rh}$  or  $^{115}\text{In}$  (for Rh determination) as an internal standard. Analyte quantification was carried out in standard mode with correction equation to avoid polyatomic interferences. Detection limit for Zr was 0.13  $\mu\text{g L}^{-1}$ , 0.29  $\mu\text{g L}^{-1}$  for Rh, 1.42  $\mu\text{g L}^{-1}$  for Zn, 0.34  $\mu\text{g L}^{-1}$  for Mg, 0.59  $\mu\text{g L}^{-1}$  for Cu, 0.71  $\mu\text{g L}^{-1}$  for Ni, 0.79  $\mu\text{g L}^{-1}$  for Co, 0.70  $\mu\text{g L}^{-1}$  for Ru and 0.10  $\mu\text{g L}^{-1}$  for Re. External Calibration was performed in the range of 0  $\mu\text{g L}^{-1}$  to 100  $\mu\text{g L}^{-1}$ . Each sample was measured with five measurement replicates, a dwell time per 50 ms and an integration time of 750 ms. The metal concentrations were blank corrected via measurement of blank samples.

### Infrared spectroscopy (Gas phase IR)

Gas phase IR spectra for isotope labelling studies were recorded with a *ThermoScientific* Nicolet 380-FT and the *OMNICTM* Spectra Software. After a given reaction time, 20 mL of the reaction headspace were transferred to an evacuated gas IR cell (20 cm path length, KBr windows) and a high-resolution transmission spectrum was collected (512 scans, 0.241  $\text{cm}^{-1}$  data spacing).

### **Nuclear magnetic resonance (NMR)**

Liquid state NMR spectra were recorded by a *Bruker* AVIII 400 US ( $^1\text{H}$ : 400.13 MHz) at ambient temperature (298 K). The  $^1\text{H}$  NMR spectroscopic chemical shifts  $\delta$  are reported in ppm relative to tetramethylsilane.  $^1\text{H}$  NMR spectra are calibrated against the residual proton and natural abundance carbon resonances of the respective deuterated solvent as an internal standard ( $\text{CDCl}_3$ :  $\delta$  ( $^1\text{H}$ ) = 7.26 ppm,  $\text{DMSO-d}_6$ :  $\delta$  ( $^1\text{H}$ ) = 2.50 ppm). The following abbreviations are used to describe signal multiplicities: s = singlet, d = doublet, t = triplet, m = multiplet.

### **Powder x-ray diffraction (PXRD)**

PXRD measurements were performed on a silicon single-crystal wafer using *Bragg-Brentano* geometry in a *Rigaku* MiniFlex 600-C diffractometer. X-ray  $\text{Cu K}_\alpha$  radiation ( $\lambda_1$  - 1.5406 Å,  $\lambda_2$  - 1.5444 Å,  $I_2/I_1$  - 0.5) was used, and  $\text{K}_\beta$  radiation was removed by a Ni-filter. The measurement range, unless stated otherwise, was from 2.0° to 50.0° ( $2\theta$ ) with a step size of 0.010 degrees and a scan rate of 5 degrees per minute.

Pawley profile fit analysis was carried out by using TOPAS v6. Standard deviations of all parameters were calculated and "randomize\_on\_errors" was used to achieve the minimum of refinement.

### **Scanning electron microscopy (SEM) – MOF synthesis**

SEM images for MOF samples (chapter 3.1.2.2.) were obtained with a *Carl Zeiss* NVision40 field emission scanning electron microscope with an acceleration voltage of 5.0 kV and a working distance of 8 – 10 nm.

### **Scanning electron microscopy (SEM) – Photocatalytic $\text{CO}_2$ reduction**

SEM images were recorded using a *Jeol* JSM-7500F field emission scanning electron microscope with the Gentle Beam mode.

### **Solid-state UV-Vis spectroscopy**

Solid-state UV-Vis spectra were recorded on a *Shimadzu* UV-3600 Plus UV-Vis-NIR spectrophotometer. Powder samples were fixed between two quartz glass slides for measurement. Measurement parameters: Medium Scan Speed, slit width (20) with External(3Detector) unit, enabled stair correction, baseline correction ( $\text{BaSO}_4$  background), S/R exchange normal, slit and detector lock normal.



### UV-Vis spectroscopy

UV-Vis spectra were recorded on an *Agilent Technologies Cary 60* with a scan rate of 600 nm/min. Baseline correction was performed with the respective pure solvent. Each sample was measured in a QS Suprasil 10.00 mm quartz glass cuvette from *Heraeus Quarzglas GmbH*.

### Variable-temperature PXRD (VTPXRD)

Variable temperature powder X-ray diffraction (VTPXRD) measurements were conducted with Debye-Scherrer geometry using a *STOE Stadi P* diffractometer (STOE & Cie, Germany) which is equipped with a *DECTRIS MYTHEN2R 1K* (Dectris, Switzerland) strip detector, with a Mo fine-focus sealed tube and a curved Ge (111) monochromator selecting Mo  $K_{\alpha}$  radiation source ( $\lambda = 0.70926 \text{ \AA}$ ). Samples were filled into borosilicate glass capillaries with a diameter of 0.5 mm (Hilgenberg, Germany). VTPXRD data were recorded in the temperature range  $T = 150\text{-}400 \text{ K}$  using a *Cryostream 800* cooler (OXFORD Cryosystems, UK) for temperature control with 20 K steps (and 10 K steps from 390 to 400 K). The obtained PXRD patterns were analyzed by Pawley profile fit analysis using TOPAS v6 software.<sup>[213]</sup> The minimum of refinement was achieved by using "randomize\_on\_errors".

## 5.3. Synthetic Procedures

### 5.3.1. (Metallo-)Porphyrin Syntheses

#### **5,10,15,20-tetrakis(4-carboxylphenyl)-porphyrin (TCPPH<sub>2</sub>)**

The synthesis was performed according to a literature known procedure.<sup>[14]</sup> First, *tetrakis*(4-methoxycarbonylphenyl)-porphyrin (TPPCOOMe) was synthesized from pyrrole (3.09 mL, 44.9 mmol, 1.1 equiv.) and methyl-p-formylbenzoate (6.93 g, 42.3 mmol, 1.0 equiv.) which were added to refluxing propionic acid (100 mL). The mixture was refluxed for 22 h. Afterwards, the precipitate was filtrated and subsequently washed with methanol (MeOH, 30 mL), ethyl acetate (EtOAc, 10 mL) and tetrahydrofuran (THF, 10 mL) which yielded the purple-colored product in 15% yield (5.45 g, 6.44 mmol). Analytics matched literature reports.

<sup>1</sup>H NMR (400 MHz, 300 K, CDCl<sub>3</sub>):  $\delta$  [ppm] = 8.82 (s, 8H,  $\beta$ -pyrrole), 8.45 (d, <sup>3</sup>J = 8.1 Hz, 8H, phenyl), 8.38 (d, <sup>3</sup>J = 8.2 Hz, 8H, phenyl), 4.12 (s, 12H, COOMe), -2.81 (s, 2H, NH).

ATR-IR:  $\tilde{\nu}$  [cm<sup>-1</sup>] = 3316 (br), 2946 (m), 2529 (s), 2217 (br), 1933 (w), 1720 (vs), 1605 (s), 1554 (w), 1434 (s), 1401 (m), 1271 (vs), 1188 (s), 1177 (s), 1100 (vs), 1019 (s), 982 (w), 961 (s), 864 (m), 804 (s), 760 (s), 737 (s), 704 (s).

UV-Vis (THF,  $\lambda_{\max}$ ): [nm] 418 (Soret band), 513 (Q band), 548 (Q band), 591 (Q band), 648 (Q band).

Anal. calcd. (%) for TPPCOOMe: C, 73.75; H, 4.52; N, 6.62. Found (%): C, 72.80; H, 4.66; N, 6.30.

For saponification, TPPCOOMe (1.00 g, 1.19 mmol, 1.0 equiv.) was dissolved in a mixture of THF/MeOH (1:1, 70 mL) to which a solution of KOH (3.5 g, 62.4 mmol, 52 equiv.) in H<sub>2</sub>O (30 mL) was added. After refluxing for 15 h, the organic solvents were removed in vacuo. Subsequently, the solid was dissolved in H<sub>2</sub>O (150 mL) and heated at 90 °C for 15 min. After filtration the solution was acidified with 1 M HCl (100 mL). Filtration of the resulting green precipitate and subsequent drying afforded the product (864 mg, 1.09 mmol, 92% yield). Analytics matched literature reports.

<sup>1</sup>H NMR (400 MHz, 300 K, DMSO-*d*<sub>6</sub>):  $\delta$  [ppm] = 13.29 (s, 4H, COOH), 8.87 (s, 8H,  $\beta$ -pyrrole), 8.40 (d, <sup>3</sup>J = 8.3 Hz, 8H, phenyl), 8.36 (d, <sup>3</sup>J = 8.4 Hz, 8H, phenyl), -2.94 (s, 2H, NH).

ATR-IR:  $\tilde{\nu}$  [cm<sup>-1</sup>] = 2983 (br), 2528 (br), 2161 (vw), 1978 (vw), 1689 (vs), 1604 (vs), 1565 (m), 1504 (m), 1402 (s), 1374 (m), 1310 (m), 1224 (vs), 1175 (s), 1100 (s), 1017 (m), 982 (w), 964 (s), 864 (m), 781 (s), 768 (s), 710 (s).

UV-Vis (THF,  $\lambda_{\max}$ ): [nm] 418 (Soret band), 513 (Q band), 548 (Q band), 591 (Q band), 648 (Q band).

Anal. calcd. (%) for **TCPPh<sub>2</sub>**: C, 72.91; H, 3.82; N, 7.09. Found (%): C, 67.85; H, 3.89; N, 6.37.  
Crystal water: 3 H<sub>2</sub>O.

### **5,10,15,20-tetrakis(4-carboxylphenyl)-porphyrinato-Rh(III) Chloride (Rh-TCPP)**

The synthesis was performed according to a literature known procedure.<sup>[134]</sup> TPPCOOMe (168.2 mg, 0.2 mmol, 1.0 equiv.) was refluxed with the precursor RhCl<sub>3</sub> · x H<sub>2</sub>O (104.2 mg, 0.8 mmol (calculated without xH<sub>2</sub>O, 4 equiv.)) in benzonitrile (5 mL) for 2 h. After cooling to room temperature and solvent removal under vacuo, the purple solid was purified by column chromatography over silica with EtOAc/DCM (1/1). Upon solvent removal the purple product Rh(TPPCOOMe)Cl was obtained (118 mg, 0.12 mmol, 60% yield).

<sup>1</sup>H NMR (400 MHz, 300 K, CDCl<sub>3</sub>): δ [ppm] = 8.88 (s, 8H, β-pyrrole), 8.41 (m, 16H, phenyl), 4.06 (s, 12H, COOMe).

UV-Vis (THF, λ<sub>max</sub>): [nm] 421 (Soret band), 532 (Q band), 566 (Q band).

Rh-TPPCOOMe (350 mg, 356 μmol, 1.0 equiv.) was dissolved in THF/MeOH 1:1 (40 mL) for saponification. Note that different batches of Rh-TPPCOOMe were combined to increase reactant amount. A solution of KOH (300 mg, 5.35 mmol, 15 equiv.) dissolved in H<sub>2</sub>O (20 mL) was added to the first solution. After refluxing for 13 h and subsequent cooling to room temperature, organic solvents were removed under vacuo and the solid was dissolved in H<sub>2</sub>O (35 mL). After heating at 90 °C for 10 min and filtration 1 M HCl solution (25 mL) was added to the aqueous solution. Centrifugation of the violet precipitate, washing with H<sub>2</sub>O (8 × 30 mL) and drying under vacuo yielded the violet product (295 mg, 318 μmol, 89% yield).

<sup>1</sup>H NMR (400 MHz, 300 K, DMSO-*d*<sub>6</sub>): δ [ppm] = 13.41 (s, 4H, COOH), 8.95 (m, 8H, β-pyrrole), 8.38 (m, 16H, phenyl), -2.93 (s, 0.33H, NH). Rh-metalation of 84%.

ATR-IR: 2971 (br), 1688 (s), 1604 (vs), 1569 (w), 1535 (w), 1501 (w), 1467 (br), 1399 (w), 1366 (w), 1353 (w), 1310 (w), 1267 (w), 1227 (w), 1172 (s), 1098 (s), 1011 (vs), 982 (w), 885 (w), 866 (m), 827 (m), 787 (w), 764 (s), 737 (w), 708 (s).

UV-Vis (EtOH, λ<sub>max</sub>): [nm] 418 (Soret band), 532 (Q band).

Anal. calcd. (%) for **Rh-TCPP**: C, 62.18; H, 3.04; N, 6.04. Found (%): C, 62.60; H, 3.84; N, 6.32.

**5,10,15,20-tetrakis(4-carboxyphenyl)porphyrin-Ru(II) [(Ru-TCPP(CO))]**

The synthesis was performed according to a literature known procedure.<sup>[137]</sup> To a solution of TPPCOOMe (100.0 mg, 0.12 mmol, 1.0 equiv.) in propionic acid (10 mL) triruthenium dodecacarbonyl (38.0 mg, 0.06 mmol, 0.5 equiv.) was added. The mixture was refluxed under argon for 72 h. After solvent removal, the crude product was purified by column chromatography (Silica, CHCl<sub>3</sub>, collecting a single red band) to remove excessive Ru precursor. Following, EtOH (25 mL) was added. The purple Ru-TPPCOOMe(CO) product was obtained by solvent removal and subsequent drying under vacuo in 99% yield (114.3 mg, 0.12 mmol).

<sup>1</sup>H NMR (400 MHz, 300 K, CDCl<sub>3</sub>):  $\delta$  [ppm] = 8.66 (s, 8H  $\beta$ -pyrrole, phenyl), 8.40 (t, <sup>3</sup>J = 7.6 Hz, 8H, phenyl), 8.26 (dd, <sup>4</sup>J = 20.6 Hz, <sup>3</sup>J = 8.1 Hz, 8H, phenyl), 4.08 (s, 12H, COOMe).

ATR-IR:  $\tilde{\nu}$  [cm<sup>-1</sup>] = 3422 (br), 2948 (m), 2544 (br), 2254 (br), 1938 (vs), 1719 (vs), 1700 (vs), 1605 (s), 1565 (vw), 1531 (m), 1433 (s), 1401 (m), 1350 (m), 1270 (vs), 1191 (m), 1178 (m), 1098 (vs), 1072 (s), 1041 (w), 1007 (vs), 967 (m), 889 (w), 865 (m), 821 (s), 793 (vs), 762 (vs), 711 (vs).

UV-Vis (THF,  $\lambda_{\max}$ ): [nm] 411 (Soret band), 529 (Q band), 563 (Q band).

Anal. calcd. (%) for **Ru-TCPPCOOMe**: C, 65.36; H, 3.73; N, 5.75. Found (%) C, 63.45; H, 3.84; N, 5.53.

For the synthesis of Ru-TCPP(CO), a solution of KOH (302.5 mg, 5.39 mmol, 53.9 equiv.) in H<sub>2</sub>O (3 mL) was added to Ru-TPPCOOMe(CO) (98.6 mg, 0.10 mmol, 1.0 equiv.) dissolved in THF/MeOH (1:1, 7 mL). After refluxing at 80°C overnight, organic solvents were evaporated and H<sub>2</sub>O (7 mL) was added. Heating at 80°C for 15 min afforded dissolution of the product. After filtration, Ru-TCPP(CO) was precipitated by adding 1 M HCl (30 mL). Centrifugation, washing with H<sub>2</sub>O (3  $\times$  35 mL) and drying under vacuo yielded the product as purple solid. (92.0 mg, 0.10 mmol, 99 %).

<sup>1</sup>H NMR (400 MHz, 300 K, DMSO-d<sub>6</sub>):  $\delta$  [ppm] = 13.23 (s, 4H, COOH), 8.57 (s, 8H,  $\beta$ -pyrrole), 8.34 (s, 12H, phenyl), 8.21 (d, <sup>3</sup>J = 5.7 Hz, 4H, phenyl).

ATR-IR:  $\tilde{\nu}$  [cm<sup>-1</sup>] = 3427 (br), 2990 (br), 2525 (br), 2239 (br), 1934 (vs), 1686 (s), 1603 (s), 1566 (m), 1529 (m), 1403 (m), 1348 (w), 1308 (w), 1234 (s), 1209 (m), 1174 (s), 1099 (s), 1077 (s), 1006 (vs), 885 (w), 865 (m), 826 (m), 788 (s), 765 (s), 713 (s), 664 (w).

UV-Vis (THF,  $\lambda_{\max}$ ): [nm] 411 (Soret band), 529 (Q band), 563 (Q band).

Anal. calcd. (%) for **Ru-TCPP(CO)**: C, 64.12; H, 3.08; N, 6.10. Found (%) C, 57.75; H, 3.22; N, 5.67.

**5,10,15,20-tetrakis(4-carboxyphenyl)porphyrinato-Mn(III) [Mn-TCPP]**

The synthesis was adapted from a literature known procedure.<sup>[14]</sup> A solution of TPPCOOMe (427 mg, 0.5 mmol, 1.0 equiv.) and manganese(II) chloride tetrahydrate (1.25 g, 6.40 mmol, 12.8 equiv.) in DMF (50 mL) was refluxed for 6 h. By water addition (75 mL), the crude product was precipitated and isolated by centrifugation. After washing with H<sub>2</sub>O (3 × 15 mL) and subsequent drying under vacuo dark green Mn-TPPCOOMe (115 mg, 0.123 mmol, 25 %) was obtained.

<sup>1</sup>H NMR (400 MHz, 300 K, CDCl<sub>3</sub>):  $\delta$  [ppm] = 8.82 (s, 8H,  $\beta$ -pyrrole), 8.45 (d,  $^3J$  = 8.0 Hz, 8H, phenyl), 8.30 (d,  $^3J$  = 8.0 Hz, 1H, phenyl), 4.12 (s, 12H, COOCH<sub>3</sub>).

ATR-IR:  $\tilde{\nu}$  [cm<sup>-1</sup>] = 2952 (w), 1722 (vs), 1608 (s), 1436 (s), 1404 (m), 1274 (vs), 1181 (m), 1104 (vs), 1012 (s), 967 (m), 867 (m), 823 (w), 801 (m), 765 (s), 710 (m).

UV-Vis (EtOH,  $\lambda_{\max}$ ): [nm] 466 (Soret band), 565 (Q band), 600 (Q band).

For saponification, a solution of KOH (317 mg, 5.66 mmol, 52.9 equiv.) in H<sub>2</sub>O (2 mL) was added to Mn-TPPCOOMe (100 mg, 0.11 mmol, 1.0 equiv.) suspended in THF/MeOH (1:1, 7 mL). After refluxing at 90°C for 15 h, the organic solvents were removed. Distilled water (15 mL) was added, and the mixture heated at 80°C for 15 min. Subsequently, the mixture was filtrated, and the solution acidified with 1 M HCl (10 mL). The precipitate was isolated via centrifugation and washed with H<sub>2</sub>O (7 × 10 mL). Drying the product under vacuo yielded dark green Mn-TCPP (80.5 mg, 0.09 mmol, 86 %).

<sup>1</sup>H NMR (400 MHz, 300 K, DMSO-d<sub>6</sub>):  $\delta$  [ppm] = 8.87 (s, 8H,  $\beta$ -pyrrole), 8.37 (q,  $^3J$  = 7.8 Hz, 16H, phenyl), -2.94 (s, 2H, NH).

ATR-IR:  $\tilde{\nu}$  [cm<sup>-1</sup>] = 2945 (br), 2519 (br), 1697 (vs), 1605 (m), 1387 (m), 1244 (s), 1177 (w), 1105 (m), 1012 (s), 867 (m), 766 (m), 716 (w).

UV-Vis (EtOH,  $\lambda_{\max}$ ): [nm] 414 (Soret band), 468 (Q band), 513 (Q band), 548 (Q band), 596 (Q band). The presence of 4 Q bands indicates incomplete metalation.

**5,10,15,20-tetrakis(4-carboxyphenyl)porphyrin-Co(II) [Co-TCPP]**

The synthesis was adapted from a literature known procedure.<sup>[100]</sup> A solution of TPPCOOMe (100.1 mg, 0.12 mmol, 1.0 equiv.) and cobalt(II) chloride hexahydrate (164.3 mg, 0.69 mmol, 5.8 equiv.) in DMF (10 mL) was refluxed for 16 h. By water addition (30 mL), the crude product was precipitated and isolated by centrifugation. After washing with H<sub>2</sub>O (3 × 35 mL) and subsequent drying under vacuo purple Co-TPPCOOMe (37.1 mg, 0.04 mmol, 34 %) was obtained.

<sup>1</sup>H NMR: paramagnetic compound, precise integration not possible.

ATR-IR:  $\tilde{\nu}$  [cm<sup>-1</sup>] = 3123 (br), 2950 (m), 2548 (br), 1719 (vs), 1607 (s), 1566 (w), 1548 (w), 1434 (s), 1401 (m), 1367 (w), 1351 (m), 1272 (vs), 1205 (w), 1177 (m), 1101 (vs), 1002 (vs), 964 (m), 889 (w), 865 (m), 820 (m), 795 (s), 763 (vs), 708 (vs), 658 (w).

UV-Vis (THF,  $\lambda_{\max}$ ): [nm] 422 (Soret band), 543 (Q band), 589 (Q band).

Anal. calcd. (%) for **Co-TCPPCOOMe**: C, 69.1; H, 4.01; N, 6.20. Found (%) C, 62.22; H, 4.31; N, 7.75.

For saponification, a solution of KOH (42.7 mg, 0.08 mmol, 20.0 equiv.) in H<sub>2</sub>O (2 mL) was added to Co-TPPCOOMe (32.1 mg, 0.04 mmol, 1.0 equiv.) suspended in THF/MeOH (1:1, 5 mL). After refluxing at 90°C for 6 h, the organic solvents were removed. Distilled water (5 mL) was added, and the mixture heated at 80°C for 15 min. Subsequently, the mixture was filtrated and the solution acidified with 1 M HCl (30 mL). The precipitate was isolated via centrifugation and washed with H<sub>2</sub>O (3 × 35 mL). Drying the product under vacuo yielded purple Co-TCPP (22.3 mg, 0.03 mmol, 75 %).

<sup>1</sup>H NMR: paramagnetic compound, precise integration not possible.

ATR-IR:  $\tilde{\nu}$  [cm<sup>-1</sup>] = 3123 (br), 2927 (br), 2512 (br), 1690 (s), 1604 (vs), 1567 (w), 1434 (s), 1401 (m), 1348 (m), 1308 (w), 1232 (s), 1206 (s), 1173 (m), 1100 (s), 1001 (vs), 964 (m), 887 (w), 864 (m), 827 (s), 763 (vs), 708 (s), 672 (w).

UV-Vis (THF,  $\lambda_{\max}$ ): [nm] 425 (Soret band), 544 (Q band), 589 (Q band).

**5,10,15,20-tetrakis(4-carboxyphenyl)porphyrin-Zn(II) [Zn-TCPP]**

The synthesis was adapted from a literature known procedure.<sup>[14]</sup> A solution of TPPCOOMe (502.4 mg, 0.59 mmol, 1.0 equiv.) and zinc(II) acetate (Zn(OAc)<sub>2</sub>, 746.3 mg, 4.07 mmol, 6.9 equiv.) in DMF (25 mL) was refluxed for 19 h. Afterwards, the solvent was evaporated under vacuo and the crude product purified by Soxhlet extraction in CHCl<sub>3</sub>. Solvent removal and drying under vacuo yielded dark purple Zn-TPPCOOMe (791.3 mg, 0.81 mmol, 137%). The excessive yield results from additional zinc species.

<sup>1</sup>H NMR (400 MHz, 300 K, CDCl<sub>3</sub>):  $\delta$  [ppm] = 8.92 (s, 8H,  $\beta$ -pyrrole), 8.45 (d, <sup>3</sup>J = 8.4 Hz, 8H, phenyl), 8.30 (d, <sup>3</sup>J = 6.2 Hz, 8H, phenyl), 4.12 (s, 12H, COOMe).

ATR-IR:  $\tilde{\nu}$  [cm<sup>-1</sup>] = 3118 (br), 2945 (m), 2567 (br), 1717 (s), 1660 (s), 1604 (m), 1539 (s), 1435(s), 1408 (m), 1385 (s), 1309 (w), 1275 (vs), 1205 (m), 1155 (w), 1105 (s), 1049 (w), 1021 (w), 996 (s), 867 (m), 820 (m), 793 (m), 745 (w), 694 (vs), 661 (w).

UV-Vis (THF,  $\lambda_{\max}$ ): [nm] 426 (Soret band), 557 (Q band), 597 (Q band).

Anal. calcd. (%) for **Zn-TCPPCOOMe**: C, 68.61; H, 3.99; N, 6.16. Found (%) C, 45.26; H, 3.46; N, 3.90.

For saponification, solution of KOH (241.7 mg, 4.31 mmol, 21.8 equiv.) in H<sub>2</sub>O (3 mL) (180.3 mg, 0.20 mmol, 1.0 equiv.) was added to Zn-TPPCOOMe suspended THF/MeOH (1:1, 7 mL). The resulting suspension was refluxed at 80°C overnight. After removal of the organic solvents distilled water (7 mL) was added. The mixture was heated at 80°C for 15 min and filtered subsequently. Precipitation of the crude product was achieved by addition of 1 M HCl (30 mL). The solid product was isolated by centrifugation and washed with H<sub>2</sub>O (3 × 35 mL). Drying under vacuo yielded dark purple Zn-TCPP (85.9 mg, 0.10 mmol, 51 %).

<sup>1</sup>H NMR (400 MHz, 300 K, DMSO-d<sub>6</sub>):  $\delta$  [ppm] = 13.27 (s, 4H, COOH), 8.87 (s, 7H  $\beta$ -pyrrole), 8.79 (s, 1H  $\beta$ -pyrrole) 8.38 (d, <sup>3</sup>J = 8.9 Hz, 16H, phenyl, phenyl), -2.93 (s, 2H, NH).

ATR-IR:  $\tilde{\nu}$  [cm<sup>-1</sup>] = 2972 (br), 2523 (br), 1687 (s), 1604 (s), 1562 (w), 1501 (w), 1483 (m), 1378 (m), 1310 (w), 1275 (vs), 1227 (s), 1176 (m), 1101 (s), 1014 (w), 986 (m), 993 (w), 866 (m), 827 (w), 767 (m), 710 (m), 671 (w).

UV-Vis (THF,  $\lambda_{\max}$ ): [nm] 422 (Soret band), 513 (Q band), 553 (Q band), 595 (Q band), 645 (Q band).

Anal. calcd. (%) for **Zn-TCPP**: C, 67.50; H, 3.30; N, 6.56. Found [%] C, 60.00; H, 3.60; N, 6.48.

**5,10,15,20-tetrakis(4-carboxyphenyl)porphyrin-Ni(II) [Ni-TCPP]**

The synthesis was adapted from a literature known procedure.<sup>[100]</sup> A solution of TPPCOOMe (500 mg, 0.59 mmol, 1.0 equiv.) and nickel(II) acetyl acetonate (1.50 g, 5.9 mmol, 10 equiv.) in toluene (50 mL) was refluxed for 6 h. By water addition (50 mL), the crude product was precipitated. The precipitate was removed by filtration. The aqueous phase and organic phase of the filtrate were separated. The solvent of the organic phase was removed under vacuo. Washing with H<sub>2</sub>O (3 × 40 mL) and drying under vacuo yielded violet Ni-TPPCOOMe (235.6 mg, 0.26 mmol, 44%).

<sup>1</sup>H NMR (400 MHz, CDCl<sub>3</sub>):  $\delta$  [ppm] = 15.46 (s, 3H, COOH), 8.71 (s, 8H,  $\beta$ -pyrrole), 8.37 (d, <sup>3</sup>J = 7.8 Hz, 8H, phenyl), 8.09 (d, <sup>3</sup>J = 7.9 Hz, 8H, phenyl), 4.08 (s, 12H, COOMe). Broad shoulder at -2.74 ppm.

UV-Vis (THF,  $\lambda_{\max}$ ): [nm] = 413 (Soret band), 527 (Q band), a second Q band could not be identified due to the low intensity (very broad peak).

For saponification, a solution of KOH (82 mg, 1.46 mmol, 11.2 equiv.) in H<sub>2</sub>O (3.6 mL) was added to Ni-TPPCOOMe (120.3 mg, 0.13 mmol, 1.0 equiv.) suspended in THF/MeOH (1:1, 8.2 mL). After refluxing for at 90°C for 9 h, organic solvents were evaporated and distilled water (8 mL) was added. The suspension was heated at 80°C for 15 min. Upon addition of 1 M HCl (10 mL) the product was precipitated and subsequently isolated by centrifugation. After washing with H<sub>2</sub>O (3 × 35 mL) and drying under vacuo, purple yielded Ni-TCPP (64.2 mg, 0.08 mmol, 58 %).

<sup>1</sup>H NMR (400 MHz, DMSO-d<sub>6</sub>):  $\delta$  [ppm] = 13.31 (s, 3H, COOH), 8.79 (s, 8H,  $\beta$ -pyrrole), 8.33 (d, <sup>3</sup>J = 7.9 Hz, 8H, phenyl), 8.17 (d, <sup>3</sup>J = 7.8 Hz, 8H, phenyl). Note that a residual signal at 4.02 is present (s, 0.57H, COOMe).

UV-Vis (THF,  $\lambda_{\max}$ ): [nm] = 411 (Soret band), 527 (Q band), a second Q band could not be identified due to the low intensity (very broad peak).

**5,10,15,20-tetrakis(4-carboxyphenyl)porphyrin-Cu(II) [Cu-TCPP]**

The synthesis was adapted from a literature known procedure.<sup>[14]</sup> A solution of TPPCOOMe (500 mg, 0.59 mmol, 1.0 equiv.) and copper(II) acetate hydrate (1.18 g, 5.9 mmol, 10 equiv.) in CHCl<sub>3</sub> (80 mL) was refluxed for 5 h. Afterwards, the crude solid was filtered off and the solvent of the filtrate is evaporated. After solvent removal, the solid was washed with H<sub>2</sub>O (3 × 40 mL) and dried under vacuo to yield purple Cu-TPPCOOMe (462.4 mg, 0.51 mmol, 86%).



$^1\text{H}$  NMR: paramagnetic contribution, precise integration not possible.

UV-Vis (THF,  $\lambda_{\text{max}}$ ): [nm] = 417 (Soret band), 540 (Q band), a second Q band could not be identified due to the low intensity (very broad peak).

For saponification, a solution of KOH (123.5 mg, 2.20 mmol, 10.0 equiv.) in  $\text{H}_2\text{O}$  (6 mL) was added to Cu-TPPCOOMe (200 mg, 0.22 mmol, 1.0 equiv.) suspended in THF/MeOH (1:1, 14 mL). After refluxing for 6 h at  $90^\circ\text{C}$ , the organic solvents were evaporated. Distilled water (15 mL) was added, and the suspension was heated at  $80^\circ\text{C}$  for 15 min. By addition of 1 M HCl (13 mL) the product was precipitated. Isolation by centrifugation, washing with  $\text{H}_2\text{O}$  ( $3 \times 35$  mL) and drying yielded dark purple Cu-TCPP (106.8 mg, 0.12 mmol, 56 %).

$^1\text{H}$  NMR: paramagnetic contribution, precise integration not possible.

UV-Vis (THF,  $\lambda_{\text{max}}$ ): [nm] 417 (Soret band), 542 (Q band), a second Q band could not be identified due to the low intensity (very broad peak).

### **5,10,15,20-tetrakis(4-carboxyphenyl)porphyrin-Mg(II) [Mg-TCPP]**

The synthesis was adapted from a literature known procedure.<sup>[214]</sup> A solution of TPPCOOMe (500 mg, 0.59 mmol, 1.0 equiv.), triethylamine (2.7 mL, 1.96 g, 19.3 mmol, 32 equiv.) and magnesium (II) bromide (0.65 g, 3.5 mmol, 6 equiv.) in DCM (50 mL) was stirred at room temperature for 19 h. Afterwards,  $\text{H}_2\text{O}$  (50 mL) was added. The crude solid is filtered off and the solvent of the filtrate is evaporated. After solvent removal, the solid was washed with  $\text{H}_2\text{O}$  ( $3 \times 35$  mL) and dried under vacuo to yield dark green Mg-TPPCOOMe (177 mg, 0.20 mmol, 35%).

$^1\text{H}$  NMR (400 MHz,  $\text{CDCl}_2$ ):  $\delta$  [ppm] = 8.84 (s, 8H,  $\beta$ -pyrrole), 8.47 (d,  $^3J = 8.1$  Hz, 8H, phenyl), 8.32 (d,  $^3J = 7.9$  Hz, 8H, phenyl), 4.14 (s, 12H, COOMe), -2.79 (s, 2H, NH). Note that the integration of the peak at -2.79 ppm is challenging due to the low signal-to-noise ratio but indicates insufficient metalation.

UV-Vis (THF,  $\lambda_{\text{max}}$ ): [nm] 432 (Soret band), 573 (Q band), 617 (Q band).

For saponification, a solution of KOH (58 mg, 1.03 mmol, 10.0 equiv.) in H<sub>2</sub>O (2.7 mL) was added to Mg-TPPCOOMe (90.0 mg, 0.10 mmol, 1.0 equiv.) suspended in THF/MeOH (1:1, 6.4 mL). After refluxing for 16 h, the organic solvents were evaporated. Distilled water (7 mL) was added, and the suspension was heated at 80°C for 15 min. By addition of 1 M HCl (9 mL) the product was precipitated. Isolation by centrifugation, washing with H<sub>2</sub>O (3 × 35 mL) and drying yielded dark purple Mg-TCPP (81.6 mg, 0.10 mmol, 100 %).

<sup>1</sup>H NMR (400 MHz, DMSO-d<sub>6</sub>): δ [ppm] = 13.34 (s, 4H, COOH), 8.88 (s, 8H β -pyrrole), 8.39 (q, <sup>3</sup>J = 7.9 Hz, 16H, phenyl, phenyl), -2.93 (s, 2H, NH). Note that the peak at -2.79 ppm indicates insufficient metalation.

UV-Vis (THF, λ<sub>max</sub>): [nm] 417 (Soret band), 513 (Q band), 550 (Q band), 592 (Q band), 648 (Q band).

Note that UV-vis and <sup>1</sup>H NMR spectroscopy suggested the absence of Mg in the porphyrin.

### **5,10,15,20-tetrakis(4-carboxyphenyl)porphyrinato-Fe(III) Chloride [Fe-TCPP]**

The synthesis was adapted from a literature known procedure.<sup>[14]</sup> A solution of TPPCOOMe (890 mg, 1.05 mmol, 1.0 equiv.) and FeCl<sub>2</sub> · 4H<sub>2</sub>O (2.54 g, 12.8 mmol, 13 equiv.) in DMF (100 mL) was refluxed overnight. By water addition (150 mL), the crude product was precipitated and isolated by centrifugation. After washing with H<sub>2</sub>O (2 × 50 mL) and subsequent drying under vacuo, the solid was purified by Soxhlet extraction with CHCl<sub>3</sub> (for 36 h). Following, extraction of the dark solution with 1 M HCl (2 × 50 mL) and with H<sub>2</sub>O (3 × 50 mL) was performed. The organic phase was dried over sodium sulfate. The organic solvent was evaporated and the solid dried under vacuo yielding brown Fe-TPPCOOMe (0.76 g, 0.81 mmol, 78 %).

<sup>1</sup>H NMR: paramagnetic compound, precise integration not possible.

UV-Vis (EtOH, λ<sub>max</sub>): [nm] 416 (Soret band), 582 (Q band, very broad).

For saponification, a solution of KOH (320 mg, 5.70 mmol, 4.8 equiv.) in H<sub>2</sub>O (2.7 mL) was added to Fe-TPPCOOMe (100 mg, 0.11 mmol, 1.0 equiv.) suspended in THF/MeOH (1:1, 6.4 mL). After refluxing for 15 h, the organic solvents were evaporated. Distilled water (14 mL) was added, and the suspension was heated at 80°C for 15 min. By addition of 1 M HCl (9 mL) the product was precipitated. Isolation by centrifugation, washing with H<sub>2</sub>O (5 × 35 mL) and drying yielded Fe-TCPP (67.0 mg, 0.07 mmol, 63 %).

$^1\text{H}$  NMR: paramagnetic compound, precise integration not possible.

UV-Vis (EtOH,  $\lambda_{\text{max}}$ ): [nm] 414 (Soret band), 573 (Q band), 644 (Q-band, shoulder).

### 5.3.2. MOF Syntheses

#### PCN-222

The synthesis was adapted from literature.<sup>[32,82]</sup> In a 20 mL screw cap vial, TCPPH<sub>2</sub> (12.5 mg, 0.016 mmol, 1.00 equiv.) and ZrOCl<sub>2</sub> · 8 H<sub>2</sub>O (23.5 mg, 0.073 mmol, 4.56 equiv.) were dissolved in N,N-diethylformamide (DEF, 3 mL). Afterwards, the modulator 4-*tert*-butylbenzoic acid (1350 mg, 7.57 mmol, 473 equiv.) was added. The mixture was ultrasonicated for 10 min. For yield enhancement, seeds of PCN-222 were added. The suspension was heated in an oven at 120 °C for 12 h. Product isolation was performed by centrifugation, followed by soaking the solid in DMF (3 × 6 mL) and drying under vacuo.

The resulting solid (12.2 mg) was dispersed in DMF (8.1 mL) and 8 M HCl (0.3 mL) was added. The green suspension was again heated in an oven at 120 °C for 12 h. Centrifugation of the solid, soaking in DMF (3 × 6 mL) and acetone (3 × 6 mL) and subsequent drying under vacuo yielded the purple product. For dehydration (=activation) the product is heated at 120 °C under dynamic vacuum (10<sup>-3</sup> mbar) overnight. Analytics are in accordance to literature reports.

#### PCN-224

The synthesis was adapted from a literature known procedure.<sup>[32,82]</sup> In a 20 mL screw cap vial, TCPPH<sub>2</sub> (16.0 mg, 0.020 mmol, 1.00 equiv.) and ZrOCl<sub>2</sub> · 8 H<sub>2</sub>O (30.0 mg, 0.093 mmol, 4.65 equiv.) were dissolved in N,N-dimethylformamide (DMF, 4 mL). Afterwards, the modulators formic acid (0.69 mL, 17.2 mmol, 860 equiv.) and 3,3-dimethylbutanoic acid (0.81 mL, 6.36 mmol, 318 equiv.) were added. The mixture was ultrasonicated for 10 min. For yield enhancement, seeds of PCN-224 were added. The suspension was heated in an oven at 120 °C for 12 h. Product isolation was performed by centrifugation, followed by soaking the solid in DMF (3 × 6 mL) and drying under vacuo.

The solid (31.1mg) was dispersed in DMF (21 mL) and 8 M HCl (1.6 mL) was added. The green suspension was again heated in an oven at 120 °C for 12 h. Centrifugation of the solid, soaking in DMF (3 × 6 mL) and acetone (3 × 6 mL) and subsequent drying under vacuo yielded the purple product. For dehydration (=activation) the product is heated at 120 °C under dynamic vacuum (10<sup>-3</sup> mbar) overnight. Analytics are in accordance to literature reports.

**MOF-525**

The synthesis was adapted from a literature known procedure.<sup>[129]</sup> In a 100 mL laboratory bottle (Schott®),  $\text{ZrOCl}_2 \cdot 8 \text{H}_2\text{O}$  (125 mg, 0.39 mmol, 11.8 equiv.) was suspended in DMF (60 mL). The suspension was ultrasonicated for 30 min.  $\text{TCPPh}_2$  (26 mg, 0.033 mmol, 1.0 equiv.) was added to the solution, followed by ultrasonication for 10 min. Acetic acid (10 mL) was added. The resulting solution was heated in an oven at 80 °C for three days. The solid was isolated by centrifugation, soaked with DMF (3 × 40 mL) and acetone (3 × 40 mL). Drying under vacuo and activation at 120 °C under dynamic vacuum ( $10^{-3}$  mbar) for 16 h yielded the product. Analytics are in accordance to literature reports.

**NU-1000**

The synthesis was adapted from a literature known procedure. In a 100 mL laboratory bottle (Schott®), 389 mg  $\text{ZrOCl}_2 \cdot 8 \text{H}_2\text{O}$  (1.21 mmol) and 17.6 g biphenyl-4-carboxylic acid (88.7 mmol) were suspended in DMF (32 mL). The suspension was heated in an oven at 80 °C for 1 h. The linker  $\text{H}_4\text{TBAPy}$  (1,3,6,8-tetrakis(p-benzoic acid)pyrene; 50.0 mg, 0.073 mmol) was dissolved with 11.6 mg NaOH (0.290 mmol) in DMF (3 mL) and ultrasonicated for 10 min. The linker solution was heated in an aluminum block at 100 °C. To the hot solution, 10 mL of the hot Zr containing solution were added. The mixture was heated at 100 °C for 24 h. Product isolation was achieved by centrifugation and washing with DMF (3 × 25 mL). For modulator removal, the solid was suspended in DMF (12 mL) and HCl (37%, 0.5 mL) and heated at 100 °C for 24 h. The solid was separated by centrifugation, washed with DMF (3 × 25 mL) and acetone (3 × 25 mL) and dried to yield yellow NU-1000 which was activated under dynamic vacuum ( $10^{-3}$  mbar) at 120 °C for 12 h.

### 5.3.3. Porphyrin MOF Metalation

In the following, different approaches (direct metalloporphyrin incorporation = pre-metalation, post-synthetic metalation) are described. Note that the yield of PCN-222(M) and PCN-224(M), respectively, was always ~10 mg.

#### PCN-222(Rh) – pre-metalation

The synthesis was adapted from literature.<sup>[82]</sup> In a 20 mL screw cap vial, Rh-TCPP (15.4 mg) and  $\text{ZrOCl}_2 \cdot 8 \text{H}_2\text{O}$  (23.5 mg) were dissolved in DEF (3 mL). Afterwards, the modulator 4-*tert*-butylbenzoic acid (1350 mg) was added. The mixture was ultrasonicated for 10 min. For yield enhancement, seeds of PCN-222 were added. The suspension was heated in an oven at 120 °C for 12 h. Centrifugation of the solid, soaking in DMF (3 × 6 mL) and acetone (3 × 6 mL) and subsequent drying under vacuo yielded the purple product. For dehydration (=activation) the product is heated at 120 °C under dynamic vacuum ( $10^{-3}$  mbar) overnight.

#### PCN-222(Rh) – Reflux

A suspension of PCN-222 (27 mg) and  $\text{RhCl}_3 \cdot x\text{H}_2\text{O}$  (14.6 mg, 2.5 equiv.) in DMF (5 mL) was refluxed for 15 h while stirring (300 rpm). The product was isolated by centrifugation and soaked in DMF (3 × 8 mL) and acetone (3 × 8 mL). Drying under vacuo yielded the dark green product.

#### PCN-222(Rh) – Microwave

A suspension of PCN-222 (30.0 mg for  $\text{RhCl}_3 \cdot x\text{H}_2\text{O}$ ; 15 mg for  $\text{Rh}_2(\text{OAc})_4$ ) and the Rh precursor ( $\text{RhCl}_3 \cdot x\text{H}_2\text{O}$ : 32 mg, 5 equiv.,  $\text{Rh}_2(\text{OAc})_4$ : 15 mg, 5 equiv.) in DMF (10 and 5 mL, respectively) was placed in a microwave tube and heated under following conditions: 135 °C, open vessel, 85 W, 10 min,  $P_{\text{max}}$  on, stirring mode high). The product was isolated by centrifugation and soaked in DMF (3 × 10 mL) and acetone (3 × 10 mL). Drying under vacuo yielded the dark green product.

For synthesis optimization, metal equivalents and reaction time were adjusted.

**PCN-222(Rh) – Oven**

A suspension of PCN-222 (10.0 mg) and  $\text{RhCl}_3 \cdot x\text{H}_2\text{O}$  (19.5 mg, 9 equiv.) in DMF (4 mL) was heated in an oven at 120 °C for 12 h. The product was isolated by centrifugation and soaked in DMF (3 × 6 mL) and acetone (3 × 6 mL). Drying under vacuo yielded the dark green product.

**PCN-222(Rh), PCN-224(Rh) and MOF-525(Rh) – Aluminum heating block**

A suspension of  $\text{RhCl}_3 \cdot x\text{H}_2\text{O}$  (38.4 mg for PCN-222 and 30.6 mg for PCN-224 and 41.5 mg for MOF-525) and the MOF powder (20 mg) in DMF (4 mL) was heated in an aluminum block at 120 °C for 24 h under stirring (300 rpm). The product was obtained by centrifugation, soaking in DMF (3 × 6 mL) and acetone (3 × 6 mL) and subsequent drying under vacuo. Various batches were combined after synthesis to allow the performance of all catalytic experiments and characterizations with the material. The product was activated 120 °C under dynamic vacuum ( $10^{-3}$  mbar) overnight.

**PCN-222(Ru) – pre metalation**

The synthesis was adapted from literature.<sup>[82]</sup> In a 20 mL screw cap vial, Ru-TCPP(CO) (13.8 mg) and  $\text{ZrOCl}_2 \cdot 8 \text{H}_2\text{O}$  (23.5 mg) were dissolved in DEF (3 mL). Afterwards, the modulator 4-*tert*-butylbenzoic acid (1350 mg) was added. The mixture was ultrasonicated for 10 min. For yield enhancement, seeds of PCN-222 were added. The suspension was heated in an oven at 120 °C for 12 h. Centrifugation of the solid, soaking in DMF (3 × 6 mL) and acetone (3 × 6 mL) and subsequent drying under vacuo yielded the red product. For dehydration (=activation) the product is heated at 120 °C under dynamic vacuum ( $10^{-3}$  mbar) overnight.

**PCN-222(Ru) – different Ru loading**

The synthesis was adapted from literature.<sup>[82]</sup> In a 20 mL screw cap vial, Ru-TCPP(CO) (6.9 mg, 0.008 mmol, 0.5 equiv.), TCPPH<sub>2</sub> (6.9 mg, 0.009 mmol, 0.5 equiv.) and  $\text{ZrOCl}_2 \cdot 8 \text{H}_2\text{O}$  (23.5 mg, 0.073 mmol, 4.56 equiv.) were dissolved in DEF (3 mL). Afterwards, the modulator 4-*tert*-butylbenzoic acid (1350 mg, 7.57 mmol, 473 equiv.) was added. The mixture was ultrasonicated for 10 min. For yield enhancement, seeds of PCN-222 were added. The suspension was heated in an oven at 120 °C for 12 h. Centrifugation of the solid, soaking in DMF (3 × 6 mL) and acetone (3 × 6 mL) and subsequent drying under vacuo yielded the violet product. For dehydration (=activation) the product is heated at 120 °C under dynamic vacuum ( $10^{-3}$  mbar) overnight. For PCN-222(Ru) with 1.2 wt% the linker equivalents were adjusted accordingly (0.15 equiv. Ru-TCPP(CO), 0.85 equiv. TCPPH<sub>2</sub>).

**PCN-222(Ru) – Reflux**

A suspension of PCN-222 (15.2 mg) and  $\text{Ru}_3(\text{CO})_{12}$  (15.2 mg) in DMF (5 mL) was refluxed under argon atmosphere. The product was isolated by centrifugation, soaked in DMF (3 × 6 mL) and acetone (3 × 6 mL) and dried under vacuo yielding a brown solid.

**PCN-222(Mn) – pre-metalation**

The synthesis was adapted from literature.<sup>[82]</sup> In a 20 mL screw cap vial, Mn-TCPP (13.9 mg) and  $\text{ZrOCl}_2 \cdot 8 \text{H}_2\text{O}$  (23.5 mg) were dissolved in DEF (3 mL). Afterwards, the modulator 4-*tert*-butylbenzoic acid (1350 mg) was added. The mixture was ultrasonicated for 10 min. For yield enhancement, seeds of PCN-222 were added. The suspension was heated in an oven at 120 °C for 12 h. Centrifugation of the solid, soaking in DMF (3 × 6 mL) and acetone (3 × 6 mL) and subsequent drying under vacuo yielded the dark green product. For dehydration (=activation) the product is heated at 120 °C under dynamic vacuum ( $10^{-3}$  mbar) overnight.

**PCN-224(Mn) – pre-metalation**

The synthesis was adapted from literature.<sup>[82]</sup> In a 20 mL screw cap vial, Mn-TCPP (17.8 mg) and  $\text{ZrOCl}_2 \cdot 8 \text{H}_2\text{O}$  (30.0 mg) were dissolved in DMF (4 mL). Afterwards, the modulators formic acid (0.69 mL) and 3,3-dimethylbutanoic acid (0.81 mL) were added. The mixture was ultrasonicated for 10 min. For yield enhancement, seeds of PCN-224 were added. The suspension was heated in an oven at 120 °C for 12 h. Centrifugation of the solid, soaking in DMF (3 × 6 mL) and acetone (3 × 6 mL) and subsequent drying under vacuo yielded the dark green product. For dehydration (=activation) the product is heated at 120 °C under dynamic vacuum ( $10^{-3}$  mbar) overnight.

**PCN-222(Mn) – Microwave**

A suspension of PCN-222 (15.0 mg) and  $\text{MnCl}_2 \cdot 4 \text{H}_2\text{O}$  (24.1 mg, 10 equiv.) in DMF (5 mL) was placed in a microwave tube and heated under following conditions: 135 °C, open vessel, 85 W, 10 min,  $P_{\text{max}}$  on, stirring mode high). The product was isolated by centrifugation and soaked in DMF (3 × 10 mL) and acetone (3 × 10 mL). Drying under vacuo yielded the dark green product.

Metalation of PCN-222, which was treated with HCl prior to metalation, was performed under analog condition.

**PCN-224(Mn) – Microwave**

A suspension of PCN-224 (15.0 mg) and  $\text{MnCl}_2 \cdot 4 \text{H}_2\text{O}$  (21.6 mg, 9 equiv.) in DMF (5 mL) was placed in a microwave tube and heated under following conditions: 135 °C, open vessel, 85 W, 10 min,  $P_{\text{max}}$  on, stirring mode high). The product was isolated by centrifugation and soaked in DMF ( $3 \times 10 \text{ mL}$ ) and acetone ( $3 \times 10 \text{ mL}$ ). Drying under vacuo yielded the dark green product.

Metalation of PCN-224, which was treated with HCl prior to metalation, was performed under analog condition.

**PCN-222(Mn) – Aluminum heating block**

A suspension of PCN-222 (30 mg) and  $\text{MnCl}_2 \cdot 4 \text{H}_2\text{O}$  (48.2 mg, 10 equiv.) in DMF (3 mL) was placed in a 20 mL screw cap vial and was heated at 120 °C for 24 h in an aluminum block (stirring 350 rpm). The product was isolated by centrifugation and soaked in DMF ( $3 \times 10 \text{ mL}$ ) and acetone ( $3 \times 10 \text{ mL}$ ). Drying under vacuo yielded the dark green product.

**PCN-224(Mn) – Aluminum heating block**

A suspension of PCN-224 (30 mg) and  $\text{MnCl}_2 \cdot 4 \text{H}_2\text{O}$  (43.2 mg, 9 equiv.) in DMF (3 mL) was placed in a 20 mL screw cap vial and was heated at 120 °C for 24 h in an aluminum block (stirring 350 rpm). The product was isolated by centrifugation and soaked in DMF ( $3 \times 10 \text{ mL}$ ) and acetone ( $3 \times 10 \text{ mL}$ ). Drying under vacuo yielded the dark green product.

**PCN-222(Co) – pre-metalation**

The synthesis was adapted from literature.<sup>[82]</sup> In a 20 mL screw cap vial, Co-TCPP (13.4 mg) and  $\text{ZrOCl}_2 \cdot 8 \text{H}_2\text{O}$  (23.5 mg) were dissolved in DEF (3 mL). Afterwards, the modulator 4-*tert*-butylbenzoic acid (1350 mg) was added. The mixture was ultrasonicated for 10 min. For yield enhancement, seeds of PCN-222 were added. The suspension was heated in an oven at 120 °C for 12 h. Centrifugation of the solid, soaking in DMF ( $3 \times 6 \text{ mL}$ ) and acetone ( $3 \times 6 \text{ mL}$ ) and subsequent drying under vacuo yielded the purple product. For dehydration (=activation) the product is heated at 120 °C under dynamic vacuum ( $10^{-3} \text{ mbar}$ ) overnight.



**PCN-224(Co) – pre-metalation**

The synthesis was adapted from literature.<sup>[82]</sup> In a 20 mL screw cap vial, Co-TCPP (17.1 mg) and  $\text{ZrOCl}_2 \cdot 8 \text{H}_2\text{O}$  (30.0 mg) were dissolved in DMF (4 mL). Afterwards, the modulators formic acid (0.69 mL) and 3,3-dimethylbutanoic acid (0.81 mL) were added. The mixture was ultrasonicated for 10 min. For yield enhancement, seeds of PCN-224 were added. The suspension was heated in an oven at 120 °C for 12 h. Centrifugation of the solid, soaking in DMF (3 × 6 mL) and acetone (3 × 6 mL) and subsequent drying under vacuo yielded the purple product. For dehydration (=activation) the product is heated at 120 °C under dynamic vacuum ( $10^{-3}$  mbar) overnight.

**PCN-222(Co) – Microwave**

A suspension of PCN-222 (15.0 mg) and  $\text{CoCl}_2 \cdot 6 \text{H}_2\text{O}$  (29.0 mg, 10 equiv.) in DMF (5 mL) was placed in a microwave tube and heated under following conditions: 135 °C, open vessel, 85 W, 10 min,  $P_{\text{max}}$  on, stirring mode high). The product was isolated by centrifugation and soaked in DMF (3 × 10 mL) and acetone (3 × 10 mL). Drying under vacuo yielded the dark green product.

Metalation of PCN-222, which was treated with HCl prior to metalation, was performed under analog condition.

**PCN-224(Co) – Microwave**

A suspension of PCN-224 (15.0 mg) and  $\text{CoCl}_2 \cdot 6 \text{H}_2\text{O}$  (26.0 mg, 9 equiv.) in DMF (5 mL) was placed in a microwave tube and heated under following conditions: 135 °C, open vessel, 85 W, 10 min,  $P_{\text{max}}$  on, stirring mode high). The product was isolated by centrifugation and soaked in DMF (3 × 10 mL) and acetone (3 × 10 mL). Drying under vacuo yielded the dark green product.

Metalation of PCN-224, which was treated with HCl prior to metalation, was performed under analog condition.

**PCN-222(Co) – Oven**

A suspension of PCN-222 (10.0 mg) and  $\text{CoCl}_2 \cdot 6 \text{H}_2\text{O}$  (9.8 mg, 5 equiv.) in DMF (3 mL) was heated in an oven at 100 °C for 24 h. The product was isolated by centrifugation and soaked in DMF (3 × 6 mL) and acetone (3 × 6 mL). Drying under vacuo yielded the dark green product.

**PCN-222(Co) – Aluminum heating block**

A suspension of PCN-222 (30 mg) and  $\text{CoCl}_2 \cdot 6 \text{H}_2\text{O}$  (57.9 mg, 244  $\mu\text{mol}$ , 12 equiv.) in DMF (3 mL) was placed in a 20 mL screw cap vial and was heated at 120 °C for 24 h in an aluminum block (stirring 350 rpm). The product was isolated by centrifugation and soaked in DMF (3  $\times$  10 mL) and acetone (3  $\times$  10 mL). Drying under vacuo yielded the purple product.

**PCN-224(Co) – Aluminum heating block**

A suspension of PCN-224 (30 mg) and  $\text{CoCl}_2 \cdot 6 \text{H}_2\text{O}$  (51.2 mg, 228  $\mu\text{mol}$ , 10 equiv.) in DMF (3 mL) was placed in a 20 mL screw cap vial and was heated at 120 °C for 24 h in an aluminum block (stirring 350 rpm). The product was isolated by centrifugation and soaked in DMF (3  $\times$  10 mL) and acetone (3  $\times$  10 mL). Drying under vacuo yielded the purple product.

**PCN-222(Zn) – pre-metalation**

The synthesis was adapted from literature.<sup>[82]</sup> In a 20 mL screw cap vial, Zn-TCPP (13.8 mg) and  $\text{ZrOCl}_2 \cdot 8 \text{H}_2\text{O}$  (23.5 mg) were dissolved in DEF (3 mL). Afterwards, the modulator 4-*tert*-butylbenzoic acid (1350 mg) was added. The mixture was ultrasonicated for 10 min. For yield enhancement, seeds of PCN-222 were added. The suspension was heated in an oven at 120 °C for 12 h. Centrifugation of the solid, soaking in DMF (3  $\times$  6 mL) and acetone (3  $\times$  6 mL) and subsequent drying under vacuo yielded the purple product. For dehydration (=activation) the product is heated at 120 °C under dynamic vacuum ( $10^{-3}$  mbar) overnight.

**PCN-222(Zn) – Oven**

The synthesis was adapted from literature.<sup>[92,143]</sup> PCN-222 (30 mg) was added to a solution of  $\text{ZnCl}_2$  (59.9 mg, 18 equiv.) in DMF (3 mL). The suspension was heated in an oven at 100 °C for 24 h. Product isolation was achieved by centrifugation. The product was soaked in DMF (3  $\times$  6 mL) and acetone (3  $\times$  6 mL) and dried under vacuo.

**PCN-224(Zn) – Oven**

The synthesis was adapted from literature.<sup>[92,143]</sup> PCN-224 (30 mg) was added to a solution of  $\text{ZnCl}_2$  (22.9 mg, 8 equiv.) in DMF (3 mL). The suspension was heated in an oven at 100 °C for 24 h. Product isolation was achieved by centrifugation. The product was soaked in DMF (3  $\times$  6 mL) and acetone (3  $\times$  6 mL) and dried under vacuo.

**PCN-222(Ni) – pre-metalation**

The synthesis was adapted from literature.<sup>[82]</sup> In a 20 mL screw cap vial, Ni-TCPPP (13.4 mg) and  $\text{ZrOCl}_2 \cdot 8 \text{H}_2\text{O}$  (23.5 mg) were dissolved in DEF (3 mL). Afterwards, the modulator 4-*tert*-butylbenzoic acid (1350 mg) was added. The mixture was ultrasonicated for 10 min. For yield enhancement, seeds of PCN-222 were added. The suspension was heated in an oven at 120 °C for 12 h. Centrifugation of the solid, soaking in DMF (3 × 6 mL) and acetone (3 × 6 mL) and subsequent drying under vacuo yielded the violet product. For dehydration (=activation) the product is heated at 120 °C under dynamic vacuum ( $10^{-3}$  mbar) overnight.

**PCN-222(Cu) – pre-metalation**

The synthesis was adapted from literature.<sup>[82]</sup> In a 20 mL screw cap vial, Cu-TCPPP (13.8 mg) and  $\text{ZrOCl}_2 \cdot 8 \text{H}_2\text{O}$  (23.5 mg) were dissolved in DEF (3 mL). Afterwards, the modulator 4-*tert*-butylbenzoic acid (1350 mg) was added. The mixture was ultrasonicated for 10 min. For yield enhancement, seeds of PCN-222 were added. The suspension was heated in an oven at 120 °C for 12 h. Centrifugation of the solid, soaking in DMF (3 × 6 mL) and acetone (3 × 6 mL) and subsequent drying under vacuo yielded the violet product. For dehydration (=activation) the product is heated at 120 °C under dynamic vacuum ( $10^{-3}$  mbar) overnight.

**PCN-222(Mg) – pre-metalation**

The synthesis was adapted from literature.<sup>[82]</sup> In a 20 mL screw cap vial, Mg-TCPPP (12.8 mg) and  $\text{ZrOCl}_2 \cdot 8 \text{H}_2\text{O}$  (23.5 mg) were dissolved in DEF (3 mL). Afterwards, the modulator 4-*tert*-butylbenzoic acid (1350 mg) was added. The mixture was ultrasonicated for 10 min. For yield enhancement, seeds of PCN-222 were added. The suspension was heated in an oven at 120 °C for 12 h. Centrifugation of the solid, soaking in DMF (3 × 6 mL) and acetone (3 × 6 mL) and subsequent drying under vacuo yielded the violet product. For dehydration (=activation) the product is heated at 120 °C under dynamic vacuum ( $10^{-3}$  mbar) overnight. Note that ICP-MS measurements did not reveal any Mg.

**PCN-222(Fe) – pre-metalation**

The synthesis was adapted from literature.<sup>[82]</sup> In a 20 mL screw cap vial, Fe-TCPP (15.4 mg) and  $\text{ZrOCl}_2 \cdot 8 \text{H}_2\text{O}$  (23.5 mg) were dissolved in DEF (3 mL). Afterwards, the modulator 4-*tert*-butylbenzoic acid (1350 mg) was added. The mixture was ultrasonicated for 10 min. For yield enhancement, seeds of PCN-222 were added. The suspension was heated in an oven at 120 °C for 12 h. Centrifugation of the solid, soaking in DMF (3 × 6 mL) and acetone (3 × 6 mL) and subsequent drying under vacuo yielded the violet/brown product. For dehydration (=activation) the product is heated at 120 °C under dynamic vacuum ( $10^{-3}$  mbar) overnight.

**PCN-222(Fe) – Microwave**

A suspension of PCN-222 (10.0 mg) and  $\text{FeCl}_2 \cdot 4\text{H}_2\text{O}$  (1.65 mg, 1 equiv.) in DMF (3 mL) was placed in a microwave tube and heated under following conditions: 135 °C, open vessel, 85 W, 10 min,  $P_{\text{max}}$  on, stirring mode high). The product was isolated by centrifugation and soaked in DMF (3 × 10 mL) and acetone (3 × 10 mL). Drying under vacuo yielded the violet product.

**PCN-222(Fe) – Aluminum heating block**

A suspension of PCN-222 (10 mg) and  $\text{FeCl}_2 \cdot 4\text{H}_2\text{O}$  (3.3 mg, 2 equiv.) in DMF (3 mL) was placed in a 20 mL screw cap vial and was heated at 120 °C for 24 h in an aluminum block (stirring 300 rpm). The product was isolated by centrifugation and soaked in DMF (3 × 10 mL) and acetone (3 × 10 mL). Drying under vacuo yielded the brown product.

## Mixed-metal porphyrin MOFs

### PCN-222(Ru, Zn)

PCN-222(Ru) was synthesized via the mixed-linker approach described above (PCN-222(Ru) – different Ru loading). For PCN-222(Ru) metalation with Zn, PCN-222(Ru) (10.4 mg, 0.006 mmol, 1.0 equiv.) and ZnCl<sub>2</sub> (0.9 mg, 0.007 mmol, 1.1 equiv.) were suspended in DMF (3 mL). The suspension was heated in an oven at 100 °C for 24 h in an oven. Centrifugation of the solid, soaking in DMF (3 × 6 mL) and acetone (3 × 6 mL) and subsequent drying under vacuo yielded the red product. This procedure afforded a Ru/Zn ratio of 2.08. For Ru/Zn ratios of 0.93 and 0.72, ZnCl<sub>2</sub> equivalents were adjusted accordingly (2.0 and 5.0 equiv., respectively).

### PCN-222(Ru, Co)

The synthesis was adapted from literature.<sup>[82]</sup> In a 20 mL screw cap vial, Ru-TCPP(CO) (7.3 mg, 0.008 mmol, 0.5 equiv.), Co-TCPP (6.7 mg, 0.008 mmol, 0.5 equiv.) and ZrOCl<sub>2</sub> · 8 H<sub>2</sub>O (23.5 mg, 0.073 mmol, 4.56 equiv.) were suspended in DEF (3 mL). Afterwards, the modulator 4-*tert*-butylbenzoic acid (1350 mg, 7.57 mmol, 473 equiv.) was added. The mixture was ultrasonicated for 10 min. For yield enhancement, seeds of PCN-222 were added. The suspension was heated in an oven at 120 °C for 12 h. Centrifugation of the solid, soaking in DMF (3 × 6 mL) and acetone (3 × 6 mL) and subsequent drying under vacuo yielded the violet product.

### PCN-222(Ru, Ni)

The synthesis was adapted from literature.<sup>[82]</sup> In a 20 mL screw cap vial, Ru-TCPP(CO) (7.3 mg, 0.008 mmol, 0.5 equiv.), Ni-TCPP (6.7 mg, 0.008 mmol, 0.5 equiv.) and ZrOCl<sub>2</sub> · 8 H<sub>2</sub>O (23.5 mg, 0.073 mmol, 4.56 equiv.) were suspended in DEF (3 mL). Afterwards, the modulator 4-*tert*-butylbenzoic acid (1350 mg, 7.57 mmol, 473 equiv.) was added. The mixture was ultrasonicated for 10 min. For yield enhancement, seeds of PCN-222 were added. The suspension was heated in an oven at 120 °C for 12 h. Centrifugation of the solid, soaking in DMF (3 × 6 mL) and acetone (3 × 6 mL) and subsequent drying under vacuo yielded the violet product.

**PCN-222(Ru, Cu)**

The synthesis was adapted from literature.<sup>[82]</sup> In a 20 mL screw cap vial, Ru-TCPP(CO) (7.3 mg, 0.008 mmol, 0.5 equiv.), Cu-TCPP (6.7 mg, 0.008 mmol, 0.5 equiv.) and  $\text{ZrOCl}_2 \cdot 8 \text{H}_2\text{O}$  (23.5 mg, 0.073 mmol, 4.56 equiv.) were suspended in DEF (3 mL). Afterwards, the modulator 4-*tert*-butylbenzoic acid (1350 mg, 7.57 mmol, 473 equiv.) was added. The mixture was ultrasonicated for 10 min. For yield enhancement, seeds of PCN-222 were added. The suspension was heated in an oven at 120 °C for 12 h. Centrifugation of the solid, soaking in DMF (3 × 6 mL) and acetone (3 × 6 mL) and subsequent drying under vacuo yielded the violet product.

### 5.3.4. SED and Photocatalyst Synthesis

#### **4,4':2',2'':4'',4'''-quarterpyridine – qtpy**

The synthesis was adapted from literature.<sup>[215]</sup> A solid mixture of 4,4'-bipyridine (2.50 g, 16.0 mmol) and Pd/C (10 wt. %, 0.50 g) were heated at 250 °C for 48 h in a Teflon bomb. After grinding, the solid was placed in a Soxhlet apparatus and extracted with DCM (300 mL) over 18 h, yielding a first fraction. A second fraction was obtained by washing the Pd residue with hot DMF (2 × 50 mL). After solvent evaporation for both fractions, the solids were combined, and purified by flash column chromatography (DCM/MeOH 91/9 v/v). Sublimation yielded the product (0.77 g, 31% yield). Analytics matched literature reports.

<sup>1</sup>H NMR (400 MHz, 300 K, CDCl<sub>3</sub>) : δ [ppm] = 8.84 (dd, 2H), 8.81 (dd, 2H), 8.79 (m, 4H), 7.74 (m, 4H), 7.62 (dd, 2H).

#### **fac-ReBr(CO)<sub>3</sub>(qtpy)**

The synthesis was adapted from literature.<sup>[216]</sup> To a solution of ReBr(CO)<sub>5</sub> (140 mg, 0.35 mmol, 1.00 eq.) dissolved in toluene/THF (25 mL, 3:1, dry and degassed) 4,4':2',2'':4'',4'''-quarterpyridine (112 mg, 0.36 mmol, 1.05 eq.) was added under *Schlenk* conditions. After refluxing for 24 h, the suspension was filtered. The orange solid was washed with CHCl<sub>3</sub> (2 mL) and dried under vacuo to yield the orange powdered product (144 mg, 63 %).

<sup>1</sup>H NMR (400 MHz, 300 K, DMSO-d<sub>6</sub>): δ [ppm] = 9.34 (s, 2H), 9.17 (d, 2H), 8.88 (d, 4H), 8.17 (d, 2H), 8.07 (d, 4H)

ATR-IR:  $\tilde{\nu}$  [cm<sup>-1</sup>] = 2019, 1929, 1886, 1615, 1592, 1536, 1476, 1402, 1332, 1233, 1070, and 816 cm<sup>-1</sup>

#### **fac-ReBr(CO)<sub>3</sub>(dcbpy)** (for control experiments, dcbpy = 4,4'-dicarboxyl-2,2'-bipyridine)

The synthesis was adapted from literature.<sup>[217]</sup> Under argon atmosphere, ReBr(CO)<sub>5</sub> (0.30 g, 0.74 mmol, 1.0 eq.) was added to ethylene glycol dimethyl ether (20 mL) to which 4,4'-dicarboxyl-2,2'-bipyridine (0.18 g, 0.74 mmol, 1.0 eq.) was given. The reaction mixture was heated at 90 °C under inert gas atmosphere overnight while stirring. After solvent removal under vacuo the solid was dissolved in ethylene glycol dimethyl ether and added to hexane (100 mL) at 0 °C. Product isolation was performed by centrifugation. Drying under vacuo yielded the orange product. Analytics match literature reports.<sup>[217]</sup>

<sup>1</sup>H NMR (400 MHz, 300 K, CD<sub>3</sub>CN): δ [ppm]= 9.20 (d, <sup>3</sup>J = 5.7 Hz, 2H), 8.95 (s, 2H), 8.06 (d, <sup>3</sup>J = 5.7 Hz, 2H)

ATR-IR (Re(CO)<sub>3</sub>):  $\tilde{\nu}$  [cm<sup>-1</sup>] = = 2021, 1915 and 1870 cm<sup>-1</sup>

### 5.3.5. Functional Linker and Catalyst (analogue) Integration

#### PCN-222 with Et-TCPPh<sub>2</sub> and TCPPh<sub>2</sub> – EtP-PCN-222

In a 20 mL screw cap vial, TCPPh<sub>2</sub>, Et-TCPPh<sub>2</sub> (2,3,7,8,12,13,17,18-octaethyl-5,10,15,20-tetrakis(4-carboxyphenyl)-porphyrin) and ZrOCl<sub>2</sub> · 8 H<sub>2</sub>O (117.5 mg, 0.35 mmol, 4.56 equiv.) were dissolved in DEF (3 mL). Afterwards, the modulator 4-*tert*-butylbenzoic acid (1350 mg, 7.57 mmol, 473 equiv.) was added. The mixture was ultrasonicated for 10 min. For yield enhancement, seeds of PCN-222 were added. The suspension was heated in an oven at 120 °C for 12 h. Product isolation was performed by centrifugation, followed by soaking the solid in DMF (3 × 35 mL) and acetone (3 × 35 mL) and drying under vacuo. For dehydration (=activation) the product is heated at 120 °C under dynamic vacuum (10<sup>-3</sup> mbar) overnight.

The amounts of the different EtP-PCN-222 materials are summarized in the following:

MOF	TCPPh <sub>2</sub>	Et-TCPPh <sub>2</sub>
20EtP-PCN-222*	100 mg (0.127 mmol)	32.0 mg (0.032 mmol)
59EtP-PCN-222	56.3 mg (0.071 mmol)	8.1 mg (0.008 mmol)
72EtP-PCN-222	50.8 mg (0.064 mmol)	15.8 mg (0.016 mmol)

\*Note that for 20EtP-PCN-222 the synthesis approach was doubled. Thus, the amounts of Zr precursor, solvents and modulators are doubled.

#### Anchoring of *fac*-ReBr(CO)<sub>3</sub>(qtpy) in PCN-222(Zn) or PCN-224(Zn)

In 20 mL screw cap vials, a suspension containing a 0.1 mM solution of *fac*-ReBr(CO)<sub>3</sub>(qtpy) in MeCN (15 mL) and the activated MOF (PCN-222(Zn) or PCN-224(Zn), 10.0 mg) was kept at room temperature for 24 h in the dark. Afterwards, the solid was isolated by centrifugation and washed with fresh MeCN (3 × 7 mL, for 2 h each). Drying under vacuo yielded the MOF with anchored catalyst.

#### Calculation of Re-Catalyst/linker ratio

The metal loadings of Re and Zn were determined by ICP-MS measurements and subtracted from the total mass. With the ideal sum formula of PCN-222 (Zr<sub>6</sub>O<sub>8</sub>(OH)<sub>8</sub>(TCPPh)<sub>2</sub>, M = 2463.82 g·mol<sup>-1</sup>) and PCN-224 (Zr<sub>6</sub>O<sub>12</sub>(OH)<sub>8</sub>(TCPPh)<sub>1.5</sub>, M = 2063.33 g·mol<sup>-1</sup>), weighting of the remaining weight% by the mass fraction of the linkers (from ideal sum formula; 0.6382 for PCN-222 and 0.5730 for PCN-224) yielded the weight% of the assembly. Since this stems from the TCPPh linker only, the molar amount can be calculated using the molar mass of the linker (786.21 g·mol<sup>-1</sup>). Dividing the catalyst molar amount (directly obtained from ICP-MS measurements) and the molar amount of the linker results in the catalyst/linker ratio.



**Anchoring of *fac*-ReBr(CO)<sub>3</sub>(4,4'-dicarboxy-2,2'-bipyridine) in PCN-222(Zn) or PCN-224(Zn)**

For the anchoring of *fac*-ReBr(CO)<sub>3</sub>(4,4'-dicarboxy-2,2'-bipyridine) the procedure for *fac*-ReBr(CO)<sub>3</sub>(qtpy) anchoring above was followed with 10 mL of a 0.1 mM solution.

**Anchoring of Et-TCPPh<sub>2</sub> in PCN-222 via SALI**

For the SALI procedure a literature known procedure was adopted.<sup>[59]</sup> PCN-222 (25 mg) and Et-TCPPh<sub>2</sub> (3.46 mg, 1 equiv. per node) were suspended in DMF (2 mL) in a 20 mL screw cap vial. The suspension was heated in an oven at 80 °C for 24 h with occasional swirling. Afterwards, the solid was isolated by centrifugation, washed with DMF (3 × 7 mL) and acetone (3 × 8.5 mL) and dried under vacuo.

Note that the mother liquor and washing solutions were used for UV-vis spectroscopy.

**Anchoring of benzoic acid (BA) and phenyl phosphonic acid (PPA) in NU-1000 via SALI**

For the SALI a literature known procedure was adapted.<sup>[178,218]</sup> In a 20 mL screw cap vial, NU-1000 (30 mg) was suspended in DMF (1.865 mL) to which 135 μL of a 0.1 M solution of the respective acid (BA or PPA) in DMF were added. The suspension was heated in an oven at 60 °C for 22 h with occasional swirling. Afterwards, the solid was isolated by centrifugation, washed with DMF (3 × 4 mL) and acetone (3 × 4 mL) and dried under vacuo yielding NU-1000-BA and NU-1000-PPA, respectively.

**Stability tests of NU-1000, NU-1000-BA and NU-1000-PPA under catalytic conditions**

For stability studies the respective solids of NU-1000 and its acid anchored analogues (10 mg) were suspended in a solution of 9.9 μL 5-hexynoic acid in 0.9 mL solvent (CDCl<sub>3</sub> or DMSO-d<sub>6</sub>). The suspension was refluxed for 17 h (stirring 350 rpm). After cooling to room temperature, the solid was washed with the respective solvent (CDCl<sub>3</sub> or DMSO-d<sub>6</sub>) and dried under vacuo.

## 5.4. Catalysis

### 5.4.1 Cyclopropanation Catalysis

#### 5.4.1.1 Catalytic Setup and reaction conditions

##### **Styrene**

For styrene as substrate cyclopropanation catalysis was conducted in 5 mL capped vials containing an 8 mm PTFE stirring bar. The activated MOF powders (2.00 mg for PCN-22(Rh), 2.53 mg for PCN-224(Rh) and 1.76 mg for MOF-525(Rh)) were suspended in 0.73 mL (6.38 mmol, 25 000 equiv.) styrene to which 56.4  $\mu$ L mesitylene was added as internal standard. The mixture was stirred at room temperature (350 rpm). To this suspension, a solution of 49.0  $\mu$ L ( $0.25 \cdot 10^{-3}$  mmol, 1.0 equiv.) ethyl diazoacetate (EDA, 10wt% in DCM) in 1.10 mL DCM was added. Addition occurred dropwise via a motorized syringe pump (0.5 mL/h). Formed  $N_2$  was released via a separate needle.

##### **4-Aminostyrene**

For the substrate 4-aminostyrene the same reaction setup was used (5 mL capped vial, 8 mm PTFE stirring bar, EDA addition via motorized syringe pump). The activated MOF (1.38 mg for PCN-22(Rh), 1.75 mg for PCN-224(Rh) and 1.21 mg for MOF-525(Rh)) was suspended in DCM (1.5 mL) to which 382 mg (3.21 mmol, 18 900 equiv.) 4-aminostyrene and 38.8  $\mu$ L mesitylene as internal standard were added. Under stirring at room temperature, a solution of 33.8  $\mu$ L ( $0.17 \cdot 10^{-3}$  mmol, 1.0 equiv.) EDA (10wt% in DCM) in 0.75 mL DCM was added dropwise. Formed  $N_2$  was released via a separate needle.

For the EDA/substrate ratio variation, the amount of substrate was adjusted accordingly.

##### **4-Chlorostyrene**

For the substrate 4-chlorostyrene the same reaction setup was used (5 mL capped vial, 8 mm PTFE stirring bar, EDA addition via motorized syringe pump). Following amounts of starting materials were applied: 2.00 mg for PCN-22(Rh) in 0.80 mL (6.6 mmol, 25 000 equiv.) 4-chlorostyrene and 56.4  $\mu$ L mesitylene as internal standard, 49.0  $\mu$ L ( $0.25 \cdot 10^{-3}$  mmol, 1.0 equiv.) of EDA (10wt% in DCM) in 1.10 mL DCM.

##### **Additive Approach**

For the addition of pyridine, aniline, phenol and ethylene diamine the standard conditions for the respective substrate were applied. Additives were introduced via stock solutions with the respective mol% of additives (regarding Rh). These solutions were directly added to the suspension of MOF, mesitylene and substrate (4-aminostyrene) in DCM.

## Recycling

For catalyst recycling styrene cyclopropanation was conducted under standard conditions with PCN-222(Rh) (2.00 mg) as catalyst. The performance was analyzed after 6 h (after complete EDA addition) by taking a sample of the suspension was taken which was analyzed by GC. Afterwards, the MOF was isolated by centrifugation (10 min, 7830 rpm), washed with DCM (3 × 4 mL) and dried. The dried MOF was used in a further catalytic cycle of styrene cyclopropanation.

## Sample preparation

After complete EDA addition, 30 µL of the reaction mixture were taken via a piston pipette and added to 1.5 mL DCM (the end of EDA addition is defined as starting point, = 0h). The suspension was filtered using a syringe filter (13 mm PTFE membrane, 0.22 µm pore size). Further samples were taken after every hour until 6 h of reaction time and a last sample after 24 h.

### 5.4.1.2 Calculation of Conversion, Yield and Selectivity

For each catalysis run a reference mixture of EDA and mesitylene was prepared (concentrations according to the catalysis) allowing for the calculation of conversion, yield and selectivity. Following equation was used for conversion calculation where A represents the area of the respective signals in the gas chromatogram:

$$C(t) = \frac{\frac{A_{EDA,0}}{A_{Mes,0}} - \frac{A_{EDA,t}}{A_{Mes,t}}}{\frac{A_{EDA,0}}{A_{Mes,0}}}$$

Dividing the areas of *cis*- and *trans* product by the sum of all products and side-products areas results in their respective selectivities. The yield is obtained by multiplication of the conversion and selectivity (divided by 100).

## 5.4.2. Epoxidation Catalysis

### Epoxidation with PCN-222(Mn) or PCN-222(Co)

In a 20 mL screw cap vial, the solid MOF sample (PCN-222(Mn) or PCN-222(Co), 6.00 mg) was suspended in MeCN (3 mL). Styrene as substrate (99.0  $\mu$ L, 90.0 mg, 864  $\mu$ mol, 1.00 eq.), cyclohexane as internal standard (15.6  $\mu$ L, 12.2 mg, 145  $\mu$ mol, 0.167 eq.) and the TBHP (70% in water; 300  $\mu$ L, 196 mg, 2.18 mmol, 2.52 eq.) as oxidant were added to the suspension. The reaction suspension was placed in an aluminum block at different temperature (rt, 50  $^{\circ}$ C) while stirring (300 rpm) for 24 h. The reaction kinetics were followed  $^1$ H-NMR spectroscopy measurements while conversion and selectivity were evaluated by comparison of the respective reactant and product signals.

### Epoxidation with PCN-222(Ru)

In a standard reaction procedure, PCN-222(Ru) (0.25 mol% regarding olefin) and 52.0 mg 2,6-dichloropyridine N-oxide (317.2  $\mu$ mol, 1.1 equiv.) were placed in a Schlenk tube to which a solution of 288.3  $\mu$ mol olefin (1.0 eq.) and 5.2  $\mu$ L cyclohexane (48.1  $\mu$ mol, 0.2 equiv.) or 8.9  $\mu$ L mesitylene (64.0  $\mu$ mol, 0.2 equiv.), as internal standard, in DCM (1 mL) was added. The suspension was heated in a closed vessel in an oil bath at 40  $^{\circ}$ C while stirring (500 rpm). Samples were taken with a syringe after every 30 min for the first hour of catalysis and followed by every hour until 8 h. The catalysis was finished after 24 h where the last sample was taken. The respective sample suspensions were diluted in  $\text{CDCl}_3$  (0.4 mL) and filtered by a syringe filter (13 mm PTFE membrane, 0.22  $\mu$ m pore size). Analyzation was performed by  $^1$ H NMR spectroscopy.

### Calculation of Conversion, Yield and Selectivity

Conversion, yield and selectivity were calculated from the respective  $^1$ H NMR spectra. A spectrum recorded at  $t = 0$  h serves as reference allowing for the determination of a reference factor  $a$ . This factor describes the ratio of the integrals of the substrate at  $t = 0$  and the sum of the remaining integrals of substrate, product and side-products at a certain time  $x$  and is calculated by following equation.

$$a = \frac{\int \text{substrate}_{t=0}}{\int \text{substrate}_{t=x} + \int \text{product}_{t=x} + \int \text{byproducts}_{t=x}}$$

Conversions (C), Yields (Y) and Selectivities (S) at  $t = x$  of the epoxidation catalysis are calculated by following equations:

$$C(\%) = \left( 1 - \frac{a \cdot \int \text{substrate}_{t=x}}{\int \text{substrate}_{t=0}} \right) \cdot 100$$

$$Y(\%) = \frac{a \cdot \int \text{product}_{t=x}}{\int \text{substrate}_{t=0}} \cdot 100$$

$$S(\%) = \frac{Y}{X} \cdot 100$$

Turnover frequencies (TOFs) were calculated in the first part of the reaction with the highest slope in conversion with following equation:

$$TOF = \frac{X \cdot n_{\text{substrate}}}{n_{\text{catalyst}} \cdot t}$$

#### 5.4.3. CO<sub>2</sub> Cycloaddition

The catalyst PCN-222 (0.25 mol% Zr regarding olefin) or PCN-222(M) (M = Ru, Zn, Co, Cu, Ni; mol% M regarding olefin) was placed in a Fischer-Porter bottle (V = 90 mL) to which 4.6 mg tetrabutylammonium bromide (5 mol% in regards to olefin) were added. A solution of 33.0 μL styrene oxide (288.3 μmol, 1.0 equiv.), 1 mL DCM and 8.9 μL mesitylene (64.0 μmol, 0.2 equiv.), as internal standard, was added. The bottle was pressurized with 4 bar CO<sub>2</sub>. Catalysis was performed at 40 °C while stirring (500 rpm). For kinetic measurements, samples were taken after 4 h and 8 h under CO<sub>2</sub> pressure. The reaction vessel was pressurized again after retrieving the sample. The catalysis was stopped after 24 h where the last sample was taken. The respective sample suspensions were diluted in CDCl<sub>3</sub> (0.4 mL) and filtered by a syringe filter (13 mm PTFE membrane, 0.22 μm pore size). Analysis was performed by <sup>1</sup>H NMR spectroscopy. Calculations of conversion, yield and selectivity were conducted according to the method described for the epoxidation catalysis.

#### 5.4.4. Sequential Conversion of Epoxides to Cyclic Carbonates

The catalyst PCN-222 (0.25 mol% Zr regarding olefin) or PCN-222(M) (M = Ru, Zn, Co, Cu, Ni; mol% M regarding olefin) and 52.0 mg 2,6-dichloropyridine N-oxide (317.2  $\mu\text{mol}$ , 1.1 equiv.) were placed in a Fischer-Porter bottle ( $V = 90 \text{ mL}$ ) to which 4.6 mg tetrabutylammonium bromide (5 mol% in regards to olefin) were added. A solution of olefin (288.3  $\mu\text{mol}$ , 1.0 equiv.), 1 mL DCM and 5.2  $\mu\text{L}$  cyclohexane (48.1  $\mu\text{mol}$ , 0.2 equiv.) or 8.9  $\mu\text{L}$  mesitylene (64.0  $\mu\text{mol}$ , 0.2 equiv.), as internal standard, was added. Catalysis was performed at 40 °C while stirring (500 rpm). After 4 h, a sample was taken and the co-catalyst tetrabutylammonium bromide (4.6 mg, 5 mol% regarding the olefin) in 0.1 mL DCM was added. The vessel was pressurized with 4 bar  $\text{CO}_2$  before heating at 40 °C while stirring again. A further sample was taken after 4 h under  $\text{CO}_2$  (8 h in total), followed by pressurizing with 4 bar  $\text{CO}_2$  and heating again. The catalysis was stopped after 24 h where the last sample was taken. The respective sample suspensions were diluted in  $\text{CDCl}_3$  (0.4 mL) and filtered by a syringe filter (13 mm PTFE membrane, 0.22  $\mu\text{m}$  pore size). Analysis was performed by  $^1\text{H}$  NMR spectroscopy.

Calculations of conversion, yield and selectivity were calculated as follows:

$$C(\%) = \frac{\sum \int \text{products} \int \text{sideproducts}}{\sum \int \text{products} + \int \text{side - products} + \int \text{substrate}} \cdot 100$$

$$S(\%) = \frac{\sum \int \text{products}}{\sum \int \text{products} + \int \text{side - products}} \cdot 100$$

$$Y(\%) = X \cdot S \cdot 100$$

Due to the presence of signals which could not be assigned (probably side-products), calculations were conducted with the sum of integrals of reactant, products and side-products. Since the styrene signal at 5.3 ppm overlaps with DCM, its integral value was derived from the other integrals of the styrene signals (6.72 ppm and 5.75 ppm).

#### 5.4.5. Thia-Michael Addition

In a standard reaction procedure performed in a 20 mL screw cap vial, the catalyst EtP-PCN-222 catalyst (3 mol% Et-TCPP regarding limiting component) was suspended in DCM (2 mL) which was previously stored over  $K_2CO_3$  for 2 days. Phenyl vinyl sulfone (2.2 mg, 0.013 mmol, 1.0 equiv.) was added to the suspension. Afterwards, the vial was closed and flushed with Ar for 1 min. Under Ar atmosphere, *tert*-butylbenzyl mercaptan (2.4  $\mu$ L, 2.3 mg, 0.013 mmol, 1.0 equiv.) was added. The Ar atmosphere was ensured by an argon balloon on top of the reaction vessel. The catalysis was conducted in the dark at room temperature under stirring (350 rpm). The catalysis was stopped after 24 h by separating the catalyst via a syringe filter (13 mm PTFE membrane, 0.22  $\mu$ m pore size). Analysis was performed by  $^1H$  NMR spectroscopy.

For reaction optimization, solvent variation was performed (MeCN and DMSO- $d_6$ ). Additionally, increased equivalents (10 equiv.) of sulfon were applied.

However, no attempt resulted in any conversion – observed by  $^1H$  NMR spectroscopy.

Temperature increase did result in the conversion of the substrate – however, this was also observed without catalyst addition.

#### 5.4.6. Henry Reaction

In a standard reaction procedure performed in a 20 mL screw cap vial, the catalyst EtP-PCN-222 catalyst (1 mg, 3 mol% Et-TCPP regarding limiting component) was suspended in methanol (MeOH, 2 mL). Benzaldehyde (3.4  $\mu$ L, 3.5 mg, 0.03 mmol, 1.0 equiv.) and nitromethane (17.6  $\mu$ L, 20.1 mg, 0.33 mmol, 10 equiv.) were added. The reaction was heated at 55  $^{\circ}C$  for 24 h. The catalysis was stopped after 24 h by separating the catalyst via a syringe filter (13 mm PTFE membrane, 0.22  $\mu$ m pore size). Analysis was performed by  $^1H$  NMR spectroscopy which did not show any conversion.

### 5.4.7. Photocatalytic CO<sub>2</sub> Reduction

#### Photocatalytic CO<sub>2</sub> reduction

In a standard procedure performed in a 50 mL *Schlenk* flask, the MOF (1.5 mg) was suspended in MeCN (4 mL) and deionised H<sub>2</sub>O (0.12 mL, 3 vol%). BIH (225 mg, 1 mmol) was added. The suspension and headspace were saturated by CO<sub>2</sub> (for 7 min), sealed, and again flushed with CO<sub>2</sub> resulting in an overpressure (total pressure = 1.45 bar).

As the irradiation source a heat-free white light generator *Asahi Spectra* MAX-303 Compact Xenon Light Source 300 W was used, with either a XVL0430-Longpass 430 nm filter (430-740 nm irradiation, ~10 mW·cm<sup>-2</sup>) or a XVL0490-Longpass 490 nm filter (490-740 nm irradiation, ~8 mW·cm<sup>-2</sup>). The catalysis was performed at room temperature while stirring. Analysis of the reaction was performed by gas chromatography (of headspace) and <sup>1</sup>H NMR spectroscopy (solution).

For reactions and measurements with the model system of a Zr<sub>6</sub> node, Zn-TCPP and the Re catalyst the 4-fold amount of Zr<sub>6</sub>(OH)<sub>4</sub>O<sub>4</sub>(OMc)<sub>12</sub> was used – preventing porphyrin aggregation. Stock solutions of all three components were combined and soaked for 1 h at room temperature before further use.

#### Turnover number (TON) calculations

For photocatalysis, the TONs were calculated according to a literature known procedure.<sup>[47]</sup> The molar amount of the catalyst was obtained by ICP-MS measurements. Results on each gas are given by GC of the headspace. Calibration was performed with reference gases. The amount of solvated CO was estimated by using Henry's law.

### 5.4.8. Cycloisomerization of 5-Hexynoic acid

In a 20 mL screw cap vial, NU-1000 (5.0 mg) was suspended in a solution of 9.9 μL 5-hexynoic acid (10.1 mg, 0.09 mmol, 1.0 equiv.) in 0.9 mL CDCl<sub>3</sub> and 6.25 μL mesitylene as internal standard. Afterwards the [Pd<sub>2</sub>S<sub>2</sub>] catalyst (2.6 mg, 5 mol% regarding the substrate) was added. Catalysis was performed at 90 °C while stirring (350 rpm) for 6 h. Analysis was performed by <sup>1</sup>H NMR analysis which showed complete substrate conversion to the desired product.



## 6. References

- [1] K.-Y. Wang, J. Zhang, Y.-C. Hsu, H. Lin, Z. Han, J. Pang, Z. Yang, R.-R. Liang, W. Shi, H.-C. Zhou, *Chem. Rev.* **2023**.
- [2] K. Chen, C.-D. Wu, *Coord. Chem. Rev.* **2019**, 378, 445.
- [3] Y. Chen, S. Ma, *Dalton Trans.* **2016**, 45, 9744.
- [4] S. Benkovic, S. Hammes-Schiffer, *Science* **2003**, 301, 1196.
- [5] A. Kirby, *Angew. Chem. Int. Ed.* **1996**, 35, 707.
- [6] G. G. Hammes, *Biochemistry* **2002**, 41, 8221.
- [7] Y. Murakami, J. Kikuchi, Y. Hisaeda, O. Hayashida, *Chem. Rev.* **1996**, 96, 721.
- [8] a) L. Marchetti, M. Levine, *ACS Catal.* **2011**, 1, 1090; b) E. Kuah, S. Toh, J. Yee, Q. Ma, Z. Gao, *Chem. Eur. J.* **2016**, 22, 8404; c) W. B. Motherwell, M. J. Bingham, Y. Six, *Tetrahedron* **2001**, 57, 4663.
- [9] Z. Dong, Q. Luo, J. Liu, *Chem. Soc. Rev.* **2012**, 41, 7890.
- [10] a) H.-J. Federsel, T. S. Moody, S. J. C. Taylor, *Molecules* **2021**, 26; b) Y. R. Maghraby, R. M. El-Shabasy, A. H. Ibrahim, H. M. E.-S. Azzazy, *ACS omega* **2023**, 8, 5184.
- [11] T. Wang, X. Fan, C. Hou, J. Liu, *Curr. Opin. Struct. Biol.* **2018**, 51, 19.
- [12] Y. Chen, T. Hoang, S. Ma, *Inorg. Chem.* **2012**, 51, 12600.
- [13] a) C. Doonan, R. Riccò, K. Liang, D. Bradshaw, P. Falcaro, *Acc. Chem. Res.* **2017**, 50, 1423; b) Z.-Y. Gu, J. Park, A. Raiff, Z. Wei, H.-C. Zhou, *ChemCatChem* **2014**, 6, 67; c) M. Zhao, S. Ou, C.-D. Wu, *Acc. Chem. Res.* **2014**, 47, 1199.
- [14] D. Feng, Z.-Y. Gu, J.-R. Li, H.-L. Jiang, Z. Wei, H.-C. Zhou, *Angew. Chem. Int. Ed.* **2012**, 51, 10307.
- [15] S. R. Batten, N. R. Champness, X.-M. Chen, J. Garcia-Martinez, S. Kitagawa, L. Öhrström, M. O'Keeffe, M. Paik Suh, J. Reedijk, *Pure Appl. Chem.* **2013**, 85, 1715.
- [16] a) H.-C. Zhou, J. R. Long, O. M. Yaghi, *Chem. Rev.* **2012**, 112, 673; b) H.-C. J. Zhou, S. Kitagawa, *Chem. Soc. Rev.* **2014**, 43, 5415.
- [17] H. Furukawa, K. E. Cordova, M. O'Keeffe, O. M. Yaghi, *Science* **2013**, 341, 1230444.
- [18] S. M. Moosavi, A. Nandy, K. M. Jablonka, D. Ongari, J. P. Janet, P. G. Boyd, Y. Lee, B. Smit, H. J. Kulik, *Nat. Commun.* **2020**, 11, 4068.

- [19] R. Freund, O. Zaremba, G. Arnauts, R. Ameloot, G. Skorupskii, M. Dincă, A. Bavykina, J. Gascon, A. Ejsmont, J. Goscianska et al., *Angew. Chem. Int. Ed.* **2021**, *60*, 23975.
- [20] Q. Yang, Q. Xu, H.-L. Jiang, *Chem. Soc. Rev.* **2017**, *46*, 4774.
- [21] P. M. Stanley, J. Haimerl, C. Thomas, A. Urstoeger, M. Schuster, N. B. Shustova, A. Casini, B. Rieger, J. Warnan, R. A. Fischer, *Angew. Chem. Int. Ed.* **2021**, *60*, 17854.
- [22] X. Liu, B. Qian, D. Zhang, M. Yu, Z. Chang, X. Bu, *Coord. Chem. Rev.* **2023**, *476*, 214921.
- [23] a) K. K. Gangu, S. Maddila, S. B. Mukkamala, S. B. Jonnalagadda, *Inorganica Chim. Acta* **2016**, *446*, 61; b) S. T. Meek, J. A. Greathouse, M. D. Allendorf, *Adv. Mater.* **2011**, *23*, 249; c) W. Fan, X. Zhang, Z. Kang, X. Liu, D. Sun, *Coord. Chem. Rev.* **2021**, *443*, 213968.
- [24] a) S. Jeoung, S. Kim, M. Kim, H. R. Moon, *Coord. Chem. Rev.* **2020**, *420*, 213377; b) O. M. Yaghi, M. O'Keeffe, N. W. Ockwig, H. K. Chae, M. Eddaoudi, J. Kim, *Nature* **2003**, *423*, 705; c) S. Yuan, Y.-P. Chen, J.-S. Qin, W. Lu, L. Zou, Q. Zhang, X. Wang, X. Sun, H.-C. Zhou, *J. Am. Chem. Soc.* **2016**, *138*, 8912.
- [25] C. Xu, R. Fang, R. Luque, L. Chen, Y. Li, *Coord. Chem. Rev.* **2019**, *388*, 268.
- [26] Web of Science, *Key word: MOF Catalysis*, search range 05.02.2004–26.06.2022.
- [27] A. Bavykina, N. Kolobov, I. S. Khan, J. A. Bau, A. Ramirez, J. Gascon, *Chem. Rev.* **2020**, *120*, 8468.
- [28] A. H. Chughtai, N. Ahmad, H. A. Younus, A. Laypkov, F. Verpoort, *Chem. Soc. Rev.* **2015**, *44*, 6804.
- [29] A. Dhakshinamoorthy, A. M. Asiri, H. Garcia, *Chem. Eur. J.* **2016**, *22*, 8012.
- [30] A. Dhakshinamoorthy, Z. Li, H. Garcia, *Chem. Soc. Rev.* **2018**, *47*, 8134.
- [31] L. Jiao, Y. Wang, H.-L. Jiang, Q. Xu, *Adv. Mater.* **2018**, *30*, 1703663.
- [32] K. Epp, A. L. Semrau, M. Cokoja, R. A. Fischer, *ChemCatChem* **2018**, *10*, 3506.
- [33] S. Dissegna, K. Epp, W. R. Heinz, G. Kieslich, R. A. Fischer, *Adv. Mater.* **2018**, *30*, 1704501.
- [34] a) S. Dissegna, R. Hardian, K. Epp, G. Kieslich, M.-V. Coulet, P. Llewellyn, R. A. Fischer, *CrystEngComm* **2017**, *19*, 4137; b) F. G. Cirujano, A. Corma, F. X. Llabrés i Xamena, *Chem. Eng. Sci.* **2015**, *124*, 52.
- [35] Y. Liu, R. C. Klet, J. T. Hupp, O. Farha, *Chem. Commun.* **2016**, *52*, 7806.
- [36] Y. Zhang, X. Yang, H.-C. Zhou, *Polyhedron* **2018**, *154*, 189.

- [37] Y. Wen, J. Zhang, Q. Xu, X.-T. Wu, Q.-L. Zhu, *Coord. Chem. Rev.* **2018**, 376, 248.
- [38] X. Jia, W. Khan, Z. Wu, J. Choi, A. C.K. Yip, *Adv. Powder Technol.* **2019**, 30, 467.
- [39] J. Guo, Y. Qin, Y. Zhu, X. Zhang, C. Long, M. Zhao, Z. Tang, *Chem. Soc. Rev.* **2021**, 50, 5366.
- [40] J. Lee, O. K. Farha, J. Roberts, K. A. Scheidt, S. T. Nguyen, J. T. Hupp, *Chem. Soc. Rev.* **2009**, 38, 1450.
- [41] a) H. Huang, K. Shen, F. Chen, Y. Li, *ACS Catal.* **2020**, 10, 6579; b) L. Hu, W. Li, L. Wang, B. Wang, *EnergyChem.* **2021**, 3, 100056; c) Y.-S. Wei, M. Zhang, R. Zou, Q. Xu, *Chem. Rev.* **2020**, 120, 12089.
- [42] D. Yang, B. C. Gates, *ACS Catal.* **2019**, 9, 1779.
- [43] A. Dhakshinamoorthy, H. Garcia, *ChemSusChem* **2014**, 7, 2392.
- [44] A. Dhakshinamoorthy, M. Alvaro, Y. K. Hwang, Y.-K. Seo, A. Corma, H. Garcia, *Dalton Trans.* **2011**, 40, 10719.
- [45] T. Kiyonaga, M. Higuchi, T. Kajiwara, Y. Takashima, J. Duan, K. Nagashima, S. Kitagawa, *Chem. Commun.* **2015**, 51, 2728.
- [46] A. L. Semrau, P. M. Stanley, A. Urstoeger, M. Schuster, M. Cokoja, R. A. Fischer, *ACS Catal.* **2020**.
- [47] P. M. Stanley, A. Y. Su, V. Ramm, P. Fink, C. Kimna, O. Lieleg, M. Elsner, J. A. Lercher, B. Rieger, J. Warnan et al., *Adv. Mater.* **2023**, 35, e2207380.
- [48] P. Deria, J. E. Mondloch, O. Karagiari, W. Bury, J. T. Hupp, O. K. Farha, *Chem. Soc. Rev.* **2014**, 43, 5896.
- [49] T. Islamoglu, S. Goswami, Z. Li, A. J. Howarth, O. K. Farha, J. T. Hupp, *Acc. Chem. Res.* **2017**, 50, 805.
- [50] A. Dhakshinamoorthy, A. M. Asiri, H. Garcia, *Catal. Sci. Technol.* **2016**, 6, 5238.
- [51] S. S. Rajasree, X. Li, P. Deria, *Commun. Chem.* **2021**, 4, 47.
- [52] P. Cui, P. Wang, Y. Zhao, W.-Y. Sun, *Cryst. Growth Des.* **2019**, 19, 1454.
- [53] P. Deria, W. Bury, J. T. Hupp, O. K. Farha, *Chem. Commun.* **2014**, 50, 1965.
- [54] S. Mandal, S. Natarajan, P. Mani, A. Pankajakshan, *Adv. Funct. Mater.* **2021**, 31, 2006291.
- [55] W. R. Heinz, I. Agirrezabal-Telleria, R. Junk, J. Berger, J. Wang, D. I. Sharapa, M. Gil-Calvo, I. Luz, M. Soukri, F. Studt et al., *ACS Appl. Mater. Interfaces* **2020**, 12, 40635.

- [56] S. M. J. Rogge, A. Bavykina, J. Hajek, H. Garcia, A. I. Olivos-Suarez, A. Sepúlveda-Escribano, A. Vimont, G. Clet, P. Bazin, F. Kapteijn et al., *Chem. Soc. Rev.* **2017**, *46*, 3134.
- [57] a) Y. Cui, M. Rimoldi, A. E. Platero-Prats, K. W. Chapman, J. T. Hupp, O. K. Farha, *ChemCatChem* **2018**, *10*, 1772; b) A. Halder, S. Lee, B. Yang, M. J. Pellin, S. Vajda, Z. Li, Y. Yang, O. K. Farha, J. T. Hupp, *J. Chem. Phys.* **2020**, *152*, 84703; c) Z. Li, N. M. Schweitzer, A. B. League, V. Bernales, A. W. Peters, A. B. Getsoian, T. C. Wang, J. T. Miller, A. Vjunov, J. L. Fulton et al., *J. Am. Chem. Soc.* **2016**, *138*, 1977; d) Q. Wang, Z. Pengmei, R. Pandharkar, L. Gagliardi, J. T. Hupp, J. M. Notestein, *J. Catal.* **2022**, *407*, 162.
- [58] J. E. Mondloch, W. Bury, D. Fairen-Jimenez, S. Kwon, E. J. DeMarco, M. H. Weston, A. A. Sarjeant, S. T. Nguyen, P. C. Stair, R. Q. Snurr et al., *J. Am. Chem. Soc.* **2013**, *135*, 10294.
- [59] X. Li, J. Yu, D. J. Gosztola, H. C. Fry, P. Deria, *J. Am. Chem. Soc.* **2019**, *141*, 16849.
- [60] J. S. Oh, Y. You, K. C. Park, G. Gupta, D.-K. Kang, C. Y. Lee, *Dyes Pigm.* **2019**, *170*, 107576.
- [61] Y.-B. Huang, J. Liang, X.-S. Wang, R. Cao, *Chem. Soc. Rev.* **2017**, *46*, 126.
- [62] A. Tombesi, C. Pettinari, *Inorganics* **2021**, *9*, 81.
- [63] C. Wang, Z. Xie, K. E. deKrafft, W. Lin, *J. Am. Chem. Soc.* **2011**, *133*, 13445.
- [64] a) J. Li, Y. Ren, C. Qi, H. Jiang, *Dalton Trans* **2017**, *46*, 7821; b) P. W. Roesky, A. Bhunia, Y. Lan, A. K. Powell, S. Kureti, *Chem. Commun.* **2011**, *47*, 2035; c) Q. Xia, Y. Liu, Z. Li, W. Gong, Y. Cui, *Chem. Commun.* **2016**, *52*, 13167.
- [65] K. L. Kollmannsberger, L. Kronthaler, J. R. Jinschek, R. A. Fischer, *Chem. Soc. Rev.* **2022**, *51*, 9933.
- [66] Z. Niu, W. Zhang, P. C. Lan, B. Aguila, S. Ma, *Angew. Chem. Int. Ed.* **2019**, *58*, 7420.
- [67] Z. Lin, Z.-M. Zhang, Y.-S. Chen, W. Lin, *Angew. Chem. Int. Ed.* **2016**, *55*, 13739.
- [68] K. Hemmer, M. Cokoja, R. A. Fischer, *ChemCatChem* **2021**, *13*, 1683.
- [69] T. Uemura, R. Kitaura, Y. Ohta, M. Nagaoka, S. Kitagawa, *Angew. Chem. Int. Ed.* **2006**, *45*, 4112.
- [70] T. Uemura, D. Hiramatsu, Y. Kubota, M. Takata, S. Kitagawa, *Angew. Chem. Int. Ed.* **2007**, *46*, 4987.

- [71] F. Gao, L. Zhang, C. Yu, X. Yan, S. Zhang, X. Li, *Macromol. Rapid Commun.* **2018**, *39*, e1800002.
- [72] M. Zheng, Y. Liu, C. Wang, S. Liu, W. Lin, *Chem. Sci.* **2012**, *3*, 2623.
- [73] S. Nießing, C. Janiak, *Mol. Catal.* **2019**, *467*, 70.
- [74] C. Kutzscher, G. Nickerl, I. Senkowska, V. Bon, S. Kaskel, *Chem. Mater.* **2016**, *28*, 2573.
- [75] K. D. Nguyen, C. Kutzscher, S. Ehrling, I. Senkowska, V. Bon, M. Oliveira, T. Gutmann, G. Buntkowsky, S. Kaskel, *J. Catal.* **2019**, *377*, 41.
- [76] S. Nießing, C. Czekelius, C. Janiak, *Catal. Commun.* **2017**, *95*, 12.
- [77] L. Liu, T.-Y. Zhou, S. G. Telfer, *J. Am. Chem. Soc.* **2017**, *139*, 13936.
- [78] D. J. Xiao, J. Oktawiec, P. J. Milner, J. R. Long, *J. Am. Chem. Soc.* **2016**, *138*, 14371.
- [79] C. Zhu, G. Yuan, X. Chen, Z. Yang, Y. Cui, *J. Am. Chem. Soc.* **2012**, *134*, 8058.
- [80] T. Zhang, Y. Shi, S. Zhang, C. Jia, C. He, C. Duan, *New J. Chem.* **2018**, *42*, 18448.
- [81] P. Deria, D. A. Gómez-Gualdrón, I. Hod, R. Q. Snurr, J. T. Hupp, O. K. Farha, *J. Am. Chem. Soc.* **2016**, *138*, 14449.
- [82] X. Gong, Y. Shu, Z. Jiang, L. Lu, X. Xu, C. Wang, H. Deng, *Angew. Chem.* **2020**, *10*, 1913.
- [83] Y. Wang, H. Cui, Z.-W. Wei, H.-P. Wang, L. Zhang, C.-Y. Su, *Chem. Sci.* **2017**, *8*, 775.
- [84] F. G. Cirujano, F. X. Llabrés i Xamena, A. Corma, *Dalton Trans.* **2012**, *41*, 4249.
- [85] A. Corma, M. Iglesias, F. X. Llabrés i Xamena, F. Sánchez, *Chem. Eur. J.* **2010**, *16*, 9789.
- [86] H.-H. Mautschke, F. Drache, I. Senkowska, S. Kaskel, F. X. Llabrés i Xamena, *Catal. Sci. Technol.* **2018**, *8*, 3610.
- [87] K. Epp, B. Bueken, B. J. Hofmann, M. Cokoja, K. Hemmer, D. de Vos, R. A. Fischer, *Catal. Sci. Technol.* **2019**, *9*, 6452.
- [88] V. L. Rechac, F. G. Cirujano, A. Corma, F. X. Llabrés i Xamena, *Eur. J. Inorg. Chem.* **2016**, *27*, 4512.
- [89] F. Vermoortele, R. Ameloot, A. Vimont, C. Serre, D. de Vos, *Chem. Commun.* **2011**, *47*, 1521.
- [90] a) C. Chizallet, S. Lazare, D. Bazer-Bachi, F. Bonnier, V. Lecocq, E. Soyer, A.-A. Quoineaud, N. Bats, *J. Am. Chem. Soc.* **2010**, *132*, 12365; b) M. Zhu, D. Srinivas, S. Bhogeswararao, P. Ratnasamy, M. A. Carreon, *Catal. Commun.* **2013**, *32*, 36.

- [91] K. Yu, P. Puthiaraj, W.-S. Ahn, *Appl. Catal. B* **2020**, 273, 119059.
- [92] J. Liang, Y.-Q. Xie, Q. Wu, X.-Y. Wang, T.-T. Liu, H.-F. Li, Y.-B. Huang, R. Cao, *Inorg. Chem.* **2018**, 57, 2584.
- [93] Z. Fan, Z. Wang, M. Cokoja, R. A. Fischer, *Catal. Sci. Technol.* **2021**, 11, 2396.
- [94] L. J. Zhang, J. C. Yuan, L. J. Ma, Z. Y. Tang, X. M. Zhang, *J. Catal.* **2021**, 401, 63.
- [95] D. E. Fogg, E. N. dos Santos, *Coord. Chem. Rev.* **2004**, 248, 2365.
- [96] N. T. Patil, V. S. Shinde, B. Gajula, *Org. Biomol. Chem.* **2012**, 10, 211.
- [97] A. Dhakshinamoorthy, H. Garcia, *ChemSusChem* **2014**, 7, 2392.
- [98] a) Y. Dong, W.-H. Li, Y.-B. Dong, *J. Org. Chem.* **2021**, 86, 1818; b) Q. Xia, Z. Li, C. Tan, Y. Liu, W. Gong, Y. Cui, *J. Am. Chem. Soc.* **2017**, 139, 8259.
- [99] M. H. Beyzavi, N. A. Vermeulen, K. Zhang, M. So, C.-W. Kung, J. T. Hupp, O. K. Farha, *ChemPlusChem* **2016**, 81, 708.
- [100] D. Feng, W.-C. Chung, Z. Wei, Z.-Y. Gu, H.-L. Jiang, Y.-P. Chen, D. J. Darensbourg, H.-C. Zhou, *J. Am. Chem. Soc.* **2013**, 135, 17105.
- [101] L. Feng, K.-Y. Wang, E. Joseph, H.-C. Zhou, *Trends Chem.* **2020**, 2, 555.
- [102] Y. Bai, Y. Dou, L.-H. Xie, W. Rutledge, J.-R. Li, H.-C. Zhou, *Chem. Soc. Rev.* **2016**, 45, 2327.
- [103] X. Gong, H. Noh, N. C. Gianneschi, O. K. Farha, *J. Am. Chem. Soc.* **2019**, 141, 6146.
- [104] M. L. Kelty, W. Morris, A. T. Gallagher, J. S. Anderson, K. A. Brown, C. A. Mirkin, T. D. Harris, *Chem. Commun.* **2016**, 52, 7854.
- [105] S. M. Shaikh, P. M. Usov, J. Zhu, M. Cai, J. Alatis, A. J. Morris, *Inorg. Chem.* **2019**, 58, 5145.
- [106] T.-F. Liu, D. Feng, Y.-P. Chen, L. Zou, M. Bosch, S. Yuan, Z. Wei, S. Fordham, K. Wang, H.-C. Zhou, *J. Am. Chem. Soc.* **2015**, 137, 413.
- [107] C. Koschnick, R. Stäglich, T. Scholz, M. W. Terban, A. von Mankowski, G. Savasci, F. Binder, A. Schökel, M. Etter, J. Nuss et al., *Nat. Commun.* **2021**, 12, 3099.
- [108] G. C. Shearer, S. Chavan, J. Ethiraj, J. G. Vitillo, S. Svelle, U. Olsbye, C. Lamberti, S. Bordiga, K. P. Lillerud, *Chem. Mater.* **2014**, 26, 4068.
- [109] S. W. Hong, J. W. Paik, D. Seo, J.-M. Oh, Y. K. Jeong, J. K. Park, *Inorg. Chem. Front.* **2020**, 7, 221.

- [110] C. Koschnick, M. W. Terban, S. Canossa, M. Etter, R. E. Dinnebier, B. V. Lotsch, *Adv. Mater.* **2023**, e2210613.
- [111] H.-Q. Xu, K. Wang, M. Ding, D. Feng, H.-L. Jiang, H.-C. Zhou, *J. Am. Chem. Soc.* **2016**, *138*, 5316.
- [112] a) M.-F. Xiong, A. Ali, W. Akram, H. Zhang, L.-P. Si, H.-Y. Liu, *Catal. Commun.* **2019**, *125*, 93; b) A. Call, M. Cibian, K. Yamamoto, T. Nakazono, K. Yamauchi, K. Sakai, *ACS Catal.* **2019**, *9*, 4867; c) M. M. Pereira, L. D. Dias, M. J. F. Calvete, *ACS Catal.* **2018**, *8*, 10784.
- [113] S. Carrasco, A. Sanz-Marco, B. Martín-Matute, *Organometallics* **2019**, *38*, 3429.
- [114] T. Higuchi, H. Ohtake, M. Hirobe, *Tetrahedron Lett.* **1989**, *30*, 6545.
- [115] S. Hiroto, Y. Miyake, H. Shinokubo, *Chem. Rev.* **2017**, *117*, 2910.
- [116] N. Huang, S. Yuan, H. Drake, X. Yang, J. Pang, J. Qin, J. Li, Y. Zhang, Q. Wang, D. Jiang et al., *J. Am. Chem. Soc.* **2017**, *139*, 18590.
- [117] T. Ishizuka, N. Grover, C. J. Kingsbury, H. Kotani, M. O. Senge, T. Kojima, *Chem. Soc. Rev.* **2022**, *51*, 7560.
- [118] M. Beller, A. Renken, R. A. van Santen (Eds.) *Catalysis. From principles to applications*, Wiley-VCH-Verlag GmbH & Co. KGaA, Weinheim, **2012**.
- [119] J. Hagen, *Industrial catalysis. A practical approach*, Wiley-VCH, Weinheim, **2015**.
- [120] A. Behr, *Angewandte homogene Katalyse*, Wiley-VCH, Weinheim, **2008**.
- [121] L. Lloyd, *Handbook of Industrial Catalysts*, Springer, New York, **2011**.
- [122] K. Epp, *Dissertation*, Technische Universität München, München, **2019**.
- [123] W. Morris, B. Voloskiy, S. Demir, F. Gándara, P. L. McGrier, H. Furukawa, D. Cascio, J. F. Stoddart, O. M. Yaghi, *Inorg. Chem.* **2012**, *51*, 6443.
- [124] C. Xu, H. Liu, D. Li, J.-H. Su, H.-L. Jiang, *Chem. Sci.* **2018**, *9*, 3152.
- [125] L. Jiao, G. Wan, R. Zhang, H. Zhou, S.-H. Yu, H.-L. Jiang, *Angew. Chem. Int. Ed.* **2018**, *57*, 8525.
- [126] H.-Q. Xu, J. Hu, D. Wang, Z. Li, Q. Zhang, Y. Luo, S.-H. Yu, H.-L. Jiang, *J. Am. Chem. Soc.* **2015**, *137*, 13440.
- [127] D. Lv, R. Shi, Y. Chen, Y. Chen, H. Wu, X. Zhou, H. Xi, Z. Li, Q. Xia, *Ind. Eng. Chem. Res.* **2018**, *57*, 12215.

- [128] S. Choi, W.-J. Jung, K. Park, S.-Y. Kim, J.-O. Baeg, C. H. Kim, H.-J. Son, C. Pac, S. O. Kang, *ACS Appl. Mater. Inter.* **2021**, *13*, 2710.
- [129] H. Zhang, J. Wei, J. Dong, G. Liu, L. Shi, P. An, G. Zhao, J. Kong, X. Wang, X. Meng et al., *Angew. Chem. Int. Ed.* **2016**, *55*, 14310.
- [130] G. C. Shearer, J. G. Vitillo, S. Bordiga, S. Svelle, U. Olsbye, K. P. Lillerud, *Chem. Mater.* **2016**, *28*, 7190.
- [131] A. M. Szczepkowska, M. Janeta, M. Siczek, W. Tylus, A. M. Trzeciak, W. Bury, *Dalton Trans.* **2021**, *50*, 9051.
- [132] J. Malone, S. Klaine, C. Alcantar, F. Bratcher, R. Zhang, *New J. Chem.* **2021**, *45*, 4977.
- [133] M. A. Fodor, P. Szabó, G. Lendvay, O. Horváth, *Z. Phys. Chem.* **2022**, *236*, 27.
- [134] J. Liu, Y.-Z. Fan, X. Li, Z. Wei, Y.-W. Xu, L. Zhang, C.-Y. Su, *Appl. Catal. B* **2018**, *231*, 173.
- [135] K. Anjali, N. J. Venkatesha, J. Christopher, A. Sakthivel, *New J. Chem.* **2020**, *44*, 11064.
- [136] Z. Gross, S. Ini, M. Kapon, S. Cohen, *Tetrahedron Lett.* **1996**, *37*, 7325.
- [137] A. Vidal, F. Battistin, E. Iengo, B. Milani, E. Alessio, *Eur. J. Inorg. Chem.* **2019**, *2019*, 2883.
- [138] a) J. Chen, M. Chen, B. Zhang, R. Nie, A. Huang, T. W. Goh, A. Volkov, Z. Zhang, Q. Ren, W. Huang, *Green Chem.* **2019**, *21*, 3629; b) A. W. Stubbs, L. Braglia, E. Borfecchia, R. J. Meyer, Y. Román-Leshkov, C. Lamberti, M. Dincă, *ACS Catal.* **2018**, *8*, 596; c) K. Yuan, T. Song, D. Wang, Y. Zou, J. Li, X. Zhang, Z. Tang, W. Hu, *Nanoscale* **2018**, *10*, 1591.
- [139] J. W. Brown, Q. T. Nguyen, T. Otto, N. N. Jarenwattananon, S. Glöggler, L.-S. Bouchard, *Catal. Commun.* **2015**, *59*, 50.
- [140] S. Singh Dhankhar, B. Ugale, C. M. Nagaraja, *Chem. Asian J.* **2020**, *15*, 2403.
- [141] J. Hui, H. Chu, W. Zhang, Y. Shen, W. Chen, Y. Hu, W. Liu, C. Gao, S. Guo, G. Xiao et al., *Nanoscale* **2018**, *10*, 8772.
- [142] J. Warnan, Y. Pellegrin, E. Blart, F. Odobel, *Chem. Commun.* **2012**, *48*, 675.
- [143] J. Jin, *Reac. Kinet. Mech. Cat.* **2020**, *131*, 397.
- [144] X. Wang, W.-Y. Gao, Z. Niu, L. Wojtas, J. A. Perman, Y.-S. Chen, Z. Li, B. Aguila, S. Ma, *Chem. Commun.* **2018**, *54*, 1170.



- [145] T. Ema, Y. Miyazaki, J. Shimonishi, C. Maeda, J.-y. Hasegawa, *J. Am. Chem. Soc.* **2014**, *136*, 15270.
- [146] Y. Mun, S. Lee, K. Kim, S. Kim, S. Lee, J. W. Han, J. Lee, *J. Am. Chem. Soc.* **2019**, *141*, 6254.
- [147] Z.-C. Sun, Y.-B. She, Y. Zhou, X.-F. Song, K. Li, *Molecules* **2011**, *16*, 2960.
- [148] S.-C. Qi, Z.-H. Yang, R.-R. Zhu, X.-J. Lu, D.-M. Xue, X.-Q. Liu, L.-B. Sun, *J. Mater. Chem. A* **2021**, *9*, 24510.
- [149] H. J. Callot, F. Metz, C. Piechocki, *Tetrahedron* **1982**, *38*, 2365.
- [150] D. Inriieri, A. Caselli, E. Gallo, *Eur. J. Inorg. Chem.* **2011**, *2011*, 5071.
- [151] J. L. Maxwell, K. C. Brown, D. W. Bartley, T. Kodadek, *Science* **1992**, *256*, 1544.
- [152] T. Niino, M. Toganoh, B. Andrioletti, H. Furuta, *Chem. Commun.* **2006**, 4335.
- [153] Aoyama Y., M. Asakawa, A. Yamagishi, H. Toi, H. Ogoshi, *J. Am. Chem. Soc.* **1990**, *112*, 3145.
- [154] a) A. F. Holleman, E. Wiberg, N. Wiberg, *Lehrbuch der anorganischen Chemie*, de Gruyter, Berlin, **2007**; b) B. Commerscheidt, R. Gruehn, *Z. anorg. allg. Chem.* **2001**, *627*, 465; c) K. Fagnou, M. Lautens, *Angew. Chem. Int. Ed.* **2002**, *41*, 26.
- [155] S. J. Thompson, M. R. Brennan, S. Y. Lee, G. Dong, *Chem. Soc. Rev.* **2018**, *47*, 929.
- [156] P. Tagliatesta, A. Pastorini, *J. Mol. Catal. A* **2002**, *185*, 127.
- [157] R. Murugesan, A. Thamarachelvan, P. Sami, *J. Incl. Phenom. Macrocycl. Chem.* **1999**, *34*, 235.
- [158] S. Akyüz, A. B. Dempster, R. L. Morehouse, *Spectrochim. Acta* **1974**, *A*, 1989.
- [159] C.-M. Che, J.-S. Huang, *Chem. Commun.* **2009**, 3996.
- [160] a) A. Farokhi, H. Hosseini-Monfared, *New J. Chem.* **2016**, *40*, 5032; b) J. Ji, F. Liu, W. Yang, M. Tan, W. Luo, S.-F. Yin, *ChemCatChem* **2020**, *12*, 4331; c) N. A. Stephenson, A. T. Bell, *J. Mol. Catal. A* **2007**, *275*, 54.
- [161] H.-F. Yao, Y. Yang, H. Liu, F.-G. Xi, E.-Q. Gao, *J. Mol. Catal. A* **2014**, *394*, 57.
- [162] J. Chen, C.-M. Che, *Angew. Chem.* **2004**, *116*, 5058.
- [163] a) P. Ji, X. Feng, P. Oliveres, Z. Li, A. Murakami, C. Wang, W. Lin, *J. Am. Chem. Soc.* **2019**, *141*, 14878; b) A. Dhakshinamoorthy, M. Alvaro, H. Garcia, *Chem. Eur. J.* **2010**, *16*, 8530.

- [164] C. A. Hunter, J. K. M. Sanders, *J. Am. Chem. Soc.* **1990**, *112*, 5525.
- [165] D. Chatterjee, *Inorganica Chim. Acta* **2008**, *361*, 2177.
- [166] D. Mohajer, G. Karimipour, M. Bagherzadeh, *New J. Chem.* **2004**, *28*, 740.
- [167] H. T. D. Nguyen, Y. B. N. Tran, H. N. Nguyen, T. C. Nguyen, F. Gándara, P. T. K. Nguyen, *Inorg. Chem.* **2018**, *57*, 13772.
- [168] M. North, R. Pasquale, *Angew. Chem. Int. Ed.* **2009**, *48*, 2946.
- [169] M. H. Beyzavi, C. J. Stephenson, Y. Liu, O. Karagiari, J. T. Hupp, O. K. Farha, *Front. Energy Res.* **2015**, *2*, 2975.
- [170] a) J. Kim, S.-N. Kim, H.-G. Jang, G. Seo, W.-S. Ahn, *Appl. Catal. A* **2013**, *453*, 175; b) P. T. K. Nguyen, H. T. D. Nguyen, H. N. Nguyen, C. A. Trickett, Q. T. Ton, E. Gutiérrez-Puebla, M. A. Monge, K. E. Cordova, F. Gándara, *ACS Appl. Mater. Inter.* **2018**, *10*, 733.
- [171] Y.-B. Huang, J. Liang, X.-S. Wang, R. Cao, *Chem. Soc. Rev.* **2017**, *46*, 126.
- [172] M. Kielmann, M. O. Senge, *Angew. Chem. Int. Ed.* **2019**, *58*, 418.
- [173] M. Roucan, M. Kielmann, S. J. Connon, S. S. R. Bernhard, M. O. Senge, *Chem. Commun.* **2017**, *54*, 26.
- [174] O. Karagiari, W. Bury, J. E. Mondloch, J. T. Hupp, O. K. Farha, *Angew. Chem. Int. Ed.* **2014**, *53*, 4530.
- [175] a) S. R. G. Balestra, R. Bueno-Perez, S. Hamad, D. Dubbeldam, A. R. Ruiz-Salvador, S. Calero, *Chem. Mater.* **2016**, *28*, 8296; b) F.-X. Coudert, *Chem. Mater.* **2015**, *27*, 1905.
- [176] H. L. B. Boström, S. Bette, S. T. Emmerling, M. W. Terban, B. V. Lotsch, *APL Mater.* **2022**, *10*, 71106.
- [177] M. J. Cliffe, J. A. Hill, C. A. Murray, F.-X. Coudert, A. L. Goodwin, *Phys. Chem. Chem. Phys.* **2015**, *17*, 11586.
- [178] P. Deria, W. Bury, I. Hod, C.-W. Kung, O. Karagiari, J. T. Hupp, O. K. Farha, *Inorg. Chem.* **2015**, *54*, 2185.
- [179] L. Valenzano, B. Civalieri, S. Chavan, S. Bordiga, M. H. Nilsen, S. Jakobsen, K. P. Lillerud, C. Lamberti, *Chem. Mater.* **2011**, *23*, 1700.
- [180] a) P. Brunel, J. Monot, C. E. Kefalidis, L. Maron, B. Martin-Vaca, D. Bourissou, *ACS Catal.* **2017**, *7*, 2652; b) A. Clerc, E. Marelli, N. Adet, J. Monot, B. Martín-Vaca, D. Bourissou, *Chem. Sci.* **2020**, *12*, 435; c) N. Á. Espinosa-Jalapa, D. Ke, N. Nebra, L. Le Goanvic, S. Mallet-Ladeira, J. Monot, B. Martin-Vaca, D. Bourissou, *ACS Catal.* **2014**, *4*,

- 3605; d) N. Nebra, J. Monot, R. Shaw, B. Martin-Vaca, D. Bourissou, *ACS Catal.* **2013**, *3*, 2930.
- [181] M. H. Beyzavi, R. C. Klet, S. Tussupbayev, J. Borycz, N. A. Vermeulen, C. J. Cramer, J. F. Stoddart, J. T. Hupp, O. K. Farha, *J. Am. Chem. Soc.* **2014**, *136*, 15861.
- [182] T. E. Webber, W.-G. Liu, S. P. Desai, C. C. Lu, D. G. Truhlar, R. L. Penn, *ACS Appl. Mater. Inter.* **2017**, *9*, 39342.
- [183] P. Asselin, P. D. Harvey, *ACS Appl. Nano Mater.* **2022**, *5*, 6055.
- [184] H.-J. Son, S. Jin, S. Patwardhan, S. J. Wezenberg, N. C. Jeong, M. So, C. E. Wilmer, A. A. Sarjeant, G. C. Schatz, R. Q. Snurr et al., *J. Am. Chem. Soc.* **2013**, *135*, 862.
- [185] A. J. Lees, *Photophysics of Organometallics*, Springer Berlin / Heidelberg, Berlin, Heidelberg, **2010**.
- [186] G. Lucazeau, L. Guemas, A. Novak, *Inorganica Chim. Acta* **1976**, *20*, 11.
- [187] a) L. Favereau, A. Crossen, J. B. Kelber, J. Q. Gong, R. M. Oetterli, J. Cremers, L. M. Herz, H. L. Anderson, *J. Am. Chem. Soc.* **2015**, *137*, 14256; b) M. A. Jinks, H. Sun, C. A. Hunter, *Org. Biomol. Chem.* **2014**, *12*, 1440.
- [188] G. Sahara, O. Ishitani, *Inorg. Chem.* **2015**, *54*, 5096.
- [189] J. Hawecker, J.-M. Lehn, R. Ziessel, *Helv. Chim. Acta* **1986**, *69*, 1990.
- [190] P. M. Stanley, C. Thomas, E. Thyraug, A. Urstoeger, M. Schuster, J. Hauer, B. Rieger, J. Warnan, R. A. Fischer, *ACS Catal.* **2021**, *11*, 871.
- [191] a) P. M. Stanley, J. Haimerl, C. Thomas, A. Urstoeger, M. Schuster, N. B. Shustova, A. Casini, B. Rieger, J. Warnan, R. A. Fischer, *Angew. Chem. Int. Ed.* **2021**, *60*, 17854; b) Y. Benseghir, A. Lemarchand, M. Duguet, P. Mialane, M. Gomez-Mingot, C. Roch-Marchal, T. Pino, M.-H. Ha-Thi, M. Haouas, M. Fontecave et al., *J. Am. Chem. Soc.* **2020**, *142*, 9428; c) X. Wang, F. M. Wisser, J. Canivet, M. Fontecave, C. Mellot-Draznieks, *ChemSusChem* **2018**, *11*, 3315; d) P. Deria, W. Bury, I. Hod, C.-W. Kung, O. Karagiari, J. T. Hupp, O. K. Farha, *Inorg. Chem.* **2015**, *54*, 2185.
- [192] a) C. D. Windle, M. W. George, R. N. Perutz, P. A. Summers, X. Z. Sun, A. C. Whitwood, *Chem. Sci.* **2015**, *6*, 6847; b) P. Lang, M. Pfrunder, G. Quach, B. Braun-Cula, E. G. Moore, M. Schwalbe, *Chem. Eur. J.* **2019**, *25*, 4509; c) C. D. Windle, M. V. Câmpian, A.-K. Duhme-Klair, E. A. Gibson, R. N. Perutz, J. Schneider, *Chem. Commun.* **2012**, *48*, 8189.

- [193] S. Meister, R. O. Reithmeier, M. Tschurl, U. Heiz, B. Rieger, *ChemCatChem* **2015**, *7*, 690.
- [194] J. Jin, *New J. Chem.* **2020**, *44*, 15362.
- [195] R. Hariri, S. Dehghanpour, *Appl. Organomet. Chem.* **2021**, *34*, e5993.
- [196] E. E. Benson, C. P. Kubiak, *Chem. Commun.* **2012**, *48*, 7374.
- [197] P. M. Stanley, K. Hemmer, M. Hegelmann, A. Schulz, M. Park, M. Elsner, M. Cokoja, J. Warnan, *Chem. Sci.* **2022**, *13*, 12164.
- [198] A. A. Yakovenko, Z. Wei, M. Wriedt, J.-R. Li, G. J. Halder, H.-C. Zhou, *Cryst. Growth Des.* **2014**, *14*, 5397.
- [199] P. M. Stanley, M. Parkulab, B. Rieger, J. Warnan, R. A. Fischer, *Faraday Discuss.* **2021**, *231*, 281.
- [200] S. M. Shaikh, S. Ilic, B. J. Gibbons, X. Yang, E. Jakubikova, A. J. Morris, *J. Phys. Chem. C* **2021**, *125*, 22998.
- [201] a) J. Yu, J. Park, A. van Wyk, G. Rumbles, P. Deria, *J. Am. Chem. Soc.* **2018**, *140*, 10488; b) S. Goswami, I. Hod, J. D. Duan, C.-W. Kung, M. Rimoldi, C. D. Malliakas, R. H. Palmer, O. K. Farha, J. T. Hupp, *J. Am. Chem. Soc.* **2019**, *141*, 17696.
- [202] S. S. Rajasree, J. Yu, S. M. Pratik, X. Li, R. Wang, A. S. Kumbhar, S. Goswami, C. J. Cramer, P. Deria, *J. Am. Chem. Soc.* **2022**, *144*, 1396.
- [203] G. Kickelbick, U. Schubert, *Chem. Ber.* **1997**, *130*, 473.
- [204] a) K. Kiyosawa, N. Shiraishi, T. Shimada, D. Masui, H. Tachibana, S. Takagi, O. Ishitani, D. A. Tryk, H. Inoue, *J. Phys. Chem. C* **2009**, *113*, 11667; b) R. T. Hayes, C. J. Walsh, M. R. Wasielewski, *J. Phys. Chem. A* **2004**, *108*, 2375; c) J. Petersson, J. Henderson, A. Brown, L. Hammarström, C. P. Kubiak, *J. Phys. Chem. C* **2015**, *119*, 4479; d) M. Morisue, N. Haruta, D. Kalita, Y. Kobuke, *Chem. Eur. J.* **2006**, *12*, 8123; e) J. Karolczak, D. Kowalska, A. Lukaszewicz, A. Maciejewski, R. P. Steer, *J. Phys. Chem. A* **2004**, *108*, 4570; f) H. Chosrowjan, S. Tanigichi, T. Okada, S. Takagi, T. Arai, K. Tokumam, *Chem. Phys. Lett.* **1995**, *242*, 644.
- [205] a) M. Pschenitzza, S. Meister, A. von Weber, A. Kartouzian, U. Heiz, B. Rieger, *ChemCatChem* **2016**, *8*, 2688; b) J. K. Nganga, C. R. Samanamu, J. M. Tanski, C. Pacheco, C. Saucedo, V. S. Batista, K. A. Grice, M. Z. Ertem, A. M. Angeles-Boza, *Inorg. Chem.* **2017**, *56*, 3214; c) Y. Kou, Y. Nabetani, D. Masui, T. Shimada, S. Takagi, H. Tachibana, H. Inoue, *J. Am. Chem. Soc.* **2014**, *136*, 6021.

- [206] S. Choi, W.-J. Jung, K. Park, S.-Y. Kim, J.-O. Baeg, C. H. Kim, H.-J. Son, C. Pac, S. O. Kang, *ACS Appl. Mater. Inter.* **2021**, *13*, 2710.
- [207] K. D. Nguyen, C. Kutzscher, S. Ehrling, I. Senkovska, V. Bon, M. de Oliveira, T. Gutmann, G. Buntkowsky, S. Kaskel, *J. Catal.* **2019**, *377*, 41.
- [208] a) J. Rouquerol, P. Llewellyn, F. Rouquerol in *Studies in Surface Science and Catalysis*, Elsevier, **2007**, pp. 49–56; b) M. Thommes, K. Kaneko, A. V. Neimark, J. P. Olivier, F. Rodriguez-Reinoso, J. Rouquerol, K. S.W. Sing, *Pure Appl. Chem.* **2015**, *87*, 1051.
- [209] F. Neese, *Wiley Interdiscip. Rev. Comput. Mol. Sci.* **2012**, *2*, 73.
- [210] a) A. D. J. Becke, *J. Chem. Phys.* **1993**, *98*, 5648; b) C. Lee, W. Yang, R. G. Parr, *Phys. Rev. B* **1988**, *37*, 785.
- [211] a) S. Grimme, J. Antony, S. Ehrlich, H. Krieg, *J. Chem. Phys.* **2010**, *132*, 154104; b) S. Grimme, S. Ehrlich, L. Goerigk, *J. Comput. Chem.* **2011**, *32*, 1456.
- [212] F. Weigend, R. Ahlrichs, *Phys. Chem. Chem. Phys.* **2005**, *7*, 3297.
- [213] a) A. A. Coelho, *J. Appl. Crystallogr.* **2018**, *51*, 210; b) G. S. Pawley, *J. Appl. Crystallogr.* **1981**, *14*, 357.
- [214] J. S. Lindsey, J. N. Woodford, *Inorg. Chem.* **1995**, *34*, 1063.
- [215] E. Rousset, D. Chartrand, I. Ciofini, V. Marvaud, G. S. Hanan, *Chem. Commun.* **2015**, *51*, 9261.
- [216] P. Wolf, S. L. Heath, J. A. Thomas, *Inorganica Chim. Acta* **2003**, *355*, 280.
- [217] B. W. Pfennig, P. Chen, T. J. Meyer, *Inorg. Chem.* **1996**, *35*, 2898.
- [218] P. Deria, J. E. Mondloch, E. Tylianakis, P. Ghosh, W. Bury, R. Q. Snurr, J. T. Hupp, O. K. Farha, *J. Am. Chem. Soc.* **2013**, *135*, 16801.

## 7. Appendix

### 7.1. Material Characterization

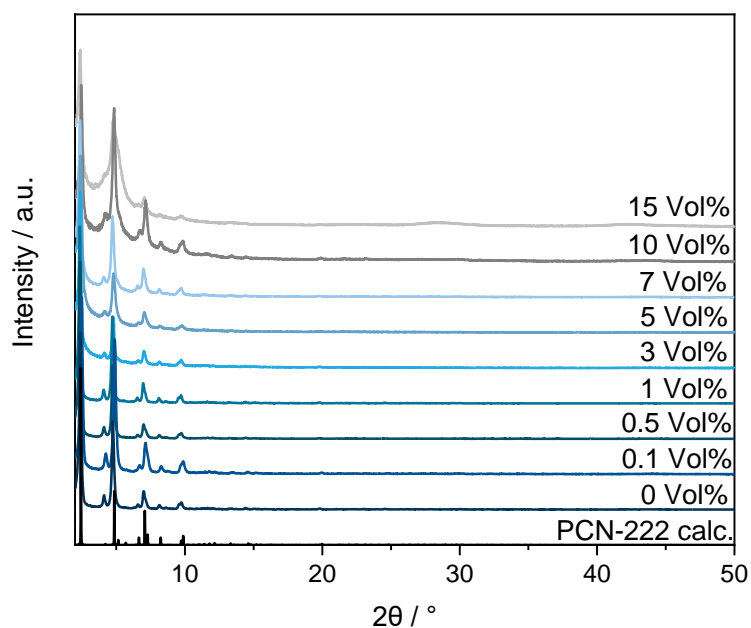


Figure A 1: PXRD pattern of PCN-222 synthesized with different Vol% of water (bidistilled) added during solvothermal synthesis in comparison to the calculated pattern of PCN-222.

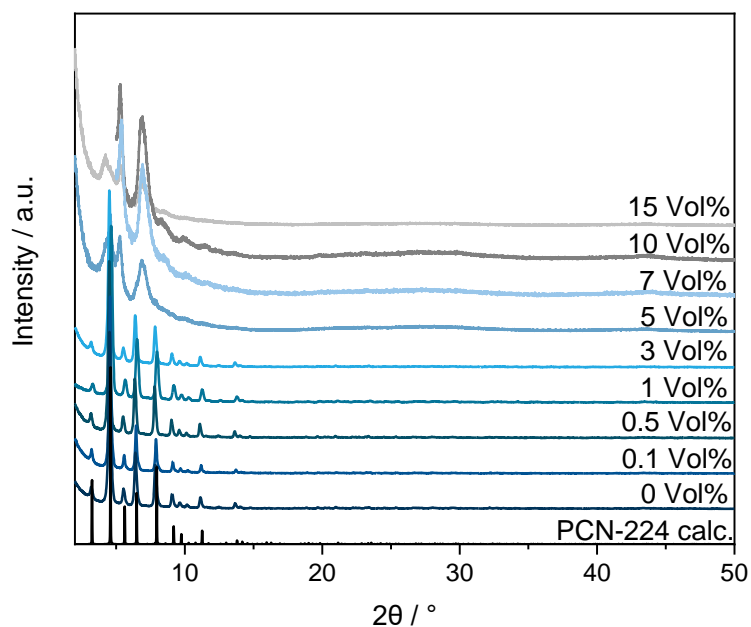


Figure A 2: PXRD pattern of PCN-224 synthesized with different Vol% of water (bidistilled) added during solvothermal synthesis in comparison to the calculated pattern of PCN-224.

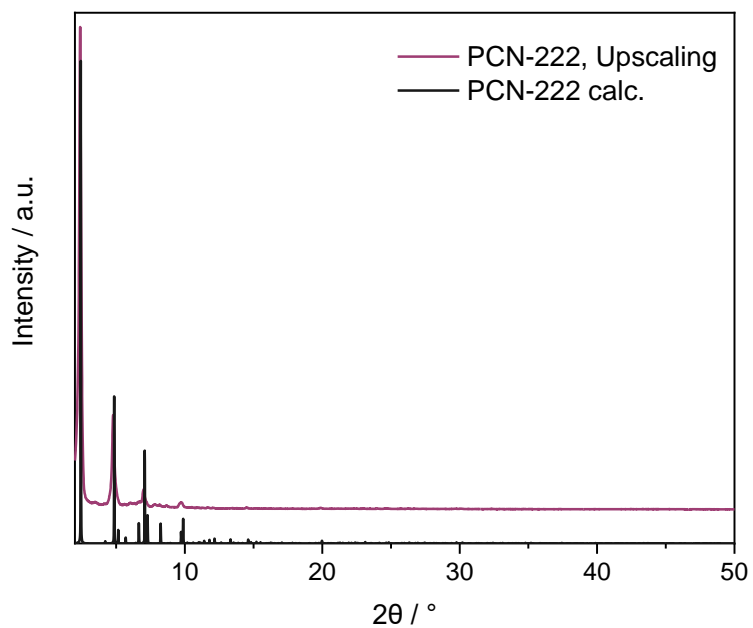


Figure A 3: PXRd pattern of PCN-222 with an upscaling factor of 5 in comparison to the calculated pattern of PCN-222.

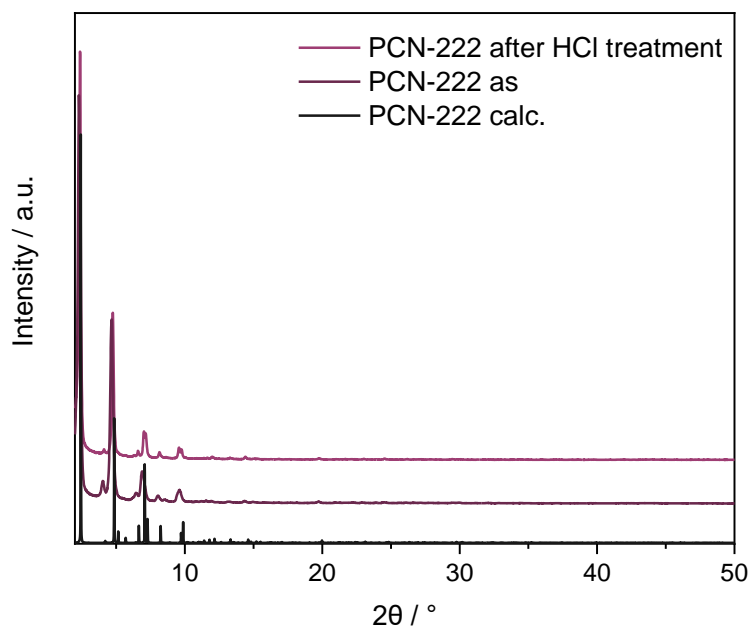


Figure A 4: PXRd pattern of PCN-222 after HCl treatment and PCN-222 in comparison to the calculated pattern of PCN-222.

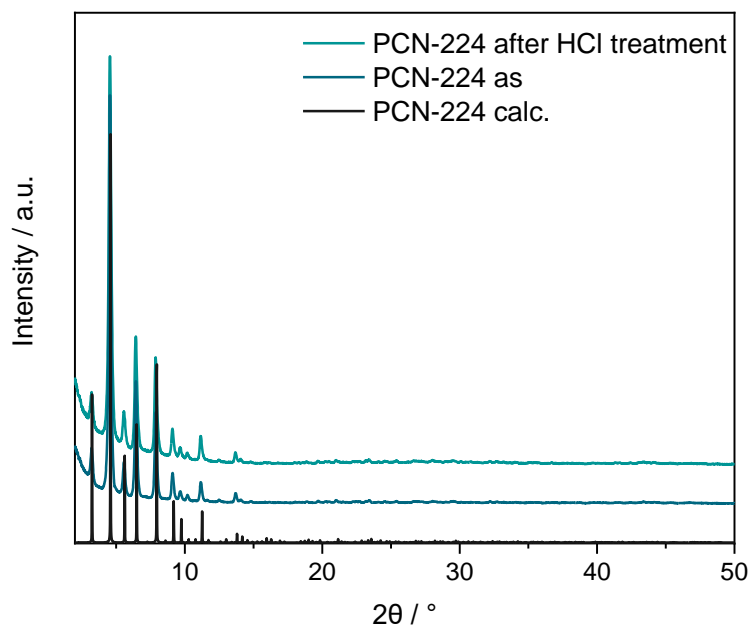


Figure A 5: PXRD pattern of PCN-224 after HCl treatment and PCN-224 in comparison to the calculated pattern of PCN-224.

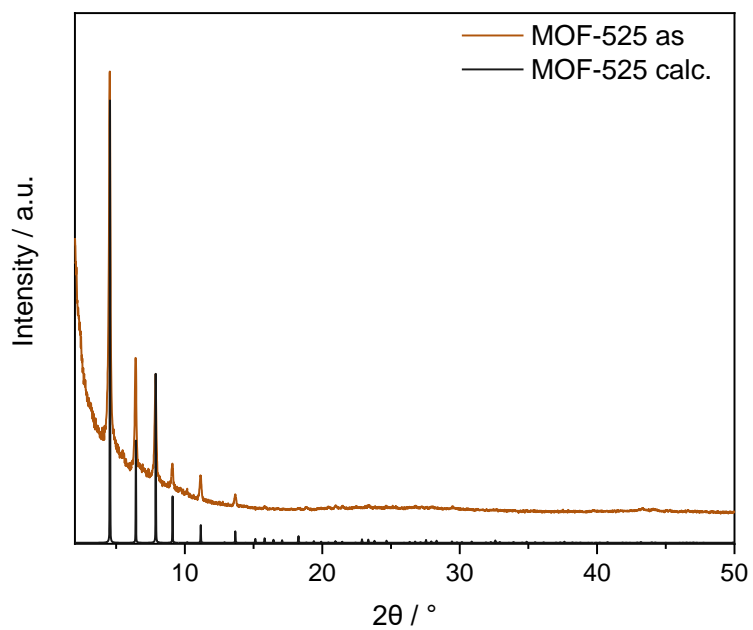


Figure A 6: PXRD pattern of MOF-525 in comparison to the calculated pattern of MOF-525.



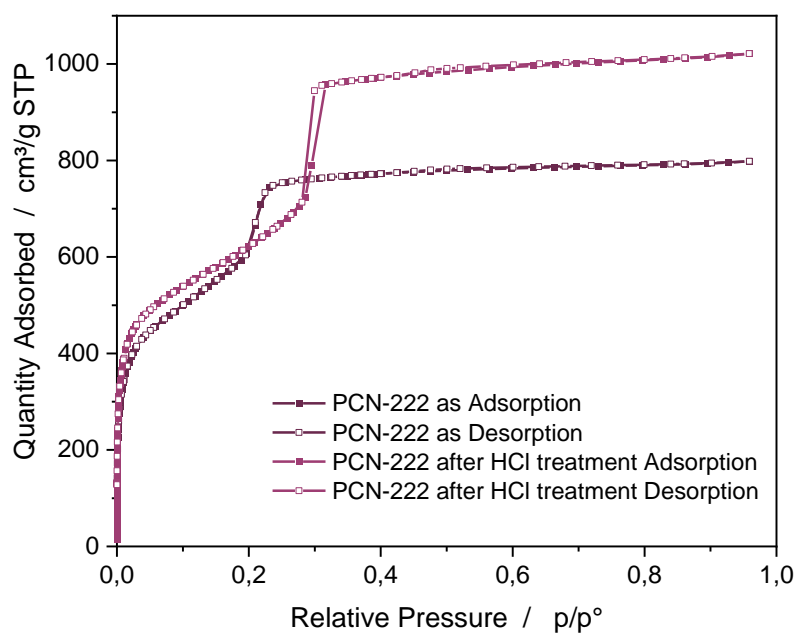


Figure A 7: N<sub>2</sub> sorption measurements at 77 K of PCN-222 and PCN-222 after HCl treatment.

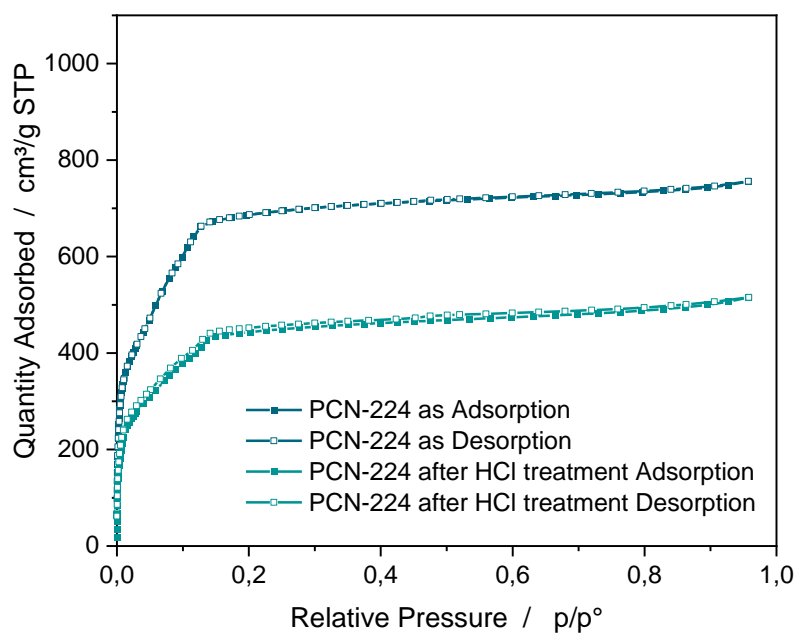


Figure A 8: N<sub>2</sub> sorption measurements at 77 K of PCN-224 and PCN-224 after HCl treatment.

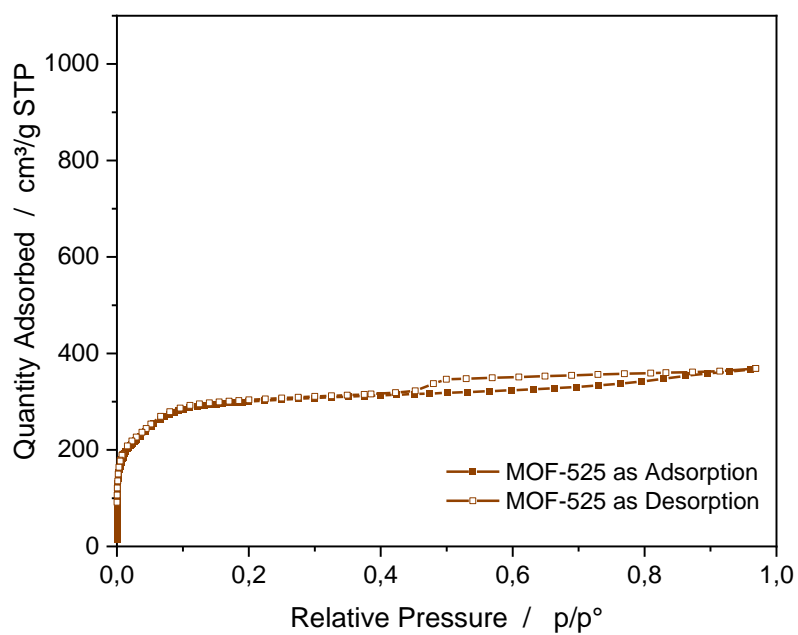


Figure A 9: N<sub>2</sub> sorption measurements at 77 K of MOF-525.

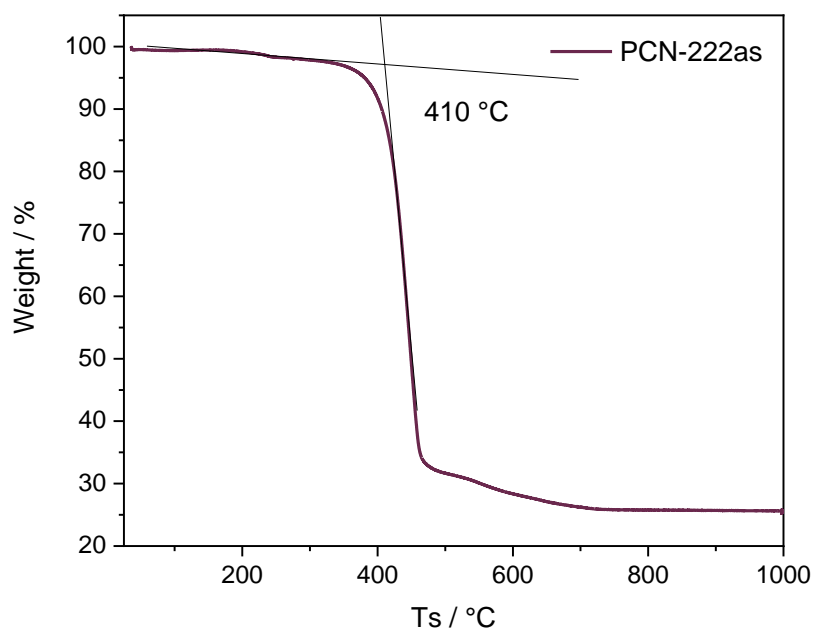


Figure A 10: TGA curve of as-synthesized PCN-222 with its decomposition temperature.

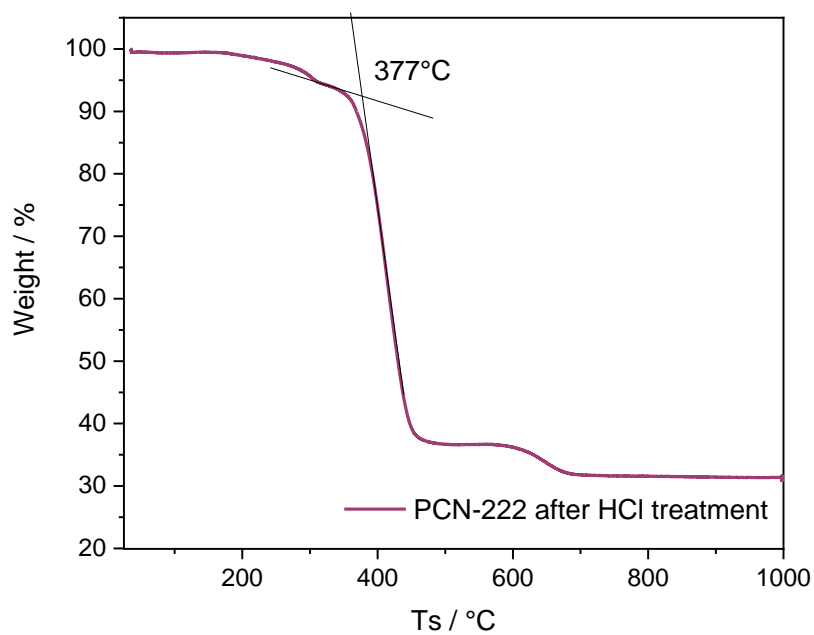


Figure A 11: TGA curve of PCN-222 after HCl treatment with its decomposition temperature.

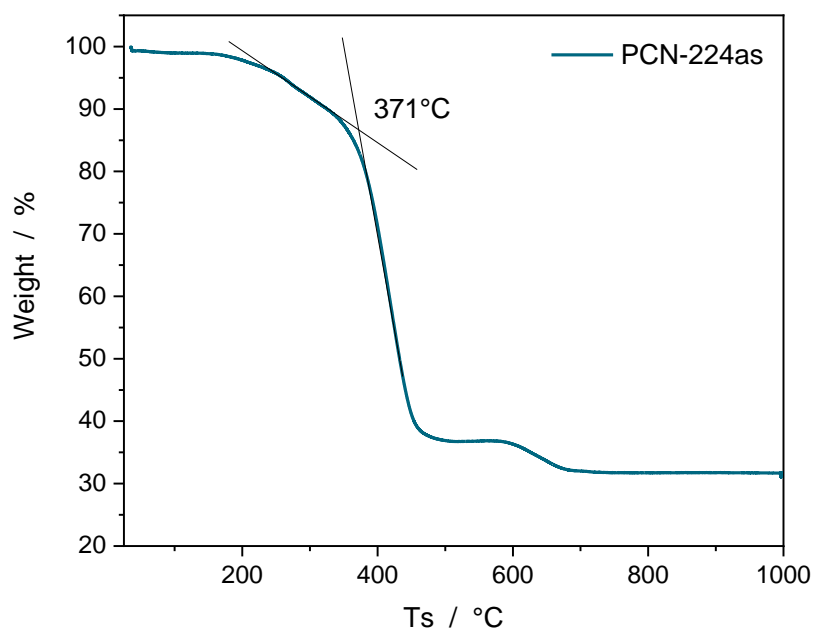


Figure A 12: TGA curve of as-synthesized PCN-224 with its decomposition temperature.

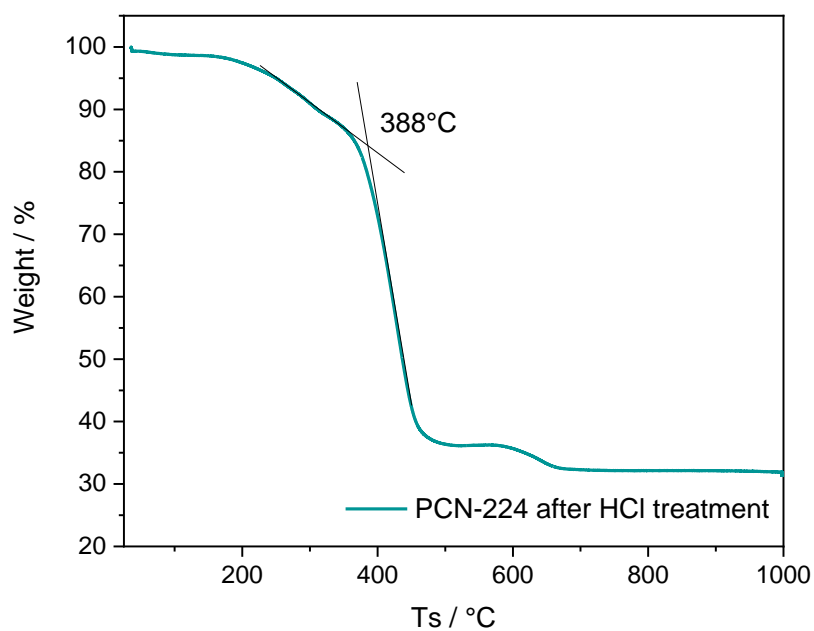


Figure A 13: TGA curve of PCN-224 after HCl treatment with its decomposition temperature.

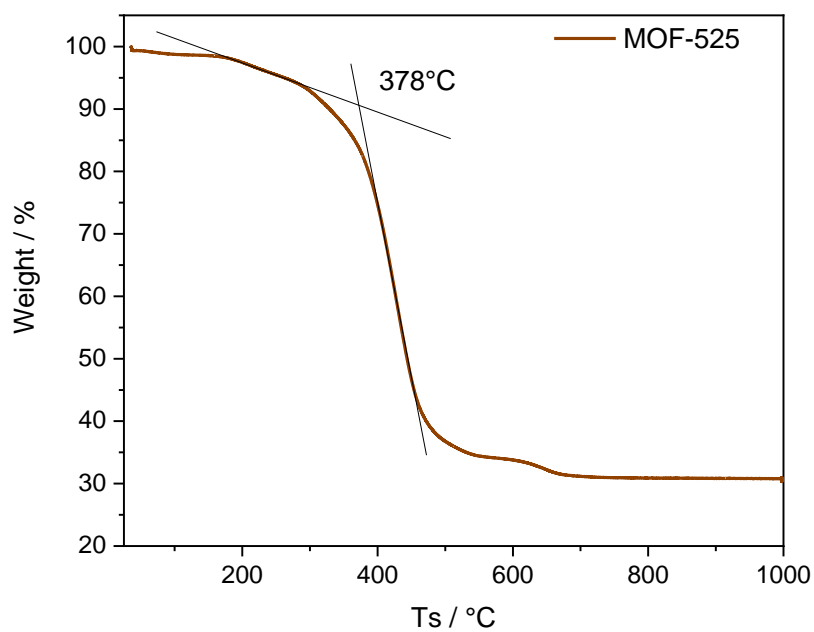


Figure A 14: TGA curve of as-synthesized MOF-525 with its decomposition temperature.

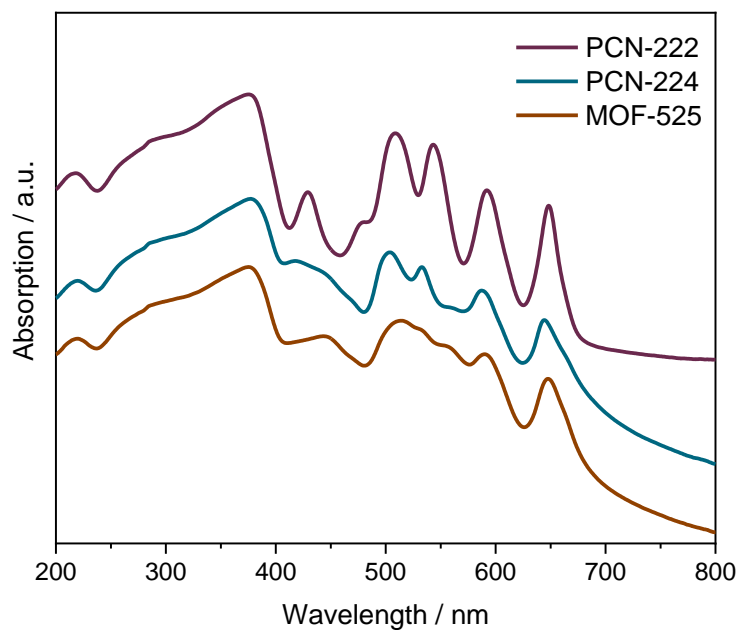


Figure A 15: Solid-state UV-vis spectra of PCN-222 (top), PCN-224 (middle) and MOF-525 (bottom).

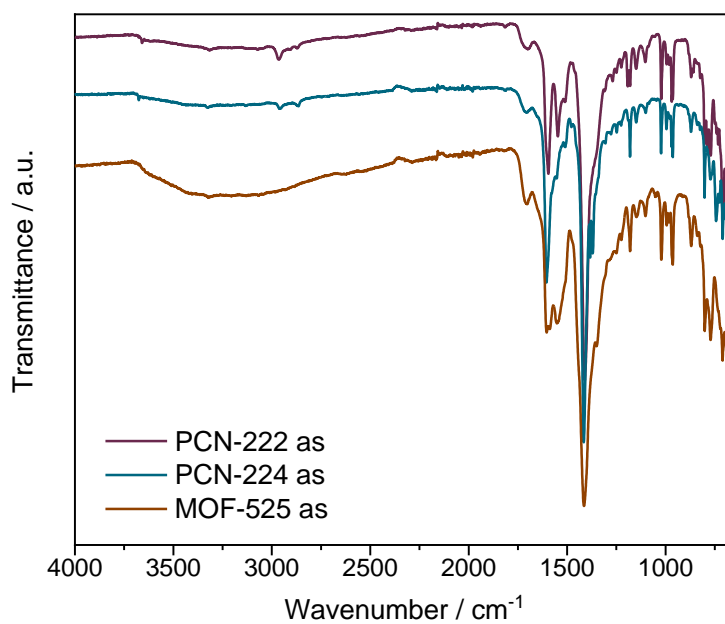


Figure A 16: IR spectra of as synthesized (as) PCN-222 (top), PCN-224 (middle) and MOF-525 (bottom).

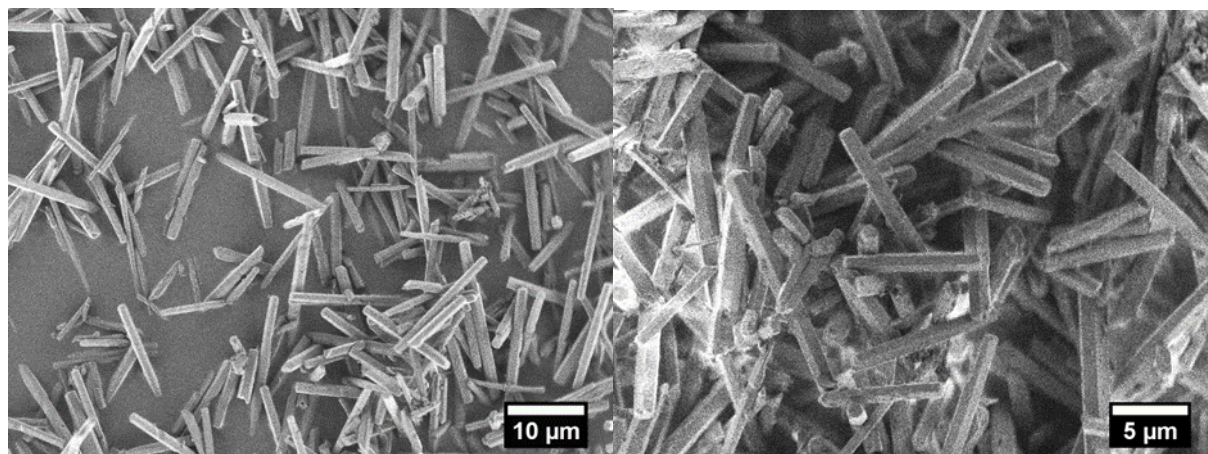


Figure A 17: SEM images of PCN-222 and different magnifications.

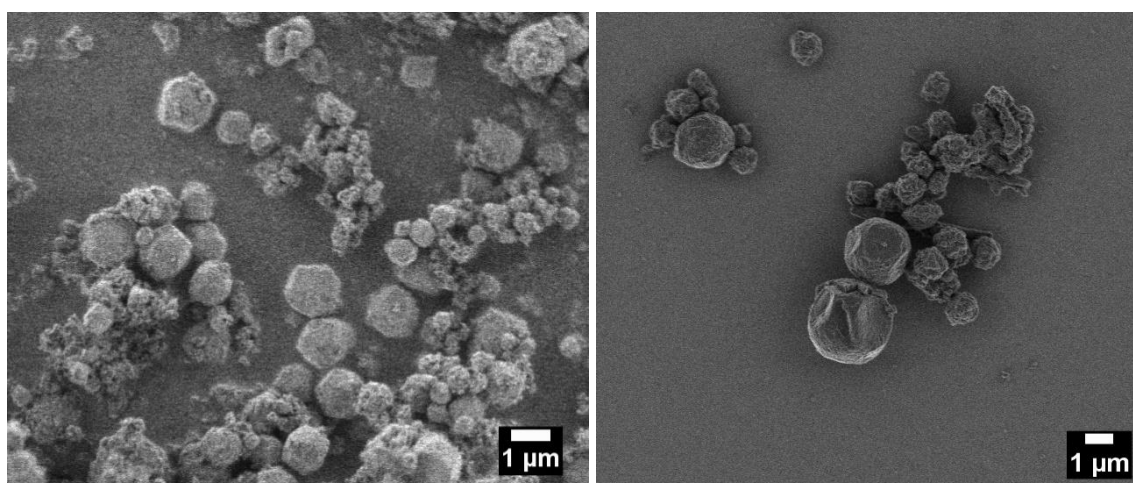


Figure A 18: SEM images of PCN-224 (left) and MOF-525 (right).

## 7.2. Metalation Strategies

### Rhodium metalation

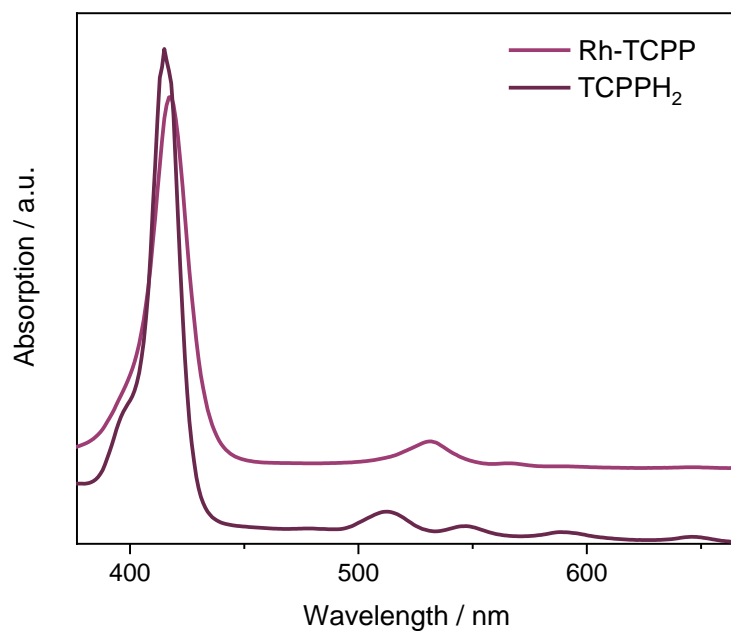


Figure A 19: UV-vis spectra of Rh-TCPP and TCPPh<sub>2</sub> in EtOH.

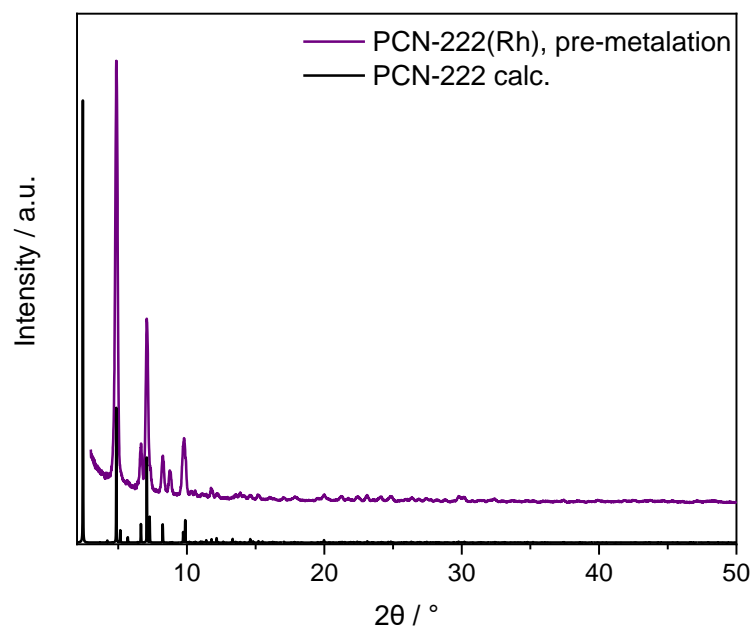


Figure A 20: PXRD pattern of PCN-222(Rh), synthesized via the pre-metalation approach, in comparison to the calculated pattern of PCN-222.

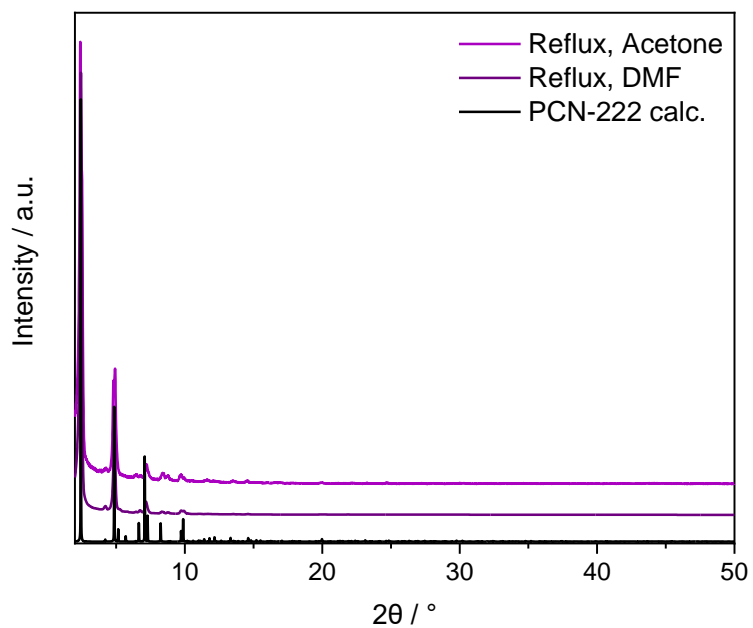


Figure A 21: PXRD pattern of PCN-222(Rh), synthesized under refluxing conditions in different solvents, in comparison to the calculated pattern of PCN-222.

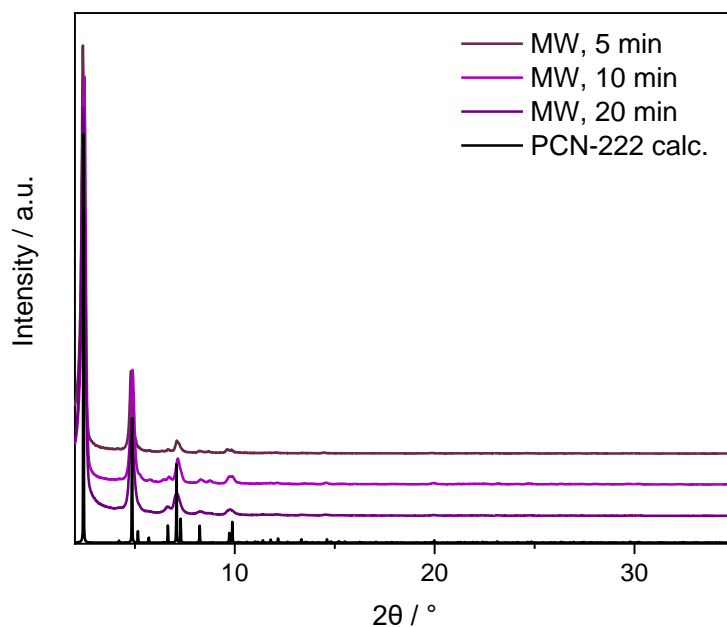


Figure A 22: PXRD pattern of PCN-222(Rh), synthesized via the microwave approach varying the reaction time, in comparison to the calculated pattern of PCN-222.



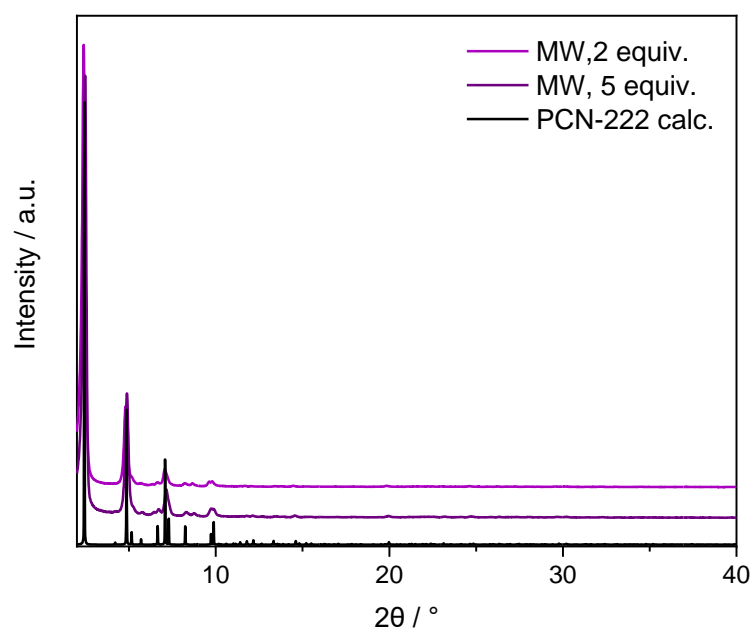


Figure A 23: PXRD pattern of PCN-222(Rh), synthesized via the microwave approach varying the metal equivalents, in comparison to the calculated pattern of PCN-222.

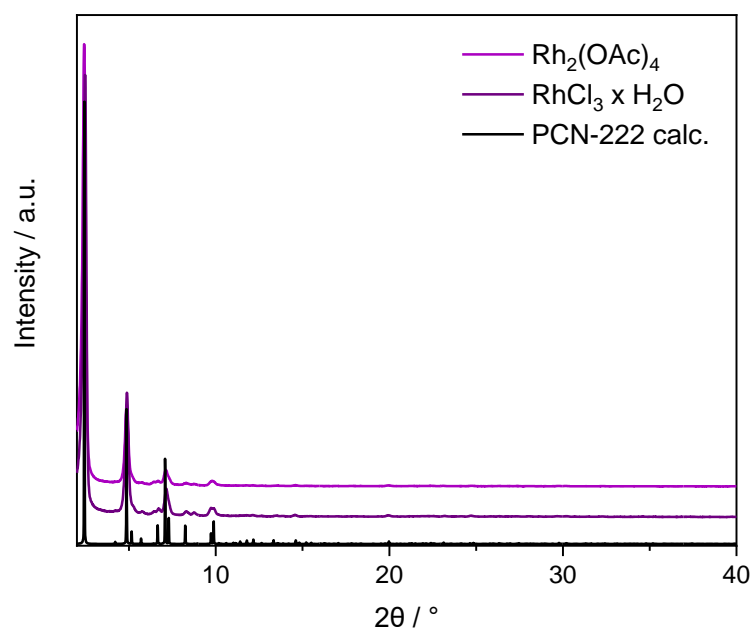


Figure A 24: PXRD pattern of PCN-222(Rh), synthesized via the microwave approach varying the Rh precursor, in comparison to the calculated pattern of PCN-222.

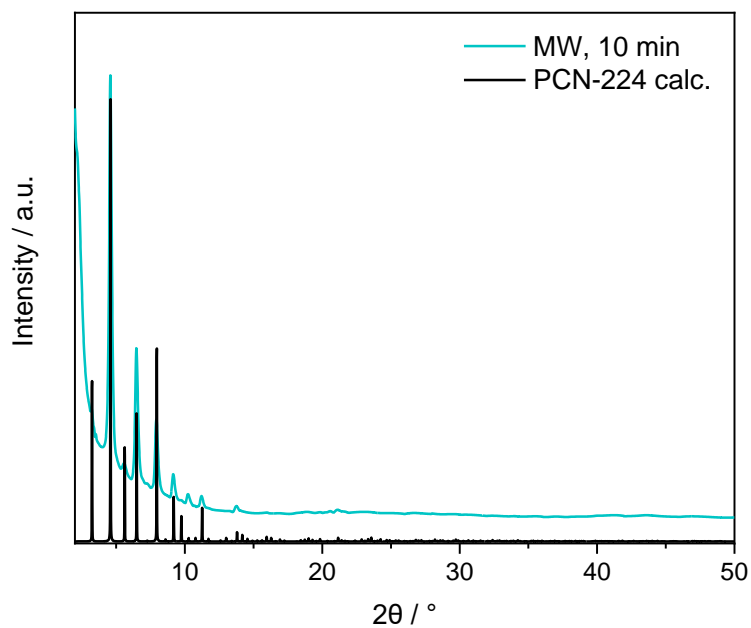


Figure A 25: PXR D pattern of PCN-224(Rh), synthesized via the microwave approach, in comparison to the calculated pattern of PCN-224.

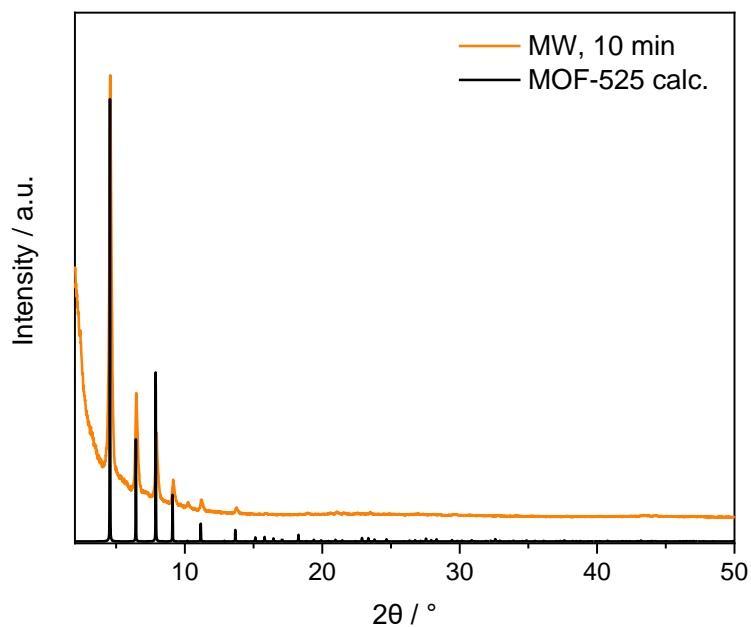


Figure A 26: PXR D pattern of MOF-525(Rh), synthesized via the microwave approach, in comparison to the calculated pattern of MOF-525.

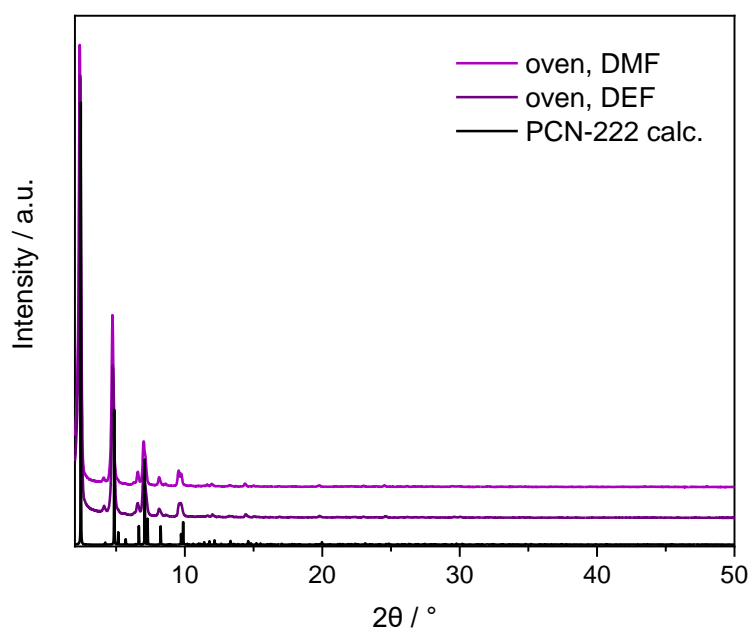


Figure A 27: PXRD pattern of PCN-222(Rh), synthesized in an oven varying the solvent, in comparison to the calculated pattern of PCN-222.

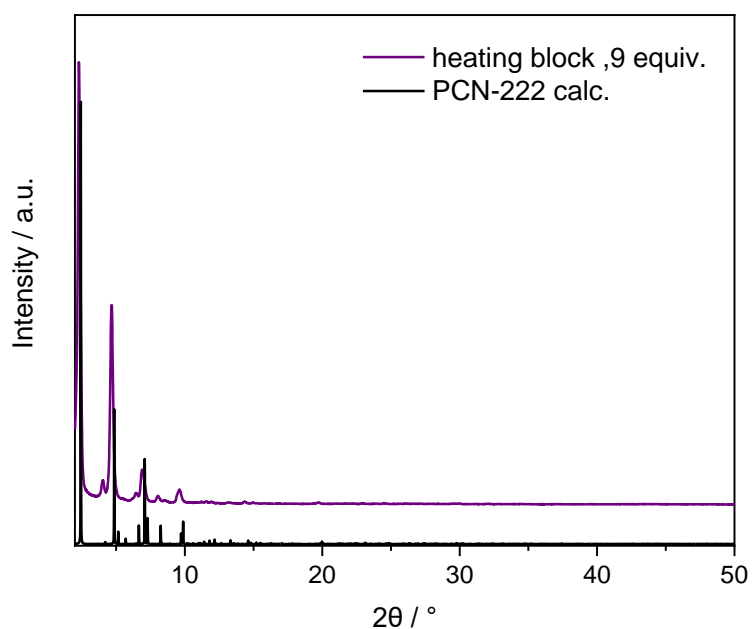


Figure A 28: PXRD pattern of PCN-222(Rh), synthesized via heating in an aluminum heating block, in comparison to the calculated pattern of PCN-222.

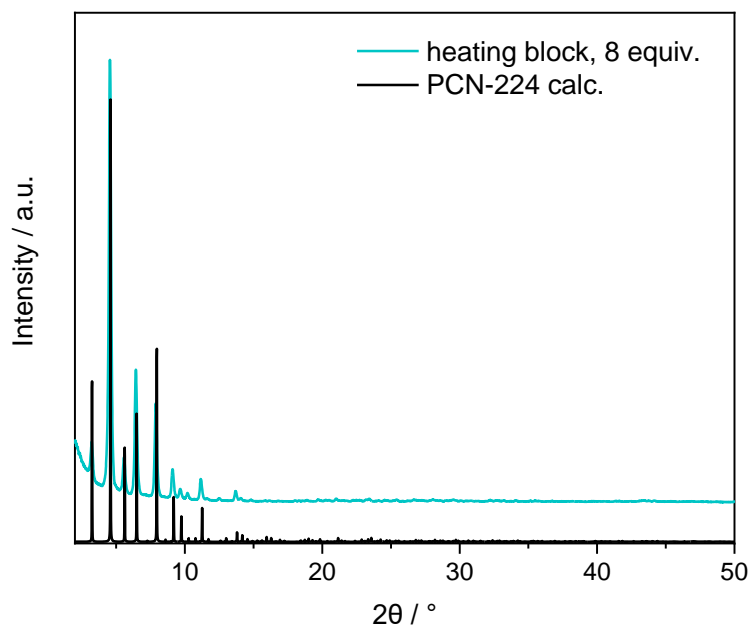


Figure A 29: PXRD pattern of PCN-224(Rh), synthesized via heating in an aluminum heating block, in comparison to the calculated pattern of PCN-224.

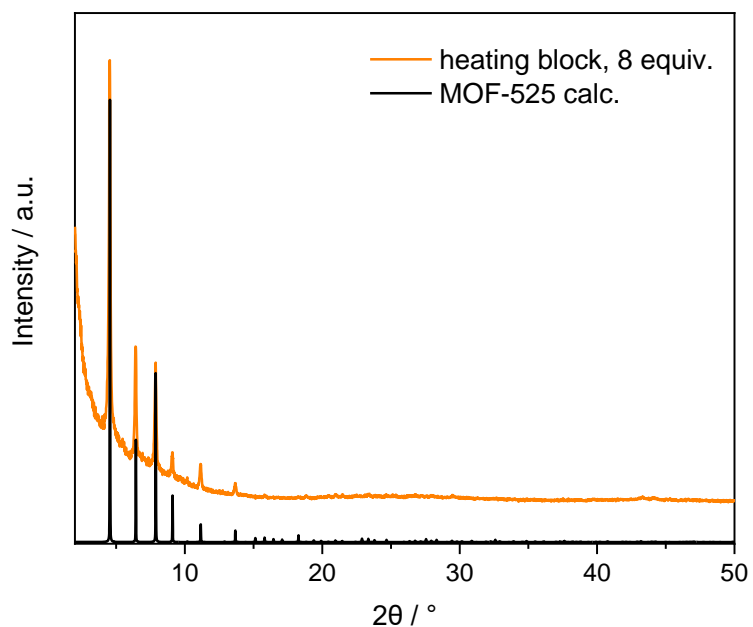


Figure A 30: PXRD pattern of MOF-525(Rh), synthesized via heating in an aluminum heating block, in comparison to the calculated pattern of MOF-525.

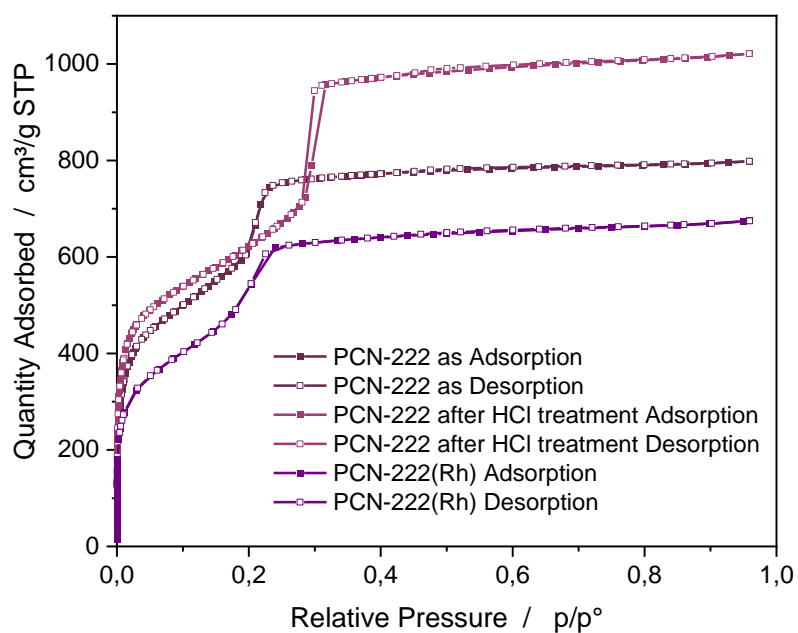


Figure A 31: N<sub>2</sub> adsorption isotherms at 77 K for PCN-222, PCN-222 after HCl treatment and PCN-222(Rh).

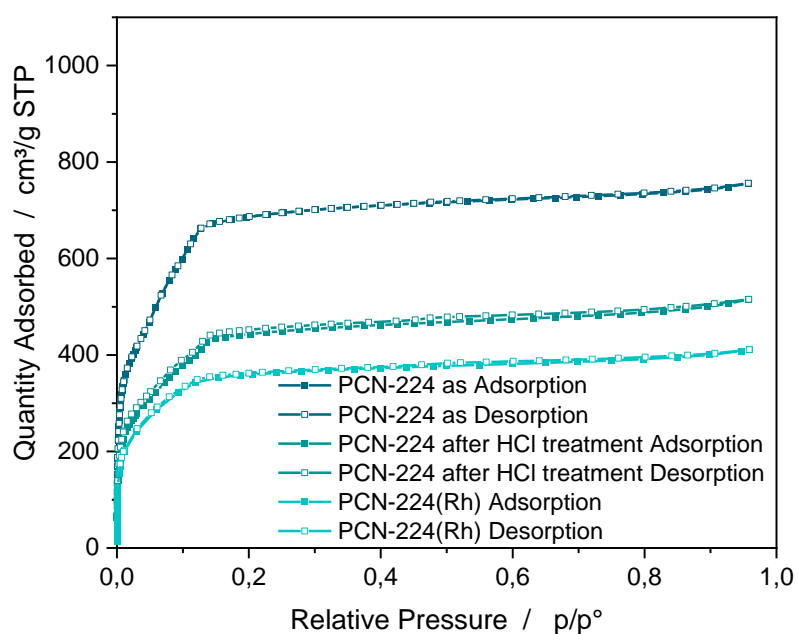


Figure A 32: N<sub>2</sub> adsorption isotherms at 77 K for PCN-224, PCN-224 after HCl treatment and PCN-224(Rh).

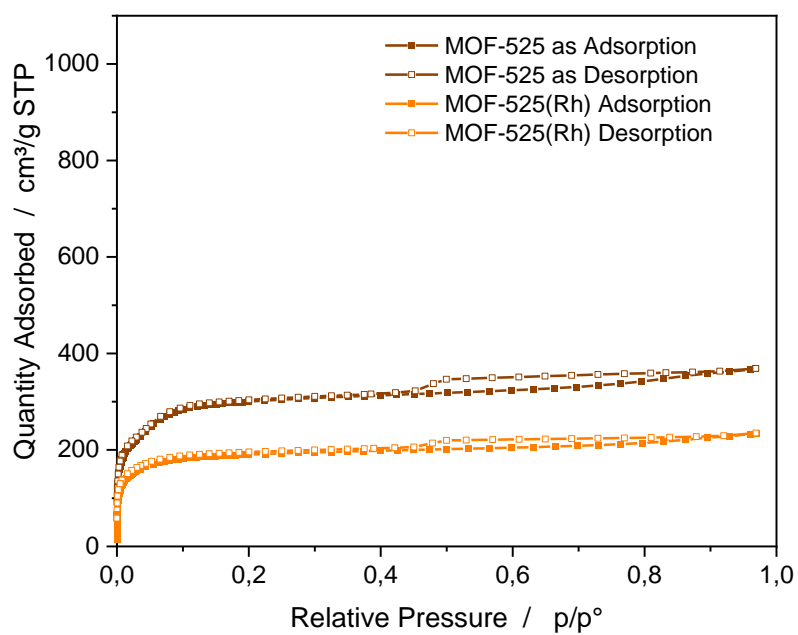


Figure A 33: N<sub>2</sub> adsorption isotherms at 77 K for MOF-525 and MOF-525(Rh).

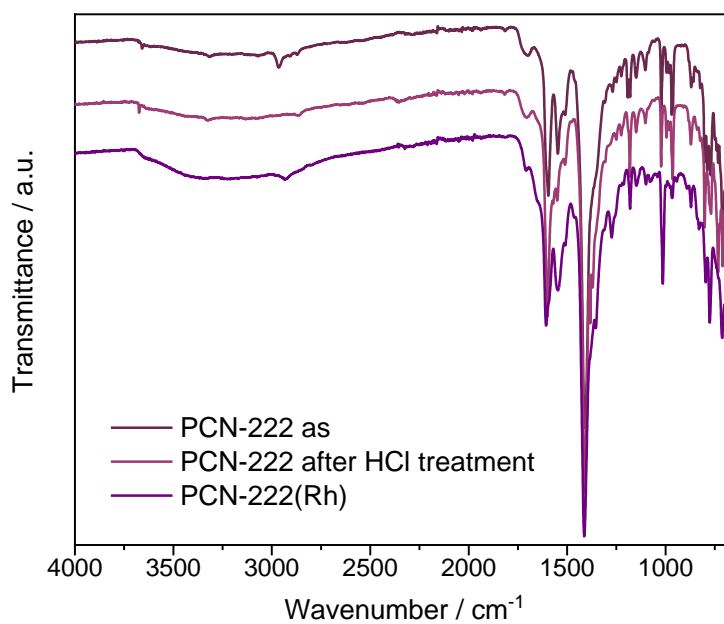


Figure A 34: IR spectra of PCN-222, PCN-222 after HCl treatment and PCN-222(Rh).

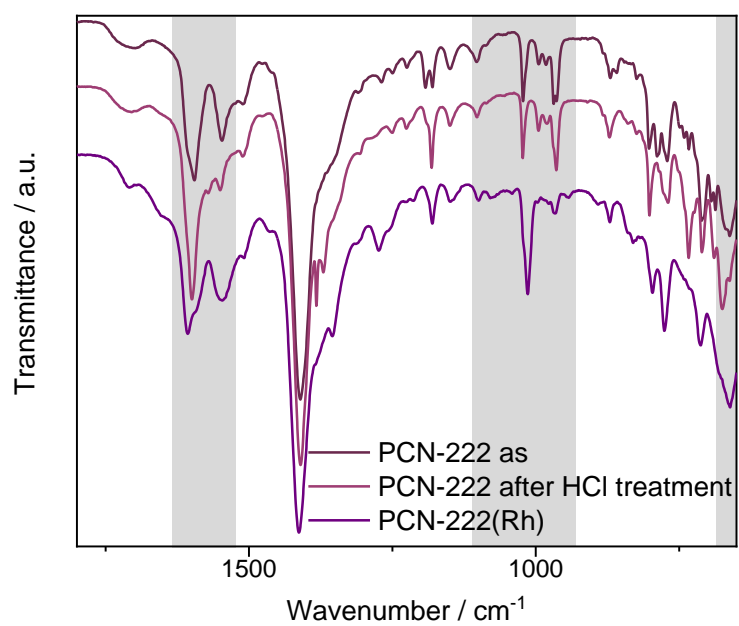


Figure A 35: IR spectra of PCN-222, PCN-222 after HCl treatment and PCN-222(Rh) in the range of 1800 – 650 cm<sup>-1</sup>.

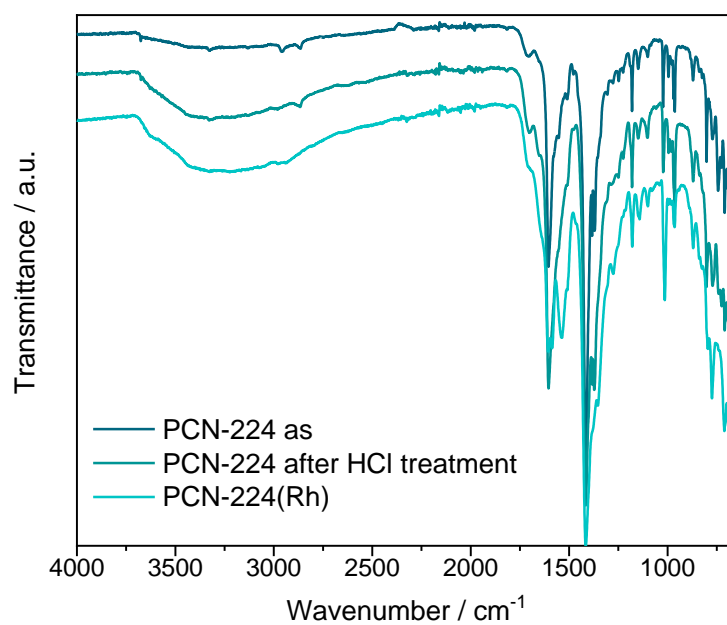


Figure A 36: IR spectra of PCN-224, PCN-224 after HCl treatment and PCN-224(Rh).

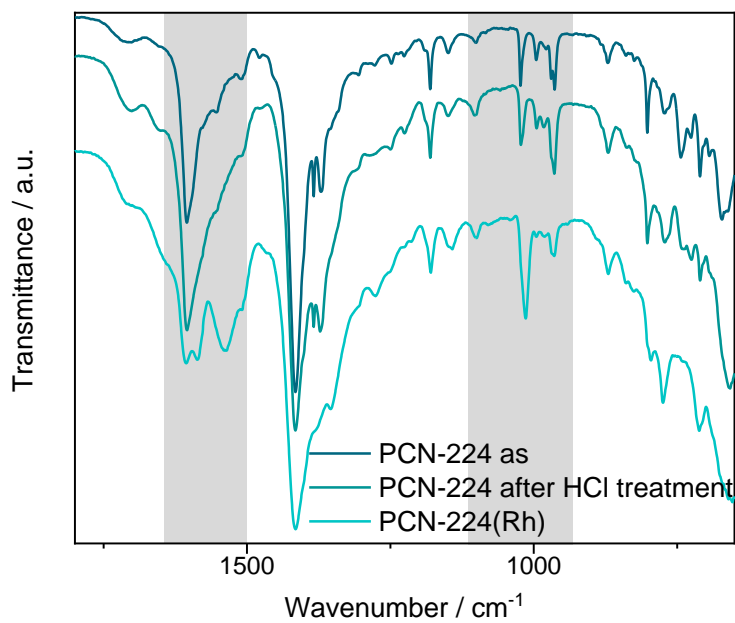


Figure A 37: IR spectra of PCN-224, PCN-224 after HCl treatment and PCN-224(Rh) in the range of 1800 – 650  $\text{cm}^{-1}$ .

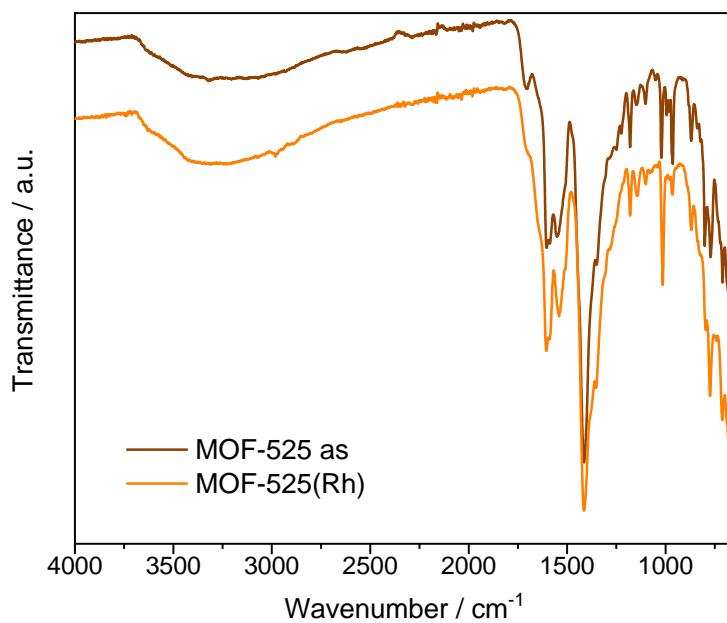


Figure A 38: IR spectra of MOF-525 and MOF-525(Rh).



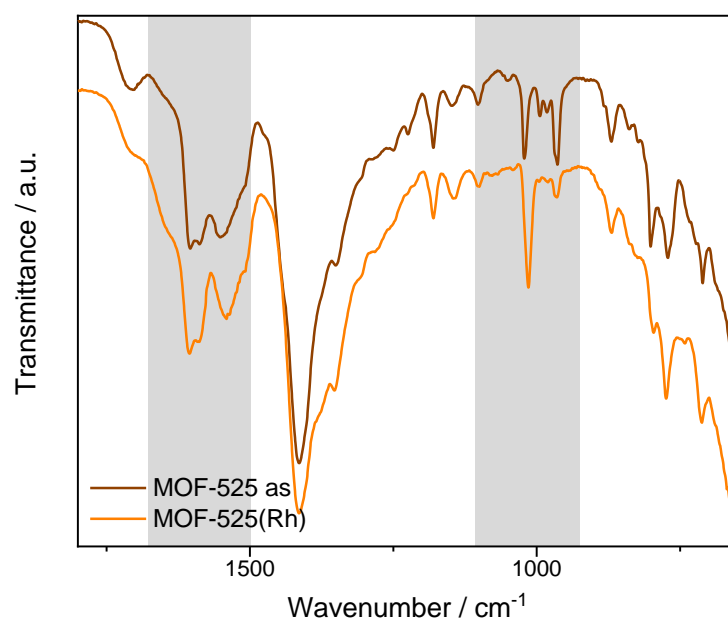


Figure A 39: IR spectra of MOF-525 and MOF-525(Rh) in the range of 1800 – 650 cm<sup>-1</sup>.

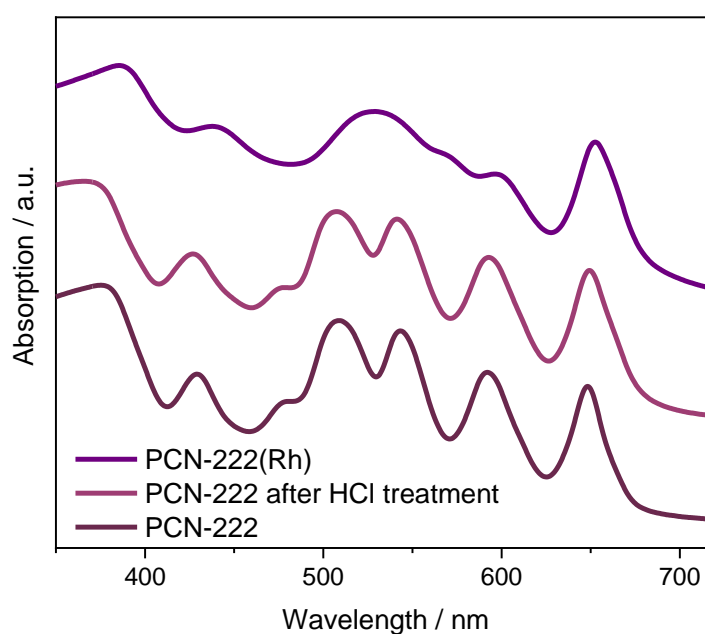


Figure A 40: Solid-state UV-vis spectra of PCN-222, PCN-222 after HCl treatment and PCN-222(Rh).

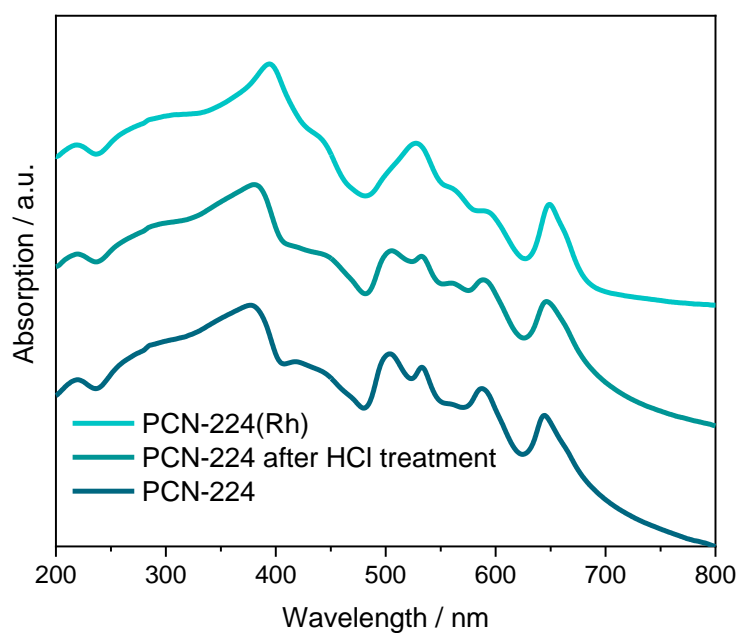


Figure A 41: Solid-state UV-vis spectra of PCN-224, PCN-224 after HCl treatment and PCN-224(Rh).

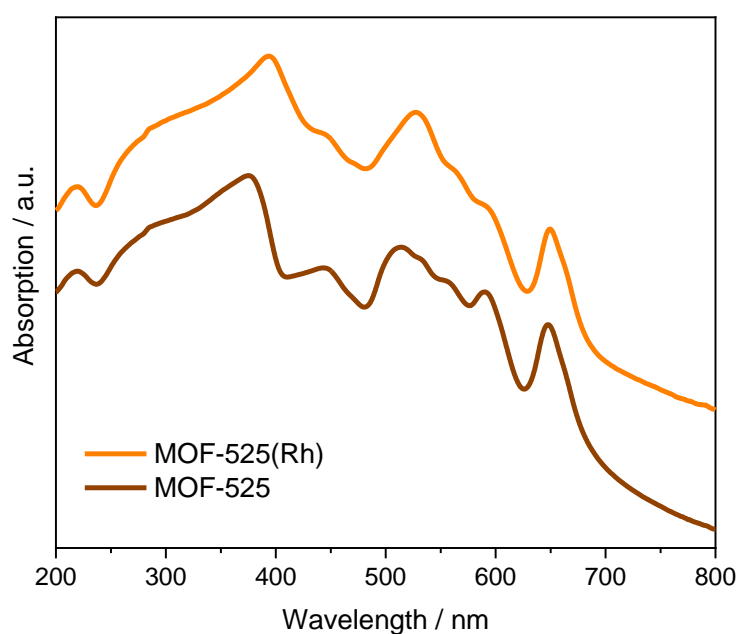


Figure A 42: Solid-state UV-vis spectra of MOF-525 and MOF-525(Rh).

Table A 1: Wt% of Rh, Zr:Rh ratios and approximated %Linker metalation (calculated with the ideal sum formula) for the metalation of PCN-222 with Rh under reflux conditions (15 h) with variation of the solvent. Quantities of Rh and Zr were determined by ICP-MS.

Entry	Metal precursor	Metal equivalents	Solvent	wt% Rh	Zr:Rh	% Linker metalated
<b>1</b>	RhCl <sub>3</sub> · xH <sub>2</sub> O	2.5	DMF	1.80	7.49	22
<b>2</b>	RhCl <sub>3</sub> · xH <sub>2</sub> O	1.2	Acetone	9.59	1.27	127

Table A 2: Wt% of Rh, Zr:Rh ratios and approximated %Linker metalation (calculated with the ideal sum formula) for the metalation of PCN-222 with Rh using the microwave approach. The metal precursor, metal equivalents, reaction time were varied. Quantities of Rh and Zr were determined by ICP-MS.

Entry	Metal precursor	Metal equivalents	Reaction time / min	wt% Rh	Zr:Rh	% Linker metalated
<b>1</b>	RhCl <sub>3</sub> · xH <sub>2</sub> O	5	5	2.18	7.18	27
<b>2</b>	RhCl <sub>3</sub> · xH <sub>2</sub> O	2	10	2.14	8.82	26
<b>3</b>	Rh <sub>2</sub> (OAc) <sub>4</sub>	5	10	1.66	12.19	20
<b>4</b>	RhCl <sub>3</sub> · xH <sub>2</sub> O	5	10	1.73	10.98	21
<b>5</b>	RhCl <sub>3</sub> · xH <sub>2</sub> O	5	20	1.22	11.15	15

Table A 3: Wt% of Rh, Zr:Rh ratios and approximated %Linker metalation (calculated with the ideal sum formula) for the metalation of PCN-222 with Rh in an oven (120 °C, 12 h) with variation of the solvent. Quantities of Rh and Zr were determined by ICP-MS.

Entry	Metal precursor	Metal equivalents	Solvent	wt% Rh	Zr:Rh	% Linker metalated
<b>1</b>	RhCl <sub>3</sub> · xH <sub>2</sub> O	9	DMF	2.40	8.16	30
<b>2</b>	RhCl <sub>3</sub> · xH <sub>2</sub> O	9	DEF	2.88	6.77	36

Table A 4: Wt% of Rh, Zr:Rh ratios and approximated %Linker metalation (calculated with the ideal sum formula) for the metalation of PCN-222 with Rh by heating in an aluminum block (120 °C, 12 h in DMF). Quantities of Rh and Zr were determined by ICP-MS.

Entry	MOF	Metal equivalents	wt% Rh	Zr:Rh	% Linker metalated
<b>1</b>	PCN-222	9	8.25	2.46	108
<b>2</b>	PCN-224	8	6.51	3.41	93
<b>3</b>	MOF-525	8	9.37	2.83	102

## Ruthenium

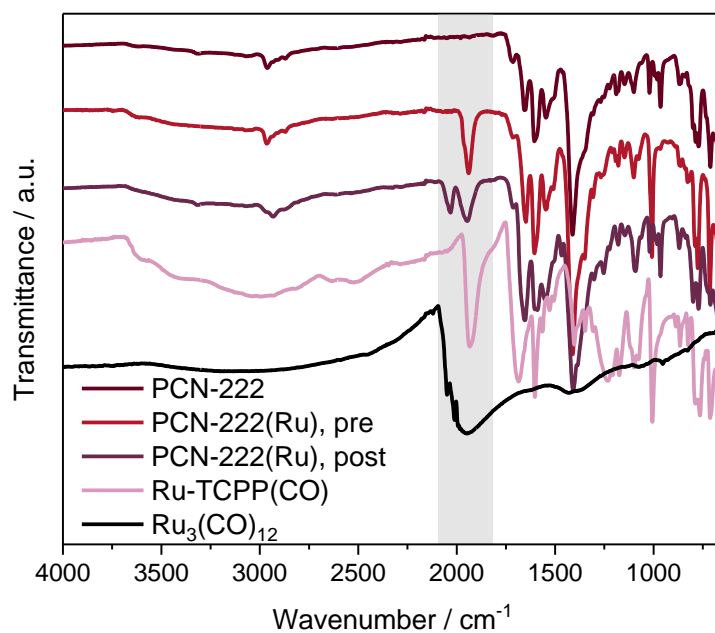


Figure A 43: IR spectra of PCN-222 and PCN-222(Ru).

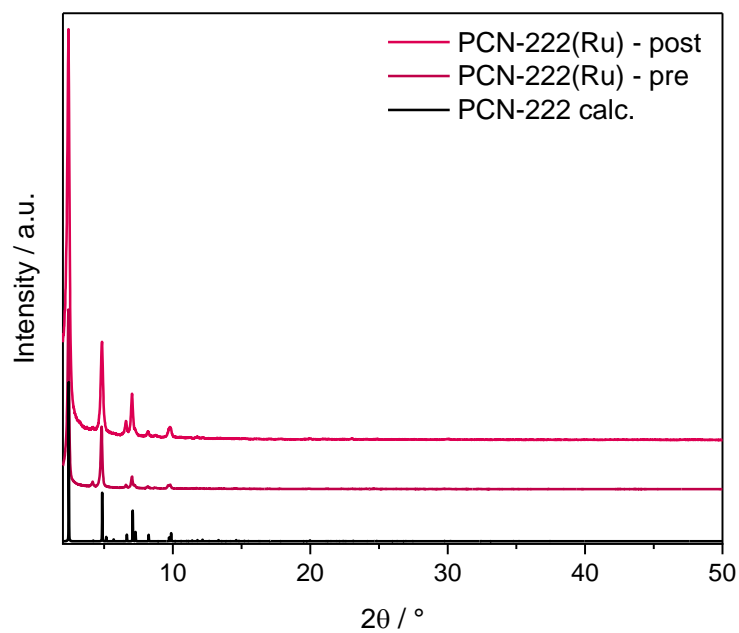


Figure A 44: PXRD spectra of PCN-222(Ru), synthesized via the pre- and post-synthetic approach, in comparison to the calculated pattern of PCN-222.

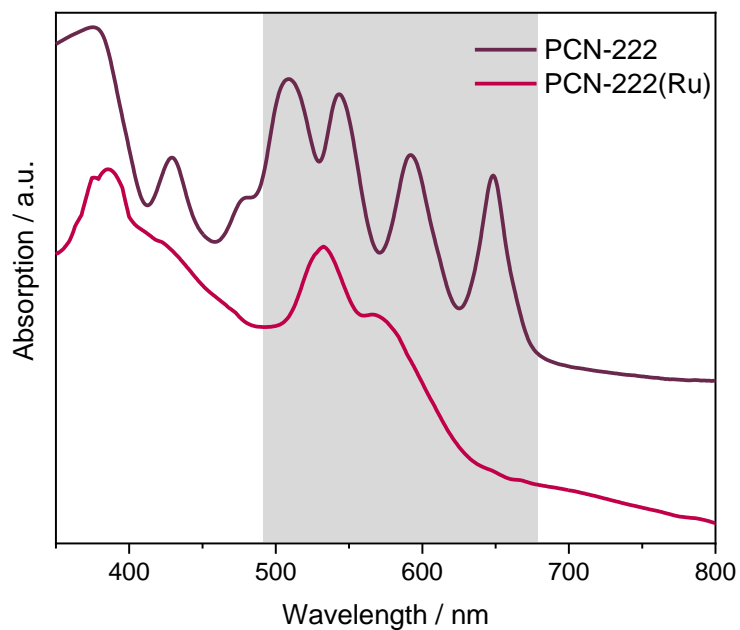


Figure A 45: Solid-state UV-vis spectra of PCN-222 and PCN-222(Ru).

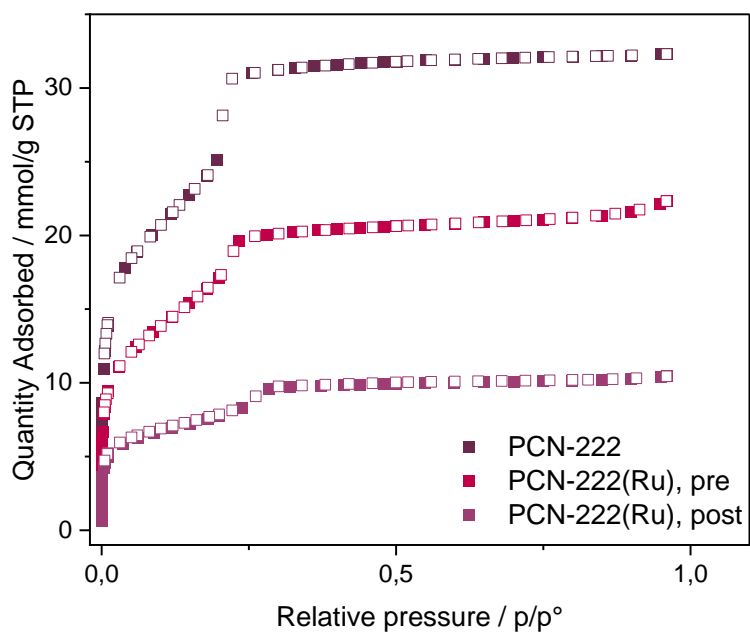


Figure A 46: N<sub>2</sub> sorption measurements at 77 K of PCN-222 and PCN-222(Ru).

Table A 5: Wt% of Ru and Zr:Ru ratios of PCN-222 post-synthetically metalated with Ru varying the Ru equivalents. Quantities of Rh and Zr were determined by ICP-MS.

Entry	Ru equivalents	wt% Ru	Zr:Ru
1	3	4.75	2.86
2	6	8.91	3.73
3	9	16.89	0.34

## Manganese

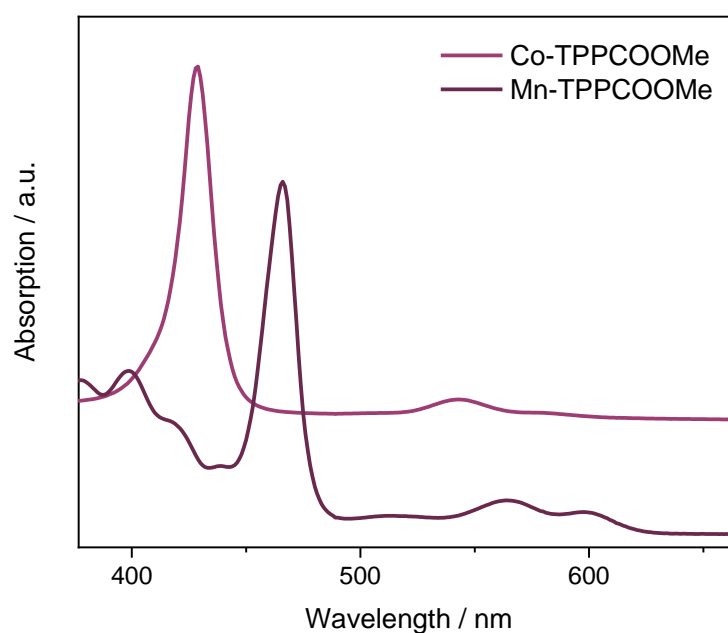


Figure A 47: UV-vis spectra of Mn-TPPCOOMe and Co-TPPCOOMe in EtOH.

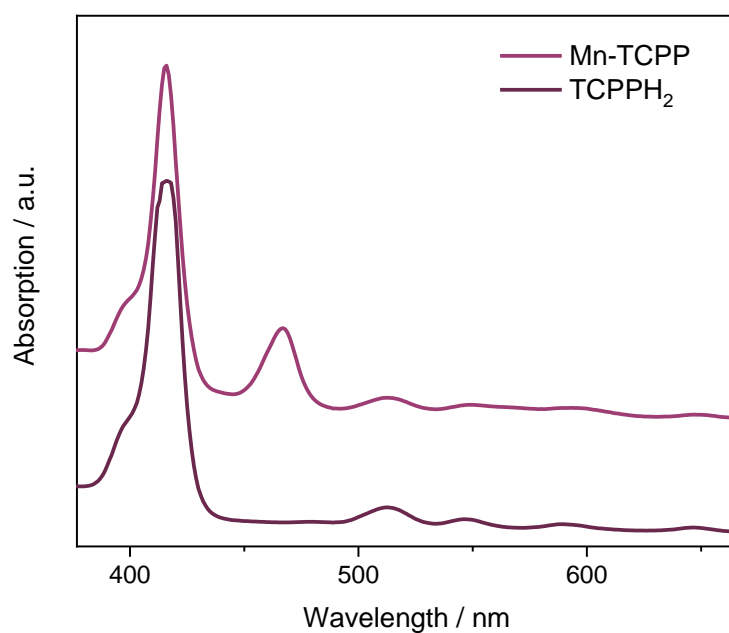


Figure A 48: UV-vis spectra of Mn-TCPP and TCPPH<sub>2</sub> in EtOH.

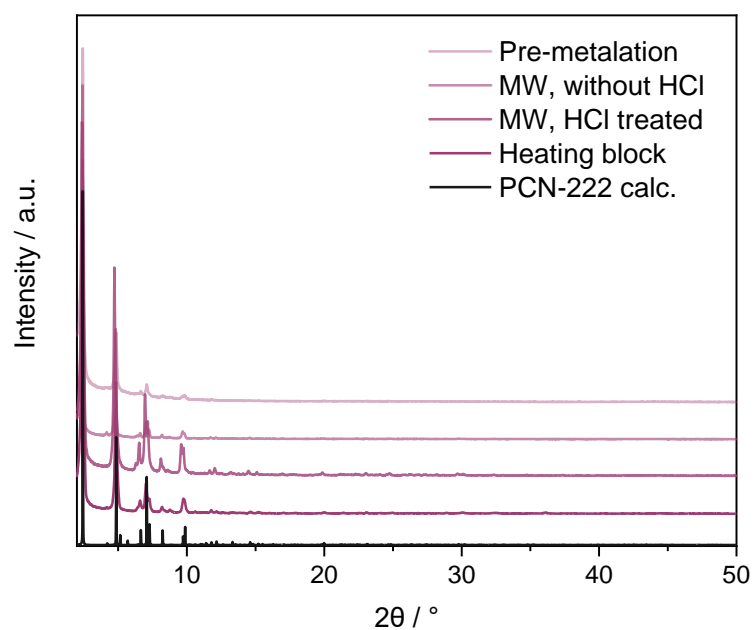


Figure A 49: PXRD pattern of PCN-222(Mn) synthesized via different approaches (pre-metalation, MW, heating block) in comparison to the calculated pattern of PCN-222. Additionally, the pattern of HCl treated PCN-222(Mn) is depicted.

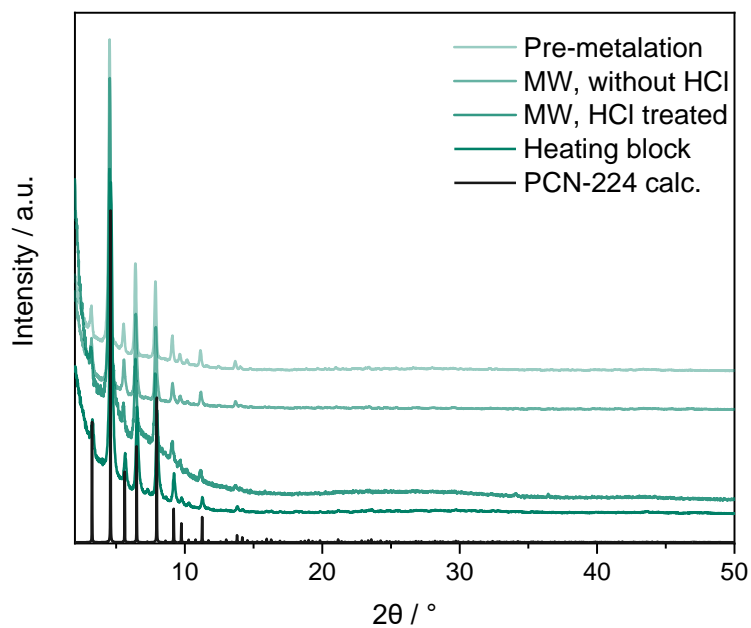


Figure A 50: PXRD pattern of PCN-224(Mn) synthesized via different approaches (pre-metalation, MW, heating block) in comparison to the calculated pattern of PCN-224. Additionally, the pattern of HCl treated PCN-224(Mn) is depicted.

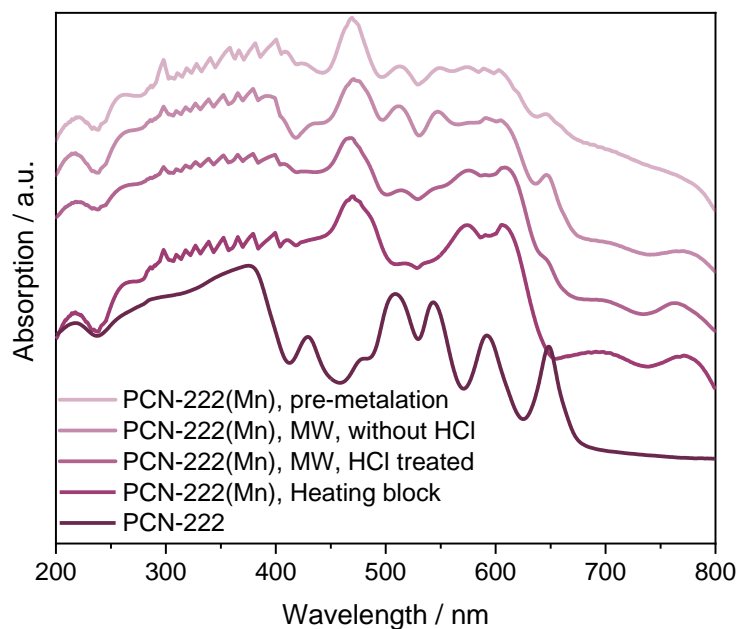


Figure A 51: Solid-state UV-vis spectra of PCN-222(Mn) synthesized via different approaches (pre-metalation, MW, heating block). Additionally, the spectrum of PCN-222 is depicted.



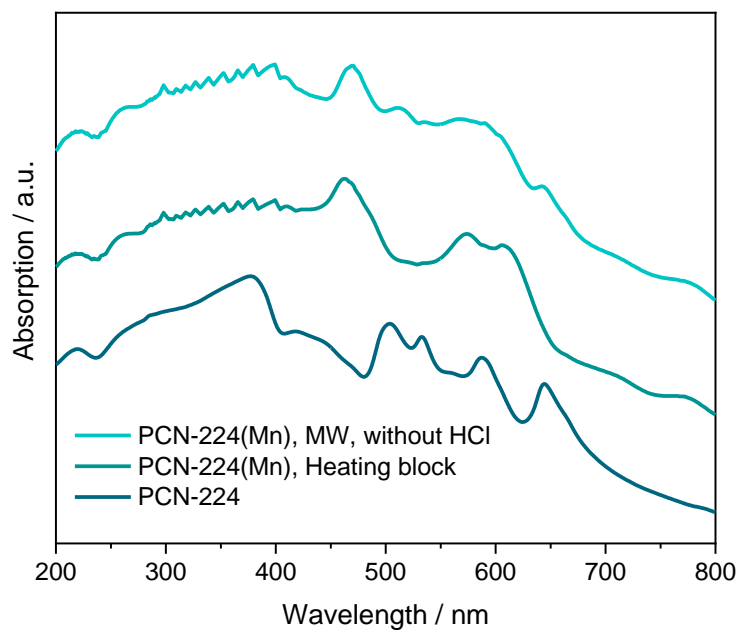


Figure A 52: Solid-state UV-vis spectra of PCN-224(Mn) synthesized via different approaches (MW, heating block). Additionally, the spectrum of PCN-224 is depicted.

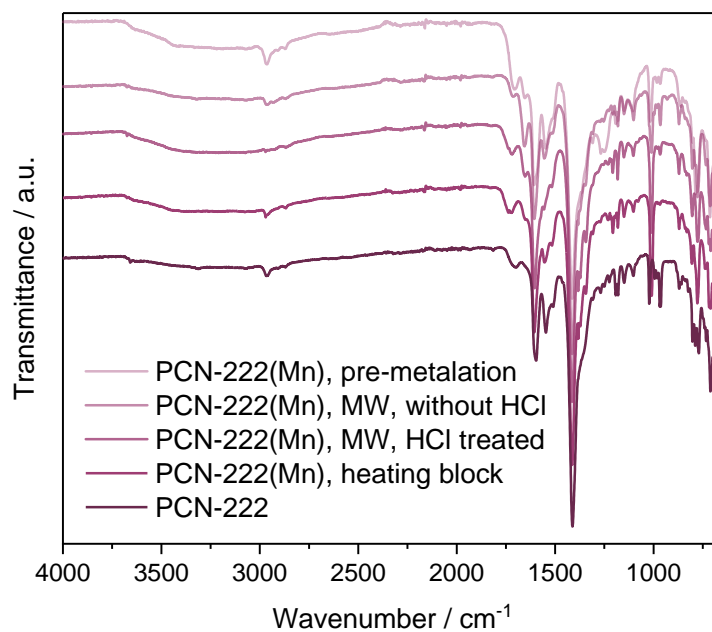


Figure A 53: IR spectra of PCN-222(Mn) synthesized via different approaches (pre-metalation, MW, heating block). Additionally, the spectrum of PCN-222 is depicted.

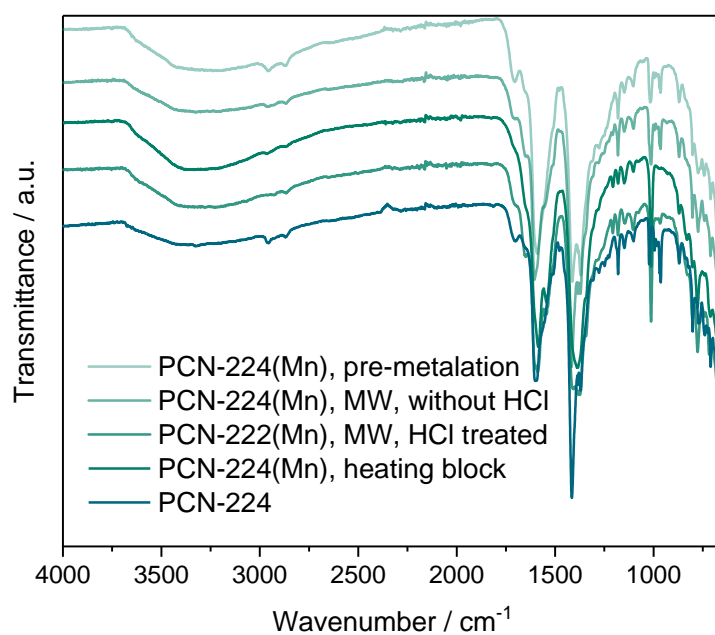


Figure A 54: IR spectra of PCN-224(Mn) synthesized via different approaches (pre-metalation, MW, heating block). Additionally, the spectrum of PCN-224 is depicted.

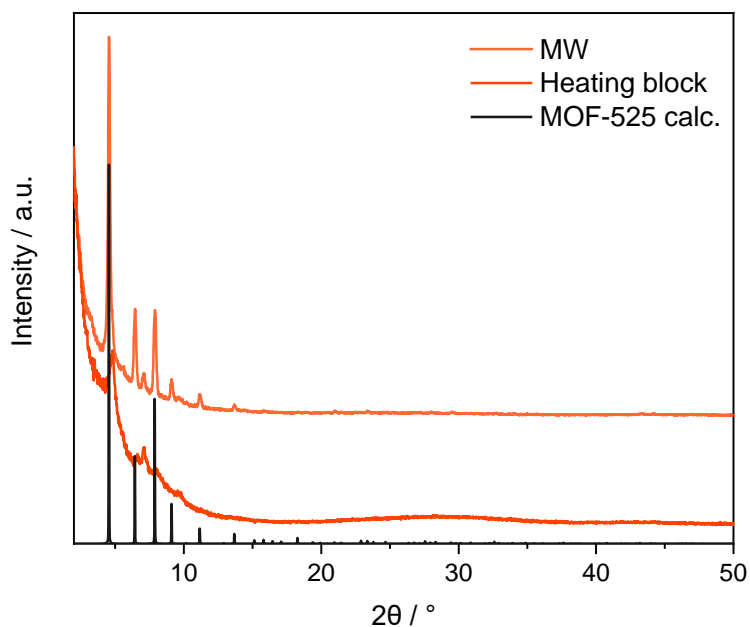


Figure A 55: PXRD pattern of MOF-525(Mn) synthesized via different approaches (MW, heating block) in comparison to the calculated pattern of MOF-525.

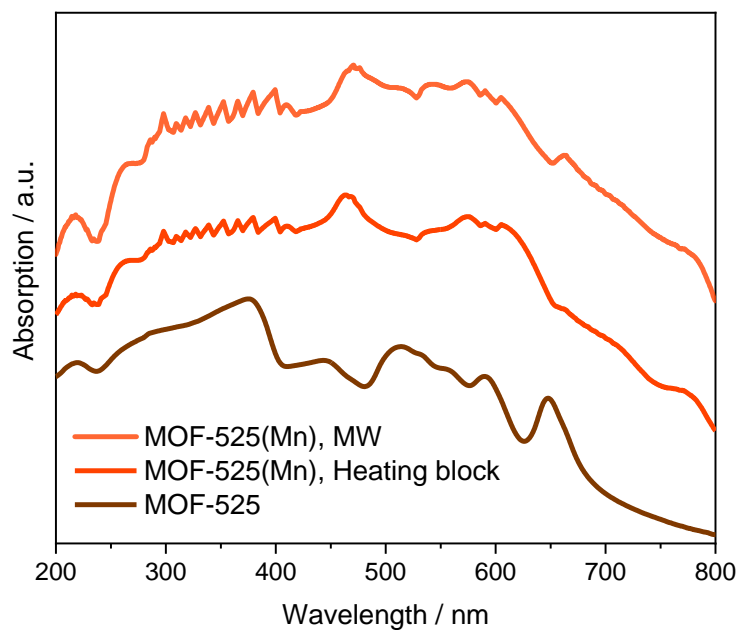


Figure A 56: Solid-state UV-vis spectra of MOF-525(Mn) synthesized via different approaches (MW, heating block).

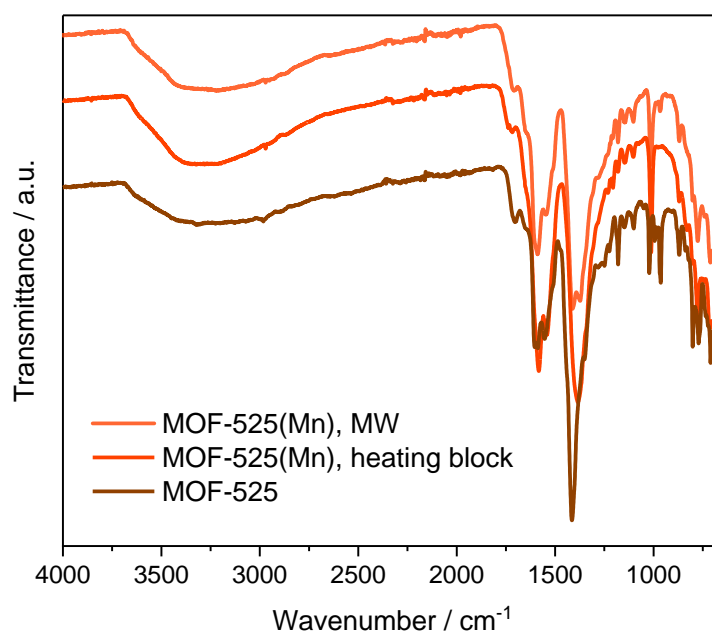


Figure A 57: IR spectra of MOF-525(Mn) synthesized via different approaches (MW, heating block).

Table A 6: Wt% of Mn and Zr:Mn ratios for the metalation of PCN-222 with Mn via different approaches. Additionally, the values for HCl treated PCN-222 are depicted. Quantities of Mn and Zr were determined by ICP-MS.

Entry	approach	HCl treatment	wt% Mn	Zr:Mn
<b>1</b>	Pre-metalation	no	0.70	8.90
<b>2</b>	MW	no	1.8	4.54
<b>3</b>	MW	yes	3.1	3.10
<b>4</b>	Al heating block	no	9.1	0.87

Table A 7: Wt% of Mn and Zr:Mn ratios for the metalation of PCN-224 with Mn via different approaches. Additionally, the values for HCl treated PCN-224 are depicted. Quantities of Mn and Zr were determined by ICP-MS

Entry	approach	HCl treatment	wt% Mn	Zr:Mn
<b>1</b>	Pre-metalation	no	0.7	15.8
<b>2</b>	MW	no	1.1	7.14
<b>3</b>	MW	yes	3.5	3.76
<b>4</b>	Al heating block	no	6.3	1.03

Table A 8: Wt% of Mn and Zr:Mn ratios for the metalation of MOF-525 with Mn via different approaches. Quantities of Mn and Zr were determined by ICP-MS

Entry	approach	wt% Mn	Zr:Mn
<b>1</b>	MW	1.2	7.70
<b>2</b>	Al heating block	8.7	0.90

## Cobalt

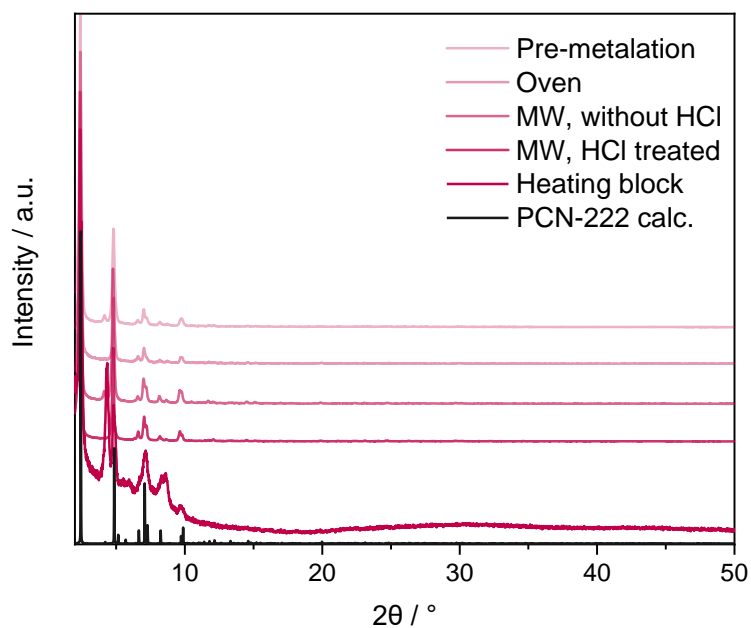


Figure A 58: PXRD pattern of PCN-222(Co) synthesized via different approaches (pre-metalation, oven, MW, heating block) in comparison to the calculated pattern of PCN-222. Additionally, the pattern of HCl treated PCN-222(Co) is depicted.

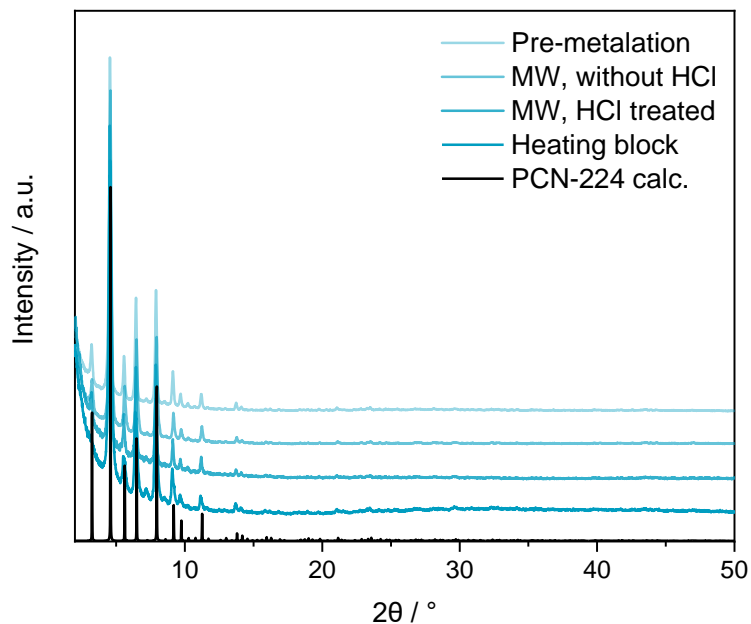


Figure A 59: PXRD pattern of PCN-224(Co) synthesized via different approaches (pre-metalation, MW, heating block) in comparison to the calculated pattern of PCN-224. Additionally, the pattern of HCl treated PCN-224(Co) is depicted.

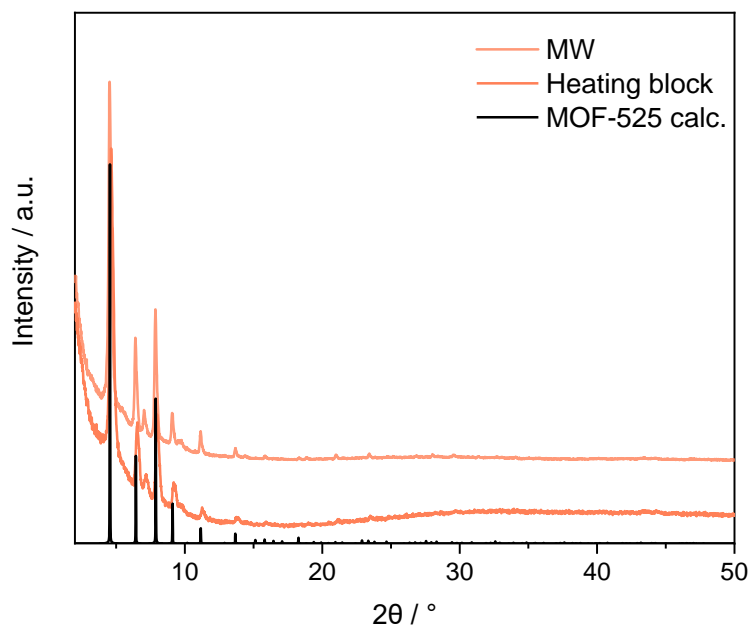


Figure A 60: PXRD pattern of MOF-525(Co) synthesized via different approaches (MW, heating block) in comparison to the calculated pattern of MOF-525

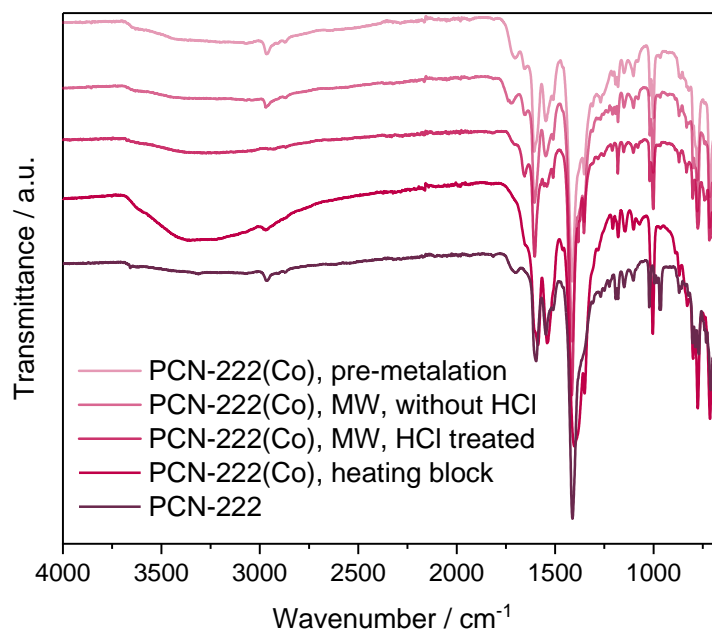


Figure A 61: IR spectra of PCN-222(Co) synthesized via different approaches (pre-metalation, MW, heating block) in comparison to the spectrum of PCN-222. Additionally, the spectrum of HCl treated PCN-222(Co) is depicted.

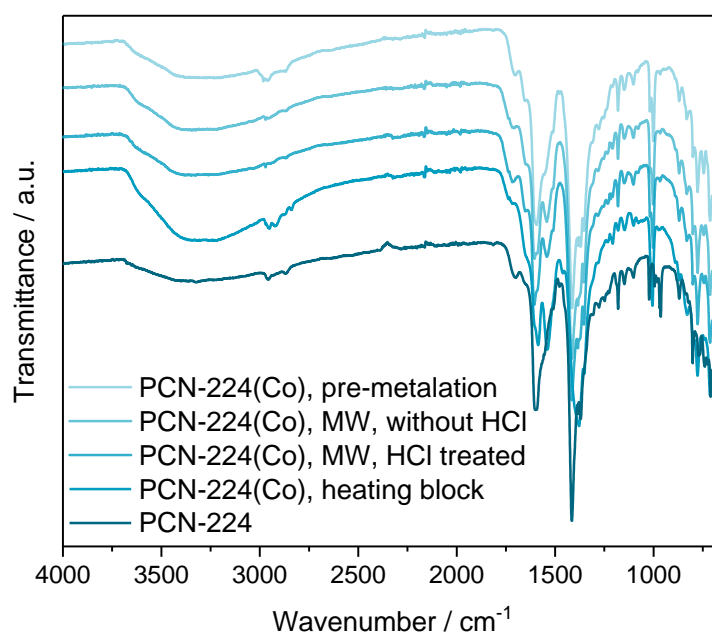


Figure A 62: IR spectra of PCN-224(Co) synthesized via different approaches (pre-metalation, MW, heating block) in comparison to the spectrum of PCN-224. Additionally, the spectrum of HCl treated PCN-224(Co) is depicted.

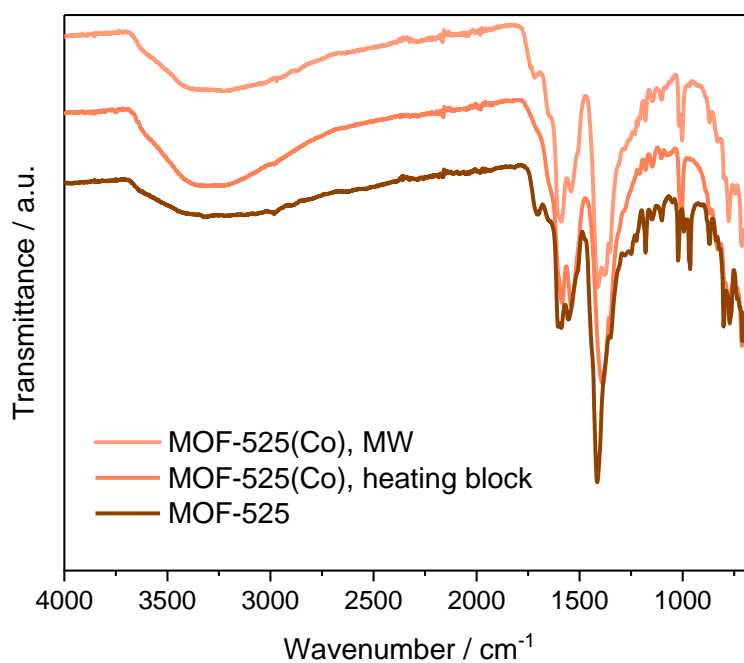


Figure A 63: IR spectra of MOF-525(Co) synthesized via different approaches (MW, heating block) in comparison to the spectrum of MOF-525.

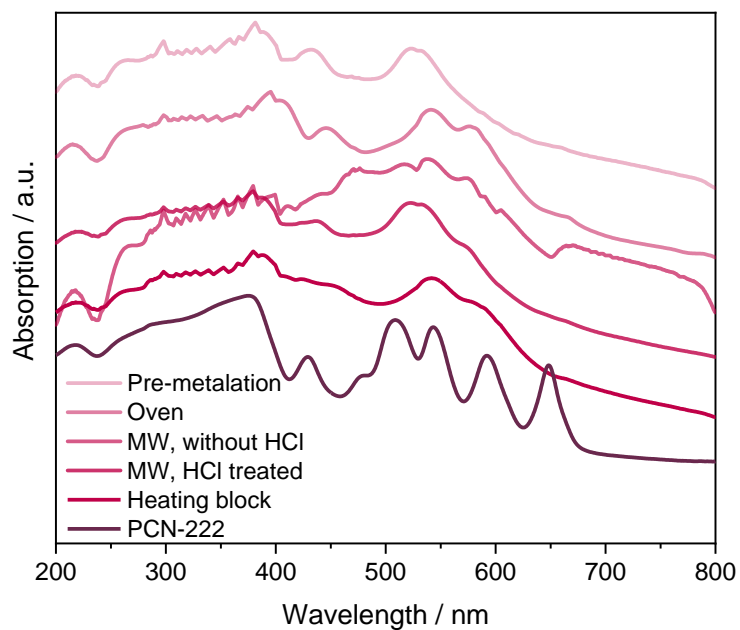


Figure A 64: Solid-state UV-vis spectra of PCN-222(Co) synthesized via different approaches (Oven, MW, heating block) in comparison to the spectrum of PCN-222. Additionally, the spectrum of HCl treated PCN-222(Co) is depicted.

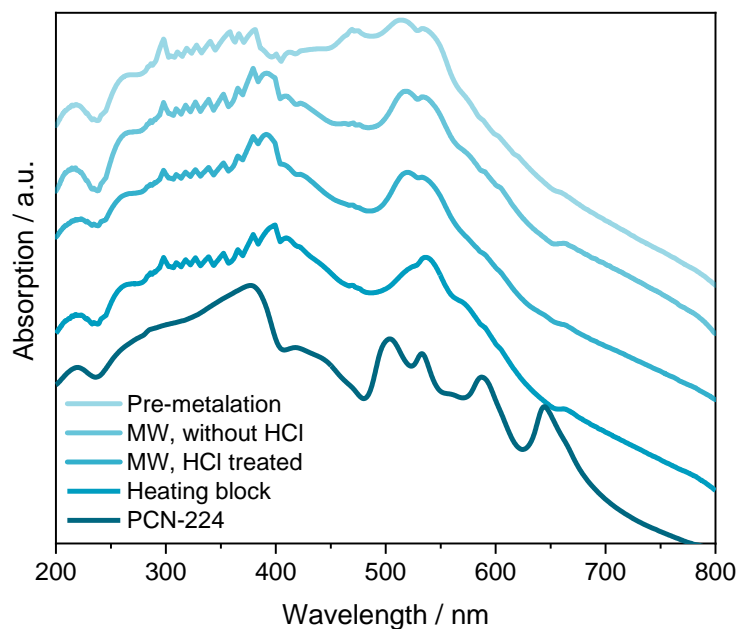


Figure A 65: Solid-state UV-vis spectra of PCN-224(Co) synthesized via different approaches (MW, heating block) in comparison to the spectrum of PCN-224. Additionally, the spectrum of HCl treated PCN-224(Co) is depicted.



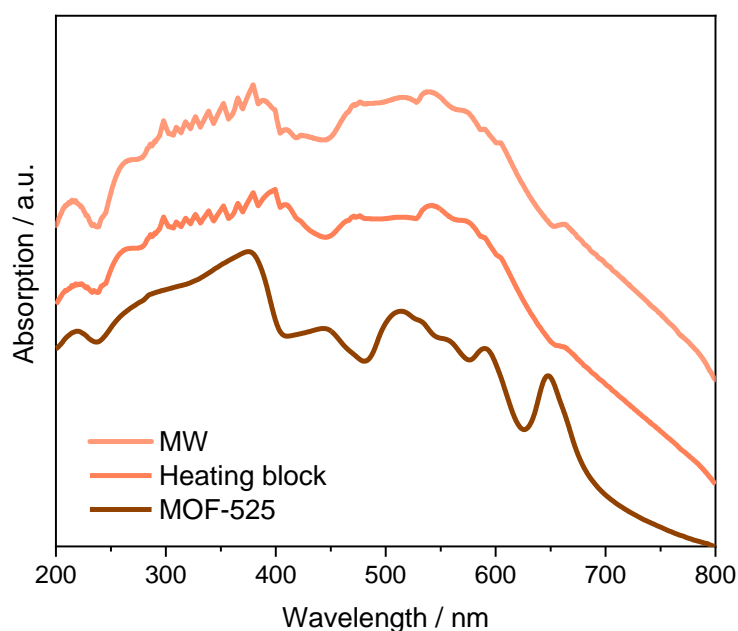


Figure A 66: Solid-state UV-vis spectra of MOF-525(Co) synthesized via different approaches (MW, heating block) in comparison to MOF-525.

Table A 9: Wt% of Co and Zr:Co ratios for the metalation of PCN-222 with Co via different approaches. Additionally, the values for HCl treated PCN-222 are depicted. Quantities of Co and Zr were determined by ICP-MS.

Entry	approach	HCl treatment	wt% Co	Zr:Co
1	Pre-metalation	no	2.3	2.94
2	MW	no	4.5	1.95
3	MW	yes	4.8	2.07
4	Al heating block	no	10.8	0.80

Table A 10: Wt% of Co and Zr:Co ratios for the metalation of PCN-224 with Co via different approaches. Additionally, the values for HCl treated PCN-224 are depicted. Quantities of Co and Zr were determined by ICP-MS.

Entry	approach	HCl treatment	wt% Co	Zr:Co
1	Pre-metalation	no	2.6	5.23
2	MW	no	4.0	2.46
3	MW	yes	3.6	3.09
4	Al heating block	no	11.5	0.72

Table A 11: Wt% of Co and Zr:Co ratios for the metalation of MOF-525 with Co via different approaches. Quantities of Co and Zr were determined by ICP-MS.

Entry	approach	wt% Co	Zr:Co
1	MW	4.0	2.62
2	Al heating block	12.9	0.57

## Zinc

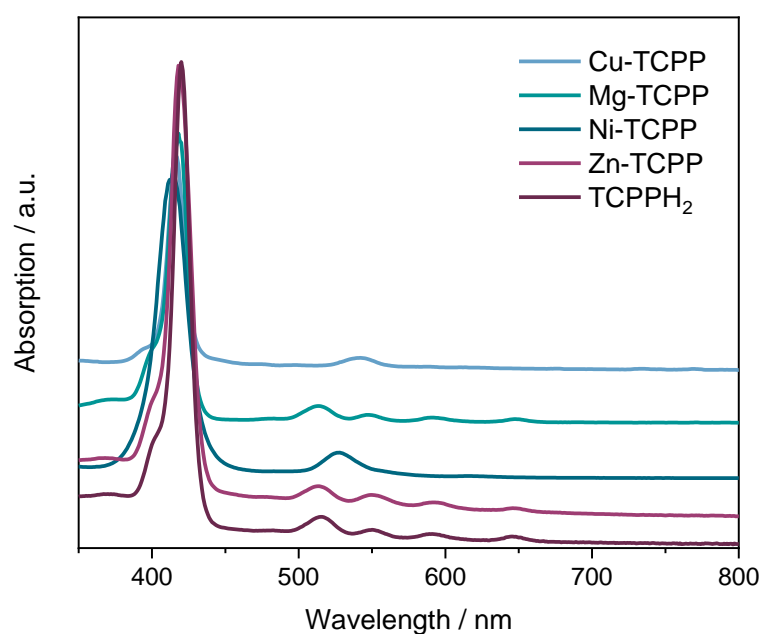


Figure A 67: UV-vis spectra of Cu-TCPP, Mg-TCPP, Ni-TCPP, Zn-TCPP and TCPPH<sub>2</sub> in THF.

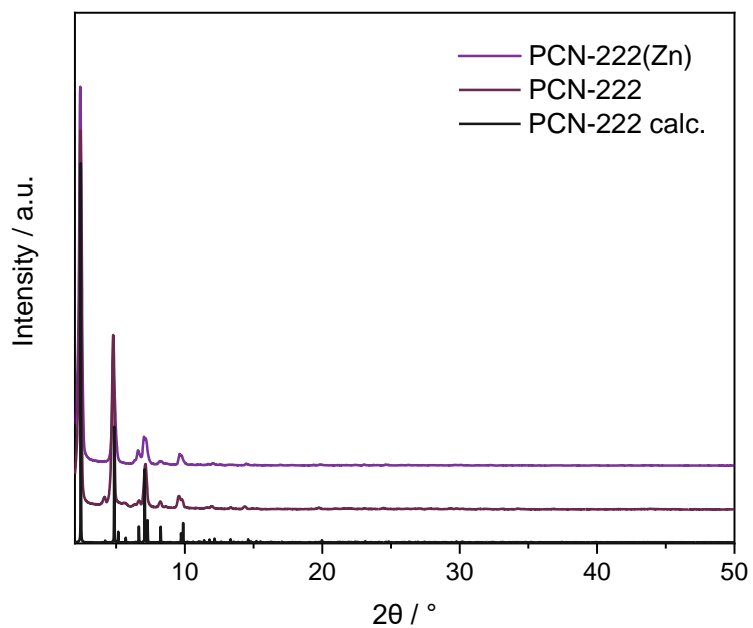


Figure A 68: PXRD pattern of PCN-222(Zn) and synthesized PCN-222 in comparison to the calculated pattern of PCN-222.

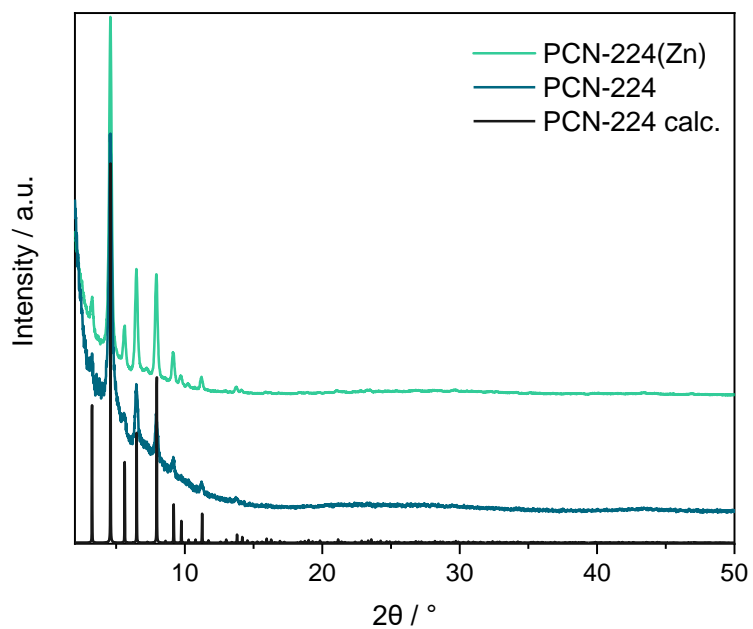


Figure A 69: PXRD pattern of PCN-224(Zn) and synthesized PCN-224 in comparison to the calculated pattern of PCN-224.

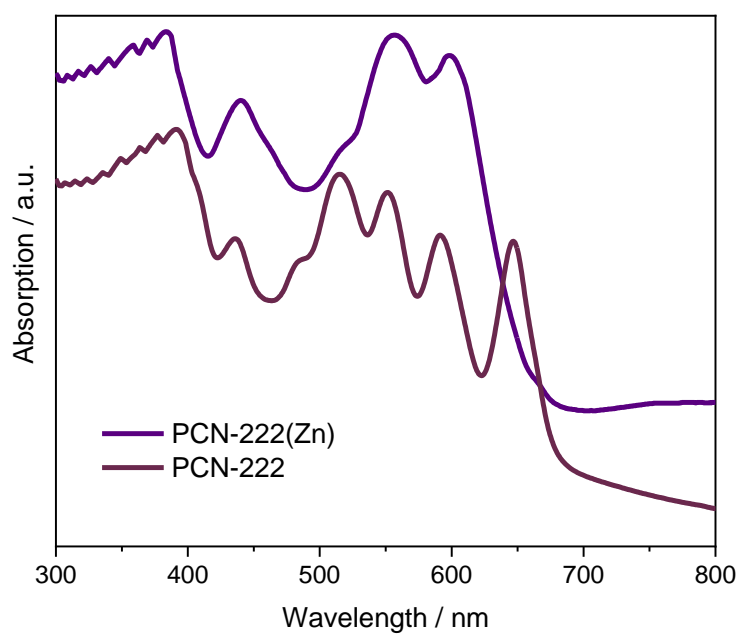


Figure A 70: Solid-state UV-vis spectra of PCN-222(Zn) and PCN-222.

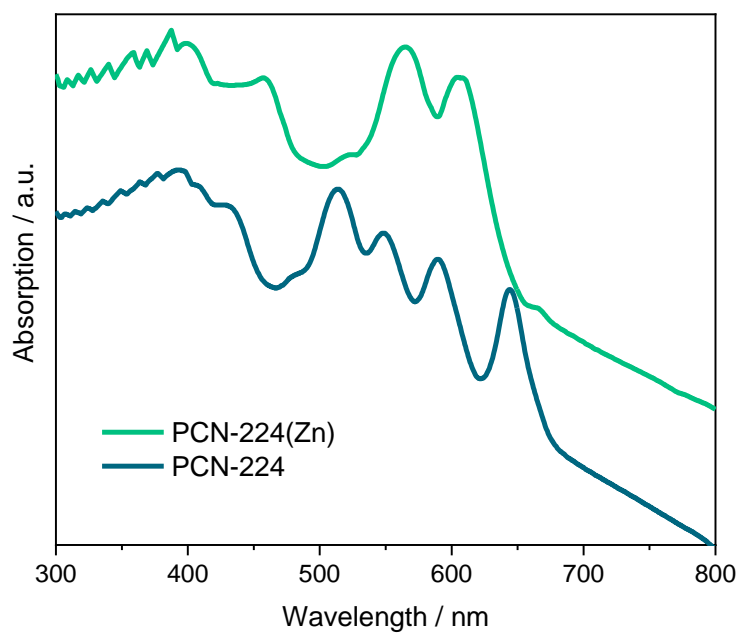


Figure A 71: Solid-state UV-vis spectra of PCN-224(Zn) and PCN-224.

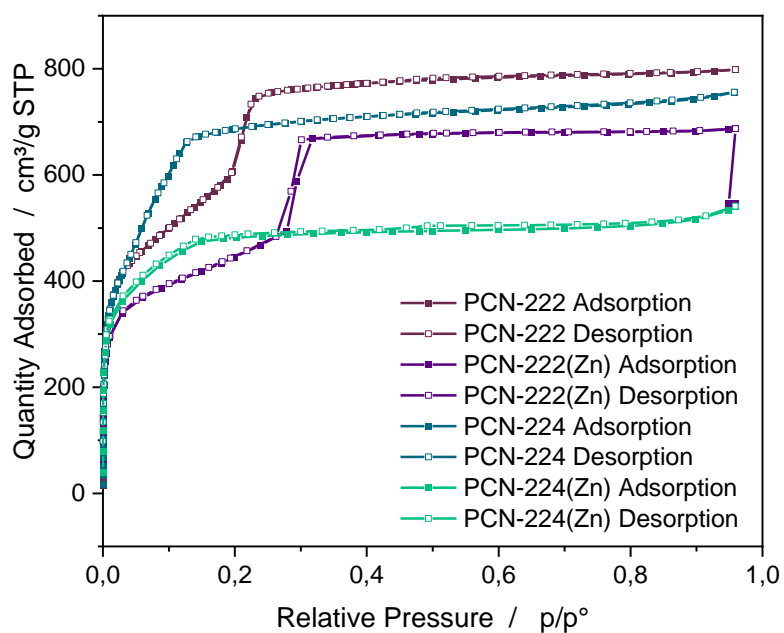


Figure A 72: N<sub>2</sub> sorption measurements at 77 K of PCN-222, PCN-222(Zn), PCN-224 and PCN-224(Zn).

## Copper / Nickel

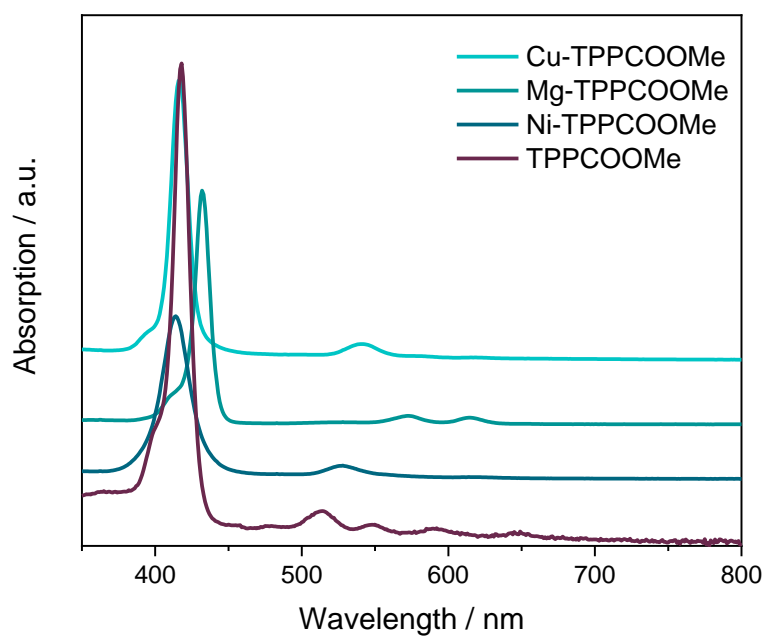


Figure A 73: UV-vis spectra of Cu-TPPCOOMe, Mg-TPPCOOMe, Ni-TPPCOOMe and TPPCOOMe in THF.

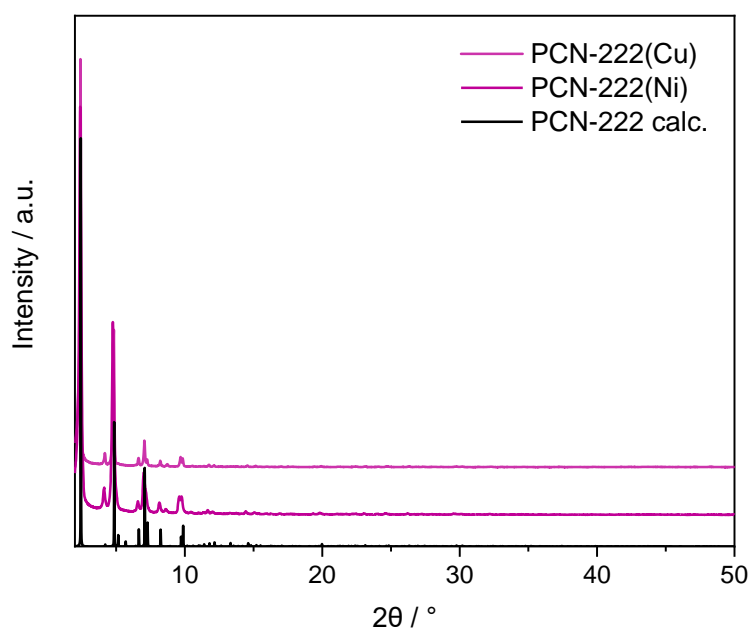


Figure A 74: PXRD pattern of PCN-222(Cu) and PCN-222(Ni) in comparison to the calculated pattern of PCN-222.

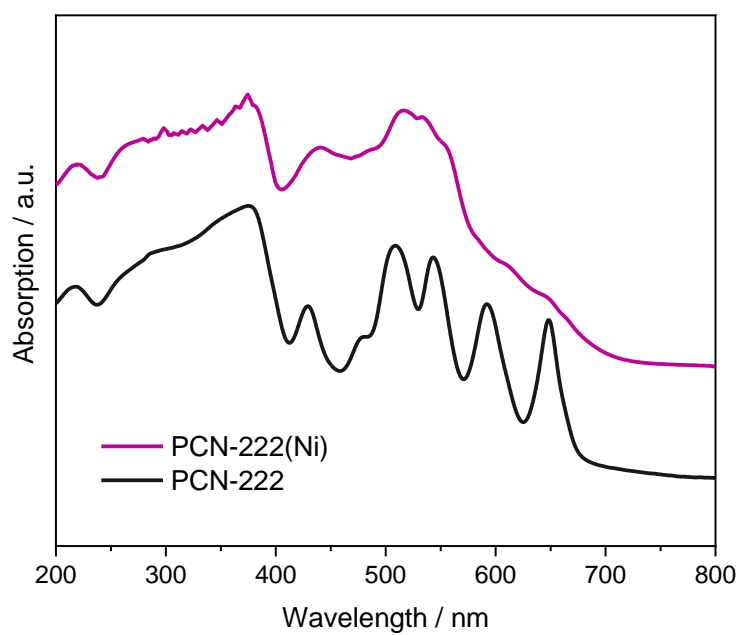


Figure A 75: Solid-state UV-vis spectra of PCN-222(Ni) and PCN-222.

## Iron

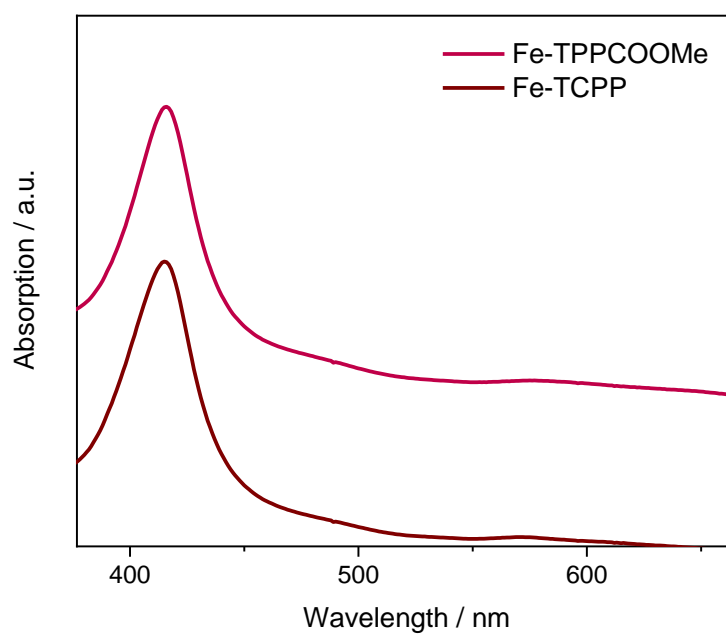


Figure A 76: UV-vis spectra of Fe-TPPCOOMe and Fe-TCPP in EtOH.

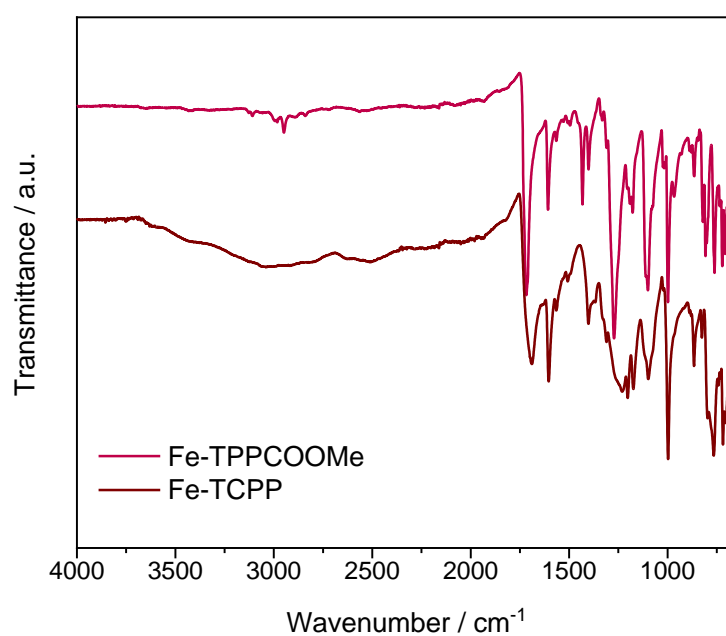


Figure A 77: IR spectra of Fe-TPPCOOMe and Fe-TCPP.

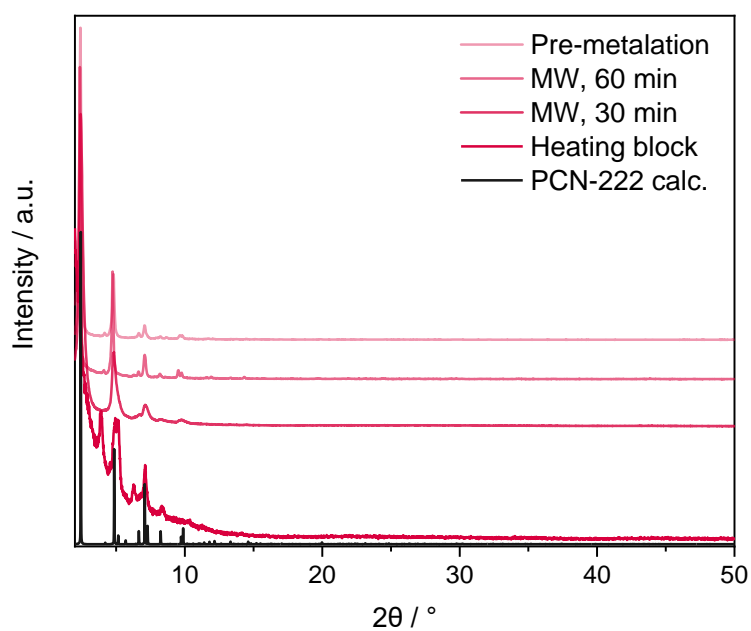


Figure A 78: PXRD pattern of PCN-222(Fe) synthesized via different approaches (pre-metalation, MW, heating block) in comparison to the calculated pattern of PCN-222.

### Mixed-metal MOFs

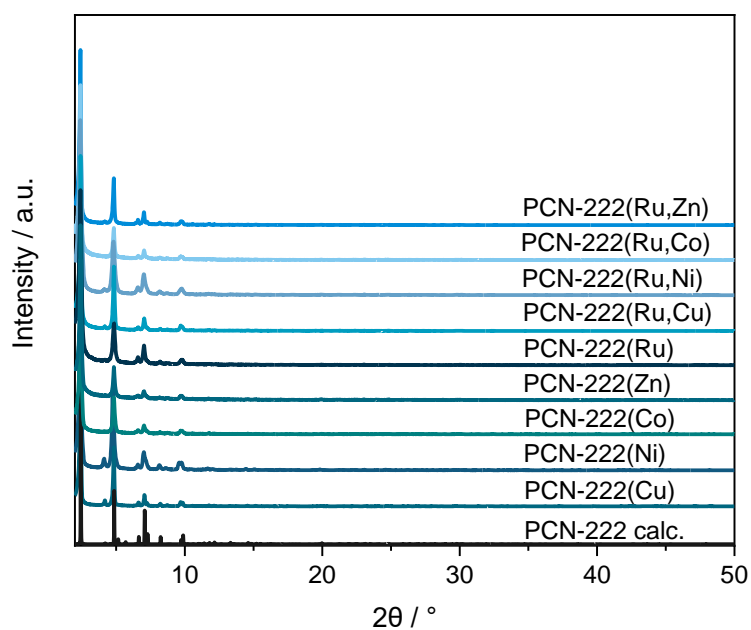


Figure A 79: PXRD pattern of PCN-222(M) (M = Ru, Zn, Co, Ni, Cu) and PCN-222(Ru,M) (M = Zn, Co, Ni, Cu) in comparison to the calculated pattern of PCN-222.



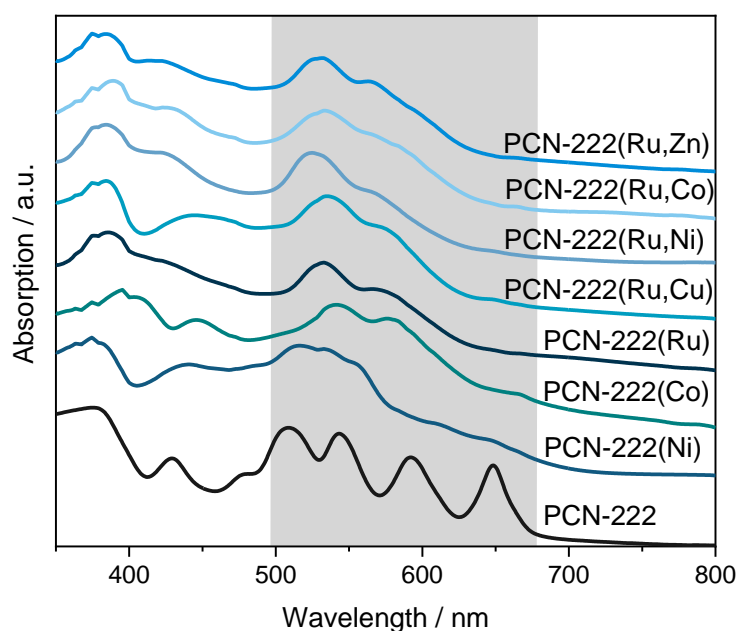


Figure A 80: Solid-state UV-vis spectra of PCN-222(M) (M = Ru, Zn, Co, Ni, Cu) and PCN-222(Ru,M) (M = Zn, Co, Ni, Cu).

Table A 12: wt% of Ru, M (Zn, Co, Cu, Ni) and Zr, and Zr:Ru and Zr:M ratios for PCN-222(Ru), PCN-222(M) and PCN-222(Ru,M) determined by ICP-MS analysis.

	wt% Zr	wt% Ru	wt% M	Zr:Ru	Zr:M	Ru:M
PCN-222(Ru)	15.85	6.56	-	2.68	-	-
PCN-222(Zn)	21.62	-	5.80	-	2.67	-
PCN-222(Co)	15.61	-	5.77	-	1.75	-
PCN-222(Cu)	17.45	-	3.23	-	3.76	-
PCN-222(Ni)	19.79	-	3.76	-	3.39	-
PCN-222(Ru,Zn) <sup>a</sup>	16.20	2.29	0.71	7.83	5.29	2.08
PCN-222(Ru,Zn) <sup>b</sup>	17.12	2.41	1.67	7.87	3.80	0.93
PCN-222(Ru,Zn) <sup>c</sup>	16.07	2.31	2.07	7.70	3.22	0.72
PCN-222(Ru,Co)	12.81	2.44	2.08	5.82	2.36	0.68
PCN-222(Ru,Cu)	12.57	2.64	1.11	5.27	7.91	1.50
PCN-222(Ru,Ni)	11.71	2.08	1.17	6.24	6.42	1.03

PCN-222(Ru,Zn) was synthesized via post-synthetic Zn-metalation using <sup>a</sup> 1.1 equiv. ZnCl<sub>2</sub> <sup>b</sup> 2.0 equiv. ZnCl<sub>2</sub> <sup>c</sup> 5.0 equiv. ZnCl<sub>2</sub>.

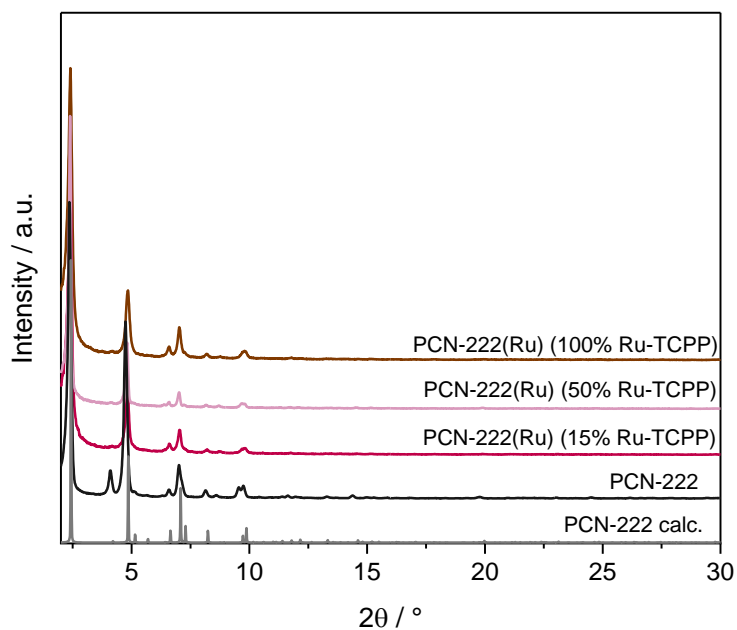


Figure A 81: PXRD pattern of PCN-222 and PCN-222(Ru), synthesized with different molar ratios of Ru-TCPP and TCPPH<sub>2</sub>, in comparison to the calculated pattern of PCN-222.

### 7.3. Cyclopropanation Catalysis

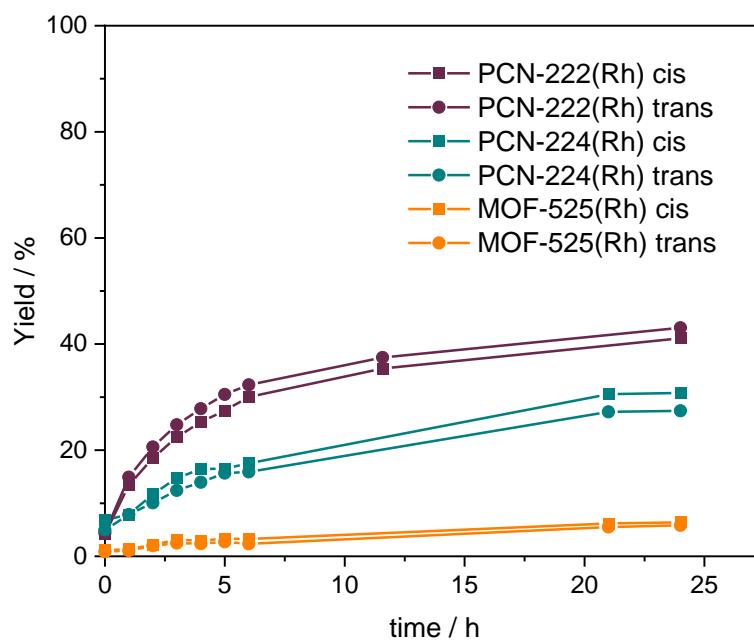


Figure A 82: Yield of the cis and trans cyclopropanation product in the styrene cyclopropanation with EDA as carbene source under standard reaction conditions. PCN-222(Rh) (violet), PCN-224(Rh) (turquoise) and MOF-525(Rh) (orange), respectively, were used as catalysts.

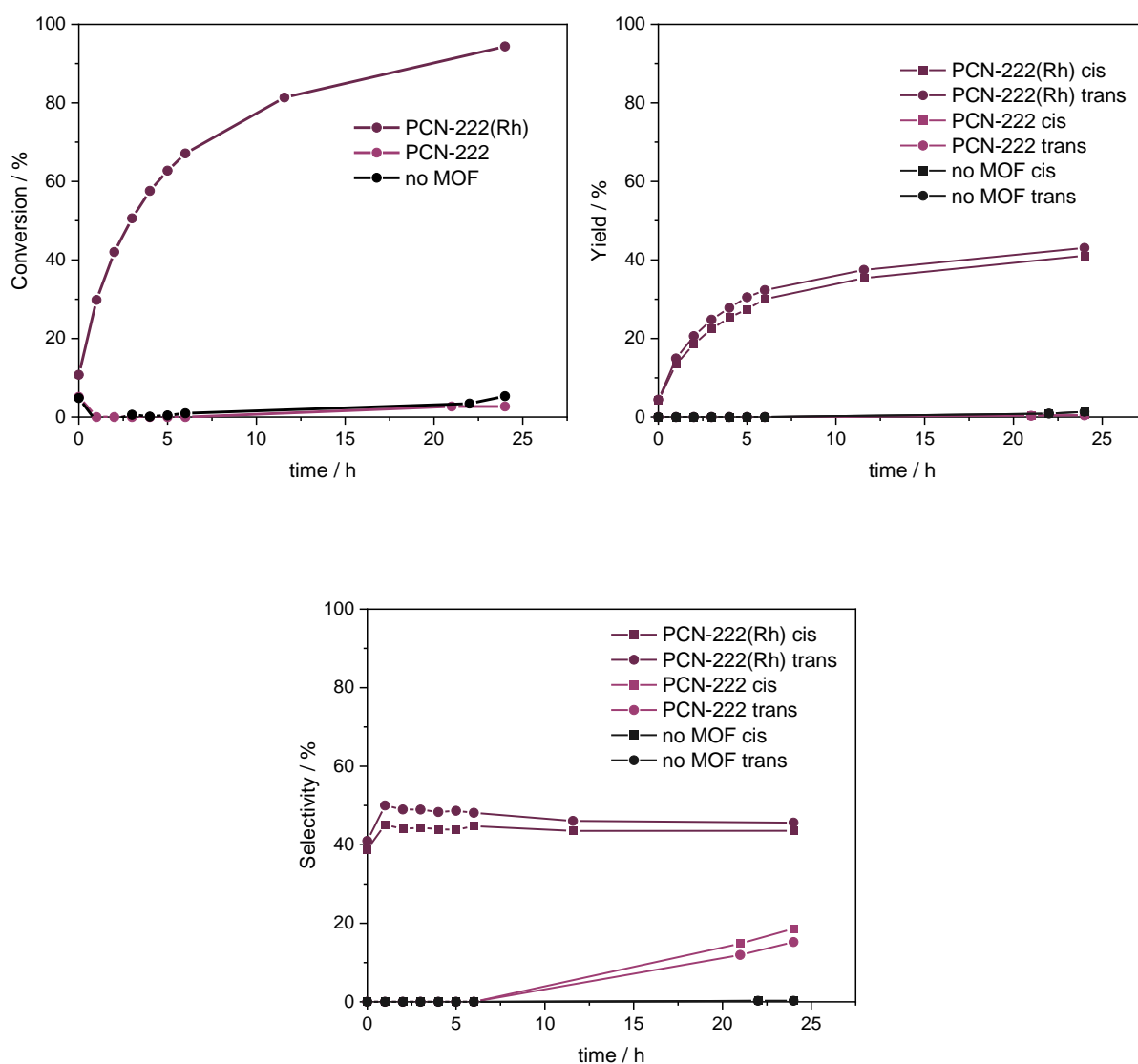


Figure A 83: Control experiments for the catalytic performance (Conversion, Yield and Selectivity) during the reaction progress of the styrene cyclopropanation with EDA under standard reaction conditions. PCN-222(Rh) and PCN-222 were used as catalysts. Additionally, no MOF was added in the catalysis.

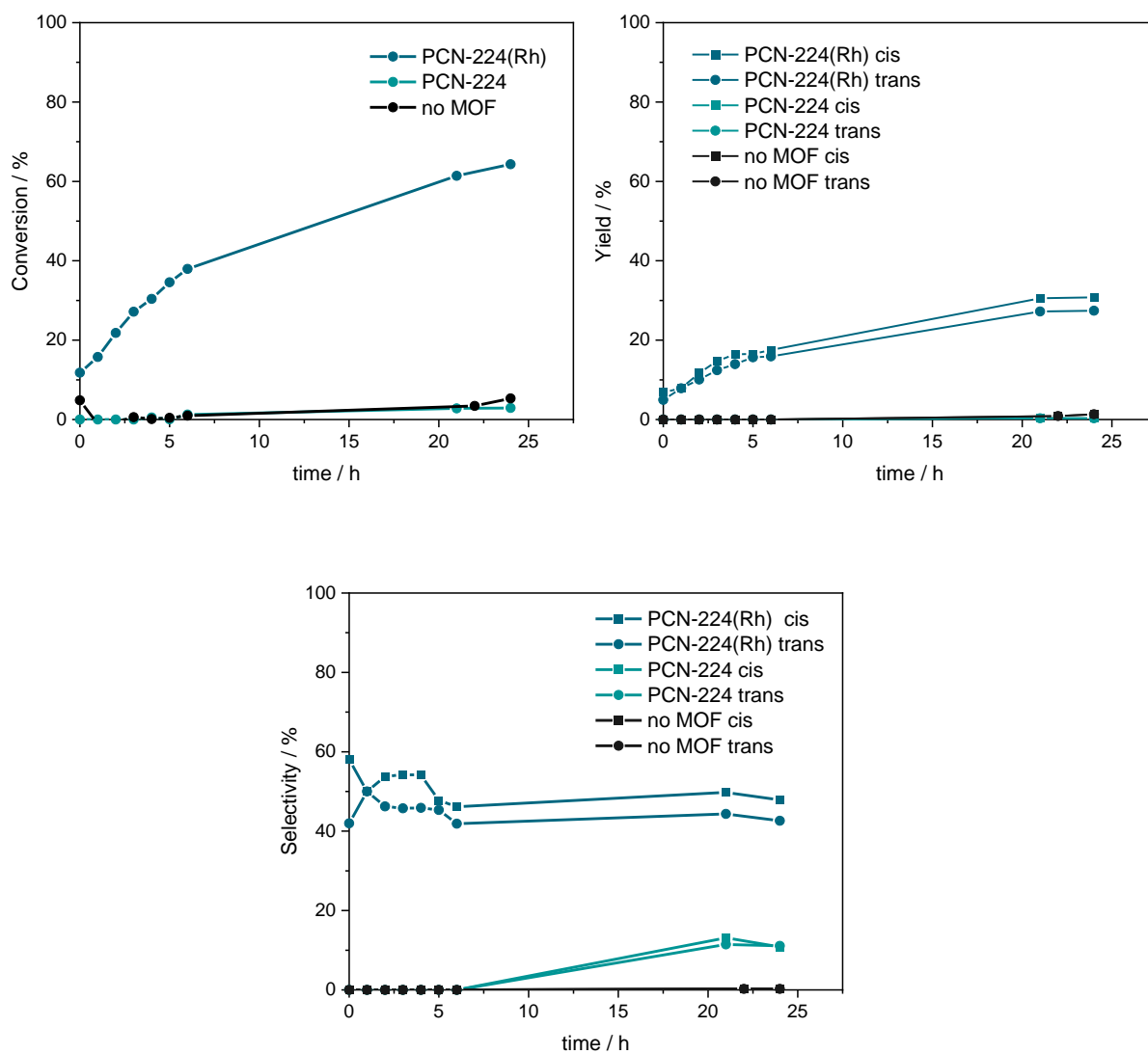


Figure A 84: Control experiments for the catalytic performance (Conversion, Yield and Selectivity) during the reaction progress of the styrene cyclopropanation with EDA under standard reaction conditions. PCN-224(Rh) and PCN-224 were used as catalysts. Additionally, no MOF was added in the catalysis.

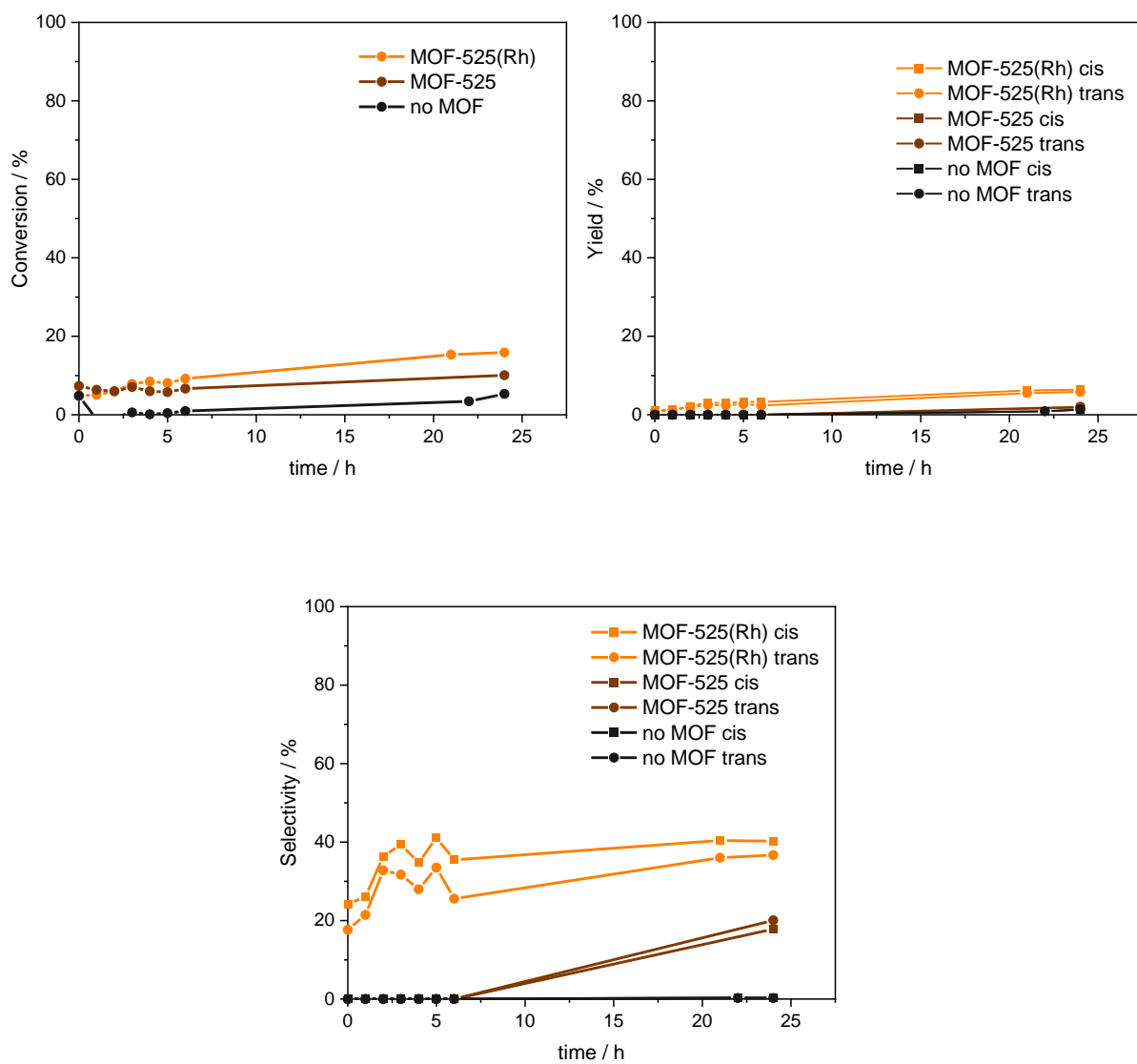


Figure A 85: Control experiments for the catalytic performance (Conversion, Yield and Selectivity) during the reaction progress of the styrene cyclopropanation with EDA under standard reaction conditions. MOF-525(Rh) and MOF-525 were used as catalysts. Additionally, no MOF was added in the catalysis.

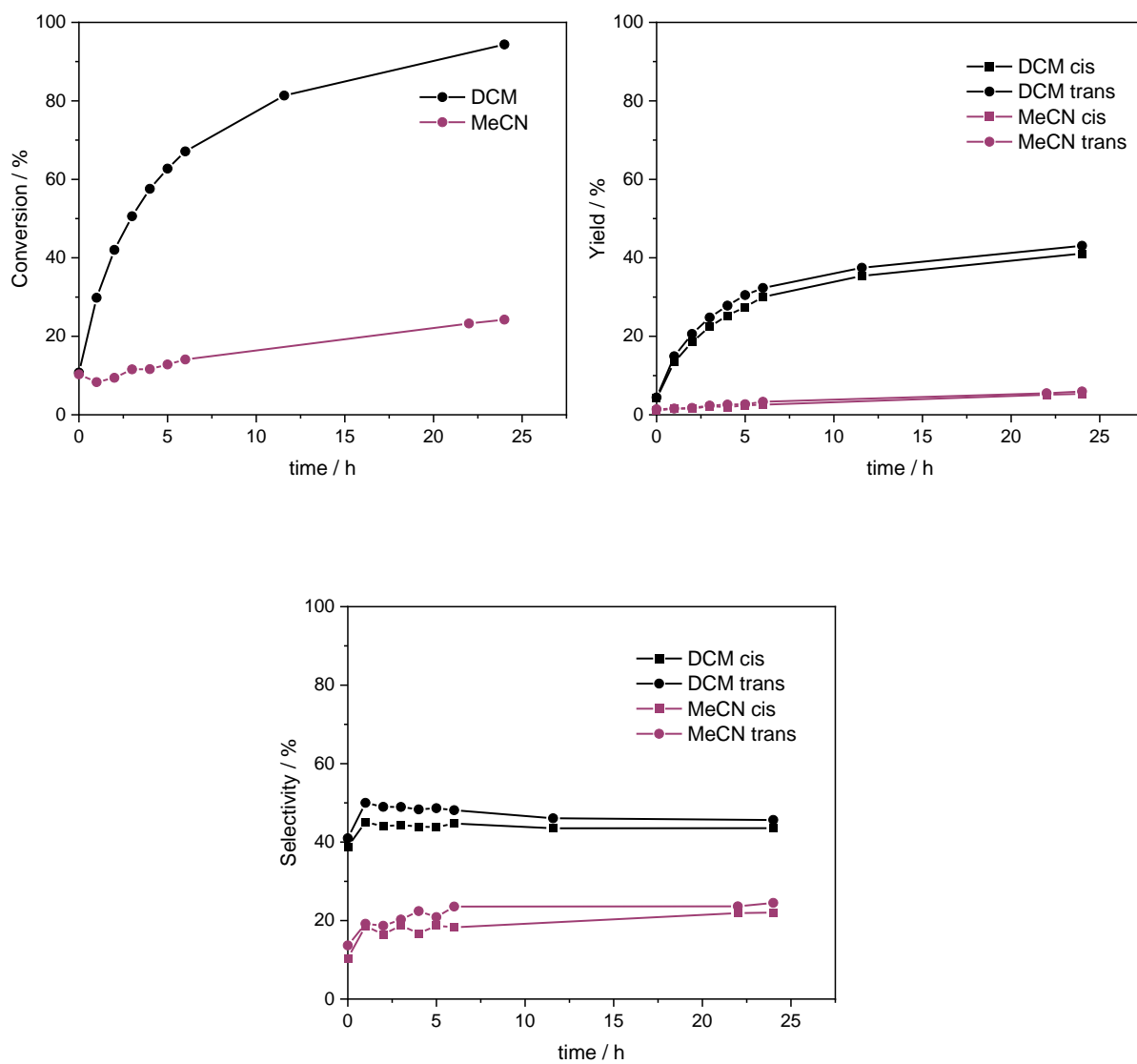


Figure A 86: Conversion, Yield and Selectivity during the reaction progress of the styrene cyclopropanation with EDA using PCN-222(Rh) as catalyst with solvent variation (DCM vs MeCN).

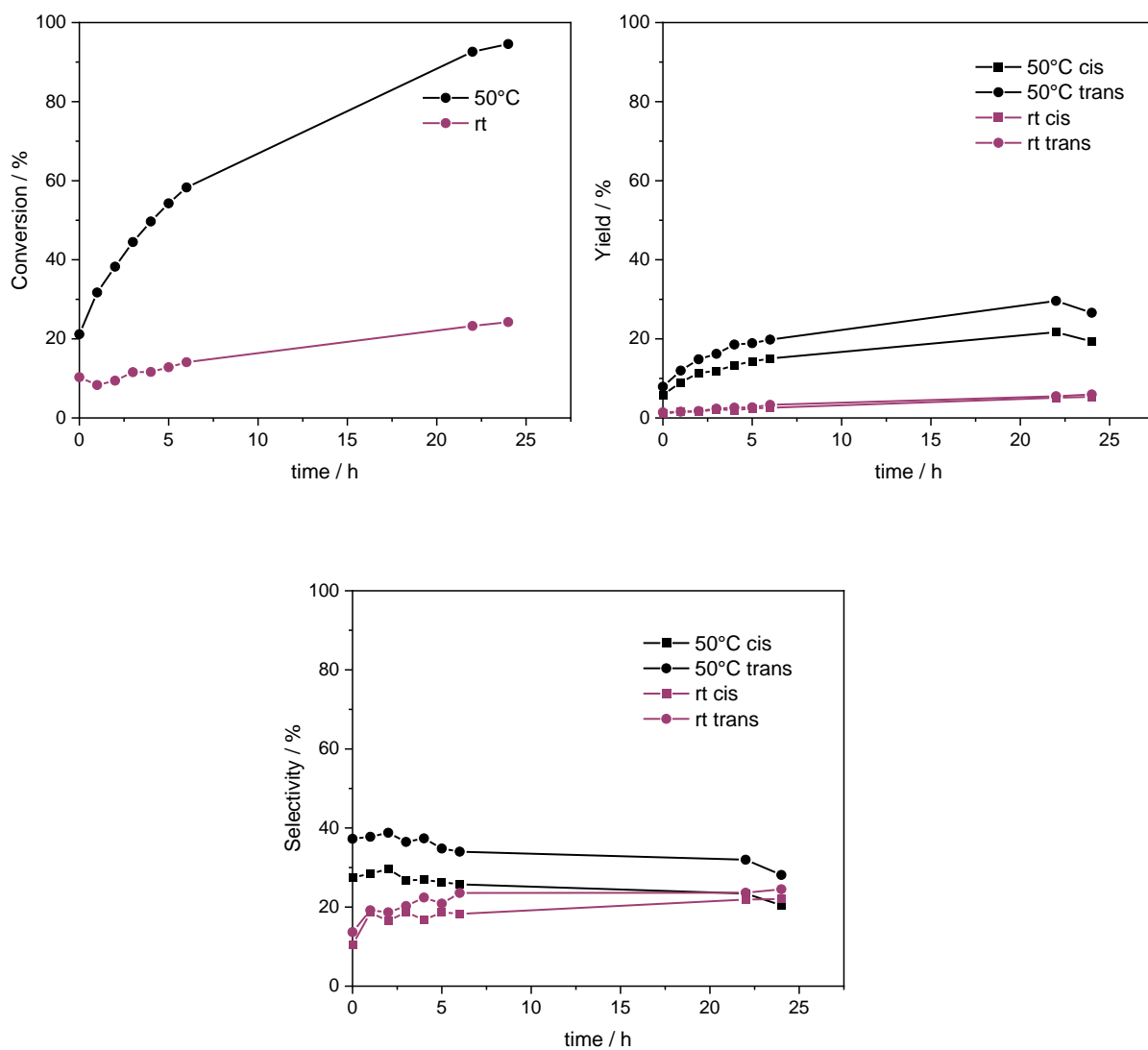


Figure A 87: Conversion, Yield and Selectivity during the reaction progress of the styrene cyclopropanation with EDA using PCN-222(Rh) as catalyst with varying reaction temperature in MeCN (room temperature (rt) vs 50 °C).

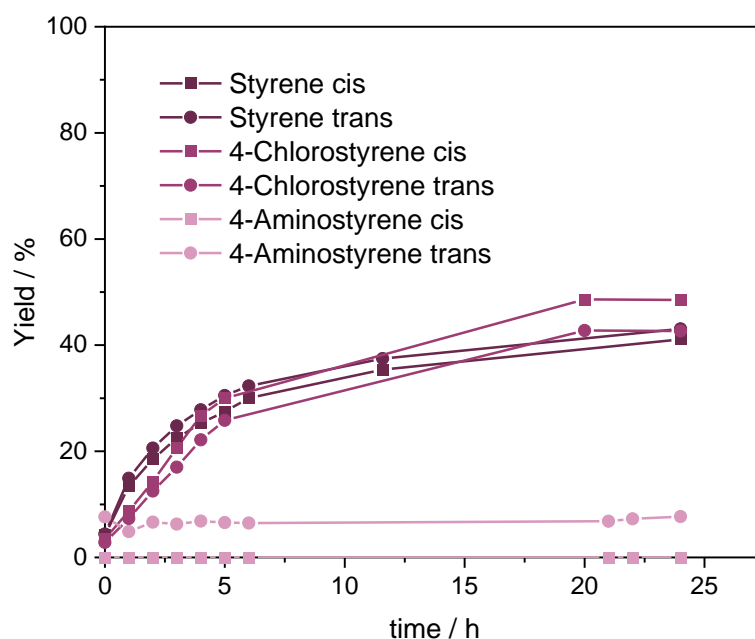


Figure A 88: Yield of the cis and trans cyclopropanation products during the reaction progress of the cyclopropanation with EDA using PCN-222(Rh) as catalyst under standard reaction conditions with substrate variation: styrene versus 4-chlorostyrene versus 4-aminostyrene.

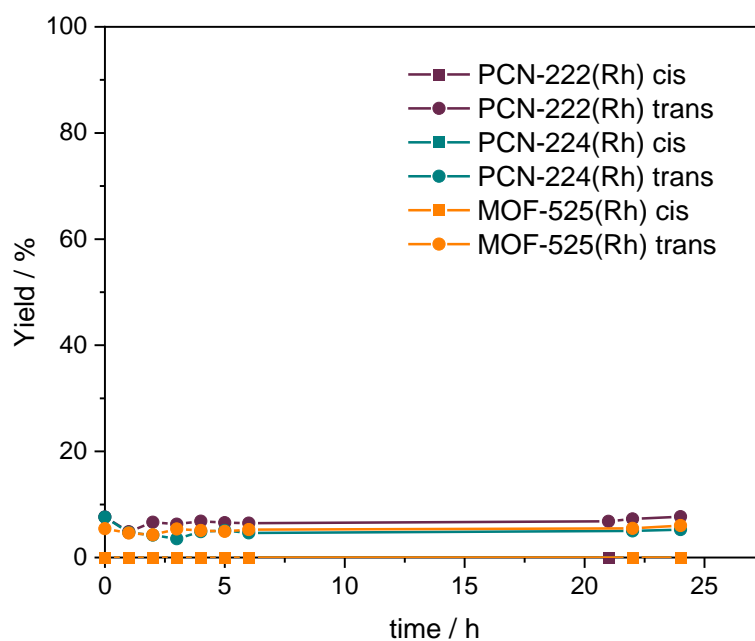


Figure A 89: Yield of the cis and trans cyclopropanation products during the reaction progress of the 4-aminostyrene cyclopropanation with EDA under standard reaction conditions varying the catalyst: PCN-222(Rh) versus PCN-224(Rh) versus MOF-525(Rh).



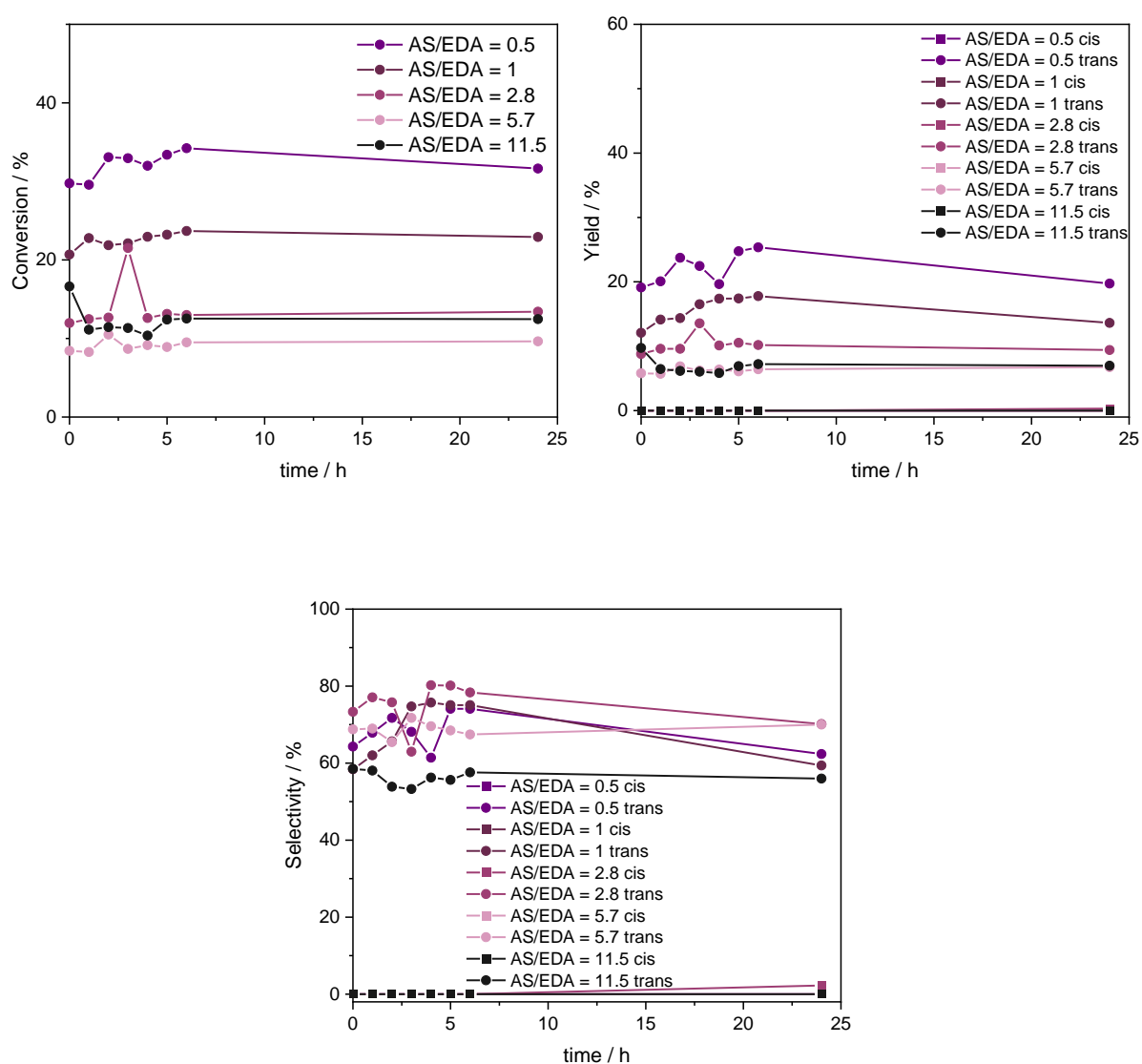


Figure A 90: Conversion, Yield and Selectivity during the reaction progress of 4-aminostyrene cyclopropanation with EDA using PCN-222(Rh) as catalyst under standard reaction conditions. The 4-AS/EDA ratio was varied (0.5 versus 1.0 versus 2.8 versus 5.7 versus 11.5).

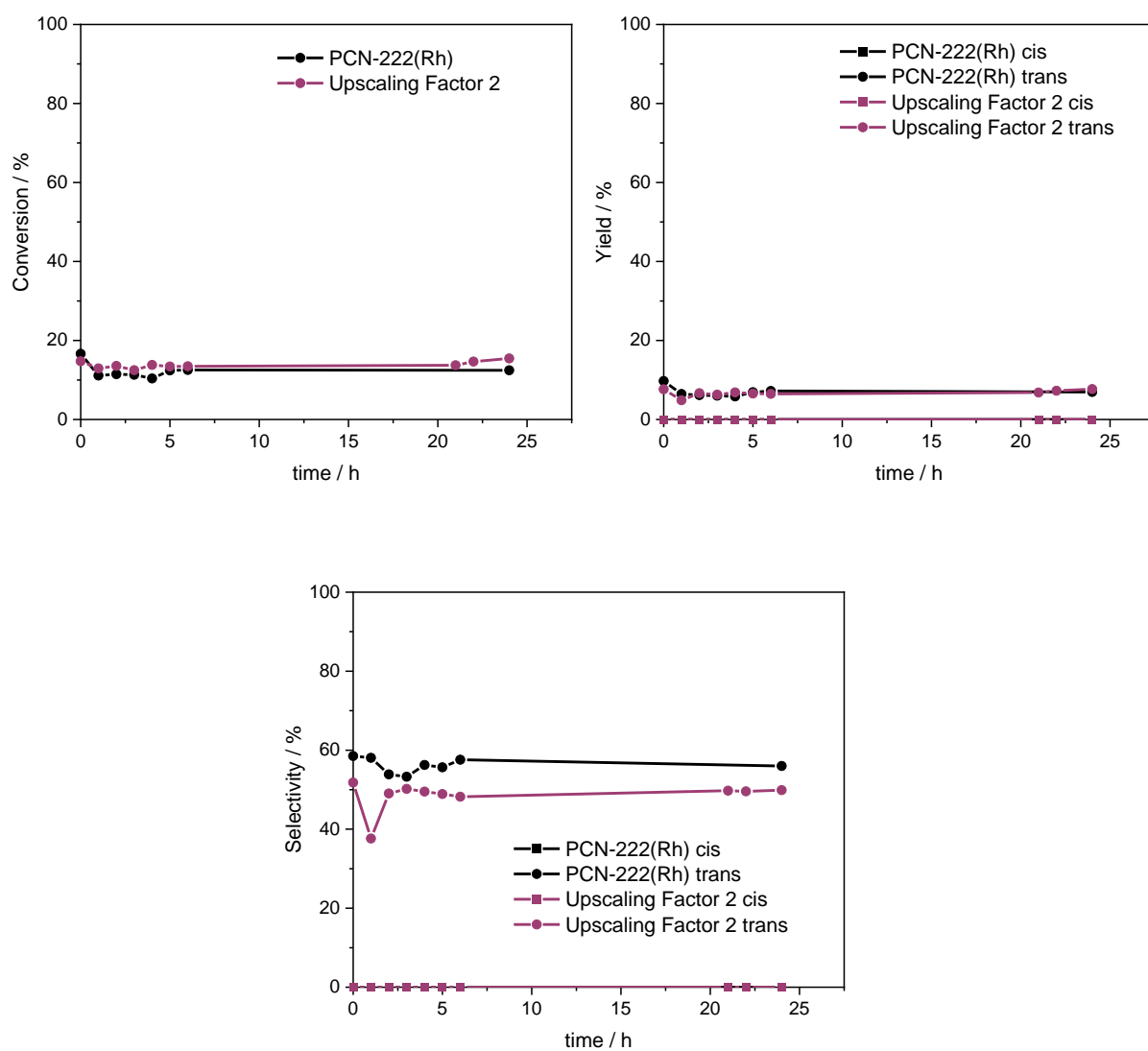


Figure A 91: Conversion, Yield and Selectivity during the reaction progress of 4-aminostyrene cyclopropanation with EDA using PCN-222(Rh) as catalyst under standard reaction conditions. The standard reaction setup is compared to an experiment with an upscaling factor of 2.

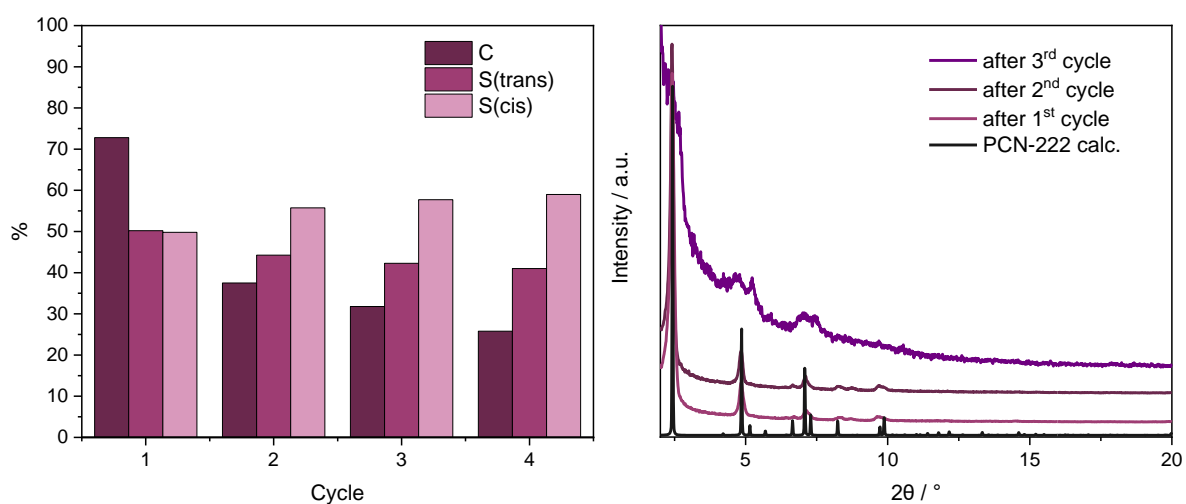


Figure A 92: Left: Recycling experiments for the catalytic styrene cyclopropanation with EDA under standard reaction conditions and PCN-222(Rh) as catalyst after 6h after complete EDA addition via a motorized syringe pump (0.5 mL/h). After the reaction, the catalyst is separated via centrifugation and washed with DCM (3x4 mL). Right: PXRD pattern of PCN-222(Rh) after each catalysis cycle compared to the calculated pattern of PCN-222.

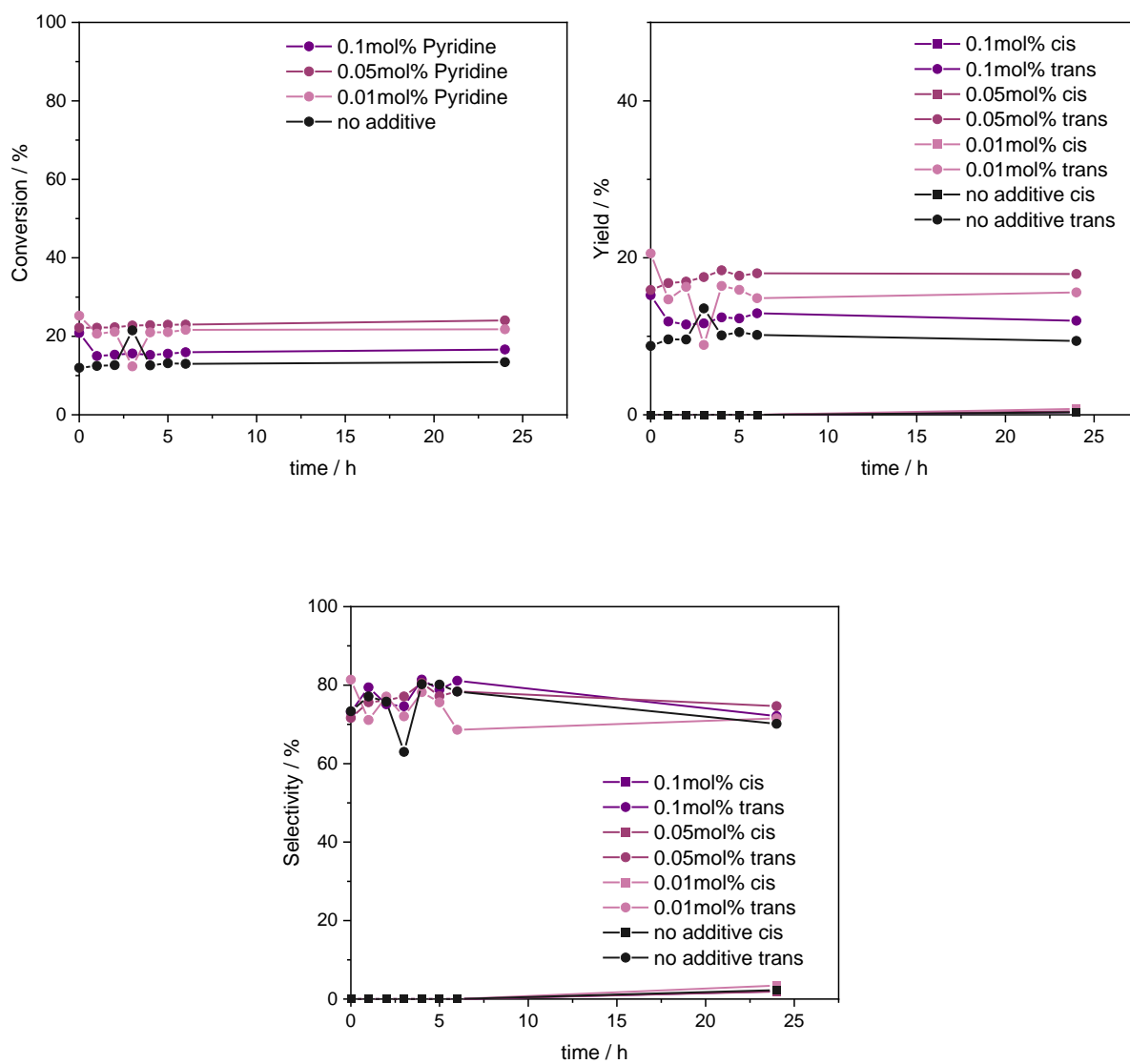


Figure A 93: Conversion, Yield and Selectivity of the cyclopropanation of 4-aminostyrene with EDA under standard reaction conditions adding different concentrations (regarding Rh) of pyridine: 0.1 mol% versus 0.05 mol% versus 0.01 mol% versus 0 mol%.

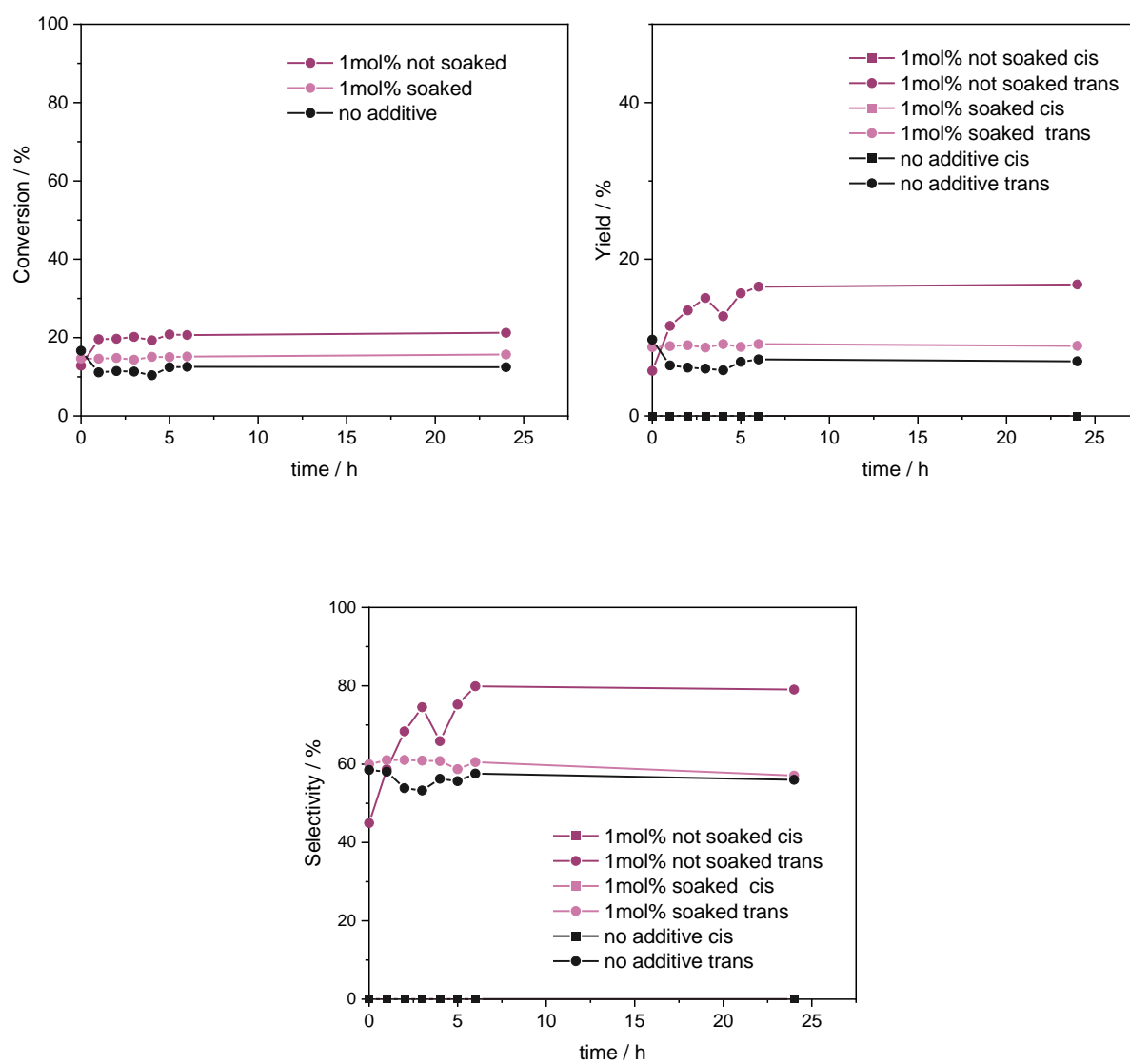


Figure A 94: Conversion, Yield and Selectivity of the cyclopropanation of 4-aminostyrene with EDA under standard reaction conditions adding 1 mol% (regarding Rh) of pyridine. For comparison, in one approach, the MOF was soaked for 2 h in a solution of additive in DCM while for a second approach pyridine was added without soaking.

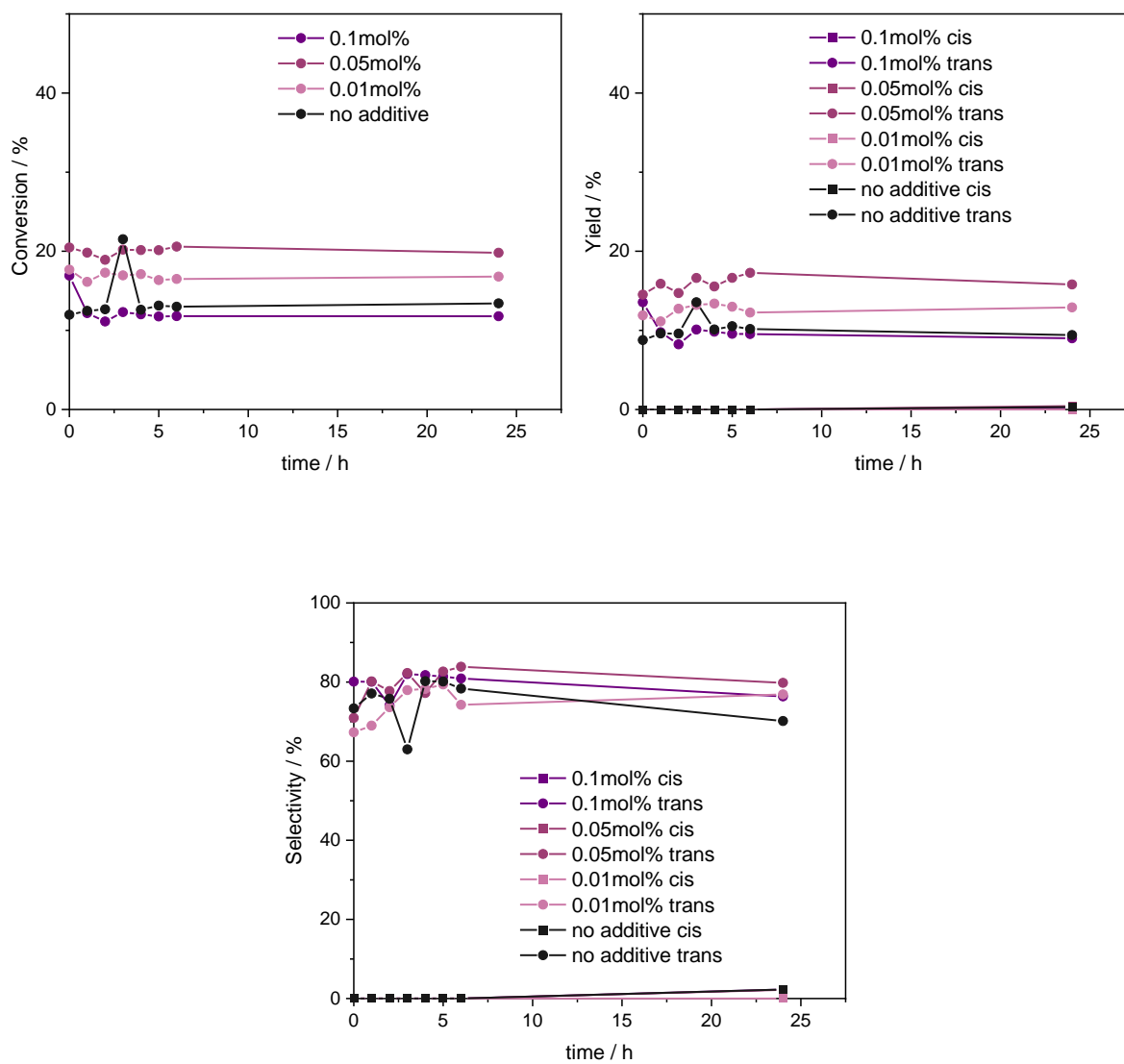


Figure A 95: Conversion, Yield and Selectivity of the cyclopropanation of 4-aminostyrene with EDA under standard reaction conditions adding different concentrations (regarding Rh) of aniline: 0.1 mol% versus 0.05 mol% versus 0.01 mol% versus 0 mol%.

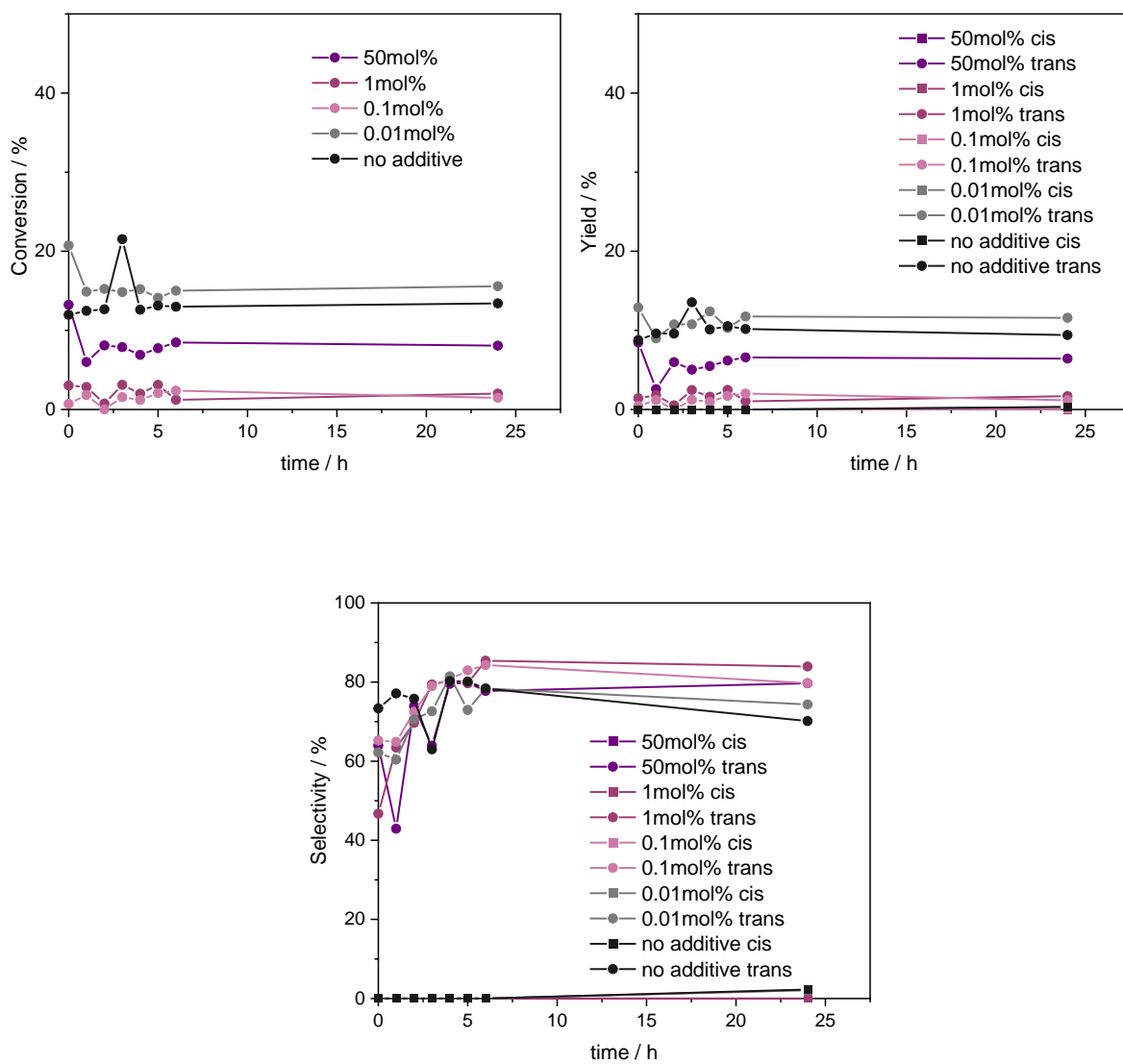


Figure A 96: Conversion, Yield and Selectivity of the cyclopropanation of 4-aminostyrene with EDA under standard reaction conditions adding different concentrations (regarding Rh) of ethylenediamine: 50 mol% versus 1 mol% versus 0.1 mol% versus 0.01 mol% versus 0 mol%.

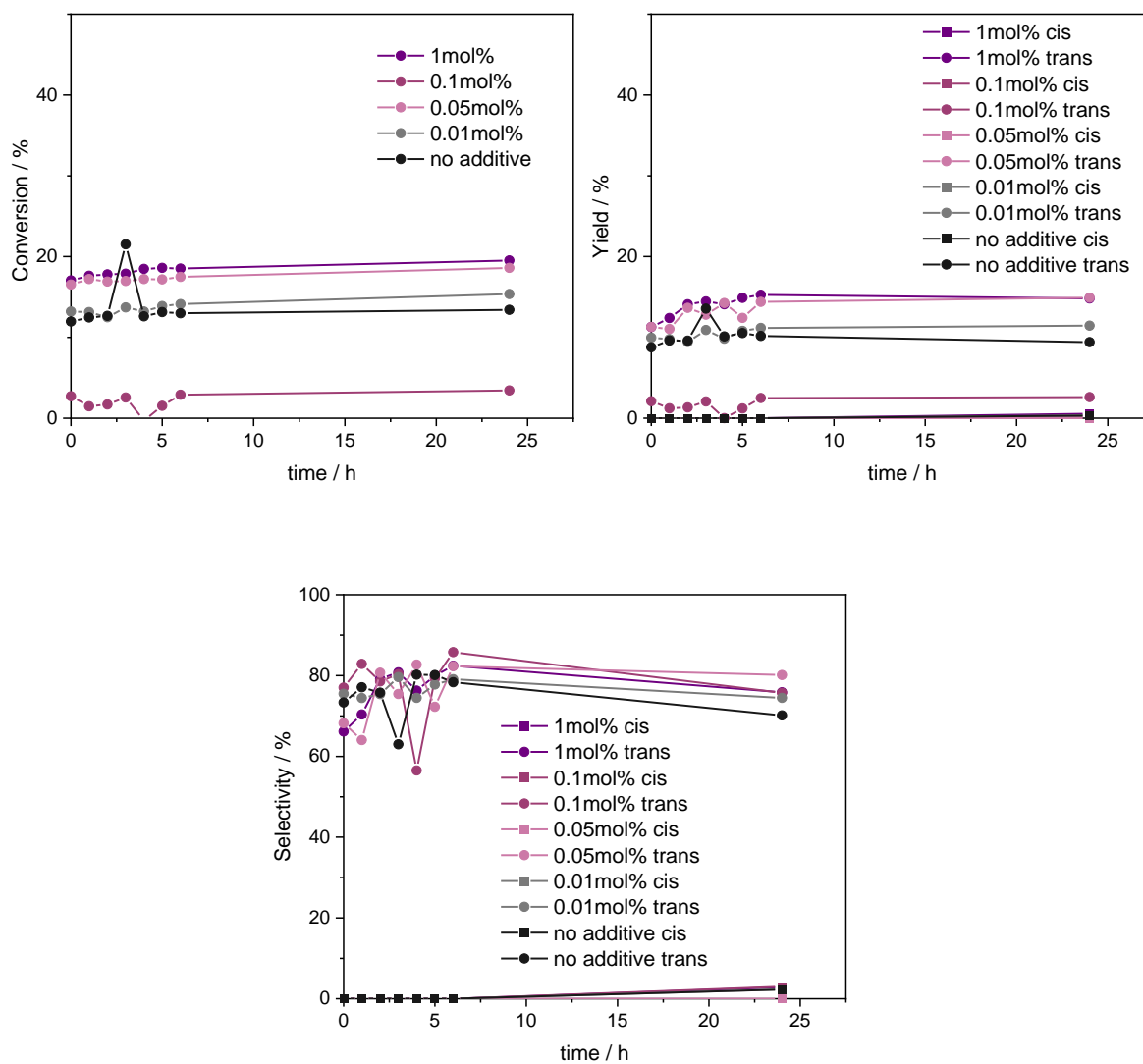


Figure A 97: Conversion, Yield and Selectivity of the cyclopropanation of 4-aminostyrene with EDA under standard reaction conditions adding different concentrations (regarding Rh) of phenol: 1 mol% versus 0.1 mol% versus 0.05 mol% versus 0.01 mol% versus 0 mol%.



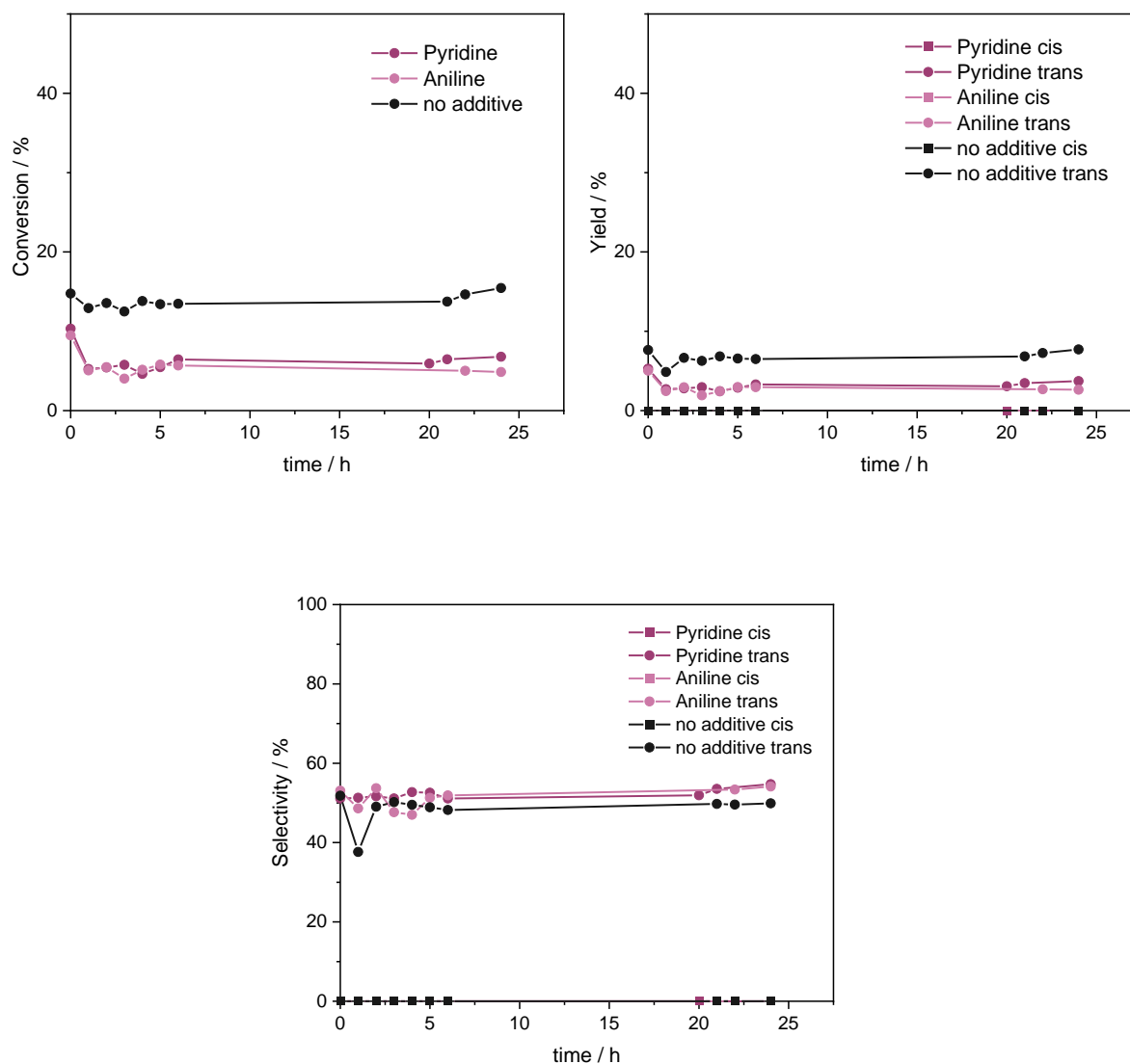


Figure A 98: Conversion, Yield and Selectivity for the cyclopropanation of 4-aminostyrene with EDA and different additives with a concentration of 50 mol% regarding Rh using PCN-222(Rh) as catalyst under standard reaction conditions.

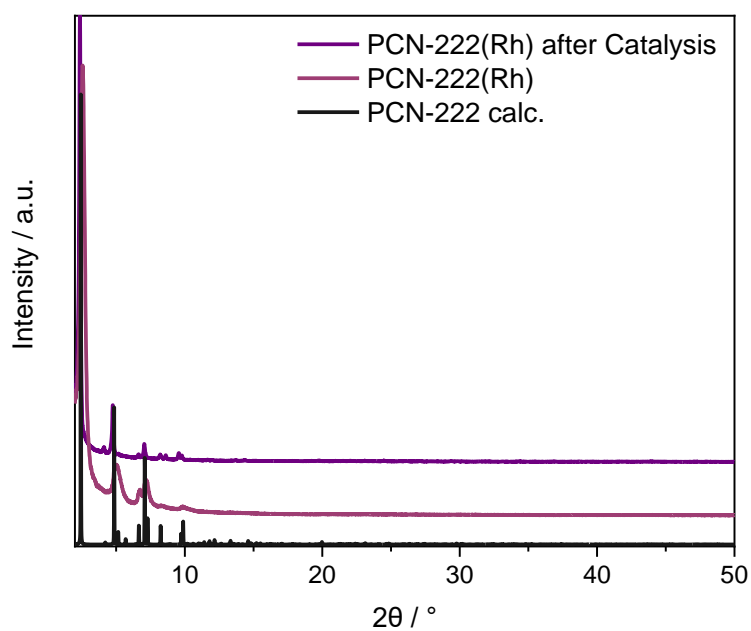


Figure A 99: PXRD pattern of PCN-222(Rh) catalysts after 24h of cyclopropanation catalysis compared to PCN-222(Rh) before catalysis and the pattern calculated from crystal structure data. MOF separation from the reaction suspension was achieved via centrifugation, following by washing with DCM (1× 8 mL) and drying under air.

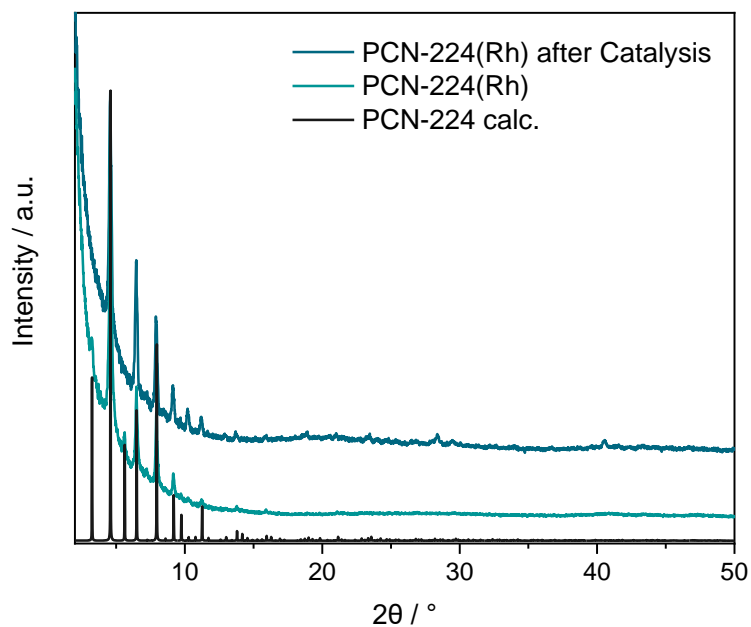


Figure A 100: PXRD pattern of PCN-224(Rh) catalysts after 24h of cyclopropanation catalysis compared to PCN-224(Rh) before catalysis and the pattern calculated from crystal structure data. MOF separation from the reaction suspension was achieved via centrifugation, following by washing with DCM (1× 8 mL) and drying under air.

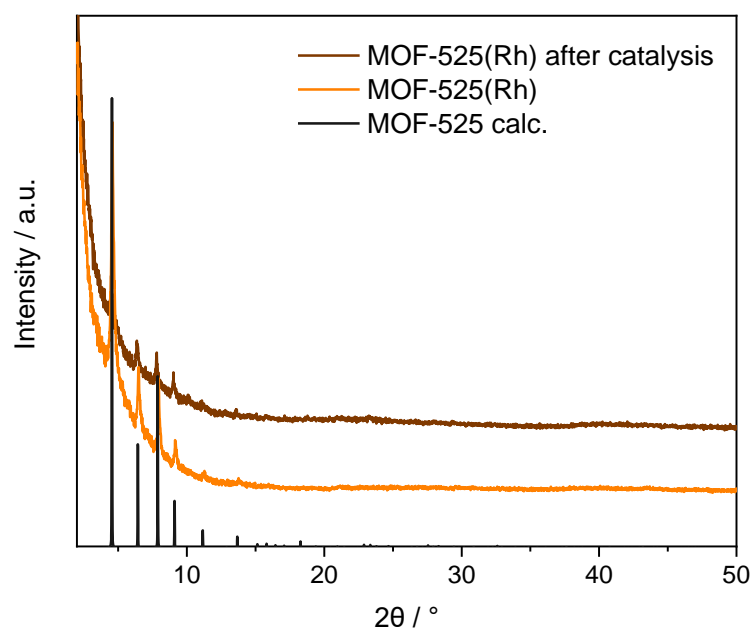


Figure A 101: PXRD pattern of MOF-525(Rh) catalysts after 24h of cyclopropanation catalysis compared to MOF-525(Rh) before catalysis and the pattern calculated from crystal structure data. MOF separation from the reaction suspension was achieved via centrifugation, following by washing with DCM (1× 8 mL) and drying under air.

## 7.4. Epoxidation Catalysis

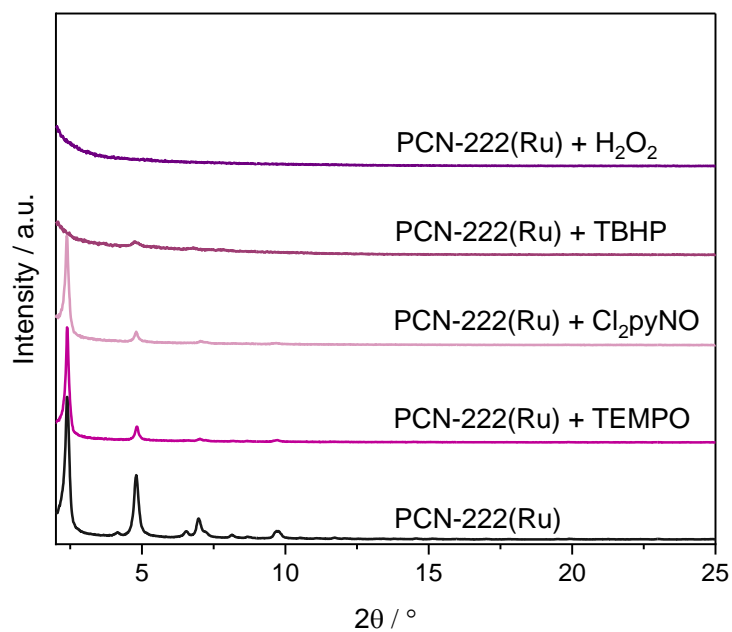


Figure A 102: PXRD pattern of PCN-222(Ru) soaked in different oxidants compared to synthesized PCN-222(Ru).

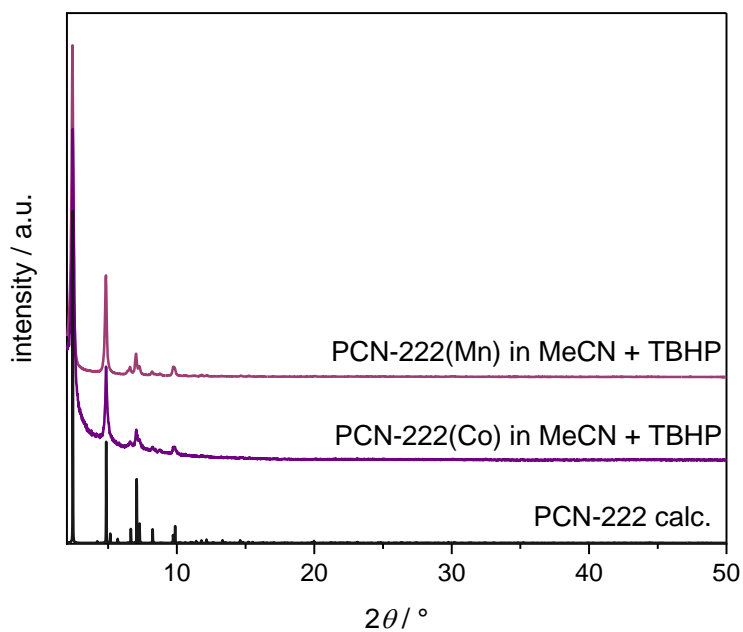


Figure A 103: PXRD pattern of PCN-222(Mn) and PCN-222(Co) soaked for 24 h in TBHP in MeCN compared to the calculated pattern of PCN-222.

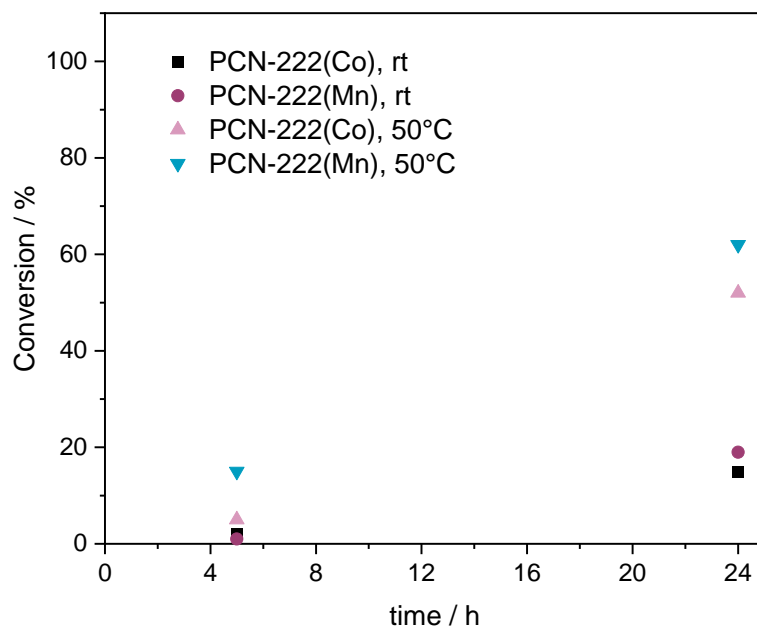


Figure A 104: Conversion of styrene in the epoxidation with PCN-222(Mn) and PCN-222(Co), respectively, as catalyst varying the reaction temperature (rt versus 50 °C). Reaction conditions: 2.00 mg MOF (9.1 wt% Mn, 10.8 wt%), MeCN, 2.4 equiv. TBHP, 1.0 equiv. styrene, 300 rpm stirring.

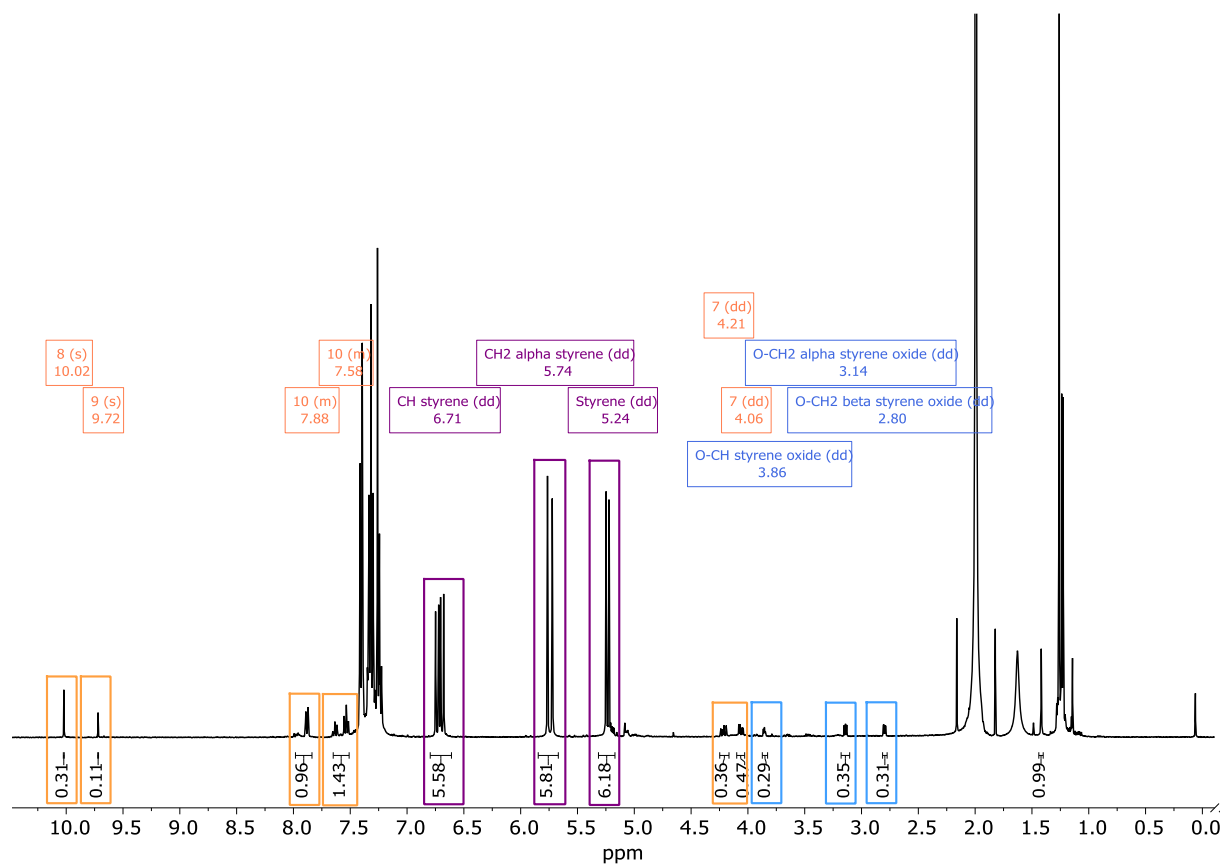


Figure A 105: <sup>1</sup>H NMR spectrum of the styrene epoxidation catalysis with PCN-222(Mn) after 24 h of reaction. Reaction conditions: 2.00 mg MOF (9.1 wt% Mn), MeCN, 2.4 equiv. TBHP, 1.0 equiv. styrene, 300 rpm stirring, 50°C. Peaks highlighted in purple correspond to the substrate styrene, blue for styrene oxide and orange for by-products (7 for 1-phenylethane-1,2-diol, 8 for benzaldehyde, 9 for 2-phenylacetaldehyde, 10 for acetophenone).

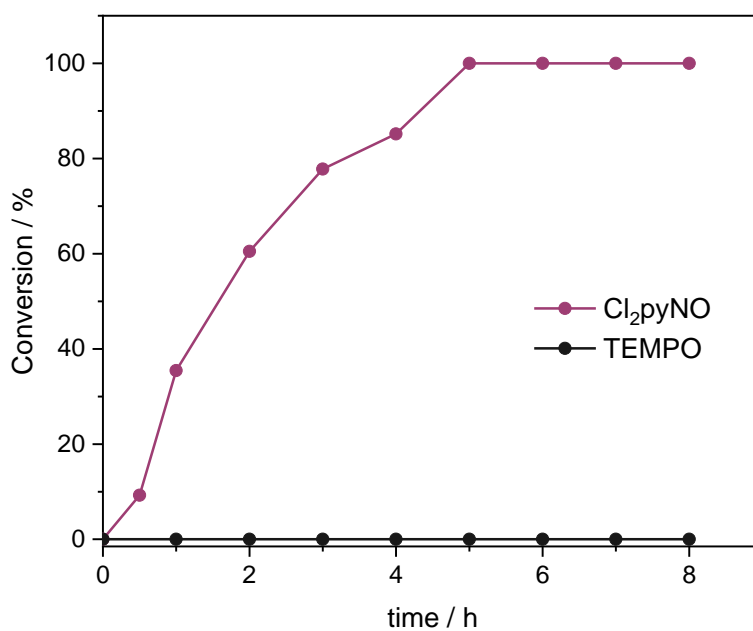


Figure A 106: Conversion of the styrene epoxidation with TEMPO and Cl<sub>2</sub>pyNO as oxidizing agents and PCN-222(Ru) as catalyst. Reaction conditions: 40 °C in DCM, 1.0 equiv. olefin, 1.1 equiv. oxidant, 0.25 mol% catalyst loading (regarding Ru)

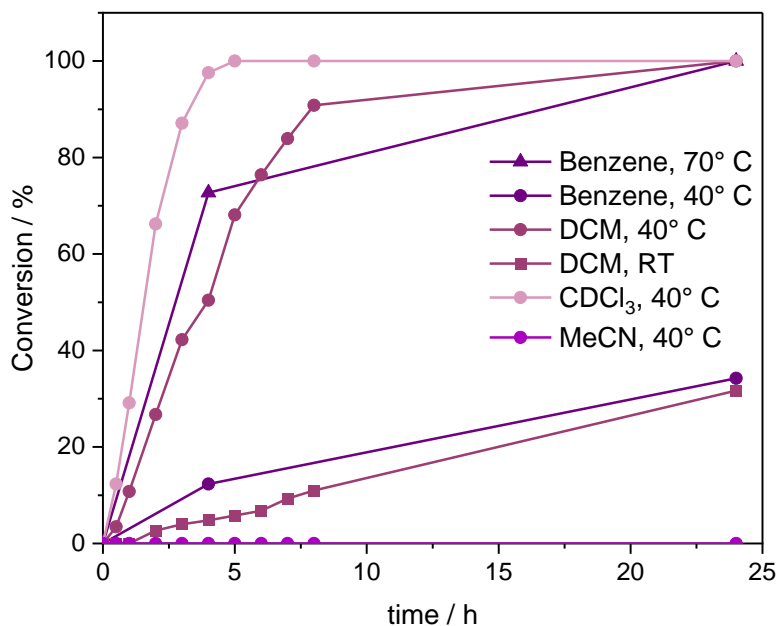


Figure A 107: Conversions of styrene epoxidation using PCN-222(Ru) as catalyst with 1.0 equiv. of olefin, 2.2 equiv. of Cl<sub>2</sub>py NO and a catalyst loading of 0.25 mol% (regarding Ru). Solvent (Benzene, DCM, CDCl<sub>3</sub>, MeCN) and temperature (RT, 40 °C, 70 °C) were varied.

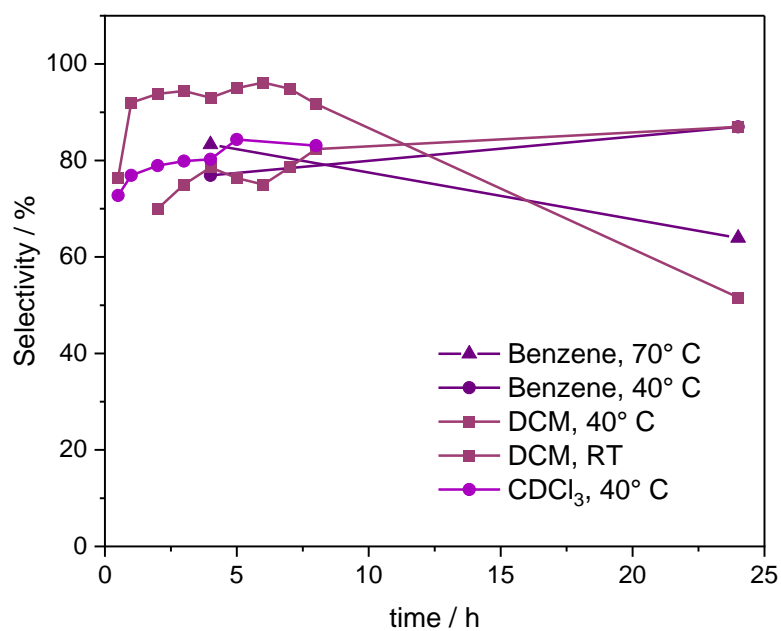


Figure A 108: Styrene oxide selectivities in the styrene epoxidation using PCN-222(Ru) as catalyst with 1.0 equiv. of olefin, 2.2 equiv. of Cl<sub>2</sub>py NO and a catalyst loading of 0.25 mol% (regarding Ru). Solvent (Benzene, DCM, CDCl<sub>3</sub>, MeCN) and temperature (RT, 40 °C, 70 °C) were varied.

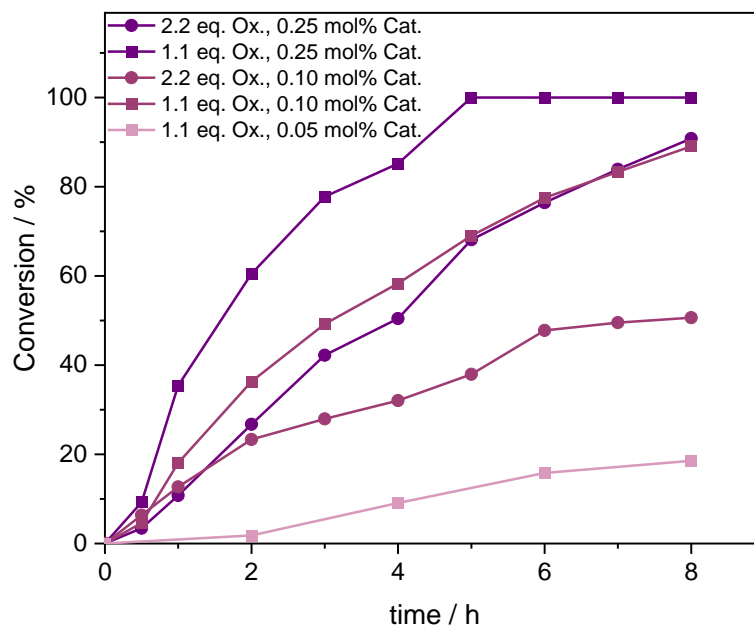


Figure A 109: Conversions of styrene epoxidation using PCN-222(Ru) in DCM at 40 °C varying the oxidant equivalents (1.1 equiv. vs. 2.2 equiv.) and catalyst loading (0.25 mol% versus 0.10 mol% versus 0.05 mol%).

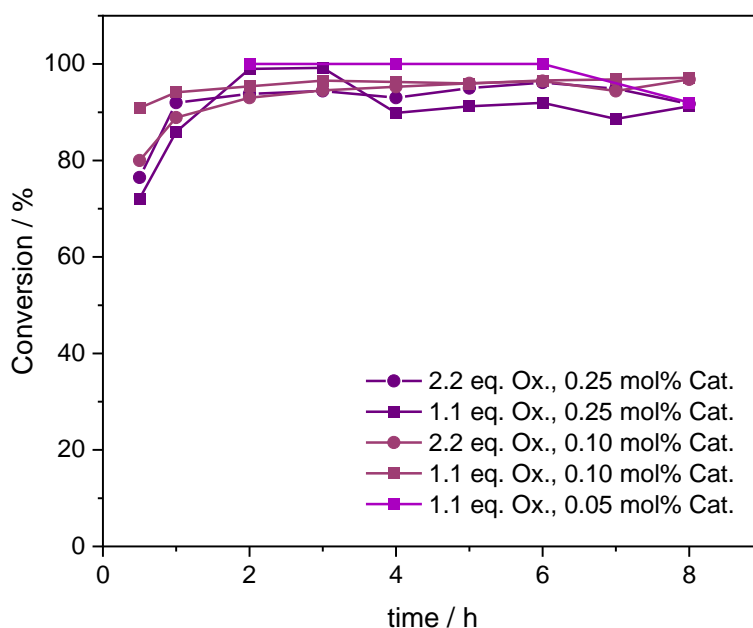


Figure A 110: Styrene oxide selectivities in the styrene epoxidation using PCN-222(Ru) in DCM at 40 °C varying the oxidant equivalents (1.1 equiv. vs. 2.2 equiv.) and catalyst loading (0.25 mol% versus 0.10 mol% versus 0.05 mol%).

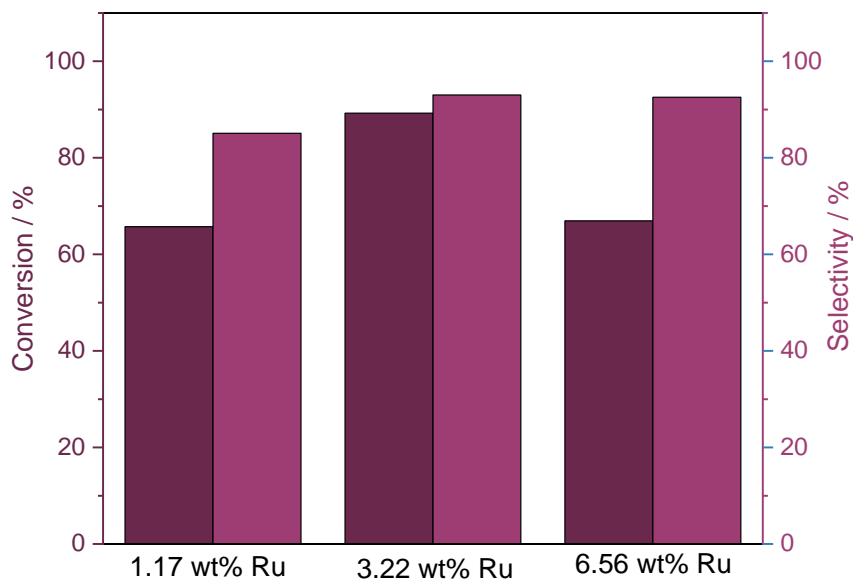


Figure A 111: Styrene conversions and styrene oxide selectivities for the styrene epoxidation after 6h in DCM at 40 °C using PCN-222(Ru) as catalyst while varying Ru dispersions within PCN-222(Ru) (1.17 wt%, 3.22 wt%, 6.56 wt%). Reaction conditions: 1.0 equiv. of olefin, 1.1 equiv. of Cl<sub>2</sub>pyNO, 0.25 mol% catalyst loading.



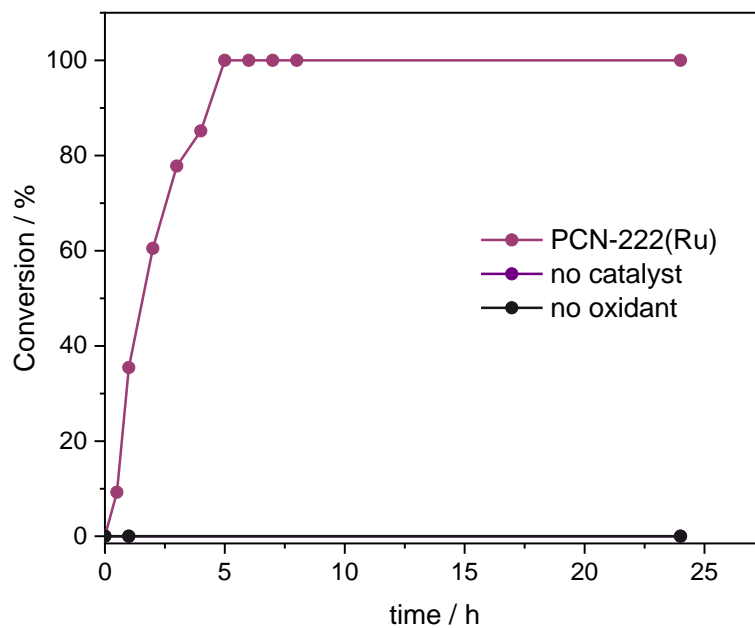


Figure A 112: Conversions of styrene epoxidation using PCN-222(Ru) and control experiments without catalyst and oxidant, respectively. Reaction conditions: 40 °C, DCM, 1.0 equiv. of olefin, 1.1 equiv. of Cl<sub>2</sub>pyNO, 0.25 mol% catalyst loading.

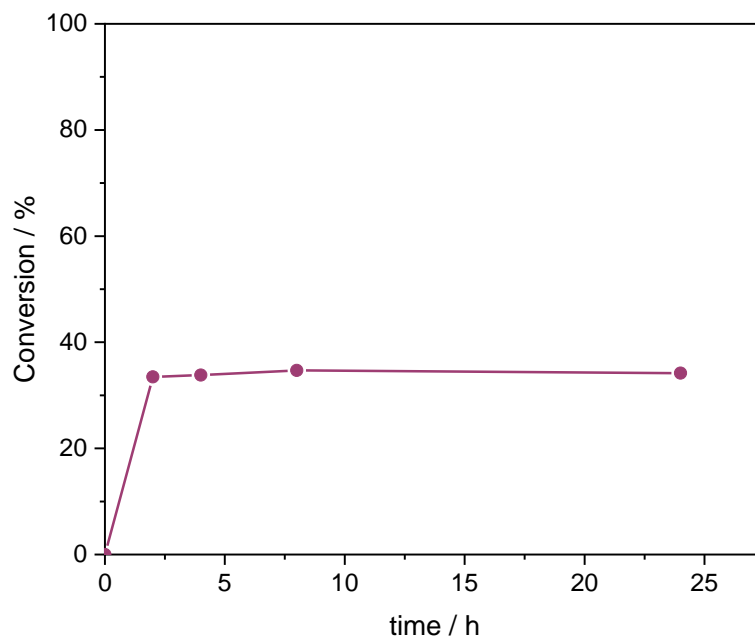


Figure A 113: Conversion of the styrene epoxidation using PCN-222(Ru) as catalyst. The catalyst was removed after 2 h of epoxidation to evaluate influence of possible metal leaching on catalysis. Reaction conditions: 40 °C, DCM, 1.0 equiv. of olefin, 1.1 equiv. of Cl<sub>2</sub>pyNO, 0.25 mol% catalyst loading.

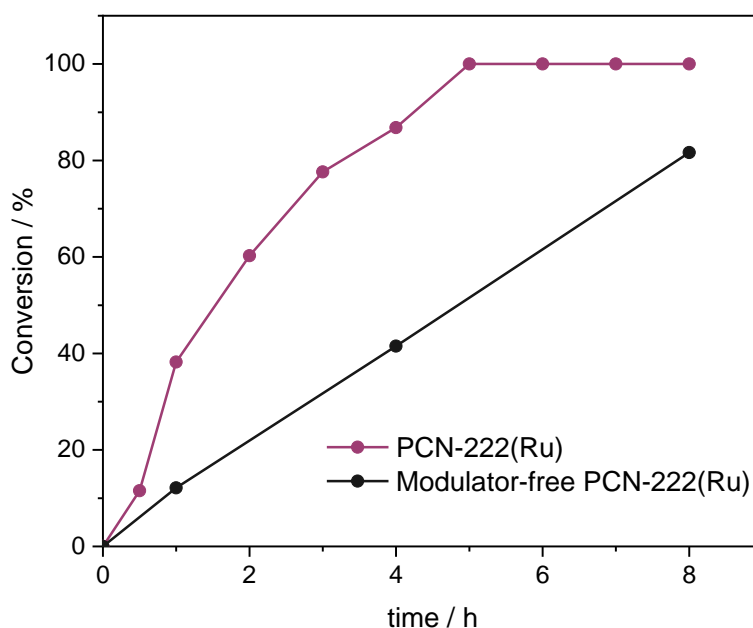


Figure A 114: Conversion of the styrene epoxidation using PCN-222(Ru) and modulator-free PCN-222(Ru), respectively, as catalysts. Modulator removal by heating a suspension of the MOF in HCl/DMF for 12 h at 120 °C. Reaction conditions for epoxidation: 40 °C, DCM, 1.0 equiv. of olefin, 1.1 equiv. of Cl<sub>2</sub>pyNO, 0.25 mol% catalyst loading.

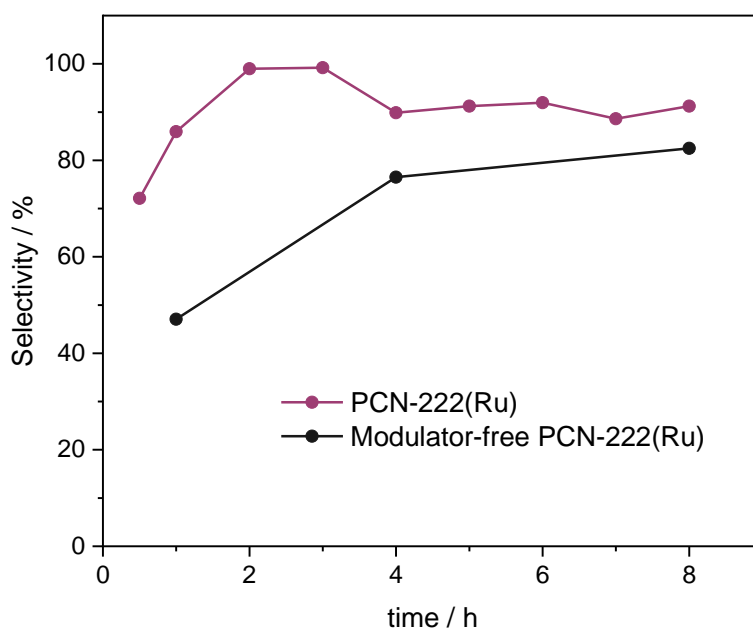


Figure A 115: Styrene oxide selectivity in the styrene epoxidation using PCN-222(Ru) and modulator-free PCN-222(Ru), respectively, as catalysts. Modulator removal by heating a suspension of the MOF in HCl/DMF for 12 h at 120 °C. Reaction conditions for epoxidation: 40 °C, DCM, 1.0 equiv. of olefin, 1.1 equiv. of Cl<sub>2</sub>pyNO, 0.25 mol% catalyst loading.

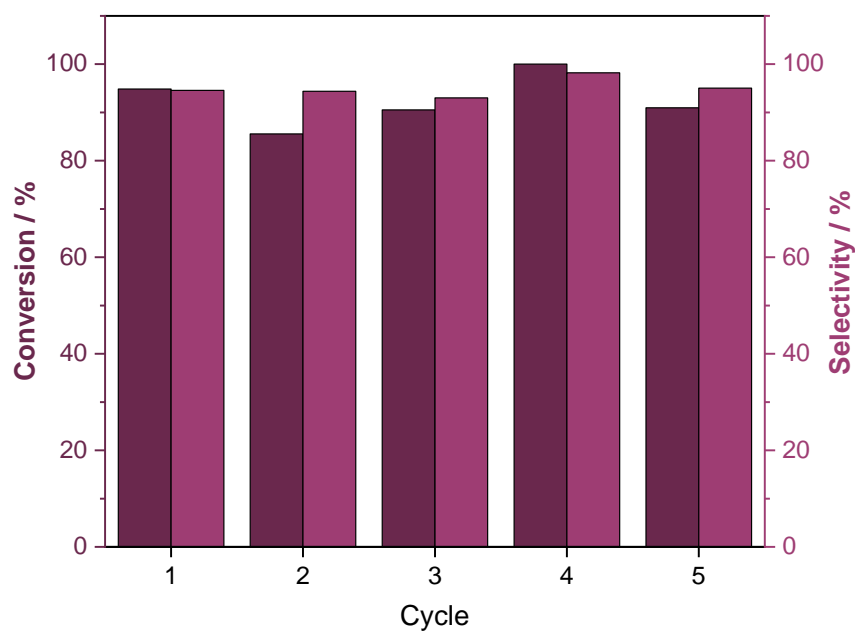


Figure A 116: Styrene conversions and styrene oxide selectivities for the styrene epoxidation with PCN-222(Ru) recycled 4 times. For recycling experiments, the catalyst was separated after 4 h of epoxidation, washed with DCM and dried *in vacuo*. Reaction conditions for epoxidation: 40 °C, DCM, 1.0 equiv. of olefin, 1.1 equiv. of Cl<sub>2</sub>pyNO, 0.25 mol% catalyst loading

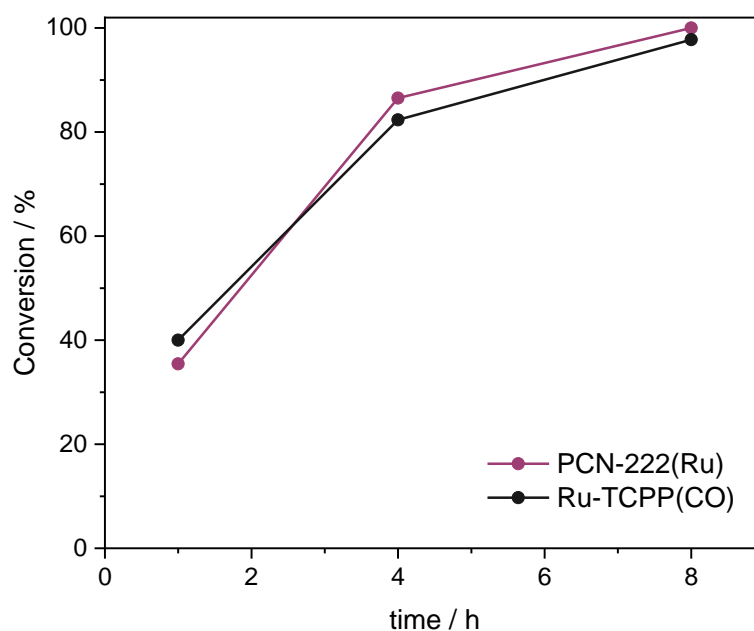


Figure A 117: Conversion of the styrene epoxidation using PCN-222(Ru) in a heterogeneous system and Ru-TCPP(CO) in homogeneous phase, respectively, as catalysts. Reaction conditions: 40 °C, DCM, 1.0 equiv. of olefin, 1.1 equiv. of Cl<sub>2</sub>pyNO, 0.25 mol% catalyst loading. For homogeneous catalysis an overestimation of conversions needs to be considered since the catalyst was not removed for <sup>1</sup>H NMR measurements

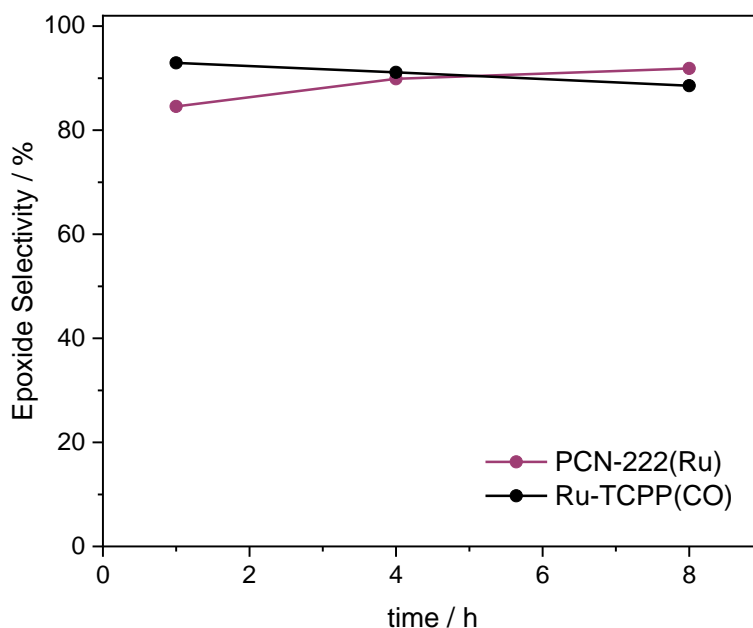


Figure A 118: Styrene oxide selectivities of the styrene epoxidation using PCN-222(Ru) in a heterogeneous system and Ru-TCPP(CO) in homogeneous phase, respectively, as catalysts. Reaction conditions: 40 °C, DCM, 1.0 equiv. of olefin, 1.1 equiv. of Cl<sub>2</sub>pyNO, 0.25 mol% catalyst loading.

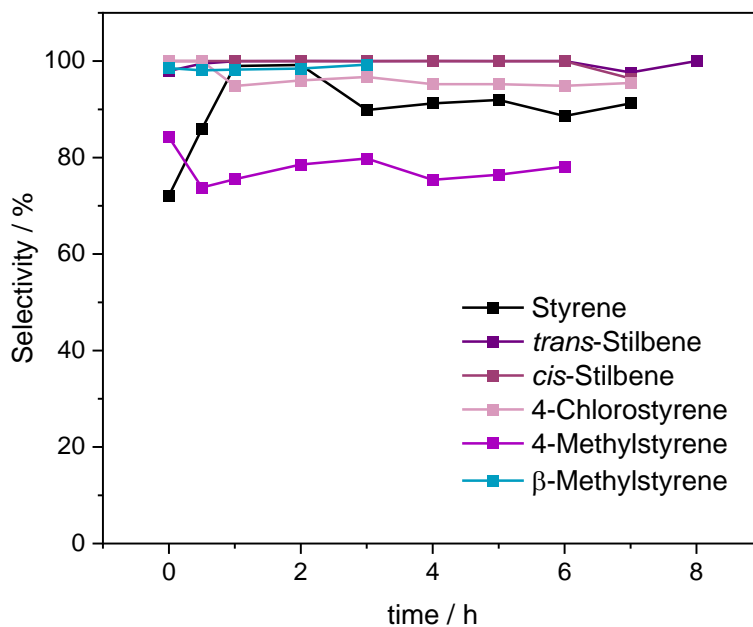


Figure A 119: Epoxide selectivities of different substrates (styrene, *trans*- and *cis*-stilbene, 4-chlorostyrene, 4-methylstyrene, β-methylstyrene) in the epoxidation catalysis using PCN-222(Ru) as catalyst. Reaction conditions: 40 °C, DCM, 1.0 equiv. of olefin, 1.1 equiv. of Cl<sub>2</sub>pyNO, 0.25 mol% catalyst loading.

## 7.5. CO<sub>2</sub> Cycloaddition Catalysis

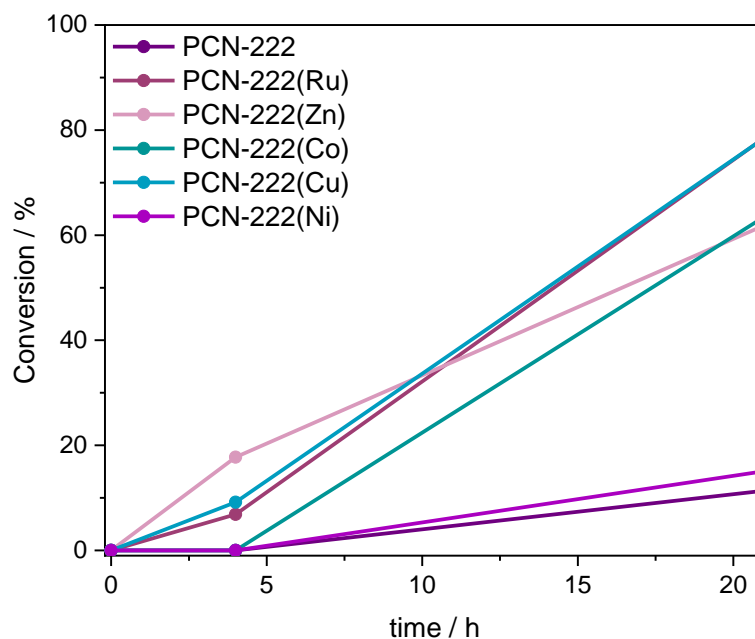


Figure A 120: Conversions of styrene oxide in the CO<sub>2</sub> cycloaddition with different PCN-222(M) catalysts. Reaction conditions: 40 °C, DCM, 4 bar CO<sub>2</sub>, 5 mol% TBAB (regarding olefin), 0.25 mol% M loading.

## 7.6. Sequential Olefin to Cyclic Carbonate Catalysis

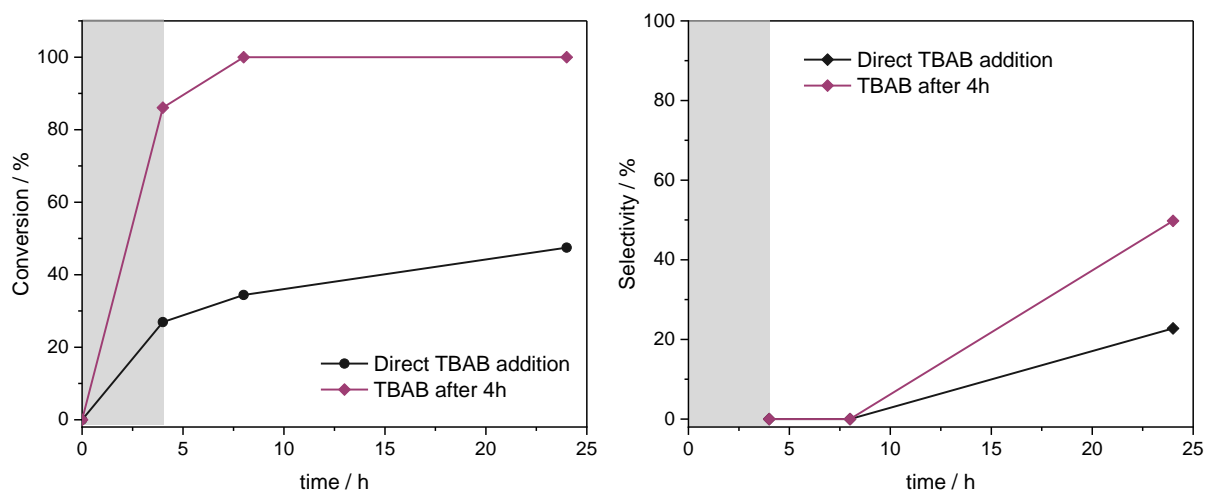


Figure A 121: Styrene conversions (left) and styrene carbonate selectivities (right) in the sequential epoxidation/CO<sub>2</sub> cycloaddition with PCN-222(Ru) as catalyst comparing two setups where 1) TBAB is directly added at the beginning of the reaction and 2) TBAB is added after 4 h of reaction. Reaction conditions: 40 °C, DCM 1.0 equiv. styrene, 1.1 equiv. Cl<sub>2</sub>pyNO, 4 bar CO<sub>2</sub> (added after 4 h reaction time), 5 mol% TBAB (regarding styrene), 0.25 mol% Ru.

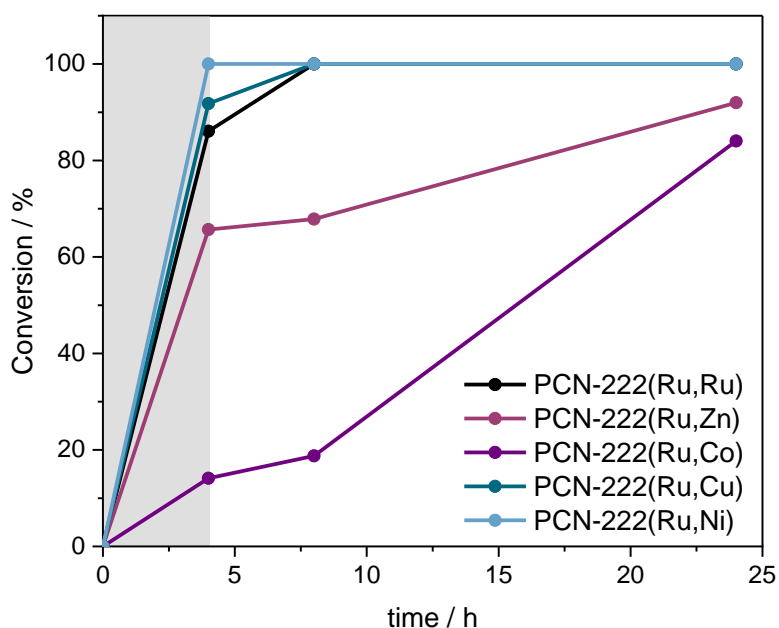


Figure A 122: Styrene conversion in the sequential epoxidation/ $\text{CO}_2$  cycloaddition with different PCN-222(Ru,M) (M= Ru, Co, Ni, Cu, Zn) as catalysts. Reaction conditions: 40 °C, DCM 1.0 equiv. styrene, 1.1 equiv.  $\text{Cl}_2\text{pyNO}$ , 4 bar  $\text{CO}_2$  (added after 4 h reaction time), 5 mol% TBAB (regarding styrene), 0.25 mol% Ru.

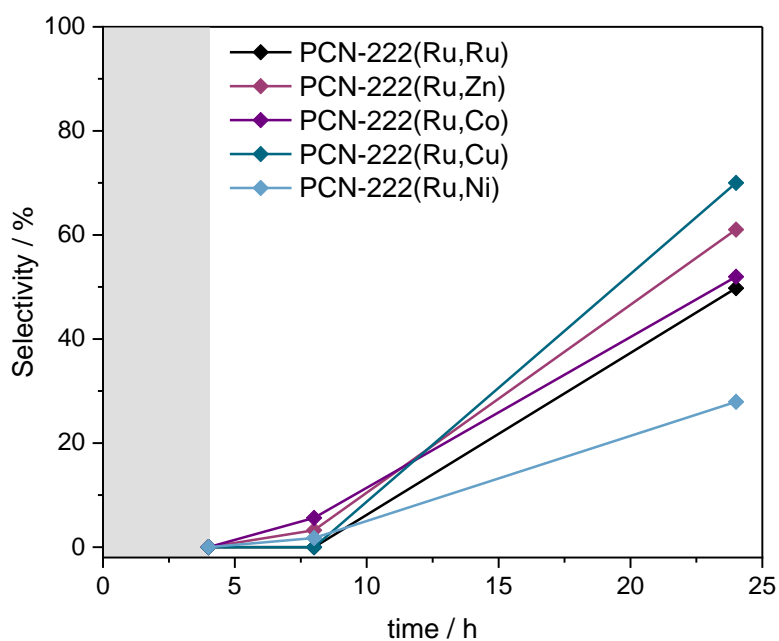


Figure A 123: Styrene carbonate selectivities of the sequential epoxidation/ $\text{CO}_2$  cycloaddition with different PCN-222(Ru,M) (M= Ru, Co, Ni, Cu, Zn) as catalysts. Reaction conditions: 40 °C, DCM 1.0 equiv. styrene, 1.1 equiv.  $\text{Cl}_2\text{pyNO}$ , 4 bar  $\text{CO}_2$  (added after 4 h reaction time), 5 mol% TBAB (regarding styrene), 0.25 mol% Ru.

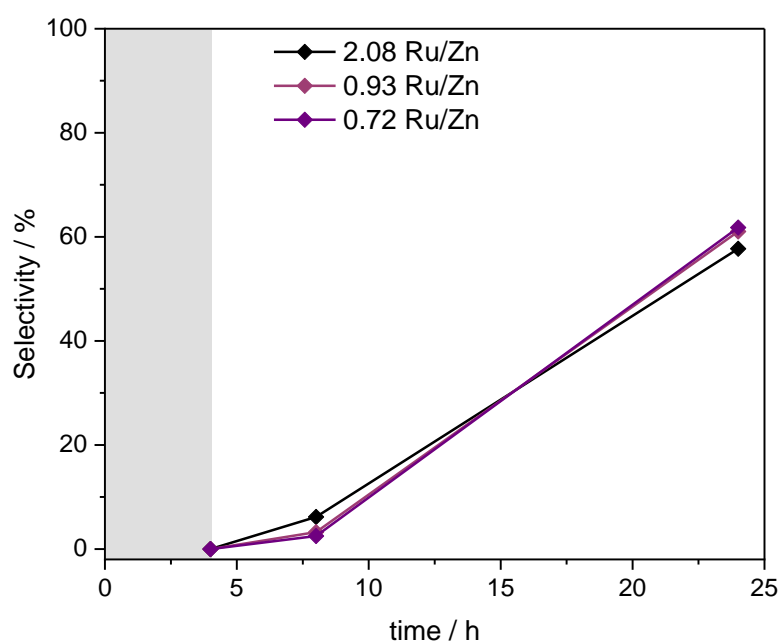


Figure A 124: Styrene carbonate selectivities of the sequential epoxidation/ $\text{CO}_2$  cycloaddition with PCN-222(Ru,Zn) as catalysts varying the Ru/Zn ratio. Reaction conditions: 40 °C, DCM 1.0 equiv. styrene, 1.1 equiv.  $\text{Cl}_2\text{pyNO}$ , 4 bar  $\text{CO}_2$  (added after 4 h reaction time), 5 mol% TBAB (regarding styrene), 0.25 mol% Ru.

## 7.7. Non-planar Porphyrin Framework Integration

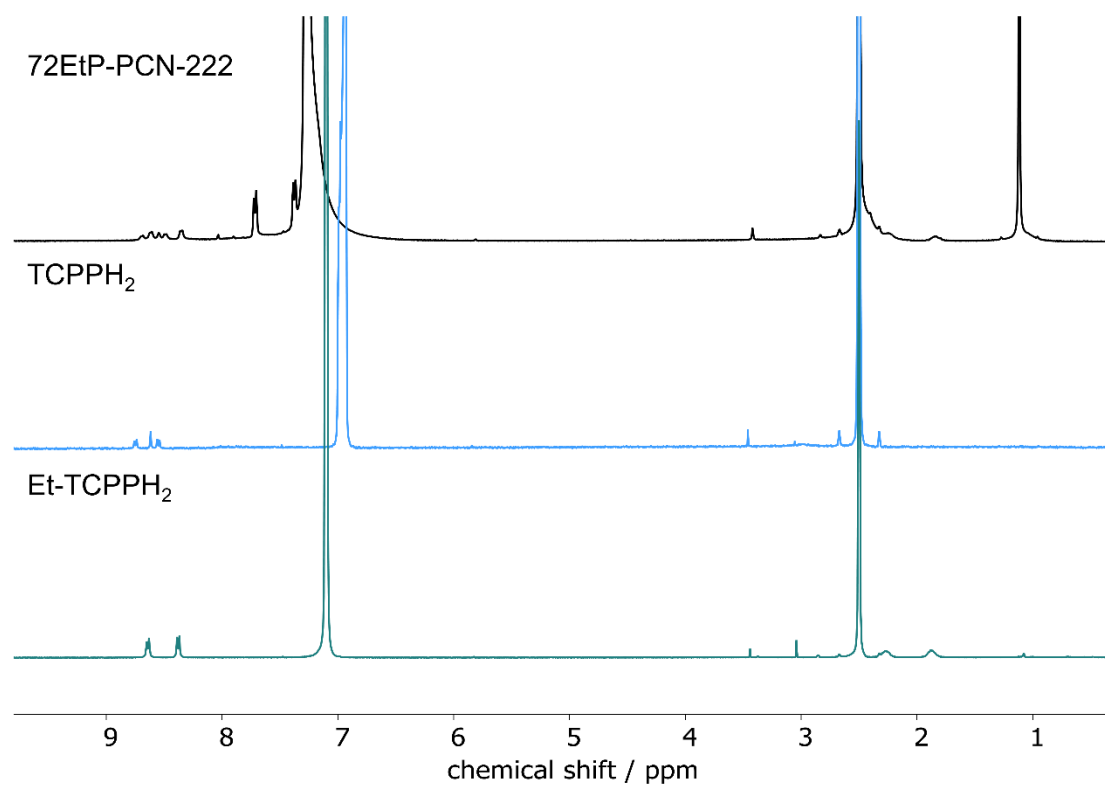


Figure A 125:  $^1\text{H}$  NMR spectra of Et-TCPPH<sub>2</sub>, TCPPH<sub>2</sub> and 72EtP-PCN-222 digested in DCI/DMSO- $d_6$  (0.1 mL/0.3 mL). For Et-TCPPH<sub>2</sub> and TCPPH<sub>2</sub> dissolved in DMSO- $d_6$  (0.3 mL) 0.1 mL of DCI was added.



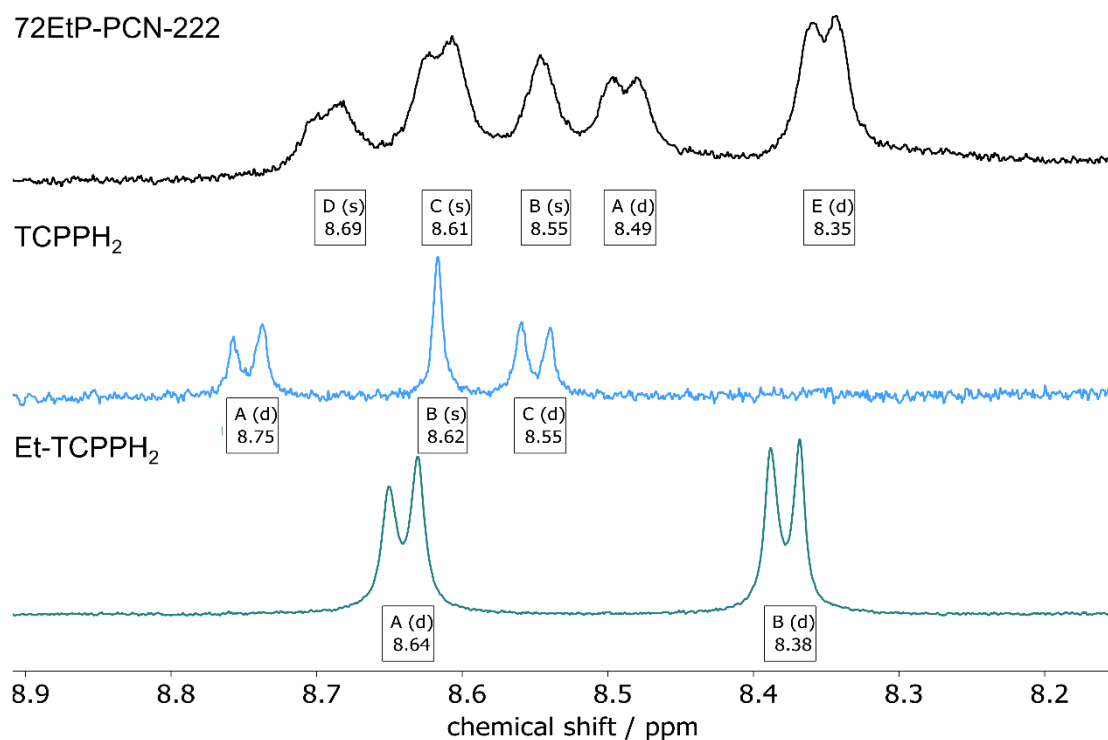


Figure A 126:  $^1\text{H}$  NMR spectra of Et-TCPPh<sub>2</sub>, TCPPh<sub>2</sub> and 72EtP-PCN-222 digested in DCI/DMSO- $d_6$  (0.1 mL/0.3 mL). For Et-TCPPh<sub>2</sub> and TCPPh<sub>2</sub> dissolved in DMSO- $d_6$  (0.3 mL) 0.1 mL of DCI was added. Porphyrin peaks in 72EtP-PCN-222 (chosen as example) are assigned to Et-TCPPh<sub>2</sub> (8.35 ppm, 8.61 ppm) and TCPPh<sub>2</sub> (8.49 ppm, 8.55 ppm, 8.69 ppm). The ratio of Et-TCPPh<sub>2</sub> and TCPPh<sub>2</sub> in in 72EtP-PCN-222 was calculated by comparing the integrals of TCPPh<sub>2</sub> (8.69 ppm) and Et-TCPPh<sub>2</sub> (8.35 ppm) while the signal at 8.69 ppm is normalized to 1 resulting in 77% ( $=3.44/4.44$ ) Et-TCPPh<sub>2</sub>.

Table A 13: Mol% of Et-TCPPh<sub>2</sub> in PCN-222 determined by  $^1\text{H}$  NMR spectroscopy of acid digested MOF by comparison of the integrals of the phenyl peaks at 8.71 ppm (for TCPPh<sub>2</sub>) and 8.36 ppm (for Et-TCPPh<sub>2</sub>).

Sample	Weigh in Et-TCPPh <sub>2</sub>	Mol% Et-TCPPh <sub>2</sub> in PCN-222 (NMR)
20EtP-PCN-222	20	20.3 ± 3.2
59EtP-PCN-222	10	59.3 ± 3.7
72EtP-PCN-222	20	72.1 ± 4.5

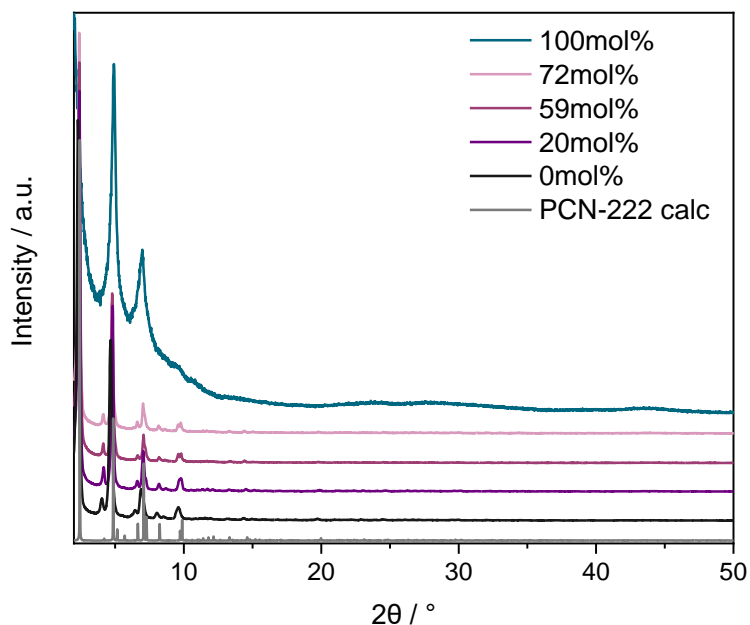


Figure A 127: PXRD pattern of PCN-222 with different Et-TCPPh<sub>2</sub> contents: 0 mol%, 20 mol%, 59 mol% Et-TCPPh<sub>2</sub>, 72 mol%, and 100 mol% Et-TCPPh<sub>2</sub>. The patterns are compared to the reflections of PCN-222 calculated from single crystal structure data.

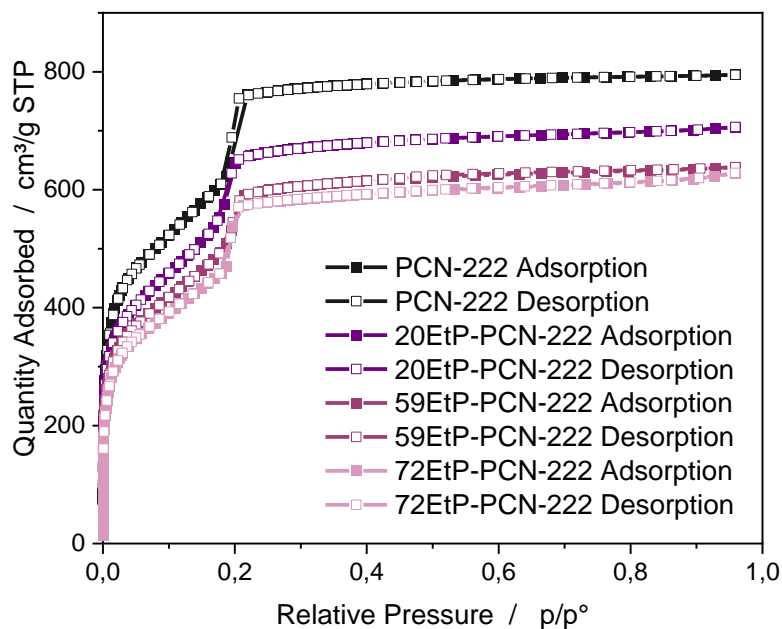


Figure A 128: N<sub>2</sub> adsorption isotherms at 77 K for PCN-222 with different Et-TCPPh<sub>2</sub> contents (0 mol%, 20 mol%, 59 mol% Et-TCPPh<sub>2</sub>, 72 mol%) - defined as 20EtP-PCN-222, 59EtP-PCN-222 and 72EtP-PCN-222 after activation at 120 °C in vacuo for 12 hours. Following BET surface areas were calculated: 2079 ± 6.9 m<sup>2</sup>·g<sup>-1</sup> (PCN-222), 1744 ± 15 m<sup>2</sup>·g<sup>-1</sup> (20EtP-PCN-222), 1594 ± 12 m<sup>2</sup>·g<sup>-1</sup> (59EtP-PCN-222), 1512 ± 10 m<sup>2</sup>·g<sup>-1</sup> (72EtP-PCN-222).

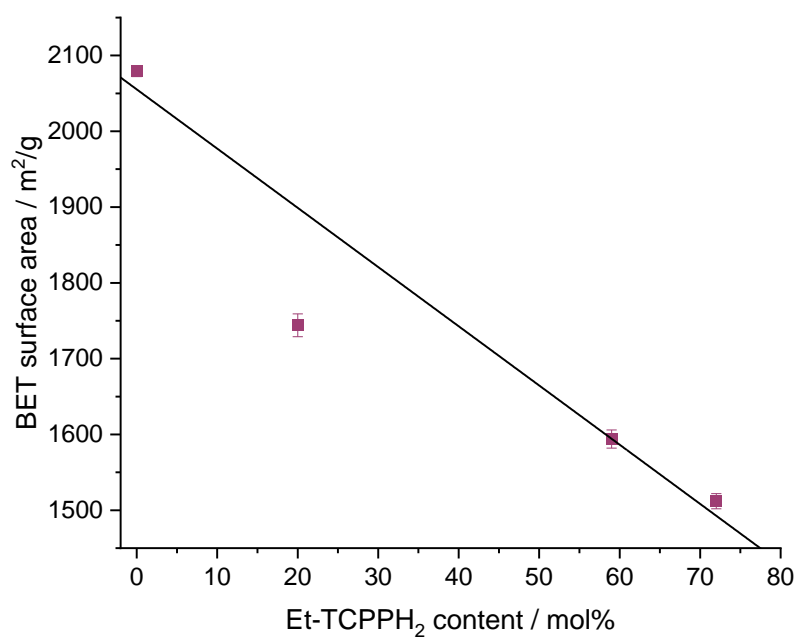


Figure A 129: BET surface areas of PCN-222 dependent on the Et-TCPPh<sub>2</sub> content (20EtP-PCN-222, 59EtP-PCN-222 and 72EtP-PCN-222) as a function of the Et-TCPPh<sub>2</sub> content. Black line: Linear fit.  $y = -7.81x + 2055$ .  $R^2 = 0.93286$ .

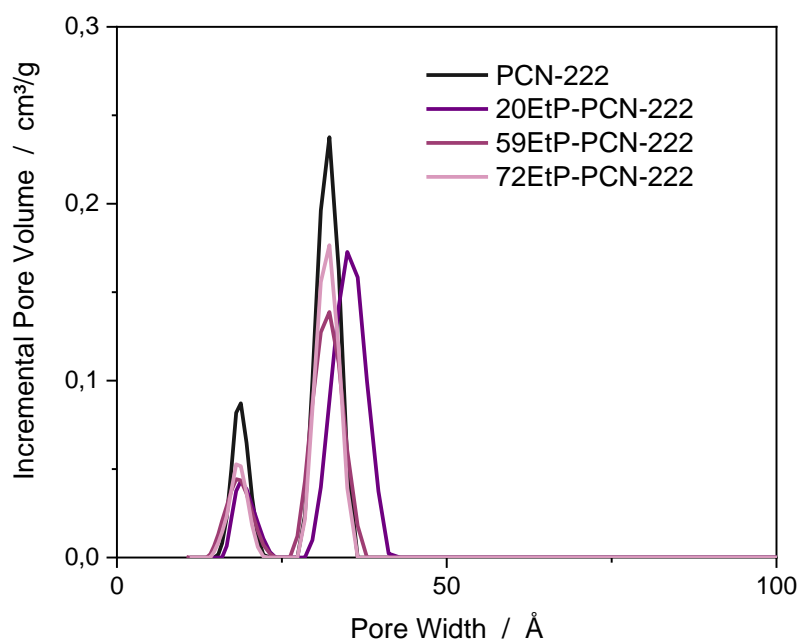


Figure A 130: Calculated pore size distributions from N<sub>2</sub> adsorption isotherms of PCN-222 materials with different Et-TCPPh<sub>2</sub> content (20EtP-PCN-222, 59EtP-PCN-222 and 72EtP-PCN-222) using sets of theoretical isotherms derived from 2D-NLDFT-based methods for specific pore sizes and geometry. As an approximation, cylindrical pores on an oxide surface were assumed for all materials.

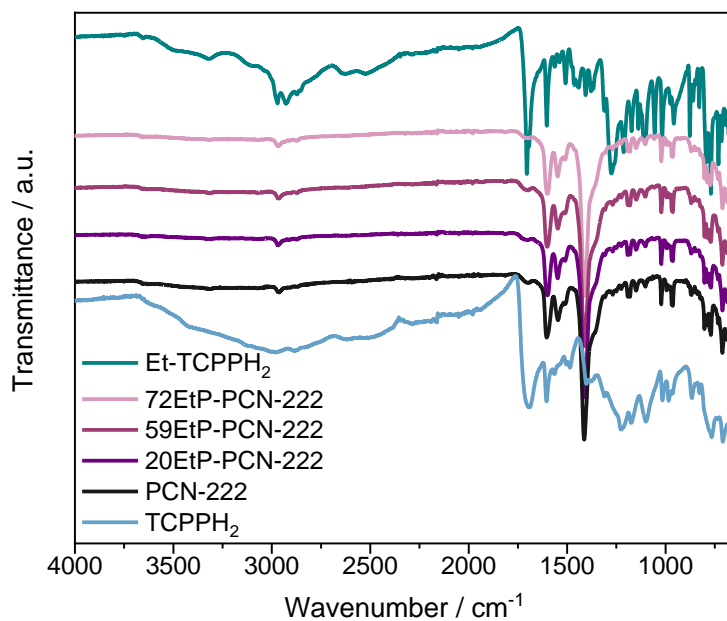


Figure A 131: Normalized IR spectra of TCPPH<sub>2</sub>, PCN-222, 20EtP-PCN-222, 59EtP-PCN-222, 72EtP-PCN-222 and Et-TCPPH<sub>2</sub>.

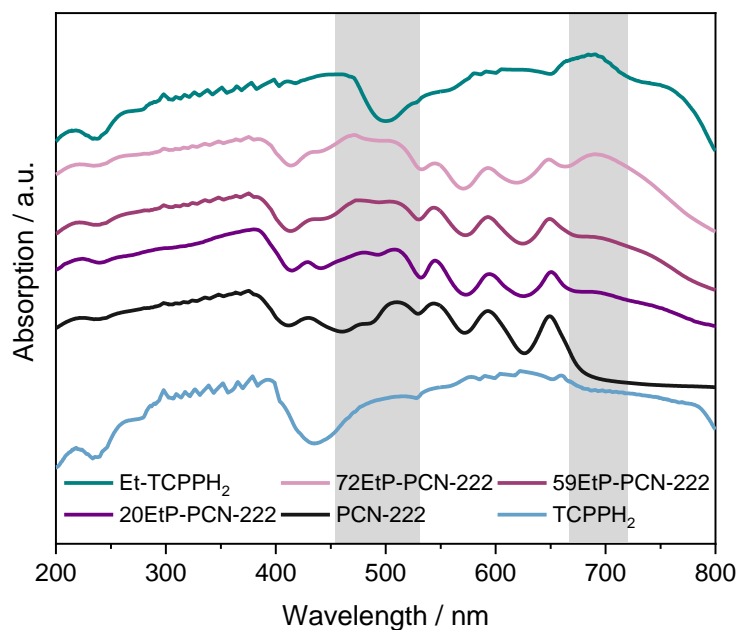


Figure A 132: Normalized solid-state UV-vis spectra of TCPPH<sub>2</sub>, PCN-222, 20EtP-PCN-222, 59EtP-PCN-222, 72EtP-PCN-222 and Et-TCPPH<sub>2</sub>. Areas of changes are highlighted in grey.

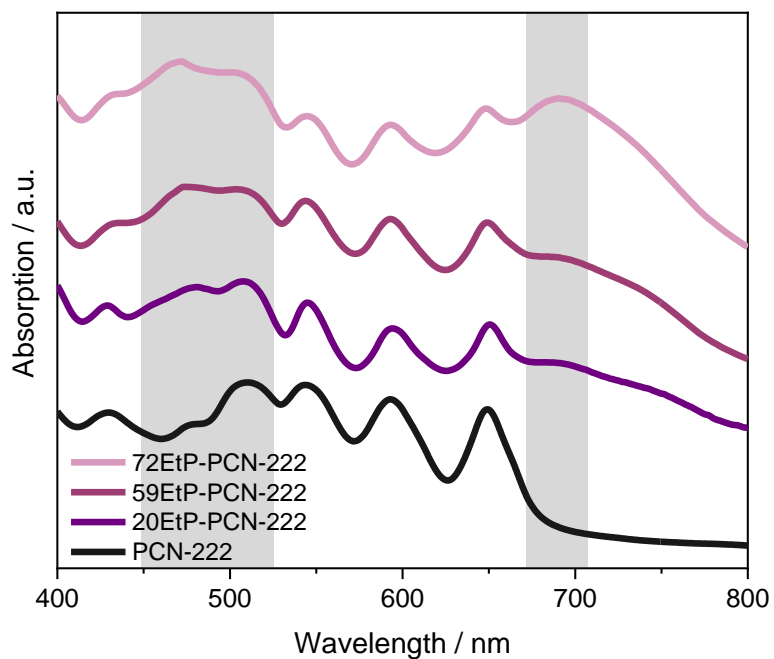


Figure A 133: Normalized solid-state UV-vis spectra of PCN-222, 20EtP-PCN-222, 59EtP-PCN-222 and 72EtP-PCN-222 in the range of 400 – 800 nm. Areas of changes are highlighted in grey.

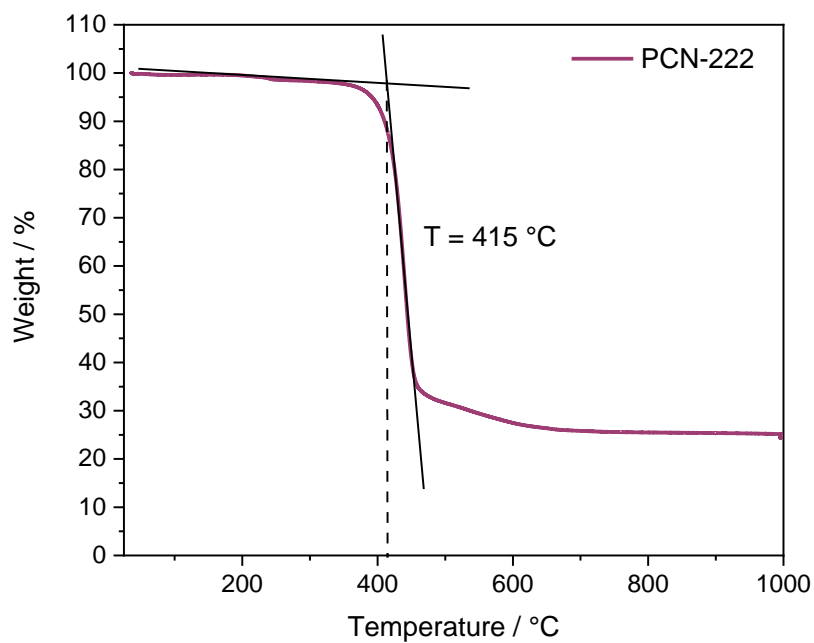


Figure A 134: TGA curve of PCN-222. Decomposition temperature was determined as 415 °C.

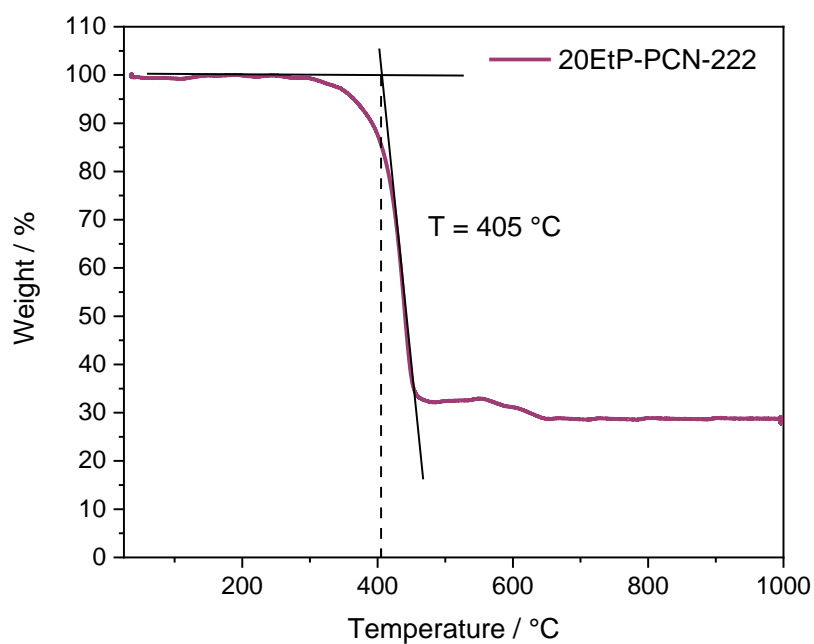


Figure A 135: TGA curve of 20EtP-PCN-222. Decomposition temperature was determined as 405 °C.

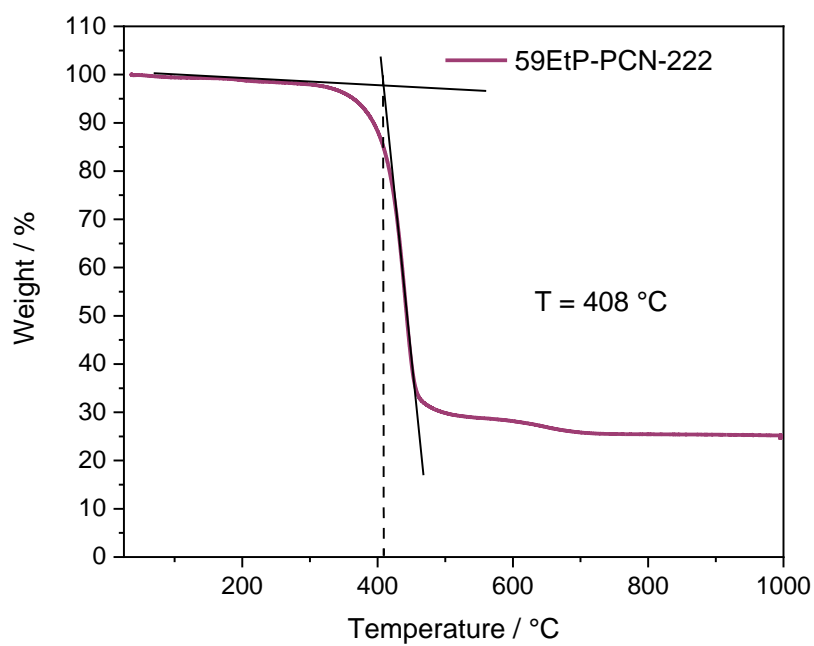


Figure A 136: TGA curve of 59EtP-PCN-222. Decomposition temperature was determined as 408 °C.

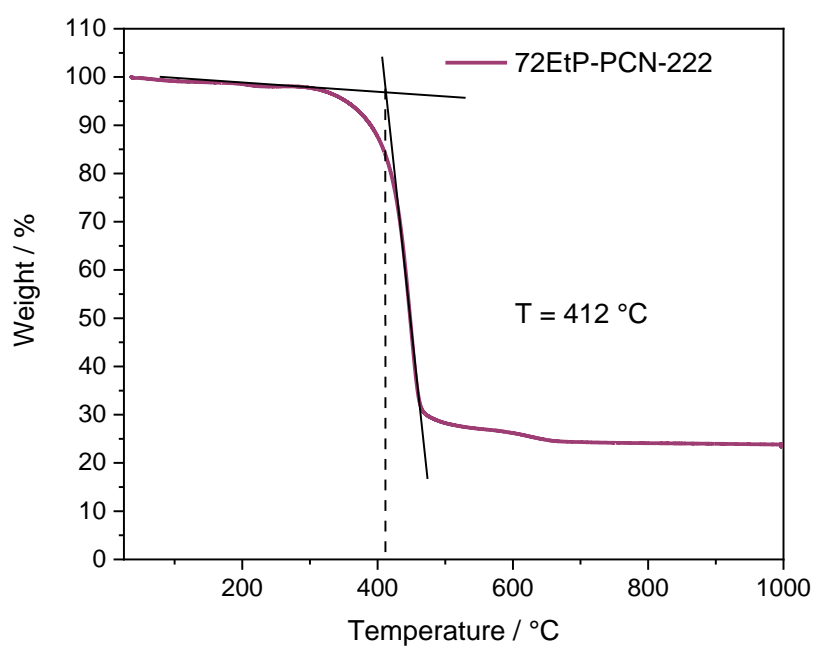


Figure A 137: TGA curve of 72EtP-PCN-222. Decomposition temperature was determined as 412 °C.

Table A 14: Linker defects of the different MOFs calculated from TGA curves. The ideal sum formula of PCN-222 is  $Zr_6(OH)_{16}(TCPP-H_2)_2$ .

	#TCPPH <sub>2</sub> linkers <sub>ideal</sub>	#TCPPH <sub>2</sub> linkers <sub>real</sub>
PCN-222	2	2.53
20EtP-PCN-222	2	2.08
59EtP-PCN-222	2	2.20
72EtP-PCN-222	2	2.27

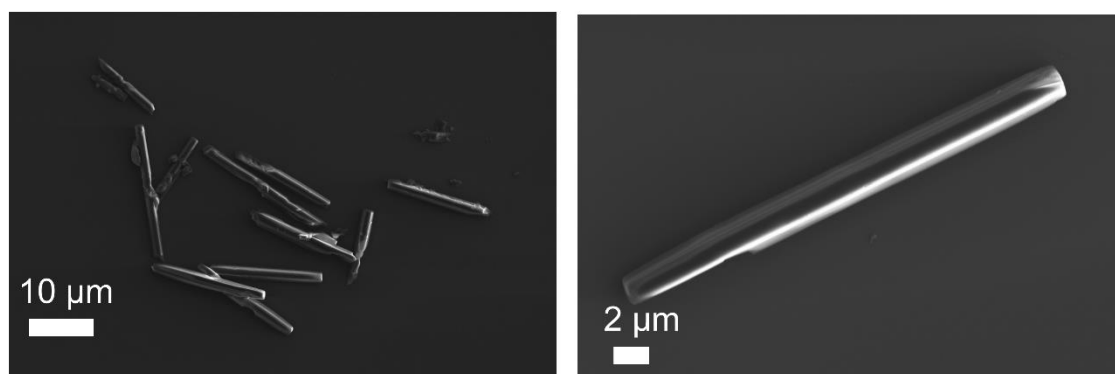


Figure A 138: Scanning electron microscopy images of PCN-222 with different magnifications.

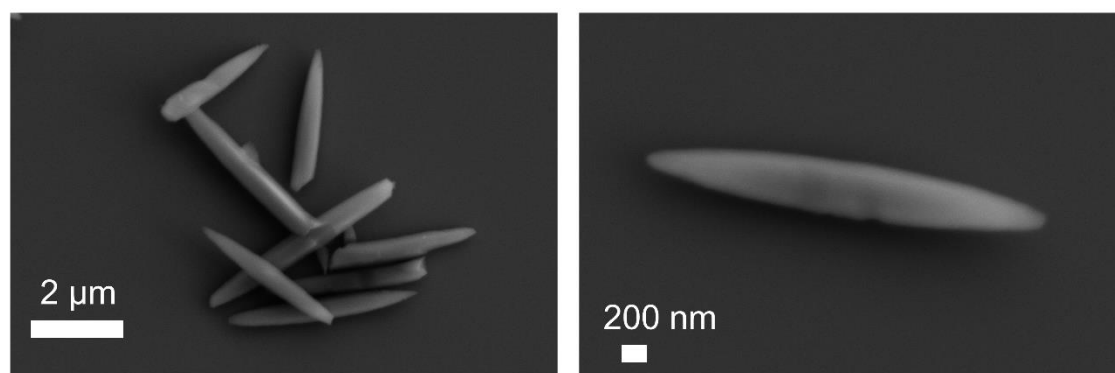


Figure A 139: Scanning electron microscopy images of 20EtP-PCN-222 with different magnifications.

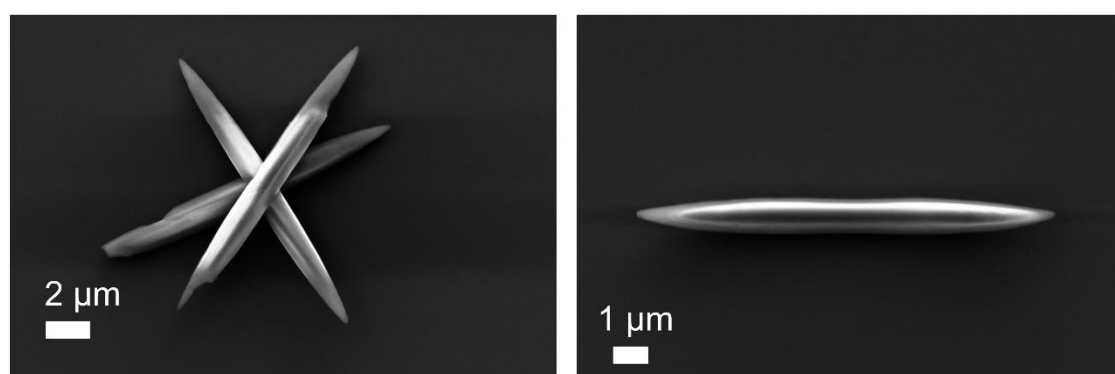


Figure A 140: Scanning electron microscopy images of 59EtP-PCN-222 with different magnifications.



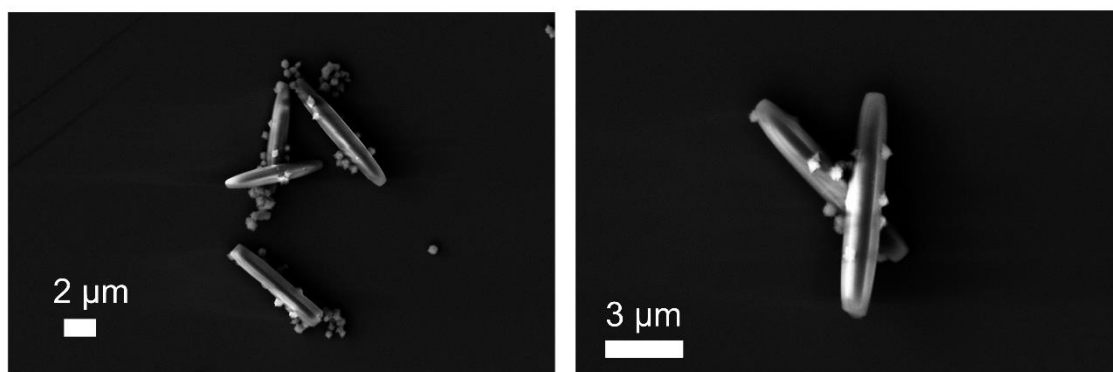


Figure A 141: Scanning electron microscopy images of 72EtP-PCN-222 with different magnifications.

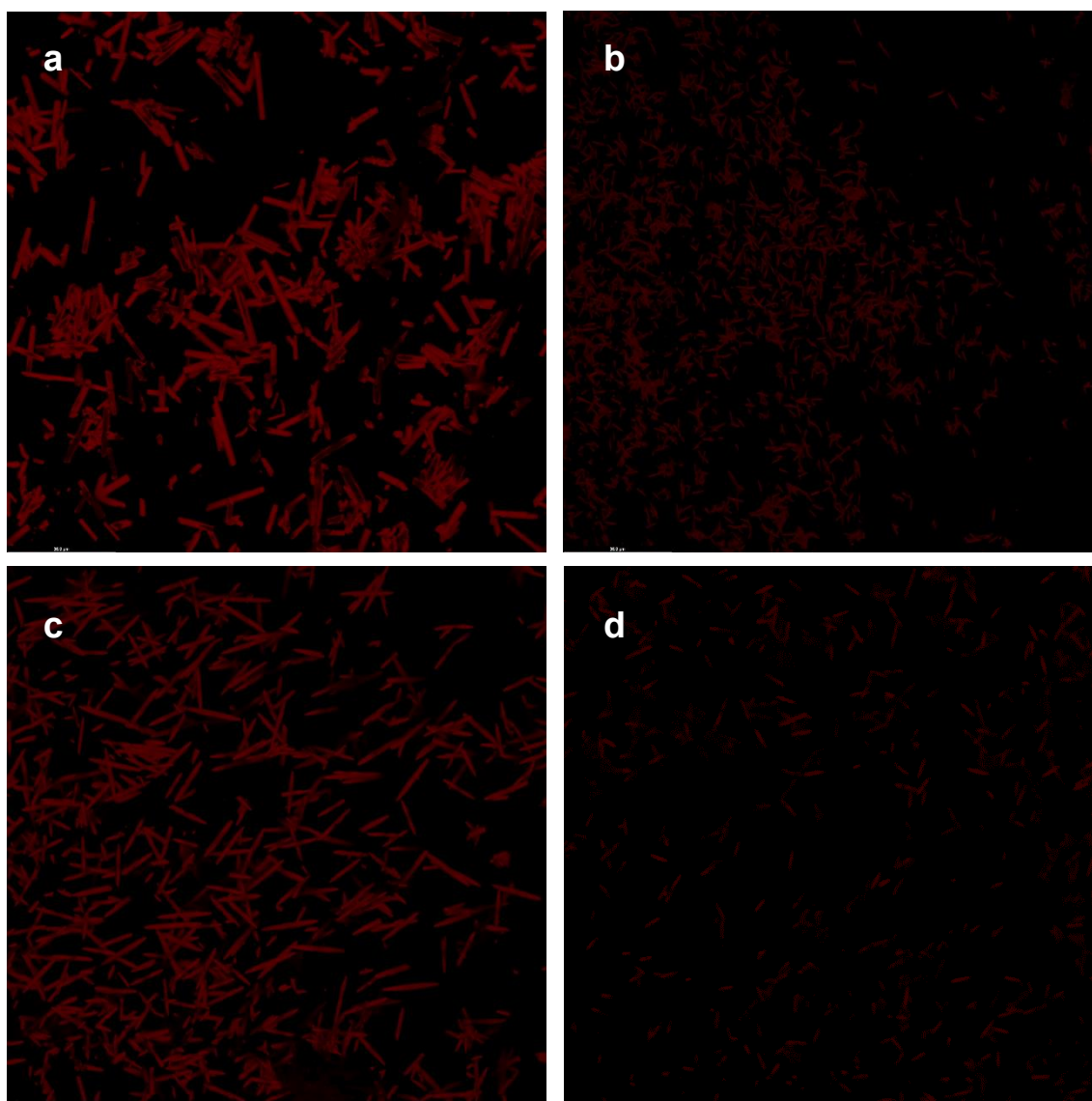


Figure A 142: Confocal microscopy images of PCN-222 (a), 20EtP-PCN-222 (b), 59EtP-PCN-222 (c) and 72EtP-PCN-222 (d). Excitation at 405 nm with a Diode 405 laser and imaged at 700 – 760 nm. All images were recorded under the same conditions allowing for qualitative comparison between the different materials.

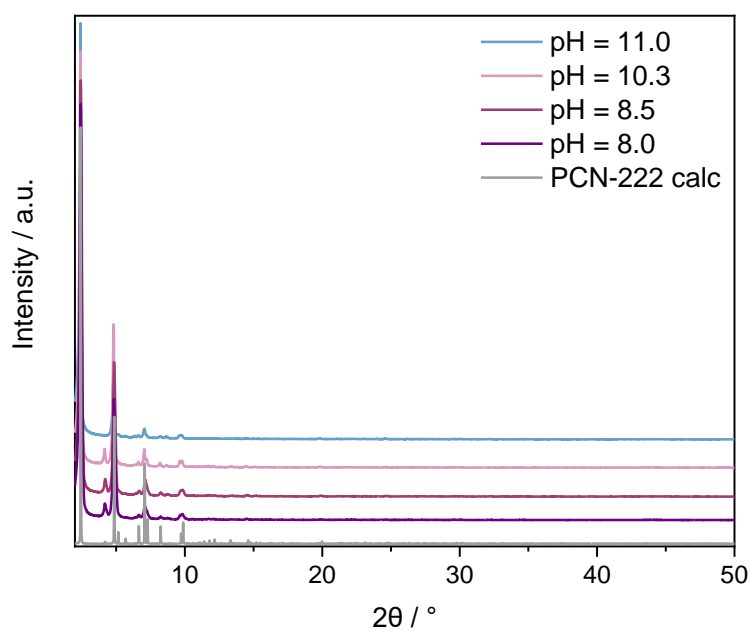


Figure A 143: PXR D spectra of PCN-222 soaked for 24 h in aqueous NaOH solutions with different pH values (8.0, 8.5, 10.3, 11.0). Before PXR D measurements, the MOF was washed with water and dried *under vacuo*.

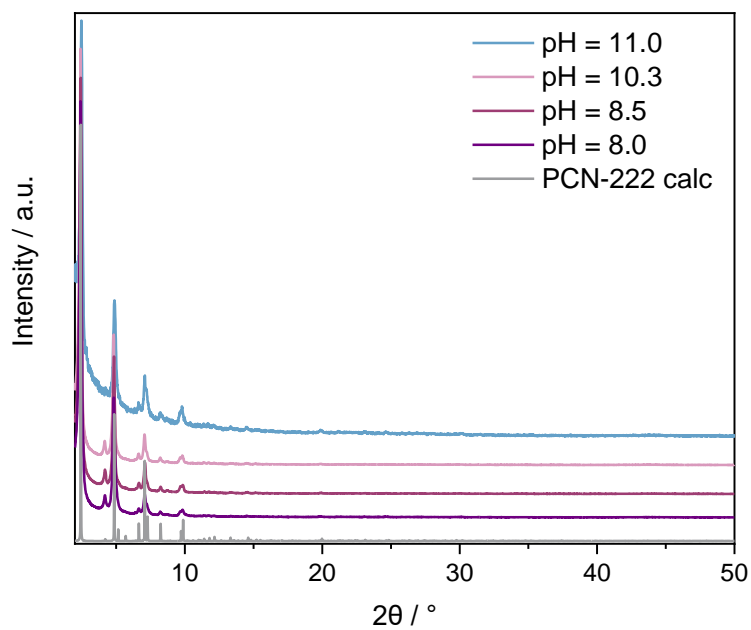


Figure A 144: PXR D spectra of 59EtP-PCN-222 soaked for 24 h in aqueous NaOH solutions with different pH values (8.0, 8.5, 10.3, 11.0). Before PXR D measurements, the MOF was washed with water and dried *under vacuo*.

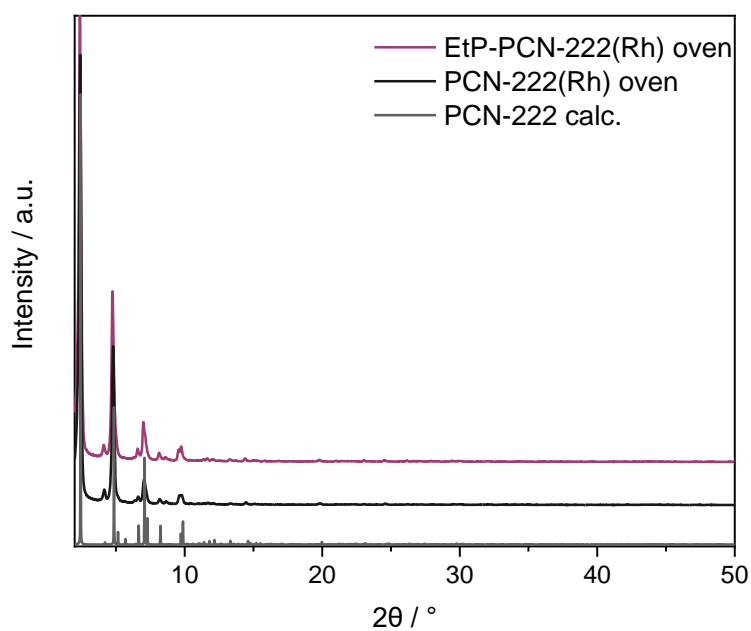


Figure A 145: PXRD pattern of PCN-222(Rh) and EtP-PCN-222(Rh) in comparison to the calculated pattern of PCN-222. For Rh metalation, synthesized MOFs were heated with  $\text{RhCl}_3 \cdot x\text{H}_2\text{O}$  in DMF in an oven for 12 h at 120 °C. After reaction, the MOF was washed with DMF and acetone and dried *under vacuo*.

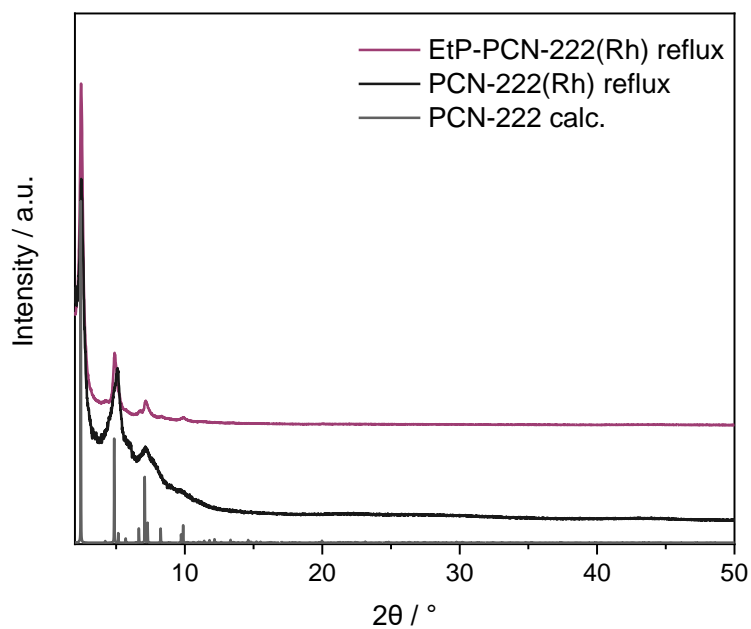


Figure A 146: PXRD pattern of PCN-222(Rh) and EtP-PCN-222(Rh) in comparison to the calculated pattern of PCN-222. For Rh metalation, synthesized MOFs were heated with  $\text{RhCl}_3 \cdot x\text{H}_2\text{O}$  in DMF under reflux for 22 h. After reaction, the MOF was washed with DMF and acetone and dried *under vacuo*.

Table A 15: wt% of Rh and Zr, approximated percentage of Linker metalation (calculated from ideal sum formula of PCN-222 and therefore only for estimation) and Zr:Rh ratios for PCN-222(Rh) and EtP-PCN-222(Rh) prepared via different methods (reflux vs oven) determined by ICP-MS analysis. The theoretical Zr:Rh ratio for complete linker metalation is 3 (calculated from the ideal sum formula and the ratio Zr:linker).

		Wt% Zr	Wt% Rh	Approximated % of linker metalation <sup>a</sup>	Zr:Rh
PCN-222(Rh)	Reflux	17.57	2.32	28.43	8.55
EtP-PCN-222(Rh)	Reflux	17.04	1.96	23.96	9.80
PCN-222(Rh)	Oven	17.62	0.80	9.62	24.94
EtP-PCN-222(Rh)	Oven	16.72	0.84	10.18	22.37

<sup>a</sup>based on the ideal sum formula of PCN-222

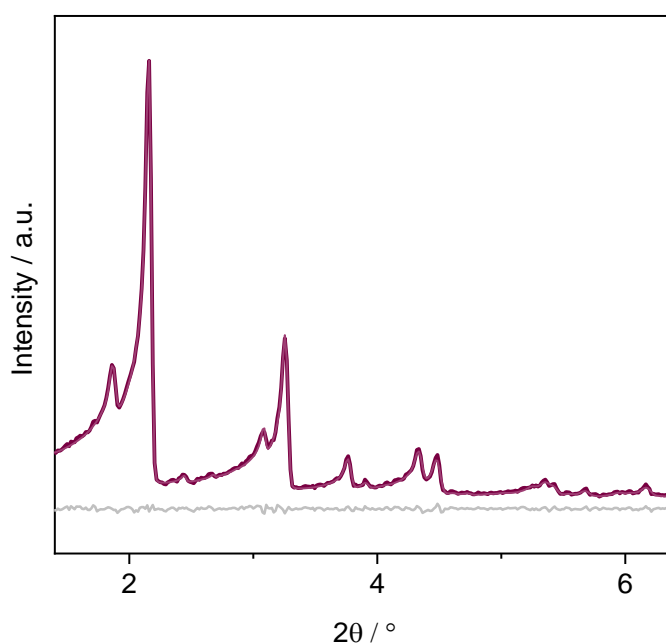


Figure A 147: Pawley fit refinement (violet) of the PXRD pattern of PCN-222 (black) at 310 K with  $\lambda=0.70926$  Å.  $R_{wp} = 3.98$ ,  $R_{exp} = 1.36$  and  $GOF = 2.92$ . Additionally, the difference curve of the profile fit (grey line) is depicted. The refinement resulted in following values:  $a = b = 42.99$  (2) Å,  $c = 18.69$  (1) Å.

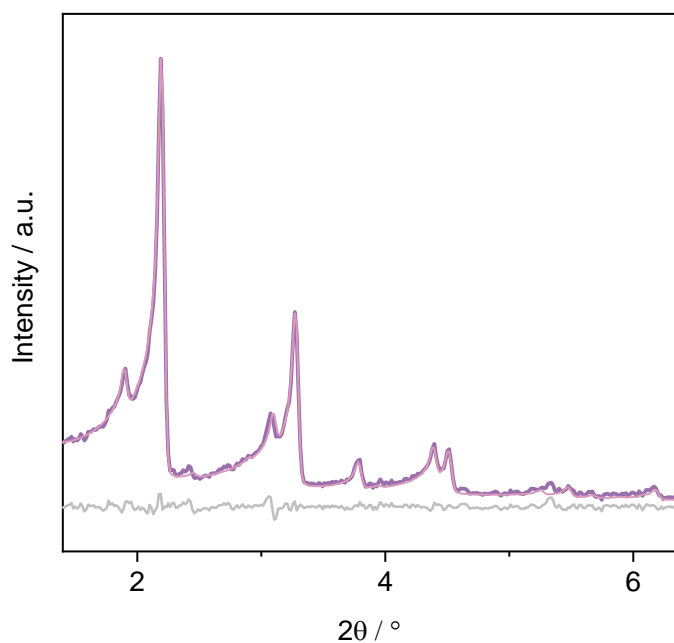


Figure A 148: Pawley fit refinement (light purple) of the PXRD pattern of 20EtP-PCN-222 (black) at 310 K.  $R_{wp} = 3.10$ ,  $R_{exp} = 1.16$  and  $GOF = 2.67$ . Additionally, the difference curve of the profile fit (grey line) is depicted. The refinement resulted in following values:  $a = b = 43.05$  (3) Å,  $c = 18.56$  (2) Å.

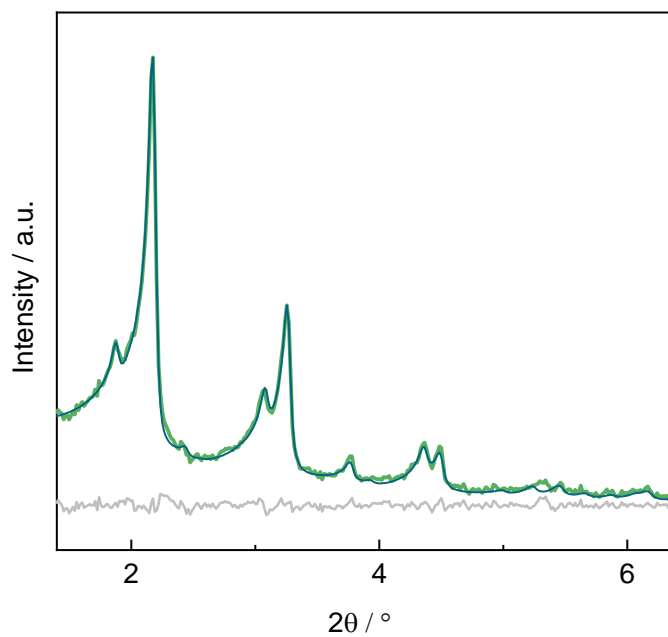


Figure A 149: Pawley fit refinement (dark green) of the PXRD pattern of 59EtP-PCN-222 (black) at 310 K.  $R_{wp} = 3.24$ ,  $R_{exp} = 1.53$  and  $GOF = 2.11$ . Additionally, the difference curve of the profile fit (grey line) is depicted. The refinement resulted in following values:  $a = b = 42.99$  (4) Å,  $c = 18.54$  (4) Å.

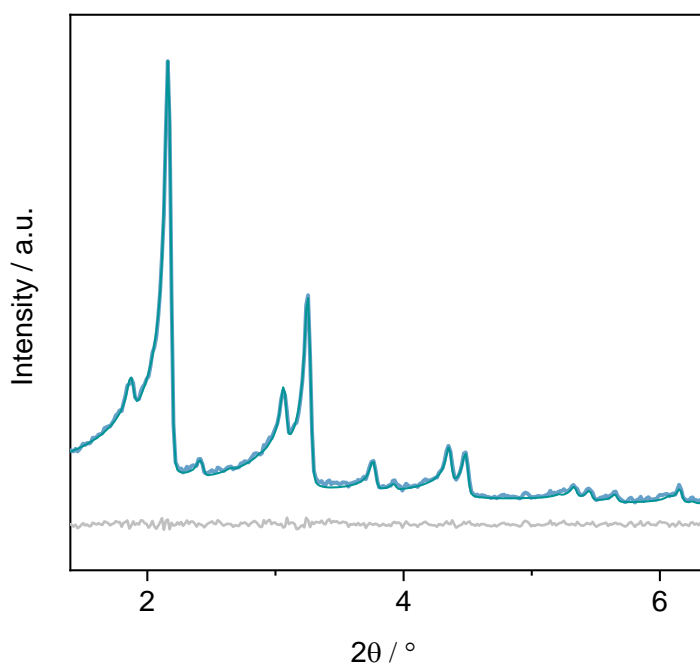


Figure A 150: Pawley fit refinement (purple) of the PXRD pattern of 72EtP-PCN-222 (black) at 310 K.  $R_{wp} = 2.73$ ,  $R_{exp} = 1.36$  and  $GOF = 2.01$ . Additionally, the difference curve of the profile fit (grey line) is depicted. The refinement resulted in following values:  $a = b = 43.01$  (2) Å,  $c = 18.60$  (1) Å.

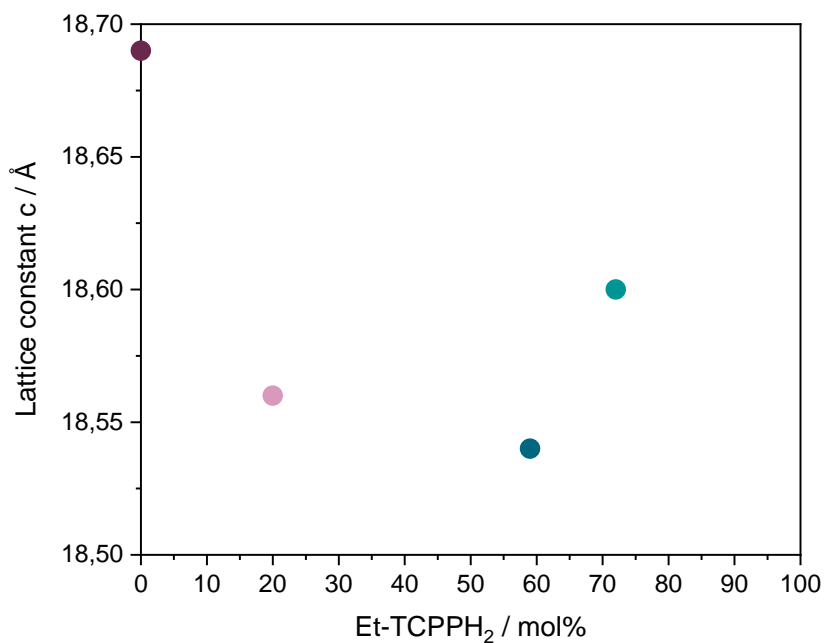


Figure A 151: Lattice parameter  $a$  of the PCN-222 series depending on the Et-TCPPH<sub>2</sub> content. Data were obtained from Pawley refinement of PXRD data at 310 K.

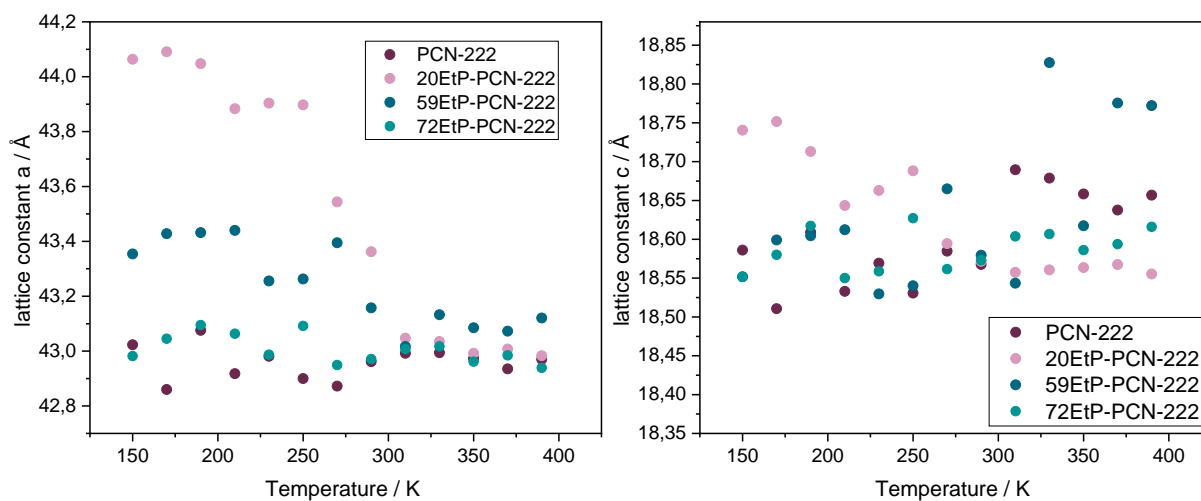


Figure A 152: Lattice parameters  $a$  and  $c$  of the EtP-PCN-222 series depending on the temperature. Data were obtained from Pawley refinement of VT-PXRD data.

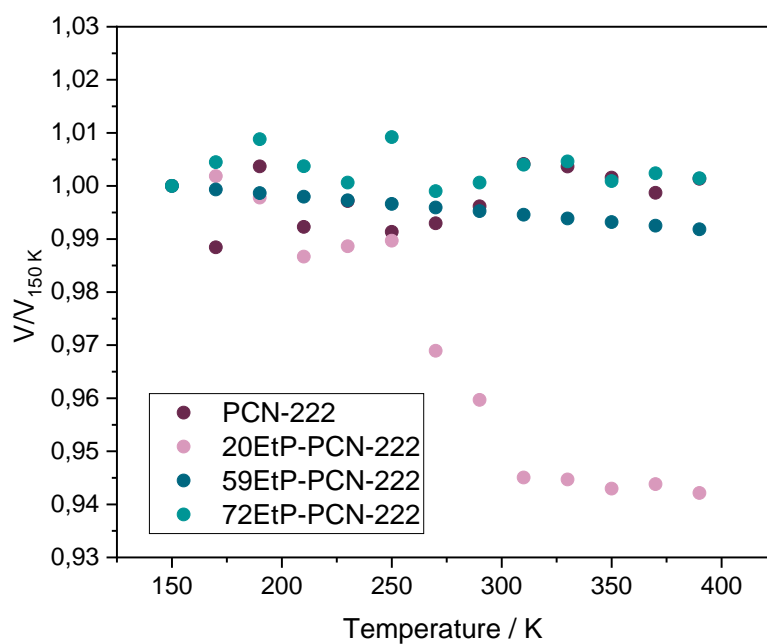


Figure A 153: Unit cell volume of the EtP-PCN-222 series depending on the temperature. Data were obtained from Pawley refinement of VT-PXRD data.

## 7.8. Node-anchored Non-planar Porphyrin

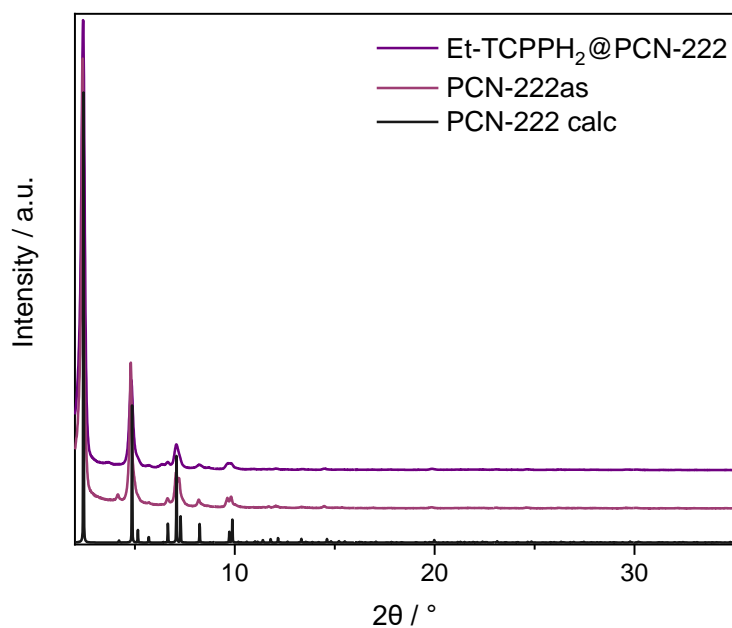


Figure A 154: PXRD pattern of PCN-222 and Et-TCPPh<sub>2</sub>@PCN-222 in comparison to the calculated pattern of PCN-222.



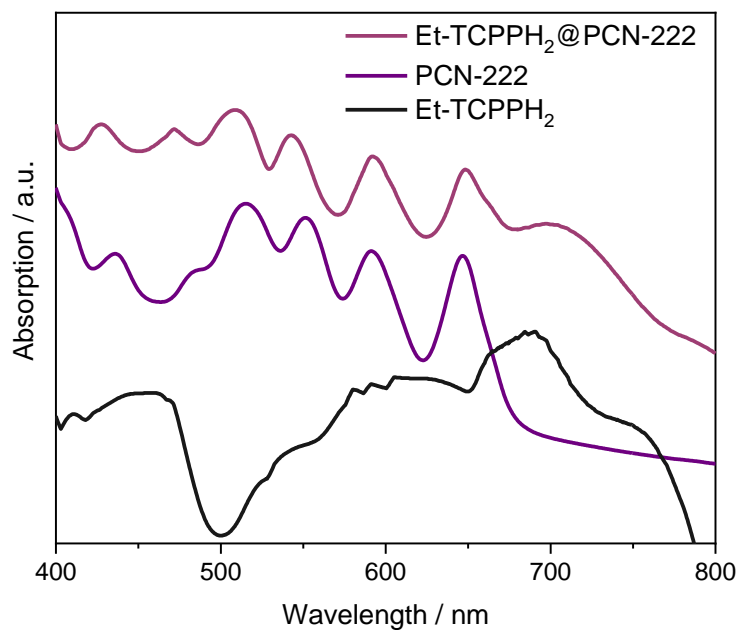


Figure A 155: Solid-state UV-vis spectra of Et-TCPPh<sub>2</sub>, PCN-222 and Et-TCPPh<sub>2</sub>@PCN-222.

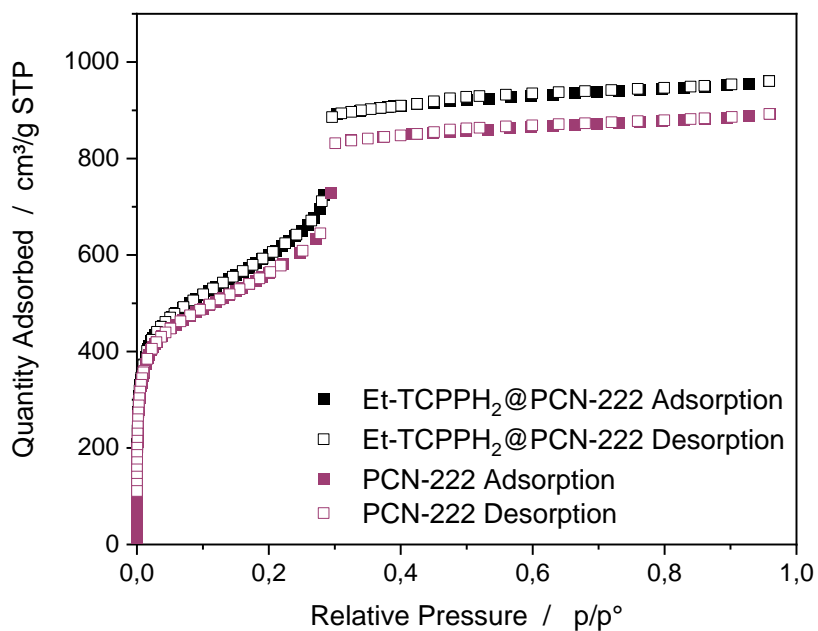


Figure A 156: N<sub>2</sub> sorption measurements at 77 K for PCN-222 and Et-TCPPh<sub>2</sub>@PCN-222.

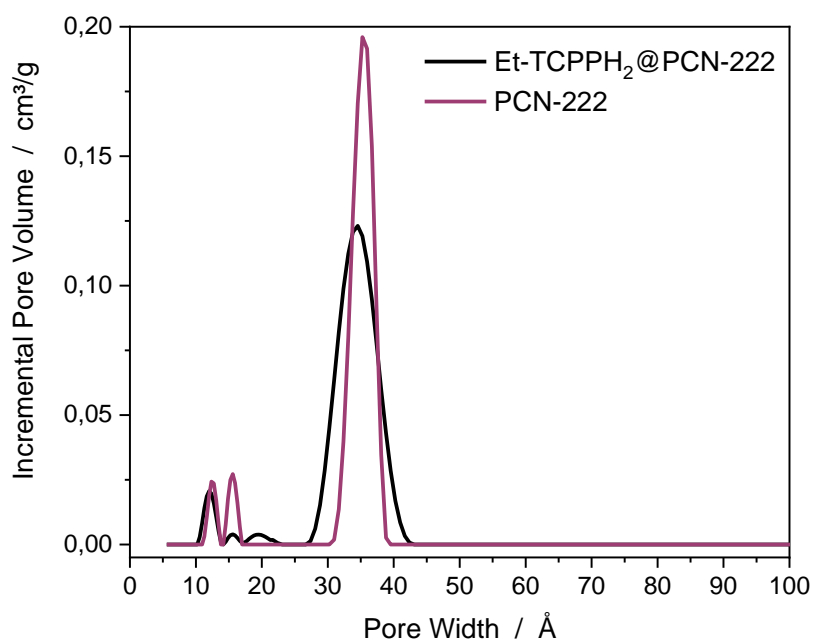


Figure A 157: Calculated pore size distributions from N<sub>2</sub> adsorption isotherms of PCN-222 and Et-TCPPh<sub>2</sub>@PCN-222 using sets of theoretical isotherms derived from 2D-NLDFT-based methods for specific pore sizes and geometry. As an approximation, cylindrical pores on an oxide surface were assumed for all materials.

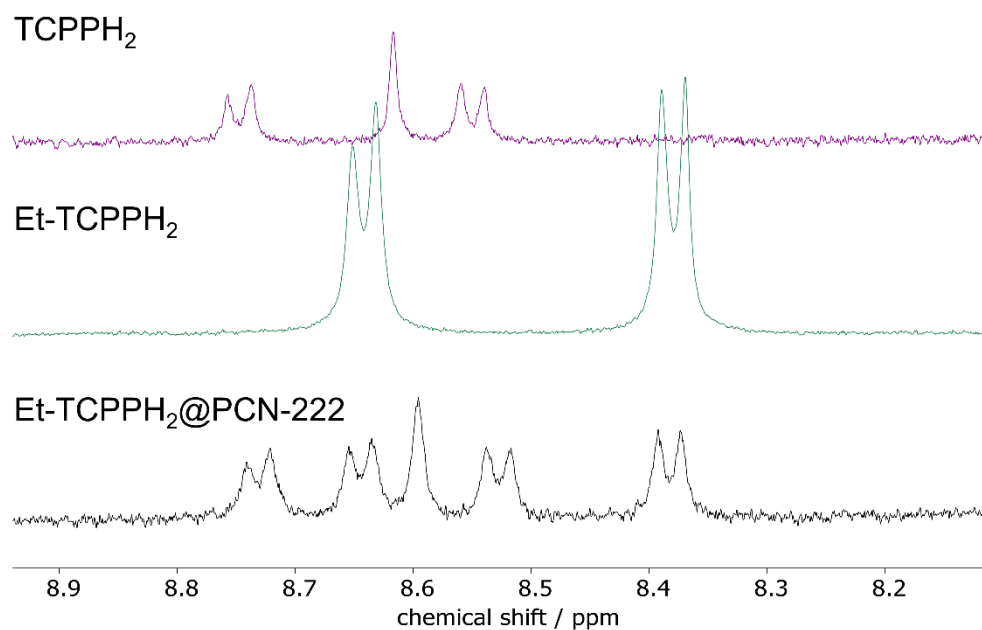


Figure A 158: <sup>1</sup>H NMR spectra of TCPPh<sub>2</sub>, Et-TCPPh<sub>2</sub> and Et-TCPPh<sub>2</sub>@PCN-222 (digested in DCI/DMSO-d<sub>6</sub>) in DMSO-d<sub>6</sub>.

## 7.9. Anchoring of Pd Pincer Complexes – Pre-study

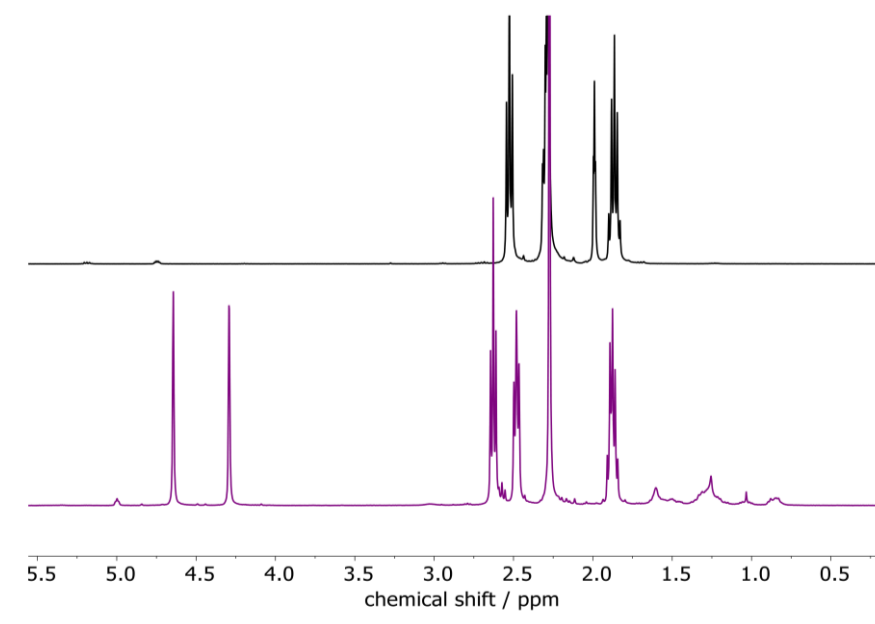


Figure A 159: <sup>1</sup>H NMR spectra of the catalysis solution of the cycloisomerization of 5-hexynoic acid before (top, black) and after catalysis (5 h, bottom, purple) in CDCl<sub>3</sub>.

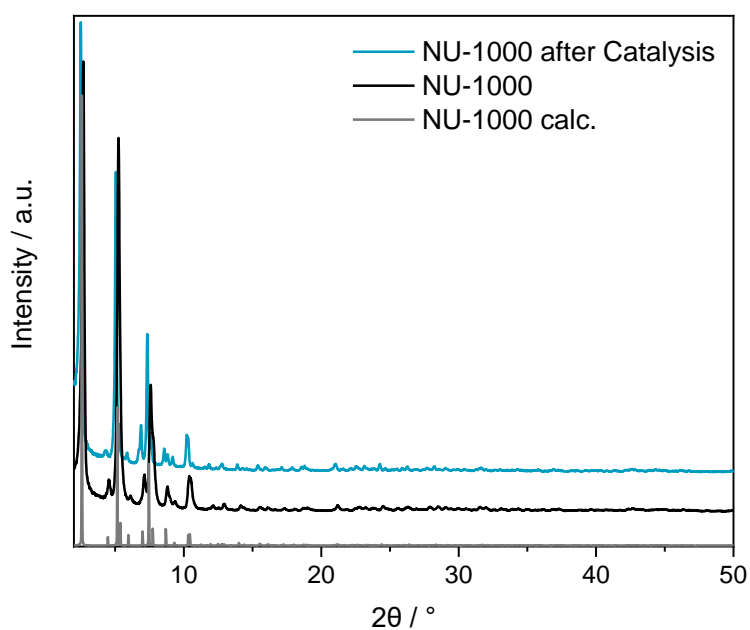


Figure A 160: PXRD pattern of NU-1000 and NU-1000 after catalysis in comparison to the calculated pattern of NU-1000.

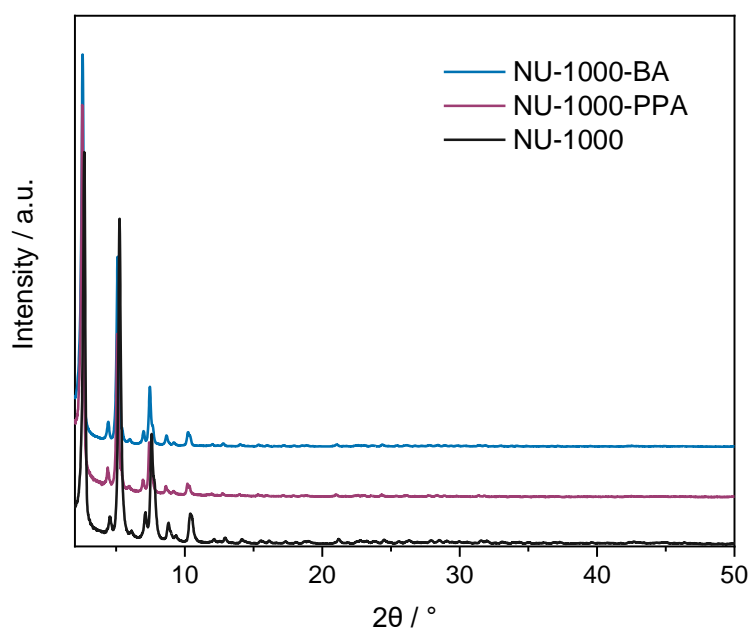


Figure A 161: PXRD pattern of NU-1000, NU-1000-BA and NU-1000-PPA.

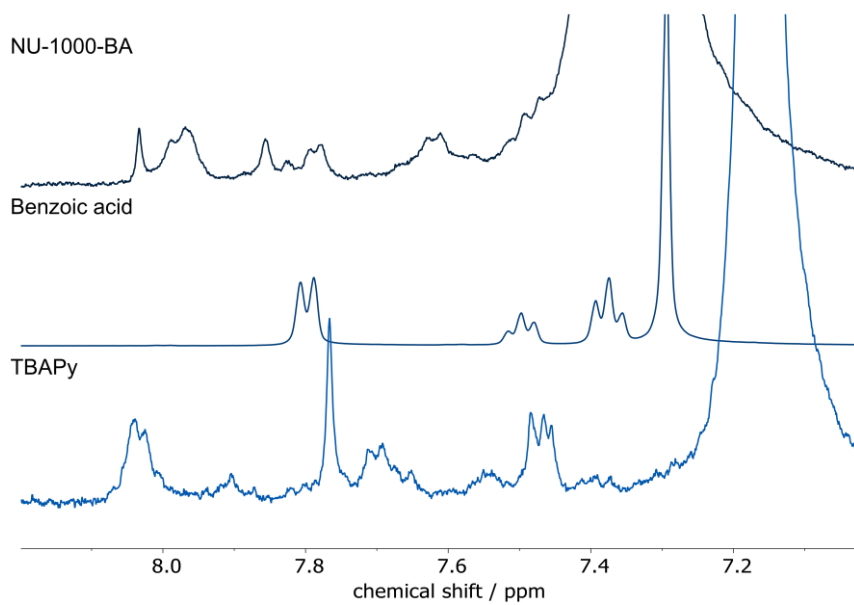


Figure A 162:  $^1\text{H}$  NMR spectra of NU-1000-BA (digested in DCI/DMSO- $d_6$ ), benzoic acid and the linker TBAPy in DMSO- $d_6$ .

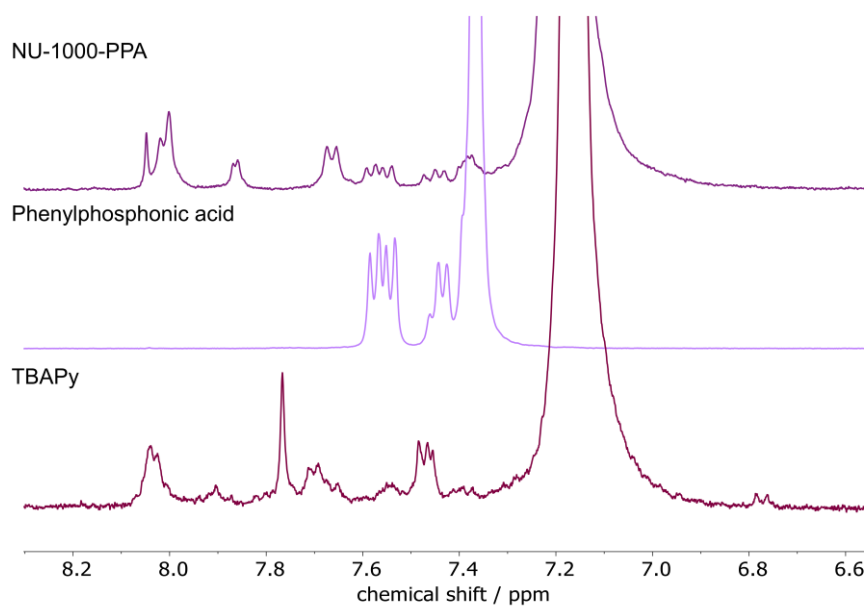


Figure A 163:  $^1\text{H}$  NMR spectra of NU-1000-PPA (digested in DCI/DMSO- $d_6$ ), phenylphosphonic acid and the linker TBAPy in DMSO- $d_6$ .

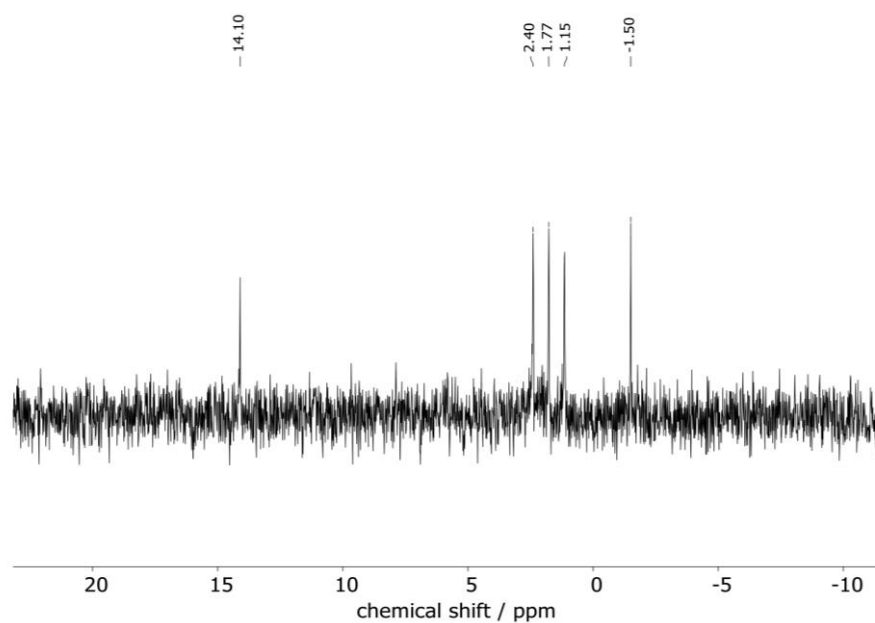


Figure A 164:  $^{31}\text{P}$  NMR spectrum of NU-1000-PPA (digested in DCI/DMSO- $d_6$ ) in DMSO- $d_6$ .

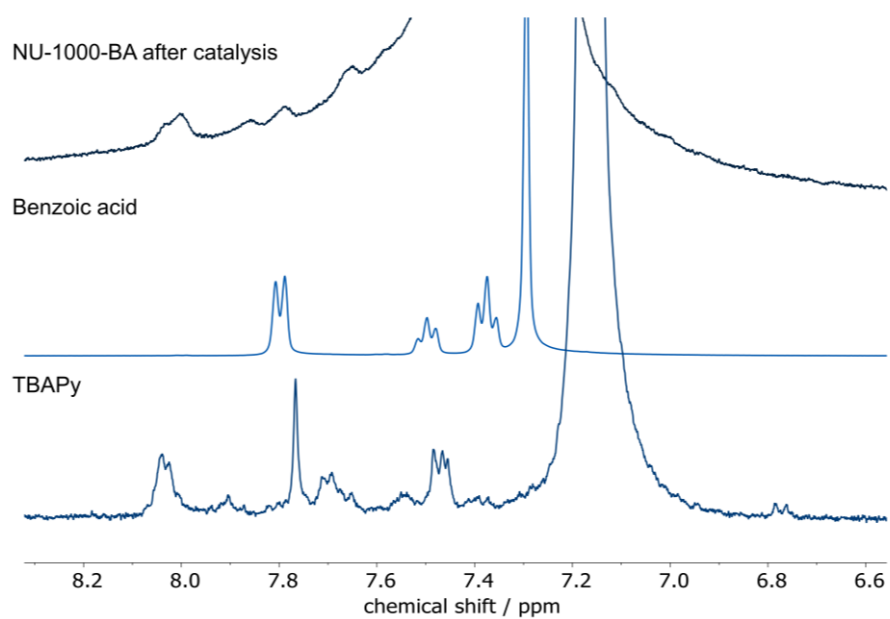


Figure A 165: <sup>1</sup>H NMR spectra of NU-1000-BA after catalysis (digested in DCI/DMSO-d<sub>6</sub>), benzoic acid and the linker TBAPy in DMSO-d<sub>6</sub>.

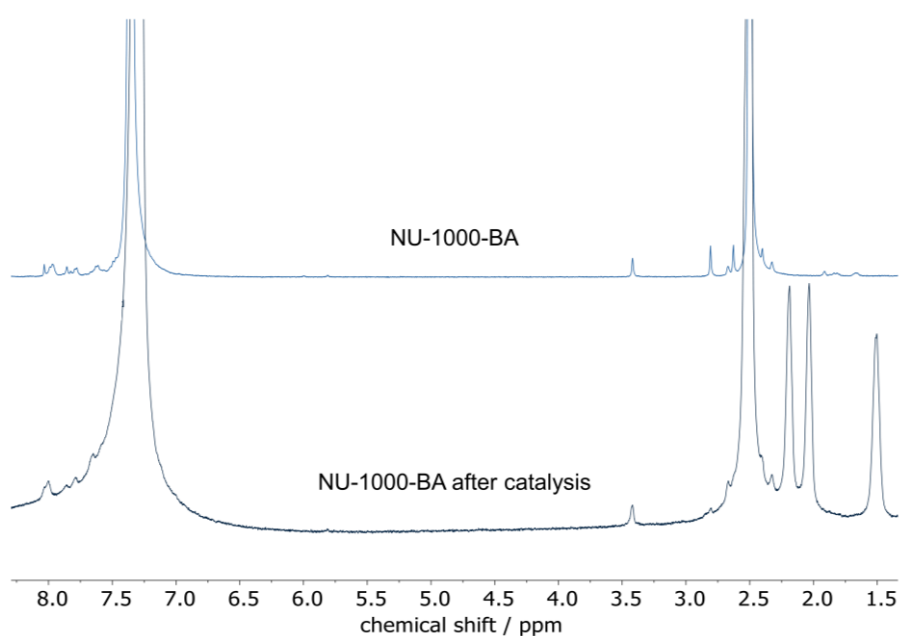


Figure A 166: <sup>1</sup>H NMR spectra of NU-1000-BA and NU-1000-BA after catalysis (both digested in DCI/DMSO-d<sub>6</sub>), in DMSO-d<sub>6</sub>.

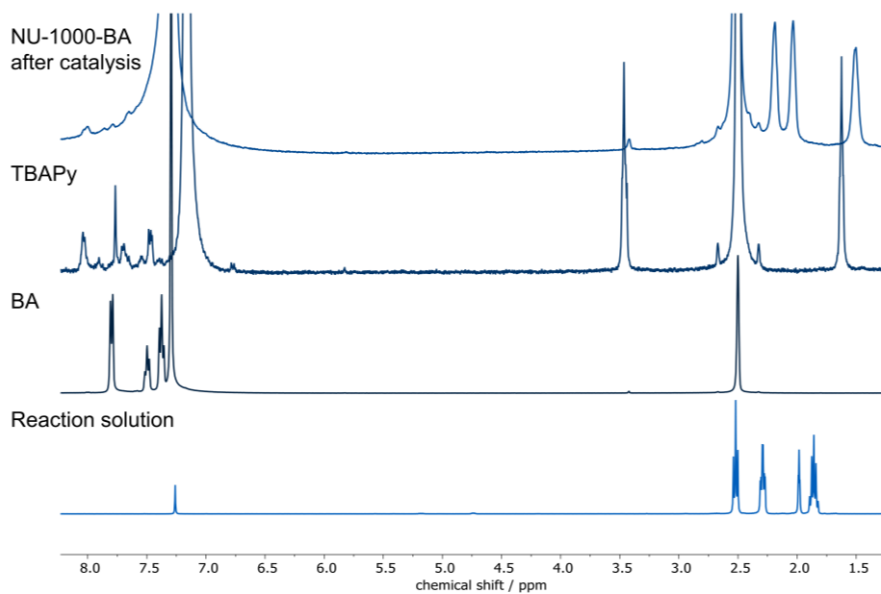


Figure A 167:  $^1\text{H}$  NMR spectra of NU-1000-BA (digested in  $\text{DCI}/\text{DMSO-d}_6$ ), the linker TBAPy, benzoic acid (BA) in  $\text{DMSO-d}_6$  and the catalysis reaction solution in  $\text{CDCl}_3$ .

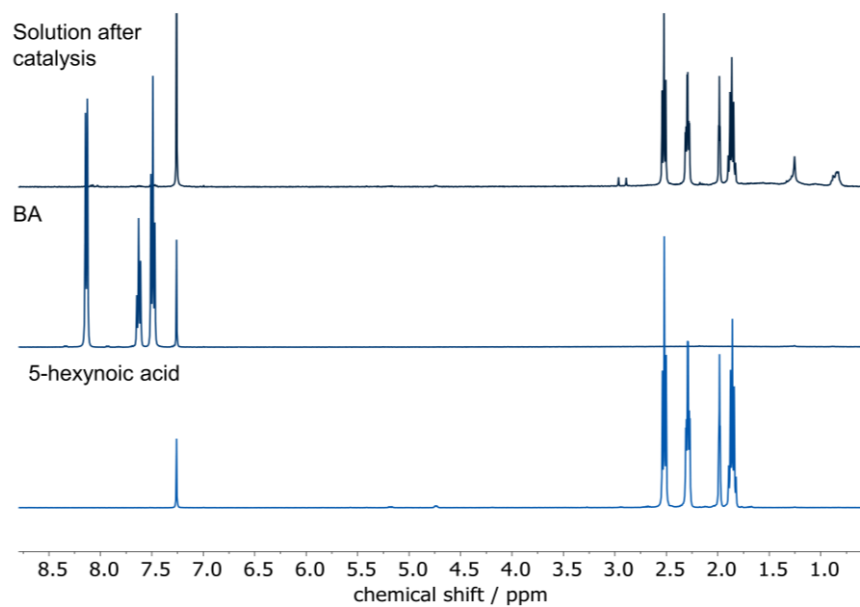


Figure A 168:  $^1\text{H}$  NMR spectra of the reaction solution after catalysis, benzoic acid (BA) and the substrate 5-hexynoic acid in  $\text{CDCl}_3$ .

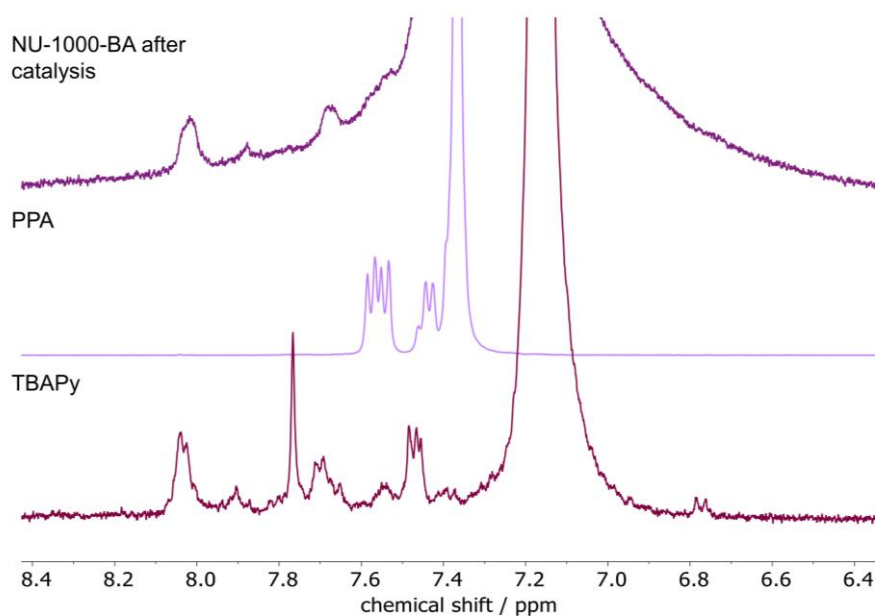


Figure A 169: <sup>1</sup>H NMR spectra of NU-1000-PPA after catalysis (digested in DCI/DMSO-d<sub>6</sub>), phenylphosphonic acid (PPA) and the linker TBAPy in DMSO-d<sub>6</sub>.

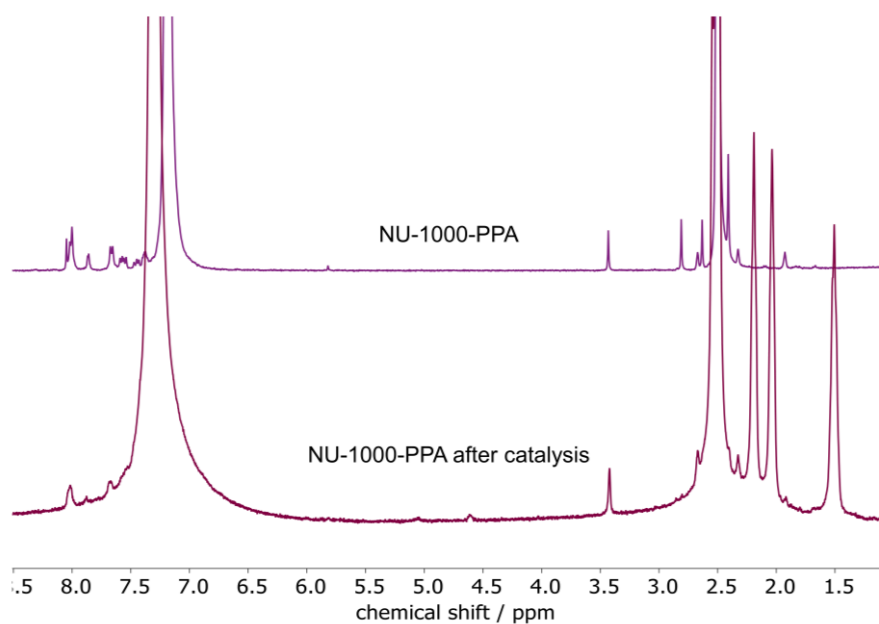


Figure A 170: <sup>1</sup>H NMR spectra of NU-1000-PPA and NU-1000-PPA after catalysis (both digested in DCI/DMSO-d<sub>6</sub>), in DMSO-d<sub>6</sub>.



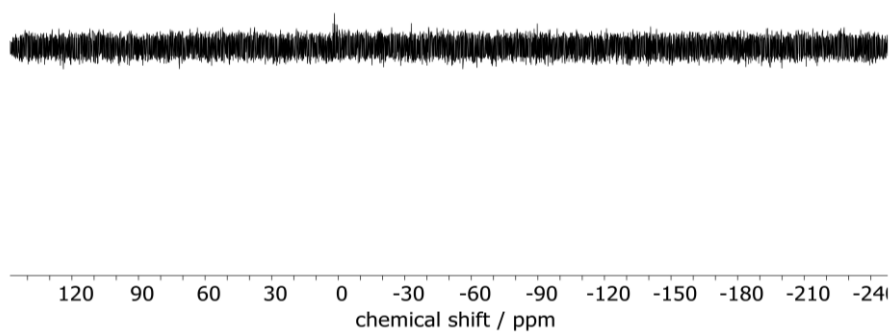


Figure A 171:  $^{31}\text{P}$  NMR spectrum of NU-1000-PPA after catalysis in  $\text{DMSO-d}_6$ .

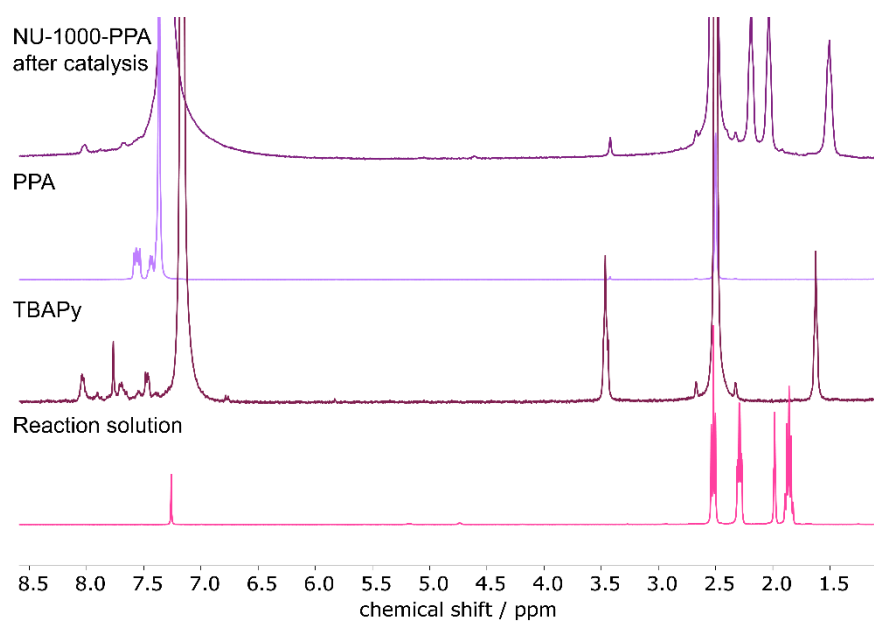


Figure A 172:  $^1\text{H}$  NMR spectra of NU-1000-PPA (digested in  $\text{DCI/DMSO-d}_6$ ), the linker TBAPy, phenylphosphonic acid (PPA) in  $\text{DMSO-d}_6$  and the catalysis reaction solution in  $\text{CDCl}_3$ .

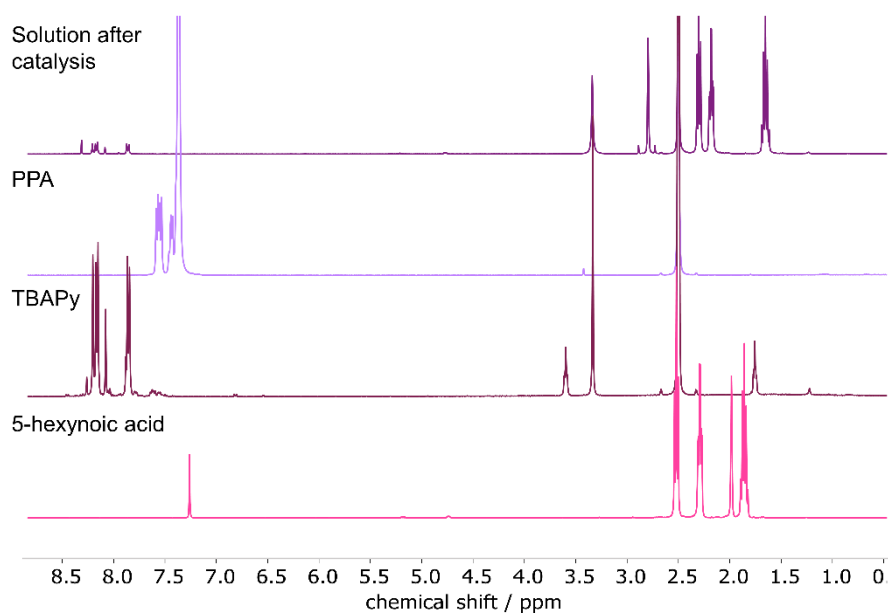


Figure A 173:  $^1\text{H}$  NMR spectra of the reaction solution after catalysis, benzoic acid (BA) in  $\text{DMSO-d}_6$  and the substrate 5-hexynoic acid in  $\text{CDCl}_3$ .

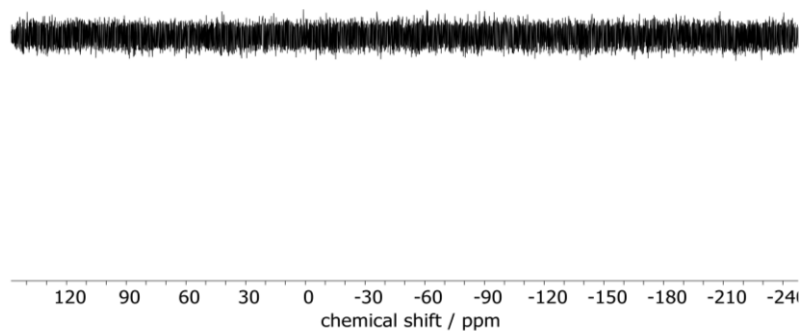


Figure A 174:  $^{31}\text{P}$  NMR spectrum of the catalysis solution after 24 h in  $\text{DMSO-d}_6$ .

## 7.10. Re-photocatalyst Anchoring in MOF Pores

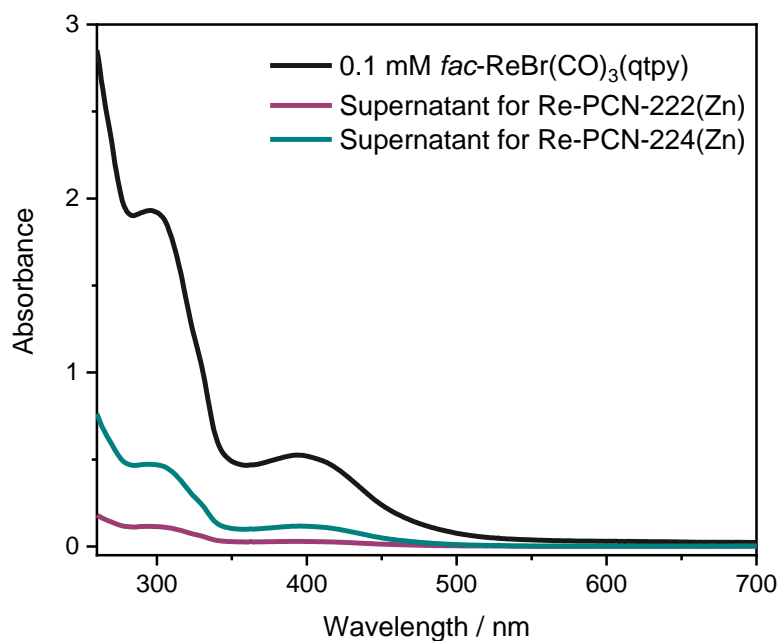


Figure A 175: UV-vis spectra of *fac*-ReBr(CO)<sub>3</sub>(qtpy) (0.1 mM in MeCN) before catalyst anchoring to PCN-222(Zn) and PCN-224(Zn), respectively. Additionally, the supernatant was measured after 24 h of soaking the MOF in the catalyst solution.

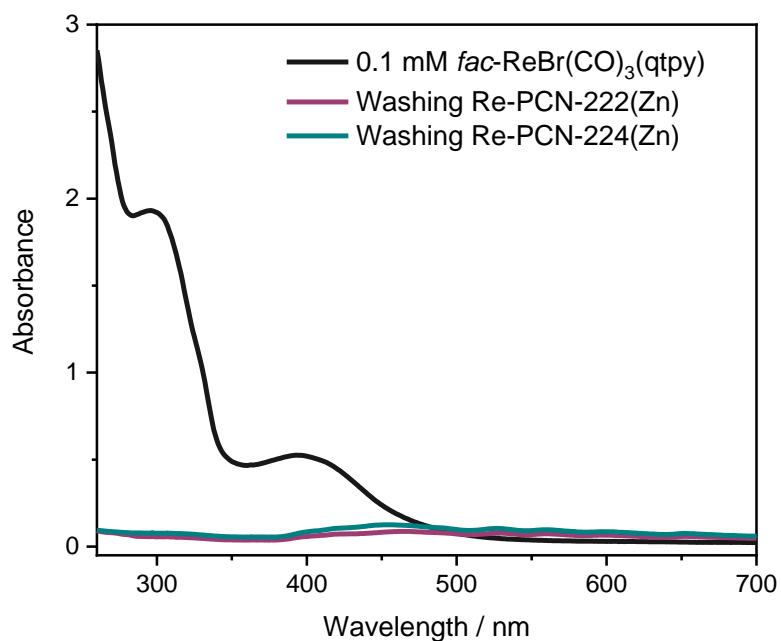


Figure A 176: UV-vis spectra of the washing solutions for Re-PCN-222(Zn) and Re-PCN-224(Zn) with MeCN excluding catalyst leaching.

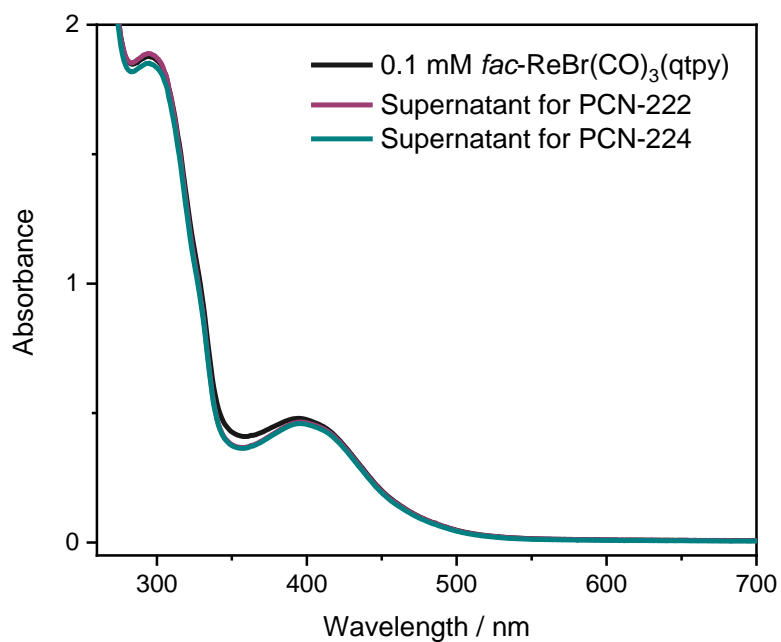


Figure A 177: UV-vis spectra of  $fac\text{-ReBr}(\text{CO})_3(\text{qtpy})$  (0.1 mM in MeCN) before catalyst anchoring to PCN-222 and PCN-224 (without Zn), respectively. Additionally, the supernatant was measured after 24 h of soaking the MOF (without Zn) in the catalyst solution confirming the importance of Zn for catalyst anchoring.

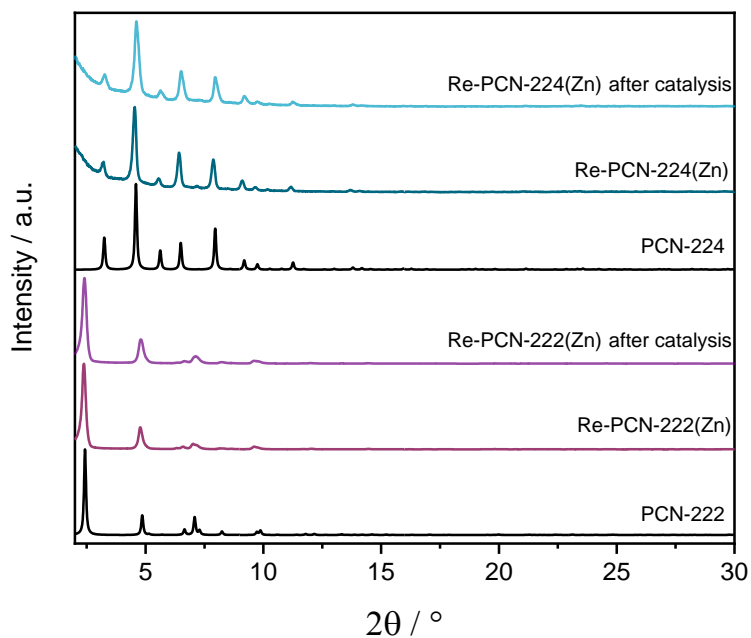


Figure A 178: PXRD of synthesized PCN-222, Re-PCN-222(Zn), PCN-224 and Re-PCN-224(Zn). Additionally, pattern of Re-PCN-222(Zn) and Re-PCN-224(Zn) after photocatalysis are depicted.

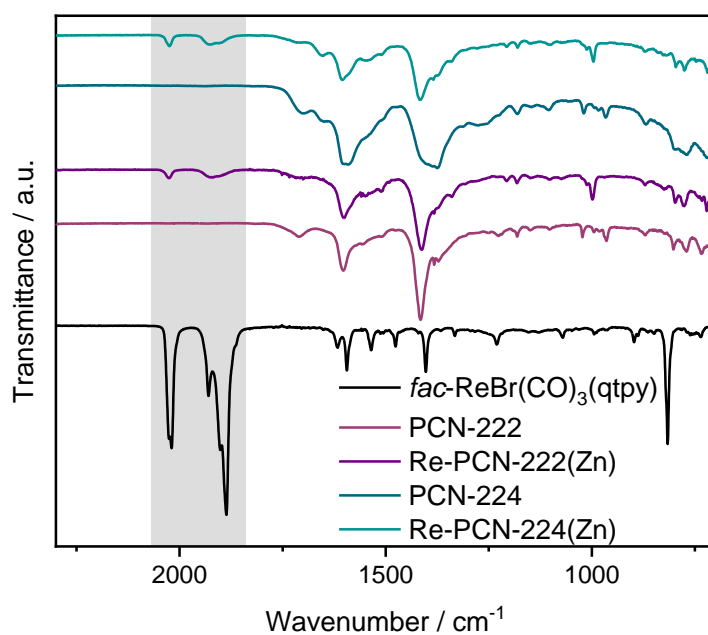


Figure A 179: IR spectra of *fac*-ReBr(CO)<sub>3</sub>(qtpy), PCN-222, Re-PCN-222(Zn), PCN-224 and Re-PCN-224(Zn).

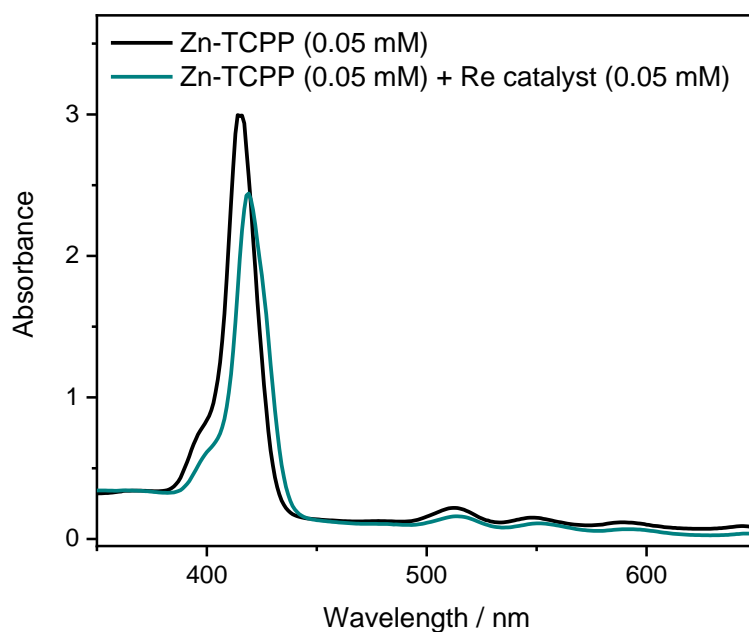


Figure A 180: Normalized UV-vis spectra of Zn-TCPP (0.05 mM) and Zn-TCPP/Re catalyst (0.05 mM each) in MeCN/DMF (v/v = 40/1).

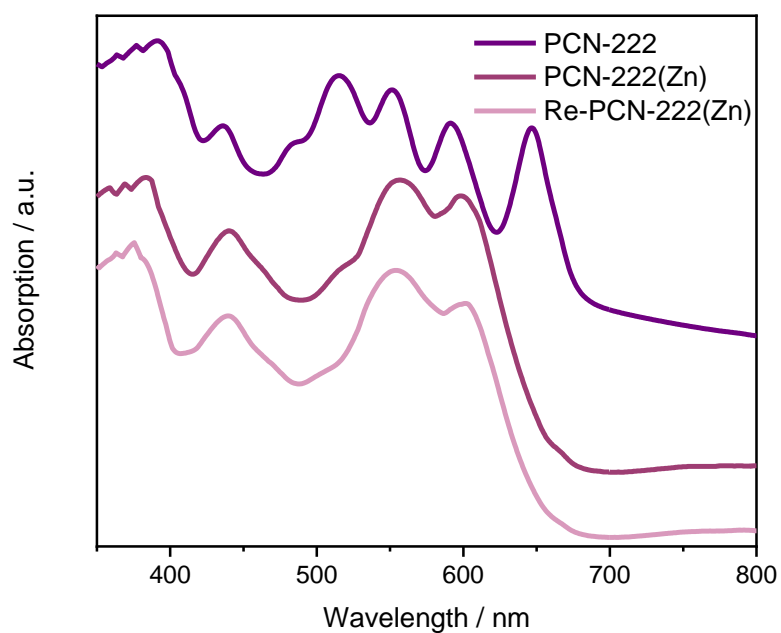


Figure A 181: Solid-state UV-vis spectra of PCN-222, PCN-222(Zn) and Re-PCN-222(Zn).

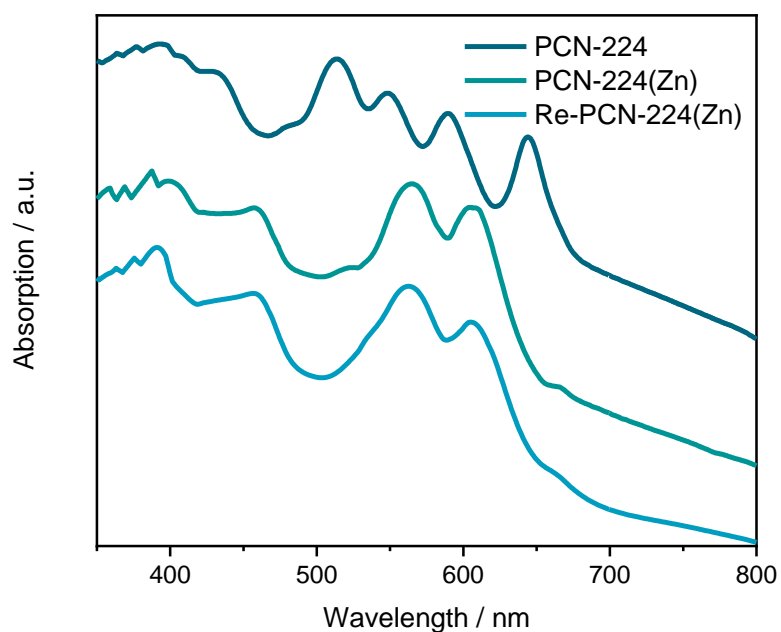


Figure A 182: Solid-state UV-vis spectra of PCN-224, PCN-224(Zn) and Re-PCN-224(Zn).

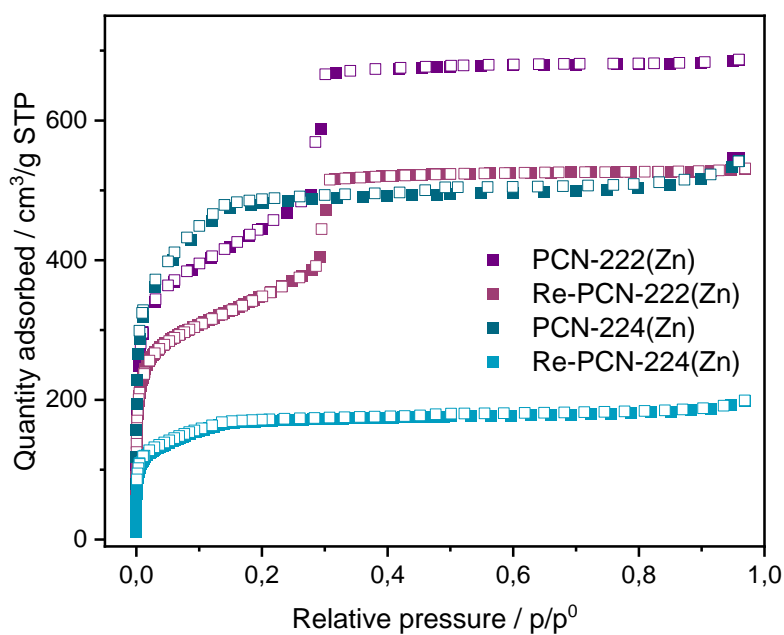


Figure A 183: N<sub>2</sub> adsorption isotherms at 77 K for PCN-222(Zn), Re-PCN-222(Zn), PCN-224(Zn) and Re-PCN-224(Zn).

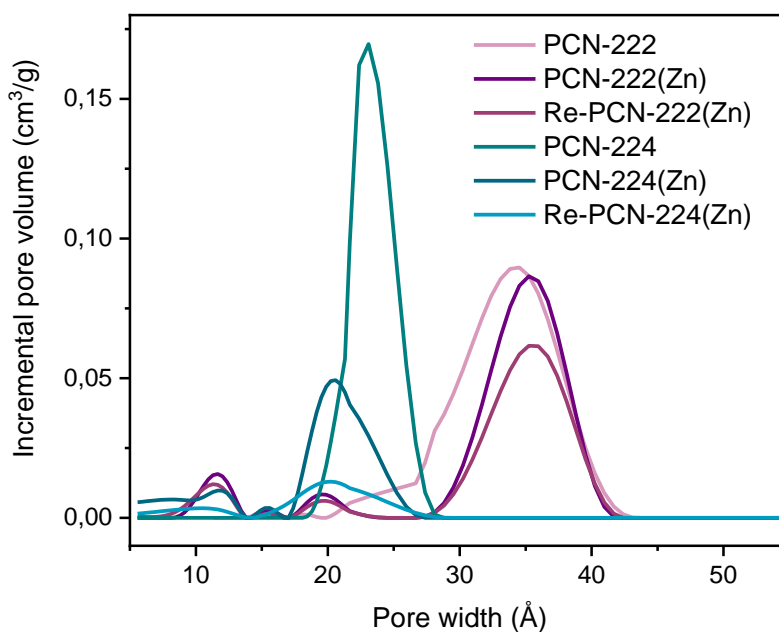


Figure A 184: Calculated pore size distributions from N<sub>2</sub> adsorption isotherms using sets of theoretical isotherms derived from 2D-NLDFT-based methods for specific pore sizes and geometry. As an approximation, cylindrical pores on an oxide surface were assumed for all materials.

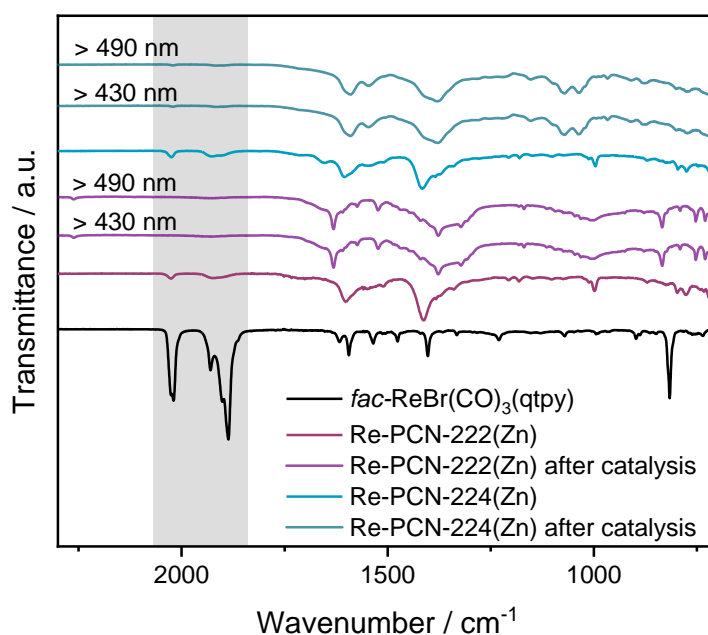


Figure A 185: ATR-IR spectra of Re-PCN-222(Zn) and PCN-224(Zn) before and after photocatalysis (72 h of irradiation).

Table A 16: Performance values for the photocatalytic CO<sub>2</sub> reduction in homogeneous phase. Re-Cat represents *fac*-ReBr(CO)<sub>3</sub>(qtpy). Standard conditions: 0.1 mM Re-Cat in MeCN and 0.1 mM Zn-TCPP in MeCN (4 mL total volume), 0.12 mL deionized H<sub>2</sub>O, BIH (1 mmol, 225 mg). Errors are calculated from three repetitions of the respective catalysis and averaging their values and the errors of catalyst quantity determined by ICP-MS. For the calculation of the TON<sub>CO</sub> the molar amount of Re is used

Sample	$\lambda$ (nm)	Comment	TON <sub>CO</sub>	Formate
<b>Re-Cat</b>	> 430		4.9 ± 0.3	n.-d.
<b>Re-Cat &amp; Zn-TCPP</b> (1:1 mol%)	> 430		10.4 ± 0.4	n.-d.
	> 430	No BIH	n.-d.	n.-d.
	> 430	No irradiation	n.-d.	n.-d.
	> 490		10.4 ± 0.3	n.-d.
	> 490		10.4 ± 0.5	n.-d.
<b>Zr<sub>6</sub>   Zn-TCPP   Re-Cat</b> (4 1 1 mol%)	> 430		0.8 ± 0.1	traces
	> 490		10.4 ± 0.5	n.-d.



Table A 17: Performance values for the colloidal photocatalytic CO<sub>2</sub> reduction. "Re" represents *fac*-ReBr(CO)<sub>3</sub>(qtpy). Standard conditions: 1.5 mg MOF assembly, 4 mL MeCN, 0.12 mL deionized H<sub>2</sub>O, BIH (1 mmol, 225 mg). Errors are calculated from three repetitions of the respective catalysis and averaging their values and the errors of catalyst quantity determined by ICP-MS. For the calculation of the TON<sub>CO</sub> the molar amount of Re is used while for TON<sub>HCOO</sub> Zr6-oxo node amounts were applied. The rates are averaged for the first 2 h.

Catalyst	$\lambda$ (nm)	Comment	CO ( $\mu\text{mol}\cdot\text{g}^{-1}\cdot\text{h}^{-1}$ )	TON <sub>CO</sub>	Formate ( $\mu\text{mol}\cdot\text{g}^{-1}\cdot\text{h}^{-1}$ )	TON <sub>HCOO</sub> <sup>-</sup> (80 h) <sup>a</sup>
<b>PCN-222(Zn)</b>	> 430		n.-d.	n.-d.	26.7 ± 0.6	5.4 ± 0.1
	> 430	No BIH		n.-d.	n.-d.	n.-d.
	> 430	No irradi.		n.-d.	n.-d.	n.-d.
<b>Re-PCN-222(Zn)</b>	> 430		4.0 ± 0.7	0.9 ± 0.2	27.0 ± 0.7	5.5 ± 0.1
	> 490		374 ± 26	101 ± 7	0.8 ± 0.4	0.2 ± 0.1
	> 490	No BIH	n.-d.	n.-d.	n.-d.	n.-d.
	> 490	No irradi.	n.-d.	n.-d.	n.-d.	n.-d.
<b>PCN-224(Zn)</b>	> 430		n.-d.	n.-d.	8.3 ± 0.4	1.4 ± 0.1
	> 430	No BIH	n.-d.	n.-d.	n.-d.	n.-d.
	> 430	No irradi.	n.-d.	n.-d.	n.-d.	n.-d.
<b>Re-PCN-224(Zn)</b>	> 430		1.5 ± 0.3	0.5 ± 0.1	8.8 ± 0.5	1.5 ± 0.1
	> 490		24.2 ± 2.1	11.5 ± 1.0	0.8 ± 0.2	0.1 ± 0.1
	> 490	No BIH	n.-d.	n.-d.	n.-d.	n.-d.
	> 490	No irradi.	n.-d.	n.-d.	n.-d.	n.-d.
<b>ReBr(CO)<sub>3</sub> (dcbpy)-PCN-222</b>	> 430			2.0 ± 0.3	27.4 ± 0.5	
	> 490			351 ± 24	0.6 ± 0.2	
<b>ReBr(CO)<sub>3</sub> (dcbpy)-PCN-224</b>	> 430			1.0 ± 0.2	8.7 ± 0.4	
	> 490			15.6 ± 0.8	0.2 ± 0.2	

<sup>a</sup>Note that the TON does not describe the entire lifetime of the catalyst since the catalyst is still active after 80 h.

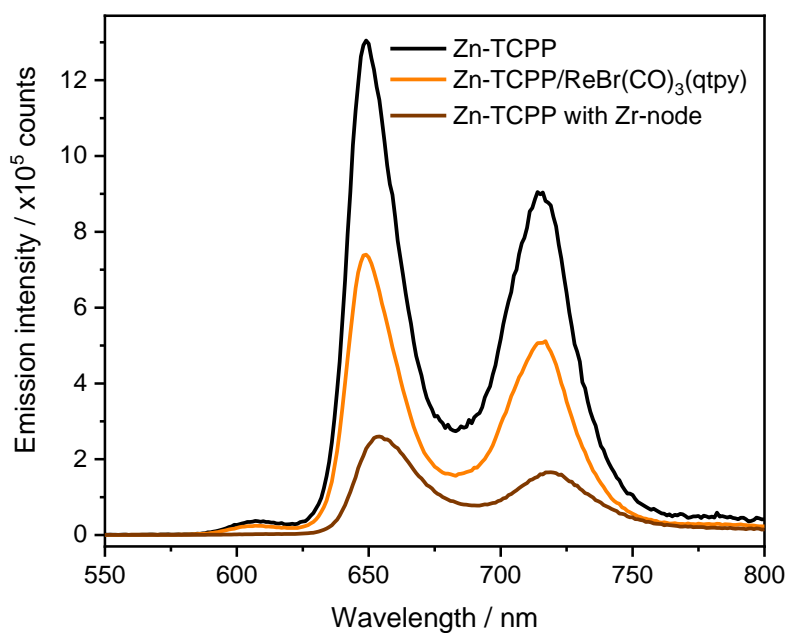


Figure A 186: Fluorescence spectra in liquid phase of solutions of Zn-TCPP (0.05 mM), Zn-TCPP (0.05 mM) and ReBr(CO)<sub>3</sub>(qtpy) (0.05 mM), and Zn-TCPP (0.05 mM) and isolated Zr<sub>6</sub>-oxo node (0.02 mM) in MeCN/DMF (v/v = 40/1). Excitation at 415 nm.

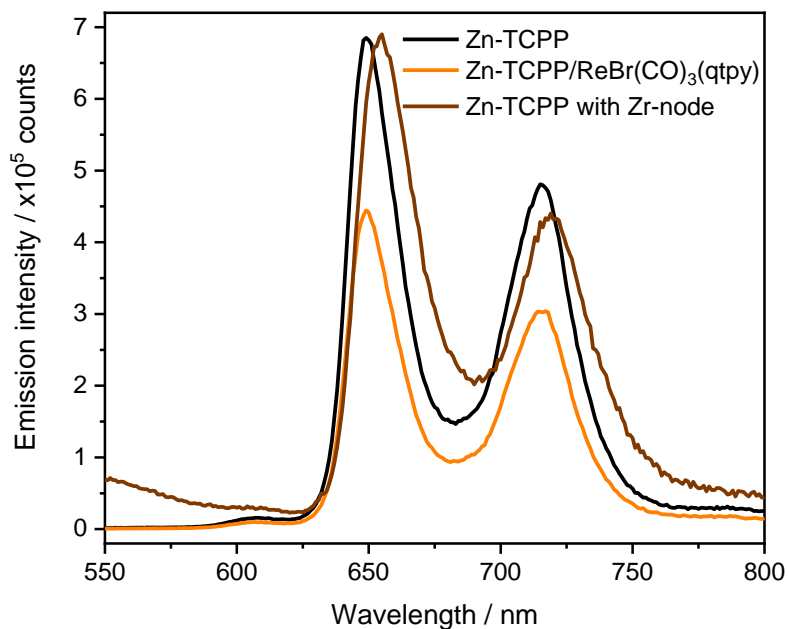


Figure A 187: Fluorescence spectra in liquid phase of solutions of Zn-TCPP (0.05 mM), Zn-TCPP (0.05 mM) and ReBr(CO)<sub>3</sub>(qtpy) (0.05 mM), and Zn-TCPP (0.05 mM) and isolated Zr<sub>6</sub>-oxo node (0.02 mM) in MeCN/DMF (v/v = 40/1). Excitation at 515 nm.

## 7.11. Author Contributions

In general, for all topics academic guidance was provided by Mirza Cokoja and Roland A. Fischer. ICP-MS analysis was performed by the group of Martin Elsner.

For porphyrin MOF metalation (chapter 3.1.2.3), the majority of experiments was conducted by Karina Hemmer including design and optimization, with contributions from Constantin Hagemann, Markus Hegelmann and Anna Tratta.

For chapter 3.2.1.1 (Confinement effects in cyclopropanation catalysis), experiments were conducted by Karina Hemmer including design and optimization. DFT calculations and their discussion were provided by Raphael Bühler.

For chapter 3.2.1.2 (Epoxidation catalysis), the design and optimization of this study was conducted by Karina Hemmer. Experiments were conducted by Karina Hemmer, Markus Hegelmann and Constantin Hagemann.

For chapter 3.2.1.3 and chapter 3.2.1.4 (CO<sub>2</sub> cycloaddition and sequential catalysis), the design and optimization of this study was conducted by Karina Hemmer. Experiments were conducted by Karina Hemmer and Markus Hegelmann.

For the study presented in chapter 3.2.1.5 (non-planar porphyrins in PCN-222 via mixed-linker strategy), Karina Hemmer conducted the experiments including design and optimization. Silva Kronawitter performed variable temperature PXRD measurements, their evaluation and discussion. The non-planar porphyrin was provided by Nitika Grover (group of Mathias Senge, Trinity College Dublin).

For the anchoring of non-planar porphyrins to the node of PCN-222 (chapter 3.2.2.1), experiments were conducted by Karina Hemmer including design and optimization. The non-planar porphyrin was provided by Nitika Grover (group of Mathias Senge, Trinity College Dublin).

For the anchoring of a [Pd<sub>2</sub>S<sub>2</sub>] catalyst to the node of NU-1000 (chapter 3.2.2.2), experiments were conducted by Karina Hemmer including design and optimization. The [Pd<sub>2</sub>S<sub>2</sub>] catalyst was provided by Julien Monot (Université Paul Sabatier Toulouse).

For the incorporation of a photocatalyst in PCN-222 and PCN-224 and its catalytic performance investigation (chapter 3.2.2.3), experiments were conducted by Philip Stanley and Karina Hemmer including design and optimization, with contributions from Markus Hegelmann, Annika Schulz and Mihyun Park. Julian Warnan gave overarching academic guidance.

## 7.12. List of Publications

### First Author Publications

#### Peer Reviewed Journal Publications

- (1) K. Hemmer, M. Cokoja, R. A. Fischer: Exploitation of Intrinsic Confinement Effects of MOFs in Catalysis, *ChemCatChem* **2021**, *13*, 1683-1691.
- (2) P. M. Stanley,<sup>‡</sup> K. Hemmer,<sup>‡</sup> M. Hegelmann, A. Schulz, M. Park, M. Elsner, M. Cokoja, J. Warnan: Topology- and wavelength-governed CO<sub>2</sub> reduction photocatalysis in molecular catalyst-metal-organic framework assemblies, *Chem. Sci.* **2022**, *13*, 12164-12174.
- (3) K. Hemmer, R. Bühler, M. Elsner, M. Cokoja, R. A. Fischer: Stereo-controlled Cyclopropanation Catalysis within the confined Pores of Porphyrin MOFs, *Catal. Sci. Technol.* **2023**, *13*, 3304-3312.
- (4) K. Hemmer, M. Hegelmann, R. A. Fischer, M. Cokoja, working title: The sequential Conversion of Olefins to Cyclic Carbonates in Multifunctional porphyrin MOFs, *manuscript in preparation*.
- (5) K. Hemmer,<sup>‡</sup> S. Kronawitter,<sup>‡</sup> N. Grover, M. Senge, G. Kieslich, M. Cokoja, R. A. Fischer, working title: Understanding and Controlling molecular Compositions and Properties in mixed-linker Porphyrin MOFs, *manuscript in preparation*.

<sup>‡</sup> Equal contribution

#### Conference Contributions

- (1) K. Hemmer, K. Epp, B. Bueken, M. Cokoja, D. de Vos, R. A. Fischer: Confinement Effects of Porphyrin MOFs in Diastereoselective Cyclopropanation Catalysis, *EFCATS Summer School: Engineering Materials for Catalysis*, **16.09.2020**.
- (2) K. Hemmer, M. Cokoja, R. A. Fischer, Confinement Effects of Porphyrin MOFs in Catalysis, *4<sup>th</sup> European Conference on Metal Organic Frameworks and Porous Polymers ("EuroMOF2021")*, **14.09.2021**.
- (3) K. Hemmer, M. Cokoja, R. A. Fischer, Confinement Effects of Porphyrin MOFs in Diastereoselective Catalysis, *ACS Spring 2022*, **23.03.2022**.
- (4) K. Hemmer, M. Cokoja, R. A. Fischer: Confinement Effects of Porphyrin MOFs in Catalysis, *8th International Conference on Metal-Organic Frameworks and Open Framework Compounds ("MOF2022")*, **05.09.2022 – 06.09.2022**

## Contributions to Other Publications

- (1) K. Epp, B. Bueken, B. J. Hofmann, M. Cokoja, K. Hemmer, D. De Vos, R. A. Fischer: Network topology and cavity confinement-controlled diastereoselectivity in cyclopropanation reactions catalyzed by porphyrin-based MOFs, *Catal. Sci. Technol.* **2019**, 9, 6452-6459.
- (2) P. Vervoorts, S. Burger, K. Hemmer, G. Kieslich, Revisiting the High-Pressure Properties of the Metal-Organic Frameworks ZIF-8 and ZIF-67, *ChemRxiv*, **2020**, DOI: 10.26434/chemrxiv.13146278.v1.
- (3) J. Mink, L. Staiger, M. Muhr, C. Gemel, M. Drees, L. Hajba, J. Mihály, C. Németh, B. V. Lokshin, K. Hemmer, M. Schütz, M. Cokoja, R. A. Fischer: Structural studies of ligand stabilized Ni/Ga clusters by means of vibrational spectroscopy and theoretical calculations, *J. Raman Spectrosc.* **2021**, 52, 2317-2337.
- (4) Z. Fan, L. Staiger, K. Hemmer, Z. Wang, W. Wang, Q. Xie, L. Zhang, A. Urstoeger, M. Schuster, J. A. Lercher, M. Cokoja, R. A. Fischer: Enhanced catalytic performance of palladium nanoparticles in MOFs by channel engineering, *Cell Reports Physical Science* **2022**, 3, 100757.
- (4) S. Burger, K. Hemmer, D. C. Mayer, P. Vervoorts, D. Daisenberger, J. K. Zaręba, G. Kieslich\*. Designing Geometric Degrees of Freedom in ReO<sub>3</sub>-Type Coordination Polymers. *Adv. Funct. Mater.* **2022**, 32, 2205343.
- (5) S. Grover, S. Burger, K. T. Butler, K. Hemmer, P. Vervoorts, G. Kieslich\*, R. Grau-Crespo\*. Tuning the Mechanical Properties of Dicyanamide-Based Molecular Perovskites. *CrystEngComm.* **2023**, 25, 3439.